STABILITY ANALYSIS OF P.F.R.P. BOX-SECTIONS

By

MUHAMMAD AFZAL JAVED

BSc., University of Engineering & Technology Lahore, PAKISTAN, 1979

MSc., University of Engineering & Technology Lahore, PAKISTAN, 1990

A thesis submitted to the Department of Civil Engineering of the

University of Newcastle upon Tyne for the Degree of

DOCTOR OF PHILOSOPHY

March 2003

In memory of my parent

CONTENTS

CHAPTER 3

DETERMINATION OF MATERIAL PROPERTIES

CHAPTER 4

BUCKLING OF GRP BOX COLUMNS – EXPERIMENTAL STUDY

LIST OF FIGURES

LIST OF TABLES

LISIT OF PLATES

Notation

a half-wavelength of buckled plate or distance between outer loading points in shear fixture

b width of the plate, or distance between inner loading points in shear fixture

c mode interaction coefficient

d diameter of the hole

e load eccentricity

e_0 initial imperfection (or curvature)

k column effective length factor

k_i normalised failure load interaction factor

p failure load ratio

q failure load ratio

r radius of gyration

t thickness of the box wall

v Poisson's ratio

w outer width of the box-profile

A cross-sectional area

A_s shear area

D bending stiffness

D_{ij} plate bending stiffness

E Young's modulus

E_L longitudinal Young's modulus

$E_{L,c}$ longitudinal young's modulus in compression

$E_{L,t}$ longitudinal Young's modulus in tension

F_u ultimate direct stress

G shear modulus

G_{LT} in-plane shear modulus

I moment of inertia

L column height or coupon length

L_{eff} effective height

P external load

P_{cr} critical buckling load for slender column

P_E Euler buckling load without shear deformation

$P_{E.sh}$ critical Euler buckling load with shear deformation

P_L failure load for short column

R restraint (support)

S_y nodal axial stress

σ normal stress

ε normal strain

ϕ angle between principal and shear strains

γ shear strain

τ shear stress

Δ lateral deflection

Δ_0 initial imperfections introduced to column in the form of lateral curvature

ρ density

ACKNOWLEDGEMENTS

I would like to express my sincere gratitude to my supervisor, *Dr. P. D. Gosling* for his guidance, advice and encouragement throughout the course of this research and production of this thesis. I would also like to thank Dr. J. T. Mottram for providing valuable information regarding material architect of the GRP box-sections and especially conducting compression testing of coupons.

I am extremely grateful to the structures laboratory technician *W. D. Cragie* for his assistance and technical support during the experimental work.

I am also thankful to the Government of Pakistan for providing the financial support.

I would like to express my deepest appreciation of my wife, Tabasum; son, Ahmad; and daughter, Ayesha; for their patience, moral support and encouragement.

Finally I would like to thank my dear friends for their moral support and encouragement.

ABSTRACT

Glass fibre reinforced plastic (GRP) structural profiles, in standard shapes and sizes are now being commercially manufactured by the process of pultrusion. GRP profiles are light weight, posses higher specific strengths and are more durable than the conventional metal or concrete counterparts.

GRP pultruded profiles have open or closed cross-sections comprising thin composite walls of low elastic moduli. Stability failure has been identified as the main cause of failure for these profiles when subjected to compressive stresses, as it may occurs at stresses much lower than the ultimate strengths. Therefore, the load carrying capacities of composite compression members mainly depends upon stability criteria. The conventional stability analyses for the prediction of buckling loads are not considered adequate as the GRP material is orthotropic and its behaviour is different from steel (non-yielding). The existing guidance for the design of composite members under compression ignores the presence of geometrical imperfections inherited in the pultruded profiles, whilst, experimental evidence suggests considerable loss of stiffness due to the imperfections particularly in the intermediate column heights. The design guidance provided by the manufacturers gives empirical equations based on data obtained from experiments on specified profiles. A universal design curve based on the experimental results of concentrically loaded GRP columns has been developed and presented. However, conducting a vast experimental study is not always feasible. The need to develop a procedure, predicting failure load numerically for the development of a design curve for GRP columns has been recognised.

Two GRP box-sections (closed square cross-sections) have been investigated for failure/buckling loads using experimental and numerical methods. In the experimental phase, specimen columns of various heights have been concentrically loaded in compression to measure the failure loads. Experimental results have been compared with the theoretical predictions made using classical methods and the equations given by the design manuals. Based on the experimental and analytical failure loads, an experimental design curve has been derived. In the numerical study, 3-dimensional full scale finite element models representing experimental configuration of the composite columns, have been analysed using both linear and nonlinear solutions. Imperfections of known amplitudes have been included parametrically to establish the

sensitivity of the failure loads towards imperfections. Imperfect model have been calibrated for the estimation of imperfection amplitude present in the profiles using experimental data. Using the numerical and analytical data, a design curve has been derived establishing interaction coefficients for each profile. The numerical design curve is compared with the experimental design curve for the validation of the numerical procedure adopted in this study.

Effects of perforations (circular holes) on the buckling stiffness of GRP box-section columns have also been investigated. Holes are drilled in the walls of profiles and tested experimentally to measure the loss in the buckling loads. Finite element models of columns with holes have been developed and analysed for buckling loads. Comparisons of experimental and numerical results are plotted.

For use in the numerical representation of the composite columns, mechanical properties of the orthotropic GRP material of the both sections have been established analytically and experimentally. In-plane shear properties have been measured by physically testing standard sized coupons, extracted along the length of profiles. However, short coupons were available in the transverse directions due to dimensional constraints. Short coupons, similar in geometry to the standard coupon, but smaller in size, have been validated for performance using finite element analyses and comparing the outcomes with the models of standard coupons. Both standard and short coupons have been used for the experimental measurement of the in-plane shear properties. Compression properties have also been measured experimentally.

Ultimate failure/buckling loads of the composite columns depend upon their heights, material properties, and the cross-sectional dimensions. These factors have been combined into one characteristic parameter 'λ', the slenderness ratio. As the later two factors are constant for a particular box-section profile, the ultimate loads depend upon column heights. Four types of failure modes; global, local, modal interaction and material failure have been observed. The loss in the buckling stiffness is minimal for smaller circular holes, provided the interval between holes is not less than 20 times the diameter of the holes. For bigger holes and an inter hole spacing of 10time the diameter, a loss of 30% have been measured. Finite element representation of pultruded columns adequately predicted the numerical failure loads and failure modes for most of the column heights.

CHAPTER 1

INTRODUCTION

1.1 COMPOSITE STRUCTURAL PROFILES

A composite material is formed when two or more materials are chemically or mechanically combined giving properties that are different from the individual components and exhibiting enhanced characteristics (e.g. strength, ductility, electromagnetic inertia, etc). Historically, composite materials such as timber (a natural composite), straw-reinforced clay, reinforced-cement-concrete and plywood have been used in civil engineering construction. New composite materials have also been conceived for fast and more versatile construction. For example, fibrous composites were proposed some fifty years ago as a lightweight material for use in military and aerospace applications, where weight reduction was the major concern (Ballinger, 1990). As indicated by their name, fibres are the essential part of these composites. Fibrous composites have two distinctive phases: a load-carrying constituent the reinforcement, and a body constituent, the matrix. Typically, the reinforcement comprises fibres of various types e.g. carbon, kevlar or glass. Principally as the reinforcing fibres impart the strength and stiffness to the composite they possess higher strength and elastic modulus than the matrix (Green 1987, Barbero 1991, Godoy and Almanzar, 1996). The matrix acts as a binding material that transfers load between fibres through shear and maintains alignment and orientation of fibres. The matrix also protects the fibres from chemical and environmental damage. Metals ceramics and polymer compounds such as polyester, vinylester, or epoxies define the matrix. Fibrous composites are now called 'advanced composites' as many types of fibres and matrix can be purposely combined to meet the demands for specific applications. Fibrous composites with those formed from polymers (plastics) as the matrices are referred to as polymer matrix composites (PMC) or fibre reinforced plastics (FRP).

Glass-fibre-reinforced plastics (GRP) represent a subset of composite FRP materials developed particularly for structural applications. Generally two types of glass fibres are in use: E -glass (electronic) and S-glass (silica) fibres (Miller 1987, Datoo 1991). S-glass fibres have superior strength and stiffness properties but are expensive, while

E-glass fibres are most commonly used being cheaper and possessing adequate and satisfactory strength and stiffness. Typically, E-glass fibres have a tensile modulus of 70kN/mm^2 and a tensile strength of 3.5kN/mm^2. The matrix component of GRP composites are normally thermoset (hardens irreversibly when cured) plastics, e.g., epoxy, vinylester or polyester resins. Epoxy resin has better adhesive and mechanical properties than polyester, though polyester resins are cheaper and cure more rapidly. The typical values for the elastic moduli and strengths of the epoxy and polyester resins are 5kN/mm^2, 100N/mm^2, 3kN/mm^2 and 60N/mm^2, respectively. Mechanical properties of the GRP composite materials depend on the properties of the constituent materials, fibre forms (filaments, mats, or fabric), fibre-direction and orientation sequence of these fibre-forms, and the volume fractions (percentage) of fibres in the composite. Typically, GRP structural profiles have a specific modulus (modulus/density) of 20mm and specific strength (strength/density) of 300mm in the direction of fibres. These properties are comparable to mild steel (25mm and 77mm) and aluminium (25mm and 160mm). GRP composite profiles offer a good alternative to conventional metallic materials. Besides having adequate strength and stiffness, GRP materials are lightweight (30% lighter than aluminium and 80% than steel), corrosion resistant, chemical resistant, non-magnetic, have good fatigue strength and require little maintenance (Liskey 1991, Zureick and Shih 1998, Turvey 2000).

Initially GRP materials have been produced by hand layup or machine buildup (layer of fibres bounded with a plastic resin) in the form of sheets (Ballinger, 1991). The method is slow and expensive. GRP sheets were cut and joined to form simple shapes to be used in non-bearing infra structural applications. Later, "pultrusion", an automated process of manufacturing FRP structural shapes, was developed. Pultrusion is a continuous process of pulling the required reinforcement (fibres) impregnated with an initially viscous liquid matrix through a heated die. Here the pre-formed composite is consolidated to the desired shape and the matrix is hot cured. The finished composite exits from the die as a solid hollow shape or profile cross-section (Starr 1983, Bonger 1990, Ballinger 1991, Davalos et al 1996, Barbero and Trovillion 1998). The process is very versatile and variations are possible relative to the nature of the operations, the type of reinforcement and matrix, and the type and size of the profile being manufactured (Martin and Sumerak, 1987). Pultrusion is the best-suited manufacturing technique for the commercial production of GRP structural profiles

(Starr 1983, Werner 1984, Strongwell 1989, Davalos et al 1996). It enables a high manufacturing performance with consistency and reproducibility in strength and stiffness, and good surface textures, which require no further treatments.

"Among the many composite manufacturing processes that have evolved during the past four decades, the pultrusion process offers the highest productivity-to-cost ratio."

(Zureick and Scott, 1997)

Today, pultrusion has a commonality in both geometry and dimensions to standard structural elements, (angles, girders, beams, hollow sections and pipes), frequently given the name 'Pultruded fibre reinforced plastic (PFRP) profiles or 'pultrudes', where the term 'structural' has been taken to assume profiles subjected to any form of load condition. These structural profiles are gaining acceptance as substitutes for conventional load bearing elements produced from steel, aluminium and timber (Barbero 1991, Ballinger 1991, Mottram, 1991, Zureick and Scott 1997, Turvey 2000). The main reinforcement in standard GRP structural profiles is glass-fibre strands (roving) placed along the longitudinal axis to produce "unidirectional profiles". Glass fibre mats are introduced to improve the transverse stiffness of the matrix and composite, leading to orthotropic material properties. Mechanical properties of the pultruded structural profiles are generally approximated as orthotropic (Vakiener et al, 1991).

Probably the largest structural application of pultruded GRP structural profiles is pipes for water or oil transportation (Ballinger, 1990), whilst they have been used in infrastructure development for air terminals and railway stations (Liskey, 1991). Purposely fabricated pultruded GRP structural elements have been used in the construction of lightweight pedestrian bridges. For example, a 51.5m span suspension bridge has been erected over A5 at Nescliff, near Shrewsbury (Plate 1.1). The deck of this footbridge has been constructed from pultruded GRP flat panels.

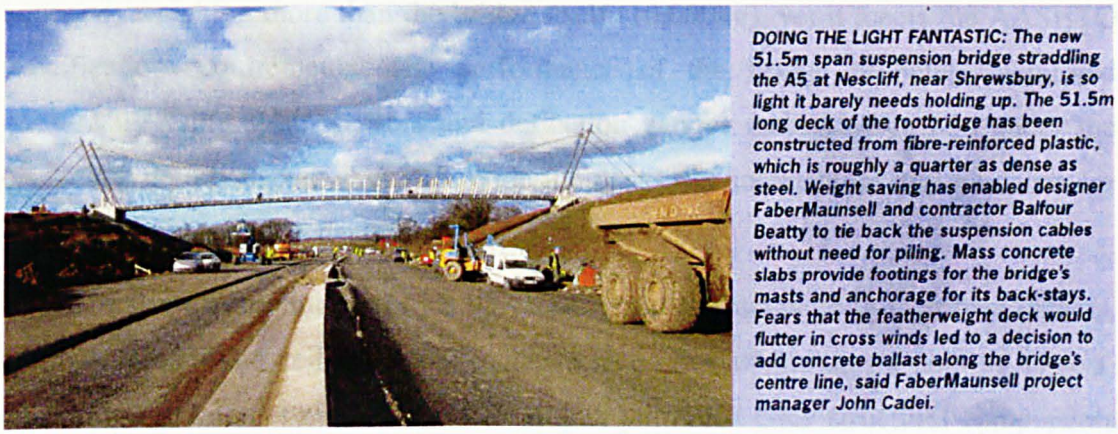

DOING THE LIGHT FANTASTIC: The new 51.5m span suspension bridge straddling the A5 at Nescliff, near Shrewsbury, is so light it barely needs holding up. The 51.5m long deck of the footbridge has been constructed from fibre-reinforced plastic, which is roughly a quarter as dense as steel. Weight saving has enabled designer FaberMaunsell and contractor Balfour Beatty to tie back the suspension cables without need for piling. Mass concrete slabs provide footings for the bridge's masts and anchorage for its back-stays. Fears that the featherweight deck would flutter in cross winds led to a decision to add concrete ballast along the bridge's centre line, said FaberMaunsell project manager John Cadei.

Plate 1.1 Pultruded GRP suspension foot-bridge, Shrewsbury, UK.

(New Civil Engineer, 6 February 2003)

A lightweight pedestrian bridge (Plate 1.2) has been built over the Tay river at the Aberfeldy golf club in Scotland (Robbins 1992, Bodamer 1998). All the components of this cable-stayed bridge are made from composite materials. The ratio of designed superimposed load to the self- weight is 10:1. This bridge has a 63m central span with back spans stayed from "A" pylons. The deck, pylons and handrails have been fabricated from pultruded cellular glass fibre reinforced plastic. The frames "A" were assembled in the factory by joining two heavy box-section legs, with pre-drilled holes to accommodate the cable stays. The deck (120m long containing 360m of GRP planks and weighing 75kg/m) was also factory prepared and assembled on site in a staggered lap arrangement with adhesive bonding. Though a considerable amount of time was expended on designing the bridge components, it took only four days to convert raw material into finished products (with no secondary finishing operations necessary), and the bridge was completed in just six weeks.

A composite road bridge (Tech 21) has been constructed in Butler County, Ohio USA (Foster et al, 2000). The bridge meets the AASHTO[†] HS-20 load requirements, equivalent of two fully loaded 18-wheel tractor/trailers, one in each lane. The bridge, 10m (33ft) long and 7.3m (24ft) wide comprising all GRP components, weighs about one-fifth the weight of a conventional concrete structure, and was installed in six weeks. The deck is covered with asphalt wearing surface (instead of polymer

[†] American Association of State Highway and Transportation Officials.

concrete) weighing more than the bridge itself (10,000kg), yet it meets the AASHTO specification requirements. The performance of the bridge is being monitored continually using strain sensors and deflection gauges embedded in and under the deck. The data collected should provide the necessary information and guidance for future composite bridge designs.

Standard shaped structural profiles have also acted as load-bearing members (beams, columns, floors and ceiling decks) in the construction of buildings, cooling towers, and bridges (Green et al, 1994). For example, pultruded GRP structural components manufactured by COMPOSITE Technology, Inc (CTI), with a brand name of Unilite® units have been used in the construction of cooling towers (Ballinger 1990 1991, Yuan et al 1991, Green et al 1994). The cooling tower components include Unicolumns, Unibeams, lintels and gusset plates with bolts and pins for connections, all made from GRP (plate 1.3). The shape of the Unicolumns was designed to support the Unibeams from all the four sides. Standard pultruded profiles have also been used in building a stair-tower (Plate 1.4) for the US Navy at Fort Story, VA, USA. The tower is designed to sustain hurricane loads (Turvey, 2000).

1.2 STABILITY AND BUCKLING ANALYSIS

Any structural system when subjected to applied loads can have two kinds of failure, namely, (i) material failure and (ii) form failure. In material failure, the stresses in the structure exceed the capacity of the material, resulting in the formation of cracks and/or rupture. In form failure, though the stresses may not exceed the yield or rupture values, the structure may not be able to maintain its original form. Here the structure does not break physically but is deformed to some other shape (or form) due to a significant external disturbance. This deformed configuration of the structure is regarded as failure because its equilibrium configuration becomes unstable and it is unable to sustain the external load. The load, at which the equilibrium of a structure (or of its component) changes from stable to neutral, is referred to as the critical load (Chen and Lui, 1987). This is the limiting load at which the original configuration of the structure ceases to be stable. This phenomenon of change of equilibrium is known as buckling and the corresponding load as the buckling load. Buckling failure is often sudden and catastrophic and is normally accompanied by large deflections and nonlinear behaviour (Chen and Lui 1987, Farshad 1994; Palmer et al 1998). The

buckling failure commences at stresses much lower than the crushing (or yield) strength of the material. Therefore, the structural components having hollow cross-sections with thin walls are more susceptible to buckling than material failure, when subjected to compressive loads in cases where the components have a large slenderness ratio.

The instability or the buckling failure of structures (or their components) is of many types; for example, overall (or global) buckling, local buckling or lateral torsional buckling. Correspondingly, their failure modes are denoted as global, local, lateral or torsional modes. In overall or global buckling the member fails with excessive deflections in a direction normal to its length and it is unable to sustain the applied load. This type of buckling develops in slender columns (in frames) or in truss members. The cross-section of the member remains un-deformed but its longitudinal axis is no longer straight (but deflected). In local buckling, on the other hand, parts of a member (under compression) fail locally with large lateral deflections. The cross-section of the member deforms (de-shapes) but the longitudinal axis remains straight. Local buckling, for example, occurs in short columns and beams (e.g. compression flange of a beam buckles locally or walls of a compressively loaded intermediate length column). In lateral torsional buckling an open-section profile buckles by a combination of twist and lateral bending of the cross-section (Timoshenko and Gere 1961, Mottram 1992, Brooks and Turvey 1995). This type of buckling usually develops in cantilever beams or in beams with unsymmetric cross-section. It is not necessary for a structure to undergo overall (global) buckling for it to be classified as having failed both under serviceability and ultimate limit states (Farshad, 1994). Local or torsional buckling in a part of the structure may lead to rapid onset of complete failure either by global buckling due to large deformations or by material degradation (crushing). Therefore the minimum buckling load (regardless of the buckling mode) may define the critical load i.e. the ultimate load carrying capacity of the structural member.

Pultruded GRP structural profiles have open or closed thin-walled cross-sections similar to their steel counterpart e.g. wide flange, I-sections, angle, channels, rectangular-hollow-box sections and square box-sections. The composite material is orthotropic in nature and remains elastic up to failure load without yielding in the direction of the primary reinforcement (Barbero, 1991). Further, GRP material has a

lower modulus of elasticity (30kN/mm^2) and shear modulus (3.5kN/mm^2) than steel (E=205kN/mm^2 and G=80kN/mm^2). For these reasons, the ultimate strength (load carrying capacity) of pultruded profiles is often governed by stiffness (buckling) and not by the actual strength of the material. It means buckling failure in pultruded sections often precedes material failure (Barbero 1991, Vakiener et al 1991). Consequently the design of structures comprising thin-walled composite members may be governed by buckling (compressive or torsional) of the flange or web segments or the overall buckling (Brown et al, 1998) in addition to deflection (or serviceability) constraints that may also prove critical.

Classical theories of elastic stability (Timoshenko and Gere, 1961) consider the analytical solutions to buckling problems of a structure or its components such as plates, beams and columns, characterised by conventional isotropic materials (metals). The formulas and design equations for the buckling analysis of these components subjected to various types of loading and boundary conditions have been developed and are well documented in the texts (Timoshenko and Gere 1961, Chen and Lui 1987, Farshad 1994, Galambos 1998). For example, the critical buckling load for a simply-supported, straight, prismatic and axially loaded column that is slender enough to buckle laterally (global buckling) at its mid-height, has been predicted by Euler (1759) as $P_E = \frac{\pi^2 EI}{L^2}$. Here E is the elastic modulus of the material, I the moment of inertia, and L, the effective length (depending on the column boundary conditions) of the column. It is quite notable that the buckling load P_E is independent of the strength or yield limit of the material but depends primarily on the elastic modulus and cross-sectional stiffness of the column. The slenderness of a column is defined by the ratio of its length to radius of gyration of its cross-section (slenderness ratio). Theoretically, above a certain slenderness ratio a column buckles in a global mode. Below this critical value the column may fail in a local buckling mode. Design curves for metallic columns along with the corresponding equations have been developed to predict the critical loads for columns of various heights and boundary conditions. Research focused on conventional material and section types (e.g. steel "I" sections), has demonstrated that critical buckling load is sensitive (decreases) to eccentric loading and initial imperfections (e.g. out of straightness and variations in the wall thickness) (Galambos 1998).

The Euler formula has initially been applied to the prediction of the critical global buckling loads for the slender GRP pultruded columns (Barbero and Raftoyiannis, 1990). The material stiffness *E,* for the orthotropic GRP, has been taken along the direction of applied load (which is same as the direction of primary fibres). Elastic modulus *E* for GRP wide-flange sections was calculated using the principles of micromechanics and lamination theory (Davalos et al, 1996) (see § 3.2). In the micromechanical approach, each thin composite wall (lamina) in the cross-section is taken as a combination of layers of different fibre forms (roving and mats). The stiffness of composite wall is calculated from the stiffness of constituent materials (fibres and matrix), percentage of their volumes in each layer (volume fraction) and configuration of layers in the wall (provided by the manufacturer). Classical lamination theory (Jones, 1975) is applied with these values to calculate the cross-sectional stiffness by algebraically adding the stiffness contributed by each layer toward the whole section, considering its orientation and position with respect to the section's neutral axis. This approach has been shown to provide estimates of cross-sectional stiffness (Salim et al 1995, Davalos et al 1996). The theoretical buckling loads predicted in the study of Barbero and Raftoyiannis (1990) have been validated by experimental results reported by Barbero and Tomblin (1992). The experimental results were evaluated from the linear regression (Southwell, 1932) of the load-deflection plot of experimental data. The close correlation of analytical and experimental results (within 6%) demonstrated that the theoretical prediction using the Euler equation could be applied to a specific GRP structural component. It was further demonstrated that the Euler formula gave an upper bound to the buckling load, as the experimental values were lower than the analytical predictions. The use of the Euler formula to predict the critical buckling loads, has also been validated by Zureick et al (1992), Scott et al (1992) and Yoon et al (1992) for GRP pultruded Wide-flange columns. These experimental studies also demonstrated the application of Southwell's method to the non-destructive testing of pultruded columns. Zureick and Scott (1997) suggested that a shear coefficient term should be added to the Euler equation, identifying the contribution of the high E_L / G_{LT} ratio that GRP composites generally display. Therefore the critical load of a slender column be estimated by the following equation, where P_E is the Euler load, A_g =gross area and n_s =form factor for shear depending on the shape of the cross-section.

$$P_{E.sh} = \frac{P_E}{1+\left(n_s P_E / A_g G_{LT}\right)}$$

Critical buckling loads for local buckling of short columns and beams have been theoretically predicted using the classical equations of elastic buckling for thin plates (Timoshenko and Gere, 1961). The thin walls of the cross-section (flanges or webs) are modelled as rectangular thin plates with appropriate boundary conditions depending upon their location and connections in the cross-section. Design curves are also available to predict the critical buckling loads for isotropic plates for different types of loadings and boundary conditions. Similar classical equations are also available for orthotropic plates (Timoshenko and Gere 1961, Galambos 1998).

Local buckling in GRP composite profiles have been studied extensively (Barbero 1991, Barbero and Sonti 1991, Mottram 1991, Vakiener et al 1991, Barbero and Raftoyiannis 1990 & 1993, Bank et al 1996, Qiao et al 2001). In these studies, thin walls of composite sections have been modelled as orthotropic rectangular plates subjected to in-plane compression. To simulate an axially loaded column, the shorter sides (loaded) of the plate are simply supported while the long sides have different boundary conditions depending upon their position in the section. For example the flange of a wide section is considered as a long plate with short edges simply supported, one long edge free and other long edge elastically connected to the web. Similarly the flange of a box-section is considered as a long plate with shorter ends simply supported and longer edges elastically connected to the web. Three types of web-flange connections have been considered in the above studies: simply supported or zero rotational stiffness, elastic connection with rotational stiffness equal to the stiffness of web or the fixed connection with restrained rotation. The plate buckles in a sine wave shape with a number of half-sign-wave lengths depending on the length of the plate. Theoretical loads have been predicted and plotted for column lengths equivalent to 2, 3, and 4 numbers of half sine waves (called as mode 2, 3 and 4 respectively). Experimentally measured local buckling loads of the short GRP wide-flange and box-section profiles are close to the results obtained from mathematical models including elastic web-flange connection. Simply supported and the fixed assumptions of the connection behaviour give the lower and upper bounds of the buckling loads. These studies further demonstrate that local buckling failure initiates a

process (tearing apart or separation of flange-web connection or material) that leads to the overall collapse and failure of the member (Bank and Yin, 1999).

A transition zone may exist between global and local buckling referred to as the 'interactive mode'. This mode has been identified in buckling tests on columns with intermediate heights. For isotropic columns the interaction between local buckling and yielding of material occurs which practically reduces the critical buckling load (Galambos, 1998). There exist column heights for an intermediate region in which the buckling load is lower than the predictions for both local and global buckling modes (Toneff et al, 1987). Column design curves (Galambos, 1998) show a maximum loss in buckling load at this height. For orthotropic columns, on the other hand, the interactive buckling is attributed to the interaction of local and global modes. Experimental studies of GRP pultruded columns (Yuan et al 1991, Tomblin 1991, Barbero and Tomblin 1992, Raftoyiannis 1994, and Tomblin and Barbero 1994) have identified an intermediate-column height range for which the measured buckling load is lower than the predictions of both local and global buckling theories. This reduction in the critical load is due to the interaction between local and global modes whilst the GRP material remains linear elastic for large values of strain without yielding (Barbero and Tomblin, 1994). An interaction constant has been defined to estimate the amount of interaction. Theoretically there exists a column height called the transition height at which both local and global modes have the same critical load. The interaction of the two isolated modes is highly sensitive to imperfections (Godoy et al 1995). In fact the interaction between local and global modes developed an unstable tertiary mode leading to imperfection sensitivity and a lower buckling load Experimental data has indicated that while the isolated local and Euler modes have stable post buckling path, the interacting path is unstable (Barbero et al, 2000).

Design curves accompanied by the corresponding equations for wide-flange pultruded sections have been proposed (Barbero and Tomblin 1994, Barbero and Evans 1997 and Barbero and DeVivo 1999). Critical buckling loads for the isolated global mode of pultruded GRP columns are plotted against a selected slenderness ratio $\lambda = \frac{L}{\pi^2}\sqrt{\frac{P_L}{EI}}$, which is function of material properties and P_L, the short column load. P_L is the load that is converged towards as the length of the column is reduced. Theoretically the short column load is equal to Euler load at λ=1. Both isolated global

and local curves converge at the transition height where the buckling load is same for global and local modes. Theoretically interaction between global and local modes occurs in the vicinity of this height, and is characterised by a reduction in the buckling load up to 25 to 35% (Barbero and DeVivo 1999). An interaction constant, 'c', indicates the level of interaction.

The finite element method has been used to predict the critical buckling loads of pultruded profiles acting as beams and columns (Vakiener et al 1991, Barbero et al 1995, Barbero et al 1996, Davalos et al 1996, Bank and Yin 1996, Palmer et al 1998 and Barbero and Trovillin 1998). The method has the ability to model the orthotropic composite material properties and to simulate the actual (physical) test conditions i.e. boundary (support) and loading states with both material and geometric nonlinearities represented.

Research into the stability of GRP pultruded sections used as columns, has been less widely reported compared with equivalent work concentrating on the behaviour of beams, where wide-flange sections have been investigated rather than box-section profiles. Furthermore, using the same sub-division of section type, wide flange and 'I' section pultruded columns with concentric axial loads have been investigated both theoretically and experimentally for local and overall (global) buckling, (Vakiener et al 1991, Barbero and Tomblin 1992, Barbero and Raftoyiannis 1993, Zureick and Scott 1997, Barbero and DeVivo 1999). Very few studies have considered the buckling behaviour of thin walled composite box-sections as columns (Barbero and Raftoyiannis 1993, Zureick and Scott 1997).

Design codes for the reliable design of structures made from conventional materials are available and approved by a number of independent international and national organisations (ASTM, ASCE, BS, Eurocode etc). For design with the pultruded profiles (composite sections), no unified design code has been available. Both the Structural Plastic Design Manual (ASCE 1984) and the Eurocomp Design Code (Clarke, 1996) summarises equations based on classical Euler buckling theory (developed for isotropic materials) for complete sections and orthotropic plates buckling formulae (Timoshenko and Gere, 1961) for limited cases of boundary conditions to predict local buckling phenomena. The use of these equations provides a reasonable estimate of the global and local buckling loads when true material properties are known (Barbero and Raftoyiannis, 1993). The theoretical equations do

not simulate the actual physical conditions of the columns, especially when section walls are thick, predicting very high buckling loads. Design manuals supplied by the manufacturers (Strongwell, 1989) provide some empirical expressions. The majority of available expressions are theoretical and have not been validated by experimental evidence (Mottram, 1992). Many authors have stressed the need for a unified and reliable design guide based on theoretical and experimental evidence (Ballinger 1990, Vakiener 1991, Green et al 1994, Brook and Turvey 1995, and Mottram 2000). It is recommended that design curves for the pultruded shapes should be developed in the same way as historical design curves for isotropic material sections. The design curve for wide-flange sections developed for the whole range of manufactured lengths (Barbero and Tomblin 1994 and Barbero and DeVivo 1999) is taken as an example.

1.3 AIMS AND OBJECTIVES OF THE RESEARCH.

The aim of the present research is to predict the stability (critical buckling loads) of pultruded GRP box-sections (homogeneous and macro-perforated) from numerical methods both quantitatively and qualitatively for dissemination to practitioners.

"It is clear to this author that the research community has not given adequate attention to creating a database with reliable geometric and mechanical properties for standard pultruded profiles."

(Mottram, 2000)

The following objectives are identified for the fulfilment of this aim:

1 To determine the current state-of-the-art in the prediction, determination, classification and dissemination of buckling phenomena in GRP composite sections with particular reference to box-section profiles.

2 To determine the experimental response (failure loads and the failure modes) of pultruded box-sections subjected to concentric compressive loads (with and without macro-perforations), contributing to the database describing the behaviour of pultruded GRP profiles.

3 To establish a numerical representation of the buckling phenomena (without mode presumptions) including the effective determination of elastic linear and non-linear material responses.

4 To verify the numerical representation against experimental evidence.

5 To develop design data and analysis procedures within the context of the experimental and numerical outcomes.

1.4 SCOPE OF THE RESEARCH

To achieve the objectives of the research, aspects of the procedures proposed by Barbero and Tomblin (1994), and Barbero and DeVivo (1999) have been followed. Two box-sections manufactured by FIBREFORCE Composites UK with nominal size of cross-section 51×51×3.2mm and 44×44×6.0mm have been selected to be studied as simply supported columns (Plate 1.5). The box-sections are made of E-glass fibres and polyester resin (Fibreforce, 2000). The box-section composition includes the following four types of layers (Figure 1.1):

1. Veil, a resin-rich layer containing polyester fibres, primarily used as a protective cover against erosion and surface damage to the reinforcing fibres. The layer provides a smooth surface for handling.
2. Continuous Filament Mat (CFM) consisting of continuous fibres randomly oriented. The layer improves the transverse mechanical properties of the section.
3. Plain Roving (PR) containing continuous unidirectional fibre bundles contributing to the stiffness and strength in the longitudinal direction.
4. Mock Spun Roving (MSR) inner protective layer covering the inner CFM layer.

Mechanical properties are measured using analytical and physical test methods. Tensile properties of the material both in longitudinal and transverse directions have been provided experimentally (Saribiyik, 2000). In-plane shear properties have been measured in longitudinal and transverse directions, by testing double V-notched specimens according to the Iosipecu test method (ASTM D5379M-93). Compressive stiffness and strengths of the material have been provided from the test procedure adopted by Mottram (1994).

Both numerical and experimental methodologies have been used to determine the critical buckling loads and failure modes of the selected pultruded box-sections columns. Numerical technologies, based on existing advanced finite element methods, have been applied to solve non-conventional structural models of pultruded columns. The experimental data has been quantified applying existing analytical and statistical approaches. Recommendations have been developed regarding the numerical

modelling of pultruded GRP box-sections. Numerical and experimental outcomes have been used to develop design curves and procedures.

1.5 THESIS OVERVIEW

The scope of the research outlined above is presented in 6 chapters.

Chapter-2 reviews the stability research carried out on the buckling of pultruded beams and columns with particular emphasis on the techniques used for the prediction of buckling loads using approaches developed for isotropic materials. Some of these techniques are used in the present research. Test methods to measure the mechanical properties of the composite material are also reviewed and suitable methods for the determination of compressive and in-plane shear are selected.

Chapter 3 presents the determination of mechanical properties of the GRP pultruded composite material. Compressive strength and in-plane shear properties are estimated analytically. Small test coupons are proposed using the finite element method for the measurement of transverse shear properties from which experimental material properties are established.

Chapter 4 details the column testing. Experimental procedure and data reduction techniques described. The outcomes of the experiments are presented and discussed.

Chapter 5 presents the numerical studies for predicting critical buckling loads using finite element models of GRP columns having different lengths. Linear elastic models with and without geometric non-linearity are analysed. Models with non-linear material properties are included. Effects of initial imperfections in the form of varying wall thickness, load eccentricities and initial curvatures are investigated. Circular holes introduced in the column walls are analysed for possible loss of buckling strength.

Chapter 6 draws together the main conclusions of the research. Recommendations for future research are also made.

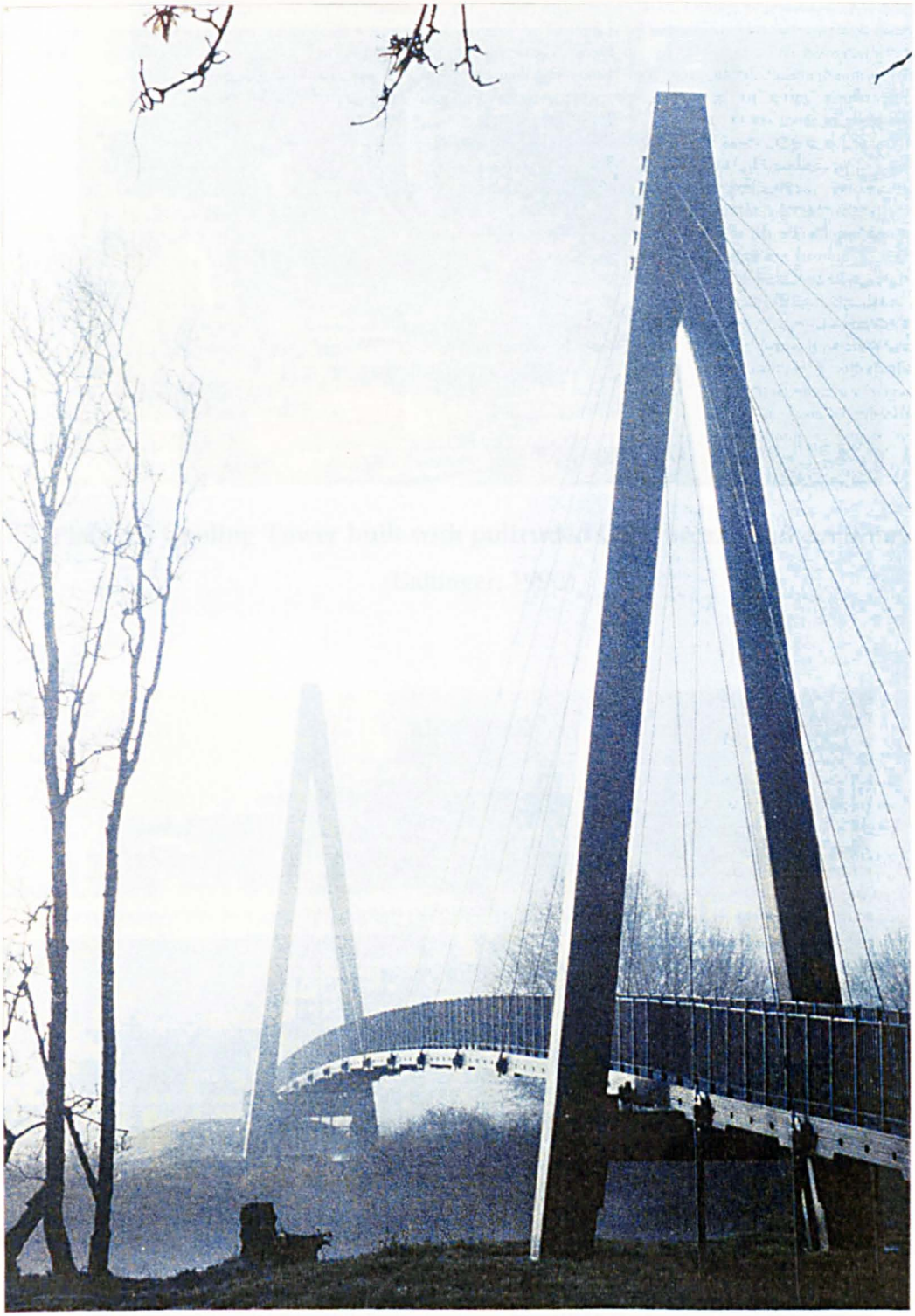

Plate 1.2. The GRP composite bridge in Aberfeldy golf-club, Scotland.

(Civil Engineering, January 1998)

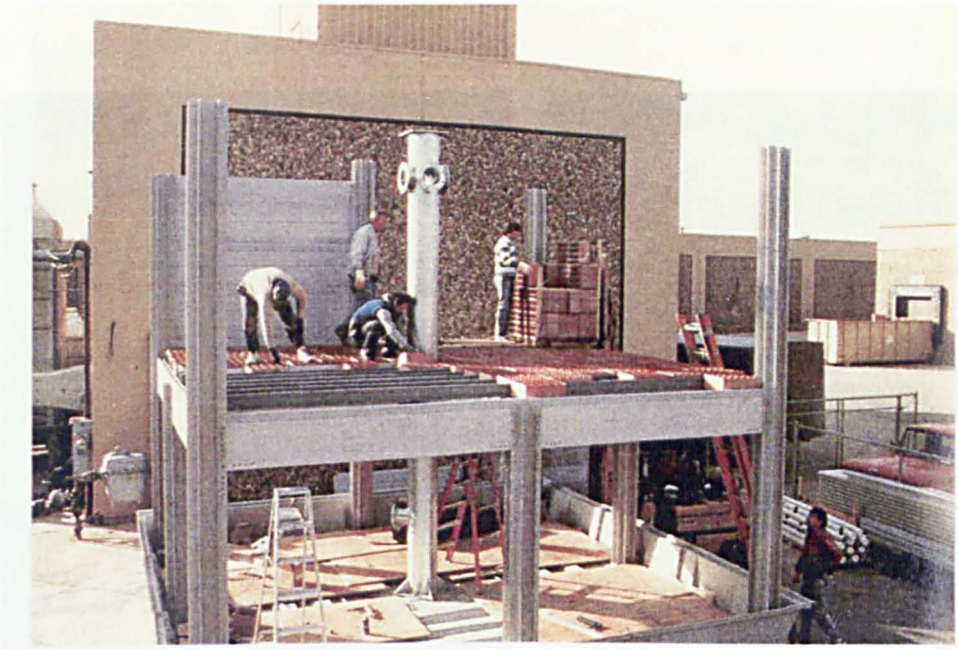

Plate 1.3 Cooling Tower built with pultruded GRP beams and columns.

(Ballinger, 1990)

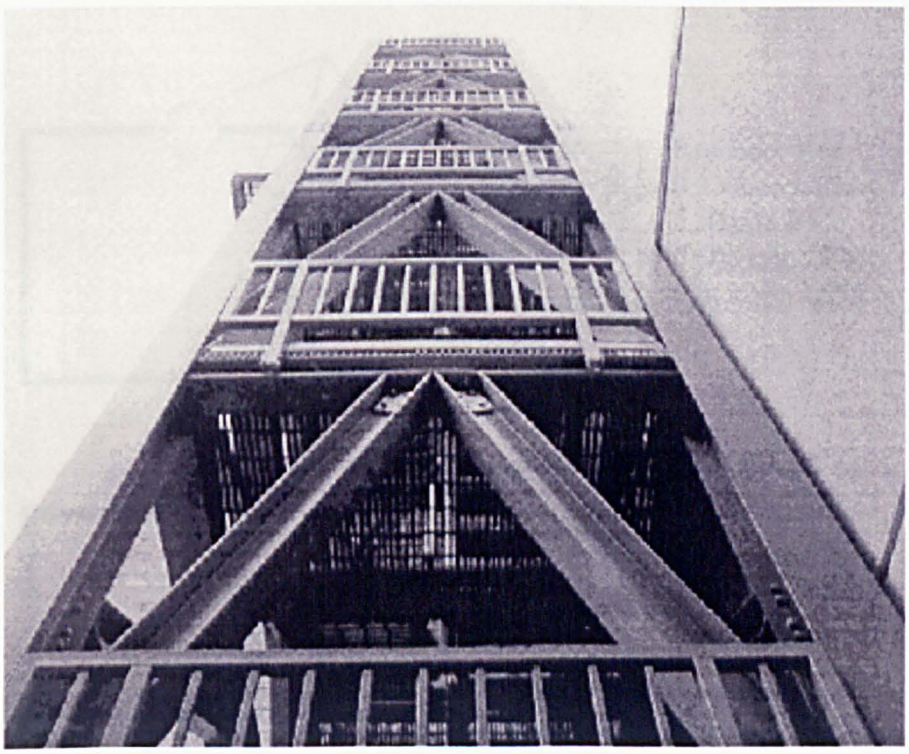

Plate 1.4 Fort Story composite stairtower built with pultruded GRP profiles.

(Turvey, 2000)

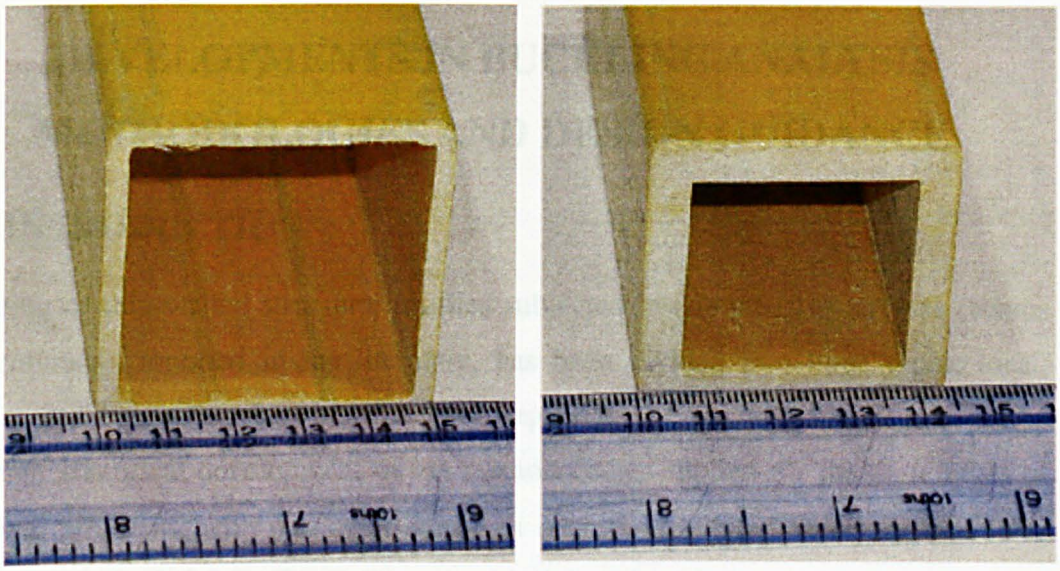

(a) (b)

Plate 1.5 Pultruded GRP box-sections (a) 51×51×3.2 mm (b) 44×44×6.0 mm.

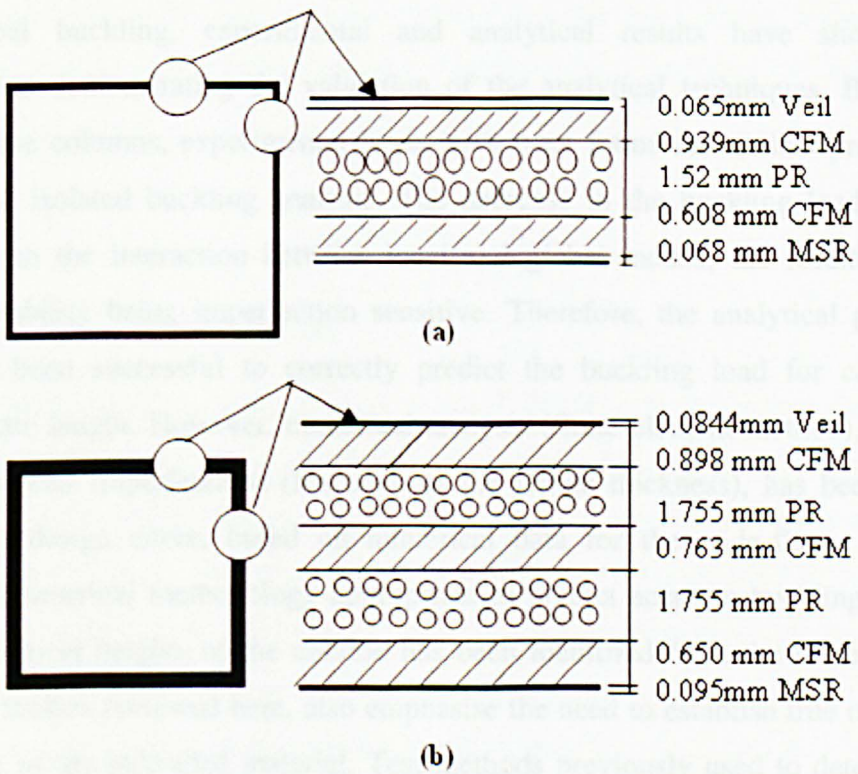

Figure 1.1 Typical Construction of pultruded box-sections.
(a) 51×51×3.2 mm (b) 44×44×6.0 mm.

CHAPTER 2

DEVELOPMENTS IN BUCKLING ANALYSIS METHODOLOGIES AND DESIGN GUIDANCE

2. I INTRODUCTION

Buckling of thin-walled structural profiles subjected to compressive stresses (beams and columns), reported in the literature, has been divided into three types; local; global; and interaction between the two, depending on the effective length of the member. Historical development of the methodologies applied for the three types of buckling problems, with particular emphasis on orthotropic pultruded sections have been reviewed (§ 2.2.2). Prediction of critical buckling loads for different column lengths has been a pre-requisite for the construction of column design curves. Universal design curves for pultruded GRP wide-flange columns has been developed by many authors, using experimental results of buckling tests performed on different lengths of various wide-flange sections (§ 2.3). For the two isolated modes i.e. local and global buckling, experimental and analytical results have shown good compromise demonstrating the validation of the analytical techniques. But for the intermediate columns, experimental loads have been found lower than predicted by any of the isolated buckling analysis. The decrease in the buckling load has been attributed to the interaction between local and global modes; the resulting mixed mode instability being imperfection sensitive. Therefore, the analytical procedures have not been successful to correctly predict the buckling load for columns of intermediate length. However, numerical analysis (finite element method), assuming different initial imperfections (fractions of the flange thickness), has been used to develop a design curve, based on numerical data for the wide-flange pultruded sections. Numerical methodology appropriate to predict accurate buckling loads for all the practical heights of the column has been identified from the review (§ 2.4). Buckling studies reviewed here, also emphasise the need to establish true mechanical properties of the pultruded material. Test methods previously used to determine the mechanical properties of the pultruded materials have been reviewed to identify their potential application in the context of dimensional limitations of the GRP box-section profiles being investigated in the present study (§2.5 onwards).

2.2 RESEARCH ON BUCKLING

2.2.1 ISOTROPIC SECTIONS

Buckling of thin-walled metal structural profiles, when subjected to compression loading, has been extensively studied and reported in the literature (e.g. Usami et al 1982, Toneff et al 1987, Key et al 1988, and Galambos 1998). The studies have covered many modes of buckling failure including overall (or global), local, lateral torsional, and interaction buckling.

Euler (1759) solved the buckling problem of a slender, isotropic, axially loaded column and presented the classic formula bearing his name (Timoshenko and Gere 1961, Galambos 1998). It was concluded mathematically that the buckling failure occurred at an axial stresses much lower than yield stress of the material, with instability due to geometry effects (length and moment of inertia) and boundary conditions of the column. For a long simply supported column under axial loading, there exists an infinite number of buckling loads, each one associated with a specific deformed shape called the buckling mode. The minimum of these loads is the critical buckling load. Once reached, the column fails with excessive lateral deflection (half sine wave) at mid height of the column. The Euler buckling load 'P_E'for a simply supported and axially loaded isotropic column is

$$P_E = \frac{\pi^2 EI}{L^2} \tag{2.1}$$

(E, I and L already defined on page 7)

Later research has solved more specific cases of slender columns where the effects of boundary conditions and load eccentricities have been investigated (Timoshenko and Gere 1961, Jones 1975). The boundary conditions (supports at the ends) determine the effective length of the column. A coefficient 'k', has been defined to calculate its effect on the critical buckling load. For example, k is 1 for a simply supported and 4 for fixed ended column. The slenderness (denoted by 'λ') of columns has been characterised by the ratio of the column effective lengths (kL) to the radius of gyration ($r = \sqrt{\frac{I}{A}}$ where A is the area of the cross-section). For a particular cross-section

(shape) of the isotropic profile, global buckling occurs above a particular slenderness ratio ($\lambda = \frac{kL}{r}$) of the column.

If the column length is short, failure occurs due to local buckling of thin walls (flanges and webs) such as in the case of I-beams and hollow box-sections. The Euler formula cannot be applied in this case. Instead, the buckling load is predicted by discrete plate theory, assuming the walls of the section as thin rectangular plates subjected to in-plane compression (Timoshenko and Gere 1961, Jones 1975, Toneff et al 1987). Equations and graphs have been developed to solve the local buckling of the thin plates with different boundary conditions depending on the position of the flange in the cross-section (Rasmussen and Rondal 1997, Faella et al 2000). The flange buckles in a number of half sine waves (mode number) depending on the length of the plate. The critical buckling load remains constant (minimum) for any number of half waves as long as they are fully developed (all half waves accommodated in the length). Extensive experimental studies have been reported to demonstrate the validity of this procedure (Usami and Fukumoto 1982, Key et al 1988, Faella et all 2000).

In the intermediate column range (short to long) a loss of buckling stiffness has been identified in experimental data on steel columns. Theoretical investigations attributed this loss to the yielding of material (Toneff et al 1987, Chin et al 1993).

2.2.2 ORTHOTROPIC SECTIONS

Like thin-walled isotropic (steel) structural profiles, the governing mode of failure for fibre-reinforced profiles, is also buckling. This instability phenomenon is well documented in the literature.

"As it is demonstrated by the experiments, local buckling of the compression flanges initiates a process that leads to the collapse of the member."

(Barbero and Fu 1990, Barbero and Raftoyiannis 1990)

"Buckling is the governing failure for this type of cross-sections (pultruded GRP) and the critical buckling load is directly related to the load carrying capacity of the member."

(Barbero and Raftoyiannis, 1993)

"In thin-walled columns made of FRP composite materials, instability is a mechanical behaviour of major interest."

(Godoy and Almanzar, 1996)

Due to low modulus of elasticity of glass fibres and the common thin-walled section geometry, pultruded FRP beams are susceptible to large deflection and buckling under service loads."

(Davalos et al, 1996)

"Since composite columns are thin-walled, buckling is a major consideration in design."

(Barbero, 2000)

"Because of the relatively low modulus of elasticity of commonly used glass fibres and the common thin-walled sectional geometry, FRP beams may be susceptible to buckling even under service loads. Due to the high strength-to-stiffness ratio of pultruded FRP composites, buckling is likely to occur before the ultimate material strength is reached."

(Qiao et al, 2001)

However, the procedures developed for the theoretical prediction of critical buckling loads of isotropic columns have not been considered appropriate for anisotropic profiles. Although the shapes of the pultruded structural profiles are similar to their steel counterparts, their material properties (and hence the behaviour under the applied loading) are different, resulting in significant variations in behaviour compared with isotropic equivalents.

GRP structural profiles have been considered as unidirectional members (§ 1.1) i.e., the main reinforcing fibres are in the longitudinal direction, with nominal reinforcement provided in directions aligned to the longitudinal axis. In general, GRP structural profiles exhibit anisotropic or orthotropic behaviour. For instance they have different elastic moduli in longitudinal and transverse directions. Also the elastic moduli in extension and bending are different (unlike steel)

"Pultruded structural elements are assumed as especially orthotropic homogeneous materials that could be characterised through four independent elastic constants: the longitudinal elastic modulus E_L; the transverse elastic modulus E_T; the in-plane shear modulus G_{LT}; and the major Poisson's ratio ν_{LT}."*

(Barbero and Raftoyiannis 1990, Zureick and Scott, 1997)

For pultruded profiles, bending moment of inertia '*I*' is a function of cross-sectional geometry and the stiffness of the material which, in turn depends upon configuration of the composite material in the cross-section. It means two sections of similar shape and size (produced by different manufacturers) may have different moments of inertia about the same axis, depending upon the type, amount, location and the percentage volume of the fibres. Therefore the bending stiffness '*EI*', used to predict the critical buckling load (Euler formula) has to be redefined for pultruded profiles to account for their orthotropic nature. Further, the pultruded material has a high ratio of extensional stiffness to shear stiffness ($E_l/G_{LT} \geq 6$ typically) compared with steel ($E/G = 2.7$ typically). Also pultruded materials do not have distinct yield points and are relatively non-ductile.

"The buckling equation has to account for the anisotropic nature of the material."

(Barbero and Tomblin, 1994)

"GRP typically features a higher ratio of elongation to shear moduli (than metals) and exhibits a non-ductile behaviour (unlike steel) without having a distinct yield point that may cause local buckling in highly stressed areas of the cross-section. There is a need to develop new design practices specifically for GRP type materials"

(Barbero and Evans, 1997)

The existence of inherited weak axes (e.g., lower bending stiffness in transverse directions), lack of yielding, high shear modulus ratio and brittle failure suggests the need of further investigation of the buckling behaviour of GRP structural sections when subjected to compression failure.

---

* When the material axes coincide with the reference axes (or loading axes), then the ply is said to by especially orthotropic (Datoo, 1991).

Global buckling (flexural mode)

Global (or overall) buckling loads of long pultruded GRP columns have been predicted theoretically and measured experimentally by many authors. These studies include Hewson (1978), Lee and Hewson (1979), Yuan et al (1991), Zureick et al (1992), Scott et al (1992), Yoon et al (1992), Barbero and Tomblin (1992), Barbero and Raftoyiannis (1990 and 1993), Zureick and Scott (1997), Brown et al (1998), Barbero and DeVivo (1999), Barbero and Turk (2000). Most of these studies include both theoretical prediction and experimental measurement of critical loads and comparative studies. The Euler formulation (2.1)* has typically been employed for the theoretical prediction of buckling loads. Effect of transverse shear has been included in the Euler formulation by Lee and Hewson (1979), Zureick and Scott (1997) and Brown et al (1998) as,

$$P_e = \frac{P_E}{1 + (nP_E / A_g G_{xy})} \tag{2.2}$$

where P_E – Euler buckling load for pin ended axially loaded column (2.1),

A_g — Area of column webs,

G_{xy} — In-plane shear modulus (assumed to be G_{LT}).

n — A form factor for shear depending on the cross-section geometry.

The bending stiffness EI has been redefined to account for the orthotropic behaviour of GRP material. Either the E has been replaced by directional modulus of elasticity 'E_x' (x being the direction of loading in Fig. 2.1) of the material (Barbero and Raftoyiannis, 1990 and 1993) or the bending stiffness 'D' of the entire cross-section is used (instead of EI, Bank 1989). The directional elastic moduli E_x and E_y (in longitudinal and transverse directions) and in-plane shear modulus 'G_{xy}' for orthotropic GRP profiles have been experimentally measured using coupons (specimens obtained from the flanges and webs of profiles) by many authors (Barbero and Fu 1990, Yuan et al 1991, Mottram 1991, Turvey 1992, Mottram 1994, Wang and Zureick 1994, Davalos et al 1996, Zureik and Scott 1997, Saribiyik, 2000). It has been

* The number in parenthesis is equation number.

demonstrated experimentally that the values of elastic modulus in tension '$E_{x,t}$' and in compression '$E_{x,c}$'are nearly equal (Zureick and Scott, 1997). It means that, for a pultruded section having uniform material architect in all its components (flanges and webs), $E_{x,t}$ or $E_{x,c}$, evaluated from coupon testing, can directly be used in the Euler formulation. Alternatively the bending stiffness 'D' for the entire cross-section of column has been experimentally measured using three- and four-point bending tests (Bank 1989 and 1989a, Barbero and Fu 1990, Mottram, 1991, Bank et al 1994, Palmer et al 1998).

Theoretically, elastic moduli E_x, E_y, Poisson ratio ν_{xy} and shear modulus G_{xy} of the composite material have been evaluated from the properties of the constituents (i.e. fibres and matrix) and the material architecture of the cross-section (Barbero and Raftoyiannis 1990, Barbero 1991, Luciano and Barbero 1994, Nagaraj and GangaRao 1997, Saribiyik 2000). Micromechanics in conjugation with the classical lamination theory 'CLT' (Jones 1975, Tsai 1989) for plates have been used to calculate the material constants of the composite walls of the pultruded cross-sections. The material properties evaluated from micromechanics has been experimentally validated by coupon testing for various pultruded shapes (Lopez-Anido et al 1995, Davalos et al 1996, Qiao et al 1998).

Experimental determination of overall buckling loads, based on performing physical tests on the pultruded GRP columns, has also been reported in the literature. Yuan et al (1991) and Hashem (1993) tested, pin-ended and concentrically loaded, square box-section columns without and with extended flanges (Unicolumns in § 1.1). The studies demonstrated that the buckling loads (and hence the strength) mainly depended on the slenderness of the column. No comparison of the experimental buckling loads to analytical predictions has been reported.

Experimental buckling loads measured by testing of slender square GRP box-sections (76×76×6.4mm) by Zureick et al (1992), Scott et al (1992), Yoon et al (1992) and Yoon (1993), and of wide-flange sections by Barbero and Tomblin (1992 and 1994), Zureick and Scott (1997) and Brown et al (1998) under similar testing conditions (simply supported and concentrically loaded) were found to be lower than those obtained using Euler formulation (2.2). It was suggested that presence of initial eccentricities (imperfections) was the main cause of this discrepancy. In these studies

Southwell plots (Southwell 1932, Tsai 1986) have been used to obtain the critical buckling loads from the test data (measured axial load and central deflection). The Southwell method also provides an estimate of cumulative imperfections (i.e. sum of material, geometric and testing equipment). In the method a nonlinear load-deflection ($P-\Delta$) plot has been transformed into a linear plot when lateral deflection Δ normalized by the axial load P, is plotted against the load ($P-\frac{\Delta}{P}$). The inverse of the slope of the linear graph, gives an estimate for the critical buckling load and the intercept the magnitude of the cumulative imperfections.

Important findings reported in these studies include;

- Theoretical predictions using the Euler equation closely agreed with the experimental results, indicating that buckling capacity mainly depends on the longitudinal modulus of elasticity. Additional fibre reinforcement placed in the longitudinal direction would improve the longitudinal modulus and hence the buckling capacity of the profiles. Evaluation of true elastic constants, theoretically or experimentally has been demonstrated. A good estimate of bending stiffness 'D' is vital for the prediction of buckling loads.
- Material properties could be found with great accuracy from the material properties of the constituents and a detailed knowledge of the lamination construction.
- The effect of transverse shear on the Euler buckling load was very small (< 4%). However the effects of shear stresses should be included to provide a conservative estimate.
- Southwell plots gave a good estimate of critical buckling loads of slender columns subjected to axial loading. The method allowed non-destructive and repeatable testing of long columns and was able to account for the presence of imperfections.
- The axial shortness is proportional to loading and can be predicted by linear theory. Theoretical and experimental observations correlate well. ($\Delta = \frac{PL}{A_g E_L^c}$)

- The typical axial deflection curve showed a linear elastic response for 75–95% of the buckling load.
- Out of straightness should comply with ASTM D3917-94 ($e_0 \leq$ L/240 where e_0 is the initial deviation from the mean dimension).
- Tension and compression moduli in longitudinal direction can be taken as equal.

Local Buckling

For short spanned pultruded GRP columns or beams, the anticipated mode of failure is primarily local buckling (§ 1.2). Pultruded profiles are essentially an assembly of laminated panels (long rectangular plates), identified as flanges and webs (Barbero and Fu, 1990). When subjected to axial or bending loads, these panels enter a state of unstable equilibrium and buckle locally. This results in a premature failure of the entire GRP section, characterised by a distortion of the cross-section. The failure may be due to local buckling of one or more panels or a web panel under the action of combined normal and shear stresses (Johnson 1985, Barbero and Fu 1990, Yoon 1993, Bank et al 1994, Qiao et al 2001).

Local buckling analyses of GRP pultruded profiles have generally been accomplished by modelling the flanges and webs individually and considering the flexibility of the flange-web connection (Vakiener 1991, Barbero and Raftoyiannis 1990 and 1993, Qiao et al 2001). Flanges and webs of the cross-sections of the pultruded shapes (box- and I-sections) have been simulated as plates analysed independently using equations for composite plate buckling (Timoshenko and Gere, 1961). The governing differential equation for buckling of a symmetric plate (having similar material architect on both sides of the central plane) where no bending-extension coupling exists, under in-plane compression loading is:

$$D_{11}\frac{\partial^4 w}{\partial x^4} + 2(D_{12} + 2D_{66})\frac{\partial^4 w}{\partial x^2 \partial y^2} + D_{22}\frac{\partial^4 w}{\partial y^4} + N_x\frac{\partial^2 w}{\partial x^2} = 0 \qquad (2.3)$$

where N_x is the in-plane stress resultant, D_{11}, D_{22}, D_{12}, and D_{66} are the plate stiffness coefficients (Galambos, 1998; Jones, 1975), given as:

$$
\begin{aligned}
D_{11} &= \frac{(EI)_x}{1-\nu_{xy}\nu_{yx}} \\
D_{22} &= \frac{(EI)_y}{1-\nu_{xy}\nu_{yx}} \\
D_{12} &= \frac{\nu_{yx}(EI)_x}{1-\nu_{xy}\nu_{yx}} \\
D_{66} &= (GI)_{xy}
\end{aligned}
\tag{2.4}
$$

For an axially loaded column, all flanges and webs are subjected to compression, while, in the case of a beam under flexure loading, only the top flange is subjected to compression. When the critical buckling load has been reached, panels buckle in a local mode.

The classical theory governing the buckling of orthotropic plates (2.3) is fundamentally the same as that for isotropic plates (Leissa, 1983). The main assumptions include: homogeneous thin plate of constant thickness; small displacements (less than the plate thickness) during buckling; elastic material; behaving kinematically according to the Kirchhoff hypothesis (normal to the middle surface remains normal and straight during deformation of the plate e.g., no shear deformations). The only difference is that: the stress-strain relationships for each ply are typically orthotropic, and may be different amongst the plies. Therefore, stresses for each ply must be transformed into a common plate co-ordinate system and the force and moment resultants must be integrated piecewise from ply to ply through the thickness of the plate (Qiao, 1997).

"The flange of a pultruded I-section can be modelled as an orthotropic plate with two simply supported loaded edges and two unloaded edges, one of which is free while the other is elastically restrained."

(Vakiener et al, 1991).

The flange-web connection plays a significant role in the determination of the critical buckling load. Three cases of flange-web connection have been considered historically: rigid flange-web connection with rigid web (fixed or clamped); rigid flange-web connection with flexible web (elastic); and hinged flange-web connection (simply supported 'SS'). A typical flange (from a pultruded section) under uniform

in-plane compression along the longitudinal axis is shown in Fig 2.2. Due to the periodic form of the buckling wave along the length of the profile, the flange has been assumed as simply supported (SS) at any of the inflection points on the buckling wave (Barbero and Raftoyiannis, 1990). The boundary conditions of the two unloaded long edges depend upon the section shape. The flange of an I-section has one long edge free with the other joined to the web. The flange of a box-section has both the long unloaded edges connected to the webs. The stiffness of the connection between intersecting flanges and webs has been denoted by 'D'. For free or simply supported connection $D = 0$, for clamped connection $D = \infty$ and for an elastic connection D is equal to the bending elastic (transverse) modulus of the webs. Typically, a flange has been considered as an orthotropic thin plate subjected to in-plane compression along two short edges and elastically supported by the web on one long side in case of an I-beam and on both long sides in the case of a box-section (Fig. 2.2).

Critical buckling loads, obtained by solving the differential buckling equations (2.3) for thin orthotropic plates for the three proposed long-sides boundary conditions, have been plotted in the form of failure envelopes (Fig 2.3) against profile lengths (Barbero and Raftoyannis, 1990). The graphs indicate lower buckling loads (lower bound) for hinged connection, higher for clamped connection (upper bound) and intermediate for elastic web-flange connection. For a short length the flange buckled in mode 1 (m=1); i.e., in the shape of $\sin\left(\frac{mx}{a}\right)$. For a longer length, the mode number increases, but the minimum critical load remains constant. This feature supports the assumption of a simply supported boundary at the inflection points along the length of the plate. It has been demonstrated that buckling of plate is independent of the length and only dependent on the bending stiffness of the material, boundary conditions and axial load applied.

Theoretical results for a 152×152×6.4mm wide flange section (using (2.3)) were compared with those from a three point bending test of same-size wide-flange beam (Barbero and Fu, 1990). The measured half wavelength (152mm) has confirmed the theoretical predicted value. The experimental buckling load however lies between the two bounds, but closer to the theoretical buckling loads predicted for clamped web-flange connection than the elastic simulation. The authors (Barbero and Raftoyiannis, 1990) attributed this to the excessive thickness of web near the flanges. However, no

experimental study giving the measured buckling loads for box-sections is available to verify the theoretical results predicted in this study.

The study reported by Tomblin and Barbero (1994) includes both the theoretical and experimental investigations on the local buckling of wide flange (102×102×6.4mm, 152×152×6.4mm, 152×152×9.5mm and 203×203×9.5mm) pultruded GRP columns in axial compression. Local buckling loads have been predicted using the discrete plate formulation (2.3) used by Barbero and Raftoyiannis (1990) and considering the web-flange connection elastic with stiffness equal to the transverse elastic modulus (D_{22}) of the web. Buckling failure envelopes (Fig. 2.3a) have been drawn for the different column lengths showing minimum (and constant) buckling loads for column heights corresponding to integral values for number of half waves along the buckled flanges. The physical axial compression tests have been performed on four wide-flange sections with lengths corresponding to 2, 3, and 4 half waves. Authors (Tomblin and Barbero, 1994) have extended the application of Southwell's method to estimate the local buckling load. Axial load has been plotted against the flange-tip deflection normalised by the applied load. The method has been used to extract the experimental buckling loads from the measured lateral deflections of the flanges. The close correlation between experimental and theoretical buckling loads indicate that simulation of web-flange connection as elastic, with stiffness of the connection equal to the transverse elastic modulus of the web, provided accurate predictions. However, the percentage difference between the two results increased as the number of half waves increased. The authors attributed this rising difference to the imperfections inherited in the pultrusion manufacturer. A careful inspection of the failure envelopes (Fig. 2.3a) and lengths of the tested specimens revealed that the flanges of the orthotropic material did not buckled in a square pattern as in the case of isotropic (steel) plates but with an aspect ratio of 1.2 to 1.3.

A numerical study predicting the local buckling loads of wide-flange sections using the finite element method and comparing these results with classical plate theory has been reported by Vakiener et al (1991). Three pultruded GRP wide flange sections have been investigated for local buckling loads using full-scale finite element models. The columns are assigned orthotropic material properties and are axially loaded with pin-ended (simply supported) boundary conditions. Classical orthotropic plate buckling analyses have also been performed considering the three general flange-web

connections discussed in the above mentioned studies, for comparison of results. Finite element results reaffirmed classically predicted buckling loads considering flange-web connections as elastic, re-establishing that the hinged (SS) web-flange connection predicting a lower load (lower bound) and the rigid web-flange connection a higher (upper bound) buckling load. Furthermore, the number of half waves obtained by the numerical method agreed fully with the number predicted using classical plate buckling theory.

The local buckling load has been referred to as short-column load 'P_L' (Barbero and Tomblin, 1994). It is a function of both material properties and the geometry of the cross-section (depends upon D_{11}, D_{12}, D_{22}, and D_{66}). P_L is independent of the length of the column and boundary conditions (Barbero and DeVivo, 1999). The value of P_L has been determined by a column test (Tomblin and Barbero, 1994) or by numerical simulation (Vakiener et al, 1991) of short columns. Barbero and Evans (1997) have suggested that the value of P_L should be reported by the industry in their design guides (also Mottram, 2000). For example it is reported (Strongwell, section 10, Eq. C-2) that $P_L = 0.5EA/(b/t)^{1.5}$, based on experimental data for their product; where A is the area of the cross-section, E is the modulus, and b and t are the width and thickness of the flange, respectively.

Local buckling of thin-walled pultruded profiles (box and I-sections) has been analytically investigated by Qiao et al (2001). Buckling loads for the flanges subjected to in plane compression have been calculated using the discrete plate method. The buckled shape has been defined as a function of plate boundary conditions, which in turn are a function of rotational stiffness (material stiffness) of the joining webs. Coefficients of restraints defined in terms of material stiffness have been used in the solution of the classical buckling differential equation (2.3). Solution to these equations has been plotted against different values of restraint coefficients. Expressions for the coefficients of restraint for I- and box-sections are presented. It has been demonstrated that actual cases of restraint lie between simply supported and fully restrained (clamped) conditions. It has been submitted conclusively;

"Although significant research has been achieved in the area of local buckling analysis of orthotropic plates with various boundary conditions, there is still a need to

develop simplified and suitable design equation for the local buckling of pultruded FRP shapes."

(Qiao et al, 2001)

Mode Interaction

An important aspect of column buckling analysis is the interaction between local and global modes for intermediate lengths of the columns. Mode-interaction (interaction of two or more isolated[†] buckling modes) occurs when the theoretical buckling loads for the two isolated modes (global and local), for the corresponding length, are close. The mode-interaction phenomenon has been physically observed during the experimental tests on GRP pultruded I-section columns, where flange buckling (local) occurred in combination with lateral deflection (Tomblin, 1991; Raftoyiannis, 1994; Barbero et al, 2000). Once the maximum load had been achieved, global (lateral) deflection combined with local flange deflection, increased rapidly with a decrease in the applied compressive load. The loss in the buckling stiffness depended on the length of the column and the magnitude of imperfections. It was further concluded that maximum interaction (and hence the maximum reduction in failure load) occurred for a column length having equal theoretical global and local buckling loads. The intermediate range of column height has been defined as the region of column heights for which interaction occurs between local and global buckling modes. The height of a column, for which the theoretical local and global buckling loads are equal, has been termed as the transition height. The occurrence of mode-interaction and resulting decrease in the experimental buckling loads has also been reported by other authors;

"The experimental data for short and long column buckling suggest the existence of an intermediate column region where the critical loads are lower than the prediction of both local and global buckling theories."

(Barbero and Tomblin, 1994)

[†] Global and local buckling modes observed in long and short columns have been termed as isolated buckling modes (Barbero et al, 1996; Barbero, 2000).

"When two modes have close critical loads, there is a possibility of having interaction between them leading to a new equilibrium path (a coupled path) with a reduction in critical load".

(Godoy, et al, 1995)

"For practical lengths of columns in frame structures, the work (Barbero, Tomblin and Raftoyannis) showed that there will be an interaction between local and global buckling.

(Mottram, 2000)

"When two or more modes of buckling correspond to loads that are close or coincident, interaction between the modes may lead to post-bucking behaviour quite different from the post-buckling behaviour of the participating modes."

(Barbero et al, 1996)

"Columns of intermediate slenderness experience mode interaction, which effectively reduces the load carrying capacity below than both predicted values, local and global, for a given slenderness."

(Barbero and Evans, 1997)

"For intermediate lengths, the local and global buckling modes interact leading to smaller failure loads than predicted by any of the two isolated modes acting alone".

(Barbero, 2000)

Experimental studies carried out by Barbero and Tomblin (1994) and Barbero et al (2000) indicated a loss of up to 30% in the buckling loads of wide-flange pultruded columns of intermediate heights and a different failure mode (flange local buckling combined with lateral deflection at mid height of column) than the participating modes. Experimental data from one of these studies (Table 2 in Barbero et al, 2000) demonstrated that interactive buckling occurred at stress/strength ratios of less than 0.4, i.e., well in the elastic range of the composite material. It was concluded that the mode-interaction in pultruded GRP columns was due to interaction between local and global buckling mode rather than between local buckling and yielding of the material as in the case of steel columns. It was further demonstrated that the interaction between the isolated modes, in the case of pultruded I-sections, mainly depended on the length of the column and not on the cross-section dimensions. For the other

structural shapes, effect of the cross-sectional geometries on the degree of interaction may further be investigated by testing additional shapes for intermediate heights. The degree of interaction between isolated modes has been defined by an empirical constant '*c*' derived from the experimental data (Tomblin 1991, Barbero and Tomblin 1994). The value of '*c*' is the ratio of measured load for a particular length of the column to its local and Euler theoretical load.

The interaction constant '*c*' has been empirically evaluated using the experimental data from tests on the pultruded I-shape columns (Tomblin, 1991; Barbero and Tomblin, 1994). The buckling strength ratios 'q' and 's' have been defined as:

$$q = \frac{\text{Experimental failure load}}{\text{Local buckling load}} = \frac{P_{cr}}{P_L}$$
$$s = \frac{\text{Experimental failure load}}{\text{Euler buckling load}} = \frac{P_{cr}}{P_E} \qquad (2.5)$$

An empirical interaction equation, based on the experimental data has been defined by the authors (Barbero and Tomblin, 1994) as:

$$q + s = 1 + cqs \qquad (2.6)$$

For each column tested, '*c*' may be calculated from (2.6) as;

$$c = \frac{q + s - 1}{qs} \qquad (2.7)$$

The interaction constant '*c*' for a profile of particular cross-section is determined by averaging the '*c*' values from all the samples (lengths in intermediate range) tested. For example, the interaction constant c=0.85 for a wide-flange I-section (152×152×6.4mm) has been determined by averaging the '*c*' obtained by testing a number of samples of 152×152×6.4 profiles having intermediate lengths (Tomblin, 1994). Similarly, interaction constant c=0.84 for the four different cross-sections of wide-flange I-sections has been averaged (Fig 2.4) in one value with the conclusion that interaction constant is independent of the cross-section, but is a function of column length and material properties (Barbero and Tomblin, 1994).

The mode interaction phenomenon (also known as modal interaction) in composite columns of intermediate heights has been investigated theoretically by many authors (Barbero et al 1993, Raftoyiannis 1994, Godoy et al 1995, Barbero et all 1996,

Barbero 2000). The investigations have been carried out within the general framework of the theory of elastic stability considering the occurrence of the buckling phenomenon within the linear range of composite material. This has been documented experimentally for pultruded columns by Barbero and Tomblin (1994) and Vakiener et al (1991) and for lateral-torsional buckling of beams by Mottram (1991). Theory of elastic stability provides a similar understanding of the critical loads as those obtained by Euler (for global) and Timoshenko (for local), but it differs in that it allows to study post-critical states, also accounting for imperfection sensitivity of the critical loads. As the mode-interaction occurs after the initialisation of the buckling process (Godoy et al 1995, Barbero et al 1996), post-buckling behaviour of the structure, has been included in addition to the pre-buckling behaviours in these analyses. Analytically, mode-interaction has been studied by Barbero and Tomblin (1994), Godoy et al (1995), Barbero et al (1996) and Barbero (2000), using a static perturbation (incremental) technique to draw the equilibrium path for the entire buckling process.

A numerical analysis considering the first order displacements (Barbero et al 1993, Raftoyiannis 1994), proved insufficient to predict the interaction behaviour, as the resulting mode was imperfection insensitive. It was concluded from the previous analytical studies on the interactive buckling of isotropic columns (Sridharan and Ali, 1986), that an interactive failure mode (similar to one observed experimentally) could be included in the analysis to notice the imperfection sensitivity of the buckling load (Ratoyiannis 1994, Barbero and Tomblin 1994). It was suggested, therefore, to add a new mode (resulting from interaction) as a third participating mode in the buckling analysis. The third mode was termed a secondary local mode as its deformed shape (flange deflection) characterised the local buckling mode.

A number of buckling modes may interact with the global and local mode (Godoy et al 1995, Barbero 2000). The criteria for the possible interacting modes are: (a) it is different from Euler or local modes; (b) it follows an interacting path; and (c) the interacting mode resembles the experimental mode shape. Once the shape of the third mode has been determined, modal displacements of the resulting interaction mode can be written as the linear combination of the three interacting modes.

The studies reported by Raftoyiannis (1994), Barbero and Tomblin (1994), Godoy et al (1995), Barbero et al (1996) and Barbero (2000) include three isolated modes: a

primary local (rotation of flanges and bending of web); a global (Euler); and a secondary local (bending of flanges), in the mode interaction analyses for I-shaped GRP columns. In the study by Godoy et al (1995) analytical functions have been chosen to model the deformed shapes of the three participating buckling modes. Contributions from the proposed displacements of the individual (a global and two local) modes, have been combined linearly to obtain the total displacement field in terms of four degrees of freedom (axial shortening, lateral web deflection, rotation of flanges and transverse displacement of flange outer-tip). The deformed shape and the buckling behaviour (loss in strength at buckling and imperfection sensitivity[‡]) were then calculated by linear analysis. The fundamental path was typically linear (for a perfect system), with three bifurcation points on the loading axis, corresponding to the three isolated modes. Two secondary paths, both stable and symmetric emerged from the lowest bifurcation point (corresponding to local mode) and next one, close or nearly coincident bifurcation point (corresponding to global mode). Two further bifurcation points were found on the local (lower) secondary path; the first one yielded a stable tertiary path similar to the Euler mode, while the second one yielded an unstable tertiary path with a different mode shape (flange and web deflection) resulting from interaction between local and global mode. Since the tertiary path is unstable, the behaviour of a real imperfect column will be imperfection sensitive and failure will be catastrophic, with no load capacity after buckling. It is worth mentioning that other modes with shapes similar to the second local mode has been chosen as the third interacting mode along with primary local and global modes. However, similar deformed shapes and buckling behaviour were obtained from the interaction analysis. This means that interaction depends exclusively on the two primary modes. The third mode needs to be considered because first order displacement is insufficient to trigger interaction (Barbero et al 1996, Barbero 2000). The finite element method has also been employed using commercial code (ABAQUS, 1998) to model the intermediate height wide flange pultruded columns (Barbero, 2000). By using a finite element discretisation as plate assemblies, all

---

[‡] Imperfection sensitivity means that the peak or failure load of the imperfect system will be lower than the bifurcation load of the perfect system, the magnitude of the reduction depends on the magnitude of imperfection (Barbero, 2000)

buckling modes as well as amplitude modulation[§] are automatically taken into account. While all the isolated mode secondary paths were found to be stable, the column was found to be imperfection sensitive once mode interaction was reached.

Material properties (like orthotropy i.e., ratio between stiffness in the transverse and axial directions) play an important role in the interactive buckling of I-section columns (Godoy et al, 1995). For higher orthotropic ratios, higher degrees of interaction have been reported in the analytical investigations performed by Godoy et al (1995). Conversely, it is possible to design the material so as to avoid the occurrence of interaction for a given length (one of the advantages of using composite materials) (Barbero, 2000).

Numerical results for 152×152×6.4mm I-section columns of intermediate lengths (Barbero, 2000) are compared with experimental results for the same columns by Barbero and Tomblin (1994), with poor agreement (difference between 14% to 55%) between the two, indicating that the interacting mode shape is different from the isolated local mode.

Barbero (2000) presented a numerical study investigating the effects of geometrical imperfections on the degree of modal interaction in pultruded columns. Imperfections of known quantities ($t/240$ to $t/2$ where 't' is the thickness of the flange) were introduced to the column corresponding to the shape of Euler, local or a combination of the both buckling modes. Euler and local imperfections, when introduced separately, produced virtually the same decrease in buckling loads, whereas a combination of both imperfections caused cumulated reduction adding the effect of both imperfections. It was concluded that besides the column slenderness, buckling load is a function of amplitude of imperfections, and is independent of the imperfection shape. Interaction plots (Fig. 2.5) for an I-section profile of intermediate lengths has been constructed numerically by Barbero (2000) similar to that developed experimentally (Fig. 2.4) by Barbero and Tomblin (1994). Numerical plots (Fig 2.5) clearly show the deviation of the peak load from the corresponding isolated mode predictions. For each imperfection amplitude, several points represent different values

---

[§] Wave modulation implies the reduction in the amplitude of the buckling shape near the supports (Barbero, 1996).

of slenderness. The simulated data for the imperfection amplitudes have been curve fitted to evaluate the empirical interaction constant '*c*' (Tomblin, 1991). The annotated plots represent the best fit to the data for the imperfection amplitudes, and the corresponding values of '*c*' are given in the legend. As the process accounts for the effect of slenderness, '*c*' represents all the various values of slenderness. Values of '*c*' taken from the best fit to the data are plotted against imperfection amplitude *e/t*, can be represented by a linear equation (straight line). From this plot '*c*' can be determined for any value of *e/t*, and peak load can be predicted using design equations (§ 2.4).

2.3 STATE -OF-THE-ART DESIGN GUIDANCE

For design purposes, simplified formulas have been provided for steel structural profiles, being used as beams and columns in the structural frames. For instance the column formulas are functions of the major parameters of strength, such as the yield point, the length, and the cross-sectional properties, with factors of safety prescribed to give designs of acceptable safety. The Column Research Council (CRC) was founded in 1944 to monitor and present theoretical and practical work related to metal column design. Later in 1976 the CRS became the Structural Stability Research Council (SSRC) with an extended scope to include research dealing with all types of structures and structural elements where stability is a controlling feature of behaviour (Johnston 1983, Galambos 1998). The council publishes up-to-date research on the stability of metal structures, on a regular basis, and maintains a working interaction between structural engineering practice and research (Galambos, 1998).

For example, "CRC**—Column strength curves" has recommended empirical equations (Galambos, 1998) based on the tangent-modulus theory as:

$$\sigma_{cr} = \sigma_y \left[1 - \frac{\lambda^2}{4} \right] \qquad \text{for } \lambda \le \sqrt{2} \qquad (2.8)$$

$$\sigma_{cr} = \sigma_y \left[\frac{1}{\lambda^2} \right] \qquad \text{for } \lambda \ge \sqrt{2} \qquad (2.9)$$

where

** CRC: Column Research Council.

$$\lambda = \frac{1}{\pi}\sqrt{\frac{\sigma_y}{E}}\frac{L}{r} \qquad (2.10)$$

The curves has been drawn for the average critical stress for small and medium-sized hot rolled wide flange sections of mild structural steel, with a symmetrical residual stress distribution typical of such members. The recent trend in column design involves column formulas which are a numerical fit of curves obtained from maximum strength analysis of representative geometrically imperfect columns. Further, the strength of columns has now been represented by more than one column curve, introducing the concept of multiple column curves, e.g., SSRC[††] curves 1 (Fig. 2.6), 2, and 3 (Galambos, 1998); Eurocode 3 (ECS, 1992) and Canadian standard (CSA, 1994).

Pultruder's Design Manuals.

The first EXTREN® Design Manual was published in 1971, updated in 1978 and republished in 1989, providing design guidance for compression members (columns) using empirical equations based on the manufacturing experience, application knowledge and test data gathered from physical tests on GRP columns (Strongwell, 1989). FIBREFORCE, UK also follows this manual. Design tables, besides the corresponding design equations have been included for the prediction of allowable axial stress and loads for different sections. Neither the test methods have been described nor are the experimental data available in public domain for independent evaluation. The column heights are divided into two groups; short and long, depending on the slenderness ratio taken as *kL/r* (like conventional steel elements). Only concentric loading conditions have been considered. For example, the allowable axial stress F_u (should be less than critical buckling stress) for:

short box-section column:

$$F_u = \frac{E}{16(b/t)^{0.85}} \qquad (2.11)$$

(b and t are width and thickness of the webs of the box-section respectively)

long box-section column:

[††] SSRC: Structural Stability Research Council, new name of CRC since 1976 (Galambos, 1998).

$$F_u = \frac{1.3E}{(kL/r)^{1.3}} \tag{2.12}$$

short wide-flange column:

$$F_u = \frac{0.5E}{(b_f/t_f)^{1.5}} \tag{2.13}$$

(b_f and t_f are the width and thickness of the flange respectively)

long wide-flange column:

$$F_u = \frac{4.9E}{(kL/r)^{1.7}} \tag{2.14}$$

"These relationships appear to correlate well with the actual failure loads encountered during testing. However, since these equations are empirical in nature, they must be supported analytically before acceptance in a general design code."

(Vakiener et al, 1991)

The Elastic moduli used for design purposes are the minimum for a range of materials of structural profiles produced by the company. Most importantly, intermediate heights of column (near to the transitional length) have been omitted from the design point of view, for which the experimental load has been found much lower than either for short or long column due to interaction of local and global buckling (Barbero, 1994; Barbero and Trovillion, 1998). Therefore these design equations can not be referred to as universal design equations.

ASCE (1984)

This code, published by the American Society of Civil Engineers, includes design equations suitable for composite fibre reinforced structural profiles. Design expressions are based on the theory of elastic stability (Timoshenko and Gere, 1961; Jones, 1975). Long column buckling has been addressed using directional modulus of elasticity in the Euler formulation (2.1). To deal with the local flange buckling, equations are presented for the limiting case of a one edge simply supported flange (simple-simple-simple-free), and a one edge fixed flange (simple-fixed-simple-free) as:

$$P_L = \pi^2 bt\left[\frac{E_x}{12(1-\nu_{xy}\nu_{yx}}\left(\frac{b}{a}\right)^2 + \frac{G_{xy}}{\pi^2}\right]\left(\frac{t}{b}\right)^2 \qquad (2.15)$$

The equation can be used to approximate the critical load for an outstanding flange (Vakiener et al, 1991). Composite columns with intermediate lengths susceptible of buckling mode interaction have not been included in the design.

Eurocomp Design Code (EDC, 1996)

"This publication represents the first independent, practical guidance on structural design of polymer composites. The EUROCOMP design code has a limit state approach to requirements for resistance, serviceability and durability of structures."

(Mottram, 2000)

The equations cited in Eurocomp design code for the prediction of design load for the concentrically loaded pultruded (FRP) column are based on elastic theory of stability (Timoshenko and Gere, 1961). It has been suggested in the code that columns should be investigated for all the possible types of buckling for that height such as global (lateral deflection), web local (flexural and shear) and flange local (compression) buckling. The Euler formula has been used (in the design code) for the determination of global buckling load assuming the material as isotropic and using the elastic modulus along the weak axis of the profile. Local buckling, on the other hand, has been solved using the classical plate buckling equation and requires the knowledge of both longitudinal and the transversal flexural stiffness of the member. For example, the local compression flange buckling for the two general cases: a long rectangular flange with both longitudinal edges simply supported (flange of a box-section); and a long rectangular plate with one longitudinal edge simply supported and the other free (outstayed of an I- or H-section); are respectively computed as

$$\sigma_{c.cr.y} = \frac{2\pi^2}{tb^2}\left\{(\sqrt{D_x D_y}) + H_0\right\} \qquad (2.16)$$

and

$$\sigma_{c.cr.y} = \frac{\pi^2}{tb^2}\left\{D_x\left(\frac{b}{a}\right)^2 + \left(\frac{12D_{xy}}{\pi^2}\right)\right\} \qquad (2.17)$$

where

$$H_0 = \frac{1}{2}\left(\nu_{xy} D_y + \nu_{yx} D_x\right) + 2\left(\frac{G_{xy} t^3}{12}\right) \qquad (2.18)$$

a = the half wave length of the buckle (taken equal to the length of the plate)

b = effective width of the plate

t = thickness of the plate

D_x, D_y, D_{xy}, and D'_{xy} are the plate stiffness and are respectively equal to D_{11}, D_{22}, D_{12} and D_{66}, given in (2.4).

The design equations presented in the EDC for design of composite structural profiles are the same as given in the ASCE (1984). Effects of apparently lower shear modulus of the composite material have not been accounted for. Also the length of half sine wave 'a' assumed by the buckled flange cannot be taken equal to the length of the long rectangular plate (equal to short column length). It is well known that a long rectangular isotropic plate buckles in half-waves, the lengths of which approach (for minimum load) the width of the plate i.e. a buckled plate subdivides approximately into squares. In a three point bending test on composite wide-flange I beam (152x152x6.35mm), both theoretical predicted (Barbero and Raftoyannis, 1990) and experimental measured (Barbero and Fu, 1990), half-wave length of 152mm was found, confirming the square divisions of the buckled flange. However these studies concluded that local buckling of the compression flange is independent of the length of the beam and only dependent of the maximum bending moment (load) applied. Further Eurocomp design code does not address the potential loss of buckling stiffness in the column of intermediate (or transition) height. The design criteria in EDC require computing the ultimate stresses for all possible modes of buckling and serviceability limitations, for every practical height. Interaction of global and local buckling develops an unstable mode, which reduces the stiffness of the section up to 30%, and is highly imperfection sensitive (Barbero et al, 1996).

Design curves for GRP columns.

A universal design curve along with the corresponding equation has been developed to estimate the buckling loads for GRP pultruded I-section structural profiles used as

concentrically loaded columns (Tomblin 1991, Barbero 1992, Barbero and Tomblin 1993). The design curve represents the whole range of practical column lengths (similar to universal design curve for steel columns). The main parameters involved in the design equation are the slenderness ratio (λ), the local buckling load (P_L) for a short column and the interaction constant (c) to account for modal interaction in columns of intermediate length range.

The universal slenderness ratio (λ) for the composite GRP columns has been defined based on similar arguments made for steel (Galambos, 1998) and timber (Zahn, 1992) column universal design curves. For example, in the case of steel columns the slenderness ratio ($\lambda = \frac{1}{\pi}\frac{L}{r}\sqrt{\frac{\sigma_y}{E}}$) has been defined as a function of σ_y (yield stress) and E (the bending stiffness) in conjunction with the normally expected $\frac{L}{r}$ (length of column divided by its radius of gyration). In case of a timber column (a natural composite) the slenderness ratio ($\lambda = \frac{1}{\pi}\frac{L}{\rho}\sqrt{\frac{F_c}{E}}$) has been defined as a function of F_c (compression strength) and E (bending stiffness) in addition to the L/ρ (ratio of column length to curvature). Likewise, the slenderness for the composite GRP column has been defined in terms of D (the sectional flexural rigidity), P_L (local buckling load which in turn depends upon D) and column length L. The P_L corresponds to the local buckling behaviour of steel sections before yielding and compressive failure of timber columns in the absence of local buckling. Note that because of various amounts, types, and orientation of fibres in the cross-section the term D cannot be separated into bending stiffness (E) and the moment of the inertia 'I' (Barbero 1990, Barbero and Trovillion 1998). Further, two columns having same ratio of L/r may have different bending stiffness and hence the bending characteristics (Barbero and Trovillion, 1998). Where as, dependency of the buckling load on column length has been established experimentally by many authors (Yuan 1991, Barbero and Raftoyiannis 1992, and Barbero and Tomblin 1994). Therefore the slenderness ratio for pultruded composite columns has been redefined (Tomblin 1991, Barbero 1992, Barbero and Tomblin 1994), as:

$$\lambda = \frac{L}{\pi}\sqrt{\frac{P_L}{D}} \qquad (2.19)$$

Since $P_E = \frac{\pi^2 D}{L^2}$, from the definition of universal slenderness (2.19), it may be written as

$$P_E = \frac{P_L}{\lambda^2} \tag{2.20}$$

which means that theoretical global and local buckling loads are same for $\lambda = 1$, giving the definition of transition height (e.g., transition between global and local buckling). Putting $\lambda = 1$ in (2.19), the transition height 'L^*'for an I-section column can be calculated as:

$$L^* = \sqrt{\frac{D\pi^2}{P_L}} \tag{2.21}$$

"For the theoretical imperfection-free situation there is a column height where the critical buckling load is identical for both the global and local buckling modes. This height is referred to as the transition height".

Mottram (2000)

The loss in the buckling stiffness (decrease in the critical buckling load due to mode interaction) of an intermediate column (imperfect or real) has been estimated by defining the interaction constant '*c*', which physically describes the degree of interaction present between the local and global buckling modes (2.7). The parameter '*c*' accounts for the effects of nonlinear compression due to inhomogeneity of the material, and physical imperfection such as out of straightness in the columns (Zahn 1992, Barbero and Tomblin 1994).

Substitution of (2.20) and (2.5) in (2.6) gives,

$$\frac{P_{cr}}{P_L} + \frac{P_{cr}}{P_E} = 1 + c\frac{P_{cr}}{P_L} \times \frac{P_{cr}}{P_E}$$

$$\frac{P_{cr}}{P_L} + \frac{\lambda^2 P_{cr}}{P_L} = 1 + c\frac{P_{cr}}{P_L} \times \frac{\lambda^2 P_{cr}}{P_L}$$

$$q + \lambda^2 q = 1 + c\lambda^2 q^2$$

$$(1 + \lambda^2)q = 1 + c\lambda^2 q^2$$

$$c\lambda^2 q^2 - (1+\lambda^2)q + 1 = 0 \tag{2.22}$$

The root of this equation is

$$q = \frac{1+\frac{1}{\lambda^2}}{2c} - \sqrt{\left(\frac{1+\frac{1}{\lambda^2}}{2c}\right)^2 - \frac{1}{c\lambda^2}} \tag{2.23}$$

replacing q by $\frac{P_{cr}}{P_L}$ gives,

$$P_{cr} = P_L\left[\frac{1+\frac{1}{\lambda^2}}{2c} - \sqrt{\left(\frac{1+\frac{1}{\lambda^2}}{2c}\right)^2 - \frac{1}{c\lambda^2}}\right] \tag{2.24}$$

which represents actual values of P_{cr} determined experimentally and presented in terms of interaction parameter c and slenderness ratio λ. Therefore, equation (2.24) has been presented as a design equation over the entire range of column slenderness, short, intermediate, and long (Fig 2.7).

Barbero and Tomblin (1994) used this equation to construct a universal design curve for the wide flange I-sections used as columns simply supported and concentrically loaded. Buckling loads for intermediate length columns (in the vicinity of transition length (2.21)) has been measured on three wide flange sections i.e. 102×102×6.4mm, 152×152×6.4mm and152×152x 9.35mm. Additional experimental data from Barbero and Tomblin (1992) and Barbero and Raftoyiannis (1993) have also been included. The interaction constant for each type of cross-section was inferred from the experimental data by averaging the value of 'c' using all data points. Theoretical buckling loads have been computed using micromechanics and classical lamination theory (Barbero and Ratoyiannis 1990, Luciano and Barbero 1995). This procedure has been validated experimentally for similar pultruded shapes (Lopez-Anido et al, 1995; Davalos et al, 1996, Qiao et al, 1998) by comparing the predicted material properties with coupon test results. Experimental loads, normalised by the local

buckling load ($\frac{P_{cr}}{P_L} = q$), have been plotted against universal slenderness 'λ' (2.19), and resulting buckling envelopes for all I-sections collapse into one universal curve. All the I-sections used in this investigation have been described by the same value of the interaction constant. It has been further recommended that the interaction constant 'c' must be determined experimentally for each new section following the procedure described. A similar design equation, design curve and the procedure for the evaluation of the interaction constant 'c' has also been reported by Barbero and Evans (1997). Determination of the interaction constant using experimental data has also been emphasised by other authors as:

"The value of the mode-interaction constant must be determined from reliable and relevant experimental data (i.e. when the load eccentricity is zero)."

(Mottram, 2000)

A further parameter needed for the construction of the universal (applicable for all range of practical heights) design curve is P_L. This should also be measured as accurately as possible. Design equation (2.24) is simpler to use than many equations for different heights (2.11-2.17) or Euler equation for long columns and local buckling equation for short columns. Equation 2.24 provides a basis for the design and use of pultruded structural columns in engineering applications Barbero and Evans, 1997).

Barbero and DeVivo (1999) have produced a design curve (Fig 2.7) for pultruded GRP I-section columns using (2.24) and experimental data from Barbero and Tomblin (1994), Zureick and Scott (1997), Barbero and Trovillion (1998), Brown et al (1998), and Barbero et al (1999). Values of 'D' and P_L were taken from the respective references. The column loads have been normalised by P_L (function of D) to compare the experimental data from various sources because for even the same cross-sections, the material properties of the columns differ among the manufacturers. The classical local and Euler curves are recovered by setting c = 1, with buckling loads showing a strong dependency on the slenderness of the column as expected. Interaction constant has been calculated to a value of 0.65. The curve with interaction constant c = 0.65 has proved to be conservative as all the experimental points fall above this curve. According to Mottram (2000), a 'c' value of 0.65 for concentric loaded columns, is

very low and indicative of very high imperfections either in the structural profiles or in the testing rig and the procedure followed to obtain concentric loading. Mottram (2000) also observed a substantial difference in the value of P_L computed analytically or measured experimentally by many authors. In this respect he submits,

"Agreement must be reached on the method or methods (either testing or numerical) that can be used to accurately determine the local flange-buckling load."

(Mottram, 2000)

Mottram (2000) did agree to the logical arguments used to define the universal slenderness ratio (λ) for the composite columns and the procedure followed to evaluate the interaction constant '*c*' from the experimental results by Barbero and his fellow researchers. It has been added,

"The methodology used to develop their equations has laid down procedures that will eventually provide a rigorous design approach for engineers to use with confidence."

(Mottram, 2000)

Zureick and Scott (1997) have undertaken an experimental study regarding the Euler buckling of pultruded GRP I-and box-sections columns, and presented a design curve based on the experimental data gathered through buckling tests on slender columns. For comparison of experimental results from different sections, a non-dimensional slenderness ratio has been defined as:

$$\lambda = \sqrt{\frac{F_L^c}{F_e}} \tag{2.25}$$

where F_L^c denotes ultimate longitudinal compression stress,

and F_e is the Euler load including the shear factor.

Note that F_L^c included in the slenderness ratio (even for long columns, where buckling occurs at stresses much lower stresses than ultimate compressive stress) corresponds to the local buckling load P_L used in the definition of slenderness in (2.19). P_L is unique property of the profile which is independent of the column height. The experimentally measured buckling stresses 'f_{exp}' have been calculated by dividing the experimental buckling load by cross-sectional area. To compare the experimental results from different sections, the buckling stress 'f_{exp}' has been normalised by the

ultimate compressive stress 'F_L^c' of the material and plotted against the defined slenderness ratio. Plots of the experimental results of all the sections (two I- and two box-sections) showed a great similarity in the behaviour of different cross-sections. The curves are similar to the Euler curves for slender columns. Based on the experimental observations, design guidelines, for concentrically loaded unidirectional fibre reinforced composite members with doubly symmetric cross-section in which the global limit controls, have been proposed as:

$$P_r = \phi_c P_n \tag{2.26}$$

where P_r is the factored axial compressive resistance, ϕ_c is the resistant factor that shall not exceed 0.85, and P_n is nominal compressive resistance given by

$$P_n = A_g F_E \tag{2.27}$$

where A_g is the gross sectional area of the member F_E is the elastic buckling stress and may be defines as

$$F_E = \frac{\pi^2 E_L}{\left(L_{eff}/r\right)^2} \tag{2.28}$$

The axial shortening in the member can be estimated as

$$\Delta_c = \frac{PL_0}{A_g\left(0.8E_L\right)} \tag{2.29}$$

where L_0 is the member length, and a reduction of 20% in the average material property E_L is an empirical factor obtained experimentally.

In the previous studies the interaction constant '*c*' has been calculated using experimental data. Barbero (2000) described a procedure to evaluate the constant '*c*' from simulation results generated from Finite Element Analysis. Critical loads for pultruded wide-flange (152x152x6.4mm) columns have been estimated using the finite element method for various constant values of slenderness (in the vicinity of transition length i.e., λ from 0.824 to 1.013) and varying the introduced imperfections (*e/t* from 1/40 to 1/2, where *e* is initial central deflection and *t* is flange thickness) at mid lengths (called the imperfection amplitude). The larger is the imperfection the greater is the reduction of the peak load. For each value of imperfection amplitude,

the simulation data were fitted with the empirical equation (2.6) which models interaction by an adjustable constant '*c*'. The lines with symbols (Fig. 2.5) represent the best fit to the data for corresponding imperfection amplitudes and corresponding values of '*c*' are given in the legend. Note that this process accounts for the effect of slenderness because all the data for various slenderness values have been represented by a single value of '*c*' corresponding to a given imperfection amplitude. Experimental data have also been include for comparison and is presented by open circle symbols in the Fig 2.5. Interaction constant '*c*' has been found inversely proportional to the amplitude of imperfection (*e/t*). Consequently, '*c*' can be obtained if the amplitude of imperfections is estimated. For design purposes, an estimate of the imperfection amplitude can be obtained from the geometric tolerance reported by the manufacturer. Once the '*c*' value has been established for a particular shape, (2.24) can be used to compute the peak load for any slenderness value.

2.4 RESEARCH METHODOLOGY

The research on the buckling strength of pultruded GRP profiles has demonstrated the application of combined experimental and analytical approaches to establish the critical buckling loads and associated buckling modes. Experimental investigations have been employed to obtain the load-deflection (overall lateral deflections or flange rotations) diagrams showing the pre- and post-buckling behaviour of the structure under the applied load. For example, overall buckling loads for pultruded GRP wide-flange and box-section columns have experimentally been measured by Yuan et al (1991), Barbero and Tomblin (1992), Zureick and Scott (1997), Brown et al (1998). Southwell method (Southwell, 1932) has been applied for the linear regression of non-linear P-Δ (axial Load versus central lateral deflection) plots. A mathematical explanation of the Southwell method has been given by Tsai (1986). Experimental methodologies not only provide the shapes of buckling modes but also measure the modal amplitude (lateral central deflection). Further, Southwell plots provide an overall estimate of initial imperfections. The experimental data has been used as the primary information for constructing the analytical models and also for the validation of the theoretical outcomes.

Analytical approaches correlate the experimental observations with the classical theories (e.g. theory of elastic stability, CLT and static equilibrium equations) and

provide explanations for the observed behaviour. The classical approaches i.e. Euler formulation and differential equation for buckling of orthotropic plates has been solved using analytical functions representing modal shapes observed in experimental configurations (Barbero and Fu 1990, Barbero and Raftoyiannis 1993). The analytical functions are required to satisfy the boundary conditions and modal displacements of the buckled shapes. Similarly in the mode-interaction investigations modal displacement fields have been analytically proposed by Barbero and Raftoyiannis (1994) and Godoy et al (1995). Modal displacements of the three isolated modes participating in the interaction process, in the form of strain energy have been added linearly to obtain the displacement field of the resulting interaction mode. The analytical investigations have been usually generalized allowing parametric studies to establish the effects of varying material properties, geometry, loading or support conditions. Numerical approaches (e.g. finite element method) have now become more useful as large and complex geometries can be solved using fast and extensive computing facilities. Theoretical investigations save time, material, and expensive laboratory resources. Parametric studies lead to identification of principal factors imparting improvements in the material architect and the buckling behaviour. For example introduction of angle-plies in the material, improves the transverse stiffness of the material and hence the local flange buckling and interaction properties (Barbero et al 1993). However, the calibration and validation of numerical simulations are essential.

Finite element method

Finite element method (FEM) has been widely used in the buckling analysis of pultruded structures during the last decade. It is the numerical method which can successfully model large and geometrically complex structures (Barbero et al, 1995). FEM has been employed to estimate the critical buckling loads for the isolated buckling modes (local and global). A linear elastic buckling analysis of a pultruded wide-flange column using a finite element model has been presented by Vakiener et al (1991). An individual flange was modelled first as an orthotropic plate (assigning orthotropic material properties) simply supported at the loaded edges, one unloaded edge simply supported and the other unloaded edge as free. FEM results, when compared with those obtained from classical plate buckling analysis, demonstrated

the validity of the approach (difference < 4%). Secondly, three whole wide-flange sections were modelled as pin ended columns under axial compression and analysed using FEM. Predicted critical buckling loads fell between the upper and lower bounds estimated by the classical simply supported and fixed flange solutions. FEM results were very close (difference < 5%) to the results obtained using web-flange interaction solutions (Barbero and Raftoyiannis 1990, Yoon and Zureick 1992). The actual observed number of half waves was the same as the number of half waves predicted.

FEM has been used to model GRP profiles like wide-flange, angles and box-sections with and without extended flanges (Barbero et al 1995). Full scale models of pin ended columns under concentric and eccentric loads were solved for the critical buckling loads. FEM results were found to provide very close correlation to that of computed by plate buckling analysis. FEM results of Vakiener (1991) were confirmed, analysing the same sections with different loading conditions. In the analysis performed by Vakiener (1991), point loads of different intensities applied along the width of flanges, while in Barbero et al (1995) model, a uniform loading on all nodes along the flange width were applied. This close correlation has provided confidence to propose that finite element methods can be used to model the complex boundary and loading conditions and solved to produce the accurate results. It has been concluded:

"With the increased capacity of present day workstations and personal computers, it is now possible to solve large problems without having to assume analytical approximations for prismatic members. Furthermore, the finite element method easily allows the modelling of non-prismatic problems, complex boundary conditions and geometries. The accuracy of the results can be improved with mesh refinement."

(Barbero et al. 1995)

Finite element method has been employed for the post-buckling analysis of the pultruded columns (Godoy et al, 1995). Post-buckling analysis is required to establish the nature of the critical state (stable or unstable bifurcation), classification of secondary paths and sensitivity of the emerging secondary and tertiary paths. The post-buckling solution has provided information on the mode-interaction in columns of intermediate length. Imperfection sensitivity and mode interaction of the pultruded columns have been assessed without having to choose appropriate analytical

functions. A perturbation technique (incremental loading) was used to draw post critical analysis to capture the mode-interaction during the nonlinear finite element analysis. The authors describe the FEM as a comprehensive tool for stability analysis of the composite pultruded profiles,

"However, engineering problems often require the modelling of a rather complex geometry, and the finite element method has been the most convenient tool to achieve this in the last three decades. Thus, it is most desirable to have finite element solutions adapted to the needs of stability analysis. "

(Godoy et al, 1995)

An experimental and numerical study to measure the buckling loads of pultruded GRP I-sections, when used as beam-columns and to construct a curve for their design has been reported by Barbero and DeVivo (1999). FEM has been used to model numerous load eccentricities and slenderness which could not practically be possible due to equipment limitations and experimental set up. For example, the load eccentricity of 25.4mm could only be applied by the testing arrangement used in the study. The buckling loads for other eccentricities were predicted using finite element simulation. Furthermore, some loading configurations are simply not possible to apply. For instant, application of a constant end-moment (due to beam bending in frames), while the axial load increased to failure load, can be introduced using finite element simulation, yet would be very difficult to apply in physical tests. Finite element simulation and statistical methods have been used to develop resistance factors that represent a lower bound to the expected beam-column load of wide-flange shapes. For other shapes the procedure described here can be used to redefine the coefficients in the resistance factors, using the relevant section properties.

A study to establish a relationship between column imperfection and the interaction constant using finite element method has been reported by Barbero (2000). Buckling and post-buckling of pultruded columns (152×152×6.4mm wide flange sections) have been modelled using a finite element code (ABAQUS 1998). For short and long columns finite element models closely predicted the bifurcation load and the curvature of the post-critical path, as long as the local and Euler bifurcation loads were far apart. For intermediate lengths, a linear combination of the isolated modes could predict a deformation field similar to the experimental deformation data.

"Finite element modelling provides the engineer with a powerful tool that consistently predicts the physical behaviour of a particular structural member without having to conduct numerous laboratory tests."

(Barbero, 2000)

"Work must be undertaken to find out if the finite element method can be used to determine the failure load that would occur in practice (assuming the column conditions remain unaltered)."

(Mottram, 2000)

It has also been demonstrated that a variety of commercial FEM codes are available now enabling the engineers and designers to perform many types of analyses including eigenvalue, linear and nonlinear (both geometrically and materially). Different types of material properties, boundary conditions and loading schemes can be assigned to different components of the structures.

2.5 COMPRESSION MATERIAL PROPERTIES

"Properties for pultruded materials are usually determined by tests in directions parallel and perpendicular to the direction of the pull. Data in the form of characteristic values are required for a limit state design approach (Eurocomp design code)".

(Mottram, 2000)

Compression testing of polymeric composite materials is extensively reported in the literature. However, the present review is limited to the testing of material in GRP pultruded structural profiles.

Design manuals prepared by manufacturers of the pultruded GRP structural profiles provide values for the compressive properties of pultrudes (Strongwell, 1989). These properties are the minimum values representing a group (members with similar constituents, fibre volume fractions and material configurations) of pultrudes and are intended to be used for structural design purposes. These properties have been measured in accordance with ASTM D695[‡‡] standard test using coupons cut from the

[‡‡] ASTM D695: "Standard Test Method for Compressive Properties of Rigid Plastics."

pultruded profiles and physically testing them in the lab. The manufacturers tend not to publish the test data, details of the size of the material specimen tested, stress-strain curves, failure modes or details of any statistical analyses. In the ASTM D695 test, a rectangular prismatic material specimen is loaded in axial compression. A steel fixture (called as compression tool) holds the specimen vertically and facilitates the axial load application. The steel fixture transfers the compressive force directly to the end faces of the test specimen (end loading). Specimen ends should be squared and kept parallel with the platens of the compression machine for uniform loading. This test is basically approved for rigid plastics and a thick prismatic specimen (length is twice the principal width) is recommended (ASTM D695M-91)[§§]. For thinner specimens (3mm or less) a supporting jig is required or a different specimen shape is used. This method is not recommended for resin-matrix composites reinforced with oriented continuous, discontinuous or cross-ply reinforcements (Note 1 in the ASTM D695M-91). In the absence of a standard test method for pultruded material, different researchers have used different test methods.

Mottram (1991) measured the compressive properties of pultruded GRP I-beams (102×51×6.6mm). Short parallel-sided and parallel-ended (nominally 40×20×6.6mm) material specimens obtained form flanges and webs of I-beams, were compressed between parallel high strength steel platens (end loading). No compression tool was used. The stroke rate of the compression machine was kept at 0.01mm/s. The measured ultimate compressive strengths in longitudinal direction were much higher than given in the design manual (design value). However the longitudinal ultimate strengths for web-specimens were lower than for the flange specimens (depending on fibre volume fraction). In the transverse direction, measured compressive stresses were close to the design value. Failure modes were undesirable (not within the central gauge length) and most specimens failed with end crushing or brooming (splitting of CFM layers and unidirectional roving). Transverse specimens (51mm long instead of 40mm) failed in a mixed mode of end crushing, brooming and buckling, giving a lower ultimate load. The specimens were obviously not restrained against end

---

[§§] ASTM D695M-91: "Standard test Method for Compressive Properties of Rigid Plastics [Metric]." (Revised in 1991).

brooming in the absence of compression tool. Neither compressive stress-strain curves nor information as the measurement of compressive moduli were reported.

Turvey (1992) used the ASTM D3410*** method to measure the compressive properties of GRP pultruded plate. A flat strip of material having a constant rectangular cross-section cut from the pultruded sheet was used as a test coupon. The test coupon was inserted in a steel fixture with a pair of rectangular steel wedge-grips at each end. The fixture (gripping the specimen) was placed vertically between the platens of the testing machine and loaded in compression. The compressive load was introduced into the coupon through shear at the wedge grip interface. Three sets of specimens with widths 15mm, 25mm and 35mm and lengths of 140mm to 155mm and a thickness of 6.4mm were tested in this study. Gripping length was 65mm on each end leaving a central gauge length of 10 to 25mm. Aluminium tabs, 1.5mm thick, were bonded on both sides gripping lengths to avoid crushing under the compressive action of the grips. The coupons failed within the gauge lengths as required. Both compressive stresses and moduli were measured and reported. The method uses a specially designed fixture and wedge grips, the latter requiring a high level of technical skill to avoid wedge-seating problems (ASTM D3410). The method may be expensive if specimens with different thickness are required to be tested, as for every thickness, separate grips are needed. Another disadvantage is the use of long specimens, which are not always possible to cut from pultruded profiles due to dimensional constraints. Fixing of aluminium tabs is a technical and time-consuming process, which may further increase the expense of the test methodology. For thicker specimens high transverse compressive stresses applied on the surfaces of the tabbed specimen can introduce errors in the results.

Wang and Zureick (1994) used ASTM standard D3410 to determine the compressive properties of GRP pultruded WF-beams (102×102×6.4mm size), with one exception; the width of the coupon was 38mm as opposed to the maximum 25mm width given in the standard. The decision to use a wider coupon was based on a study made by the same authors (Wang and Zureick, 1994A) to measure the tensile properties of the same material. Longitudinal compressive strain in the coupon was measured using a

*** ASTM D3410: "Standard Test for Compression properties of Polymer matrix Composite Materials with Unsupported Gauge Section by Shear Loading."

single uniaxial extensometer, which was removed at a stress level of about one-half of the expected ultimate strength, to avoid damage. Compressive moduli were estimated from stress-strain curves (not up to failure loads) for the coupons, while the ultimate strength was calculated from the load recorded by the machine at failure of the coupon. A similar study using the ASTM standard D3410-95M (revised counterpart of D 3410) method to determine longitudinal compressive properties of pultruded GRP I- and box-beams has been reported by Zureick and Scott (1997). Prismatic material coupons, whose lengths (not given) were determined from the classical stability analysis to avoid buckling, were used in this study. During preliminary tests, tabs were found unnecessary and coupons were tested without tabs using hydraulic grips. Coupons failed within the gauge lengths confirming to the desired mode of failure.

Tomblin (1994) measured the compressive properties of pultruded GRP cylindrical rods using a non-standard end loading method. The cylindrical specimen was encircled by a steel ring attached to the bottom plate of a compressive testing machine to position the specimen for axial loading and to confine it against end brooming. The steel ring was not thick and whole length of the specimen acted as the gauge length. The appropriate specimen length was calculated using the classical formulation for global buckling, with a safety factor of two. Favourable failure modes (failure in the central gauge length) were obtained. Tomblin (1994) observed that the method used for a specific compression-testing programme depends upon the objective of the particular investigations and no universally accepted test configuration exists for characterising the compressive properties of composite material.

Mottram (1994) tested GRP pultruded sheet (6.4mm thick) using a non-standard method, as none of the existing standard methods has been specified for the pultruded material. A special test rig was designed for the axial compression of a flat rectangular material specimen on its ends (end loading), essentially a modified version of compression rig used by Barker and Balasundaram (1987) and Haeberle and Matthews (1990) to measure the compression properties of carbon fibre reinforced plastics (CFRP). The salient features of the test rig are shown in Fig. 2.8. A high precision die set consisting of two (one upper and one lower) parallel plates, comprises the rig. The lower plate is fixed while the upper plate can move in the vertical direction, guided by four vertical columns using linear bearings to ensure

frictionless and concentric loading. Each plate is fitted with an adjustable mounting block into which either end of a rectangular straight-sided specimen is inserted. The internal faces of the adjustable mounting blocks are smooth enough to minimise the transmission of any transverse load to the specimen and also confine the specimen avoiding end-brooming and end splitting. The die set is fixed (screwed) to the lower platen of the compression-testing machine while load is applied at the centre of the top plate. The GRP specimens used were 70mm long, 20mm wide and 6.4mm thick. Of the 70mm overall length, 25mm on each side is inserted in mounting blocks leaving on open gauge length of 20mm. Strain gages were bonded to the specimen at the centre of gauge length to measure the compressive strain. Some specimens were strain gauged on both sides to enable the identification of any bending or buckling.

Typical stress strain curves, measured compressive properties, failure modes and statistical analyses are included in the paper. The measured compressive strengths using more than fifty coupons obtained from the same GRP material (sheet) in longitudinal direction range from 210 to 343 MPa. This large range of scatter in the strength values has been attributed to the non-homogeneous placement of roving bundles in the material. The author (Mottram 1994), suggested that five specimens in a batch required by the ASTM D3410 are not enough to estimate a representative value of the material property and that the test method used in this study (other than the ASTM standards) is equally valid method.

The test method proposed by Mottram (1994) has the following advantages:

1. Simple and shorter rectangular prismatic material specimens
2. No tabs, adhesives or time consuming preparation procedures required
3. No expensive wedge shaped grips or size dependent fixture required
4. Specimen ends directly loaded in axial compression. Hence no introduction of transverse compression into the strain measuring (gauge-length) area
5. Simple die-sets to insert specimen, which is screwed to base platen of compressive machine to ensure alignment for axial loading.
6. Adjustable mounting block to accommodate variable specimen thickness.
7. Free and frictionless vertical movement of the top plate guided by four posts, using linear bearings, ensure concentric loading

8. Screw-tight lateral supports to confine the specimen and avoid end brooming.

2.6 IN-PLANE SHEAR PROPERTIES

ASTM Designation D5379/D5379M-93[†††] is the standard test method recommended for the determination of in-plane shear properties of the composite materials reinforced by high modulus fibres. Note 1 of the designation D5379/D5379M-93 states

"The shear test concept was originally developed without reference to fibre direction for use on isotropic materials such as metals or ceramics."

The method, originally introduced by Iosipescu (1967), can produce failure of specimen under the action of pure shear stresses, with maximum and uniformly distributed values of shear strains at the central test section. The test has been successfully used for measuring shear properties of steel, aluminium alloys and welds (Iosipescu, 1967). Rectangular specimens cut from the metals were loaded in pure shear through a specially designed steel fixture. The original specimen used by Iosipescu was notched on all four sides and through an extensive photo-elastic study, the author found a region of maximum and uniform pure shear stress in the central test section (Iosipescu, 1967, Herakovich and Bergner, 1980).

In 1977 the Composite Materials Research Group of the University of Wyoming USA adopted the procedure to test composite materials. A double v-notched rectangular coupon was used for the measurement of the shear properties of the composite materials with and without fibre reinforcements (Walrath and Adams, 1983). The schematic of the test coupon and fixture used by the group is shown in Fig. 2.9. The test configuration (coupon geometry and fixture loading) achieves a state of pure shear loading at specimen mid-length by application of two counteracting moments produced by two force couples. These moments exactly cancel each other at the mid-length of the specimen producing a pure shear loading state. The shear force and moment diagrams of the schematic demonstrate a region of pure shear at the centre (Fig. 2.10). With the introduction of 90-deg notches on both longer sides of the test specimen, the shear-stress distribution across the middle cross-section is altered from

---

[†††] ASTM D 5379/D 5379M-93: "Standard test method for Shear Properties of Composite Materials by the V-notched Beam Method."

the parabolic shear-stress distribution (evidenced in constant cross-section beams) to a constant shear-stress distribution. The notches do not cause any stress concentration at the centre, as the sides of the notches are parallel to the normal stress directions at that point in the specimen (Walrath and Adams, 1983). Therefore the shear stress distribution at the central cross-section is simply equal to the shear force divided by the net cross-sectional area between the notches. Also, the notches create a central test section with a minimal cross-sectional area, where failure may occur due to maximum shear stresses. The test was applied to measure the shear properties of a wide variety of the composite materials, ranging from unidirectional reinforced glass/epoxy and graphite/epoxy to chopped-glass fibre-reinforced polyester sheet moulding components (SMC), and even materials such as wood and foam.

Sleptz et al (1978) adopted a slightly different loading scheme (Fig. 2.11) to test a similar double v-notched composite material coupon and adopted the title 'asymmetrical four-point bend (AFPB) test'. The fixture is simpler than the Wyoming fixture, but under this arrangement the induced shear stress depends on the location of the loading-points. The test was subjected to numerical analysis using finite element method to investigate the effect of notch geometry on the shear stress distribution achieved at the central notched section of the coupon. It was found that 90-degree notches produce a maximum and uniform shear stress distribution at the mid-section. The experimental study was also conducted to compare with numerical predictions for different notch geometries. Ultimate shear strengths were not achieved experimentally due the material failure under the loading points. The test was used to measure the shear stiffness of many composites with different lay up configurations. Although, the test fixture is simple in fabrication and use, but is limited to the determination of shear modulus only.

Herakovich and Bergner (1980) used an alternative loading arrangement (Fig. 2.12). The ends of a flat rectangular double v-notched composite coupon are gripped (either bolted or bonded) in steel fixture and then loaded in tension. The Finite element method was used to investigate the suitability of this arrangement to measure the shear properties of composites with different lay-up configurations ([0], [0/90], [±45] and [0/90/±45]). It was numerically established that a uniform, pure shear region exists in the test section of a flat v-notch coupons, and a laminate with fibres parallel to the axis between the notches is most desirable for determining the ultimate shear

strength (showing pure shear failure mode) of unidirectional materials. The findings are in agreement with those of Slepetz et al (1978).

Adams and Walrath (1987) made a detailed finite element study of the Wyoming test (Walrath and Adams, 1983) to investigate the stress states in the specimen under the influence of the specific test fixture configuration. The influences of coupon parameters including notch depth, notch angle, and notch-root radius were also investigated. Finite element analyses indicated that the shear stress distribution was heavily concentrated near the edge of the notches, even though the loading surfaces were flat and extended over a considerable length remote from the notch. The normal stresses in the specimen length direction were low, indicating minimal bending effects, but the normal stresses in specimen width direction, induced by the inner load points did intrude into the gauge section. As a result, in the redesign, these loading points were moved outward. Another disadvantage considered was the use of a relatively small specimen. The small specimen meant that the region of constant shear strain between notches was small, thus making shear strain measurement more difficult. Also loading of a specimen in a small fixture was difficult, and the specimen was not fully exposed for inspection during a test. It was decided to increase the specimen size by 50 percent in the redesigned (termed 'second version') Wyoming fixture. The finite element investigations for optimum specimen geometry concluded that for orthotropic materials, the greater ($< 90°$) notch angle reduced the notch-root shear-stress concentrations. However, the effect was not significant for unidirectional composites. Furthermore, the greater the notch angle, lead to a reduction in the notch depth and hence the uniform distribution of the shear stresses in the notched section. A notch depth equal to 20 to 25 percent of coupon-width, with a notch angle of 90-deg was recommended. The analysis also demonstrated that the stress state obtained with an Iosipescu shear test is truly pure shear in the test region, and that the test is a viable method of measuring both shear strength and shear modulus of anisotropic as well as isotropic material. No experimental studies were included to produce test data using the redesigned coupon and fixture for comparison with the original Wyoming test configuration. However, the revised version of the Wyoming test configuration is now the part of the ASTM standards for the measurement of shear properties of the composite materials (ASTM D5379/D 5379M-93).

Lee and Munro (1986) evaluated different in-plane shear test methods for advanced composite materials by the decision analysis technique, considering many factors including cost of fabrication, cost of testing, producibility of the test and accuracy of experimental results. The Iosipescu test method has been rated as one of three best testing methods been used for the composite materials.

A detailed numerical and experimental investigation was conducted by Spigel et al (1987), to analyse and compare the performance of Wyoming and AFPB loading-fixtures with respect to loading positions, notch angles and notch-root radii. A linear-elastic finite element analysis was used to demonstrate that both the Iosipescu and AFPB shear test produce a region of uniform shear stress in the central notched section. Notch geometry and load locations were found to significantly influence the magnitude and the uniformity of the shear stress in this region. The findings are similar to those of Sleptz et al (1978). Experimentally, a 90° (without radius) notch gave the best results with both fixtures. It was concluded (most important from this study's point of view) that the Iosipescu and AFBP test fixtures are essentially the same test with the difference that in AFPB test, induced shear stress at the notched section is a function of the loading point location. The criterian for the selection have been the time and cost spent for preparation and test and the simplicity and ease of its use. The authors found the Iosipescu fixture was difficult to use because of the necessary strict dimensional tolerance to prevent bending of the specimen. The AFBP fixture was found to be easier to use, to provide greater exposure of the test section for monitoring and measuring the strains, but required tabs to prevent crushing of the specimen under the round loading rods. Abdullah and Gsacoigne (1989) concluded that even the revised (modified) version of Iosipescu fixture produced large undesirable bending in the specimen, where as, the AFPB fixture gave a symmetric distribution in the gauge section.

ASTM shear coupon and Wyoming fixture has been used by many researchers in the determination of shear properties of pultruded GRP structural profiles. Bank (1990) used the second version of Wyoming test fixture (Fig. 2.9) to measure the shear modulus and ultimate shear strength of specimens extracted from pultruded glass-fibre reinforced wide-flange beams. Shear strains were measured using three element strain rosettes. From the plots of stresses and strains, shear properties were measured. Sonti and Barbero (1995) measured the shear properties (modulus and ultimate

strength) of pultruded composite (GRP) I-beam material using the Iosipescu test method. Coupons (ASTM standard size) were cut from the flanges and webs of the I-beam. Strains were measured using ±45-degree two-element strain gauges bonded at the centreline of the coupon between the notches. Graphs between applied shear stress and measured shear strain were plotted to abstract the shear properties. A considerable amount of scatter in the results was found which was attributed to the fact that test area was very small and material was not uniform. The use of an asymmetric four-point bending test is reported by Zureick and Scott, (1997) to measure the shear properties of pultruded GRP I- (102×102×6.4mm and 152×152×9.5mm) and box-sections (76.2×76.2×6.4mm and 102×102×6.4mm). The test was performed in accordance with ASTM D5379 with one notable exception; the coupons used were bigger than given in the standard. The bigger coupons were used to account for the degree of inhomogeneity of pultruded material. Tests were performed on coupons measuring 203mm in length and 38 mm in width with a 90° notch at mid-span of the longer sides to a depth of 6.4mm. The in-plane shear modulus was taken as the chord modulus for the region between 1,000 and 6,000μm (as required in ASTM procedure) on the stress strain curve.

It is concluded from the above discussion that a double V-notched shear coupon is capable of measuring in-plane shear properties of the composite materials. Size of a standard shear coupon has been recommended in the ASTM designation D5379/ D5379M-93, and should be adopted where ever available. Further, different sizes of test coupon can be adopted depending upon the degree of non-homogeneity and size of the section available. However, the suitability of other sizes may be established using theoretical or experimental investigations. Numerical investigations have been opted by many others as parametric analysis may be performed using these techniques. Many researchers have successively used this coupon configuration for the experimental measurement of shear properties of the pultruded materials. It has also been demonstrated that Iosipescu and AFBP shear fixtures produces the similar pure shear loading and stress distribution at the central test section of the v-coupon. However, doublers (tabs) have been recommended to avoid the material crushing of the coupon under the fixture's loading points.

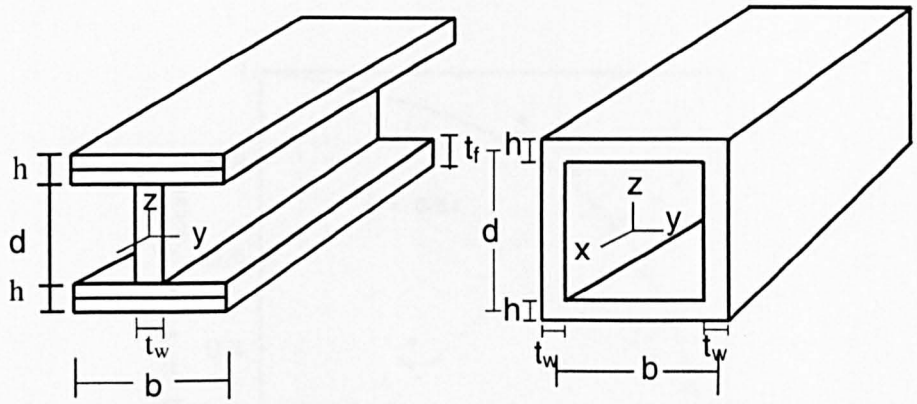

Fig 2.1 Typical I- and box-sections with co-ordinate system.

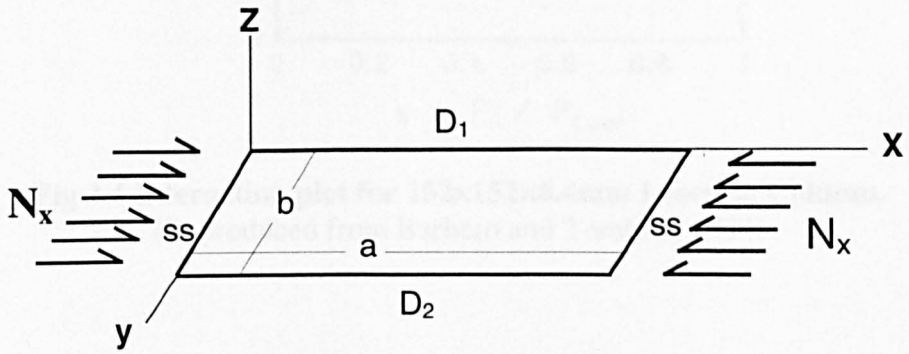

Fig 2.2 Flange of I- or box-section modelled as orthotropic plate

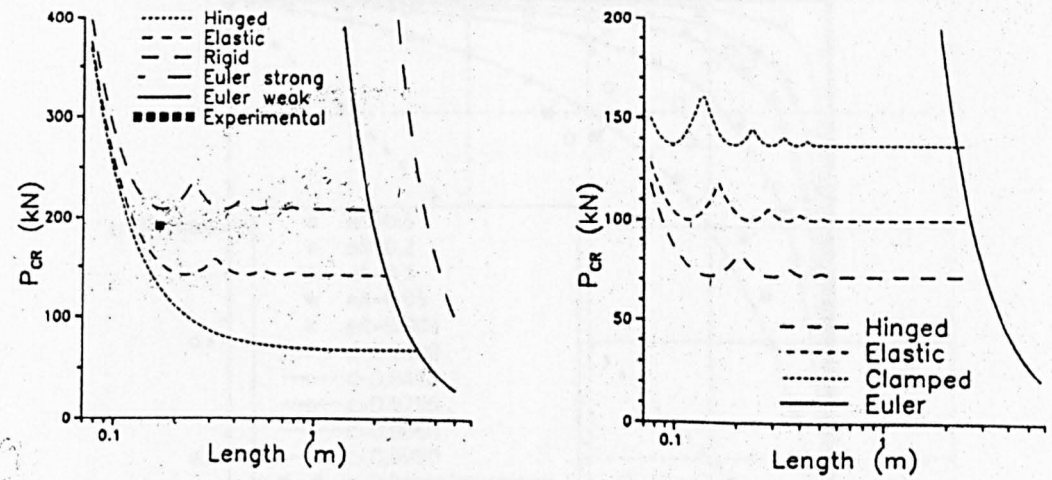

(a) **(b)**

Fig. 2.3. Failure envelopes (a) 152×152×6.4mm I-beam, Euler strong and weak curves represent buckling loads with respect to strong and weak axes of the column respectively (b) 102×102×6.4mm Box-beam.
(Reproduced from Barbero and Raftoyiannis, 1990).

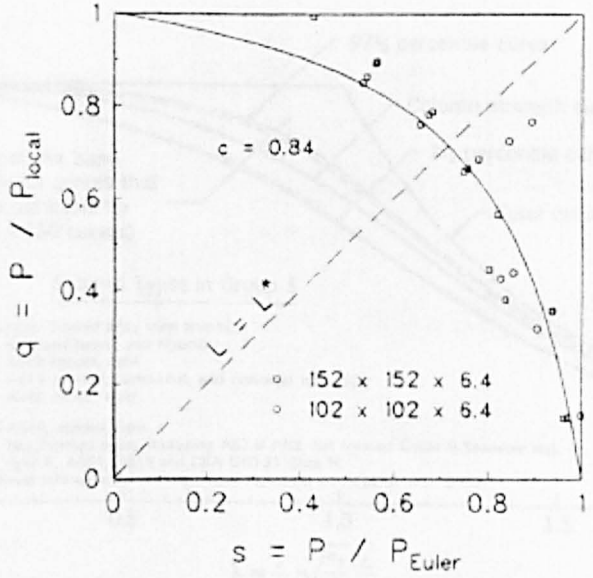

Fig 2.4 Interaction plot for 152×152×6.4mm I-section Column.
(Reproduced from Barbero and Tomblin, 1994)

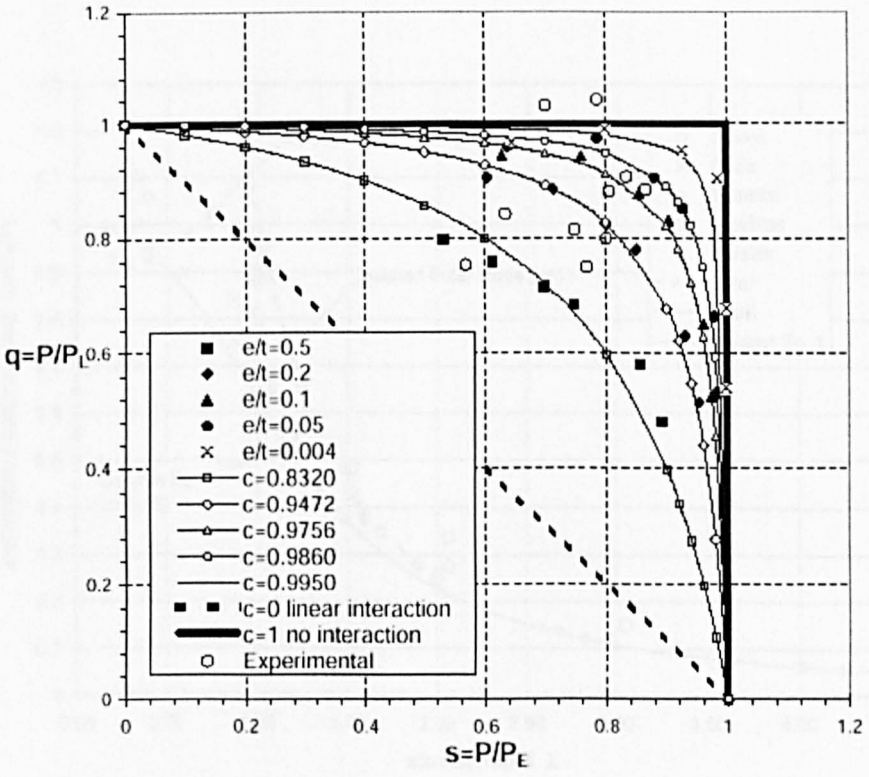

Fig 2.5 Interaction plots for 152×152×6.4mm I-section columns.

(Reproduced from Barbero, 2000)

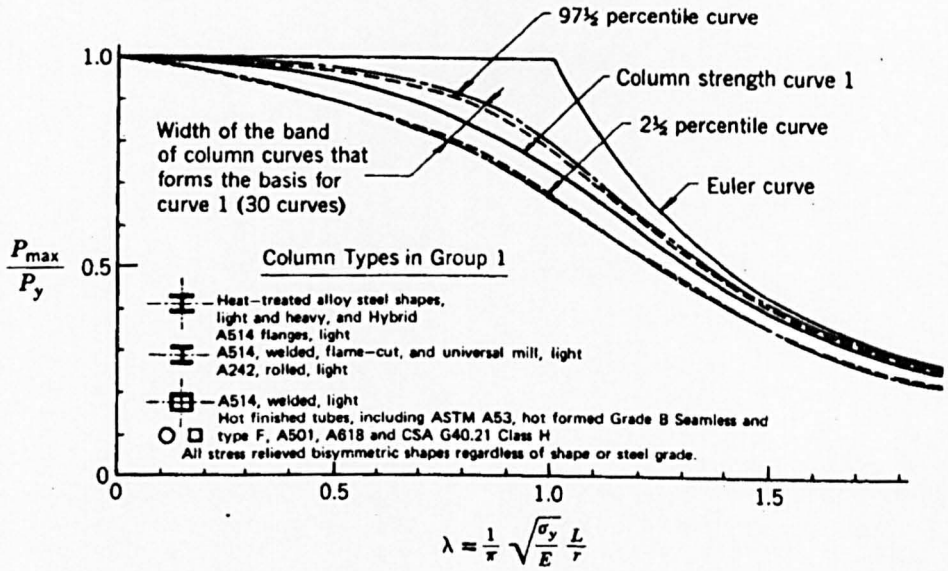

Fig. 2.6 SSRC column strength curve 1 for structural steel.
(Reproduced from Galombos, 1998)

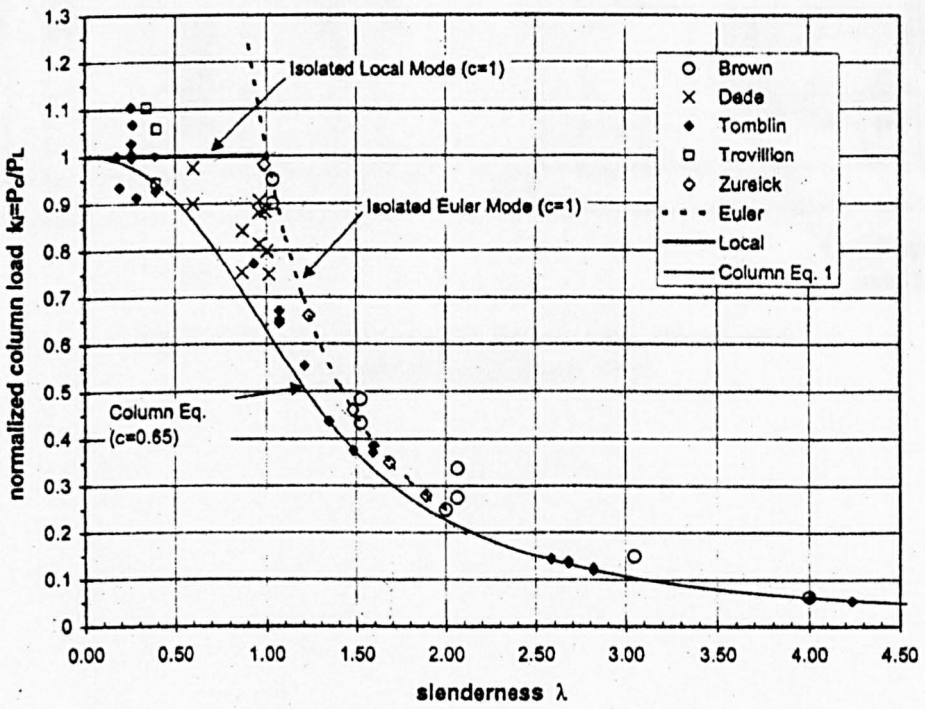

Fig. 2.7 A typical design curve for concentrically loaded pultruded I-section.
(Reproduced from Barbero and DeVivo, 1999)

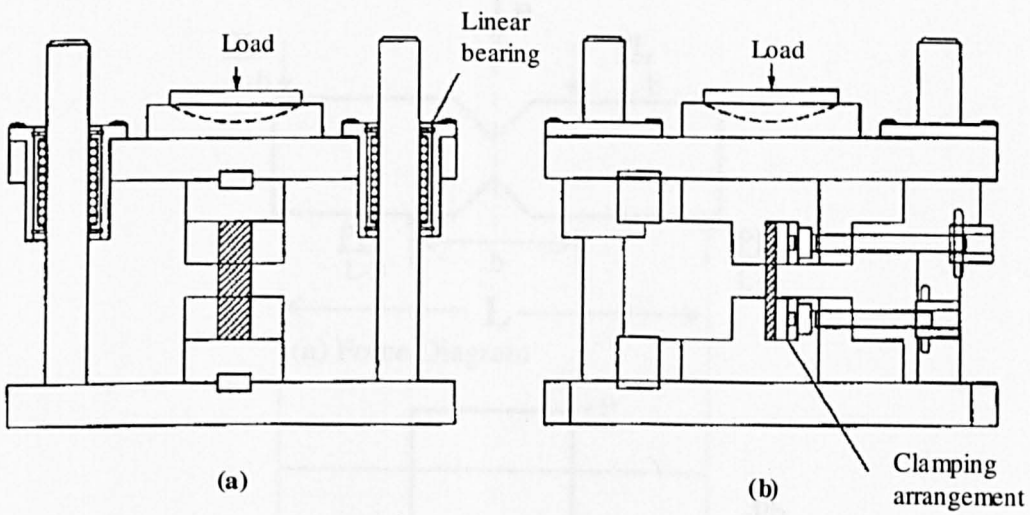

Fig. 2.8 Compression testing rig (a) front view; (b) side view.
(Reproduced from Mottram, 1994)

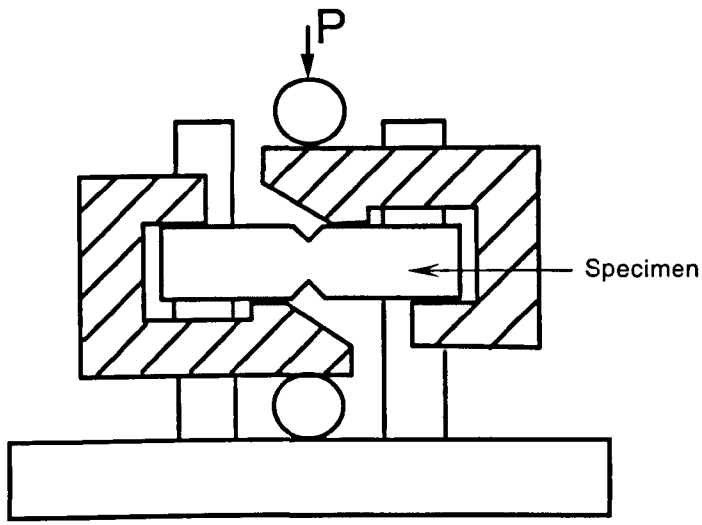

Fig. 2.9 Schematics of the Wyoming group shear fixture with shear coupon
(reproduced from ASTM D5379D/D 5379M)

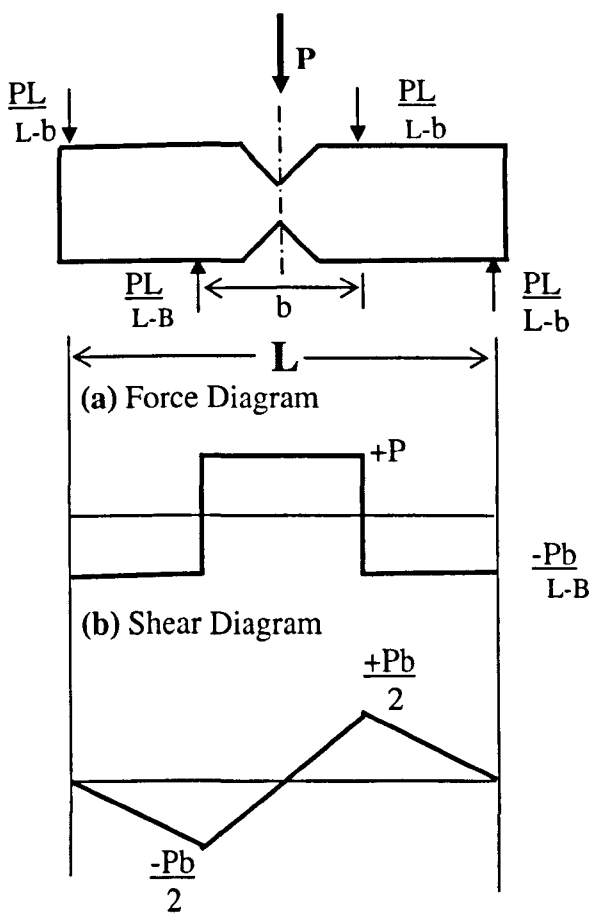

Fig 2.10 Idealized force, shear and moment diagrams for shear coupon loading
(reproduced from ASTM D 5379/D5379M)

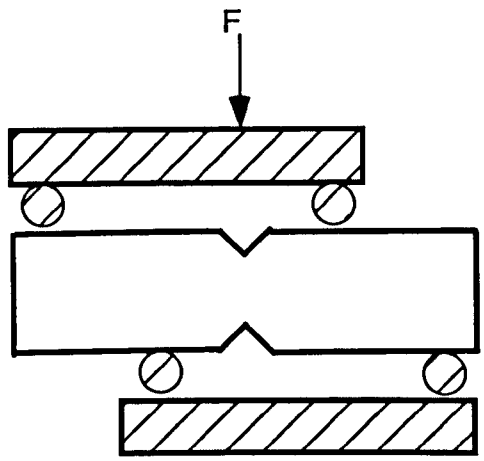

Fig. 2.11 Schematics of AFPB Shear fixture with ASTM shear coupon.

(Reproduced from Walrath and Adams, 1983)

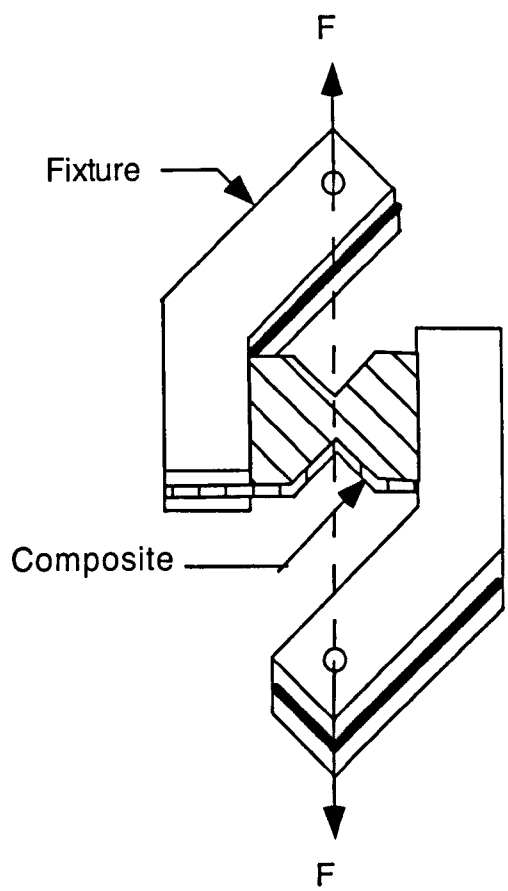

Fig. 2.12 Schematics of a tensile load steel fixture with double v-notched coupon.

(Reproduced from Herakovich and Bergner, 1980)

CHAPTER 3

DETERMINATION OF MATERIAL PROPERTIES

3.1 INTRODUCTION

Material properties of two pultruded GRP box-section structural profiles have been established analytically and experimentally. Analytically, four orthotropic material constants (E_x, E_y, G_{xy} and ν_{xy}) have been estimated using micromechanics and classical lamination theory. Coupons extracted from the sides (walls) of two GRP box-sections (51×51×3.2mm and 44×44×6mm) have been tested in the laboratory to measure these properties.

In-plane shear properties (modulus and ultimate strength) have been measured in both longitudinal and transverse directions using the V-notched beam method (ASTM D5379M-93). A standard (ASTM) shear-coupon (76×20mm) is available only in the longitudinal direction due to dimensional constraints. A short coupon, similar in geometry to the standard ASTM coupon, is proposed to measure the transverse properties. The most appropriate geometry of the proposed short coupon has been established from a parametric (geometry) study using the finite element method (FEM), with the best geometry defined as that with the most uniform shear strain distribution at the central test section of the coupon. For comparison, FEM models of the standard ASTM shear coupon have also been analysed for shear strain distribution across the central section.

Asymmetric four point bending (AFPB) steel fixtures have been developed to load the ASTM and short coupons in shear. Longitudinal properties of the materials have been measured experimentally using standard and short coupons in the longitudinal direction for validation against the short coupon performance. Once validated through comparison of numerical and experimental evidence, short coupons have been used to measure the transverse material properties.

Compression properties have been measured using material coupons in the longitudinal direction only. The tests were performed by Mottram using a specific compression test rig (Mottram, 1994). Tensile properties have been assumed equal to compression properties (Bank et al 1994, Zureick and Scott 1997).

3.2 THEORETICAL PREDICTIONS

GRP box-sections (Plate 1.5) manufactured by the pultrusion process comprise fibres and fibre mats (impregnated in resin matrix) arranged in layers. The box-sections consist of four composite walls (webs), having the same material architect and layer thickness. The typical layer architect of the two pultruded GRP box sections (51×51×3.2mm and 44×44×6.0mm) is shown in Fig. 1.1. Theoretically, each wall has been simulated as a laminate (laminated plate) of specified thickness, consisting of a number of laminae or plies (thin layers) with varying thicknesses and properties (Barbero 1991, Davalos et al 1996, Nagaraj and GangaRao 1997). Mechanical properties of the GRP material (of box-sections) depend on the properties of the fibres and matrix, fibre volume fraction, and the architecture of fibres in the laminae. The fibre volume fraction in each lamina is the ratio of volume of fibres present to the total volume of lamina. Details of the architect, types and amount of fibres, and fibre volume fraction in each layer, for the box-sections, under investigation, have been provided by Mottram (1999). These details have been used to calculate the weight of fibres and matrix (per meter), fibre volume fractions, layer thickness, for each lamina (layer), and are presented for 51×51×3.2mm and 44×44x6.0mm box-sections in Tables 3.1-3.2. The mechanical properties of the constituent materials i.e., glass-fibre and the vinylester matrix, (Fibreforce Ltd) are given in Table 3.3.

MICROMECHANICAL APPROACH

In micromechanics each wall of the cross-section has been assumed as a laminate formed by combining a number of thin laminae. A lamina either contains unidirectional roving or randomly oriented filament mats combined using a matrix. A layer with unidirectional fibres as reinforcement exhibits orthotropic properties (e.g. plane roving), whilst a lamina containing fibre mats behaves as isotropic (e.g. veil, CFS, and MRS layers in Fig. 1.1). For each layer, Young's modulus in the longitudinal direction (fibre direction) has been denoted by E_x, in the transverse (normal to fibre direction) by E_y, the major Poisson's ratio by ν_{xy}, and the in-plain shear modulus by G_{xy}. For a unidirectional (plane roving) layer, E_x, E_y, ν_{xy} and G_{xy} are calculated from equations 3.1 (Jones 1975).

$$
\begin{aligned}
E_x &= (V_f \times E_f) + (V_m \times E_m) \\
E_y &= \frac{(E_f \times E_m)}{[(V_f \times E_m) + (V_m \times E_f)]} \\
\nu_{xy} &= (V_f \times \nu_f) + (V_m \times \nu_m) \\
\nu_{yx} &= \frac{E_y \nu_{xy}}{E_x} \\
G_{xy} &= \frac{(G_f \times G_m)}{(V_m G_f + V_f G_m)}
\end{aligned}
\tag{3.1}
$$

where V_f is the fibre volume fraction and E_f the elastic modulus of fibres along x-axis, V_m the volume fraction and E_m the elastic modulus of matrix, ν_f and ν_m are the Poisson's ratio of the fibres and matrix, G_f and G_m are the shear modulus of the fibres and matrix respectively. Using the information provided in Tables 3.1-3.2, and Table 3.3, the material properties for the plain roving (PR) lamina have been calculated and are reported in Table 3.4. The outer layer 'veil' contains polyester fibre (instead of glass fibres), added for the protection of the outer surface, and assumed not to contribute towards the stiffness. It has, therefore, been excluded from the calculations.

CFM and MSR laminae are made up of continuous filament mats in which fibres are randomly oriented. They are, therefore considered isotropic layers. Approximate mechanical properties for these layers have been computed using the following equations derived by Akasaka (1974):

$$
\begin{aligned}
E &= \frac{3}{8} E_x + \frac{5}{8} E_y \\
G_{xy} &= \frac{1}{8} E_x + \frac{1}{4} E_y \\
\nu &= \frac{E}{2G} - 1
\end{aligned}
\tag{3.2}
$$

Where E_x and E_y can be determined by the mechanics of materials approach given in (3.1). Substituting the appropriate values from Tables 3.1-3.2 into (3.1) and using these results in (3.2), the isotropic elastic properties of the CFM and MSR layers have been calculated (Table 3.4).

Having estimated the material properties of each lamina using micromechanics, classical lamination theory 'CLT' has been used to evaluate the laminate properties. The main assumptions made in micro-mechanics approach are:

- the laminates consists of perfectly bonded layers (laminae),
- each layer is a homogeneous material with known effective properties,
- properties of a layer can be isotropic, orthotropic, or transversely isotropic.
- each layer is in a state of plane stress.

It is recognised that the ensuing equations relate only to state of plane stress and not bending. In the latter case the positions of the layers with respect to a neutral axis would need to be used to define an equivalent bending stiffness. However, the material property estimates derived here are to be used in a finite element simulation in which facets are used to construct the complex box section. Global bending associated with overall buckling is fully represented by this approach. Local buckling in which a facet of the section deforms is approximated in the post-buckling range, and fully simulated in the pre-buckled state. As the latter is the focus of this research, the proposed CLT approach is appropriate, therefore. This also applies to the adoption of experimentally obtained plane-stress elastic constants.

The stress-strain relation for a single orthotropic lamina in a state of plane stress where the principal material axes are aligned with the *x-y* system can be derived from the generalised form (Jones, 1975) as:

$$\begin{Bmatrix} \sigma_x \\ \sigma_y \\ \tau_{xy} \end{Bmatrix} = \begin{bmatrix} Q_{11} & Q_{12} & 0 \\ Q_{12} & Q_{22} & 0 \\ 0 & 0 & Q_{66} \end{bmatrix} \begin{Bmatrix} \varepsilon_x \\ \varepsilon_y \\ \gamma_{xy} \end{Bmatrix} \tag{3.3}$$

where the stiffness components $Q_{11}, Q_{12}, Q_{22}, Q_{66}$ are given by engineering constants of the laminate in three mutually orthogonal directions as:

$$Q_{11} = \frac{E_x}{1-\nu_{xy}\nu_{yx}}, \quad Q_{22} = \frac{E_y}{1-\nu_{xy}\nu_{yx}}, \qquad Q_{12} = \nu_{xy}Q_{22} = \nu_{yx}Q_{11}, \quad Q_{66} = G_{xy} \tag{3.4}$$

The strain-stress relations in terms of compliance ($[S]=[Q]^{-1}$) are given by,

$$\begin{Bmatrix} \varepsilon_x \\ \varepsilon_y \\ \gamma_{xy} \end{Bmatrix} = \begin{bmatrix} S_{11} & S_{12} & 0 \\ S_{12} & S_{22} & 0 \\ 0 & 0 & S_{66} \end{bmatrix} \begin{Bmatrix} \sigma_x \\ \sigma_y \\ \tau_{xy} \end{Bmatrix} \tag{3.5}$$

where the compliance components S_{11}, S_{12}, S_{22}, S_{66} in terms of engineering constants are,

$$\begin{aligned} S_{11} &= \frac{1}{E_x}, & S_{22} &= \frac{1}{E_y}, \\ S_{12} &= \frac{\nu_{xy}}{E_x} = \frac{\nu_{yx}}{E_y}, & S_{66} &= \frac{1}{G_{xy}} \end{aligned} \tag{3.6}$$

The engineering properties (E_x, E_y, ν_{xy}, and G_{xy}) of the section-wall (laminate) are computed by assembling the stiffness coefficients Q_{ij} (of laminae) into the extensional stiffness matrix $[A]$ (extending the single lamina case to N laminae). The coefficients A_{ij} of the matrix $[A]$ are calculated as (Jones 1975),

$$A_{ij} = \sum_{k=1}^{N} (\bar{Q}_{ij})_k t_k \tag{3.7}$$

where $i,j = 1,2,6$ and t_k is the thickness of the k^{th} ply.

$[A]$ is the in-plane stiffness matrix relating strains to resultant forces.

Similarly $[S]$ is replaced by $[\alpha]$ with the $[\alpha]=[A]^{-1}$ defined as the compliance matrix of the laminate.

Using the law of micromechanics, the material properties of the laminate of thickness t ($t = \sum_{k=1}^{N} t_k$) are obtained as (Davalos, 1996):

$$\begin{aligned} E_x &= \frac{1}{\alpha_{11} \times t}, & E_y &= \frac{1}{\alpha_{22} \times t}, \\ G_{xy} &= \frac{1}{\alpha_{66} \times t}, & \nu &= -\alpha_{12} \times E_x \times t \end{aligned} \tag{3.8}$$

The stiffness matrix $[A]$ is calculated for 3.2mm thick laminate using the layer properties listed in Table 3.4 as

$$[A]=\begin{bmatrix}89.9 & 13.7 & 0\\ 13.7 & 35.9 & 0\\ 0 & 0 & 12.1\end{bmatrix}$$

and matrix $[A]$ for 6mm thick laminate as;

$$[A]=\begin{bmatrix}197 & 21.2 & 0\\ 21.2 & 63.6 & 0\\ 0 & 0 & 23.6\end{bmatrix}$$

The compliance matrix, $[\alpha]$ which is the inverse of $[A]$, becomes:

for the 3.2mm thick laminate $[\alpha]=\begin{bmatrix}0.0118 & -0.00452 & 0\\ -0.00452 & 0.0296 & 0\\ 0 & 0 & 0.0824\end{bmatrix}$, and

for the 6mm thick laminate $[\alpha]=\begin{bmatrix}0.00529 & -0.00193 & 0\\ -0.00193 & 0.0160 & 0\\ 0 & 0 & 0.0426\end{bmatrix}$

The quantities in the compliance matrix give the box section elastic moduli, E_x, E_y, G_{xy}, and ν_{xy} by using the following equations (Davalos et al 1996).

$$E_x=\frac{1}{\alpha_{11}t}=\frac{1}{0.0118\times 3.2}=27.3\ \text{kN/mm}^2$$

$$E_y=\frac{1}{\alpha_{22}t}=\frac{1}{0.0296\times 3.2}=10.9\ \text{kN/mm}^2 \qquad (3.9)$$

$$G_{xy}=\frac{1}{\alpha_{66}t}=\frac{1}{0.0824\times 3.2}=3.91\ \text{kN/mm}^2$$

$$\nu_{xy}=\alpha_{12}tE_x=(0.00452\times 3.2\times 27.3)=0.38$$

where t = 3.2mm is the box section wall thickness. For the 6mm thick box sections, the elastic constants are calculated as;

$$E_x = \frac{1}{\alpha_{11} t} = \frac{1}{0.00529 \times 6} = 31.5 \text{ kN/mm}^2$$

$$E_y = \frac{1}{\alpha_{22} t} = \frac{1}{0.016 \times 6} = 10.4 \text{ kN/mm}^2 \qquad (3.10)$$

$$G_{xy} = \frac{1}{\alpha_{66} t} = \frac{1}{0.0426 \times 6} = 3.92 \text{ kN/mm}^2$$

$$v_{xy} = \alpha_{12} t E_x = (0.00193 \times 6 \times 31.5) = 0.37$$

The results are summarised in Table 3.4. The outcomes (mechanical properties) of the micro-mechanical study are used as guidelines for the subsequent finite element studies, to analyse the models of short coupons proposed to measure the transverse properties of the composite material.

Table 3.1 Laminae detail of 51×51×3.2mm GRP box-section.

Layer	Weight of Fibre (gm) (W_f)	Weight of Matrix (gm) (W_m)	Volume of fibre (%) (V_f)	Layer volume in wall (%)	Thickness of layer (mm)
Veil	1.05	2.95	24	2.1	0.06
CFM	54.4	67.8	28	49.9	1.61
PR	110	32.8	62	45.8	1.46
MSR	4.8	1.83	56	2.2	0.07

Table 3.2 Laminae detail of 44×44×6.0mm GRP box-section

Layer	Weight of Fibre (gm) (W_f)	Weight of Matrix (gm) (W_m)	Volume of fibre (%) (V_f)	Layer volume in wall (%)	Thickness of layer (mm)
Veil	0.975	2.75	24	1.40	0.08
CFM	57.9	72.0	28	38.5	2.31
PR	194	57.7	62	58.5	3.51
MSR	4.8	1.87	56	1.58	0.10

Table 3.3 Properties of the constituent materials

Material	Tensile Modulus E (kN/mm^2)	Shear Modulus G (kN/mm^2)	Tensile Strength (N/mm^2)	Poisson Ratio ν	Density ρ (gm/cm^3)
E-glass fibres	72 (E_f)	29 (G_f)	3400	0.25 (ν_f)	2.56
Vinyl-ester matrix	3.5 (E_m)	1.6 (G_m)	103	0.35 (ν_m)	1.24

Table 3.4 Calculated material properties for each lamina

Layer	E_x (kN/mm^2)	E_y (kN/mm^2)	ν_{xy}	G_{xy}
CFM	11.5	11.5	0.43	4.01
PR	46.0	8.53	0.29	3.86
SMR	20.4	20.4	0.43	7.11

Table 3.5. Estimated elastic properties of the box-sections

Box-section	E_x (kN/mm^2)	E_y (kN/mm^2)	ν_{xy}	G_{xy}
51x51×3.2mm web or flange	27.3	10.9	0.38	3.91
44×44×6.0mm web or flange	31.6	10.4	0.37	3.92

3.3 IN-PLANE SHEAR PROPERTIES

The shear coupon described in ASTM D5379/D5379M specifications (referred to as the "ASTM coupon" hereafter and shown in Fig. 3.1) is 76mm (3.0 in) long, 20 mm (0.75 in) wide and may be of any thickness up to 12.7mm (0.5 in). The ASTM coupon has two 4mm deep 90° v-notches cut symmetrically along the two longer sides at mid-length. The notches have a dual purpose, creating a test-section (smallest across the notch tips) for failure at the centre, and also converting the parabolic shear stress distribution (typical in a rectangular beam section) to a uniform stress distributed across the test section (Walrath and Adams 1983, ASTM D5379/D5379M-93). The fixture required to hold the coupon in position and to load it in a state of pure shear, should be a four point asymmetric flexure fixture as recommended in the ASTM testing procedure. The fixture described in the ASTM specification was developed by Adams and Walrath (1987) and referred to the earlier work of Iosipescu (1967) and Arcon et al (1978). The coupon loading, using this fixture, has been idealised as asymmetric flexure, as shown by the shear force and bending moment diagrams in Fig. 2.10 (ASTM D5379/ D5379M).

A relatively simpler, more intuitive and easier to fabricate shear fixture has been proposed by Sleptz et al (1978) denoted as the "asymmetric four-point bending" (AFPB). In this type of fixture, the shear loading at the central test-section is not equal to the applied load, but depends upon the distance between the loading points. The main draw back of the AFPB fixture is the specification of round loading bars (Fig. 2.11), which cause local crushing of the coupon edges under high compressive loading.

A similar loading scheme has been adopted for the development of an AFPB type fixture for the present study, keeping in mind the simplicity of fabrication. A detailed sketch of the AFPB shears fixture (made from steel) showing components and dimensions has been provided in Fig. 3.2, and a schematic of ASTM coupon loaded in the AFPB fixture in Fig. 3.3. The round loading bars in the new fixture have been replaced by rectangular broad faced bars to spread the compressive loading over a wider area. The cross-sectional dimensions of the loading bars (and hence the contact area) have been calculated from the expected maximum compressive load (a function of material's shear strength and position of the loading bars) and ultimate compressive

(bearing) strength of the coupon material. The minimum unsupported coupon length at the centre has been kept to 13mm to comply with the recommendations of standard specifications (ASTM D5379/D5379M). The behaviour and performance of the ASTM shear coupon loaded by the proposed AFPB type fixture is investigated using the finite element method.

Finite element models of the ASTM type shear coupon without and with the AFPB fixture are analysed for the shear stress/strain distribution at the coupon's central test section. The validity of the performance of the AFPB fixture is established by examining the stress/strain distribution at the central test section, under a known applied load. The effects of material orthotropy on the shear stress/strain distribution across the central test section are also investigated.

A short shear coupon geometry is proposed to measure the transverse shear properties. Having a similar shape to the ASTM shear coupon, the short coupon has a reduced length of 40mm, constrained by the dimension in the transverse direction of the 44mm box-section. The test section of the coupon should provide a region of pure, uniform shear stress, which is uniquely related to the applied load. The central notched section should also exhibit a uniform and predictable shear stress, whilst stress concentrations due to the load introduction and free edge effects should be minimal in the proposed coupon. The finite element method provides a relatively efficient tool for assessing the configuration of candidate specimens most adequately meeting these requirements. The analysis goes some way to predicting the effects of load locations and notch parameters on the stress/strain distribution across the central notched section of shear coupons. FEM modelling and analysis has been conducted using 'LUSAS', (v.12.3, Finite Element Analysis UK (FEA)). The adequacy and suitability of the short shear coupon has been established by comparing the consistency of numerical results with the predicted distribution of the ASTM coupon. The short configuration is also used to measure experimentally the longitudinal shear properties, in-order to compare and validate the performance of short coupon with the standard coupon. Following validation, short coupons have been used for the experimental measurement of the transverse shear properties of the GRP box profiles.

3.3.1 ASTM SHEAR COUPON AND AFPB FIXTURE

The ASTM shear coupon (Fig 3.1) is a rectangular flat strip of composite material, 76mm long and 20mm wide, with a thickness as received. Two symmetrical centrally located v-notches with a notch depth of 4mm and notch angle of 90° have been cut on the longer sides of the coupon. 'Longitudinal coupons' are those having reinforcing fibres along the length (longitudinal axis) of the coupon i.e., extracted from the box-sections (Plate 1.5) in a direction parallel to the longitudinal axis. 'Transverse coupons' on the other hand have reinforcement parallel to the shorter direction of the coupon (normal to the longitudinal axis) and are extracted width-wise from the GRP box-sections. Both longitudinal and transverse coupons are orthotropic. Four material constants (E_x, E_y, ν, and G_{xy}) are established for their complete characterisation. To investigate the effect of material orthotropy on the behaviour and performance of the ASTM shear coupons, 'isotropic coupons' have also been included in the present investigations. They have been defined by two material constants (E, and ν), whilst G is taken equal to $\frac{E}{2(1+\nu)}$. The isotropic coupons could either be obtained from a composite material mainly made from fibre mats, or from metals.

The asymmetric four point bending (AFPB) fixture developed for the loading of the ASTM coupon is shown in Fig.3.2. The fixture has two loading beams; an upper to which the compressive load 'P' is applied, and a lower providing the reaction to the applied load. The lower loading beam is fixed to the side posts, and rests on a rectangular cross beam to locate the reaction point. The cross beam is clamped to the lower platen of the testing machine. The upper loading beam can move vertically downward under the applied load, guided by groves cut in the side posts. Attached to the loading beams are the rectangular loading bars designed to transfer the compressive forces on to the coupon edges. The bars near the central notch location are referred to as inner loading bars, with those at the extremities as outer loading bars. The location of the inner loading bars is fixed to keep the central 13mm of the coupon length (6.5mm on each side of the notch) unsupported (ASTM standard D5379M-93). This amount of clearance is required to avoid the introduction of effects of vertical normal stresses into the central test-section. The cross-sectional areas of the inner and outer loading bars have been calculated from the maximum expected load (multiplied by a safety factor of 2), the ultimate compressive strength, and the

contact area between the loading bars and the coupon. Inner loading bars have twice the width (10mm) of the outer (5mm), reflecting the relative magnitude of the applied compressive forces. The shear loading applied by the AFPB fixture can be idealized as asymmetric and dependent upon the location of the loading bars with respect to the central notched section (Fig 3.4). The actual load application is "distributed and imperfect" along the contact area of the loading bars (ASTM D5379M-93), contributing to asymmetry in the shear strain distribution. This fact has also been recognised by the ASTM standard for the fixture used in the standard procedure, as:

"While the idealization indicates constant shear loading and zero bending moment in the specimen at the notches, the actual load application is distributed and imperfect, which contributes to asymmetry in the shear strain distribution and to a component of normal stress that is particularly deleterious to [90]n specimens."*

(ASTM D5379/D5379M footnote 9)

However, in the analytical solutions, the load application has been assumed to act through the central vertical axis of the loading bars. Under the idealized loading configuration, the central test section (notched section) is subjected to maximum shear force as the coupon has a minimum cross-sectional area at this section, and further, '*b*' is always less than half the length (*L*) of the coupon (see Fig 3.4). Contact surfaces have been assumed in the numerical representation to simulate the distributed load application.

Finite Element Models

A two-dimensional, surface model of the ASTM coupon has been developed considering plane stress loading (Fig. 3.5). Rectangular, eight node, isoparametric, plane stress elements (QPM8)†, having two translational degrees of freedom *u* and v (i.e., in *x* and *y* directions) at each node have been used. These elements can accommodate curved boundaries, varying thickness and are capable of accounting for membrane and shear deformations. As the loading is asymmetric, the entire *x-y* plane

---

* A laminate with *n* layers having fibres at right angles to the longitudinal direction.

† LUSAS™ element library code.

of the coupon has been modelled. Non-eccentric geometric properties with a thickness equal to the nominal web-thickness of pultruded profiles (3.2 and 6.0mm) have been assigned to surface elements.

Material properties have been assigned to the surface finite elements in x and y directions denoted as the local material co-ordinates. Isotropic material has been simulated as having E=27.3kN/mm^2 and ν=0.38 (Table 3.5). Three types of orthotropic coupons using the estimated material properties (Table 3.4) has been modelled as: a 'pseudo orthotropic'‡ having E_x=E_y=E=27.3kN/mm^2, ν=0.38, and G_{xy}=3.91kN/mm^2; a 'longitudinal coupon' having E_x=27.3kN/mm^2, E_y=10.9 kN/mm^2, ν =0.38 and G_{xy}=3.91 kN/mm^2; and a 'transverse coupon' having E_x=10.9kN/mm^2, E_y=27.3kN/mm^2, ν=0.38, and G_{xy}=3.91kN/mm^2. The longitudinal coupon has been loaded by a shear force in a direction normal to the direction of the fibres whilst the transverse coupon is subjected to a shear force parallel to the direction of fibres.

Boundary conditions simulate a simply supported beam, i.e., the supports (indicated by green arrows R1 and R2 in Fig. 3.5) allow coupon movement in vertical direction (in the direction of applied load), but restrict any horizontal or transverse (in z-direction) movements. For an idealised loading situation (Fig. 3.4), point supports have been considered (Fig. 3.5(a)). Similarly, two point loads, L1 and L2 (Fig 3.5), have been adopted for the simple calculation of the shear force acting at the coupon's mid-section. A regular mesh grid in local x and y directions of the specimen has been used to divide the surfaces into the finite elements. Comparison of un-averaged and averaged nodal stress/strains results has been used to determine the necessary degree of mesh refinement throughout this study.

The FE model of the ASTM coupon loaded in AFPB fixture (Fig. 3.6) comprises the same eight node QPM8 elements. The fixture posts have been ignored in the model as the vertical movement of the upper loading beam has been assumed to be friction free. To simulate coupon-fixture interaction, slide lines 'SL' (indicated by red lines) have been introduced along the contact lines between loading bars and the coupon. One, of the four contact lines, is non-sliding to hold the specimen in position and prevent

‡ Orthotropic properties with zero orthotropy (E_x=E_y) has been assigned to establish the effect of change in shear modulus in isotropic and orthotropic coupons and to validate the adequate performance of the model.

rigid-body motion. This simulates the simply supported boundary conditions of the coupon. The upper loading beam has been assigned side supports (R2 in Fig. 3.6) which allow vertical movement but prohibit horizontal and transverse movements. A fixed support (R1 indicated by green arrows in Fig 3.6), generating a reaction equal to the applied load '*P*' has been assigned to the cross beam supporting the lower loading beam. A compressive point load '*P*' has been applied at the mid position of the upper loading beam, to model the external testing load. Only isotropic linear material properties for the steel fixture have been considered. A similar (to that of coupon) regular mesh grid in local x and y direction has been used to divide the surfaces into elements.

Finite Element Results

A theoretical unit load (P=1kN)[§], has been applied externally to the fixture. The shear force resultant at the central test section of the coupon due the application of this load has been calculated from the shear force diagram (Fig 3.4), knowing the value of 'b' and 'L' (e.g., the distance between idealised lines of load application through the inner and outer loading bars respectively), leading to a theoretical average shear stress distribution. For P=1kN, b=23mm, L=71mm, and thickness t=3.2mm, a shear force (S.F) of 0.51kN has been calculated. Corresponding to this S.F, shear stress and strain has been obtained using simple elastic theory principles (e.g., Hook's law):

$$\text{Shear stress} = \frac{\text{shear force}}{\text{area of the cross - section}} = \tau = \frac{\text{S.F}}{\text{A}} \tag{3.11}$$

$$\text{Shear Strain} = \frac{\text{Shear Stress}}{\text{Shear Modulus}} = \gamma = \frac{\tau}{\text{G}} \tag{3.12}$$

For a S.F of 0.51kN and area A=12×3.2=38.4mm^2, a shear stress of 1.33×10^{-2} kN/mm^2 has been calculated. Because of the rectangular loading bars, load applied by the fixture is different from point loading (Fig. 3.5-3.6), the shear force actually applied by the fixture (for an external load of 1kN) to the coupon's mid-section has

---

[§] As the analysis is linear elastic, an arbitrary value of P has been applied within the elastic range and the ultimate shear strength of the material. Minimum ultimate shear strength of similar pultrates quoted by STRONGWELL is more than 20 N/mm^2. An external load of 1kN produces a shear stress of 13.3N/mm^2 at the central test section (A=12×3.2mm^2) of the ASTM coupon. Shear strains for other applied loads (in the linear range) can be evaluated by simple scaling of the applied load with the numerical results.

been established by the finite element analysis of the testing configuration. The deformed shape of the model (post analysis configuration, Fig 3.6(b)) indicated bending in the upper loading beam under the applied load. Due to this bending, the shear stresses along the lengths of the loading bars are no longer uniformly distributed. The resultants of shear force exerted by each loading bar have been calculated by measuring the shear stress intensities along the length of the bars (at sections L1, L2, R1 and R2, shown in Fig 3.6 (b)) and multiplying by the cross-sectional area of the respective loading bars. A graphical representation of the variation of the shear stress intensities along the loading bar lengths have been shown in Fig 3.6(c). The stress resultants** calculated using the vertical nodal stresses (S_y), gave a shear resultant of 0.51kN and shear stress of 1.33×10^{-2} kN/mm^2 at the central test section, which are equal to the theoretical values obtained from shear force diagram of Fig 3.4. This outcome, indicates (also evident from the graphs in Fig 3.6 (c)) that the stress resultants pass through the centre of the loading bars maintaining the idealised distances 'b' and 'L' (shown in Fig. 3.4). This theoretical shear stress is expected to be constant across the section between the notches (due to the introduction of the notches).

A corresponding theoretical shear strain has been calculated from the shear stress and the estimated shear modulus (from micromechanics and CLT). For isotropic coupons the shear modulus has been taken as $G = \frac{E}{2(1+\nu)}$, whilst for orthotropic coupons G_{xy} is taken as 3.91kN/mm^2 (Table 3.5). Numerical shear strains across the central test section have been obtained from finite element analyses and plotted against the distance between the notch roots at the central test section, measured from the central longitudinal axis of the coupon, positive upward and negative downward.

The shear strain distributions in the entire ASTM isotropic coupon, under the idealised point loading, and for the loading applied by using AFPB fixture, have been shown in Fig. 3.7. The distribution is asymmetric about the axis between the notches (as expected due to asymmetric loading). A contour interval of 0.5×10^{-4} has been used to display the strain distributions in both the loading cases for comparison. For the point loading case (Fig. 3.7 (a)), a higher shear strain (of the order of $\pm2.0\times10^{-3}$)

** Mid section method is used where each nodal stress is multiplied by half the area between two nodes.

can be seen under the point loads which is 1.8 times greater than the numerical and theoretical shear strain (1.15×10^{-3}) at the mid-section of the coupon. This high strain concentration at the points of load application implies possible damage to the coupon edges and produces a premature coupon failure preventing the determination of ultimate shear strength of the material. In the case of loading with the proposed AFPB fixture the intensity of the shear strains under the loading points is less than half (of the order of 0.5×10^{-3}) of the mid-section strains. This justifies the use of broader loading bars in the present version of the AFPB fixture. A central region with uniform shear strain (with no contours i.e., strain variations are less than the contour interval of 0.5×10^{-4}) has been observed in the middle of the coupon. Similar contour plots showing shear strain distributions in the orthotropic coupons have been given in Figs 3.8 - 3.10. To obtain a similar number of contours (for comparison) in a specified coupon area, the contour interval for orthotropic strain distributions is taken as 0.15×10^{-3} (three times of that for isotropic coupon) since the shear modulus of the orthotropic material is nearly one-third of the shear modulus of the isotropic and the range of shear strains obtained is three times larger than in the latter.

Theoretical and numerical (computed using FEM) results agree closely for the isotropic assumption for the majority of the depths of the coupon with a negligible strain concentration at the notch roots (Fig 3.11). The coupon loaded by the proposed fixture produced very similar results to the coupon only model. The quality and uniformity of numerically computed shear strains demonstrate the potential of the AFPB test fixture. This outcome is consistent with the findings of Adams and Walrath (1987), in that 90° notches minimise shear stress concentrations when notch sides are parallel to the direction of maximum shear stress. Pseudo orthotropic coupons also show a close agreement between the theoretical and numerical results for the central 9mm width (± 4.5mm from the longitudinal axis) of the mid-section and a strain concentration of less than 5% at the notch roots. These results also contribute to establishing appropriateness of the finite element model representation of the ASTM coupon.

Similar higher strain concentrations can be seen under the loading points in the case of longitudinal coupons modelled individually and loaded using point loads (Fig. 3.9(a)). For the longitudinal coupons loaded using the proposed AFPB fixture, the magnitude of the strain concentrations under the loading bars is smaller than the

strains at the central test section (Fig. 3.9(b)), anticipating failure in the gauge section. A central region with uniform shear strain (without contours) is indicative of the proper use and validation of the purpose of v-notches in the testing of orthotropic materials. The shear strain distribution is more symmetric and constant over a wider area than obtained in isotropic coupon, establishing the validity of the designed test fixture. However, strain values are slightly higher (7%) than the theoretical strains and larger strain concentrations (28%) have been computed at the notch roots (Fig 3.11). ASTM standard D5379/D5379M states that stress/strain concentrations arise as an effect of the orthotropy of the material and can be minimised by adjusting the notch angle (e.g., see FEA results for notch angle parametric study for small coupon, Fig. 3.20).

Shear strain contours for transverse coupons are illustrated in Fig. 3.10. Strain concentrations can again be seen under the loading points in the case of individual coupon point loading (Fig.3.10(a)). For both the loading cases, the shear strain distribution is constant (no contours are displayed as the variations are less than the contour interval) in the central test section. Sufficient area of constant shear strain at the centre of the coupon is available to accommodate a rosette strain gauge for the experimental determination of shear properties. The shear strain values at the centre are slightly lower (4%) than the theoretical strain values. A higher strain concentration (34%) has been observed in the case of transverse coupon (Fig 3.11)[††].

From the numerical results obtained from finite element analysis of the ASTM coupon model and their comparison with the theoretically calculated values it is predicted that proposed AFPB shear fixture (Fig. 3.2) is capable of testing ASTM shear coupons for the determination of in-plane shear properties (modulus and ultimate strength). The fixture applies a unique shear resultant at the central test section of the test coupon, which can be theoretically calculated by using values of length (L) and loading point separation 'b' and simple shear force diagram (Fig. 3.4). The strain concentrations at the notch roots in the cases of isotropic and special orthotropic coupons are low. Higher strain concentrations in the cases of longitudinal

[††] The ASTM shear coupon in transverse direction is not used in this study owing to geometry restraints. This analysis is only for completeness and validation of the AFPB shear test fixture. A new short coupon to measure transverse shear properties is proposed in the subsequent section.

and transverse coupons are attributed to the orthotropy of the material and not to the fixture's performance. A close agreement between numerical and theoretical shear strain for isotropic and special orthotropic coupons goes some way to validate the performance and behaviour of the designed steel fixture. This validation is used in the subsequent section to design a smaller version of the proposed fixture to test the short shear coupon for the measurement of transverse shear properties.

3.3.2 SHORT COUPON AND FIXTURE

Finite Element Models

Finite element models for short shear coupon and the corresponding (short) AFPB fixtures are geometrically similar to those for ASTM coupon. To maintain a similar aspect ratio, a coupon width of 10mm for a length of 40mm has been adopted. Initially a base model with 90° sharp V-notches and a notch depth of 2.5mm (25% of overall depth) has been modelled (Fig 3.12). Keeping the inner loading bars 2.5mm from either of the notch edges, a length of 10mm at the centre of the coupon remains unsupported (as compared to 13mm in the case of the ASTM coupon), when loaded in the fixture. Another important difference is that the widths of the inner and outer loading bars are identical (5mm) in the case of short AFPB fixture[‡‡] (Fig. 3.13). Correspondingly, the short coupon has supports and loading surfaces all equal to 5mm. For a 5mm width of the loading bars, a loading point separation 'b'=15mm has been obtained. Different loading bars have been used for 3.2mm thick (Fig. 3.13 (b)) and for 6mm thick (Fig 3.13 (c)) coupons. Models of shear coupons with varying notch-angles, notch depths and loading point separations have been developed through variations in the base model.

A two dimensional (2-D) surface model of the short coupon using the isoparametric, rectangular plane-stress elements 'QPM8' has been constructed. The entire coupon has been modelled considering an asymmetric loading (Fig 3.14(a)). The model comprises points, lines and surfaces, defining the geometry of the coupon. Thickness of the coupon has been assigned to the surfaces using non-eccentric geometric

---

[‡‡] The width of loading bars are calculated from the maximum expected applied load (depending on the cross-sectional area of the test section and the shear strength of the coupon) and the compressive strength of the coupon. A width of 5mm for the inner loading bars is found sufficient to keep the applied stress lower than the bearing strength of the coupon material.

properties. Estimated material properties (Table 3.5) have been used to represent the isotropic, pseudo orthotropic, longitudinal and transverse coupons in the similar way as described for the modelling of ASTM coupon material properties. The coupon model has been simply supported using a set of fixed support R1 ($u=0$, $v=0$, $z=0$) and a hinged support R2 ($u=0$, $v\neq0$, $z=0$) to restrain the horizontal movement of the coupon and to allow the vertical displacement due to the applied loads. Point loads L1 and L2 acting vertically downward have been applied at the upper edges of the coupon. A regular mesh in x and y directions, with more refined mesh in the central region of interest, has been assigned to the surfaces. Surface models (2-D) have been used to represent isotropic, special orthotropic and longitudinal coupons.

A finite element representation of a short coupon schematically loaded in the proposed short AFPB fixture is shown in Fig. 3.14 (c). The model is similar to that for ASTM coupon and fixture except the dimensions of the coupon, inner loading bars and fixture size. Similar eight nodded isoparametric rectangular finite elements have been used to construct the model. Slide lines (SL1-SL4) have been introduced to simulate the contact of coupon and loading bars and one of the slide lines has been fixed to avoid the rigid body motion. Rectangular mesh grid, loading and supports (similar to ASTM coupon and fixture model) are shown in Fig. 3.14 (a), and (c). The vertical reactions in the loading bars of the short fixture (Fig. 3.14 (d)) are discussed under the heading "Fixture effect".

Aluminium tabs[§§] have been bonded to the transverse coupons at locations of loading (under loading bars) to avoid compressive failures at sections directly under the compressive loads. The size of the tabs has been calculated from the bearing capacity (maximum compressive strength) of the material in the transverse direction and the maximum expected load. A three dimensional (3-D) volume model has been prepared

---

[§§] Compressive failure of short transverse coupons without aluminium tabs, beneath the loading bars, has been observed during preliminary shear testing. To avoid this type of failure and to ensure a true shear failure at the central test sections, aluminium tabs have been used. The thickness and width of the aluminium tabs were calculated from the expected total load for the shear failure, multiplied be a safety factor of 2, and the ultimate transverse compressive strength of the material. Ultimate transverse strength in tension has been measured for the 51x51x3.2 box section profile by Saribiyik (2000) and taken equal to the compressive strength as stated previously.

using the isoparametric solid continuum elements (HX20***) to represent the coupon and tab thicknesses. 3-D continuum elements has been defined by volumes and do not require geometric (thickness) assignments. To compare and investigate the effect of the tabs, on the shear strain distribution at the central test section of the coupon, 3-D volume models of the transverse short coupon without tabs have also been prepared (Fig. 3.15) and analysed. Boundary conditions (supports) are assigned to the lower surfaces of the volume model. Similarly the loading has been assigned to the upper surfaces of the volumes comprising the 3-D model. Loading has been applied as uniformly distributed over the surface (load per unit area) idealising the loading applied by the fixture. 2D-surface and 3D-volume models of transverse shear coupons have been compared to predict the intensity and distribution of shear strains across the test section. Aluminium tabs have been added to the model to simulate the tabbed models of the GRP coupon (Fig. 3.16). The steel fixture has not been included in the analysis as no modification was required to the fixture geometry. However plane inner loading bars (without grooves, Fig 3.13 (d)) have been used to accommodate the tabs.

As previously stated, the main region of interest in this study is the area between the notches where an approximately uniform shear strain distribution should be exhibited when a known shear force is applied. This is the region where shear strains are measured using strain gauges during the experimental measurement of the shear properties. Different parameters relating to the geometry of the shear coupon including notch depth, notch angle and distance of loading ends from notch root are investigated for their influence on the shear stress distribution. In addition to establishing the geometry of a short shear coupon and appropriate interpretation of test results, the study also aims to identify the effects of orthotropy on the performance of this test, as making it suitable for the measurement of the shear properties of the GRP material of varying orthotropy. To investigate this, analyses has been performed for a range of orthotropy by simply modifying elastic constant values E_x and E_y in isolation.

*** LUSAS™ element library code.

Finite Element Results

Overall Depth

Initially the depth of the coupon has been taken as 10 mm to maintain the aspect ratio of 4.0 as compared to 3.8 for ASTM coupon used in the standard specification. Numerical analyses has been performed to investigate the effect of changing the overall depth 'D' of the short coupon on the shear strain distribution across the central notched section. Notch depth (25% of the overall depth) and notch angle (90°) have been kept constant in the analyses. An isotropic material coupon with point loading has been assumed. Numerical shear strains for four values of overall depth i.e., D = 9, 10, 11, and 12mm, normalised by the respective theoretical shear strains has been plotted for comparison (Fig. 3.17). The shear strain distribution is of a similar form for all four values of 'D'. A gradual increase in the deviation of computed shear strain from the theoretical uniform distribution with an increase in the coupon depth is observed. However, the deviation is small e.g., 1.5% to 2.8% for a D value of 9mm to 12mm. Furthermore, the strain concentration near the notch root increases with the increase in depth. These effects imply the consistent selection of coupon depth with notch depth.

For practical reasons i.e., to accommodate the notches and strain gauge between the notches, a minimum depth of 10mm has been maintained. A 2% difference between numerical and theoretical shear strain values have been observed for an overall depth of 10mm (Fig 3.17).

Loading Bars Separation

The separation between the inner loading bars controls the shear force intensity at the central notched section (shear force diagram in Fig. 3.4). The distance between the central vertical axes of the inner loading bars (where the loads are visualised to act) is denoted 'b' (Fig. 3.14(b)). The ASTM specification recommends locating the loading bars at 2.5mm from the notch edges to avoid the introduction of vertical direct stresses into the central test section. Starting from a minimum 1.5mm distance between the notch edge and inner loading bar on each side of the notched section, values of 'b' of 13mm to 19mm, with a difference of 2mm, have been investigated to establish its effects on the shear strain distribution at the centre. For comparison, values has been normalised by theoretical shear strains (Fig. 3.18). No significant

difference is observed in the strain distribution for the values of 'b' ranging from 13 to 19mm. The apparent reason for this similarity and consistency in the results is that for each value of 'b' the moments produced at the mid-section by the load couples that are equal and opposite, thus cancelling (Fig. 3.4). For practical reasons, 'b'=15mm (corresponding to an unsupported coupon length of 10mm between the inner loading bars), giving a maximum difference between numerical and theoretical strain values of 2% only, has been selected. This deviation from the theoretical value is similar to that arising from the depth of the coupon, as discussed earlier. Consequently the proposed loading configuration does not further compromise the quality of shear strain distribution at the centre.

Notch Depth

The effect of variation in notch depth has been studied by changing the notch depth from 1.5mm to 3.0mm (15% to 30% of overall depth) with a difference of 0.5mm. Numerical results are shown to straddle the theoretical target (Fig. 3.19). For small values of notch depth the shear strain distribution is relatively broader (8% for 1.5mm and 3% for 2mm notch depth) than the theoretical strains. For large values of notch depth the strain distribution is 7.5% lower than the theoretical values. The ASTM standard recommends a notch depth between 20 to 25% of the depth of the coupon (e.g., 2.0 to 2.5mm for a 10mm deep coupon). Interestingly, this recommendation is fully consistent with the numerical results obtained in this study, with results for notch depths of 2.0mm (20%) and 2.5mm (25%) enclosing the theoretical solution. In this study a 2.5mm notch depth is recommended, providing closest correlation to the expected or desired distribution.

Notch Angle

Strain distributions predicted for notch angle values of between 60° and 120° with 10° increments (Fig 3.20) clearly support the recommendation of the ASTM standard (ASTM D5379) that the preferred notch angle is 90°. While lower and higher angles generate numerical shear strain deviations of -5% to +14.9% (from the theoretical expectation), high strain concentrations (+100% to -50%) result from the same variation of notch angles. In contrast, the strain concentration associated with a 90° notch angle is approximately ±6%. It is clear that the notch angle is significant in strength measures rather than elastic modulus determination, given the relative insensitivity of the strain concentration to the notch angle.

Effect of Orthotropy

The main object of the study is to measure the shear properties of the orthotropic (composite) material using short shear coupon. The behaviour and performance of the short coupon has been investigated by varying the material properties along the longitudinal and transverse (x and y) directions of the coupon. The degree or amount of orthotropy of an orthotropic material has been defined as the ratio between elastic moduli in the longitudinal and transverse direction ($E_x : E_y$). For example for material with longitudinal elastic modulus of 30kN/mm^2 and transverse elastic modulus of 5kN/mm^2, the degree of orthotropy has been taken as 6:1. The strain distributions across the central notched sections of short coupons of materials with varying degrees of orthotropy have been plotted in Fig. 3.21. Two special orthotropic materials have also been included; one with E_x=E_y=30kN/mm^2 with shear modulus of 3.91kN/mm^2[†††] (denoted as 1:1), and the second as E_x=E_y=30kN/mm^2 with shear modulus of 11.54kN/mm^2[‡‡‡] (denoted by 1:1+), with the later as isotropic material specification but has been treated as orthotropic material. For comparison, the shear strains have been normalised by the theoretical shear strain.

For a zero degree of orthotropy (1:1+), the strain distribution shows a small deviation across the notched section with strain concentrations at the notch root that are low (4.4 to 5.4%). For the pseudo isotropic case (1:1) with a lower shear modulus, results are similar, with the most noteworthy difference a reduction in strain concentration at the notch tips. For higher degrees of orthotropy, the strain distribution deviates further from the uniform theoretical results. The deviation increases with an increase in the degree of orthotropy (Fig. 3.21), is positive for longitudinal coupons (e.g., E_x>E_y, 6:1), and negative for transverse coupons (e.g., E_x:E_y=1:6). Similar results have been produced by Herakovich and Bergner (1980) and are in agreement with the observations made in ASTM specifications;

"The actual degree of uniformity varies with the level of material orthotropy and the direction of loading. Both analysis and full-field experimental strain measurement

---

[†††] This value of shear modulus has been derived from micromechanics and CLT, see Table 3.5.

[‡‡‡] This value of shear modulus has been derived from the expression $E/2(1+\nu)$.

have shown that when testing in the 1 – 2 plane, [0]n[§§§] *specimen result in an elastic modulus estimate that is too high (about 10% too high for carbon/epoxy), while [90]n specimens of the same material result in a value that is about 20% too low. The most accurate measurement of in-plane shear modulus for unidirectional material have been shown to result from the [0/90]ns specimens."*

(ASTM D5379/D5379M, 1996, §6.3)

The most adverse effect of orthotropy has been observed on the strain concentration at the notch roots. Particularly in highly orthotropic transverse coupons (1:6), the strain concentration is almost double the theoretical strain at the centre of the section. Therefore a premature failure at the notch root may result within the coupon not capable of measuring all material characteristics, including strength. The strain concentration decreases whilst lowering the degree of orthotropy. For a transverse coupon with an orthotropy ratio of 1:3 (GRP material in the present study), the strain concentrations are 44% higher than the uniform theoretical strain at the centre. For a longitudinal coupon with same ratio of orthotropy i.e. 3:1, however, the strain concentration is 13% higher than at the centre. But for a higher ratio i.e. 6:1, the strain concentrations increases to 60% more than theoretically expected value. Interestingly, the strain distribution is uniform along the central section for orthotropy ratio of 3:2 (though paradoxically not for 2:3) and the strain concentration is acceptable (within 5%).

Fixture effect

Finite element models of the short shear coupon separately and within the AFPB fixture (Fig 3.14) have been analysed to investigate the effect of the fixture on the shear strain distributions at the central notched section. Contours of numerically obtained shear strains over the entire plane of short isotropic coupons without and with the fixture are shown in Fig 3.22. A contour interval of 0.9E-04 (corresponding to the 0.5E-04 for ASTM isotropic coupon where shear strains' range is nearly 60%

---

§§§ The digit in square parentheses indicates the direction of reinforcing fibres i.e., [0] means fibre are at 0 angle to direction 1 and *n* out side the parentheses indicates the number of layers in the composite laminate. In the present study the longitudinal coupons have fibres at 0 angles to longitudinal axis of the coupon. In transverse coupons, fibres are at 90 degree to the longitudinal axis. [0/90]n represents a composite made from alternate longitudinal and transverse layers in a multilayered composite. Carbon/epoxy has a high ratio of orthotropy(typically 17:1, Herakovich and Bergner,1980)

of the range for the short coupon) has been chosen to obtain comparable contour plots. The patterns of the contours (strain distributions) are alike in the coupon subjected to idealised loads and the coupon loaded via the fixture. The obvious difference is that in the case of the isolated coupon loaded by point loads (theoretical), a large strain concentration (almost double the strain values at centre of the coupon) is manifested beneath the loading point indicating potential local compression failure of the coupon. By using broader loading bars, the loading has been converted to a distributed load and with a corresponding strain concentration beneath the loading bars lower than the strain at the centre, ensuring the coupon failure at the central section under the influence of pure shear loading. A "uniform" shear strain distribution has been obtained along the central notched section in both cases of the isolated and fixture encapsulated coupons. The similarity of the contour patterns suggests that the AFPB fixture simulation is representative of the overall expected behaviour.

However, a disparity has been noted between the predicted magnitudes of the shear strains at the centre test section of the isolated and fixture encapsulated coupons. In expecting the results to be the same it has been assumed that the load applied to the coupon via the loading and reaction bars/beams of the fixture is uniform and consistent with the fundamental idealisation illustrated in Fig. 3.4. The vertical (normal) stresses acting through the upper and lower loading bars have been plotted along the width (5mm) of the loading bars (Fig 3.14 (e). The net loading applied to the coupon by integrating graphs L1 and L2 has been calculated. Similarly the reaction to the loading exerted by lower bars has been calculated by integrating R2 and R1 graphs. The calculations showed that a relatively lower (0.37 kN) shear force than the theoretically calculated (0.4 kN from bending force diagram of Fig. 3.4) shear force has actually been applied. The apparent reasons for this difference are; a slight bending in the upper loading beam, and a slight change in the load separation 'b' due to non-uniform (nearly triangular) load distribution through the upper loading bars (Fig 3.14(e)). However the loading remains asymmetric and the opposite couples induced by the loading are equal, maintaining a zero bending moment at the central notched section in the coupon. It has been concluded therefore, that for this size of coupon and AFPB fixture used in this analysis, the resultant shear force applied to the coupon is 0.37 kN when an external load of 1 kN has been applied to the fixture (and

not 0.4kN as predicted by classical elastic theory). For other sizes of coupon and testing fixture arrangement, the resultant shear force should also be established through a finite element analysis. This is identified as a key observation in characterising the fixture and proposing a procedural approach to the analysis.

The quantitative comparison of the shear stress distribution across the central notched section of the point loaded coupons and coupons loaded with fixtures has been made in Fig. 3.28. Four types of short coupons have been included (e.g., isotropic, pseudo-orthotropic, longitudinal and transverse). The numerical strains obtained from FEA agree closely with the theoretical solution. The presence of the uniform shear strain along the central section up to a width of nearly 4mm infers the capability of the short coupon to accommodate strain gauges in the middle of the notched section within a "uniform" strain field.

2-D and 3-D Models

The performance of the 2-D short shear coupon has been assessed by comparing the strain contour patterns and the uniformity of the shear strain distributions across the central notched section of the ASTM and short coupon. The 2-D surface model has been further used to assess the performance of a 3-D volume model of the short coupon, which in turn has been used to indicate the effect of tabs (Fig 3.26).

Shear strain contours plots are given for isotropic 2-D coupon (encapsulated in the fixture), 3-D coupon only and 3-D coupon including tabs (Fig 3.26). Essentially the results from the 2-D and 3-D (coupon only) simulations demonstrate the numerical validity of the latter through the similarity of the contour plots whilst recognising the necessary applied load modification compared with the classical solution, as discussed in a preceding section. These results are included for completeness as it is unnecessary to represent a coupon in 3-D when tabs are not used. When simulating the addition of tabs bonded to the sides of the coupon in line with the primary load bars it is expected that the shear strain distribution will be altered (e.g. see Fig 3.26 (b) and (c)). However, the quality (e.g. uniformity) of the strain field within the centre test area has been maintained with a clear zone of low strain variation. This is also best quantified in Fig 3.29. With the transverse coupon prone to degradation of the uniformity of the strain field it is also useful to provide equivalent results for comparison (Fig. 3.27). Again the proposed short coupon is shown to perform adequately on comparing the FE results given in Figs 3.27 and 3.29).

Comparison of ASTM and short coupon

The shear strain distributions for the isotropic and orthotropic material ASTM and short coupons have been plotted in Fig 3.30 for comparison. Clearly the patterns of deviations of numerical strains from the theoretical distributions are alike. Isotropic coupons produce least deviations at the centre and minimum strain concentration under the notch roots. Longitudinal coupons show a 2% increase in the shear strain distribution at the centre while a strain concentration of 30% under the notches. Conversely in the case of transverse coupons, the shear strain distribution is 4% less than the theoretical strain but a strain concentration of 30% (ASTM) to 45% (short coupon) has been observed.

Short Shear Coupon and Fixture Specification

The geometry and dimensions of a short shear coupon adequate for measuring the longitudinal and transverse shear properties, is proposed following the outcomes of the parametric study. The recommended short shear coupon is 40mm long, 10mm wide and as supplied thickness. A 90° sharp V-notch with a notch depth of 2.5mm machined on each of the longer sides of the coupon (Fig. 3.12). The geometry is similar to the standard ASTM shear coupon (Fig. 3.1).

The proposed AFPB type fixture shown in Fig 3.13 is capable of testing the short coupon for the measurement of the in-plane shear properties. The shear loading applied by the fixture on the coupon's test section is less than the theoretical value calculated from the shear force diagram visualised for the AFPB fixture (Fig. 3.4). It has been established that a shear resultant equal to 0.37P corresponding to an externally applied load 'P' has been applied at the central test section of short coupon loaded by this fixture.

3.3.3 SUMMARY OF OUTCOMES

- The proposed finite element models of the ASTM and short coupons adequately represent the behaviour of orthotropic material under the shear loadings. 2-D models using plane stress elements can represent the thick prismatic coupon and fixture components. This is validated through the comparison of the FEA results of 2D and 3D coupon models. Both isotropic and orthotropic models adequately predict the theoretical strain distribution at the central test section of the coupons.

- The introduction of V-notches at mid lengths of longer sides of rectangular shear coupons transforms the shear stress distribution, from parabolic to uniformly distributed, across the central notched section.
- The proposed numerical models, are utilised for defining the most efficient "short" shear coupon, having the lowest strain deviation at the centre and minimum stress concentration at the notch tips, for the measurement of shear properties when a standard length is not available.
- Proposed AFPB fixture applies a pure shear loading across the central test section during a shear test. Use of broader loading bars reduced the strain concentration (from 1.8 to 0.5 times the average theoretical strain at centre) beneath the loading points, eliminating the possibility of failure at these points rather than at the centre of coupon. Numerical results are used to calculate the amount of resultant shear force applied by the proposed test fixtures on the shear coupons. In the case of ASTM coupon loaded in the fixture the numerical shear force calculated at the centre is equal to 0.51P, where P is the total applied load on the fixture by the compression testing machine. This agrees with the theoretically calculated shear force using the shear force diagram of Fig. 3.4. In the case of short coupon, the numerical value of the shear force applied by the test fixture (0.37P) is less than the theoretical value (0.4P). Therefore, for any other arrangements of coupon loading the intensity of shear resultant should be established using finite element analyses.

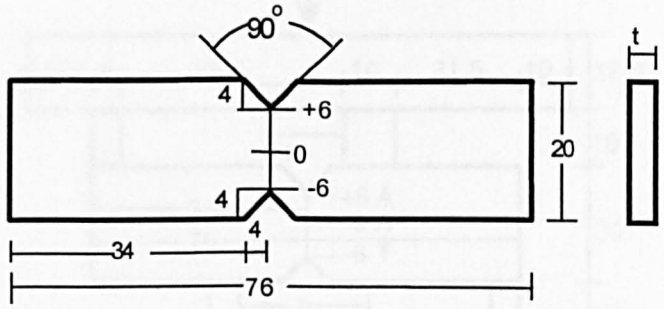

Fig 3.1 Schematic of ASTM shear coupon.
(all dimensions in mm)

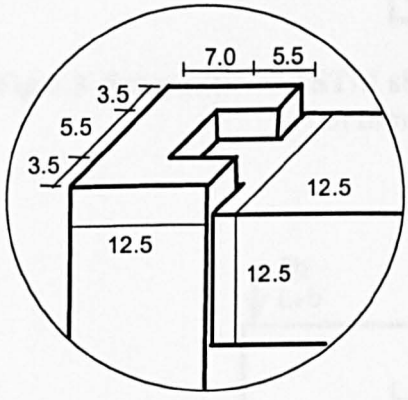

Details at A

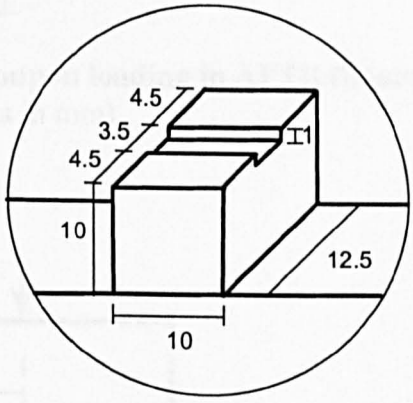

Details at B

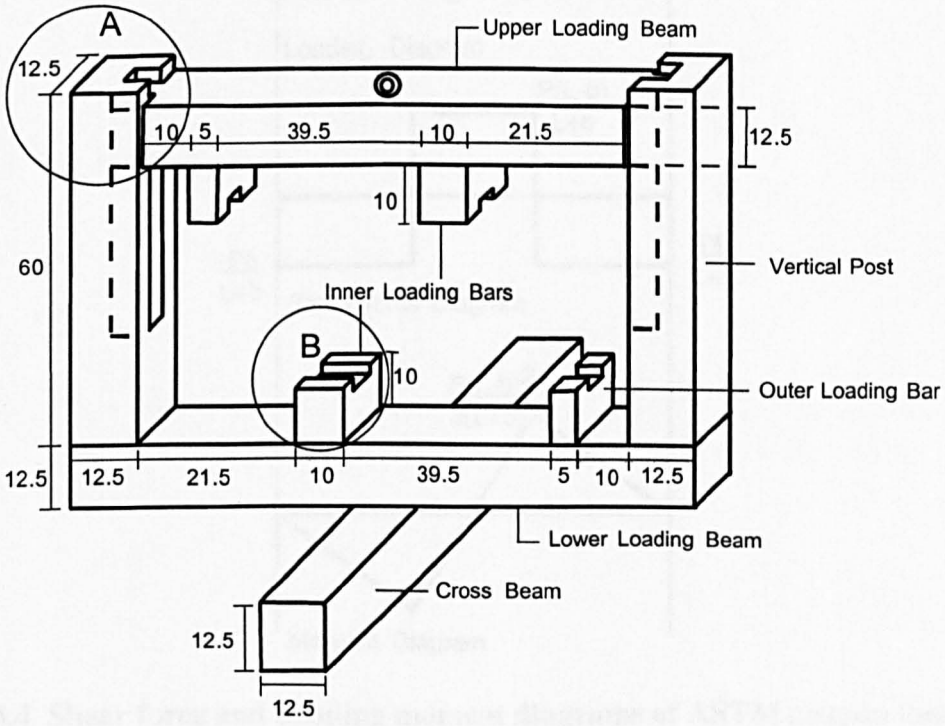

Fig 3.2 Designed AFPB shear test fixture.
(all dimensions in mm)

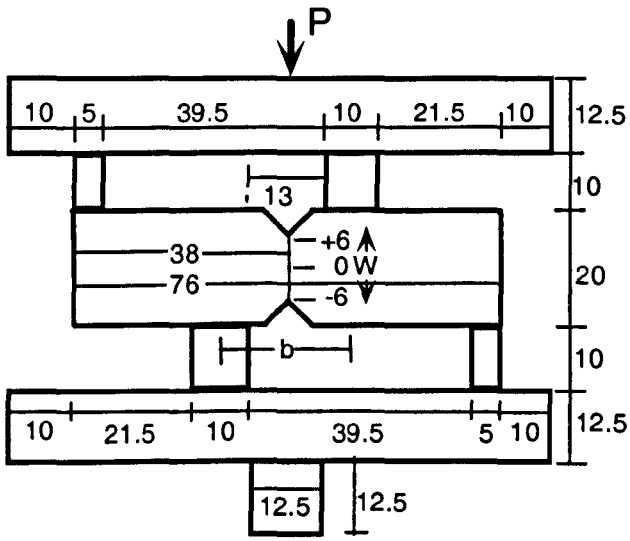

Fig 3.3 Schematic of ASTM shear coupon loading in AFTB fixture.
(all dimensions in mm)

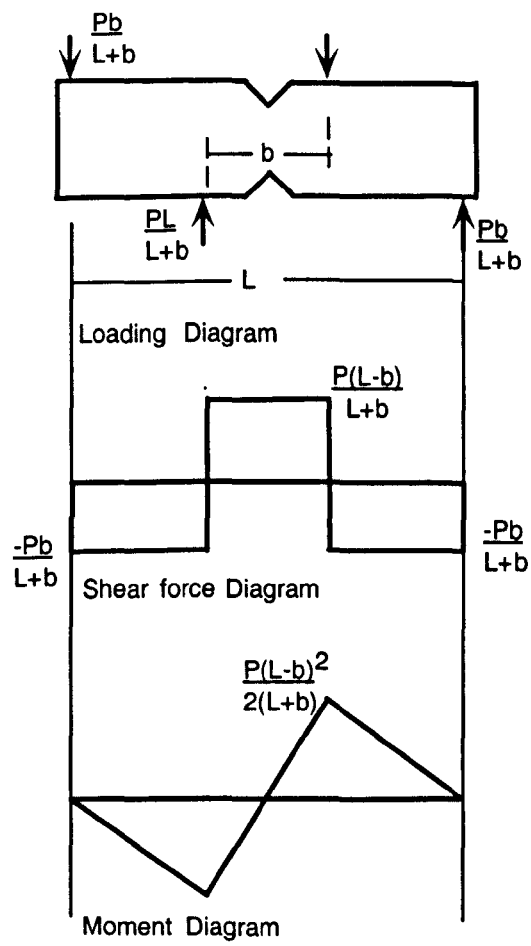

Fig. 3.4 Shear force and bending moment diagrams of ASTM coupon loaded in AFPB shear fixture.

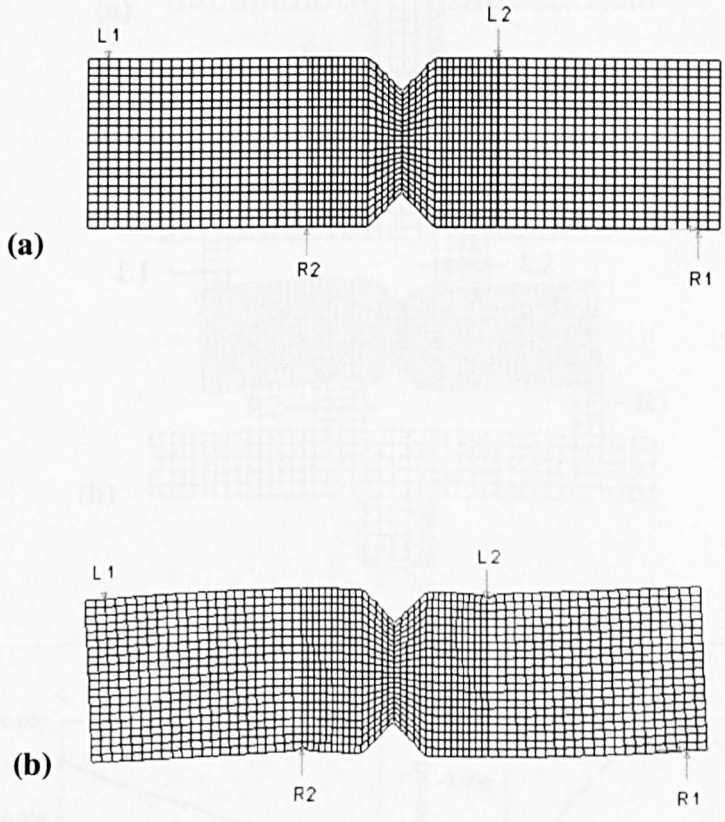

Fig 3.5 FEM model of ASTM Coupon showing mesh, loading 'L' and supports 'R'; (a) un-deformed, (b) deformed (exaggeration factor = 30).

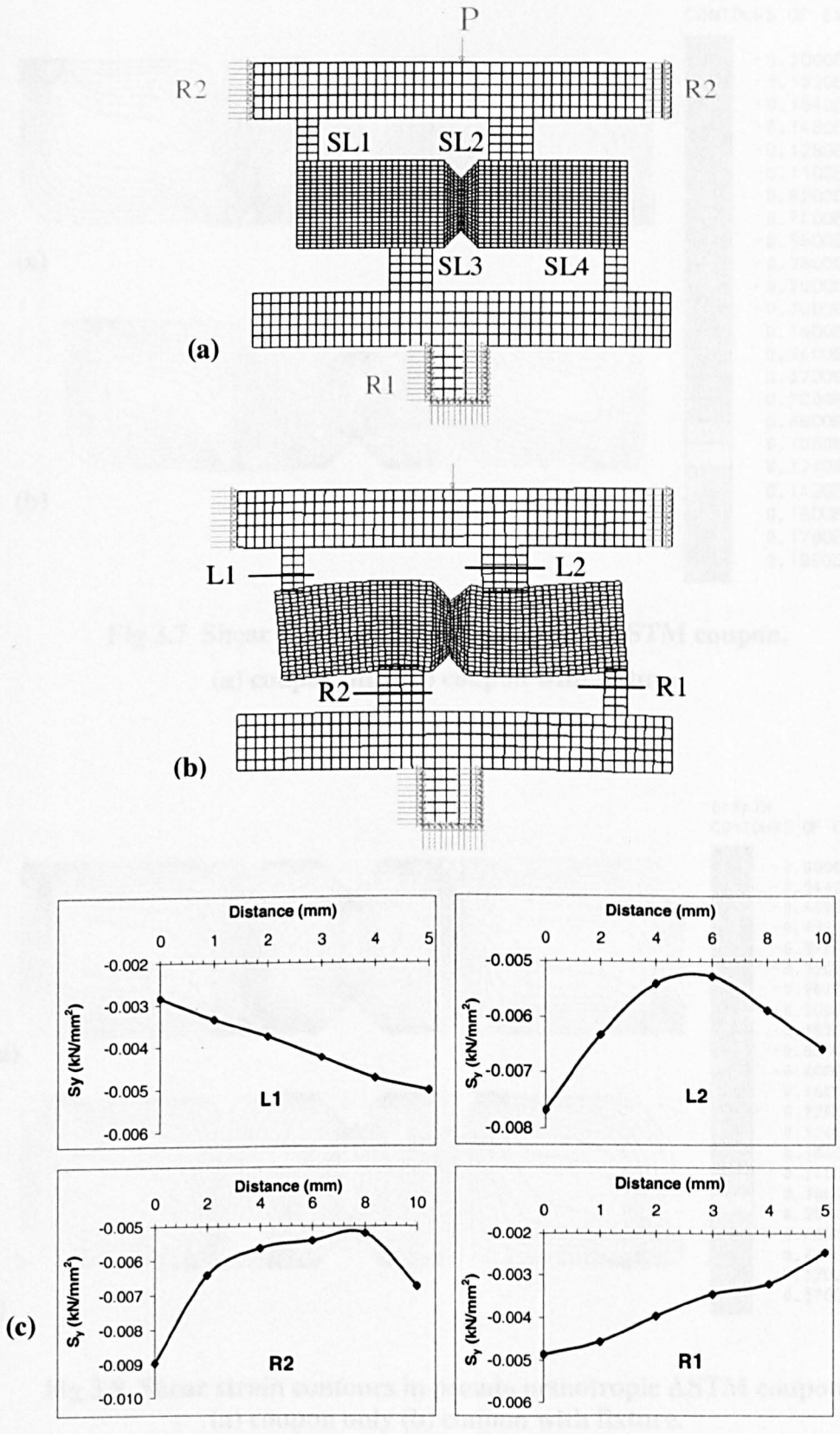

Fig 3.6 FEM model of coupon and fixture (showing mesh, slide lines 'SL', loading 'L' and supports 'R'), (a) un-deformed (b) deformed (exaggeration factor = 30), (c) normal stress (S_y) distribution across the loading bars.

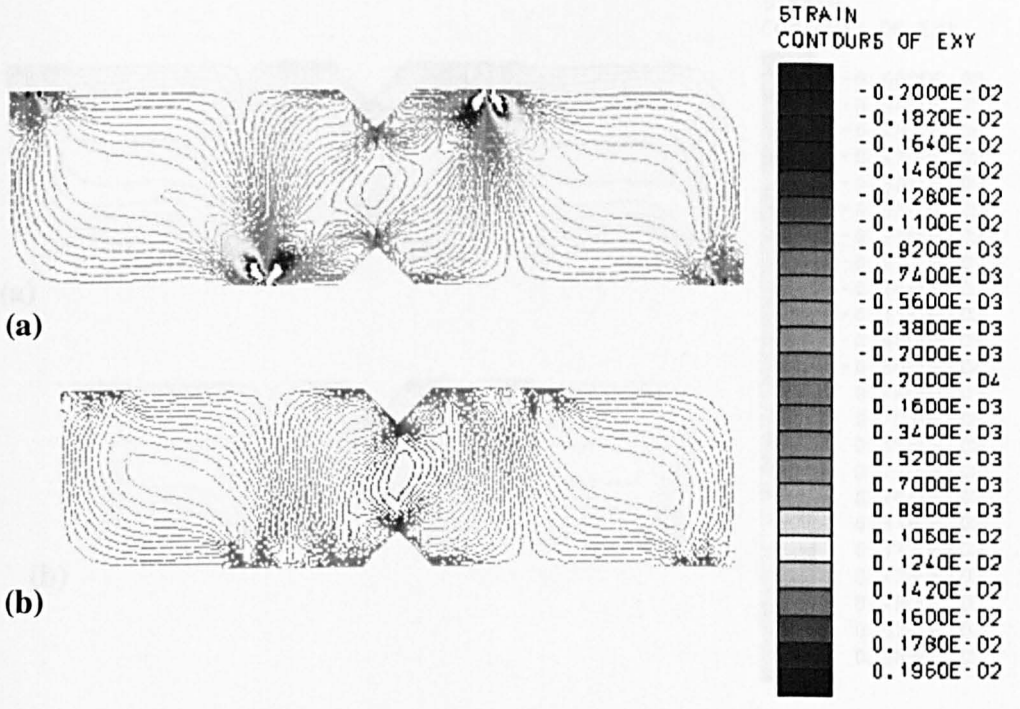

Fig 3.7 Shear strain contours in isotropic ASTM coupon.
(a) coupon only (b) coupon with fixture.

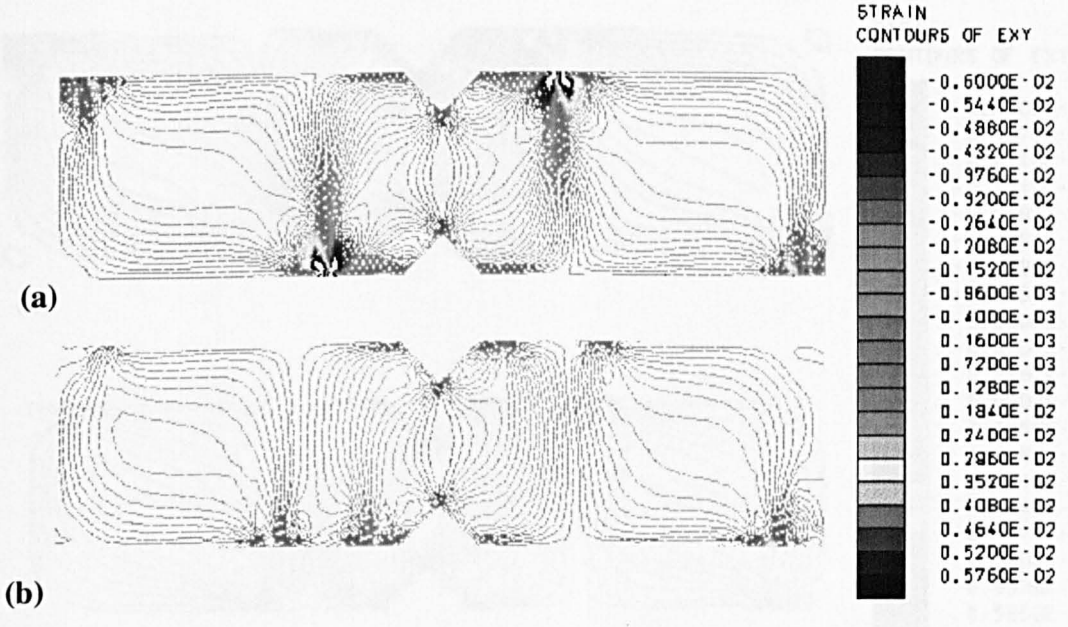

Fig 3.8 Shear strain contours in pseudo orthotropic ASTM coupon.
(a) coupon only (b) coupon with fixture.

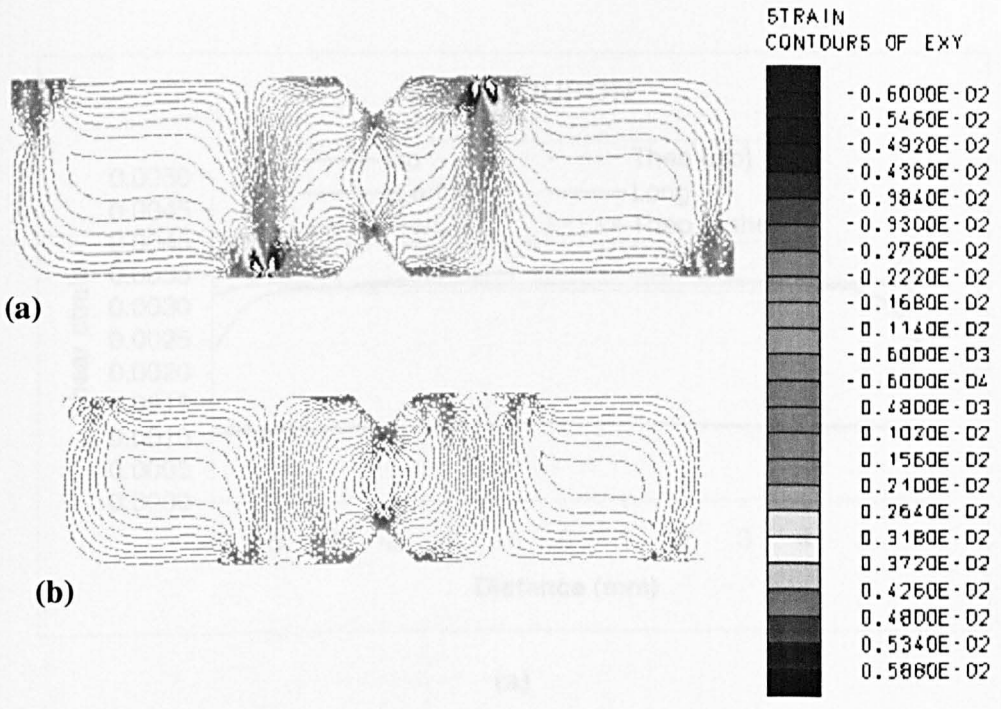

Fig 3.9 Shear Strain contours in longitudinal ASTM coupon.
(a) coupon only (b) coupon with fixture.

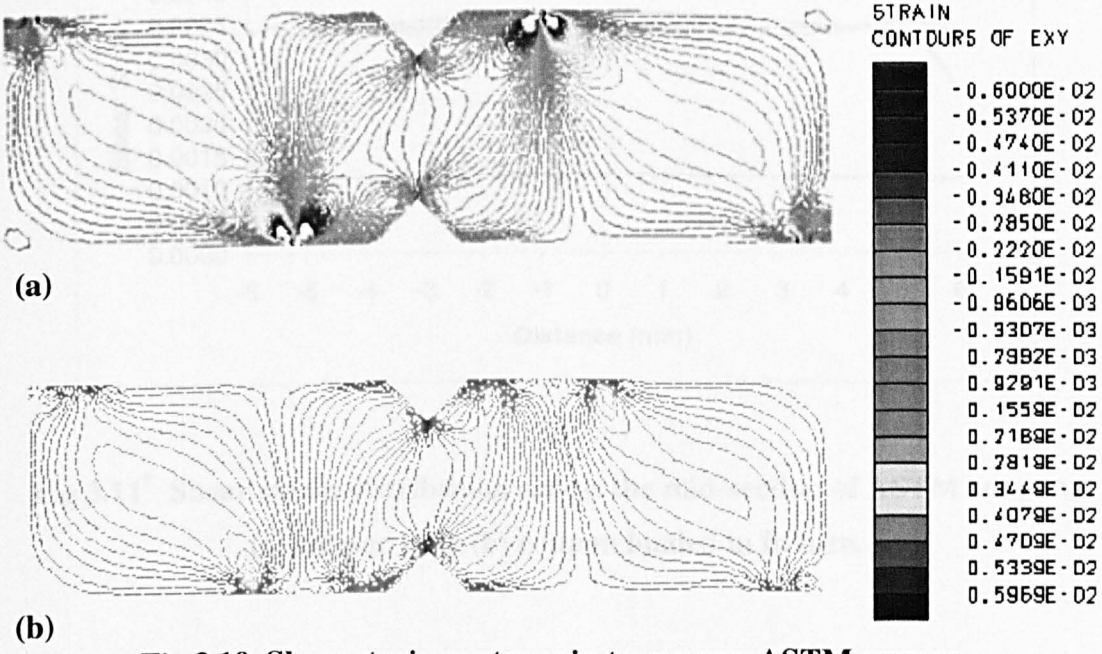

Fig 3.10 Shear strain contours in transverse ASTM coupon.

(a) coupon only (b) coupon with fixture

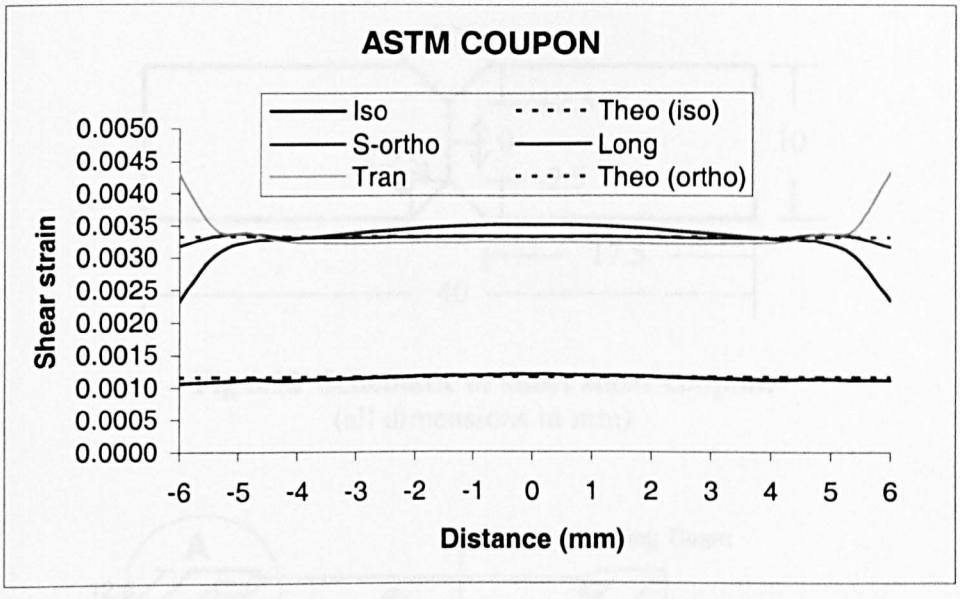

(a)

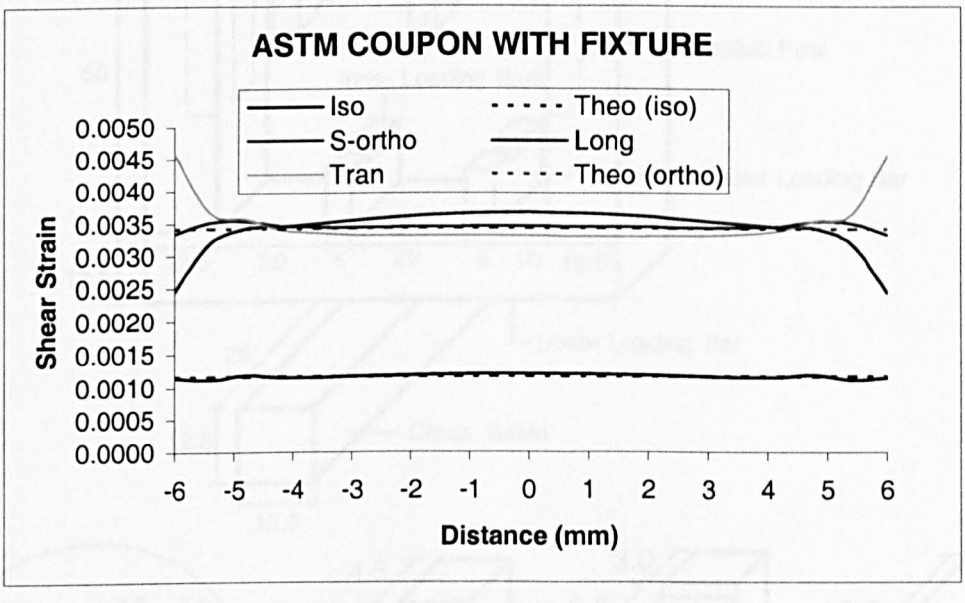

(b)

Fig 3.11[*] Shear strain distribution across the mid-section of ASTM coupon; (a) coupon only (b) coupon loaded in fixture.

---

[*] Legend: "Iso"=Isotropic coupon; "S-ortho"=Pseudo orthotropic coupon; "Long"=Longitudinal coupon; "Tran"=Transverse coupon; "Theo (iso)" and "Theo (ortho)" = theoretical shear strains for isotropic and orthotropic coupons respectively. Assumed material values are on page 81.

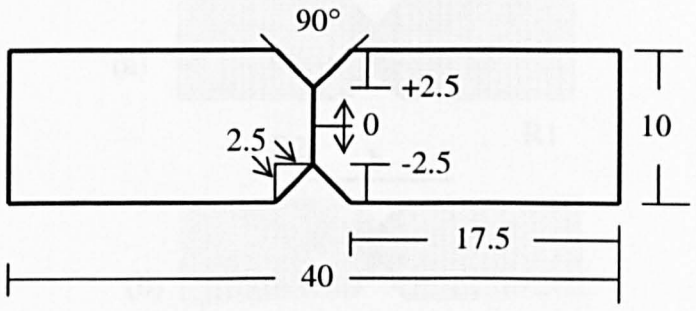

Fig 3.12 Schematic of short shear coupon.
(all dimensions in mm)

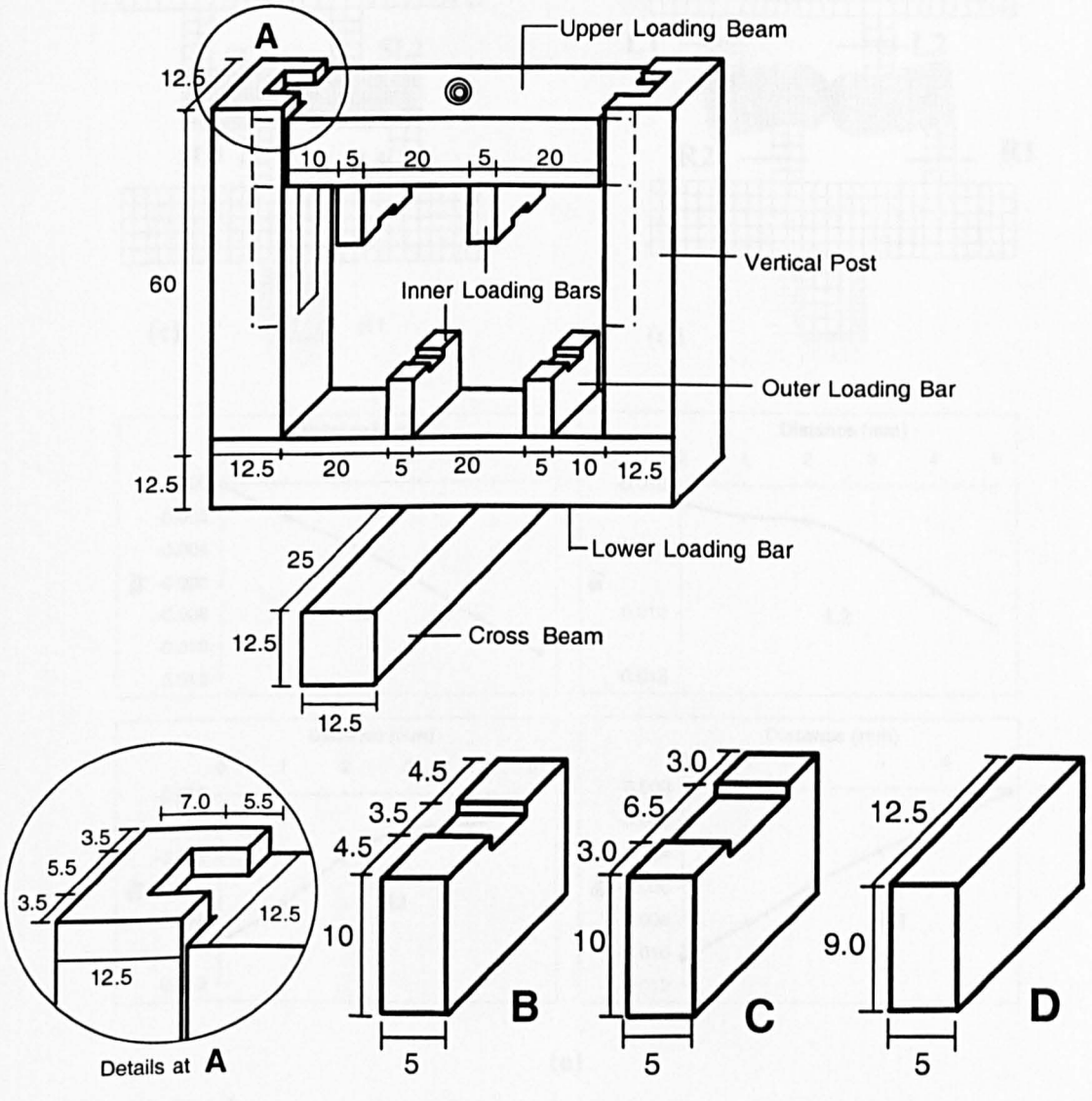

Fig 3.13 Schematic of the short AFPB shear fixture and attachable loading bars (B) for 3.2mm longitudinal coupon, (c) for 6mm longitudinal and (D) inner loading bars for 3.2mm and 6mm tabbed transverse coupons.
(all dimensions in mm)

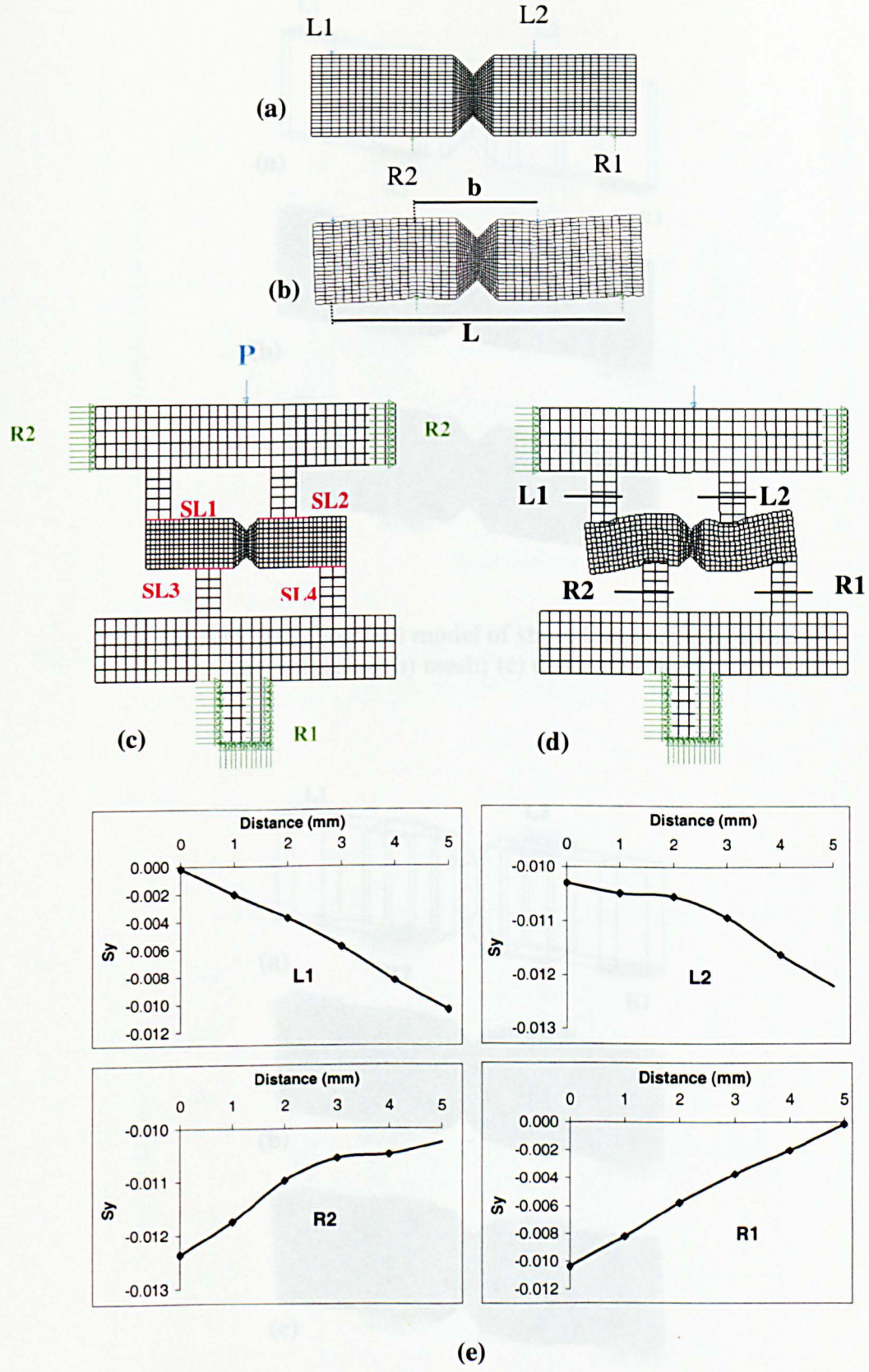

Fig 3.14 Finite element models of short shear coupon and fixture; (a) coupon under point loading (b) deformed under point loading (c) loaded in AFPB fixture (d) deformed under fixture loading (exaggeration factor = 30) (e) normal stress (S_y) across the loading bars.

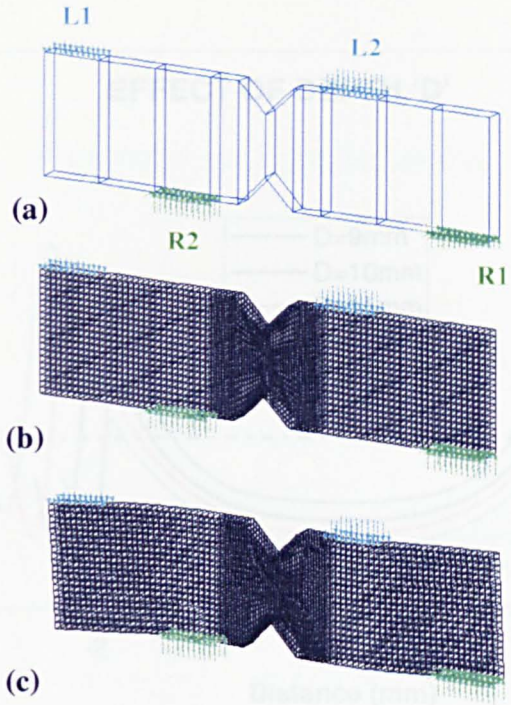

Fig 3.15 3-D (volume) model of short transverse coupon
(a) Volumes; (b) mesh; (c) deformed mesh.

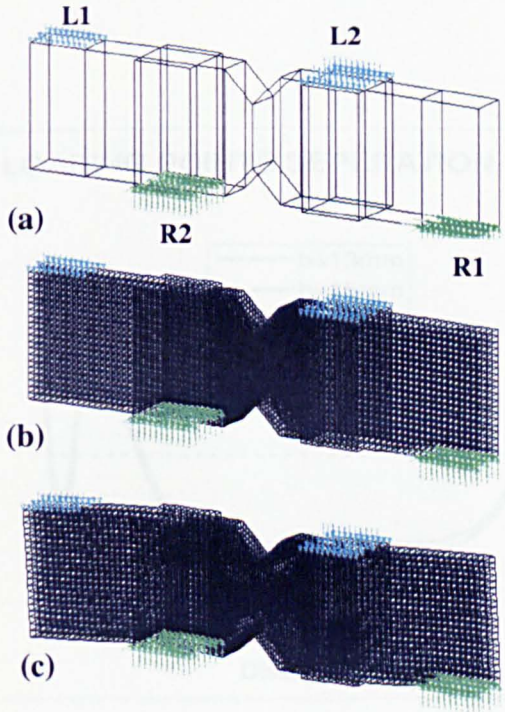

Fig 3.16 3-D (volume) model of short transverse coupon with tabs:
(a) Volumes; (b) mesh; (c) deformed mesh.

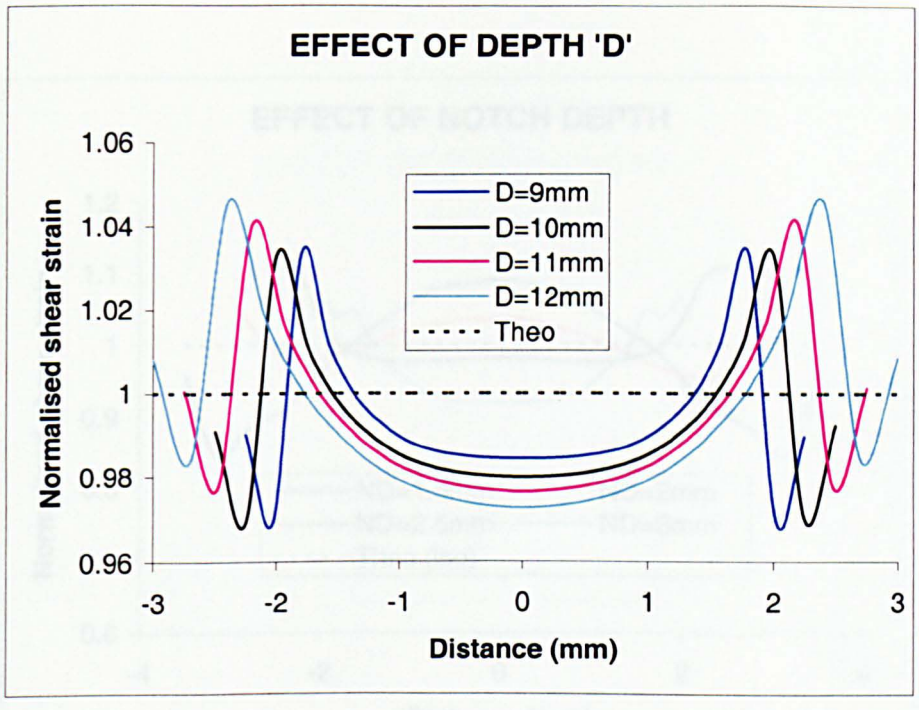

Fig 3.17 Effect of overall depth on the shear stress distribution across the mid-section of the coupon.

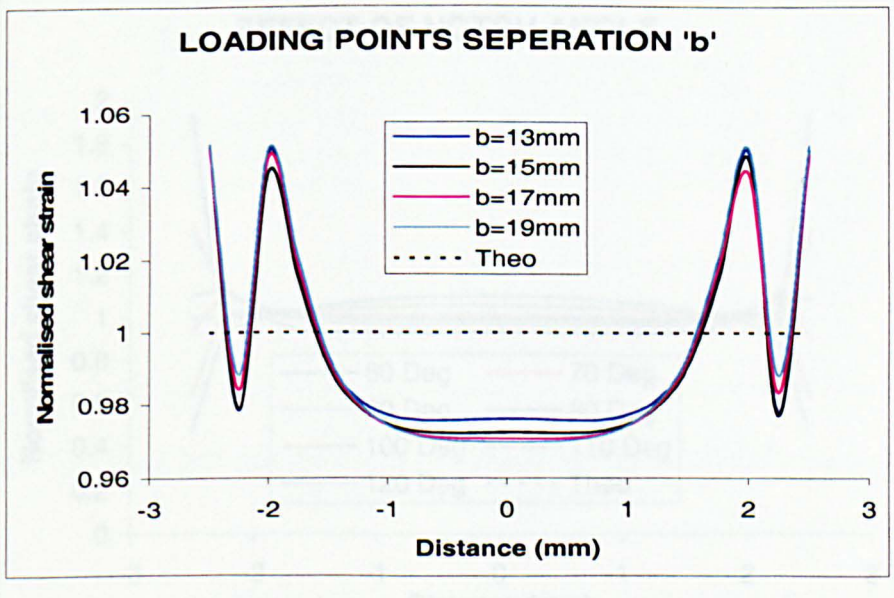

Fig 3.18 Effect of loading points separation 'b' on the strain distribution across the mid-section.

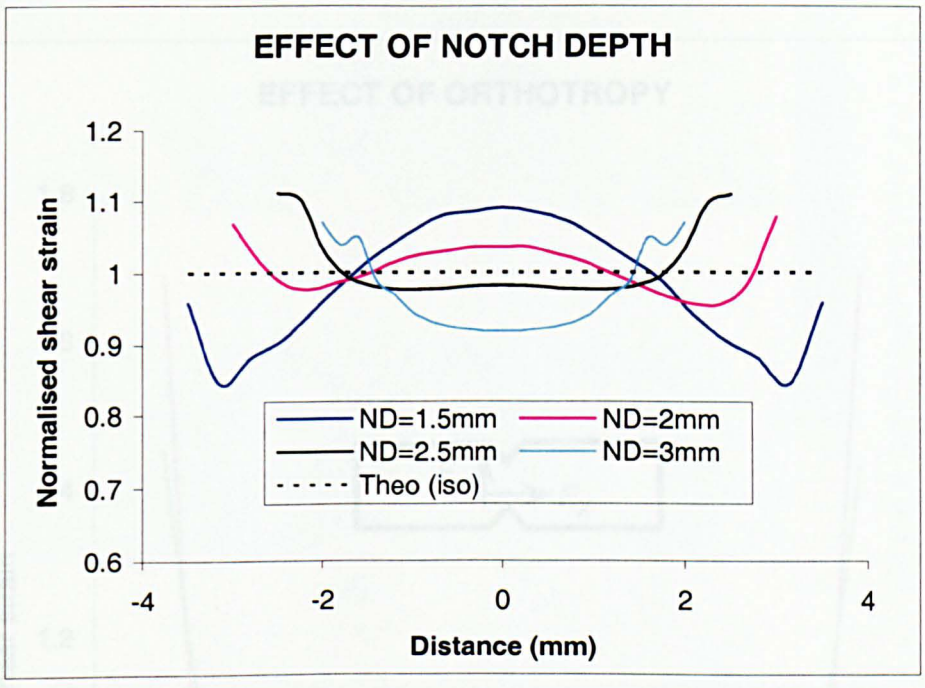

Fig 3.19 Effect of notch depth on the shear strain distribution.

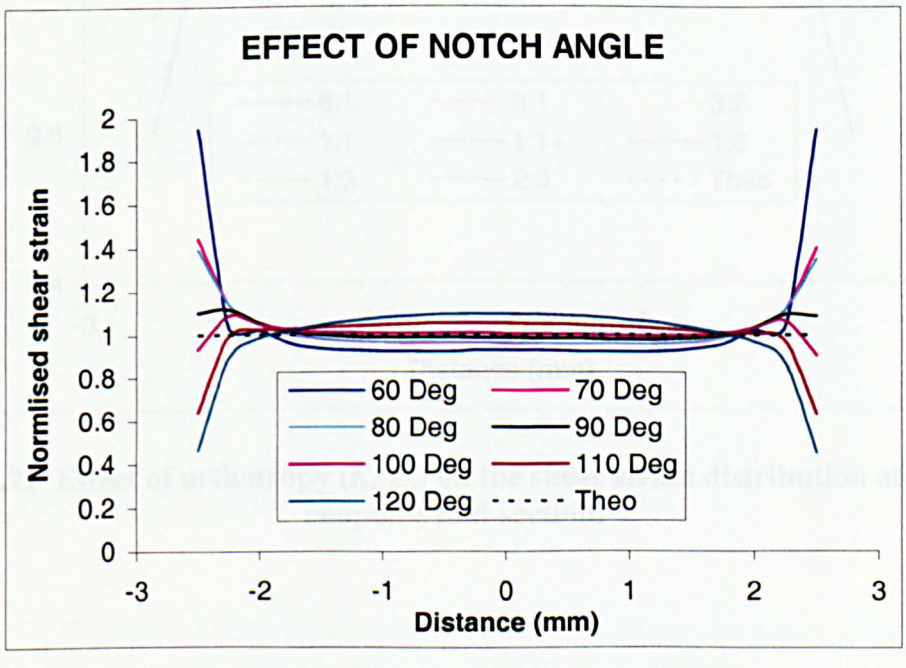

Fig 3.20 Effect of notch angle on the shear strain distribution.

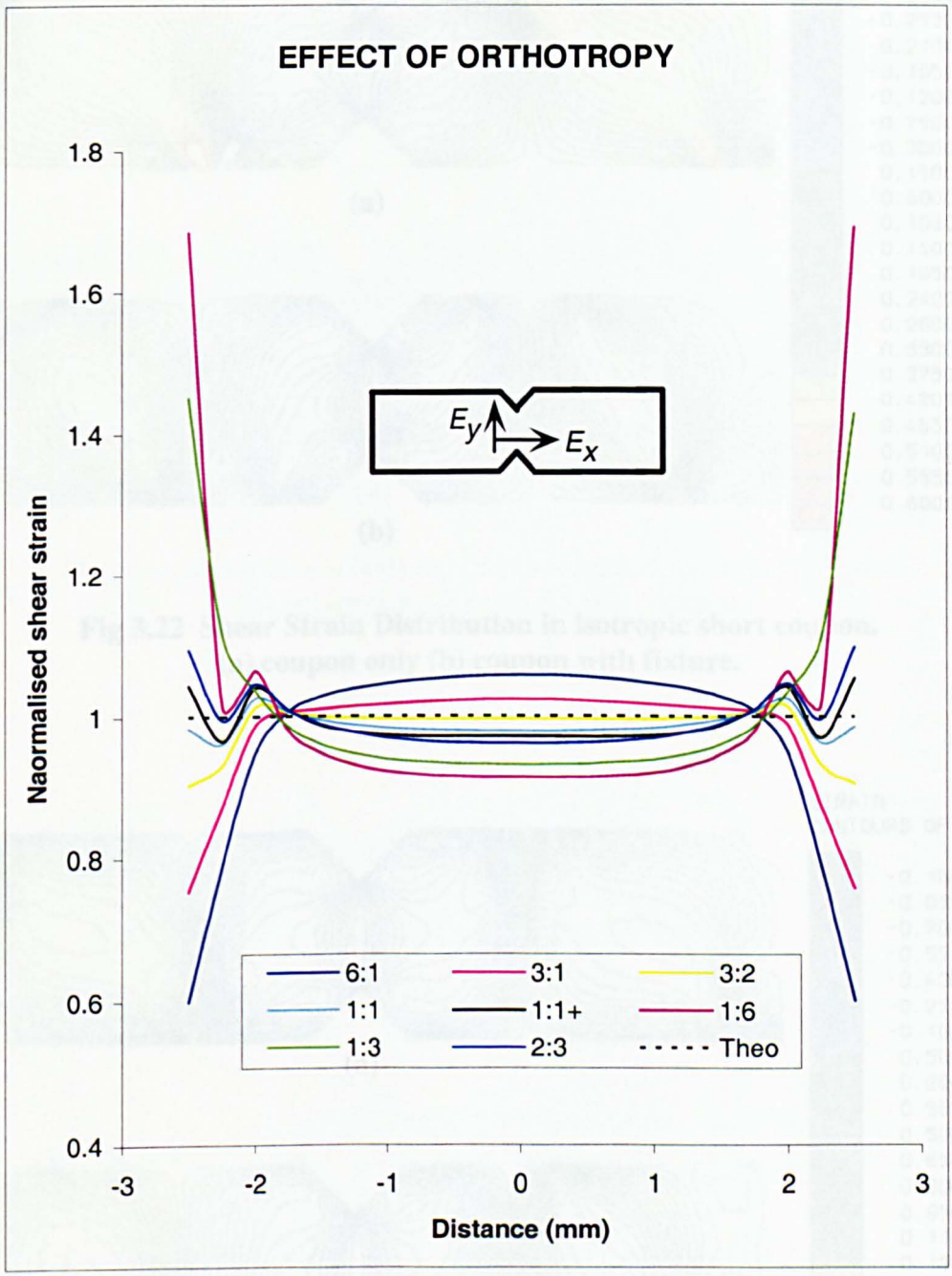

Fig 3.21 Effect of orthotropy (E_x:E_y) on the shear strain distribution at short coupon's mid-section.

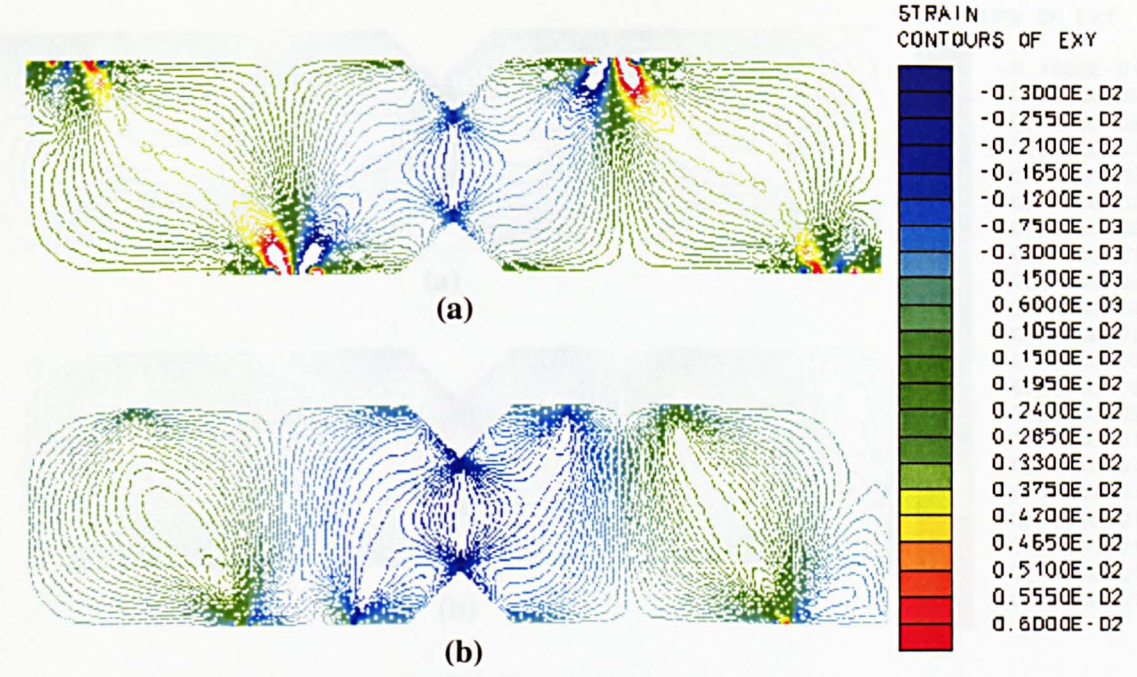

Fig 3.22 Shear Strain Distribution in isotropic short coupon.
(a) coupon only (b) coupon with fixture.

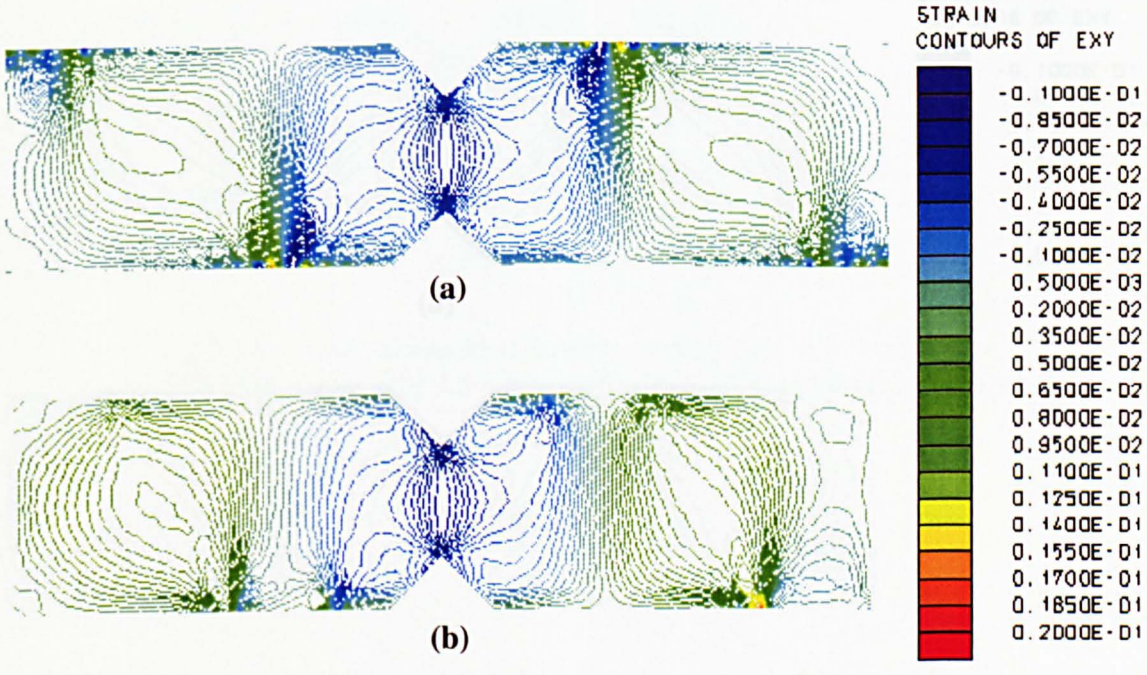

Fig 3.23 Shear strain distribution in pseudo orthotropic short coupon.
(a) coupon only (b) coupon with fixture

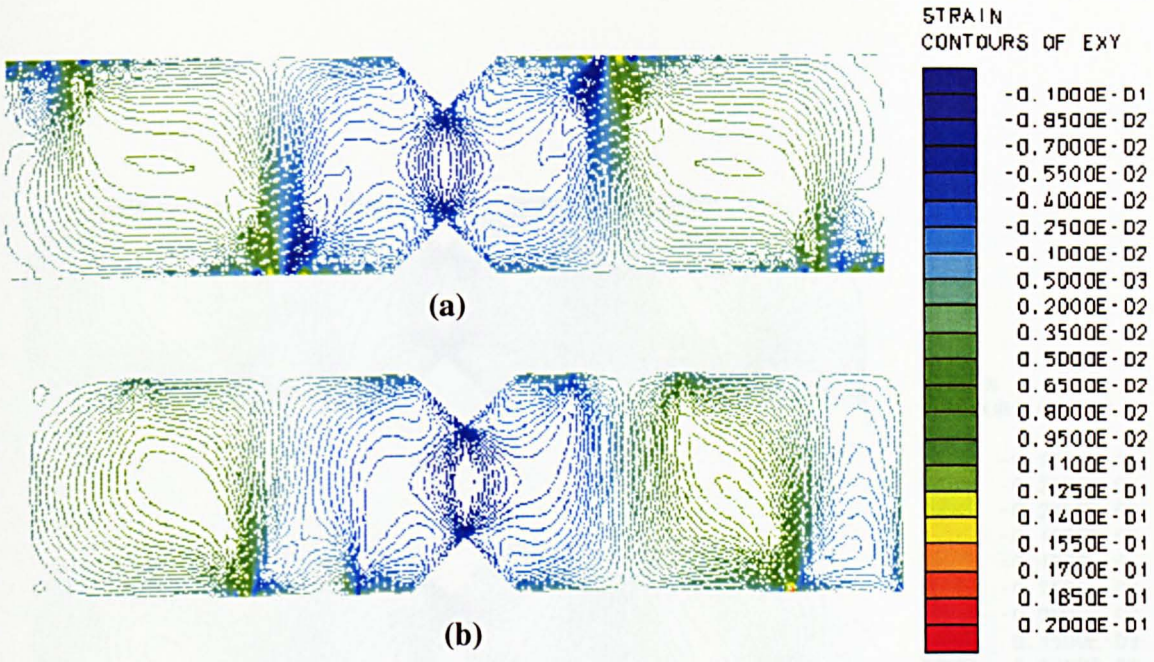

Fig 3.24 Shear strain distribution in longitudinal short coupon.
(a) coupon only (b) coupon with fixture

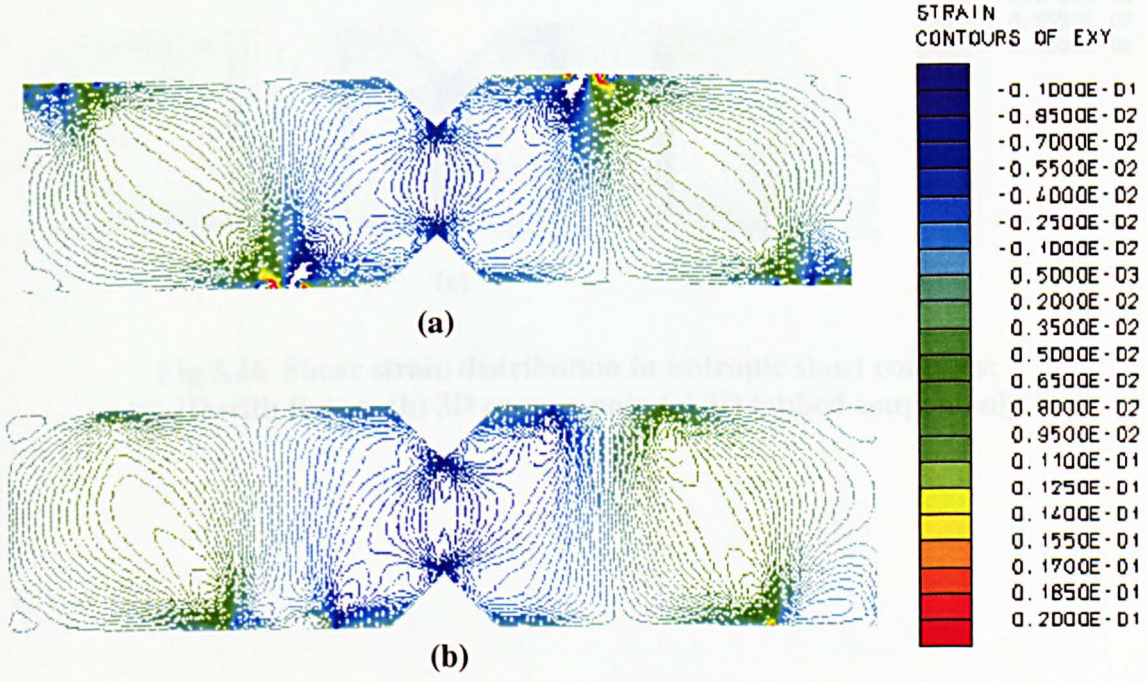

Fig 3.25 Shear strain distribution in transverse short coupon.
(a) coupon only (b) coupon with fixture

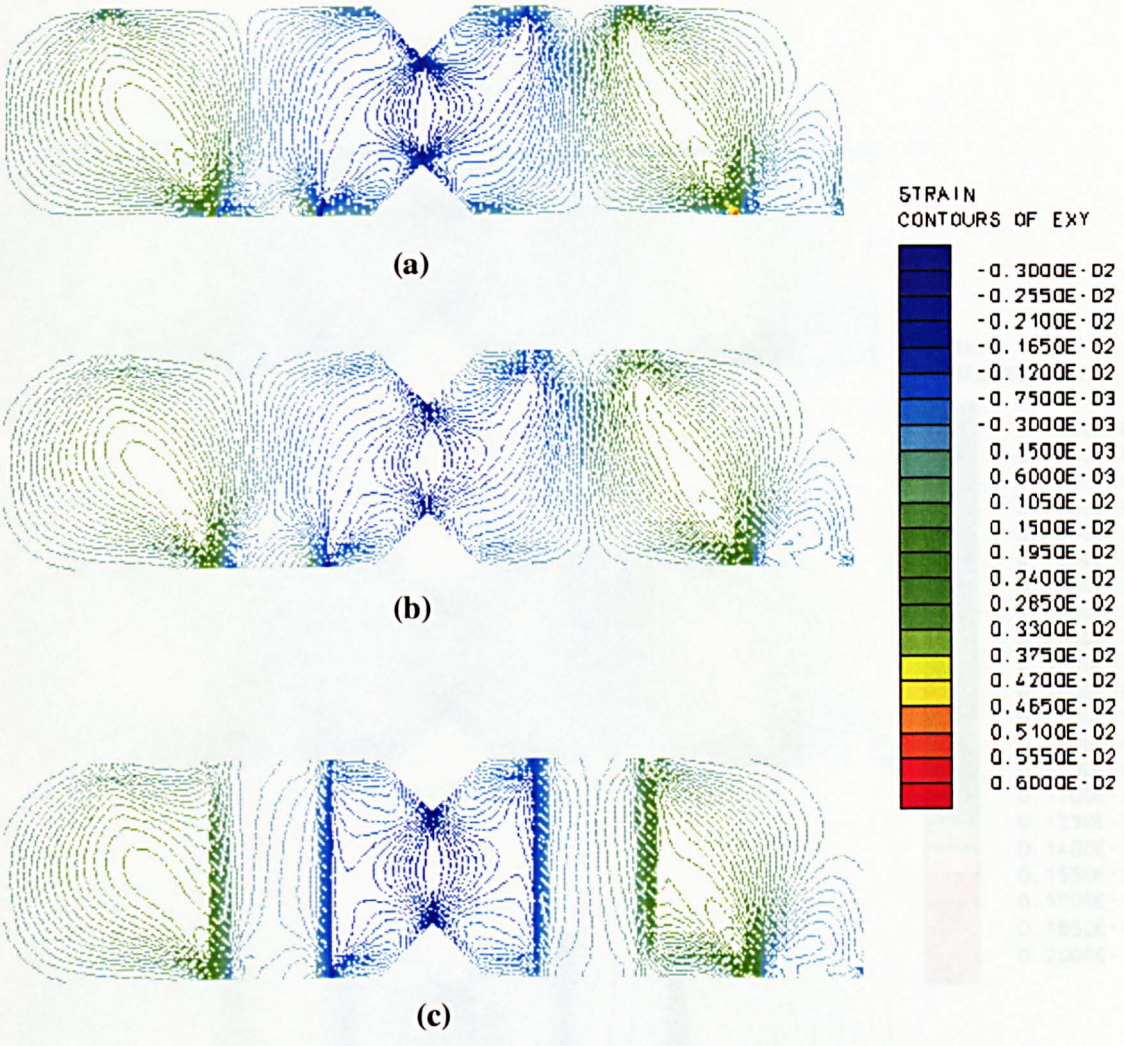

Fig 3.26 Shear strain distribution in isotropic short coupons; (a) 2D with fixture (b) 3D coupon only (c) 3D tabbed coupon only.

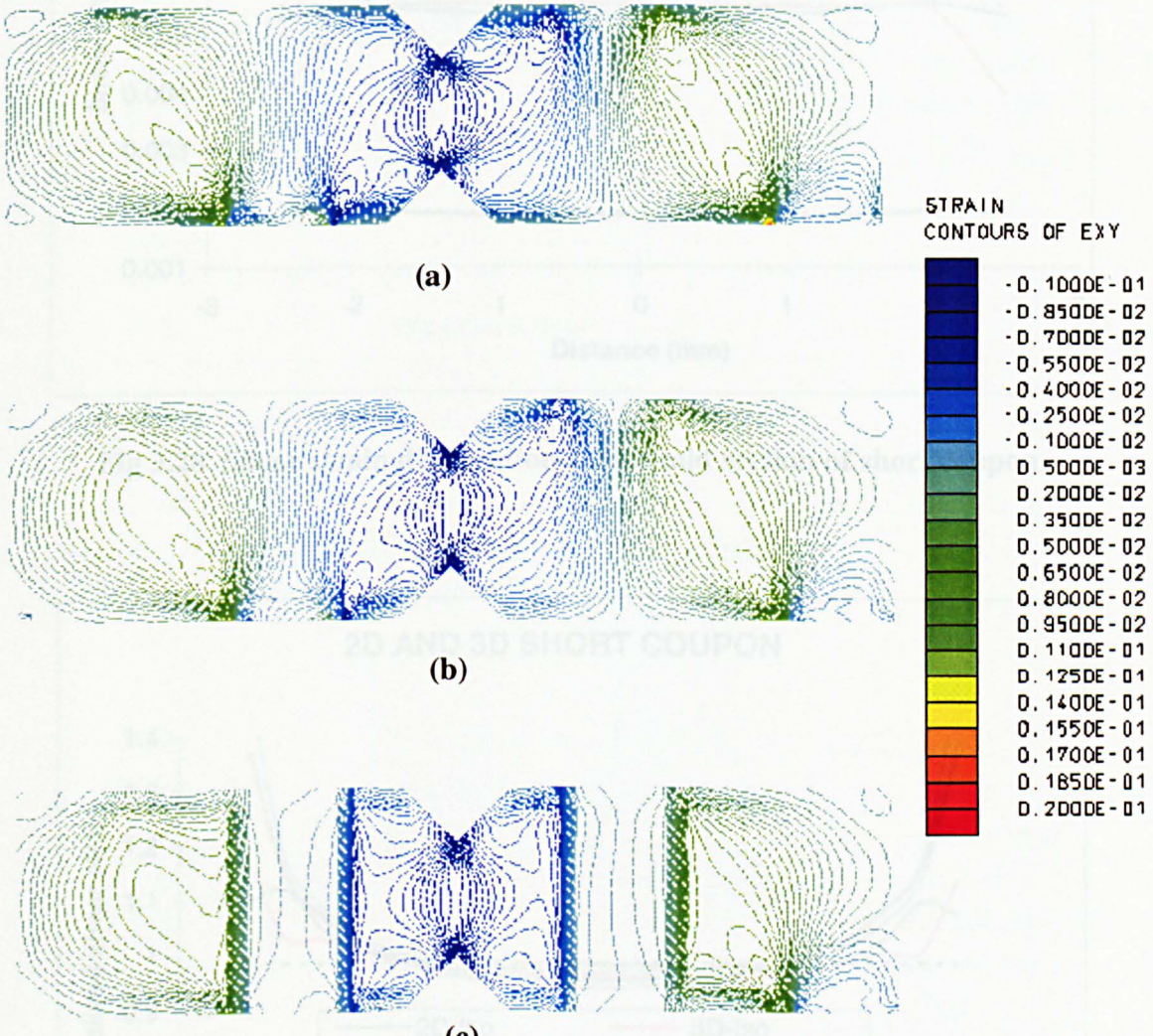

Fig 3.27 Shear strain distribution in transverse short coupons; (a) 2D coupon with fixture (b) 3D coupon only (c) 3D tabbed coupon only.

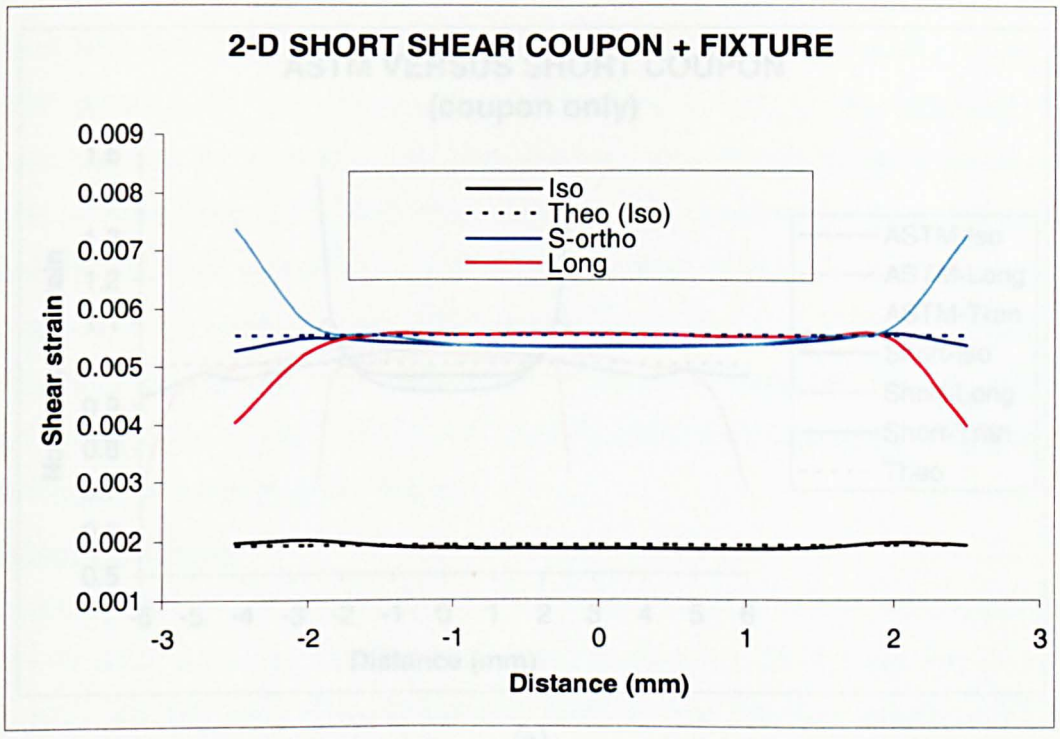

Fig 3.28 Shear strain distribution across mid section of short coupon.

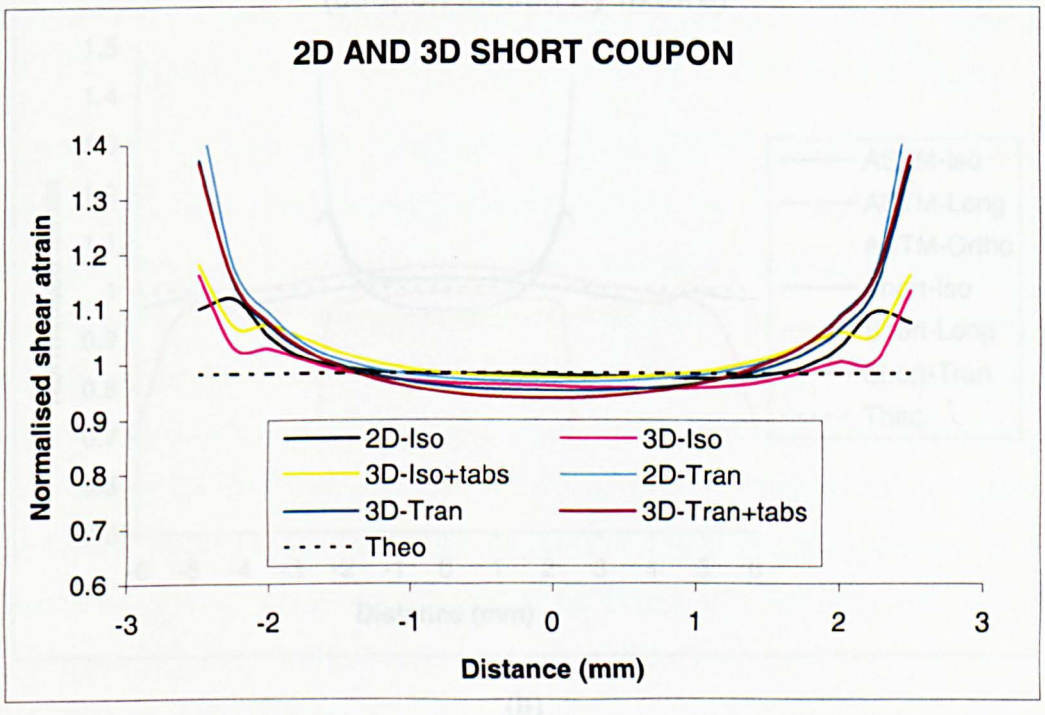

Fig 3.29 Comparison of 2D and 3D short shear coupon models

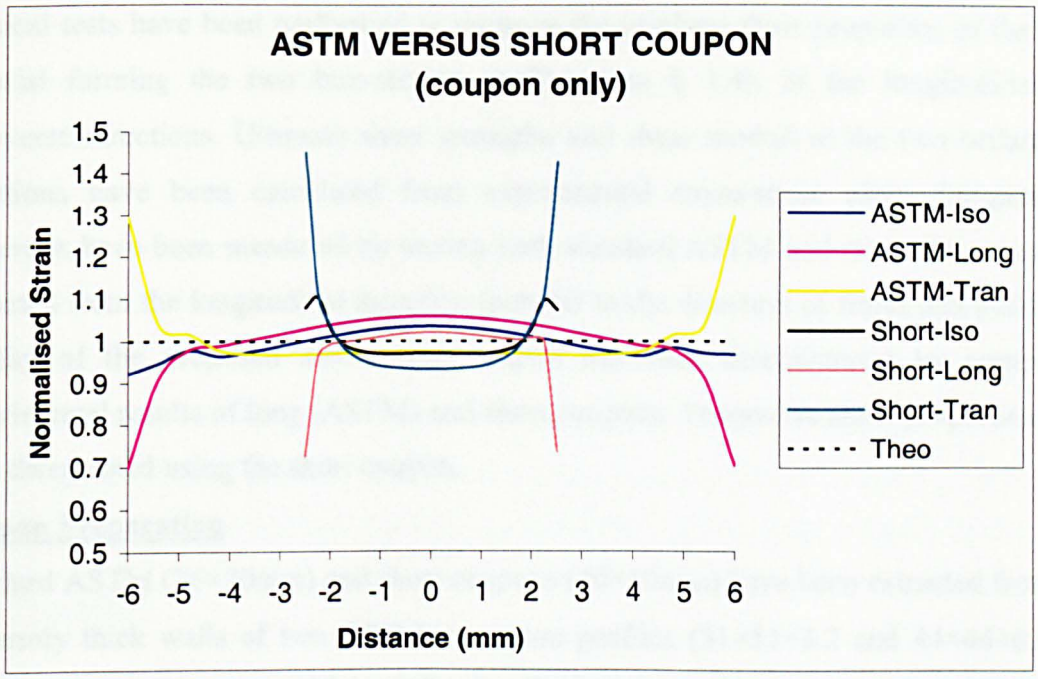

(a)

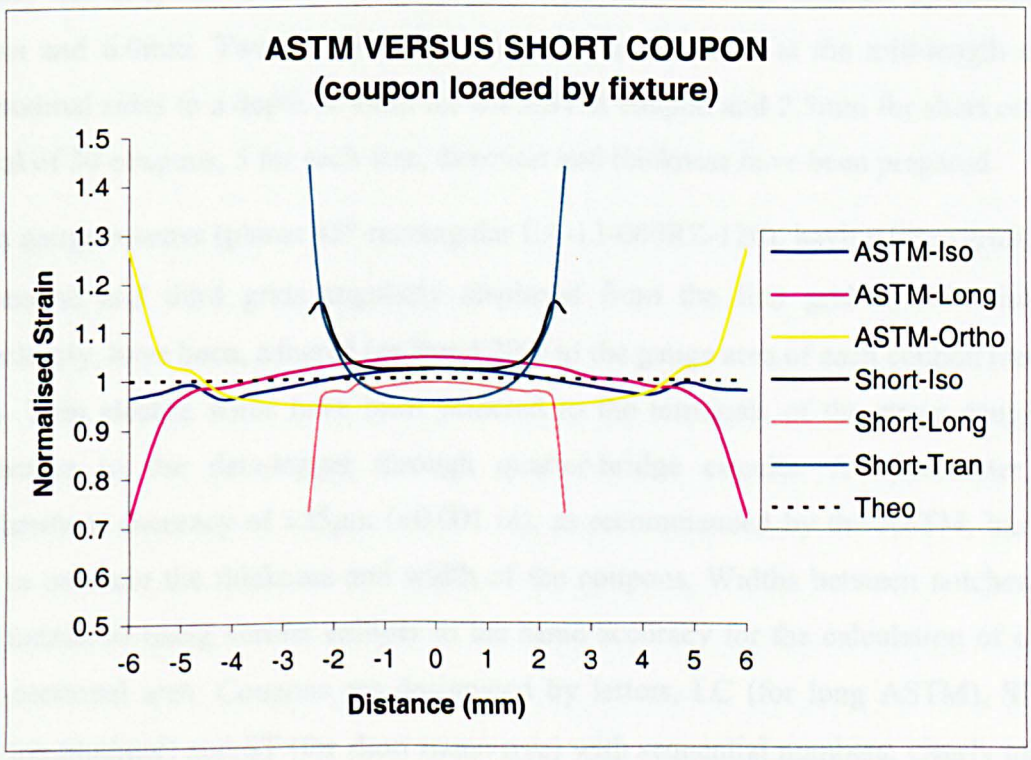

(b)

Fig 3.30 Comparison of ASTM and short coupon (a) coupon only (b) coupon loaded by fixture.

3.3.4 EXPERIMENTAL STUDY

Physical tests have been performed to measure the in-plane shear properties of the GRP material forming the two box-section profiles (see § 1.4), in the longitudinal and transverse directions. Ultimate shear strengths and shear moduli in the two orthotropic directions have been calculated from experimental stress-strain plots. Longitudinal properties have been measured by testing both standard ASTM and short shear coupons extracted from the longitudinal direction (parallel to the direction of fibres and pull). The validity of the proposed short shear coupon has been demonstrated by comparing experimental results of long (ASTM) and short coupons. Transverse shear properties have been determined using the short coupon.

Coupon Preparation

Standard ASTM (76×20mm) and short coupons (40×10mm) have been extracted from the uniformly thick walls of two GRP box-section profiles (51×51×3.2 and 44×44×6.0mm (see plate 1.1)). Direction of the reinforcing fibres (roving) has been taken parallel to the longitudinal axis of the GRP profiles, defining longitudinal and transverse coupons. Initially the coupons have planer rectangular geometries with nominal thicknesses of 3.2mm and 6.0mm. Two 90° V-notches have been machined at the mid-length of the longitudinal sides to a depth of 4mm for the ASTM coupon and 2.5mm for short coupon. A total of 30 coupons, 5 for each size, direction and thickness have been prepared.

Strain gauge rosettes (planar 45°-rectangular EA-13-060RZ-120), having three grids, with the second and third grids angularly displaced from the first grid by 45° and 90°, respectively, have been, adhered (m-Bond 200) to the gauge area of each coupon (see Fig. 3.31). Thin electric wires have been soldered to the terminals of the strain gauges for connection to the data-logger through quarter-bridge circuits. A micrometer with measurement accuracy of ±25μm (±0.001 in), as recommended by the ASTM, has been used to measure the thickness and width of the coupons. Widths between notches have been measured using vernier calliper to the same accuracy for the calculation of central cross-sectional area. Coupons are designated by letters, LC (for long ASTM), SL (for short longitudinal) and ST (for short transverse) with sequential numbers, clearly marked on both sides, for identification.

Fabrication of AFPB Steel fixture

Two steel fixtures illustrated in Fig. 3.2 for long (ASTM) coupon and in Fig. 3.13 for short coupon have been fabricated from steel. Dimensions of all the components have been marked in the figures. The vertical posts have grooves on their internal faces to guide the vertical movement of the upper loading bar. The vertical loading bars, 10mm deep with rectangular cross-sections, have been fixed to the upper and lower rigid beams. The inner loading bars in the case of fixture for ASTM coupon are wider (10×12.5mm) than the outer loading bars (5×12.5mm). The loading bars have been grooved (1mm deep) to hold the specimen vertical and to avoid twisting of the coupon during testing. Two sets of loading bars having grooves 3.5mm and 6.5mm wide have been prepared. Further sets of loading bars may be fabricated to accommodate the coupons with different thicknesses.

Test Procedure

The typical experimental set-up for testing the shear coupons, inserted in the AFPB steel fixture and loaded in compression by a universal testing machine is indicated in Plate 3.1. A horizontal thick (rigid) circular steel platform has been fabricated and fixed to the main frame of the testing machine. The cross beam of the shear fixture has been fixed to this circular platform using adjustable clamps, which allow the necessary alignment for concentric loading. A rectangular rigid steel plate has been used to fix the load cell to the upper platen of the testing machine. The load cell in turn is connected to the upper loading beam of the fixture by a conical bar having round lower tip to apply a concentric load. A load cell measures the applied load and is connected to an electronic data acquisition system which records the load values every two seconds with strains simultaneously. The compression machine applies a direct load, which is converted into a shear couple by the fixture. The loading rate has been adjusted to complete a test within ten to fifteen minutes (consistent with ASTM D5379/D5379M §11.3). The speed of testing may be approximated by repeated monitoring and adjusting of the rate of load application to maintain a nearly constant strain rate as measured by strain gauge response versus time. A standard shear strain rate of 0.01/min (ASTM guidance) has been adopted in this experimental study.

Coupons have been loaded up to the ultimate load i.e. up to failure. Mode and location of failure of each tested specimen has been recorded. All coupons failed in the test section. Their failure modes are shown in Plate 3.2 to 3.5.

Calculations

Shear stress

The shear stress applied by the fixture at the test section (central notched section) of the coupon had been calculated from the experimental data as under,

for the ASTM (long) coupon $$\tau_i = \frac{0.51P_i}{w \times t} \quad (3.13)$$

where τ_i is the shear stress at ith data point, P_i the applied load at ith data point, w is width between the notches and t is the thickness of the specimen. The factor 0.51 corresponds to the location of the loading bars (for a 'b' value of 23mm and L=71mm, as indicated in Fig. 3.4 and confirmed by the FEA of AFPB fixture for reactions) on the test coupon;

for the short coupon is $$\tau_i = \frac{0.37P_i}{w \times t} \quad (3.14)$$

with the same notation as above. The factor 0.37 is obtained by FEA of fixture effect on the short coupon (see fixture effects in § 2.3, FEA results of short coupon), and is less than the theoretically calculated (shear force diagram of Fig. 3.4) factor of 0.4.

Ultimate shear Strength

The load that accompanies failure in the test section is used as the failure load, normally the maximum load attained on the load-deflection curve (ASTM D5379M, § 6.6.2). The ultimate shear strength is calculated as;

for ASTM coupon $$F_u = \frac{0.51P_{max}}{w \times t} \quad (3.15)$$

and for short coupon $$F_u = \frac{0.37P_{max}}{w \times t} \quad (3.16)$$

where F_u is ultimate shear strength, P_{max} the maximum load prior to failure, w the width between the notches and t the thickness of the coupon.

Shear Strain

The strain rosette bonded to the coupon has three gauge elements, numbered sequentially anticlockwise as 1-3. The rosette has been fixed at the centre of section between the notches such that gauge 1 is in vertical direction and gauges two and three are at 45° and

90° from the first (Fig 3.31). Strains measured by gauges 1-3, are denoted as $\varepsilon_1, \varepsilon_2$ and ε_3, respectively. From the measured strain values ($\varepsilon_1, \varepsilon_2$ and ε_3), the following can be calculated (Measurement Group, 1990):

$$\varepsilon_{P,Q} = \frac{\varepsilon_1 + \varepsilon_2}{2} \pm \frac{1}{\sqrt{2}}\sqrt{(\varepsilon_1 - \varepsilon_2)^2 + (\varepsilon_2 - \varepsilon_3)^2}$$

$$\phi_{P,Q} = \frac{1}{2}\tan^{-1}\left(\frac{2\varepsilon_2 - \varepsilon_1 - \varepsilon_3}{\varepsilon_1 - \varepsilon_3}\right) \qquad (3.17)$$

$$\gamma_{max} = \varepsilon_P - \varepsilon_Q$$

where ε_P and ε_Q are maximum and minimum principal strains, ϕ is the angle from axis of the strain gauge 1 (reference gauge) to the principal strain and γ_{max} is the maximum shear strain. The angle ϕ = 45° between the axis of gauge 1 (set parallel to the loading axis) and the maximum principal stress direction indicates the state of pure shear at the central section.

Shear Modulus

For each coupon the shear stress and strain values measured during the experiment have been plotted. A typical stress-strain plot for the ASTM coupon is given in Fig 3.32, and for longitudinal and transverse short coupons in Fig 3.33 and Fig 3.34. ASTM D5379/D 5379M–93 recommends the determination of shear chord modulus of elasticity, if values are available for an interval of 5000με (at points 1000με and 6000με), the total strain is more than 12000με and the curve does not exhibit a transition region. The experimental results from the present study show a considerable degree of non-linearity in the initial region and in some cases results in the initial region are not reliable. The ASTM standard in this case suggests the use of another equivalent range in the vicinity of this range. Chord modulus is then defined (reporting the accepted range) as:

$$G^{chord} = \frac{\Delta\tau}{\Delta\gamma} \qquad (3.18)$$

where

G^{chord} = shear chord modulus of elasticity (kN/mm^2),

$\Delta\tau$ = change in shear stress (kN/mm^2) between the specified strain interval and

$\Delta\gamma$= specified strain range interval.

The experimental results obtained from tests on long and short coupons are given in Tables 3.6 - 3.11.

As the stress-strain curves are nonlinear, a second definition of the shear modulus -'secant modulus'- has also been evaluated (Lee and Munro 1990, Dickson and Munro 1995). To determine secant modulus, the stress-strain curves for each test are fitted with least-square polynomial curves (third-order polynomials are found sufficient to yield a correlation coefficient above 0.995). Shear stress values corresponding to 1000με and 6000με are calculated using polynomial expressions for each test. The difference between the two stresses ($\Delta\tau$) is divided by the strain interval ($\Delta\gamma$=5000με) to calculate the secant shear modulus. This procedure compensates any discrepancies in the initial range of data caused by specimen, fixture or load settings, as the polynomial represents a smooth curve between the data points. Secant modulus values are included in the Tables. 3.6- 3.11

Statistics

For each series of tests, the average value (AV), standard deviation (SD), and coefficient of variation (CV in percent) are calculated for each property using the following relations (ASTMD5379M93, §12.5);

$$\bar{x} = \left(\sum_{i=1}^{n} x_i \right) / n \tag{3.19}$$

$$S_{n-1} = \sqrt{\left(\sum_{i=1}^{n} x^2 - n\bar{x}^2 \right) / (n-1)} \tag{3.20}$$

$$CV = 100 \times S_{n-1} / \bar{x} \tag{3.21}$$

where

$\bar{x}$ = sample mean (average), x_i = measured or derived property, n = number of specimens

s_{n-1} = sample standard deviation, and CV=sample coefficient of variation (%).

Tolerance for material properties

Tolerance in each property is estimated at a confidence level of 95% (Kennedy and Neville 1976, Wang and Zureick, 1994) ;

$$\bar{x} \pm \frac{1.96SD}{\sqrt{n}} \qquad (3.22)$$

Experimental Results

Stress-strain plots have been drawn, using the experimental data, to establish the in-plane shear properties of the composite material comprising the GRP box-profiles. Stresses and strains are calculated using relations (3.15 - 3.18) summarised in the previous section. Typical stress-strain plots for ASTM, and proposed short (in longitudinal and transverse directions) shear coupons are shown in Figs. 3.32-3.34. The range of shear strain calculate from the experimental data (3.17) is higher than 12000με (35000 to 50000με). Therefore, a strain interval of 5000με (1000 to 6000με or the closet available data points)[††††] and the corresponding stress interval have been used for the calculation of both chord and secant moduli ($=\frac{\Delta\tau}{\Delta\varepsilon}$). Ultimate shear strength (F_u) has been derived from the maximum stress measured from each plot using (3.15, 3.16). The number of shear coupon tested in each set is five (n=5). Average properties from each set of tested coupons ($\bar{x}$), along with standard deviation (SD) and coefficients of variation (CV) have also been calculated (3.19 – 3.21). The experimental results for the six sets of shear coupons, each set comprising five coupons, are summarised in Tables 3.5-3.10.

ASTM coupons.

For the 3.2mm (nominal) thick ASTM coupons (Table 3.6), the average values of the chord and secant (3.94 and 3.92kN/mm^2) shear moduli are close to the theoretically predicted shear modulus (3.91 kN/mm^2, Table 3.5) using micromechanics and CLT. The low values of SD and CV show a consistency in the shear properties (and hence the material configuration) and in the testing procedure. The longitudinal shear strength of the GRP material (coupons loaded normal to the direction of fibres) is 82.8 N/mm^2 with a SD=1.82 and CV=2.2%. No theoretical or experimental value of ultimate shear strength of this material is available in the literature for comparison. However, Fibreforce Ltd, UK quotes a value of shear strength of 60MPa (1MPa=1N/mm^2) for a group of series 800 GRP profiles, of which the current profile (51×51×3.2) is a member. The quoted value is a minimum average established through experimental studies carried out by the

[††††] ASTM D5379M Table 1, giving the strain ranges for the chord modulus.

manufacturers. Therefore the measured strength may be taken as comparable and conservative.

For 6mm thick ASTM coupons, the average ($\bar{x}$) values of chord and secant shear moduli (3.96 and 3.98kN/mm^2) agree closely with the predicted value of (3.92kN/mm^2, Table 3.5) establishing the validation of test fixture, testing equipment and procedures. Calculated values of SD and CV (0.07 and 1.77) are lower than corresponding values for the set of 3.2mm thick coupons, indicating a reduced scatter and increased consistency of the specimen coupons. However a higher scatter (SD=4.48 and CV=5.12%) has been observed in the calculation of ultimate shear strength.

The angle $\phi_{P,Q}$ indicates the direction of principal normal stresses (ε_P and ε_Q) from the direction of orientation of strain gauge 1 in the rosette. The strain gauge 1 is aligned in the direction of loading (see Fig. 3.31). As the direction of max shear stress is normal to the directions of principal stress direction, and $\tan\phi = \tan(\phi+90)$, $\phi_{P,Q}$ is the direction of maximum stress from the orientation of strain gauge 1. The calculated angles '$\phi_{P,Q}$' (Tables 3.6-3.7) are close to 45°, indicating the maximum shear stress at the centre (measured by the strain rosette) of the coupon is parallel to the sides of the notches, minimising the strain concentrations at the notch roots.

All the ASTM coupons failed along the central notched sections under shear (maximum shear being at the centre) (see Plates 3.2 - 3.3). The reinforcing fibres delaminated from the matrix, deformed under the shear load (normal to the direction of fibres) but did not break (the two halves remained in tact). This type of failure and the failure locations are typical of those approved as satisfactory by the relevant test standards.

Short Longitudinal coupons

Average chord and secant moduli of five 3.2mm thick short longitudinal shear coupons are 3.95 and 3.96kN/mm^2 (Table 3.8) respectively. The measured moduli are in close agreement (difference being only 1.3%) with the predicted shear modulus (3.91kN/mm^2, Table 3.5). Whilst for 6mm thick coupons the average chord and secant moduli are calculated as 3.95kN/mm^2 (Table 3.9), which are very close (with 0.25% difference) to the predicted value of 3.94 kN/mm^2 (Table 3.5). The low values of the SDs and SVs for the short longitudinal shear coupons demonstrate the uniformity of the shear properties of the box-sections in the longitudinal directions and the consistency of the test procedure. Average ultimate shear strengths for the two sets of 3.2mm and 6mm thick coupons are

85.2 and 85.7N/mm^2, which are similar to the shear strengths measured by ASTM standard coupons. The SD and CV value for the shear strength are also acceptably low. All the short longitudinal shear coupons failed (see Plates 3.4-3.5) at the central sections under the applied shear force. The failure modes are similar to the failure of ASTM coupons and are admissible according to the ASTM specifications (ASTM D5379M).

Validation of the short coupon

Experimental results of ASTM coupon are used to validate the performance of the short longitudinal coupons. The shear moduli measured by short coupons (3.95 to 3.96kN/mm^2) are very close to that obtained by ASTM coupons (3.92 to 3.98kN/mm^2) (difference being 0.05 to 0.08 %). Similarly the ultimate shear strengths measured by short coupon (85.2 to 85.7N/mm^2) are very close to the strengths measured by ASTM (82.8 to 86.4N/mm^2) with a small difference of 0.07 to 2.7%.

The representation of short coupon test results to the outcomes of ASTM coupon results has been established using the "Student's t test" (Kennedy and Neville, 1976), where a significance of difference't' is calculated as;

$$t = \frac{\bar{x}_1 - \bar{x}_2}{S_d} \tag{3.23a}$$

$$S_d = S_c \sqrt{\frac{n_1 + n_2}{n_1 \times n_2}} \tag{3.23b}$$

$$S_c^2 = \frac{SD_1^2(n_1 - 1) + SD_2^2(n_2 - 1)}{(n_1 - 1) + (n_2 - 1)} \tag{3.23c}$$

where S_c is the combined variance and S_d is the standard deviation of the difference of the means, n is the number of coupons in each set, SD is standard deviation for each set, and subscripts 1 and 2 are used for ASTM and short coupon sets respectively.

The 't' value for the chord and secant shear moduli obtained from the ASTM and short coupon results fall in a range of 0.69 to 1.67, whilst 't' values for the shear strength results are calculated as 0.06 and 0.44 for the 3.2 and 6 mm coupons respectively. For a degree of freedom = [(5+5)-2]=8, the 't' value given in Table A-8 in Kennedy and Neville (1976), for a 5 percent level of significance (in the difference of the data) is 2.4. The greater value of 't' as tabulated (2.4) compared with the calculated values (0.06 to 1.67), suggests that the difference between the ASTM and the short coupon data is significant to less than 5%. There is at least 95% confidence that the short coupon is able to represent

the behaviour of ASTM coupon in determining the shear properties of the composite material. Further the SD and CV values of the ASTM and the short coupons compare favourably (Tables 3.6-3.9).

The failure modes observed in the ASTM and short coupon are also similar. All the coupons failed at the central test section in a similar fashion i.e., delamination of fibres and matrix and bending (rather than breaking) of fibres under shear.

It is concluded, therefore, that short coupon results are valid, and that short coupon can be used to evaluate the in-plane shear properties in the longitudinal direction where a standard ASTM coupon would normally be used.

Short transverse coupons

The chord and secant shear moduli (in transverse direction) range from 2.81 to 2.95kN/mm^2 with an average value of 2.85 kN/mm^2 for both the 3.2mm and 6mm thick transverse coupons. The moduli in the transverse coupons are lower than the moduli calculated in the longitudinal direction. The roving are in a direction parallel to the direction of load in comparison to the longitudinal specimens. The matrix (resin), is established as the unreinforced failure plane, possessing a lower shear strength and failing prior to any fibre failure.

These results are more consistent than the results produced by the ASTM and short longitudinal coupons. The SD and CV values are also in a narrow range (0.10 to 0.13) and (4.21 to 4.56%) showing uniform transverse moduli. No specific theoretical or experimental values are found from the literature to compare the experimental outcomes of this study. However, having established the validity of the short longitudinal shear coupons, results obtained from the transverse coupon are also considered valid. The average of ultimate shear strengths from the 3.2mm and 6mm thick coupons are 64.4N/mm^2 and 68.0N/mm^2 respectively (Tables 3.9-3.10). Although no study to the relevant box-sections has been reported in the literature, the ultimate strength is comparable to the minimum shear strength (60 N/mm^2) specified by FIBREFORCE, Ltd, UK, for the structural design of similar GRP profiles.

The short transverse coupons failed at the centre under the applied shear loading (Plates 3.6-3.7) consistent with the ASTM and longitudinal specimen failure modes.

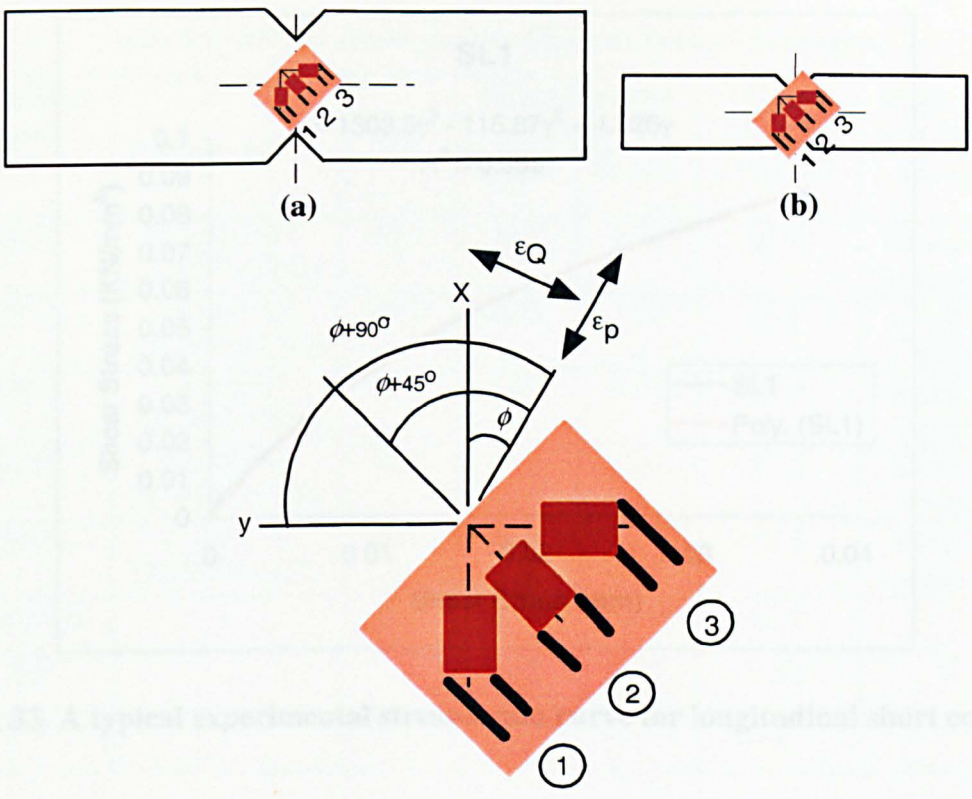

Fig 3.31 Strain rosette (45° rectangular) bonded to (a) ASTM coupon (b) Short coupon. (c) Angle ϕ represents the acute angle from gauge 1 to the principal axis

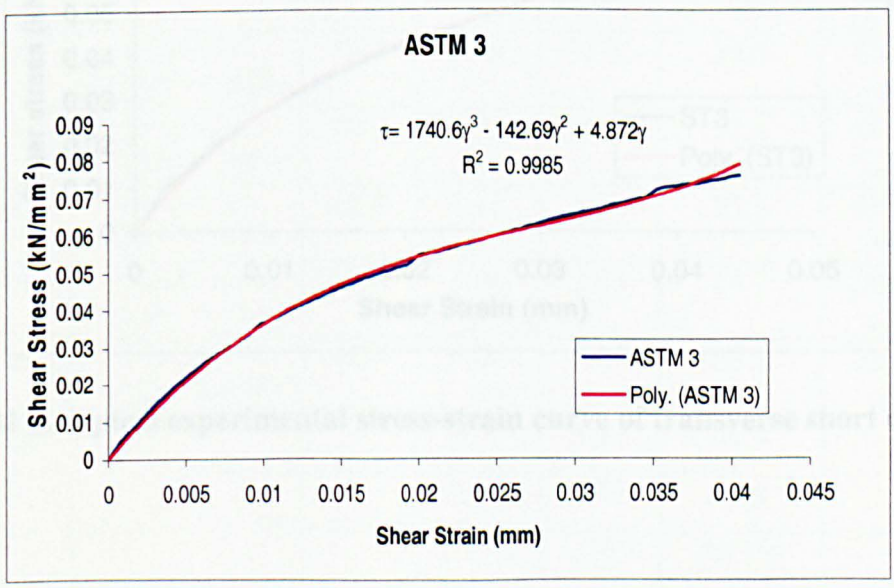

Fig 3. 32 A typical experimental stress-strain curve for ASTM coupon .

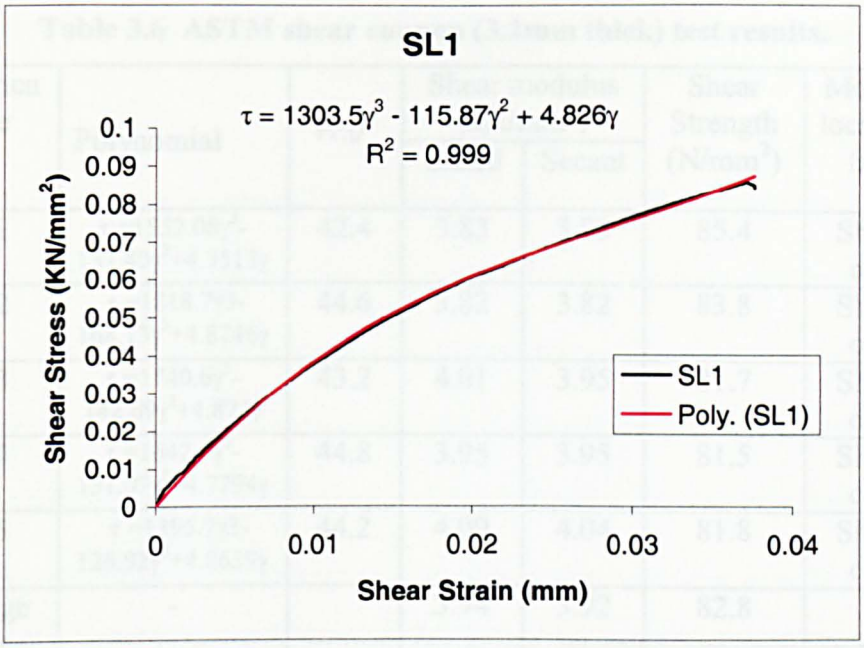

Fig 3. 33 A typical experimental stress-strain curve for longitudinal short coupon

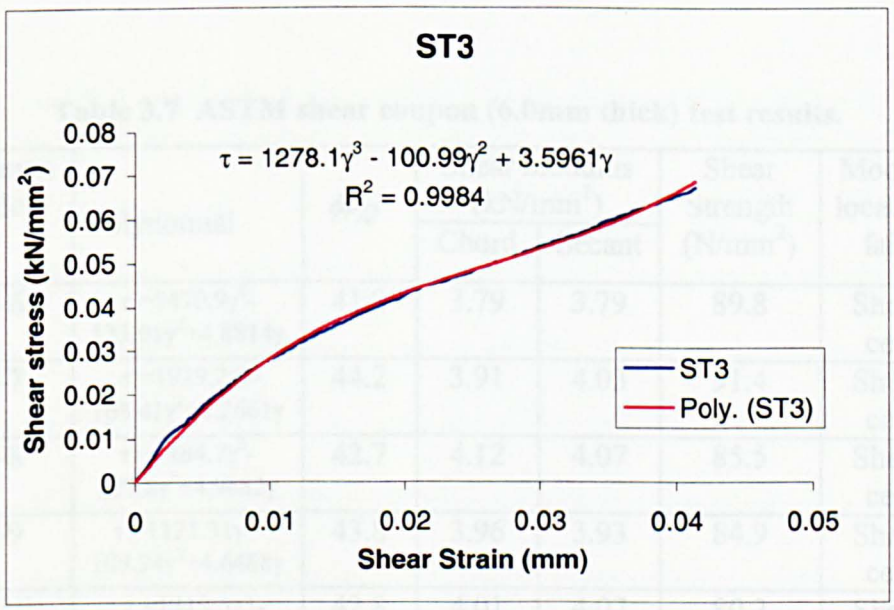

Fig 3. 34 A typical experimental stress-strain curve of transverse short coupon.

Table 3.6 ASTM shear coupon (3.2mm thick) test results.

Specimen Code	Polynomial	$\phi_{P,Q}°$	Shear modulus (kN/mm^2)		Shear Strength (N/mm^2)	Mode and location of failure
			Chord	Secant		
LC-1	$\tau = 1552.08\gamma^3 - 137.40\gamma^2 + 4.3513\gamma$	42.4	3.83	3.83	85.4	Shear at centre
LC-2	$\tau = 1818.7\gamma 3 - 168.13\gamma^2 + 4.8746\gamma$	44.6	3.82	3.82	83.8	Shear at centre
LC-3	$\tau = 1740.6\gamma^3 - 142.69\gamma^2 + 4.872\gamma$	43.2	4.01	3.95	81.7	Shear at centre
LC-4	$\tau = 1642.9\gamma^3 - 131.07\gamma^2 + 4.7794\gamma$	44.8	3.95	3.95	81.5	Shear at centre
LC-5	$\tau = 1395.7\gamma 3 - 126.92\gamma^2 + 4.8639\gamma$	44.2	4.09	4.04	81.8	Shear at centre
Average	-		3.94	3.92	82.8	-
SD	-		0.12	0.11	1.82	-
CV	-		3.05%	2.81%	2.2%	-

Table 3.7 ASTM shear coupon (6.0mm thick) test results.

Specimen Code	Polynomial	$\phi_{P,Q}°$	Shear modulus (kN/mm^2)		Shear Strength (N/mm^2)	Mode and location of failure
			Chord	Secant		
LC-6	$\tau = 1470.9\gamma^3 - 123.01\gamma^2 + 4.8814\gamma$	41.9	3.79	3.79	89.8	Shear at centre
LC-7	$\tau = 1929.2\gamma 3 - 164.41\gamma^2 + 5.2661\gamma$	44.2	3.91	4.03	91.4	Shear at centre
LC-8	$\tau = 1484.7\gamma^3 - 127.8\gamma^2 + 4.9682\gamma$	42.7	4.12	4.07	85.5	Shear at centre
LC-9	$\tau = 1121.31\gamma^3 - 109.94\gamma^2 + 4.6488\gamma$	43.8	3.96	3.93	84.9	Shear at centre
LC-10	$\tau = 1319.5\gamma 3 - 119.79\gamma^2 + 4.8493\gamma$	42.8	4.01	4.07	80.2	Shear at centre
Average	-		3.96	3.98	86.4	-
SD	-		0.07	0.07	4.48	-
CV	-		1.77%	1.76%	5.12%	-

Table 3.8 Longitudinal short shear coupon (3.2mm thick) test results.

Specimen Code	Polynomial	$\phi_{P,Q}°$	Shear modulus (kN/mm^2)		Shear Strength (N/mm^2)	Mode and location of failure
			Chord	Secant		
SL-1	$\tau = 1303.5\gamma^3 - 115.87\gamma^2 + 4.826\gamma$	44.3	3.97	3.96	86.7	Shear at centre
SL-2	$\tau = 1013.6\gamma 3 - 111.04\gamma^2 + 4.6558\gamma$	43.2	4.01	3.95	82.9	Shear at centre
SL-3	$\tau = 1324.6\gamma^3 - 114.05\gamma^2 + 4.6447\gamma$	44.1	3.93	3.90	82.5	Shear at centre
SL-4	$\tau = 897.83\gamma^3 - 94.431\gamma^2 + 4.7329\gamma$	42.4	3.89	3.92	87.4	Shear at centre
SL-5	$\tau = 1161.1\gamma 3 - 102.78\gamma^2 + 4.7174\gamma$	43.7	3.95	4.05	86.3	Shear at centre
Average	-		3.95	3.96	85.2	-
SD	-		0.05	0.19	1.82	-
CV	-		1.14%	4.8%	2.2%	-

Table 3.9 Longitudinal short shear coupon (6.0mm thick) test results.

Specimen Code	Polynomial	$\phi_{P,Q}°$	Shear modulus (kN/mm^2)		Shear Strength (N/mm^2)	Mode and location of failure
			Chord	Secant		
SL-6	$\tau = 706.38\gamma^3 - 82.16\gamma^2 + 4.426\gamma$	44.5	3.95	3.91	86.1	Shear at centre
SL-7	$\tau = 596.46\gamma 3 - 82.37\gamma^2 + 4.5924\gamma$	44.6	4.03	4.04	92.1	Shear at centre
SL-8	$\tau = 725.71\gamma^3 - 84.81\gamma^2 + 4.5408\gamma$	44.7	3.92	3.98	80.5	Shear at centre
SL-9	$\tau = 838.61\gamma^3 - 89.779\gamma^2 + 4.5315\gamma$	44.2	3.94	3.94	84.8	Shear at centre
SL-10	$\tau = 810.54\gamma 3 - 87.147\gamma^2 + 4.413\gamma$	44.8	3.89	3.87	85.2	Shear at centre
Average	-		3.95	3.95	85.7	-
SD	-		0.19	0.12	3.13	-
CV	-		4.81%	3.04%	3.65%	-

Table 3.10 Transverse short shear coupon (3.2mm thick) test results.

Specimen Code	Polynomial	$\phi_{P,Q}°$	Shear modulus (kN/mm^2)		Shear Strength (N/mm^2)	Mode and location of failure
			Chord	Secant		
ST-1	$\tau = 1263.9\gamma^3 - 101.78\gamma^2 + 3.4713\gamma$	44.3	2.81	2.81	64.1	Shear at centre
ST-2	$\tau = 1418.2\gamma 3 - 97.58\gamma^2 + 3.2413\gamma$	43.8	2.84	2.87	65.3	Shear at centre
ST-3	$\tau = 1278.1\gamma^3 - 100.99\gamma^2 + 3.5961\gamma$	42.6	2.85	2.94	68.9	Shear at centre
ST-4	$\tau = 1239.9\gamma^3 - 90.888\gamma^2 + 3.4174\gamma$	43.2	2.86	2.83	62.6	Shear at centre
ST-5	$\tau = 996.96\gamma 3 - 84.205\gamma^2 + 3.3481\gamma$	42.5	2.88	2.80	60.9	Shear at centre
Average	-		2.85	2.85	64.4	-
SD	-		0.12	0.12	1.82	-
CV	-		4.21%	4.21%	3.02%	-

Table 3.11 Transverse short shear coupon (6.0mm thick) test results.

Specimen Code	Polynomial	$\phi_{P,Q}°$	Shear modulus (kN/mm^2)		Shear Strength (N/mm^2)	Mode and location of failure
			Chord	Secant		
ST-6	$\tau = 579.24\gamma^3 - 58.475\gamma^2 + 3.549\gamma$	44.1	2.85	2.88	68.1	Shear at centre
ST-7	$\tau = 593.72\gamma 3 - 59.937\gamma^2 + 3.6377\gamma$	41.6	2.79	2.83	71.4	Shear at centre
ST-8	$\tau = 535.8\gamma^3 - 54.09\gamma^2 + 3.2828\gamma$	42.4	2.87	2.79	70.5	Shear at centre
ST-9	$\tau = 640.62\gamma^3 - 63.577\gamma^2 + 3.4124\gamma$	31.7	2.94	2.95	64.9	Shear at centre
ST-10	$\tau = 679.1\gamma 3 - 63.667\gamma^2 + 3.8734\gamma$	43.5	2.81	2.79	65.2	Shear at centre
Average	-		2.85	2.85	68.0	-
SD	-		0.13	0.10	2.89	-
CV	-		4.56%	3.51%	4.25%	-

3.4 COMPRESSIVE PROPERTIES

The compressive properties (strength and stiffness) of the pultruded box profiles, investigated for buckling behaviour, in this study (Fig. 1.4 & 1.5) have been experimentally measured. The procedure adopted for this experimental study has been introduced by Mottram (1994). The material specimen is a parallel sided rectangular coupon (70×20mm) obtained from the uniformly thick walls (sides) of the box sections. Only longitudinal coupons have been extracted and tested as transverse coupons are not available due the profiles dimensional constraints. Furthermore, the profiles are only to be tested in longitudinal compression.

Coupon Preperation

The coupons, cut from the side walls of box-sections, in a direction parallel to the longitudinal axis and remote from the edges (joints) to avoid edge effects (Mottram, 1991), have been machined to the required dimensions (70×20mm). Five coupons from each of the 51×51×3.5mm and 44×44×6.0mm box-section profiles have been extracted. Coupons have been cleaned and numbered sequentially. The exact dimensions of the finished coupons have been measured up to 0.01mm accuracy, using a micrometer and recorded for subsequent calculations. To each coupon, two single-element strain gauges, one on each side at its geometric centre, have been bonded (M-Bond 200 adhesive) having aligned the longitudinal axes of the both specimen and gauge. Pair of gauges being used to enable identification of bending arising from imperfections.

Bondable terminals have been used to secure the solder joints between the strain-gauge conductors and the connecting wires, with double wires (two with each terminal) able to provide temperature compensation during the test. The prepared coupons were dispatched for testing to the School of Engineering University of Warwick, Coventry, for testing (for a schematic of the testing see Fig 2.8).

Compression testing

A prepared coupon is inserted to a depth of 25mm into lower mounting block of the testing rig. The upper mounting block (attached to upper platen of the compression testing machine) is lowered gradually and the coupon aligned to fit in the upper block. The clamping arrangement of the rig holds the coupon vertical, aligning and confining at the ends against brooming or splitting. Consequently 25mm of coupon length on each end is

gripped by the mounting blocks, leaving an un-supported length of 20mm at the centre to act as the test section. The failure of the coupon under the compression load is expected to occur in this section. The test-rig has been loaded in a DARTEC 9500 compression machine for compression and concentric loading. The rate of loading has been maintained by controlling the stroke rate at 0.01mm/sec. Strain produced at the central test section and corresponding applied loads have been recorded in addition to real-time stress strain graphs.

Compression test results

All the coupons failed in a similar failure mode i.e. material failure near the ends (Plate. 3.9 and 3.10). Ideally the failure should have occurred in the test section i.e., at the mid-length of the coupon. The similarity in the failure pattern in all tested coupons implies the inability of the clamping arrangements to promote gauge section failure. However the compression properties obtained (Tables 3.12 and 3.13) in the tests suggest that the coupons were loaded to a maximum strength prior at "failure". The test data has been processed using a similar procedure to that described for the shear tests within the exception that a second degree polynomial was used in the curve fitting. The longitudinal compressive modulus has been calculated from polynomial stress values against strain values of 1000 and 6000με, as:

$$E_{x,c} = \frac{\Delta\sigma}{\Delta\varepsilon}$$

where $\Delta\sigma$ is the difference between stresses (in kN/mm^2) at strain values of 1000 and 6000με and $\Delta\varepsilon$ is the difference between the strain values i.e., 0.005mm (corresponding to strain interval of 1000 and 6000με). Stress-strain plots for three 3.2mm and five 6mm compressive coupons are given in Fig 3.35. The ultimate compressive stress has been evaluated from the maximum load at failure. Results from the eight coupons (three 3.2mm and five 6mm thick) are summarised in Table 3.12 and 3.13. Two of the 3.2mm thick coupons could not be tested owing to failure of the gauges. Stress-strain graphs for the tested coupons along with the polynomial curve fits are given in Fig. 3.35. Average compressive modulus (quoted as one representative value of the material) for the two box-sections has been calculated using (3.19). Similarly ultimate compressive stresses have been averaged to quote one value as the compressive strength of the material.

Standard deviation (SD) (3.20) and coefficients of variation (CV) (3.21) have also been calculated and included in Tables 3.12-3.13.

3.5 TENSILE PROPERTIES

Tensile properties in the longitudinal (parallel to the fibres) direction have been taken equal to the longitudinal compressive properties of the GRP composite profiles (Bank et al 1994, Zureick and Scott 1997).

Tensile properties of one of the box-sections, being investigated in this study, i.e. 51×51×3.2mm were measured by Saribiyik (2000). The properties have been predicted numerically by micromechanics and experimentally by testing coupons in longitudinal and transverse directions. Standard ASTM coupons were used in longitudinal direction while short coupons were used in the transverse direction. The experimental outcomes for the 51x51x3.2mm box-sections are;

$E_{x,t} = 26.7\text{kN/mm}^2$ $(E_{x,c} = 30.3\text{kN/mm}^2)$[15]

$\sigma_t = 388\text{N/mm}^2$ $(\sigma_c = 385\text{N/mm}^2)$

where $E_{x,t}$ is the longitudinal elastic modulus in tension; σ_t is the ultimate longitudinal tensile strength; $E_{x,c}$ is longitudinal elastic modulus in compression; and σ_c is the ultimate compressive strength.

3.6 TOLERANCE FOR MATERIAL PROPERTIES

Using the average property values for GRP material, from Tables 3.5 -3.12, tolerance for elastic properties has been estimated at 95% confidence level, using (3.24) (Kennedy and Neville 1976, Wang and Zureick 1994):

$$\bar{x} \pm \frac{1.96SD}{\sqrt{n}} \qquad (3.24)$$

51×51×3.2mm box-section

Longitudinal shear Modulus =3.95±0.12kN/mm^2

Transverse shear Modulus =2.85±0.04kN/mm^2

Longitudinal shear strength =82.8±2.6N/mm^2

Transverse shear strength =64.4±2.5N/mm^2

Compressive longitudinal Modulus = 30.3±0.40N/mm^2

Compressive longitudinal Strength = 385±8.0N/mm^2

---

[15] Values in the parenthesis are compressive properties for 3.2mm thick coupon from the present study.

44×44×6mm box-section

Longitudinal shear Modulus =3.95±0.13kN/mm^2

Transverse shear Modulus =2.85±0.05kN/mm^2

Longitudinal shear strength =85.8±3.3N/mm^2

Transverse shear strength =68.0±3.73N/mm^2

Compressive longitudinal Modulus = 33.2±1.5kN/mm^2

Compressive longitudinal Strength = 385±16.3N/mm^2

3.7 CONCLUSIONS AND RECOMENDATIONS

Material properties of the two GRP structural profiles (51×51×3.2 and 44×44×6.0mm box-sections) have been established using theoretical and experimental studies, for use in stability analysis of these profiles used as columns in the composite structures. The outcomes of the research presented in this chapter are summarised here;

1. Elastic constants for the composite material have been predicted using constitutive information (manufacturer supplied) and a theoretical approach (micromechanics and CLT) and reported (Table 3.5).
2. Experimental studies have been conducted to measure the in-plane shear and compressive properties of these profiles. Standard ASTM shear coupon, 76×20mm rectangular notched beam (ASTM Designation D5379M-93), has been used to measure the longitudinal in-plane shear properties (modulus and strength). An alternative, enhanced, AFPB type shear test fixture has been proposed and adopted to apply a uniform pure shear load across the central test section of ASTM coupon.
3. The performance of the ASTM shear coupon under the shear loading has been assessed using the finite element method as a benchmark to the establishment of a short equivalent. The agreement of the theoretical and numerical results validated the FEA model and analysis itself.
4. A short shear coupon, similar in shape and geometry to the ASTM coupon, has been proposed to measure the in-plane transverse shear properties in cases where the ASTM coupon cannot be extracted from the pultruded sections. The proposed short coupon is 40×10mm rectangular notched beam. FEA models (2D, surface) of an individual short coupon and fixture encapsulated short coupon subjected to idealised (point loading described in Fig. 3.4) loading and of coupon loaded in AFPB test fixture has been analysed for the shear stress/strain distributions across the central test section and compared with the theoretical values. The effects of variations in the geometric

parameters (overall width of coupon, notch depth, notch angle) have been investigated numerically. A short coupon with a length = 40mm, depth = 10mm, thickness equal to webs of the box-sections, grooved at the mid-length of each long side with one 90° sharp V-notch of notch depth = 2.5mm is recommended.

5. Aluminium tabs have been proposed located parallel to the loading bars to avoid premature failure of coupon in the contact regions. Analysis of a volume model (3D) of the proposed short shear coupon has been indicated that the tabs do not alter the uniformity of the shear strain distribution across the central section of the test region.
6. A finite element analysis of the coupon encapsulated in the test fixture is essential in determining the loading applied to the coupon for use in calculating the elastic moduli and strength constants.
7. In-plane shear properties have been measured experimentally using ASTM and short shear coupons extracted from both box-profiles. ASTM coupons show consistent values of the shear moduli and shear strengths with low SD and CV values.
8. Short coupons in the longitudinal directions gave consistent and similar results to the ASTM outcomes demonstrated by the statistical "Student's t test". The test validates the performance of the short shear coupon for the measurement of in-plane shear properties where a standard ASTM coupon would normally be used and by inference, where geometric constraints apply. Short coupons with aluminium tabs are recommended when measuring transverse shear properties of the two box-profiles.
9. All the coupons failed at the central test section (between the notches). Longitudinal coupons failed by delamination of fibres and matrix, whilst the overall integrity of the coupon was maintained. Conversely transverse coupons with tabs failed at the centre by matrix failure splitting the coupon into two halves with the consequent loss of integrity.
10. From the experimental outcomes of the ASTM and short coupons, the average shear properties of the box-sections are G_{xy} = 3.95kN/mm^2; $F_{u,t}$ = 85N/mm^2, G_{yx}= 2.85kN/mm^2 and $F_{u,}$t = 66N/mm^2. The material's shear response behaves behaviour is non-linear but elastic.
11. The compressive properties measured by testing the material coupons 3.2mm thick, are $E_{c,t}$ = 30.3kN/mm^2 and $\sigma_{u,c}$ = 385N/mm^2. The average compressive properties for the 6.0mm thick box-section are $E_{c,t}$ = 33.23kN/mm^2 and $\sigma_{u,c}$ = 523N/mm^2.

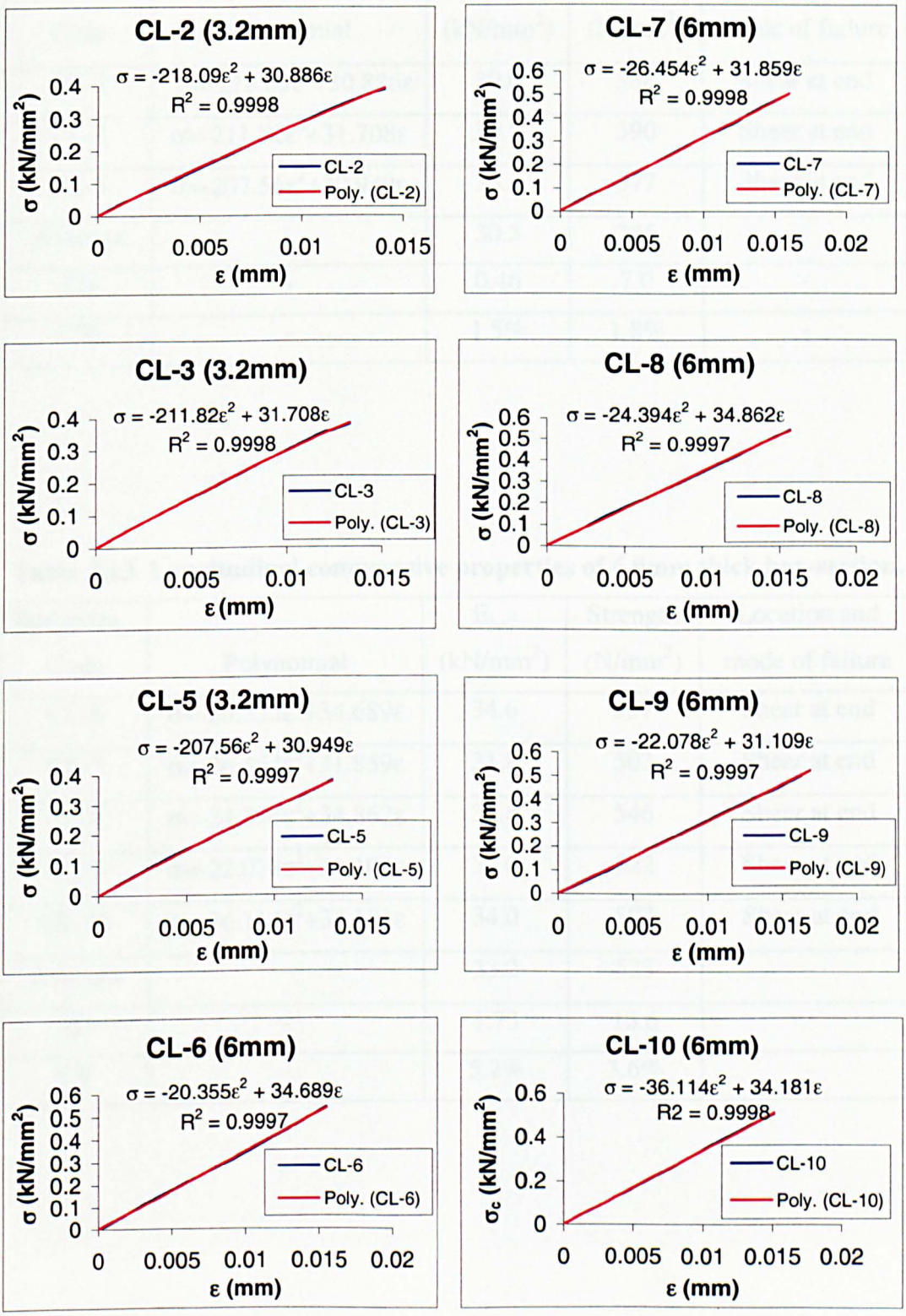

Fig. 3.35. Stress-strain curves for the compression coupons.

Table 3.12 Longitudinal compressive properties of 3.2mm thick box-section.

Specimen Code	Polynomial	$E_{L,c}$ (kN/mm^2)	Strength (N/mm^2)	Location and mode of failure
CL-2	$\sigma=-218.09\varepsilon^2+30.886\varepsilon$	30.0	388	Shear at end
CL-3	$\sigma=-211.82\varepsilon^2+31.708\varepsilon$	30.8	390	Shear at end
CL-5	$\sigma=-207.56\varepsilon^2+30.949\varepsilon$	30.1	377	Shear at end
Average		30.3	385	-
SD	-	0.46	7.0	-
CV	-	1.5%	1.8%	-

Table 3.13 Longitudinal compressive properties of 6.0mm thick box-section.

Specimen Code	Polynomial	$E_{L,c}$ (kN/mm^2)	Strength (N/mm^2)	Location and mode of failure
CL-6	$\sigma=-20.355\varepsilon^2+34.689\varepsilon$	34.6	537	Shear at end
CL-7	$\sigma=-26.454\varepsilon^2+31.859\varepsilon$	31.8	503	Shear at end
CL-8	$\sigma=-24.394\varepsilon^2+34.862\varepsilon$	34.8	546	Shear at end
CL-9	$\sigma=-22.078\varepsilon^2+31.109\varepsilon$	31.0	522	Shear at end
CL-10	$\sigma=-36.114\varepsilon^2+34.181\varepsilon$	34.0	507	Shear at end
Average		33.2	523	-
SD	-	1.73	18.6	-
CV	-	5.2%	3.6%	-

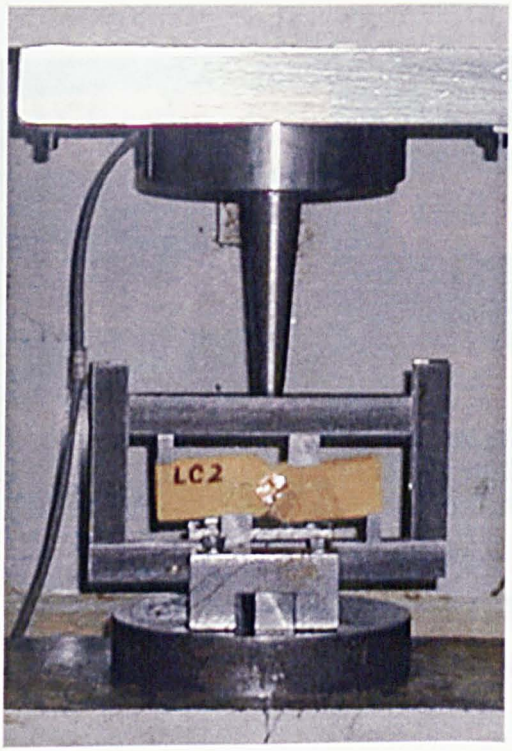

(a)

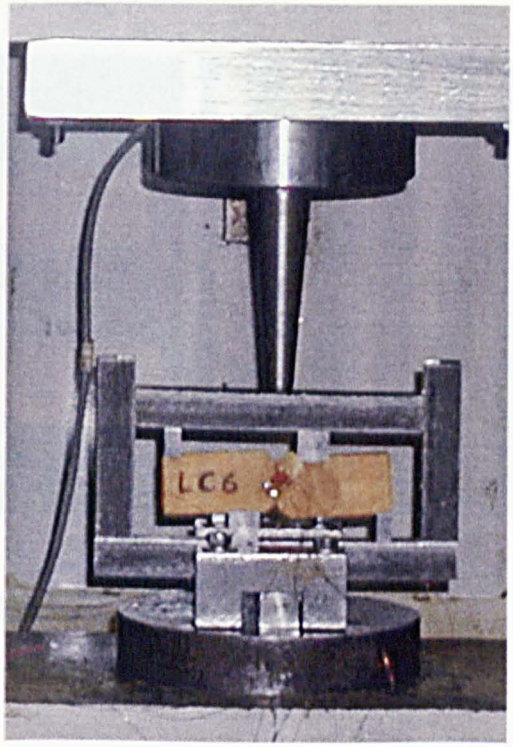

(b)

(c)

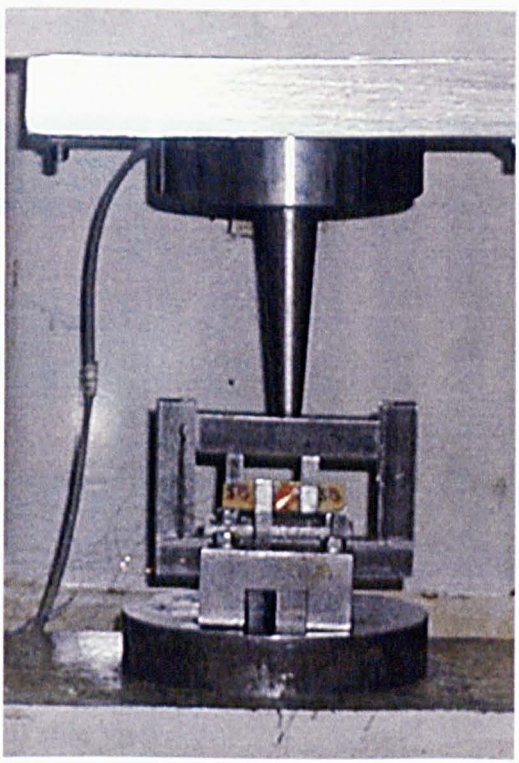

(d)

Plate 3.1 Testing arrangements for shear coupons;

(a) ASTM coupon 3.2mm thick; (b) ASTM coupon 6.0mm thick;

(c) short longitudinal coupon 6.0mm thick; (d) short transverse coupon with tabs.

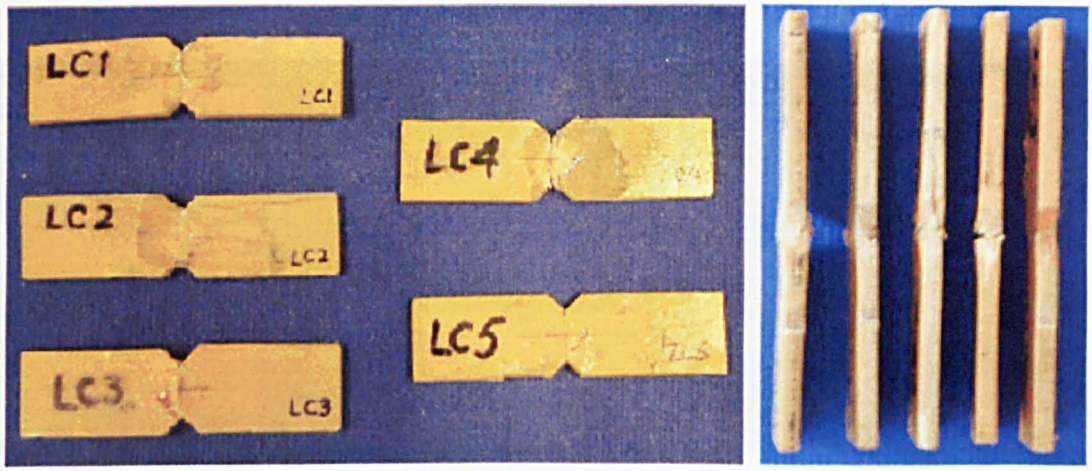

(a) (b)

Plate 3.2 Failure modes of ASTM shear coupons (3.2mm thick): (a) front view; (b) side view.

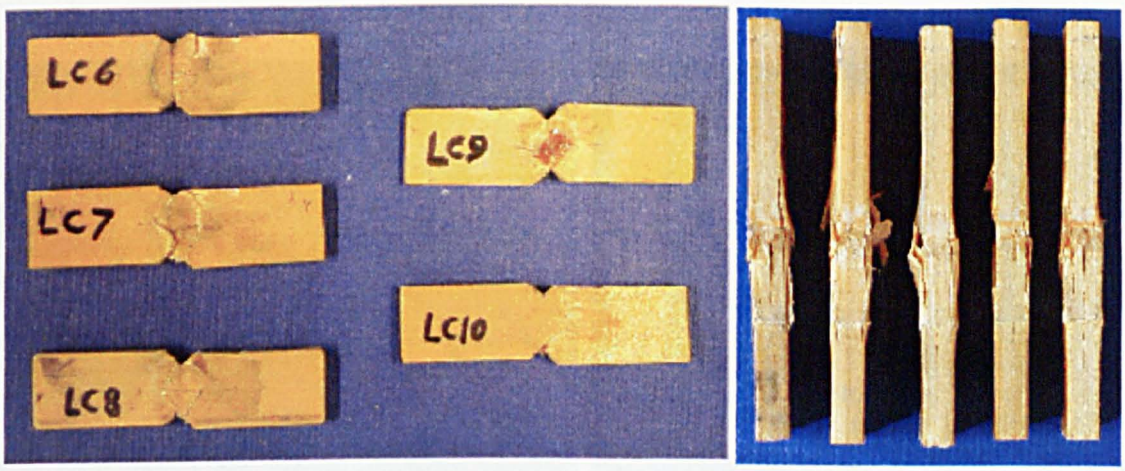

(a) (b)

Plate 3.3 Failure modes of ASTM shear coupons (6.0mm thick): (a) front view; (b) side view.

(a) (b)

Plate 3.4 Failure modes of short longitudinal coupons (3.2mm thick): (a) front view; (b) side view.

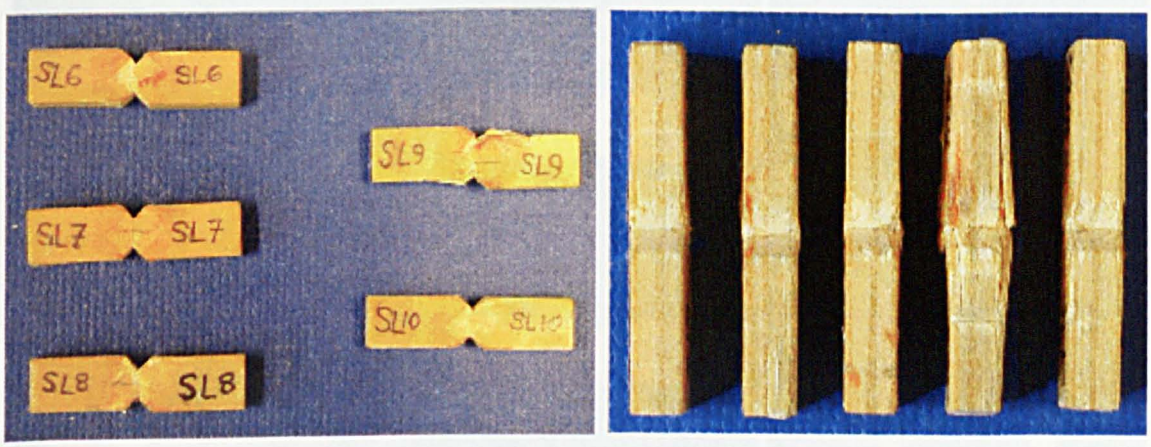

(a) (b)

Plate 3.5 Failure modes of short longitudinal coupons (6.0mm thick): (a) front view; (b) side view.

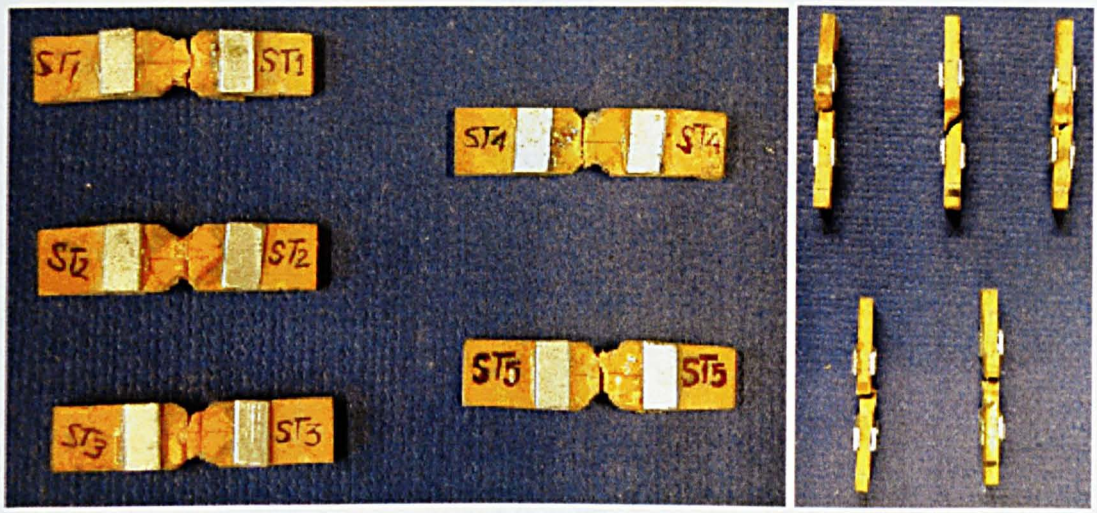

(a) (b)

Plate 3.6 .Failure modes of short transverse coupons (3.2mm thick): (a) front view; (b) side view.

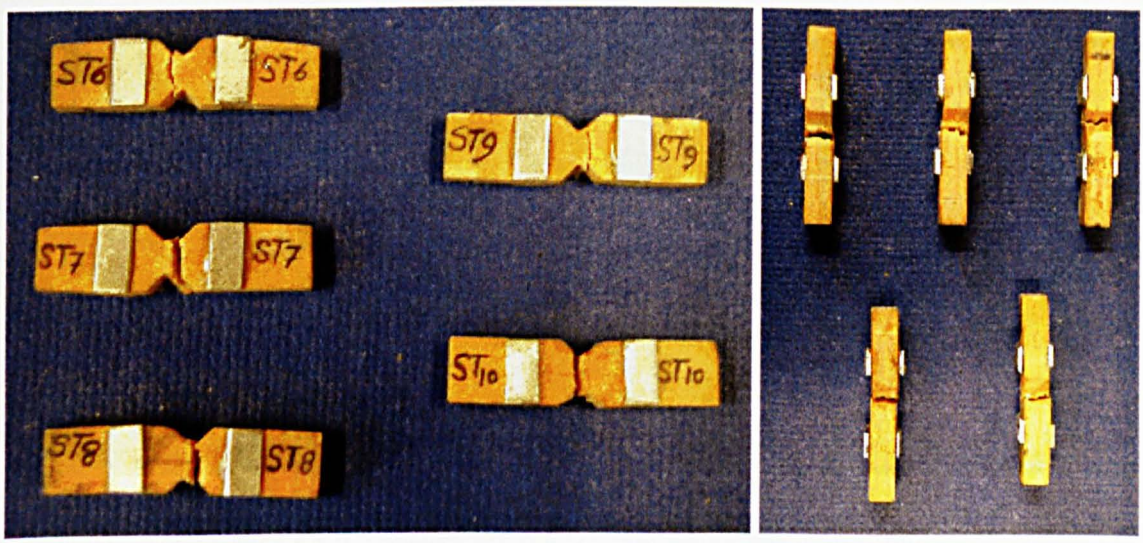

(a) (b)

Plate 3.7 Failure modes of short transverse coupons (6.0mm thick): (a) front view; (b) side view.

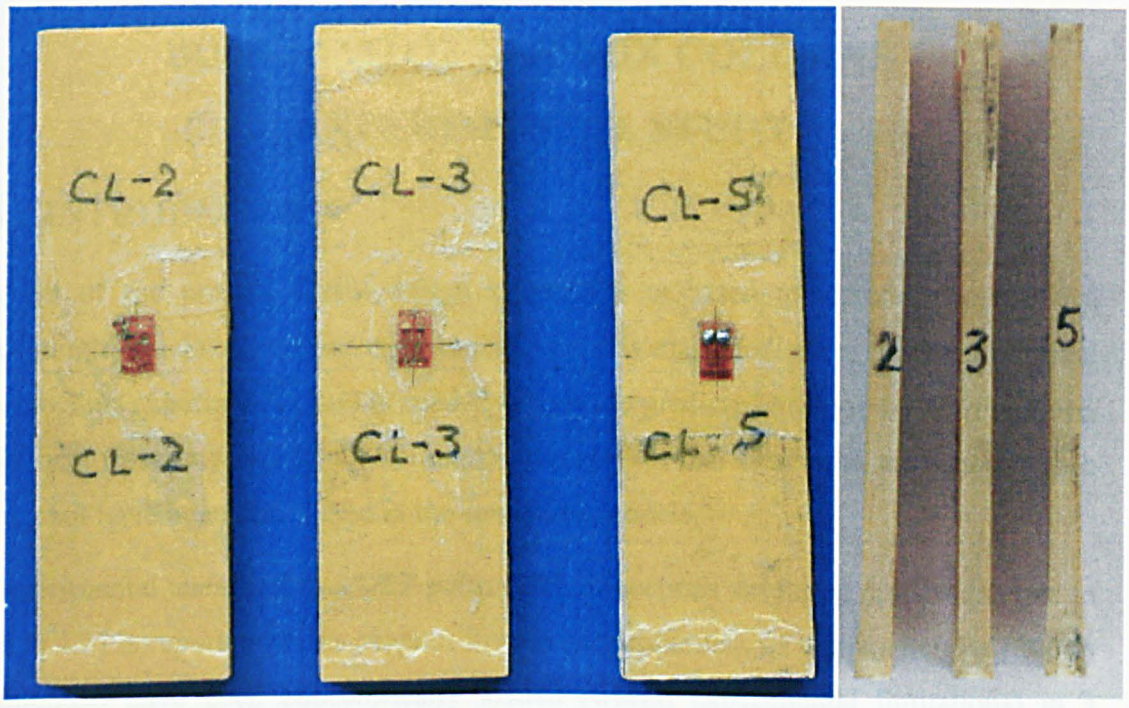

(a) (b)

Plate 3.8 Failure modes of compressive coupons (3.2mm thick): (a) front view; (b) side view.

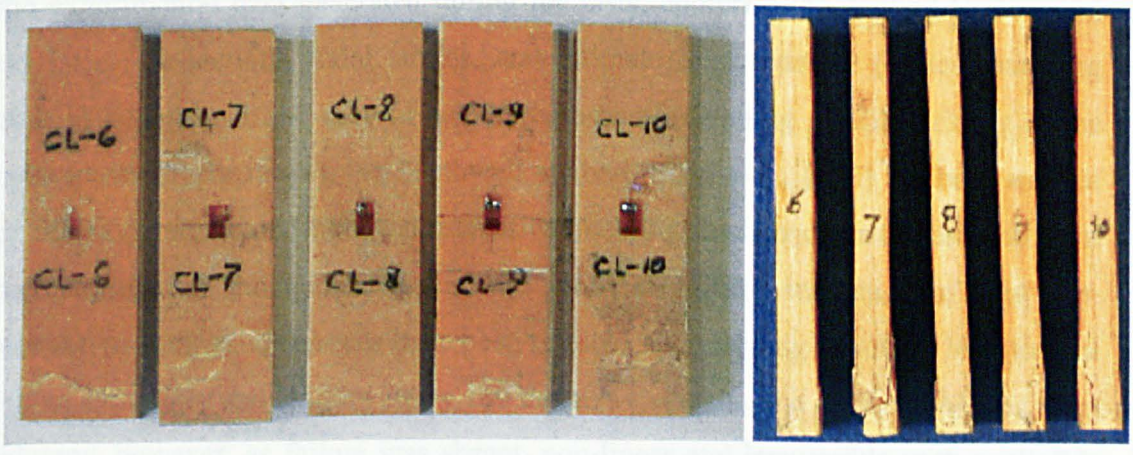

(a) (b)

Plate 3.9 Failure modes of compressive coupons (6.0mm thick): (a) front view; (b) side view.

CHAPTER 4

BUCKLING OF GRP BOX COLUMNS – EXPERIMENTAL STUDY

4.1 INTRODUCTION

Much of the present useful design knowledge is based on careful experiments. Although judiciously chosen mathematical models may predict the expected physical behaviour, experimental data is needed to validate predicted behaviours. Furthermore, physical tests may exhibit the complete behaviour of real structures, aspects of which may not have been considered in the simplified models.

Experimental testing of two GRP pultruded box-sections structural profiles (shown in Plate 1.5) is reported in this chapter. Specimens (columns), of various heights (200 to 2000mm) have been concentrically loaded (within experimental limitations) in a purposely constructed test rig with pin supports (knife-edges) and vertical alignment. The main objectives of the experimental programme include the determination of critical buckling loads and failure modes, with classifications into global, local, material failure and compound sets.

The experimental data generated during the tests, comprise the applied loads, axial and lateral deflections, axial strains, and ultimate load capacity (critical buckling loads in general). In the case of slender columns (exhibiting global buckling in the linear elastic linear range), the Southwell method (Southwell, 1932) has been applied for the calculations of single representative buckling loads and for the estimation of imperfections in the geometries of the profiles. Taking advantage of this non-destructive method, specimens have been retested after rotating about the longitudinal axis of symmetry and lengthwise by 180 degrees (reversing the orientation). For short columns, however, as failure was abrupt, non-linear and irreversible with negligible transverse deflections, the Southwell method could not be applied.

The experimental outcomes have been compared with the theoretically predicted results using classical approaches and the design guidance from Eurocomp design code and manufacturers' design manuals. A unified design curve for the two-box sections under investigation, have been produced using the procedure prescribed by

Barbero and DeVivo (1999). Comparisons with linear and non-linear analyses are given in Chapter 5.

To establish the effects of perforations on the load carrying capabilities of the composite columns circular holes have been drilled through the webs of pre-tested (with known buckling load) long specimens. Three sizes (diameters) of the holes have been adopted, one for each member comprising a group of specimens of one length. For example, three 51×51×3.2mm specimens of length 2000mm, tested for critical buckling loads have been retested with holes 14, 25 and 35mm diameter respectively. Similarly three 44×44×6.0mm specimens of length 2000mm are retested with holes 14, 20, and 25mm diameter respectively.

4.2 BUCKLING TESTS

4.2.1 PREPARATION OF SPECIMENS

Specimen extraction

Test specimens (columns of lengths ranging from 200 to 2000mm) have been extracted from standard lengths (6m ≅ 20ft as supplied) of the two GRP box profiles (51×51×3.2 and 44×44×6.0mm). Three specimens have been prepared for each length of the two cross-sections. Specimens in each length-group are marked with sequential numbers (1, 2, 3 for 51mm box-sections and 4, 5, 6 for 44mm box-sections) and their sides (webs) with letters A, B, C, and D for identification and tabulation of the test results. The specimens are machined to the idealised lengths and their ends squared i.e., ends made flat, smooth and normal to the longitudinal axis of the columns. End squaring promotes uniform distribution of applied load over the whole cross-sectional area and helps to reduce the onset of premature localised failure (Brown et al 1998, Barbero and Truk 2000).

Initial measurements

Outer dimensions (width on all four sides) have been measured every 100mm along the length of the specimens. The cross-sectional dimensions have been measured to establish the geometrical properties (e.g., area 'A' and moment of inertia 'I'). As the box-sections have a closed cross-section, wall-thicknesses and internal measurements are only available at the ends. Outer and inner widths have been measured using a vernier calliper with minimum increment of 0.01mm, whilst the wall-thicknesses are

measured using a micrometer with same resolution. Wall-thicknesses have been measured at twelve locations (shown by dotted lines in Fig 4.1) around each end-cross-section. In the case of 51mm box-section, four thin plateaus (two on each opposite sides (see Fig 4.1) are included during manufacture to accommodate adhesive for joining purposes. The formation of these plateaus has been assumed to be as a result of consolidation of the material during the manufacturing process, and that the material configuration (reinforcements and matrix) remain uniform across the entire cross-section. Therefore, average measured values from both ends of a specimen, for the geometry of the box-sections, has been used in calculating the average web-thickness, mean cross-sectional area 'A' and the moment of inertia 'I' for each specimen. The minimum and maximum wall-thickness has been recorded as 3.07 and 3.54mm as compared to 3.2mm nominal thickness specified by the manufacturer (FIBREFORCE Ltd UK). As an example, the thickness variations (between 3.07 and 3.54mm) for 51mm box-section differ from a mean thickness value (3.3mm) by ±0.25mm and are within the standard tolerance (ASTM D3917-94).

Initial imperfections

Initial imperfections i.e., out of straightness and variations in the outer cross-sectional dimensions (inherited in sections due to pultrusion process) have been measured along the specimen length on all four sides. For this purpose, the length of the specimen is marked every 50mm starting from one end. The specimen is placed horizontally on a lathe table (marking table) and a dial gauge with 0.01mm accuracy, mounted on a vertical stand, is moved along the specimen length to measure the widths along the centre line of the upper face (see plate 4.2). The procedure is repeated for each side. The imperfections of cross-section on each side have been calculated by subtracting the mean width from the measured values (Fig 4.2). The initial imperfections have been compared with the allowable imperfections (tolerance) from the ASTM standard D3917-94. For the box-sections used in this investigation, the tolerance specified by the ASTM standard is:

$$e_0 \leq \frac{L}{240} \qquad (4.1)$$

where e_0 is the initial deflection (deviation) from the mean dimension and L is the height of the specimen. All measured deviations from straightness are significantly within the tolerance specified by ASTM. For example the variations in the outer

dimensions are within ±0.3mm from the average values (5.09mm and 43.8m for 51mm and 44mm box-sections respectively). Considering the minimum height of the column i.e., 200mm, e_0 calculated using (4.1) is 0.83mm (> 0.3mm). For longer columns the variations are very small as compared to standard limits. An important observation made here is that specimens deflect under self weight when placed on the marking table, showing very little out of straightness. Consequently measured imperfections are mainly cross-sectional variations with indications of out of straightness reduced or neglected.

Fixing strain rosettes and bondable terminals

To obtain a full representation of the strain field at the mid height of the column, A 45° rectangular strain rosette (EA-06-060RZ-120 from Measurement Group) is bonded on each side (M-Bond 200 adhesive and catalyst C used) of the specimen, symmetrically about the longitudinal centre line (see Plate 4.2). The surface is cleaned (using methane) and prepared (rubbed smooth) to ensure a sound bond and to maximise bondable area. The pre-treatment processes were carried our using a clean absorbent material and neutraliser with the briefest delay before bonding, to minimise re-contamination of the surface. A similar procedure has been used for the fixing of the bondable terminal. Thin wires are soldered to connect the gauges to the bondable terminals that in turn are wired, to a data-logger for data recording, via quarter bridge circuits.

4.2.2 EXPERIMENTAL SETUP

In establishing the experimental setup, the primary considerations adopted have been:

- Columns are tested in the vertical position, to negate the introduction of initial imperfection arising from self weight deflections.
- Friction free knife-edge supports to simulate pin ended conditions, with rotation admissible about the knife-edge axis only.
- Concentric loading i.e., knife-edge centre line aligned with the axes of loading.

Test Rig

The test rig (main frame) comprises two vertical steel channel-sections, bolted rigidly via a thick steel base plate to the laboratory strong floor (Fig 4.3). To the frame base

are welded steel plates (one horizontal and two vertical) forming a platform that provides support to the test specimen at one end and makes the frame further rigid, vertical and parallel. To the upper end, a steel saddle bolted across the channels, supports a hydraulic jack fitted to the underside by a steel plate. A second 'assembly saddle' containing four horizontal rectangular supporting posts is attached (bolted) below the upper saddle. Both, upper and assembly saddles can be relocated by repositioning the bolts (Plate 4.3) along the steel channels, to suit various lengths of the specimens. The supporting posts accommodate the load guiding mechanism (see Fig 4.3 and Plate 4.3(a)). Two guide bars (25.4mm diameter steel rods) slide smoothly and vertically through four holes, lined with copper bushes. A plate, fastened to the guide bars between the supporting posts, accommodates a knife-edge support (wedge shaped steel prismatic bar, see Plate 4.3). A steel shoe (locating the specimen) comprising of a fabricated hollow steel box-section (65×65×6mm) and thick base plate (37.5mm) having a "V" notch along the centre line for the afore mentioned prismatic bar forming a simple (pinned) support (see Plate 4.4(b)). The specimen is restrained in the horizontal (x and z) plane but can move in the vertical direction under the axial load. Also, the steel shoe distributes the applied load uniformly to the specimen cross-section, reducing the possibility of localised material failure. The hollow box (of steel shoe) encapsulates the column end to a depth of 50mm (2 inches) as a safeguard against slipping or breaking of the specimen at failure. Steel shimming plates and screws on all four sides are provided to tighten and align the column end in the shoe (Plate 4.3 (a)). Centre lines, on all four sides of the steel shoe, are marked to centre (align) the test specimen for concentric loading. A similar knife-edge plate and shoe have been fabricated for the lower end (Plate 4.4 (b)). The lower plate is fixed i.e., the displacements in horizontal and vertical directions are restrained about the centre line but free to rotate on a knife edge. A second load cell is located beneath the lower knife-edge plate (atop of the base platform), to measure the reaction produced by the lower platform (Plate 4.3(b)) and to check friction losses in the total assembly.

Holes along the main frame (steel channels) has been used to fix LVDTS (Linear variable differential transducers) at the required locations. Simple steel holders have been fabricated and welded to bolts to fit in these holes. The test assembly is, therefore, fully integrated (see Plate 4.5).

Alignment of test rig and specimen

The reaction frame should be vertical and components orthogonal for concentric loading. A surveying theodolite has been used to check the verticality of the frame. The theodolite has been centred and levelled at a distance (3 to 4 meters) from the test rig to cover whole height of column. The top internal edge of one of the channel sections comprising the frame has been sighted and followed downward along the length. The same procedure has been followed to note the alignment of second steel channel. Misalignment, if detected, is eliminated using steel tie-rods. The verticality of the frame from in the orthogonal plane was similarly determined and the procedure iterated until the reaction frame was square. Equivalent accuracy in the components comprising the reaction frame has been assumed throughout.

The specimen (column) has been inserted into the lower shoe (remote from the rig) and centred by aligning preset marks. Thin shimming plates have been tightened around the specimen by screws, leaving equal gaps between shoe walls and the specimen. The opposite end of the specimen has then been inserted into the second shoe and centred by repeating this procedure. The specimen with steel shoes on both ends has been inserted into the test rig by gradually pushing the upper shoe against upper knife edge, lifting it until enough room has been available to place the lower shoe on top of lower knife edge. The specimen has been aligned as straight and vertical between the knife edge plates, using the theodolite. Screws in the lower shoe are used for adjusting the specimen position for the specimen alignment. The theodolite has been used only to align the specimen from the front face. In the orthogonal plane, the sight from the theodolite was restricted by the steel channels. Lateral alignment has been achieved using steel strips bolted to the main frame at the locations of knife edge plates. A steel strip fixed at lower knife-edge is shown in Plate 4.3(b). Internal and external callipers have been used to align the upper and lower knife-edge plates at equal distance from the aligning strips. Adjusting screws on sides of the shoe centre the specimen.

The specimen has been loaded to one third of the expected load to allow initial setting of the specimen ends. The steel shoes have then been loosened, the alignment checked and the shoes retightened to allow the specimen to destress before the start of actual test.

Effective Height (L_{eff})

The height between the knife-edges (pivots) of the upper and lower supports is the effective length for each test specimen. An additional length of 55mm to the physical length of the GRP specimens, due to the introduction of the upper and lower steel shoes, has been measured. For example the effective lengths (L_{eff}) for 200 and 2000mm GRP specimens while testing are 255 and 2055mm respectively (assuming pin supports). The presence of two steel shoes does not affect the column's deformation characteristics as in a theoretical analysis Chilver (1956) showed that even when the total length of two fully rigid end fixtures is 0.2 of the column height between simple supports, the increase in the Euler load is approximately 1.3%.

4.2.3 MEASUREMENTS

Axial Load

Axial load has been measured using two load cells; an upper and a lower. The upper load cell is directly mounted on the hydraulic jack and connected to the upper steel plate via a copper cylindrical attachment (copper being a relatively soft material, acts as a shock absorber protecting the load cell from impact damage). This load cell measures the axial compressive load applied to the specimen through the knife edge and steel shoe. The lower load cell has been placed under the lower steel plate, measuring the reaction to the above load (Plate 4.3(a) and 4.3(b)). Ideally these loads should be equal given a frictionless system and the induced gravity loads arising from the moving plate, knife-edge, steel shoes and specimen are included. Comparing the load cell readings a difference of 0.1 to 0.3kN has been recorded corresponding approximately to the self weights of the components listed previously. The test rig has a demonstrably low friction error, therefore.

During testing the load has been applied in small increments to reach the ultimate load (estimated from theoretical solutions) within 10 minutes. The load is measured and recorded digitally every two seconds (i.e. 300 readings in 10 minutes). The capacities of the load cells (e.g., 89kN to 898kN) and the hydraulic jack have been selected depending upon the height and cross-section of the columns.

Deflections

Axial deflection (vertical shortening) is measured by the downward movement of upper plate accommodating the knife edge support. An LVDT fixed to the upper

saddle measures the axial deflection of the specimen (see LVDT 1 in Fig 4.3 and Plate 4.3(a)).

For longer columns showing global buckling, lateral deflections are measured at three points (mid, upper one-quarter, and lower one-quarter of the length, see Plates 4.6-4.7), whilst for short columns, where local buckling is expected and locations of the maximum deflections are not known before hand, more than three LVDTs have been used (see Plate 4.8(d)).

The cross-sectional rotation of the specimen at mid height is measured indirectly. A flat steel (or plastic) strip is clamped to on side of the specimen and horizontal displacements at two equal distant points from the centre are measured using two LVDTs (see Plate 4.4 (a)). However, the cross-sectional rotation of the column ends is not admissible due to the rotational restraint of the knife-edge supports.

Strains

Strains produced by the compressive loads are measured by strain gauge rosettes bonded to each face of the specimen at mid-heights. Each strain rosette comprises three strain grids (see Fig 4.3 and Plate 4.2). Strain grids are numbered anticlockwise. Grid 2 of the strain rosette is at the centre of each web at mid-height parallel to the vertical axis. Grid 1 and 3 are at ±45° to vertical axis. Maximum principal strains are calculated from the strains measured by three grids of a rosette (using 3.17). The angle (ϕ) from the axis of grid 1 to the maximum principal strain is calculated to confirm the verticality of the bonded gauge in the case of the column tests. If the angle ϕ is 45°, the maximum principle strain (-ve compressive and +ve tensile) is in the axial direction. Strain measurements in the initial loading range are not only used to calculate the compressive modulus, but also indicate equal and uniform distribution of compressive load on the all four sides of the specimen, confirming the proper alignment of the specimen and concentric loading.

4.2.4 TESTING PROCEDURE

- Rig adjusted to fit a particular specimen height.
- Specimen inserted and aligned.
- Load-cells, LVDTs and strain-gauges connected to the data-logger.
- Instrumentation initialised and initial values set to zero.

- Specimen loaded to one-third of the expected load. Instrumentation checked for proper functioning. Load released, alignment re-checked and instrumentation brought to initial zero readings.
- Loading applied gradually.
- Instrumentation continuously monitored. Data filtered through noise and recorded using a data acquisition system (every 2 seconds).
- Load increased in intervals until either the central lateral displacement increased uncontrollably or material failure occurred.
- Mode of failure recorded.
- In the case of Euler buckling (non-destructive), specimen either rotated through 90° about the longitudinal axis or inverted and retested.
- In the case of local failure i.e., tearing of the cross-section, half sine wave-length measured to within a reasonable accuracy of ± 0.5mm.

4.3 EXPERIMENTAL RESULTS

The results comprise buckling/failure loads and the resulting failure shapes. Critical loads are presented in the tabular form (Tables 4.1-4.3), and failure modes have been illustrated with photographs (Plates 4.6-4.7, 4.9-4.15, and 4.17-4.19). Four types of column failure have been observed during the experiments:

- Global buckling exhibiting lateral deflection at the critical load. Buckled shape is half sine wave with maximum deflection at mid-height,
- Local buckling of the webs followed by tearing of the cross-section,
- Compression failure of the material.
- Interaction between global and local buckling modes followed by tearing of the cross-section or global and material failure.

Critical buckling (or failure) loads depend on the column heights and the material properties of the parent materials (Barbero and Tomblin 1994, Brown et al 1998, Barbero 2000). These factors has been combined together to define the universal

slenderness ratio $\lambda = \frac{L}{\pi}\sqrt{\frac{P_L}{D}}$ * (2.19) of each specimen. By definition 'λ' is a function of material stiffness and geometric properties, in addition to the column height. The experimental evidence suggests that specimens having $\lambda > 1$ buckle globally, whilst specimens having $\lambda < 1$ exhibited local or material failure. Specimens having $\lambda = 1$ showed mode-interaction. This observation is in line with the findings of the previous studies (Barbero and Tomblin 1994, Barbero and Evans 1998, Brown et al 1998, Barbero and DeVivo 1999).

As a reference of demarcation between the global and local failure, critical heights L^* (2.21) (for the occurrence of maximum mode interaction), for the two box-section profiles (51mm and 44mm) have been calculated taking $\lambda = 1$. The columns have been assumed to be of uniform cross-sectional area and moment of inertia (mean value given in Tables 4.4-4.5) throughout the length. The bending stiffnesses D have been taken equal to $E_{L,c} \times I$, where $E_{L,c}$ are the measured compressive moduli for the two sections (Tables 3.11-12). P_L^* for either of the box-sections has been taken equal to experimental load for the short columns†. The critical lengths for 51mm box-section (with P_L = 120kN) and 44mm box-section (with P_L = 220kN) have been calculated as 771 and 569mm respectively.

4.3.1 GLOBAL BUCKLING

Global buckling has been observed in specimens of height 1000mm (L_{eff}= 1055mm and λ= 1.37) and longer in the case of the 51mm box-section and for the heights 750mm (L_{eff}= 805mm and λ = 1.41) and longer in the case of the 44mm box-sections. As the global buckling is the characteristic of the slender columns, these specimens (and hence the column heights) have been categorised as slender columns. The specimens remain vertically straight (with no or very little lateral deflections) before buckling commences. As the buckling loads approach, the specimens abruptly deflect laterally to one side (with respect to the knife edge axis) and deflection continues to

---

* P_L has been taken from the short column tests on the two box-sections (Tables 4.2-3). P_L has been confirmed to be independent of the column height in the short range as at least one specimen from each height group reached this experimental failure load. This is in line with the definition of P_L.

† The minimum acceptable length for short column has been suggested to accommodate at least 4 half sine waves when buckled in a local mode (Mottram, 2000).

increase without further increase in the applied load. The buckled shape is a half sine wave (Fig 4.4 and plates 4.6-4.7) with maximum lateral deflection at the mid-height. The maximum lateral deflection at the centre is limited to height/100 to avoid any cracks or permanent damage to the material (Mottram et al, 2000). The cross-section of the specimen remained un-distorted (square with right angles) and uniform throughout the length of the specimen. The supports (knife edges) at the both ends of the specimen are rotated about the knife edge (see pin ended rotation in Plates 4.7(c, d)) without orthogonal movement. The upper support moves axially downward under the application of external compressive load. Specimens fail (without any damage or breakage) due to buckling in the elastic range (i.e., buckling stress is much lower than the ultimate compressive stress). They are retested with change in sides or rotation by 180°. Experimental results are given in Table 4.1 in which sides A, B, C, and D indicate the side of specimen in the observation reference plane (parallel to the knife-edge axis and in contact with LVDTs to measure lateral deflections), and the negative (-) sign indicates the rotation about the transverse axis by 180° (specimen longitudinal orientation reversed). The critical buckling loads measured experimentally 'P_{Exp}' and determined by Southwell method using experimental data '$P_{S.well}$' have been included in the results (Table 4.1)

The global buckling modes for the slender columns are given in Plates 4.6-4.7. The classic half sine wave deflected shape is clearly demonstrated with rotation (pin action) of the supports. The plates also indicate the position of LVDTs to measure the lateral deflections, cross-sectional rotation and central location of bonded strain rosettes.

The characteristics of the global buckling in composite GRP columns have been studied by plotting the following graphs:

Axial Deflection verses axial load

Typical plots of axial deflection verses the applied loads, for the various lengths of specimen, have been presented in Fig 4.5 for 51mm box- and in Fig 4.6 for 44mm box-sections. Axial deflection increases with load until ultimate load and remain constant after buckling. As is evident from the Figs 4.5-4.6, the behaviour is linear up to the ultimate load in all specimens. Therefore, it has been established experimentally that the global buckling of GRP slender columns occurs in the linear elastic range of

the material. Despite the reconditioning of the specimen by loading to a third of the expected failure load prior to initialising the complete test, it is clear from the initial stages of the plots (Figs 4.5-4.6) that the response of a column is less stiff than the nominal (mid-range stiffness). This characteristic is consistent for both 51mm and 44mm box-section tests. It suggests that there exists a certain amount of elastic behaviour (< 5kN) that is fully recoverable under unloading that induces a limited non-linearity at low loads that may include both material and testing flexibilities.

Axial Load (P) verses Lateral Deflection (Δ)

Lateral deflections have been measured at three points along the specimen height i.e., mid, upper quarter ($L/4$) and lower quarter ($L/4$) heights. Maximum lateral deflection (Δ_3 measured by LVDT 3)[‡] has been measured at the mid height of the specimen. The deflections measured at the upper and lower quarter lengths of the column are lower. At the buckling load, the measured values of the lateral deflection at three locations are compared with a half sinusoidal buckled shape such that $\Delta_2 \approx \Delta_4 \approx 0.707\Delta_3$ (see Fig 4.4). It is clear that the 51mm box section approximates the normally assumed half-sine wave deformation. The smaller section (44mm box) with considerably thicker walls displays a much greater curvature at the centre. Typical plots between the lateral deflections (at mid-height and upper and lower quarter lengths) and the applied axial loads for 51mm and 44mm box-sections have been shown in Figs 4.7-4.8.

It is evident from the graphs that lateral deflections are minimal until the onset of global buckling, increase abruptly without any further rise in the applied load and are asymptotic to the theoretical (Euler) buckling loads. Euler lines indicate the buckling of ideal columns perfectly straight and free from imperfections (bifurcation theory in elastic buckling). Any deviation from the ideal behaviour i.e., increasing lateral deflection from the lower range of the loading and/or decreasing buckling load, has been attributed to the initial imperfections and the limited ability of LVDTs to measure very small displacements consistently. The potential imperfections causing deviation of the column behaviour from approaching the theoretical bifurcation point

---

[‡] In all the global buckling tests, LVDT3 has been placed at mid-height and measured deflection is denoted as Δ_3. Likewise Δ_2 and Δ_4 represent deflections at upper and lower quarter lengths.

include misalignment of the testing rig (equipment limitations), geometrical tolerance (specimen limitations) and non-homogeneity of the composite material (inherited limitations).

Misalignment of the test rig causes a load eccentricity if the centroids of the sections at both ends do not coincide with the line of action of the compressive load (Mottram, 2000). It can be minimised (if not eliminated) by the proper alignment of the specimen and the components comprising the test rig e.g. knife-edge supports and steel shoes housing the specimen. In the present study surveying equipments have been used to align the upper and lower knife-edge supports with the loading line (§ 4.2.2). Both ends of the specimen are properly centred in the steel shoes, using the guiding centre lines and the adjusting screws. A close agreement (difference < 5%, Table 4.1) between the measured buckling loads P_{Exp} and the loads predicted form Southwell plots $P_{S.well}$ confirms the achievement of an adequate alignment using the adopted technique. Also, the measured (P_{Exp}) and Southwell ($P_{S.well}$) loads (Table 4.1) for the same specimen when tested in upright and upside down (rotated by 180° about the transverse axis), are very close, indicating minimal alignment imperfections. This comparison further substantiates that the test rig performed well regarding loading (frictionless and concentric) and pin-ended support conditions.

In the paper by Barbero and DeVivo (1999), a loss of 35% in the buckling loads of GRP wide-flange profiles of intermediated heights has been suggested and attributed to the interaction between the buckling modes. Mottram (2000) reviewed the contents of this paper considering this loss (35%) in buckling load to be too high and suggested that the greater part of this loss in stability was due to load eccentricity produced by the misalignment of the testing rig, as the specimen could move within the larger steel fixtures during the test. Mottram (2000) is of the opinion that mode-interaction may reduce the buckling loads but this loss is proportional to the specimen's imperfections (imperfection sensitive). Therefore, in the context of Barbero's work, a loss of 35% was deemed too high to be attributed to mode-interaction only, as recent profiles exhibit low section imperfection, and may be due to the influence of other imperfections i.e., load eccentricity due to misalignment in applied loading. This demonstrates the adverse effects of rig-misalignment on the buckling stiffness of slender columns.

Out of straightness and cross-sectional variations (e.g., varying thickness of walls and outer measures) manifest a small shift in the position of the neutral axis of cross-sections (along the column height) from the nominal centroidal axis, producing a load eccentricity leading to increased lateral deflection and the loss if buckling loads. Initial imperfections, like out of straightness and cross-sectional variations measured for both the box-sections (typically shown in Fig 4.2) are very small (of the order of less than 1mm). A small difference of less than 5% between the experimental and predicted loads suggests low level initial imperfections.

GRP composite material is non-homogeneous; i.e., the distribution of the reinforcing fibres is not uniform over the cross-section leading to a non-uniform distribution of applied load in the cross-section. The determination of material properties (Chapter 3, compressive and shear moduli), using coupons obtained from both the box-sections, established small variations in the measured material constants (Tables 3.5-3.12). However small the variations are, they still contribute toward the small eccentricities produced in the compressive loading leading to the deviations of actual behaviour of the specimens from the ideal case.

Southwell Plots

The presence of imperfections prevents the P-Δ response from following the theoretical bifurcation behaviour with its distinct limit point. These imperfections induced an initial curvature producing lateral deflections well before P_E could be attained, justifying the need to use the Southwell plot method to predict the experimental load. The method has been used efficiently to analyse the linear elastic test data from a column with initial curvature to determine the buckling capacity which the column would have if it were perfectly straight (Tsai, 1986). The capacity is estimated from the measured lateral deflection and the applied axial load. The basic assumption enforced for the validity of the Southwell method is that the deviation of the P-Δ curve from bifurcation theory equates to an out of straightness (Δ_0) in the form of a half sine wave. It is further assumed that the deformations (lateral) are in the linear range of the material. The method is especially useful in non-destructive testing (like the present study) since the specimens are required to be loaded within the elastic limit (Barbero and Tomblin 1992, Brown et al 1998). However, the accuracy of the predicted buckling capacity becomes poor if the initial curvature is small. The reason is that the actual deflection dwells within the deviation range of employed

gauges (LVDTs). To overcome this limitation, experimental data only for loads in the ranges of 80 to 100% of ultimate loads have been used (Southwell 1932, Mottram et al 2003). In the method, lateral deflections normalised by the applied load (Δ_3/P) have been plotted against deflections (Δ_3) for each test. Typical Southwell plots for various tested lengths of the 51mm and 44mm box-sections have been shown in Figs. 4.9-4.10. A linear regression curve (trend line) with equation (slope and ordinate) and correlation coefficient has been obtained for each plot. For most of the curves the correlation coefficient (R-squared value) is either unity or more than 0.99, indicating high linearity of Southwell curves, and low physical imperfections in the specimens. The inverse of the slope of the regression line yields the critical buckling load of the corresponding specimen whilst the ordinate of the equation estimates initial imperfections (including all the practical imperfections). Critical buckling loads '$P_{S.well}$' obtained from the Southwell plots for 51mm and 44mm box-sections have been reported in Table 4.1.

It is assumed here that Southwell method is valid for data where the deflections are due to combination of several imperfections and not just Δ_0. In other words two P-Δ curves due to overall eccentricity e_0 or due to a higher Δ_0 (higher to account for all imperfections), have very similar shapes.

Cross-sectional rotation

The knife edge supports at the ends of the specimen prevent its rotation about the longitudinal (vertical in the present experimental study) axis. However its mid-height section may rotate under the applied compressive load. To measure this rotation, a long rectangular (steel or plastic) strip has been fixed to the cross-section. Lateral deflections (normal to the knife edge axis) at two equidistant points from the centre of the strip are measured using LVDTs (D5 and D6 in the case of slender columns). Both deflections are normally in the same direction, indicating the lateral deflection rather than cross-sectional rotation. The difference of the two deflections (D5-D6) gives the amount of net deflection associated with rotation of the mid-height section (see Figs 4.11-4.12 for 51mm and 44mm box-sections respectively). The small values of these deflections suggest that specimen undergoes lateral deflections due to lateral imperfections rather than twisting of the specimen. Furthermore, it is interesting to note that after initial loading, the relative deformation (D5-D6) remains constant.

Axial strains and compressive modulus

The axial stresses resulting from the applied compressive loading have been plotted against the strains measured during the buckling experiments. Axial stress has been calculated by dividing the applied load by the cross-sectional area of the specimen. Experimental strains at each load-increment have been measured by strain-rosettes fixed at mid-height of all the four sides of each of the box-sections. Each strain rosette comprise of three gauges numbered anticlockwise as 1, 2, and 3. The gauge 2 (central) has been fixed parallel, whilst the gauges 1 and 2 are at 45° to the longitudinal axis of specimen (Plate 4.2). The strains measured by gauges 1, 2, and 3 are denoted as ε_1, ε_2 and ε_3 respectively.

Principal strains $\varepsilon_{P,Q}$ (maximum and minimum axial strains) and ϕ (angle between principal strains and the direction of gauge 1) have been calculated using (3.17, Measurement Group, 1990). The angle 'ϕ', in most of the tests has been calculated between 40° and 45° indicating satisfactory alignment of the strain rosettes with the longitudinal axis and demonstrating that principal strains are in axial direction. For a properly aligned strain rosette, strains measured by gauge 2 and principal strains (calculated from ε_1, ε_2 and ε_3) should be similar. For example stress-strain plots, for the 2000mm high 51mm box-section specimen, using strain data from a single gauge (central 2) and principal strains, have been presented in Fig 4.13 (a) and (b). Both the plots show very close results establishing proper gauge alignment. Typical stress-strain plots for various specimen heights using calculated maximum principal strains and average stresses have been presented in Figs 4.14-4.17.

Fig 4.14 presents stress-strain plots for specimens representing 51×51×3.2mm box-sections. The first three plots are for long columns (heights of 2000, 1500 and 1000mm). In the plots, sides A and C[§] have arbitrarily been taken for the sides of the specimen parallel to the knife edge axis, towards front i.e., in the observation reference plane and the back (opposite side), which may deflect laterally. Other two sides i.e., B and D are restrained against lateral deflections due to knife-edge supports.

[§] The notation of the side may not agree with the notation given in result table (Table 4.1). The strains gauges fixed to the front side are numbered as 1, 2, and 3. Arbitrary side B have gauges 4, 5, and 6. The back side (again parallel to the knife-edge axis) is denoted C and is associated with strain gauges 7, 8, and 9. Like wise side D contains strain gauges 10, 11 and 12.

Principal strains measured on each side have been shown in different colours. As can be seen from the plots (Fig 4.14), initially all the four sides are under compression (negative strains) and remain alike until the onset of global buckling. It is important to note here that response of the material is linear and the plots have similar slopes. The evidence that stresses and strains on all the four sides are identical for a range of applied load establishes that; the loading is concentric, alignment of test-rig and specimen is adequate, material is uniform, and above all stresses and strains are linearly proportional.

At the onset of buckling, specimen deflects laterally about the knife-edge axis and the bulging (convex) side develops tensile strains due to bending. For example compressive strains (-ve) in side C in 2000mm long specimen (Fig 4.14) reverse the direction (+ve strain) abruptly at the buckling load and go on increasing without further increase in stress. The opposite side (side A), after buckling takes the convex shape resulting further increase in compression strains with no increase in the applied load. In other words, after buckling, lateral deflection (and hence the strains) demonstrably increase without an increase in the buckling load. The other two opposite sides (side B and D) remain undeflected due to the restraint imposed by the knife-edge supports and show no change in the strain state after buckling of the specimen. Stress-strain plots in the linear elastic range (before buckling) can be used to determine the experimental compressive modulus of the GRP material. The plots for the two un-deflected opposite sides (B and D) have normally been used for the determination of the compressive modulus as the stress-strains are due to compressive loading only. For each plot a trend line giving the slope of the plot and the correlation coefficient has been drawn (using the same colour as of the plot). The correlation coefficient for all the plots in Fig 4.14 is higher than 0.99, indicating high degree of linearity of these graphs. The compressive elastic modulus $E_{L,C}$ measured from the stress-strain plots (of the un-deflected sides) varies from 28.2 to 32.4kN/mm^2 as compared with 30.2kN/mm^2 measured by coupon testing (Table 3.11). Another important point to note here is that elastic modulus of the composite material can accurately be measured using the stress strain data measured during the concentric compression testing of the long composite columns.

Figure 4.16 gives the stress-strain plots for slender 44mm box-section showing linear response of the material in the case of overall or global buckling. An abrupt change in

the direction of strains (compression to tension), at buckling loads, can be seen from the plots of convex sides and increase in compressive strain for the concave sides. Similar slopes of the plots representing all the four sides, suggest accurate alignment of the test-rig and specimens and presence of minimal imperfections. Elastic moduli have been calculated (from plots of sides B and D) with a range from 28.4 to 33.7kN/mm^2 as compared with 32.2kN/mm^2 measured by the coupon testing (Table 3.12).

4.3.2 LOCAL BUCKLING

51mm Square Box-Sections

Specimens made from 51×51×3.2mm box-sections, having heights 200, 300, 400 and 500mm that did not develop global buckling have been grouped as short columns. These specimens failed by abruptly splitting at the web-interfaces and breaking across the sides. The failure is catastrophic and specimens lose their integrity.

Three specimens have been tested for each length. The effective height for each specimen is obtained by adding 55mm to its physical height. The loading (concentric) and support conditions (pin-ended), application of load in incremental intervals, number of observations, and the testing procedure, have been adopted from the long columns tests. As the locations of the peak web-deflections are not known before hand, more than three LVDTs have been employed**. The arrangement of LVDTs for the measurement of lateral deflection in different height specimens have been shown in Plate 4.8. Each specimen was tested once only due to catastrophic failure. Critical failure loads for short columns has been given in Table 4.2, and failure modes (shapes) can be seen in Plates 4.9-4.12.

Although the failure of short 51mm square specimens occurred by sudden tearing of the sections, a careful inspection of the failed specimen suggested that a type of local buckling existed prior to section breaking. For example, in the case of 200mm (L_{eff} = 255mm) specimen sides (webs) A and C bulge out whilst sides B and D deflect inwards at mid-height (see plate 4.9(a) and 4.9(b)). The local deformations (at the critical load) increase rapidly without further increase in the buckling load and cause

** Numerical analysis for short columns (included in Chapter 5) has also been used for guidance for the location of LVDTs at locations of maximum web-deflection.

catastrophic (bursting) failure comprising rupture of the interfaces and side C at the bulge crest. Similar horizontal ruptures of webs (and fibres) are observed in sides B and D (under compression). After failure the specimen looses stiffness and the end restraints (knife edges) rotate showing a pseudo global mode. The plot between axial deflection and the axial load has been included in Fig. 4.5, indicating linear elastic behaviour up to the failure of the specimen. The lateral deflections measured during the test have been plotted in Fig. 4.7, showing very little deflection with the increasing load (less than 1mm). Surprisingly all the LVDTs measuring deflections along the specimen height showed similar readings. It indicates that local web buckling could not be measured while the web interfaces were in tact. It was only after the interface failure that webs buckled locally and breaking along the crests due to excessive strains. At this point the material behaviour changed to nonlinear as evidenced by the stress strain plot for 200mm GRP length in Fig 4.15. Due to the tearing of the section and breaking of the webs, it was not possible to measure the length of half sine wave (web local buckling). Furthermore, different length cracks on different sides prevented the measurement of true half sine wave length. Two other specimens of the 51mm square box-section with equivalent heights showed similar failure modes.

Failure of the 300mm specimen (L_{eff} = 355mm) was characterised by the opposite sides (webs) A and C deforming inwards and mirrored by sides B and D (Plate 4.10(a) and 4.10(b)). Rapid increase in displacements again causes splitting (tearing) of web-joints. Sides A and C (under high compression) fail with horizontal cracks. Side B takes the form of a long strip, splitting at the interface and buckling globally. Interestingly side D (with outward bulge like side B) fails with horizontal rupture (breaking fibres). Typical axial and lateral deflection plots for 300mm height (Figs 4.5 and 4.7) indicate linear elastic behaviour of the short column. However the stress strain plot for 300mm height (Fig 4.15) shows possible non-linearity at the failure load. Other 300mm GRP specimens failed in a similar fashion (Plates 4.10(c) and 4.10(d)).

The web of the 400mm specimen (L_{eff} = 455) on sides A, B and D bulge outwards while side C has deformed inwards (see Plate 4.11(a) and 4.11(b)). Only side C failed under compressive stresses, while the remaining three sides deflected outwards. Side A may have deflected inwards at first and deflected outwards subsequently after

failure of side C and rotation at the lower support showing a pseudo global buckling mode. The interface at sides A and B remained in tact after damage, but a vertical crack in side D ruptured near the joint. Another important observation is that buckling was initiated in the lower *L*/4 rather than at mid-height. In the second specimen of 400mm GRP height (see Plate 4.11(c) and 4.11(d)) buckling commenced at upper L/4 with rotation of upper support, but two opposite sides (B and D) bulge out while the other two sides (A and C) move inwards. All four interfaces rupture by tearing and the section lost integrity. Sides B and D (bulging out) show overall buckling while the sides A and C (moving inward) break under compression with horizontal cracks. Typical stress-strain graphs for the 400 mm length column (Fig 4.15) support the proposition that local buckling initiated the subsequent tearing failure.

Failure modes of 500mm high 51mm square sections have been shown in Plate 4.12. All the three specimens fail near the mid-height. Sides B and D in the first specimen (Plate 4.12 (a), (b)) deflect outwards tearing the web-interfaces with side C. Side A and C deflect inwards whilst side C breaks under compression. However, side A remains in tact (even after developing cracks) following stress-relieving from tension developed by pseudo global mode. The pseudo global mode is also local as the knife-edge supports show no rotation. Typical stress strain plot for 500mm height (Fig 4.15) establish the local buckling mode as two opposite sides A and C increase in compression whilst the other sides B and D develop tensile strain at the failure. The other two 500mm specimens (Plates 4.12(c)-4.12(e)) showed similar failure modes i.e., two opposite sides deflecting inwards, the other two outwards, and failed with excessive strains.

This behaviour is different from the local buckling behaviour of open sections (wide-flange profiles) observed by Barbero and Tomblin (1994) and Mottram (2000), where flange of the sections buckled locally in sine wave forms along the length of the column. It has been demonstrated in the study reported by Zuerick and Scott (1997) that the profile with the highest flange outstand-to-thickness (b_f/t_f = 10.7) ratio requires the lowest stress to induce the local mode of instability. It has also been reported that in sections with short flange outstands, the buckling stresses are higher when the failure has been catastrophic by tearing of the flange-web connections (Brown et al, 1998). It is obvious that the cross-section dimensions play an increasingly important role in determining the failure mode for short lengths of

composite columns. Observations related to tests conducted as part of the research presented in this thesis indicate that specimen shape and relative web thickness also contribute towards the failure mode (mechanism) of the short length columns. Closed form sections such as square box-sections do not exhibit a well-developed wave-like deformed shape as obviously as open sections in the local buckling mode, but a catastrophic rupturing failure particularly for short length columns (see Plates 4.9-4.12). In short columns (L_{eff} =255, 355, 455 and 555mm) local buckling commences first as small lateral deflections, followed by abrupt bursting (tearing and breaking), leaving the web in strip forms, which then deform in global buckling under the compressive loads (see Plates 4.11, 4.12). It is noted in this case that the rotation of one or both end restraints (similar to the global mode) is due to post-buckling deformations and not due to co-existence of the buckling mode. The failed geometry is the result of buckling of webs after failure and not of the whole section and in some cases (see plate 4.11) no end-restraint rotations have been observed.

4.3.3 COMPRESSIVE FAILURE

44mm Square Box-Sections

Short specimens comprising 200, 300, and 400mm heights, extracted from 44mm square box-sections failed by material failure under higher compressive stresses (Plates 4.13-4.14). In these specimens, the interfaces between the side walls are sufficiently stiff such that side walls neither locally buckle (wave like formation) nor rupture along their interfaces. As a result the cross-section of the box section maintains its shape and specimen remains straight. With further increase in the load, the ends of the specimen inside the shoes fail under direct compression (crushing). As the material is not perfectly homogeneous and longitudinal axis of the end sections may not exactly be in the line of the axial loading, a portion of the section at one end may be subjected to a local stress concentration, causing local failure of the cross-section (Plate 4.13) and rotation of one (or both) of the supporting shoes. All the 44mm box-section short specimens (200, 300, and 400mm heights) failed with local compressive failure at the lower ends (see plate 4.14).

To avoid end brooming failure of these short specimen wooden blocks were inserted inside the ends to confine the sides of the GRP sections. These blocks displaced as a result of end failure (Plate 4.13(c)), indicating that the failure was due to the crushing

of the material under high compressive stresses and not lateral bending action of the sidewalls (in the form of a plate supported on two sides).

The universal slenderness ratio 'λ' for effective heights of 255, 355 and 455mm, 44mm box-section profiles (for a maximum measured short column load P_L of 220kN), have been calculate as 0.45, 0.62 and 0.80. As $\lambda < 1$ for these specimens, grouping them as short columns is in line with the previous studies (Barbero and Tomblin 1994, Brown et al 1998, Barbero 2000). The observed failure modes suggest that short columns having slenderness less than one, do not necessarily exhibit local web buckling, but can directly fail by material degradations. Interestingly, the material failure has occurred at an averaged applied stress of 250N/mm^2 which is a nearly 50% of the ultimate compressive stress (523N/mm^2) measured by coupon tests (Table 3.12). The large reduction (50%) in the compressive capability of the section cannot be attributed solely to the material non-homogeneity only as the typical stress strain plots (Fig 4.17) for these specimens indicate a uniform and linear stress and strain distribution from the beginning to failure loads. It is proposed, therefore, that if a closed narrow cross-section with thicker webs is unable to exhibit local web buckling due to stiffer web-interfaces, the section fails by the development of a complex three-dimensional stress state (see finite element results, §5.4.2) at compressive stresses lower than those indicated by simple coupon tests. The observed behaviour of the short 44mm square specimens further demonstrate the need of experimental evidence for the validation of any numerical approach to predict failure loads for closed cross-sections with relatively thick walls.

4.3.4 MODE-INTERACTION

The phenomenon of mode interaction has been observed during the compression testing of 750mm (L_{eff} = 805mm, λ = 1.04) high 51mm box-section and 500mm (L_{eff} = 555mm, λ = 0.98) high 44mm box-section specimens. These heights of the specimens have been grouped as intermediate heights, where either global and local buckling or global and material failure modes interact.

In the case of 750mm high 51mm square specimens, the buckling process began with lateral deflection of the columns (maximum at mid-height) i.e., in global mode (see P-Δ graph for L=750mm in Fig 4.7). Lateral deflection increased with load and reaches a typical value of 9mm ($\Delta > L/100$) at mid-height. Also the rotation of knife-edge

supports (Plate 4.15(a)-4.5(d)) confirms the on-setting of the global buckling. At this stage, the specimen failed catastrophically by breaking from the concave side (under compression) at mid-height (see Plate 4.15).

It is proposed that the specimen failure mode is such that (Plate 4.15(a)) the inner web-interfaces (towards concave side) broke (tearing) initially due to outward displacement (bulging) of the compression side, leaving the inner web in the form of a vertical strip under compression. This further buckled and ruptured with horizontal crack (fibre failure). The convex side (under tension) had not ruptured. Interestingly the two other sides deflected inward and broke with horizontal cracks. The resulting pattern of deformation (and ultimate failure), i.e., two opposite sides (inner and outer) bulged outwards and the other two opposite sides deformed inward, is clearly a characteristic of local buckling (Plate 4.15(a)-4.15(b)). It implies that the specimen developed global buckling in the first phase with lateral deflection of more than $L/100$, and at the same load local buckling commenced starting from the mid-height section, with the specimen failing catastrophically by tearing at interfaces and breaking across the webs. Plates 4.15(c) and 4.5(d) show similar failure modes for an additional 750 mm high 51mm square box-section specimen. The lateral deflections measured at mid heights and upper and lower quarter lengths have been used to draw P-Δ and Southwell plots for the determination of experimental buckling loads (Fig 4.9). Buckling loads for 750mm high 51mm square box-sections are given in Table 4.3. Due to the destructive nature of the tests, only one test per specimen was done. Typical stress-strain plots (Fig 4.14) indicate a nearly uniform (parallel slopes) stress distributions on all the four sides and determine a range for experimental compressive modulus (27.2 to 32.2kN/mm^2) close to the measured $E_{L,c}$ by coupon testing (30.3kN/mm^2).

The failure of 500mm high, 44mm square box occurred by the interaction of global and material failure modes. At the buckling load the specimen buckled globally with maximum lateral deflection at mid-height. Maximum deflection reached $L/100$ (Fig 4.8) after which the specimen failed at one end without further increase in the loading. All three 500mm specimens gave the same mode of failure.

It has therefore been demonstrated, using experimental evidence, that composite columns with universal slenderness ratio close to unity (λ=1) based on P_L e.g., 750mm high 51mm square box-sections and 500mm height 44mm square box-

sections, exhibit mode interaction at failure loads. The critical failure loads for these specimens measured during the experiments have been presented in Table 4.3.

4.4. COMPARISON OF EXPERIMENTAL AND THEORETICAL RESULTS

Different approaches from the literature have been used to predict the theoretical buckling and failure loads for long and short columns. In using these approaches two types of material properties; measured using coupons (Chapter 3); and minimum specified by the manufacturer, have been used.

Measured Properties

51×51×3.2 Box-section

Longitudinal compressive modulus $E_{L,c}$ = 30.3 kN/mm^2. (Table 3.12)

Maximum longitudinal compressive stress = 385 N/mm^2. (Table 3.12)

Transverse compressive modulus $E_{T,c}$ = 9.2 kN/mm^2. (Saribiyik, 2000)

In-plane Shear Modulus (normal to fibres) G_{xy} = 3.95 kN/mm^2. (Table 3.6)

In-plane Shear Modulus (parallel to fibres) G_{yx} = 2.85 kN/mm^2. (Table 3.10)

Longitudinal Poisson's ratio ν_{xy} = 0.29 (Saribiyik, 2000)

Transverse Poisson's ratio ν_{yx} = 0.15 (Saribiyik, 2000)

44×44×6.0mm Box-section

Longitudinal compressive modulus $E_{L,c}$ = 33.2 kN/mm^2. (Table 3.13)

Maximum longitudinal compressive stress = 523 N/mm^2. (Table 3.13)

In-plane Shear Modulus (normal to fibres) G_{xy} = 3.95 kN/mm^2. (Table 3.7)

In-plane Shear Modulus (parallel to fibres) G_{yx} = 2.85 kN/mm^2. (Table 3.11)

Transverse compressive modulus $E_{T,c}$ and Poisson's ratios measured by Saribiyik (2000) for 51×51×3.2mm box-section have been adopted for 44×44×6.0mm box-section.

Minimum properties supplied by manufacturer

Material properties provided by the FIBREFORCE Ltd UK are the minimum characteristic properties for the both (51mm and 44mm) GRP box-sections.

Longitudinal compressive modulus $E_{L,c}$ = 17.2 kN/mm^2.

Maximum longitudinal compressive stress = 207 N/mm^2.

Transverse compressive modulus $E_{T,c}$ = 6.9 kN/mm^2.

In-plane Shear Modulus $G_{xy} = G_{yx}$ = 2.9 kN/mm^2.

Longitudinal Poisson's ratio v_{xy} = 0.33

Transverse poisson's ratio v_{yx} = 0.11

Theoretical buckling and failure loads for long and short columns for both the box-sections have been presented in Tables 4.4-4.5, along with the measured loads (average of many loads for each height of the column).

Average cross-sections

The measured outer dimension (A B, C, and D in Fig 4.1) for several specimens are very close with an average difference of ±0.3mm from the mean values (50.9 and 43.8mm for 51mm and 44mm box-sections respectively (see Fig 4.2). Furthermore, the web-thicknesses at either ends of each specimen vary by less than ±0.25mm, with variations sufficiently random and distributed that it is practically impossible to include all the variations. As all specimens have been extracted from a single batch of profiles, dimensional variations are very similar in all the prepared specimens. Average cross-sections for the two profiles with average geometrical properties (A_{ave} and I_{ave}) have been calculated for the subsequent determination of experimental as well as theoretical results (for comparison). The average geometrical properties have been used for the characterisation of the specimens with the standard deviations used to indicate data variations. The calculated values of A_{ave} and I_{ave} are included in Tables 4.4-4.5.

4.4.1 GLOBAL BUCKLING

Classical Column Theory

The critical buckling load for a slender, perfectly straight, centrally compressed column, pinned at the both ends with the upper end free to move vertically has been given by Euler (1759) as $P_E = n^2 \frac{\pi^2 EI}{L^2}$ (2.1) where E is Young's modulus, I is the moment of the inertia of the cross-section, L is the height of the column between the

pin-ends, and n is the order of the buckling load. Euler assumed that the cross-section of the column does not distort during buckling and failure, the parent material obeys Hooke's law and the wave length is of the order of the column length. The smallest or critical buckling load occurs for n = 1[††]. Including the transverse shear effects (Engesser, 1889), the Euler equation, becomes $P_{E.sh} = \dfrac{P_E}{1+(n_s P_E / A_g G_{xy})}$ (2.2), where P_E is given by (2.1); A_g = gross cross-sectional area and n_s = form factor for shear (taken as 2 for square box-section (Zureick and Scott, 1997)). Average cross-sectional areas and the moments of inertia representative of the two box-sections (Table 4.4) have been used in (2.2). Directional compressive modulus $E_{L,c}$ replaces E in (2.2) for composite materials (Barbero and DeVivo, 1999) and effective length (between the pivots of the knife edge end restraints) has been used for L, for the calculation of $P_{E.sh}$. The critical buckling loads '$P_{E.sh}$' calculated using (2.2), for both box-sections (slender columns) have been reported in Table 4.4.

Eurocomp Design Code (EDC)

EDC (Clarke, 1996) uses Euler equation (2.1) for the determination of global buckling loads of pultruded profiles (section 4.4 for designing compression members in EDC). The effects of low shear stiffness of the composite material have not been included. For example (4.7) in EDC gives the member's buckling resistance N_c as

$$N_c = \frac{k\pi^2 E_x I_{zz}}{\gamma_m L^2} \qquad (4.2)$$

The modulus of elasticity (E_x) used here is the directional modulus of elasticity ($E_{L,c}$) in the longitudinal direction (direction of loading), k = 1 for pin ended column, L = effective length and γ_m is partial safety factor for material resistance (taken equal to 1 for comparison). The moment of inertia I_{zz} used in the above equation is the moment of inertia for the average section. For a conservative design, including the shear effects, EDC design criteria predicts the same results $P_{(EDC)}$ as calculated using the classical approach (Table 4.4).

[††] n=1 represents first order buckling i.e., column buckles in a single half sine wave. Higher-order buckling loads can be attained only by using very slender column and by appling external constraints at the points of inflection to prevent the lateral deflection associated with the lower order modes (Timoshenko and Gere, 1961; Chen and Lui, 1987).

Included in Table 4.4 are the buckling loads $P_{E.sh}$ and $P_{(EDC)}$ calculated using minimum material properties supplied by the manufacturer (given on page 166) for comparison.

Manufacturer's manual

Both the pultruded box-sections (51×51×3.2 and 44×44×6.0mm) are manufactured by Fibreforce Ltd UK, for which the design manual is under preparation. However, the Fibreforce (in a private communication), recommended to following the design manual prepared by Strongwell (Strongwell, 1989) for column design because the material and proportions (fibre content percentages and lay-up) used for the both types of profiles are very similar. The empirical expression for the design of long square tubes (box-sections) suggested by Strongwell is;

$$F_u = \frac{1.3E}{\left(\frac{kl}{r}\right)^{1.3}} \tag{4.3}$$

Using the minimum specified material properties and (4.3), the buckling loads $P_{(STRONGWELL)}$ have been calculated and included in the last column of Table 4.4.

From Table 4.4 the following observations have been made;

- The classical buckling theory (Euler formulation) predicts the global buckling loads very well for the slender columns. The experimental loads ($P_{S.well}$)) confirm the theoretical prediction ($P_{E.sh}$), with a difference of no more than 5%. These results infer that longitudinal elastic modulus (in the direction of applied load) mainly contributes towards the buckling capacity of the axial columns. Furthermore, transverse shear properties have minimal effects on the global buckling loads. It also indicates that initial imperfections incorporated in the manufacturing process of these profiles and the cross-sectional tolerance, are minimal, as the Euler load normally corresponds to the buckling load of a perfect column. Finally, measured elastic constants are reasonably representative of the box-section material.
- EDC adopts the Euler formulation for the prediction of the global buckling load. The effects of lower shear stiffness possessed by composite material have been ignored as the effect is less than 4% (Barbero and Tomblin, 1994). However the predictions depend mainly on the value of elastic constant ($E_{L,c}$)

used in the formulations. Higher buckling capacities are predicted if the true material properties are used and likewise lower capacities are achieved if minimum specified properties are considered. As the EDC is a limit state approach, true properties with adequate factors of safety should be used. Alternatively, a lower factor of safety is required if the minimum representative properties are used. Nevertheless, the EDC approach is capable of predicting safe global buckling loads.

- Buckling loads using Strongwell expression (4.3) are higher than the measured loads. The loads are even higher for the longer columns. If the factor of safety recommended in the manual (Strongwell, 1989) of γ_m=3 is used, the predicted loads can be considered safe. However, the empirical expression given in Strongwell's design manual has been derived by curve fitting to the experimental data evolved from a range of particular profiles and though stated to be equivalent by FibreForce, may not represent profiles from other manufacturers. Significantly, the EDC approach (based on Euler formulation and having theoretical background) is applicable to composite profiles from various manufacturers, provided reliably measured material constants are available.

In light of above discussion it is shown that Euler formulation (also adopted by EDC) is capable of predicting the global buckling loads for long box-section profiles. It is further demonstrated that the global loads measured experimentally confirm the theoretical predictions, suggesting little initial imperfection.

4.4.2 LOCAL BUCKLING

Classical plate buckling

Consider an orthotropic rectangular plate, with width 'b' equal to the width of web in the box-sections (Fig. 2.2). The two short edges (x = 0, a) are considered as simply supported and compressed axially with an axial stress resultant N_x. The longer edges (y = 0, b) are each elastically restrained against rotation by side walls (webs with known transverse stiffness D_2). The critical value of the N_x causing local buckling of plate is give by the governing differential equation (2.3). An approximate solution to (2.3) is (Galambos, 1998) as:

$$N_x = \frac{\pi^2 D_3}{(b)^2}\left[\left(\frac{bm}{a}\right)^2 \frac{D_1}{D_3} + 2 + f_2(\varepsilon) + f_3(\varepsilon)\frac{D_2}{D_3}\left(\frac{a}{mb}\right)^2\right] \qquad (4.4)$$

where f_2 and f_3 are functions of rotational restraint applied at the two longer edges of the rectangular plate, $\varepsilon = Kb/D_2$, K = stiffness of supporting webs per unit length per radian of rotation, a is the length of the plate equal to half sine wave length of the plate buckling. The half sine wave length 'a' can either be measured during the local buckling tests (Barber and Tomblin, 1994; Bank et al, 1996; Barbero and Turk, 2000), or theoretically determined as $a = b\left(\frac{E_x}{E_y}\right)^{1/4}$ (Iyenger, 1998). As the length of half sine wave could not be measured experimentally, the theoretical approach has been used.

51×51×3.2mm Box-section

Moment of inertia 'I' of a small strip (of plate) of 1mm wide $= \frac{1\times(3.2)^3}{12} = 2.73\,\text{mm}^4$,

Average section internal width b = 51.0- 3.2 = 47.8mm,

E_x = 30.3kN/mm^2, E_y = 9.2kN/mm^2, a = 64.4, and G_{xy}= 3.95kN/mm^2 .

$$D_1 = \frac{(EI)_x}{1-\nu_{xy}\nu_{yx}} = \frac{30.32\times(2.73)}{1-(0.29)(0.15)} = 86.5\,\text{kN-mm}^2 \qquad (4.5a)$$

$$D_2 = \frac{(EI)_y}{1-\nu_{xy}\nu_{yx}} = \frac{9.2\times 2.73}{1-(0.29)(0.15)} = 26.3\,\text{kN-mm}^2 \qquad (4.5b)$$

$$D_3 = \frac{1}{2}(\nu_{yx}D_1 + \nu_{xy}D_2) + 2(GI)_{xy} = 25.9\,\text{kN-mm}^2 \qquad (4.5c)$$

Considering short loaded as well as long unloaded edges simply supported $f_2(\varepsilon) = f_3(\varepsilon) = 0$ the resultant N_x = 0.42 kN /mm, and

P_L = 0.42×47.8×4 = **80.3** kN.

Considering loaded edges simply supported and unloaded edges (longer sides) clamped, an approximate solution has been given by Wittrick (1952) (Galambos, 1998) as:

$$N_x = \frac{\pi^2 \sqrt{D_1 D_2}}{(b)^2}\left[k - c\left(1 - \frac{D_3}{\sqrt{D_1 D_2}}\right)\right] \qquad (4.6)$$

where c = 2.4 and k (buckling coefficient for orthotropic plate) is taken from curve drawn for orthotropic plate with ends simply supported and sides clamped (Fig. 4.30 in Galambos, 1998).

$$N_x = \frac{9.87 \times 47.67}{(47.8)^2}\left[7.7 - 2.4\left(1 - \frac{25.86}{47.67}\right)\right] = 1.32$$

and P_L = 1.42×47.8×4=**252** kN

44×44×6.0mm Box-section

Moment of inertia 'I' of a small strip of 1mm wide $= \frac{1 \times (6)^3}{12} = 18\,\text{mm}^4$,

b= 44.00-6.00=38.00mm

E_x= 33.2 kN/mm^2, E_y = 9.2 kN/mm^2, a = 52.4mm and G_{xy} = 3.95 kN/mm^2.

$$D_1 = \frac{(EI)_x}{1 - \nu_{xy}\nu_{yx}} = \frac{33.32 \times 18}{1 - (0.29)(0.15)} = 627 \qquad (4.7a)$$

$$D_2 = \frac{(EI)_y}{1 - \nu_{xy}\nu_{yx}} = \frac{9.2 \times 18}{1 - (0.29)(0.15)} = 174 \qquad (4.7b)$$

$$D_3 = \frac{1}{2}(\nu_{yx} D_1 + \nu_{xy} D_2) + 2(GI)_{xy} = 175 \qquad (4.7c)$$

For the case of loaded edges simply supported and long side also simply supported, using (4.4),

N_x = 4.64 kN/mm and P_L = 4.64×38.0×4 = **705** kN

For clamped long sides, using (4.6), c = 2.4 and k = 7.5,

N_x = 14.4 kN/mm and P_L = 14.4×38.0×4 = **2181** kN

Eurocomp design code

For an element of the section which can be defined as a long rectangular plate with two longer edges simply supported the buckling stress is calculated using the following equation (equation 4.9 in Eurocomp, 1996);

$$\sigma_{cr} = \frac{2\pi^2}{tb^2}\left[(D_1 D_2)^{1/2} + H_0\right] \qquad (4.8)$$

Where $H_0 = D_3$, and D_1, D_2 and D_3 have been defined in (4.5) for 51×51×3.2mm box-section and in (4.7) for 44×44×6.0 mm box-section.

For 51mm box-section (4.8) gives σ_{cr} = 0.20 kN/mm and P_L = 0.20×628 = **126**kN

For 44mm box-section (4.8) gives σ_{cr} = 1.26kN/mm and P_L = 1.26×882 = **1111**kN.

Using minimum material properties (manufacturer's supplied) in (4.8),

For 51mm box-section (4.8) gives σ_{cr} = 0.14 kN/mm and P_{cr} = 0.14×628 = **88**kN

For 44mm box-section (4.8) gives σ_{cr} = 0.80kN/mm and P_{cr} = 0.80×882 = **706**kN.

EDC design approach includes checking of the box-section for the ultimate compressive capacity of the cross-section. According to (4.6) in EDC, the design ultimate resistance of the cross-section is;

$$N_c = A\sigma_{cr} / \gamma_m \qquad (4.9)$$

where A is average cross-sectional area of the cross-section, σ_{cr} is the critical compressive stress and γ_m is the partial safety factor (taken equal to 1 for comparison).

Ultimate compressive capacities of the box-sections have been calculated using (4.9) and given in brackets under the $P_{(EDC)}$, for $E_{L,c}$ measured and minimum $E_{L,c}$ provided be Fibreforce.

STRONGWELL Approach

The empirical design equation in the Strongwell's manual for the allowable design loads of short square tubes is;

$$P_a = \frac{AE}{16\left(\frac{b}{t}\right)^{0.85}} \qquad (4.10)$$

where A is the average cross-sectional area of box-sections, b the web width, t the web-thickness and E is taken as $E_{L,c}$ given by manufacturer.

Using the minimum material properties supplied by the Fibreforce, in (4.10), allowable loads for short columns have been calculated and listed in the Table 4.5.

From Table 4.5, following observations have been made;

- Classical orthotropic plate buckling theory predicts a range of buckling load for the short columns depending on the assumed behaviour of the web connections. Experimental loads for the 51×51×3.2mm box-section do fall between the predicted ranges but towards the lower bound. This indicates that the stiffness of the connection between the webs approaches a simple support with nominal rotational restraint. However, it is interesting to note that the plate equations bound the experimental findings, suggesting that the local buckling of the columns may be represented by a plate with loaded edges simply supported longer edges with a nominal restraint. Adopting all four edges as simply supported results in a conservative estimate of the local buckling load.

- In the case of 44×44×6.0mm box-section, the range predicted by the plate buckling theory is far from the experimental evidence. The apparent reason for this disagreement is that failure is due to compression of webs and not the web local buckling. It is interesting to note that experimental failure load (220kN) is almost half the ultimate compressive capacity for this cross-section. It is recommended therefore that in the absence of local flange buckling, the failure load must be predicted by experiments.

- EDC, predicted a buckling load close to the experimental values, but non-conservative, in the case of 51mm box-section. The EDC expression is for elements that could be assumed as long rectangular plates with all the four edges simply supported. The bounding by the plate solutions suggests that the web interface in the case of 51mm box-section may be assumed to have little rotational stiffness. The mode of failure observed for these sections are different to the uniform wave like local buckling mode characteristic of long rectangular plates. The failure is catastrophic and material breaks along the web-interfaces following horizontal cracks. The failure of pultruded profiles

with small outstands (small I-sections) by tearing of material at the web-flange junctions have been reported by Zureick and Scott (1997) concluding the potential affect of the flange thickness to width ratio (t_f/b_f) on the failure mode. Brown et al (1998) have used Bank and Rhodes (1983) expression for the prediction of P_L in I-sections, where ratio of flange-thickness to its width (*tf*/*bf*) is a parameter. EDC expression (4.8) also includes the width and thickness of the composite plate. It indicates that if this ratio is small, local buckling of flange can cause bursting of the profile. On the other hand if this ratio is large, local web buckling may occur. For thicker sections (lower *tf*/*bf*), local buckling is replaced by a complex three-dimensional stress state (as observed in 44mm short columns). Relative cross-sectional dimensions greatly influence the failure mode of the short column, compounded by low ratios of (*tf*/*bf*). Furthermore, as web local buckling is not fully developed, correct length of the half buckled sine-wave cannot be determined with the prediction of P_L using classical approach perhaps is appropriate.

- Contrary to the findings associated with the long columns, assuming a material factor of unity, predictive failure loads given by the Strongwell design equation are conservative (safe) compared with test results. The correlation to the 44mm box is approximately 15%, reducing to 40% in comparison with the 51mm box experimental data. It is clear, therefore, that short columns with low *tf*/*bf* ratios do not follow a behaviour consistent with Euler buckling or basic material crushing across the section.

4.5 UNIVERSAL DESIGN CURVE

Design codes such as Eurocomp design code (EDC, 1996), ASCE (1984) and manufacturer's manuals (Strongwell, 1989) recognise global and local buckling in addition to material crushing but assume no interaction between these modes of failures. The common practice recommended by these guides is to evaluate a column's load bearing capability against global, local and compression failure modes and to accept the lowest value of buckling load for design (Brown et al, 1998). The outcomes of the present experimental investigations, however, do not support this approach.

It has been established experimentally (in the present and previous studies, e.g., Barbero and Tomblin, 1994) that there exist intermediate heights (in the vicinity of transition height) for a section, which exhibit lower experimental buckling loads than either of global, local or material failure predictions. This situation can become more adverse in the case of smaller (with small outstands) or closed form sections where the failure is catastrophic, and happens by tearing and breaking of webs or web/flange connections. A different approach that can be used for the design of columns having various (including slender, intermediate and short) heights, is required. For example, a "universal design curve", along with corresponding equation (2.24) has been proposed before by Barbero and Tomblin (1994), for the design of composite wide-flange profiles. Later Barbero and DeVivo (1999), extended the scope of this curve to wide-flange profiles of various sections manufactured by different pultruders, using experimental data from various sources (Fig 2.7). A similar procedure has been adopted here to construct a universal design curve for the design of pultruded box-section profiles when used as concentric columns.

The parameters involved in the development of the universal design curve in Fig 4.19 are given in Tables 4.6-4.7. These include the effective heights of the column (L_{eff}); experimental buckling loads $P_{(Exp)}$; Euler buckling loads P_E; short column failure load P_L; mode interaction coefficient c; compressive modulus of elasticity in longitudinal direction $E_{L,c}$ and the cross-sectional moment of inertia I. The dimensionless slenderness ratio 'λ' (2.19) has been defined, as a function of column length L_{eff}, stiffness EI and short column failure load P_L, to represent the various heights of composite box-sections. It has been established that P_L, the maximum buckling (or failure) load for a short column depends upon both material properties and the geometry of cross-section (Barbero and DeVivo, 1999, Mottram, 2000), and could either be determined experimentally or predicted theoretically.

The ultimate loads measured testing three 200mm (L_{eff} = 255mm) long 51mm square specimens average to a value of 120kN (Table 4.2). It can also be seen from Table 4.2 that at least one specimen from 300 to 500mm (range for short columns for 51mm box) reaches a maximum load of 120±1.51kN. This observation demonstrates that maximum measured load is independent of the specimen height. Similarly maximum loads measured using the shortest 44mm specimens i.e., 200mm (L_{eff}= 255mm) averages to 220kN and others 44mm specimens 300 to 400mm high, showed even

higher buckling loads than 220kN. This further demonstrates that although P_L is constant over the specimen lengths in the short column range but depends upon material properties and geometry of the cross-sections. These findings are in line with the basic assumptions made for the construction of the universal design curves for composite columns. The minimum affective height of the specimens (255mm) taken here is more than sufficient to accommodate four half sign-waves (using ¼ power formula by Iyengar, 1998) to eliminate any fix-end effects, recommended in previous studies (Mottram, 2000). The short column slenderness ratios λ (0.33 for 51mm and 0.45 for 44mm box-sections) are also well below the transition heights (λ=1) to avoid potential reduction of buckling stiffness due to mode interaction. Consequently 120 and 220kN has been established as P_L for 51 and 44mm box-section short specimens.

Material properties $E_{L,c}$ and G_{xy} have been measured experimentally (Table 3.12-3.13, 3.6-3.11) whilst moment of inertia 'I' and A_g used for Euler load calculation are the average sections properties (Table 4.4). The slenderness ratio λ for each specimen height has been calculated using actually measured parameters (L_{eff}, P_L, $E_{L,c}$ and I,) and presented in Tables 4.6-47.

The second important step in the formation of design curve is the determination of mode-interaction coefficient 'c' (2.7) using buckling load ratios 'q' and's' (2.5). Calculated q and s values using average experimentally measured loads for each specimen (Tables 4.1-4.3), have been plotted in Fig. 4.18 and values are compared (curve fitted) using several theoretical curves for c values ranging from 0.90 to 0.95. The curve with c = 0.91 is conservative enough to provide a lower bound for all the experimental values in the intermediate column range (around λ =1). Alternatively, from the c values for tested specimens in Tables 4.6-4.7, average values of c as 0.92 and 0.91 have been found for 51mm and 44mm box-section. Using these c values, k_i (2.23) and design compressive loads P_{cr} (2.24) for all the tested heights have been calculated (Table 4.6-4.7). The design curve (Fig. 4.19) has been plotted between the universal slenderness ratio λ and k_i using design loads.

The experimental loads have been include in Fig 4.19 showing that most of the theoretical loads are above the design plots or very close to it. The thick solid line (k_i=1) gives the maximum buckling load equal to P_L. Dotted lines represent the Euler buckling loads for the sections tested. The experimental loads for short and slender

lengths of the specimens lie on these lines indicating that measured load is either equal to P_L or P_E. For these cases $c = 1$ (no interaction). The maximum reduction in the design load P_c has been observed at $\lambda = 1$ (Fig 4.19). The loading capacity of the columns at this height reduces by 8% ($c = 0.92$) and 9% ($c = 0.91$) in the case of 51mm and 44mm box-sections respectively. It has already been demonstrated that reduction in load capacity of the axial columns of intermediate height due to mode interaction is imperfection sensitive. Experimental observations and design loads plotted in Fig. 4.19, indicate that the imperfections (overall as discussed under the heading Lateral Deflections) are very small. Experimental loads for slender and short columns (Table 4.1-3) are only 5% lower than the theoretical loads in the presence of small initial imperfections. In the view of this observation, mode interaction (maximum at λ=1) may have caused a further 3 to 4% loss in the buckling resistance of the intermediate columns.

In the view of above discussion it is proposed that "Universal Design Curve" plotted in Fig 4.19 can predict the ultimate load for any length of both box-section columns. Furthermore, this design curve is based on the experimental evidence. Such curves for the different composite sections (pultruded profiles) should be developed for the safe and confident design of structures using these profiles.

4.6 FFECTS OF HOLES

Three heights (2000, 1500 and 1000mm) of specimens from each cross-section (51mm and 44mm square boxes) have been retested after drilling holes through their webs to measure the loss of stiffness due to the introduction of holes. These specimens have already been tested and their buckling loads (without holes) are known. As each height group comprise three specimens, three diameters of the holes have been selected for the study. The diameters of holes made in the webs of the 51mm box-section are d= 14, 25 and 35mm respectively whilst for 44mm box-section the diameters are taken to be 14, 20 and 25mm (Plate 4.16). The resulting diameter to box-width ratios (d/w) are 0.28, 0.49 and 0.69 for the 51mm box-section while for 44mm box-section these ratios are 0.32, 0.46 and 0.57 respectively. Initially the holes are drilled on one side at distances 20d from centre to centre, starting at mid-height. The presence of a hole at mid-height is considered more onerous as maximum deflection (and hence the stresses) occurs at mid-height. Specimens have been tested

in both longitudinal orientations (as the testing is non-destructive). Additional holes are subsequently made in the two opposite sides (2 Holes) at 20 diameter distances and tested for buckling loads, with the process repeated giving holes on all four sides (4 Holes). Furthermore, to investigate the effect of the distance between holes, holes on all four sides are made at 10 times the diameter (mid-distance between the previous holes). Buckling loads for holes on all four sides at a distance of 10 times the diameter of holes are listed as '8 Holes' in the Table 4.8. The arrangement of the holes i.e., 1 Hole, 2 Holes, and 4 Holes at mid-height are shown in Plate 4.16. Short specimen could not be included in the study as they were tested to destruction whilst determining short column loads.

Table 4.8 presents the percentage loss in the buckling stiffness of the specimens due to the introduction of holes. These results have also been plotted against the diameter size in Fig 4.20. The graphs show a tendency of loss in the buckling stiffness with increase in the *d/w* ratio. The loss of stiffness is small (under 10%) for a *d/w* ratio of 0.5 for up to four holes at an interval of 20 times the diameter. Further increase in the hole-diameter reduces the stiffness more rapidly. More adverse effects can be seen in the plots for 8 Holes i.e., when holes are drilled at intervals of 10*d*. For the smallest size holes the loss is more than 10% in 51mm box-sections, increasing rapidly to up to 30% for a d/w ratio of 0.7. However for a *d/w* ratio of 0.5, the losses due to 8 Holes remain under 20%.

The effect of holes in the 44mm box-sections is less compared to with 51mm box. The main reason is the additional thickness of the walls and a lower width to thickness ratio. Introduction of 4 holes at 20*d* reduces the critical load by only 6 to 8% up to *d/w* ratios of 0.5. Decreasing the interval between holes (8 Holes) to half, reduces the stiffness of the specimens up to 20% for the same *d/w* ratio (0.5).

The buckling modes of the slender columns with circular holes are shown in Plates 4.17-4.19 for the three GRP heights of the box-sections 1000, 1500 and 2000mm. Buckling shapes clearly suggest the global buckling of the columns with maximum lateral deflection, at mid-heights. The specimens buckled in a half sine wave with the length of the half wave equal to the effective length of the specimens.

4.7 CONCLUSIONS

Buckling or failure loads for concentrically loaded composite columns depend upon their heights, material properties and the cross-sectional dimensions. These factors have been combined into one characteristic parameter 'λ' the slenderness ratio governing the ultimate load carrying capacity and behaviour of these columns. Slenderness ratio (λ) of each specimen is calculated using its effective height (L_{eff}), material ($E_{L,c}$) and sectional (I_{ave}) constants and the short column buckling (or failure) loads (P_L). Material constants should be measured using suitable methods (standard test methods where available) reported in the literature. Material properties given in the manufacturer's manuals are minimum values representing a group of pultrudates and their use in the prediction equations normally underestimates the critical buckling loads (and hence the load carrying capacities) of the pultruded profiles. Measured values of $E_{L,c}$ (Table 3.12-13), average values of I (Table 4.4) and experimental failure loads for short columns (Table 4.2), for the two sections have been used for the determination of respective slenderness ratios of all specimen (Tables 4.6-4.7). It can be seen from the data given in Tables 4.6-4.7 that experimentally measured loads P_{Exp} decrease with increase in 'λ'. The four types of failure modes, observed in the present study are; global buckling, local flange buckling followed by tearing and rupture of the cross-section, crushing of material at ends and interaction between two modes. The main outcomes of the experimental study are:

1. Slender columns (λ>1) buckled globally with no permanent damage to the material (without breaking). These specimens deformed in a half sine wave shape with maximum deflections at mid height (Fig 4.4). In the post buckling stage lateral deflection continued increasing without any further increase in the applied load (Figs. 4.5-4.8 for slender heights). Specimens retain their stiffness whilst the deflections increase beyond the serviceability limits (Zuerick and Scott, 1997). Furthermore, global buckling occurred in the linear elastic limits of the composite material (Figs. 4.5-4.6 for axial shortening and 4.14-4.18 for stress-strain plots). Specimens regained their straight configurations on unloading establishing the elastic behaviour of the material. Establishing the global buckling response as linear elastic, Southwell method has been used to determine the critical buckling load using measured load (P) and lateral deflection (Δ) data (Figs 4.9-4.10). Southwell method provides a critical load

$P_{S.well}$ considering the column as if it were a perfectly straight column free from imperfections. The ordinate of the Southwell plot gives an estimate of total imperfections present in the specimen and the test configuration. Twelve values of $P_{S.well}$ loads are available for every slender specimen with mean load and *SD* values. The lower *SD* values (less than 6%) for specimens (Table 4.1) establish the applicability of the Southwell method in the determination of the consistence global buckling loads. The close agreement (with difference less than 5%) of the measured P_{Exp} and $P_{S.well}$ loads (Table 4.1) demonstrate that not only the Southwell method is desirable in the case of composite slender columns but also that the pultruded box-section profiles used in this study possess minimal inherited imperfections.

2. Short columns ($\lambda<1$) extracted from 51mm box-section failed by tearing of the joints and breaking of the webs after local buckling was initiated. The web connection failure leaves the section comprising four thin composite strips which buckle globally and break at the centre due to excessive deformation. Therefore, failure of short column is not purely due to local buckling but precipitates material failure. The phenomenon has been found dependent on the web (and hence the connection) thickness and related to the thickness to width ratio of the web. Such a failure has also been reported by Zureick and Scott (1997) in the buckling experiments on I-section columns, where sections with small flange outstand failed due to tearing along the web-flange connection. This effect has been established in the case of thick section (44×44×6mm) short columns, where failure was not due to failure at the web interface, rather the material crushing at the ends (Plates 4.13-4.14). Specimens remained straight up to failure without any distortion of the cross-sections along the entire length Stress-strain plots for short specimens (Figs 4.15-4.17) conform that material behaved linearly prior to the failure followed by a minor non-linearity at failure. The failure loads (Table 4.2) indicate higher scatter (*SD* = 12.4) for longer specimens (in short column range) with a decreasing trend towards 255mm (*SD* = 2.14), establishing more consistent results for shorter heights (approaching to P_L). The failure loads for these specimens range from 202 to 226kN (Table 4.2) with a difference of -8 to +3% from the chosen P_L (220kN) for this section. However these loads are lower (45 to 47%) than the

crushing strength of the 44mm box-section, indicating a complex type of three dimensional stress distribution.

It is concluded therefore, that the conventional procedures for the prediction of buckling loads (e.g., orthotropic plate buckling formulation) are not applicable to the pultruded profiles with narrow and closed sections. Also the empirical design equations recommended by the manufacturers can only be valid for some particular sections as cross-sectional dimensions and material configuration varies from manufacturer to manufacture. Hence for the determination of design resistance when the pultruded profiles are used as concentric columns, a universal design equation is recommended.

3. Interaction between the global and local buckling has been observed in the case of 51mm box-section specimens with effective height 805mm (λ=1.05). The specimen first developed global mode at the critical load, with half sine configuration of the order of effective height. Then at the same load developed local web-buckling and failed with huge bang by tearing at the joints and rupture of webs (Plate 4.15). The experimental loads P_{Exp} for the three 750mm GRP (L_{eff} = 805mm) specimens are given in Table 4.3 with an average of 97.1kN (SD = 1.65), which is less than P_E (110kN) and P_L (120kN for 51mm box-section) indicating loss in the resistance due to the interaction between the buckling modes. It may be noted here that the λ for the columns may slightly vary as the experimentally measured values of $E_{L,c}$ for various specimens (from stress strain graphs in Fig 4.15) differs from the $E_{L,c}$ (from Table 3.12) used in the calculation of λ. This establishes that specimens having effective heights in the vicinity of λ=1 will exhibit mode-interaction leading to loss of resistance depending on the amount of imperfections present in the testing system.

4. Interaction between the global and material crushing has been exhibited by 500mm (L_{eff} = 555mm and λ=0.99) high specimens of 44mm box-section. The specimens first develop global buckling with a lateral deflection >L/100 (see Fig 4.8 for L = 500mm) and then failed by material crushing at the lower end (Plate 4.14 (c)). The measured load (195kN) is less than either P_E (224kN) or the P_L (220 kN) for the 44mm box-section.

5. Comparison has been made between measured and predicted loads (§ 4.4) to establish the method or methods capable of predicting buckling (or failure) loads for composite box-sections. The classical approach to predict the global buckling of slender columns (Euler formula) is applicable in the case of composite pultruded profiles. Correlation between the $P_{S.well}$ and calculated P_E results (Table 4.4) suggests that the Euler predictions are reasonable. The shear effects may be included in the analysis for a conservative prediction. Eurocomp design code (EDC) also recommends Euler formula for the prediction of buckling loads for slender columns. However use of minimum material properties underestimates the buckling capacities of the long composite columns. EDC recommends checking the sections against web local buckling or crushing of the material. Again using minimum properties EDC formulations underestimate the buckling resistance. Using Strongwell empirical formulations, bucking loads for long columns are too high whilst low for the short columns. Classical orthotropic plate buckling approach give a reasonable range of buckling loads for short 51mm box-sections (80.3 to 252kN) as compared to P_L (120kN) indicating a nominal stiffness of the web-interfaces. However the predictions for the short 44mm box-section columns, using classical orthotropic plate buckling theory, are far from the experimental loads (Table 4.5). EDC also predicts a very high load for the 44mm box-section profiles. It is concluded therefore, that the conventional procedures for the prediction short column failure loads are not applicable to the pultruded sections having closed and narrow sections.

6. Strain gauge readings have proved useful in providing some insight into the implied load carrying mechanisms. Stress strain plots (Figs 4.14-4.17) have been constructed using the measured strain and loading data. The changes in the directions of the graphs at buckling or failure loads indicate the nature of deformations (strains) and buckling behaviour. Compressive modulus calculated from the stress-strain plots is close to the $E_{L,c}$ values established by coupon testing (Tables 3.12-3.13) for majority of specimens but, in some cases, varies in the range of ± 12.5% . The potential reasons include non-homogeneity of material, poor alignment, testing and measuring inconsistencies. The small variations among the measured values of $E_{L,c}$ on four sides of a specimen are

attributed to material non-homogeneity and initial minor deflections of the specimens webs, and bending induced strains. Nevertheless, identical slopes of the plots in the initial loading ranges confirm the satisfactory alignment of the test specimen and the concentric loading. This establishes that a theodolite and callipers can be effectively used to align specimens. Similarly the use of strain gauges can infer the correct alignment of the specimens.

7. The conclusions drawn here also establish the fact that pultruded profiles tested in this study are straight, having reasonably uniform cross-section and the imperfections (due to manufacturing process) are well within specified limits.

8. Experimental buckling loads for the intermediate heights are lower than either of the predicted global or local buckling loads. For example, for 750mm high specimen (51mm box-section having L_{eff} = 805mm), the averaged measured load (Table 4.3) is 97.10kN as compared with $P_{E.sh}$ = 108kN and P_L = 120kN. When $P_{E.sh}$ and P_L are close, buckling modes can interact. The resulting mode is highly sensitive to the imperfections. In the case of perfect column, the measured load should approach the P_E value.

9. Universal design equation constructed, in Fig 4.18, is based on the experimental evidence considering the actual material and geometric properties and includes all the practical column heights. Most of the experimental results fall above the design curve confirming it as a conservative one.

   Determination of 'P_L' needs careful consideration and a well defined procedure (preferably experimental) as the design of the column, particularly in the intermediate range, greatly dependents on its value. P_L may be reported as an empirical parametric expression (e.g., $P_L = \frac{0.5EA}{(b_f/t_f)^{1.5}}$ has been suggested by Strongwell, 1989).

10. Holes do not affect adversely the critical buckling loads, provided *d/w* ratio is not large (< 0.3). For higher ratios (*d/w* = 0.6) buckling stiffness can be reduced by up to 30%. Sections with thicker webs demonstrated lower sensitivity towards the effects of holes.

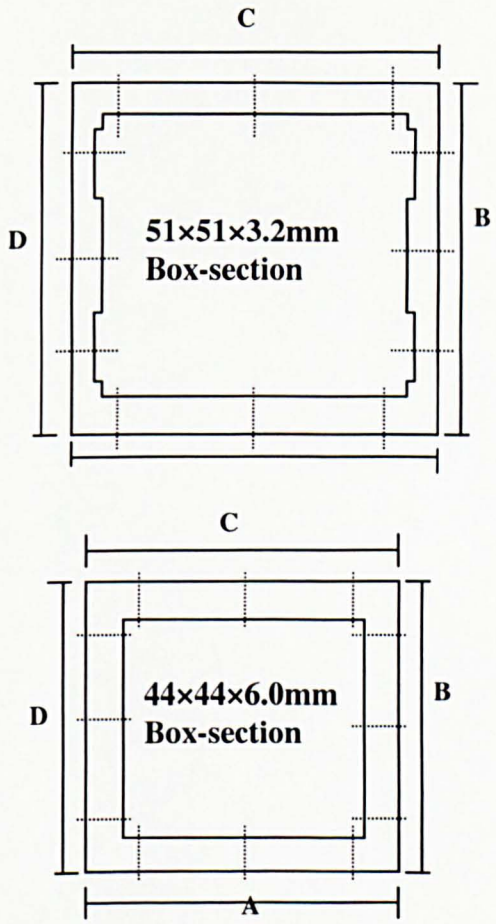

Fig 4.1 Outer dimensions (A, B, C and D) measured every 100 mm along the specimen height and web-thickness measured at 12 locations, shown by dotted lines, at both ends.

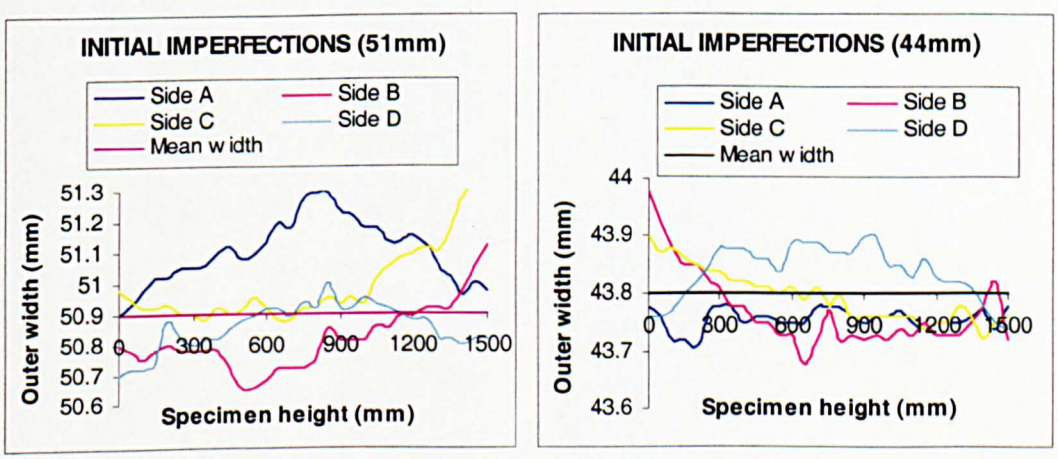

Fig 4.2 Initial imperfections in 1500mm long 51mm and 44mm box specimens.

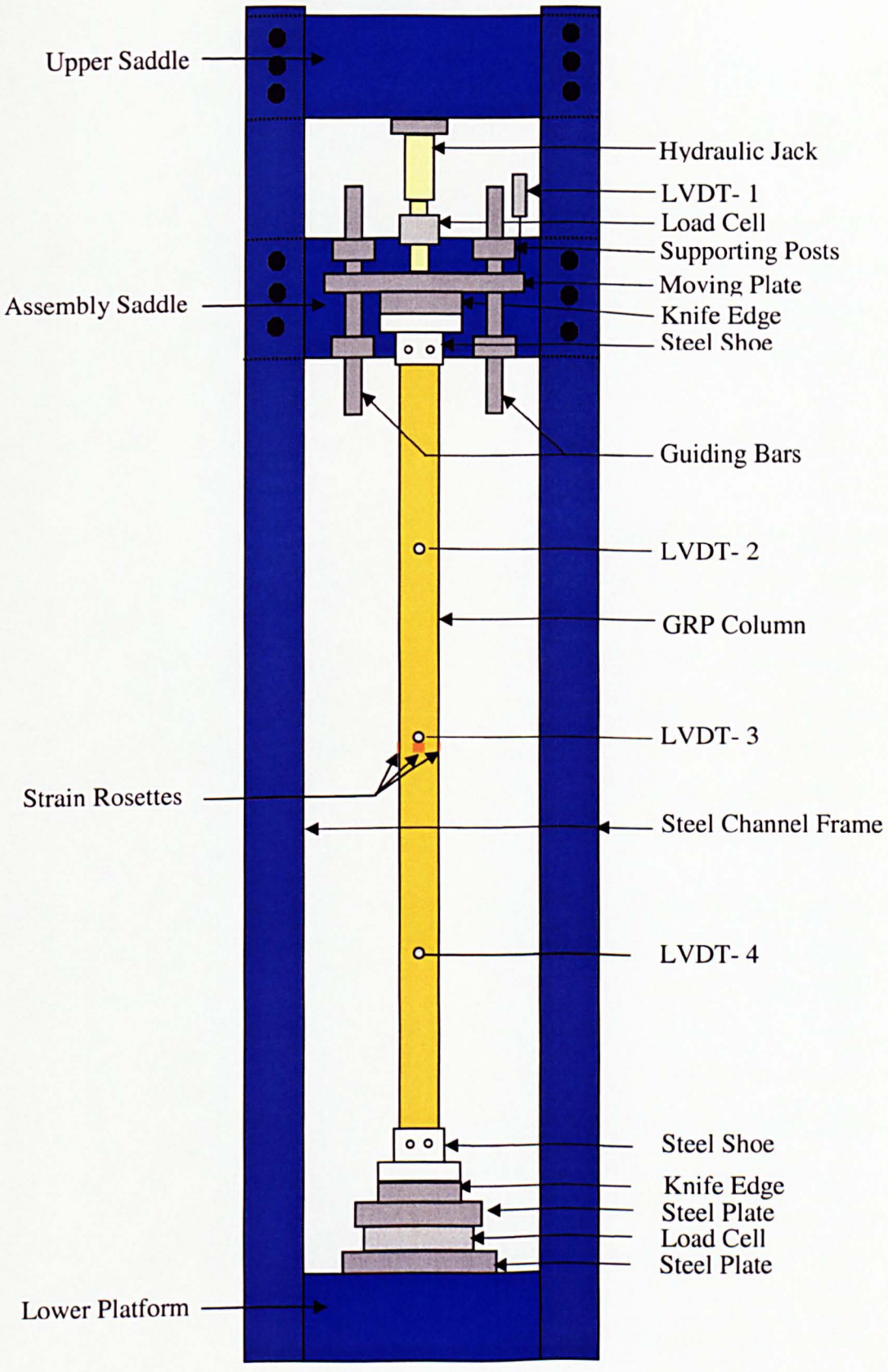

Fig 4.3 Test setup for axial loading of GRP box-section specimens.

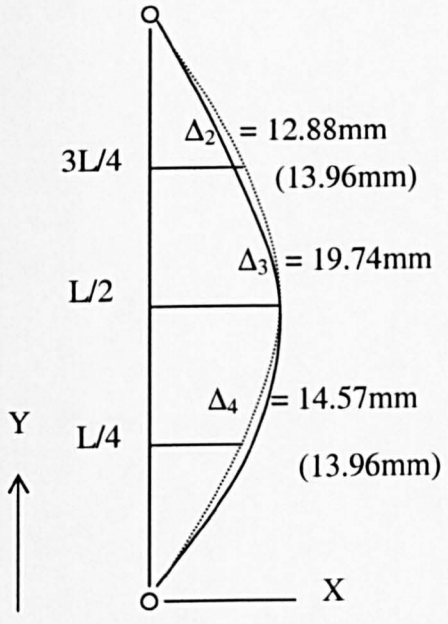

(a) 51mm box, L=2000mm

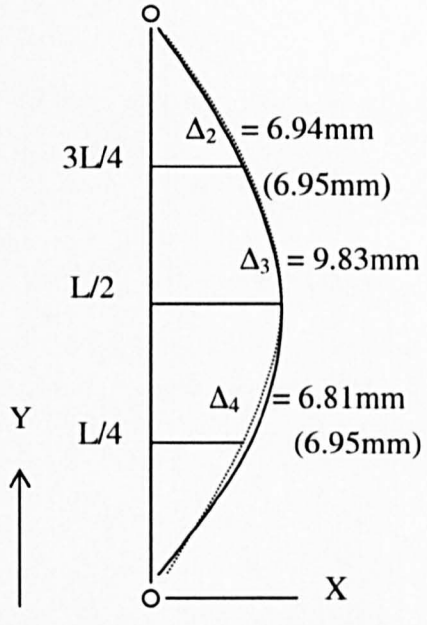

(b) 51mm box, L=1000mm

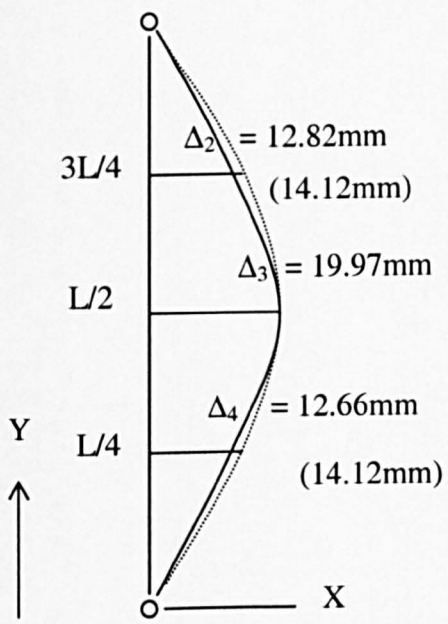

(c) 44mm box, L=2000mm

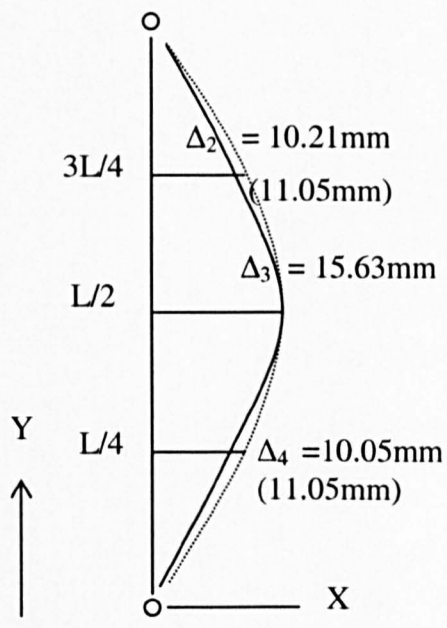

(d) 44mm box, L=1500mm

Fig. 4.4 Typical curves confirming half sinusoidal buckled shapes. (Dashed line show the sine curve with $\Delta_2 = \Delta_4 = 0.707\ \Delta_3$)

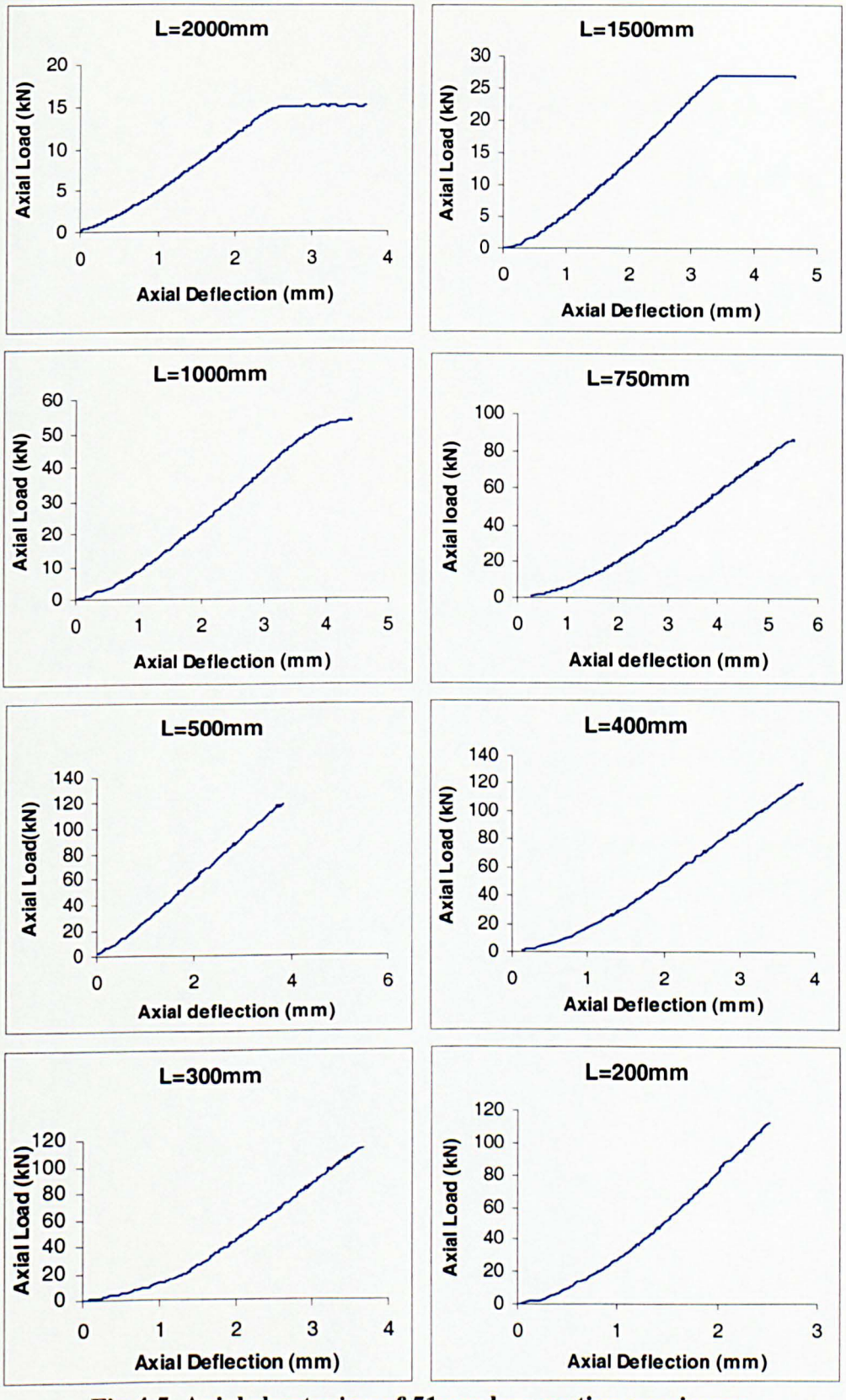

Fig 4.5 Axial shortening of 51mm box-section specimens.

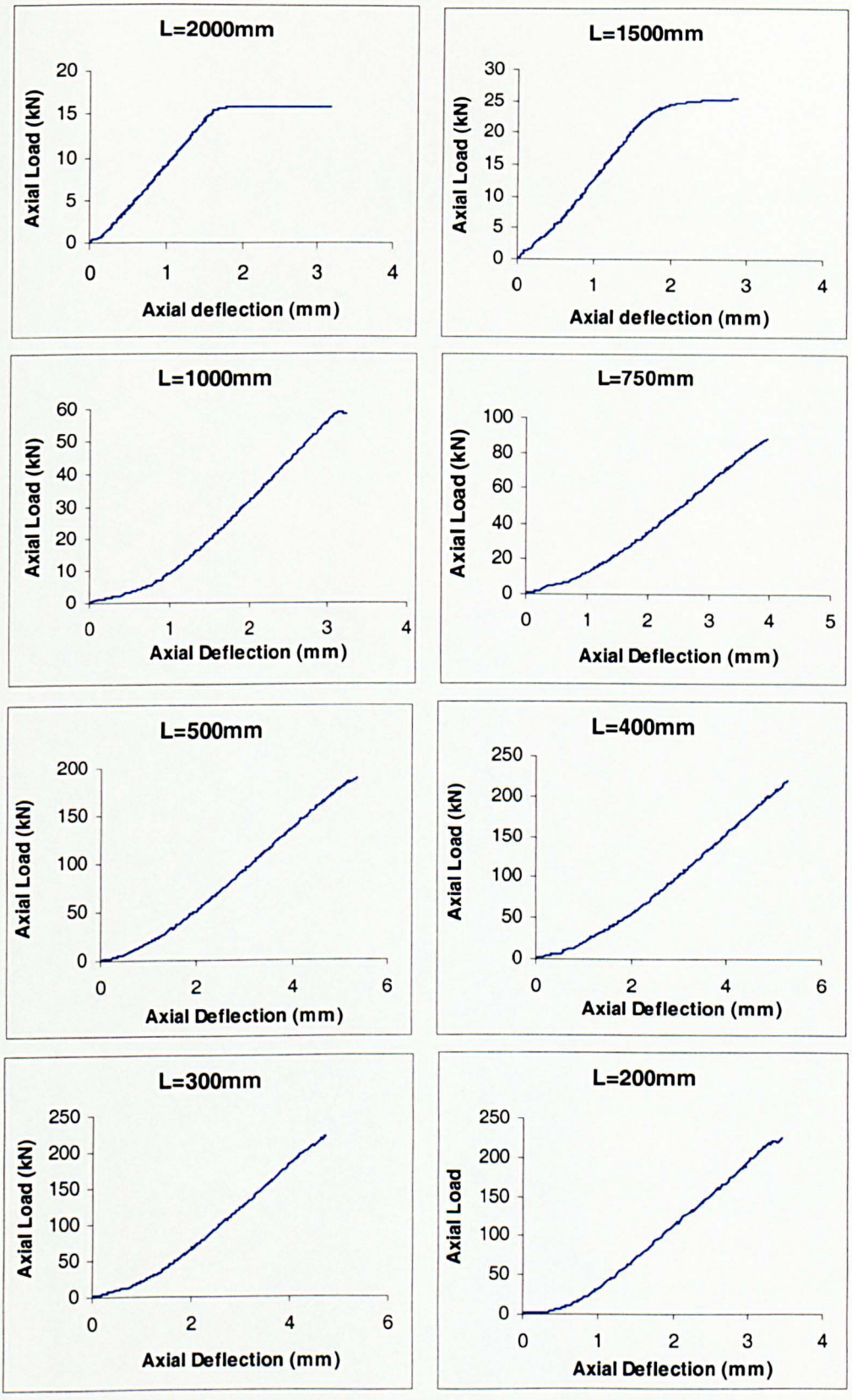

Fig 4.6 Axial shortening of 44mm box-section specimens.

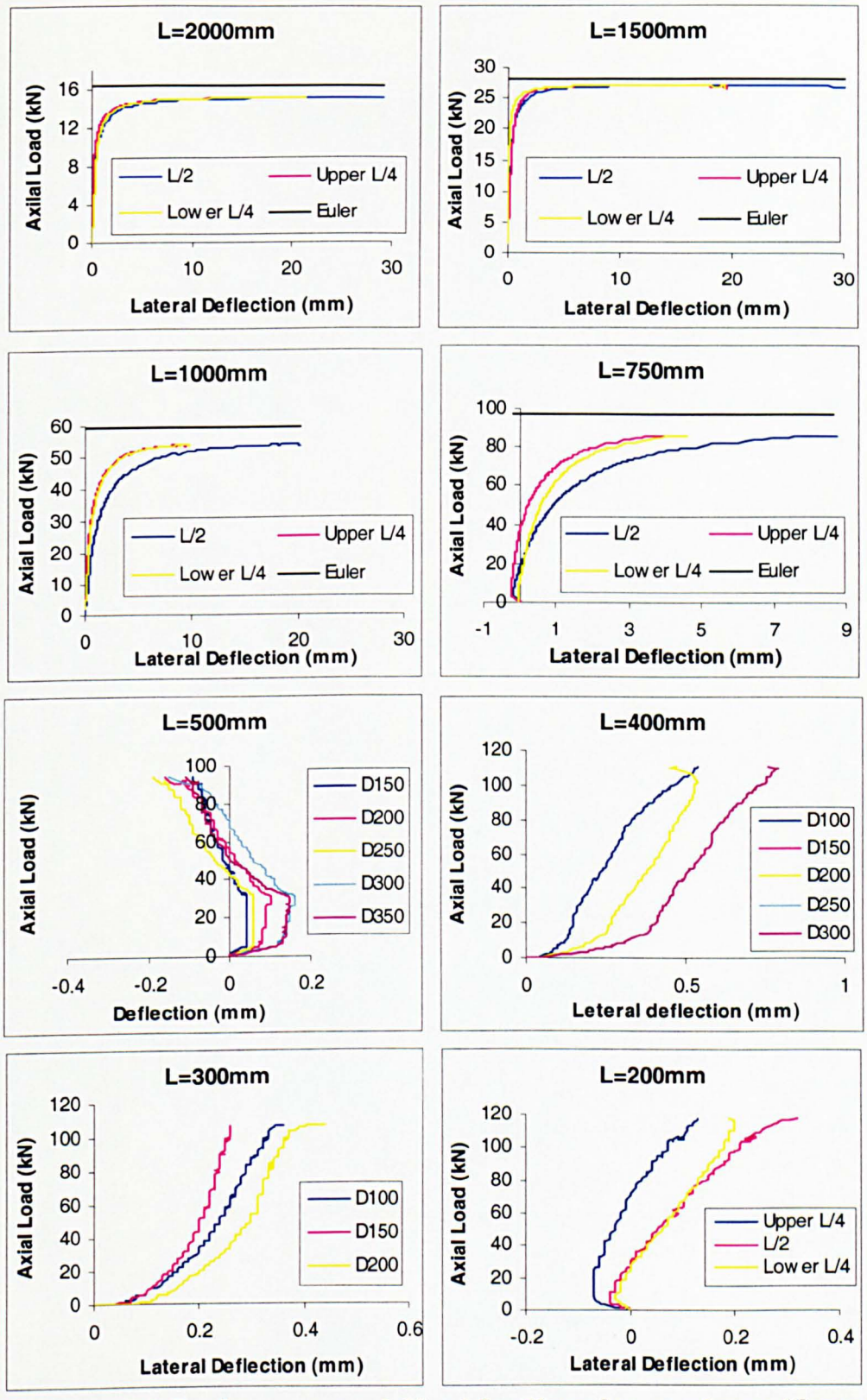

Fig 4.7 Lateral deflections verses axial load for 51mm box specimens ((legends in plots for 500 to 300mm specimens indicate the distance in mm from the lower column ends, of respective LVDTS measuring the lateral deflections).

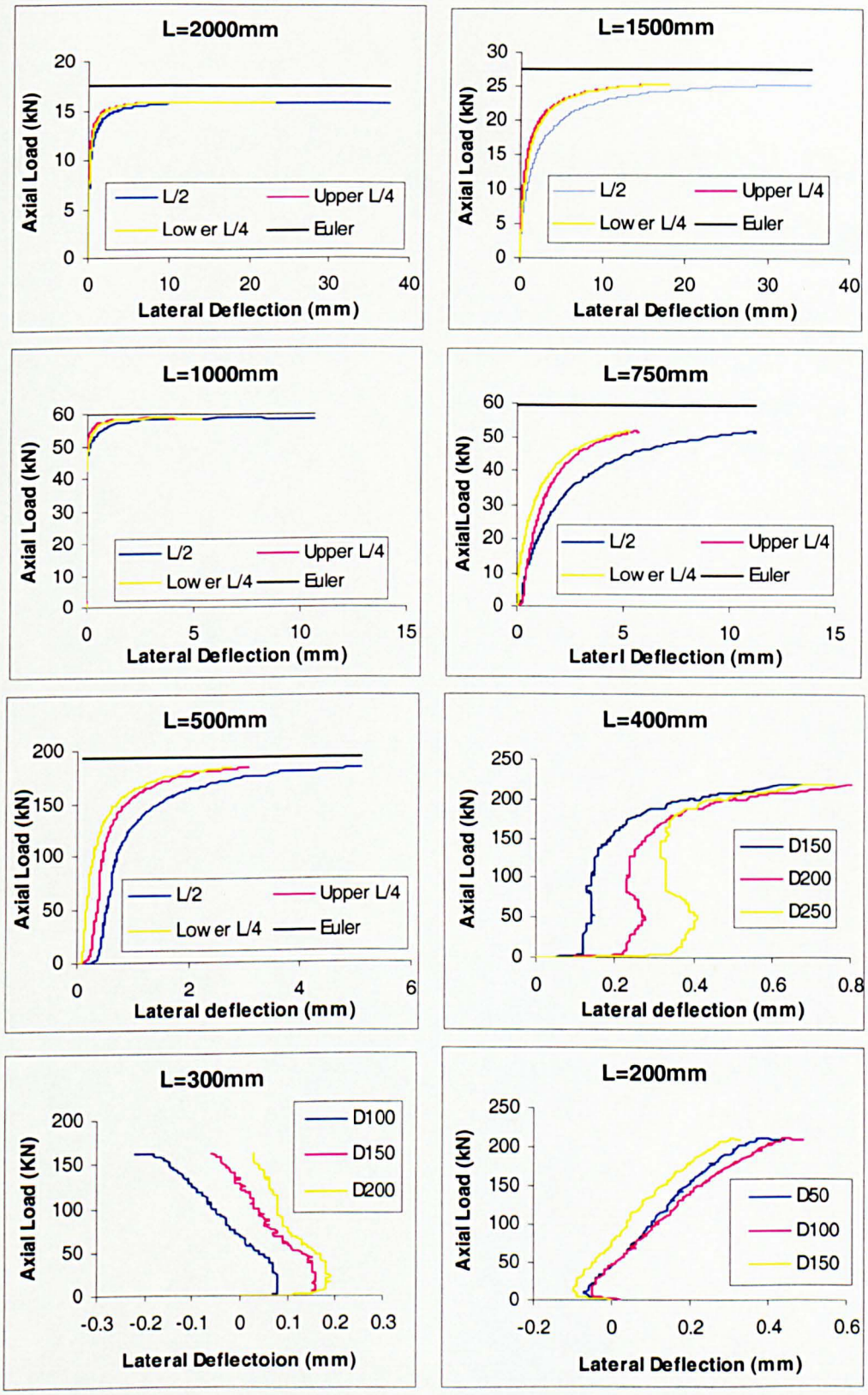

Fig 4.8 Lateral deflections verses axial load for 44mm box specimens (legends in plots for 500 to 200mm specimens indicate the distance in mm from the lower column ends, of respective LVDTS measuring the lateral deflections)

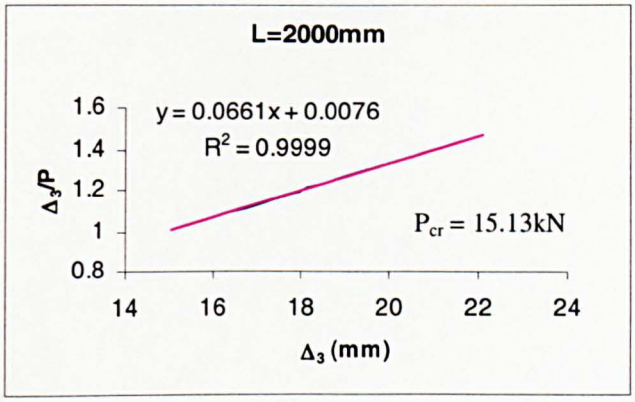

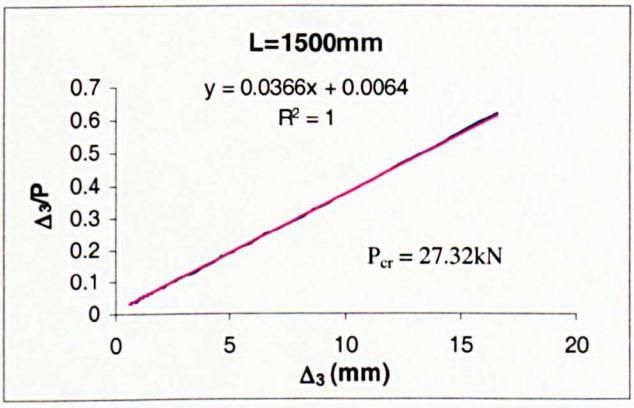

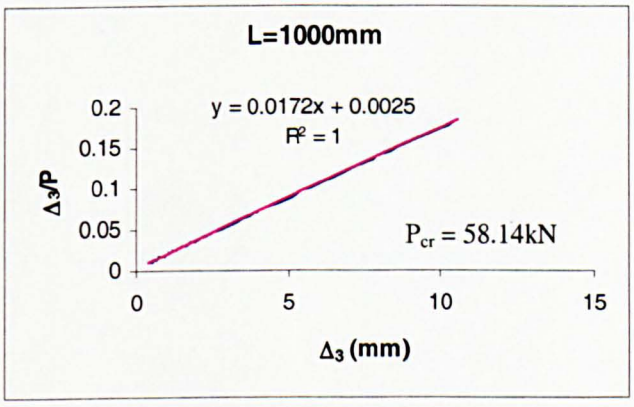

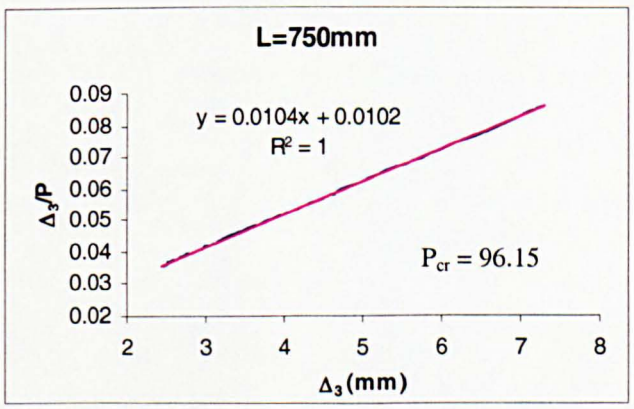

Fig 4.9 Southwell Plots (typical) for 51mm box specimens

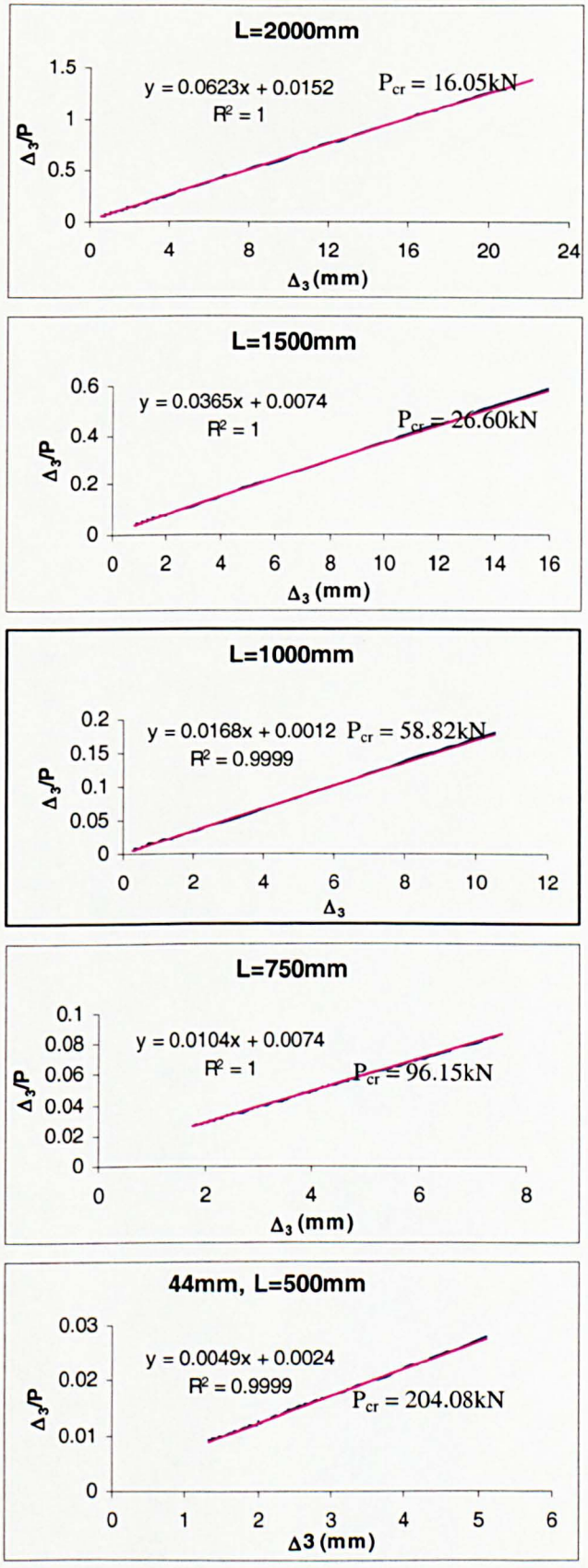

Fig 4.10 Southwell plots (typical) for 44mm box specimens.

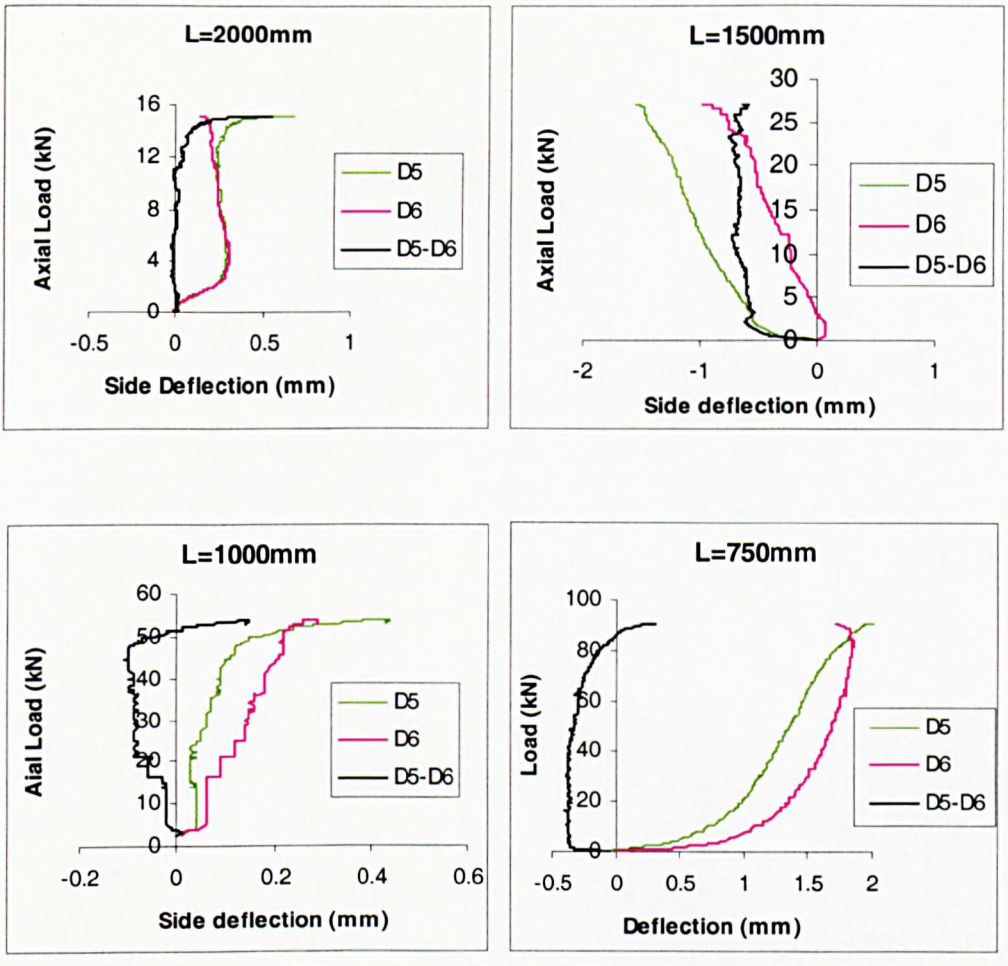

Fig. 4.11 Rotation of middle cross-section in 51mm box-section slender columns

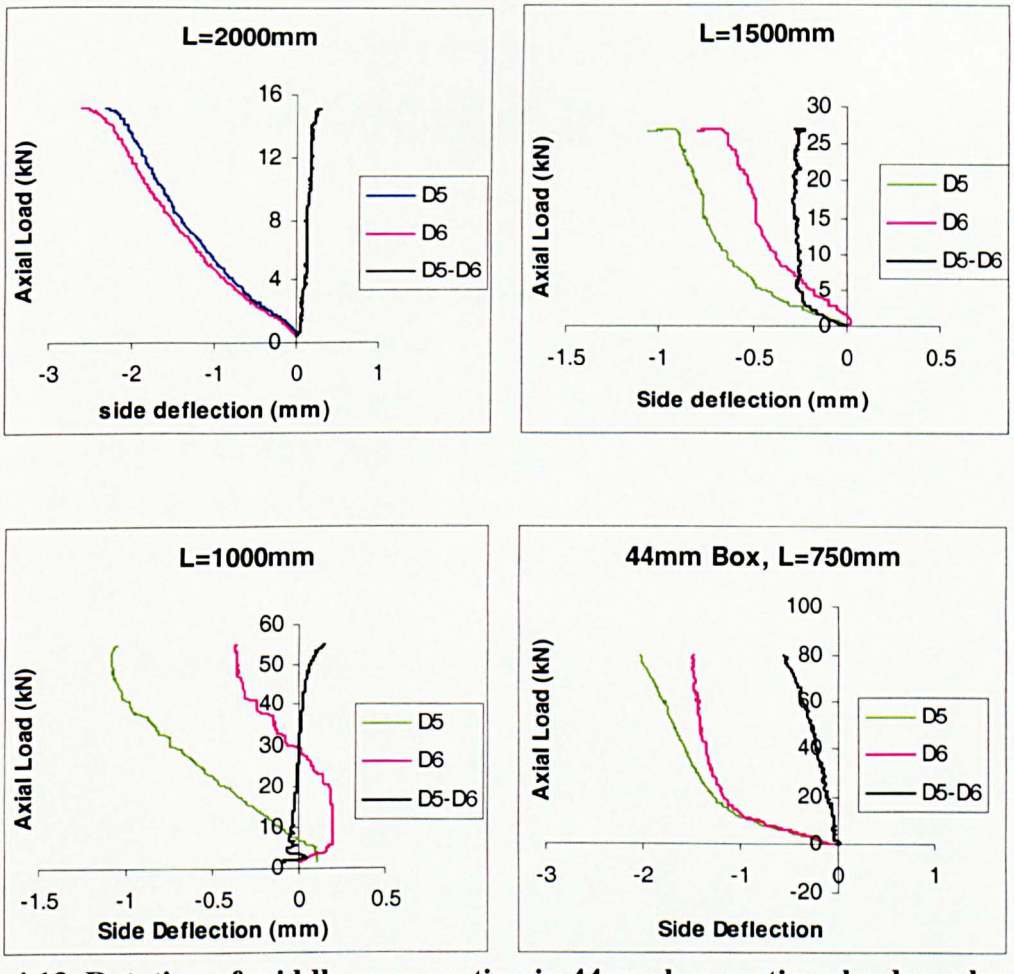

Fig. 4.12 Rotation of middle cross-section in 44mm box-section slender columns.

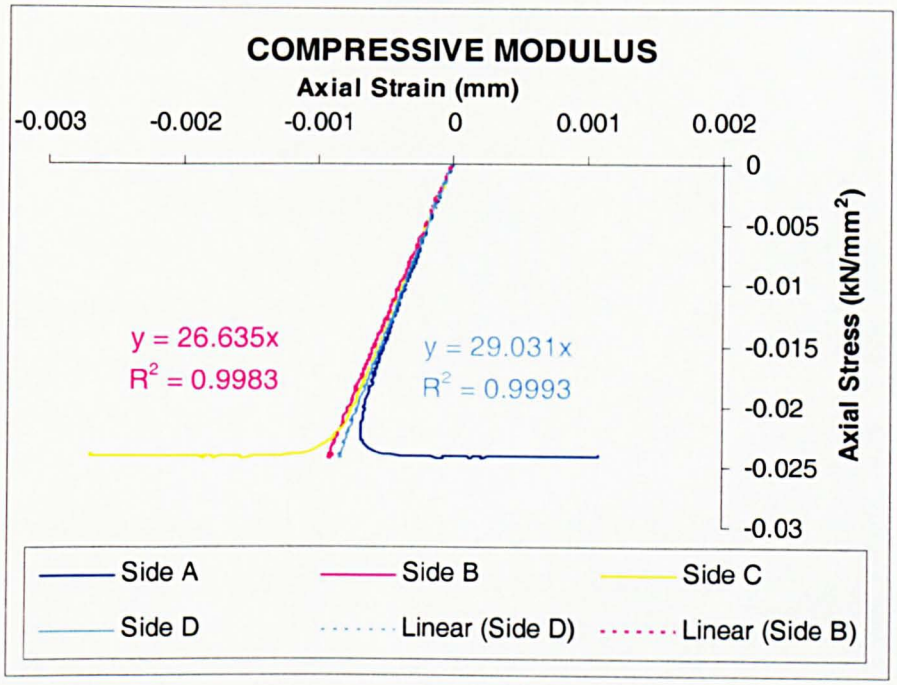

(a)

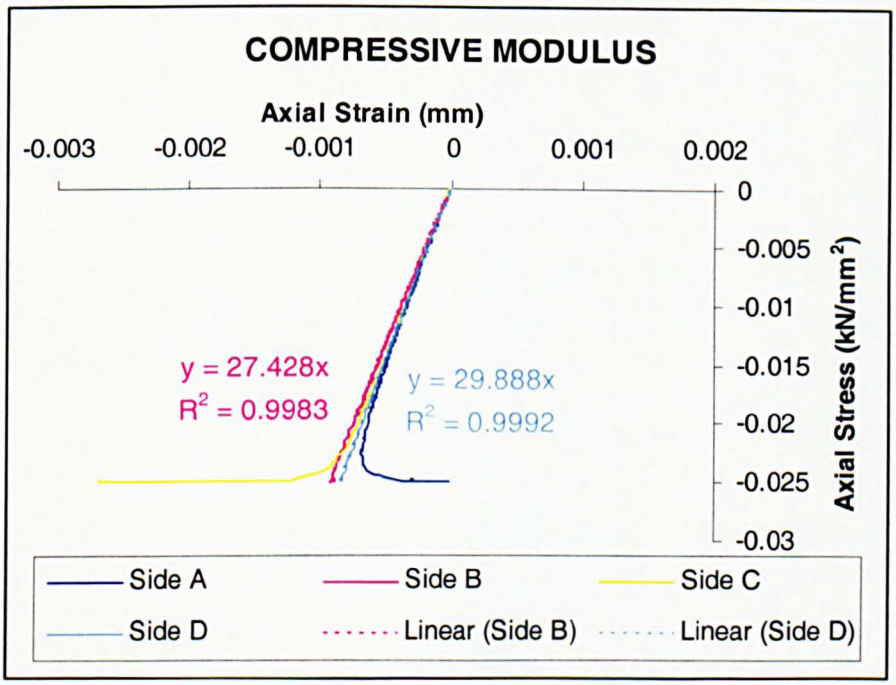

(b)

Fig. 4.13 Stress strain plots for 51mm , 2000mm high GRP specimen; (a) strain evaluated by central gauge only, (b) principal strain calculated from three gauges of a strain rosette.

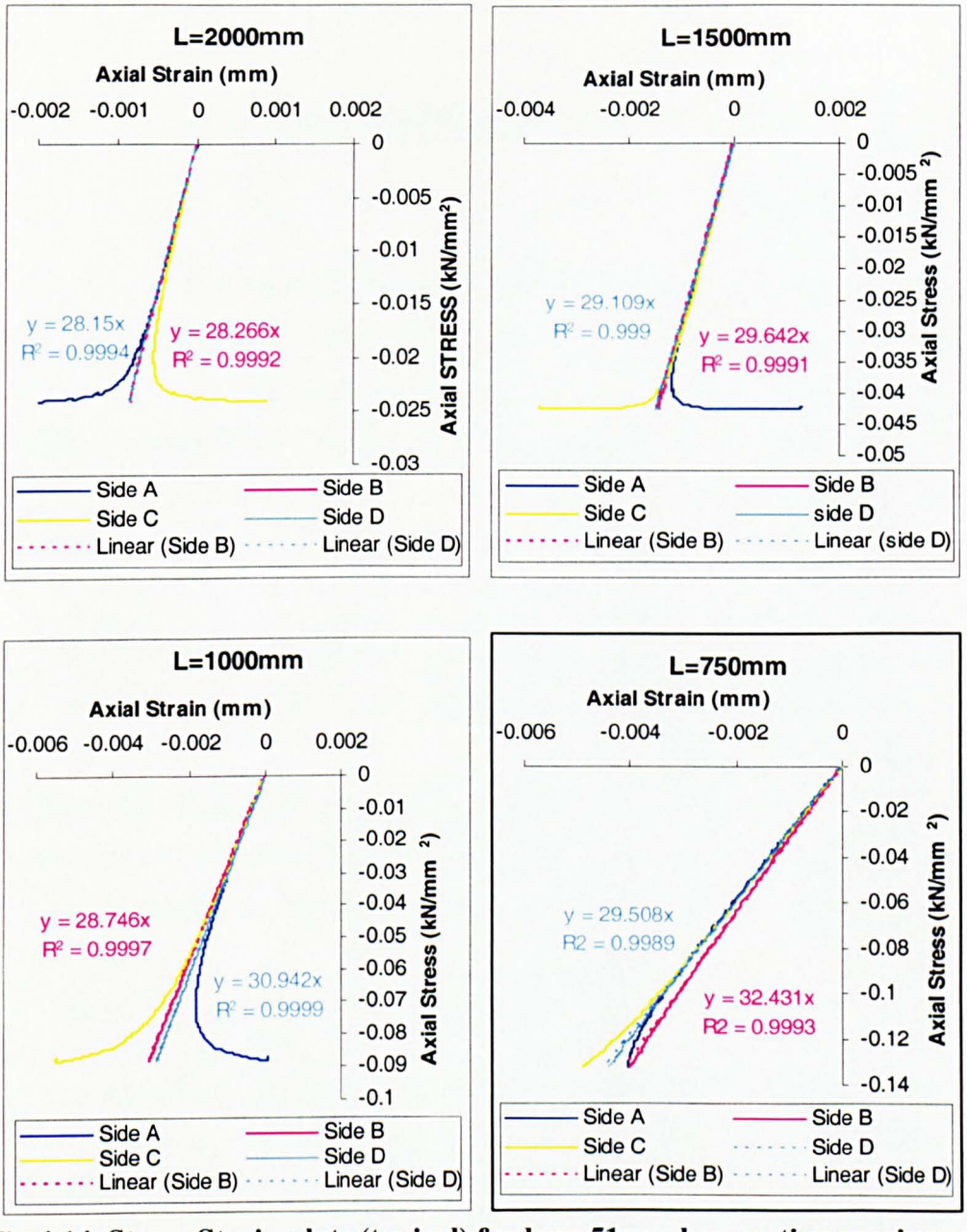

Fig 4.14 Stress-Strain plots (typical) for long 51mm box-section specimens.

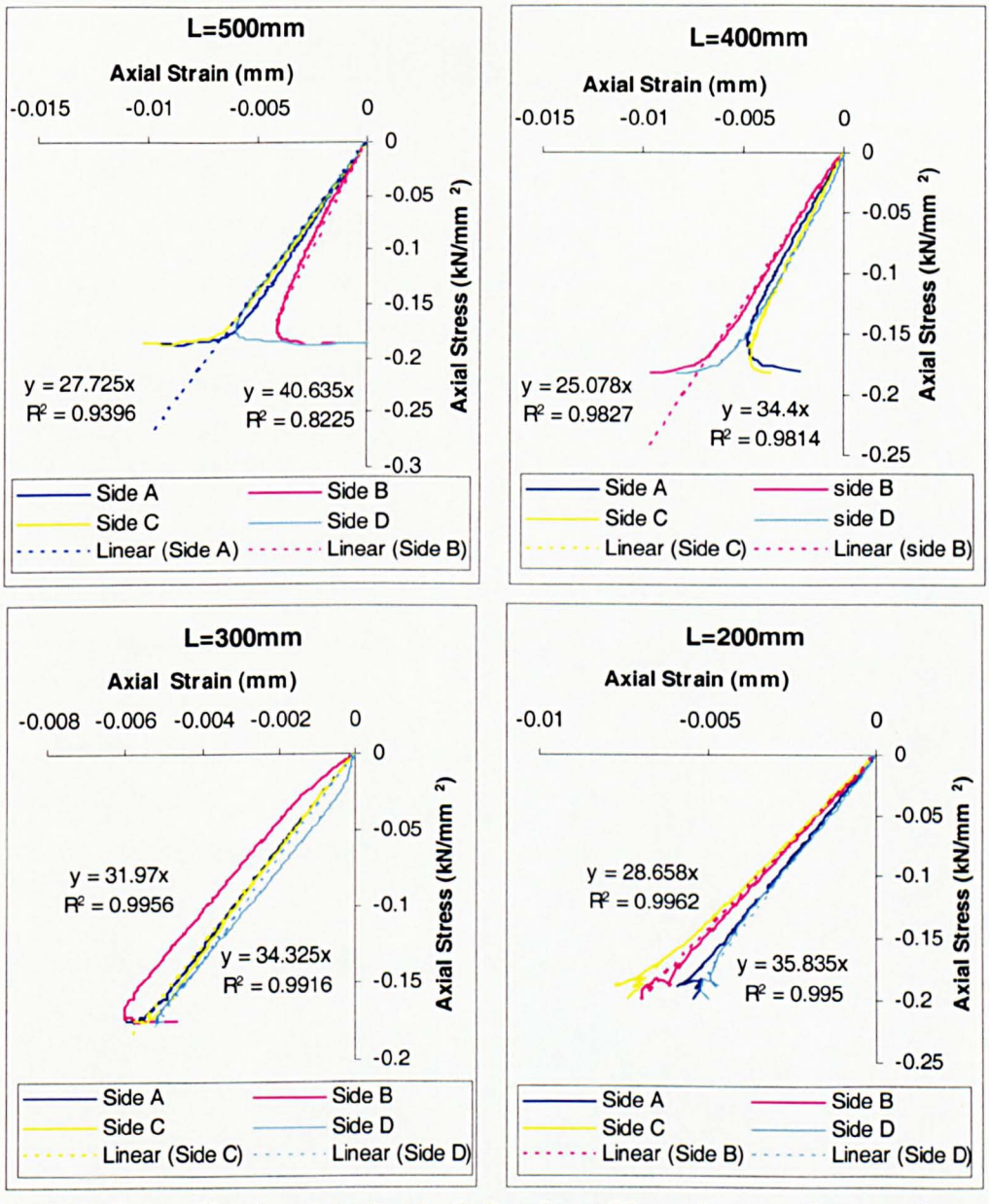

Fig 4.15 Stress-Strain plots (typical) for short 51mm box-section specimens.

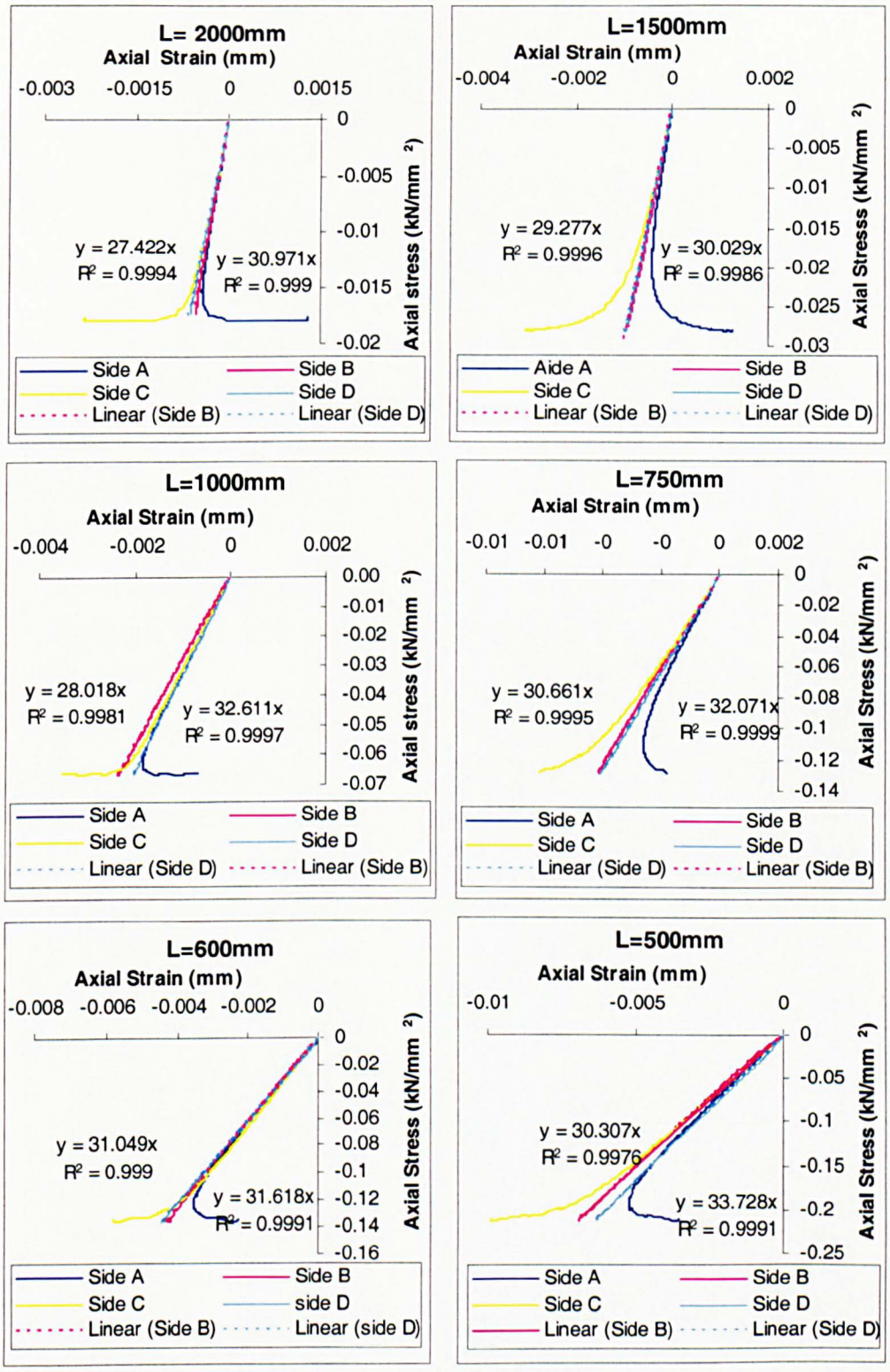

Fig 4.16 Stress-Strain plots (typical) for long 44mm box-section specimens.

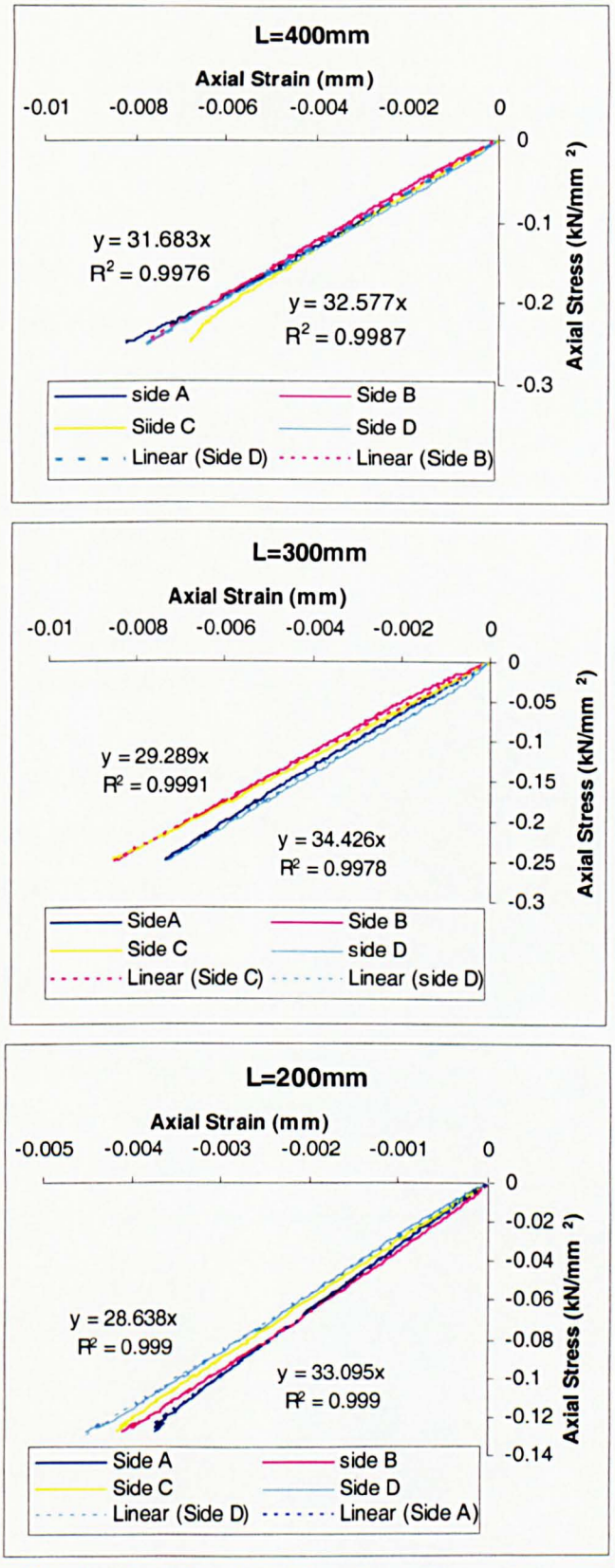

Fig 4.17 Stress-Strain plots (typical) for short 44mm box-section specimens

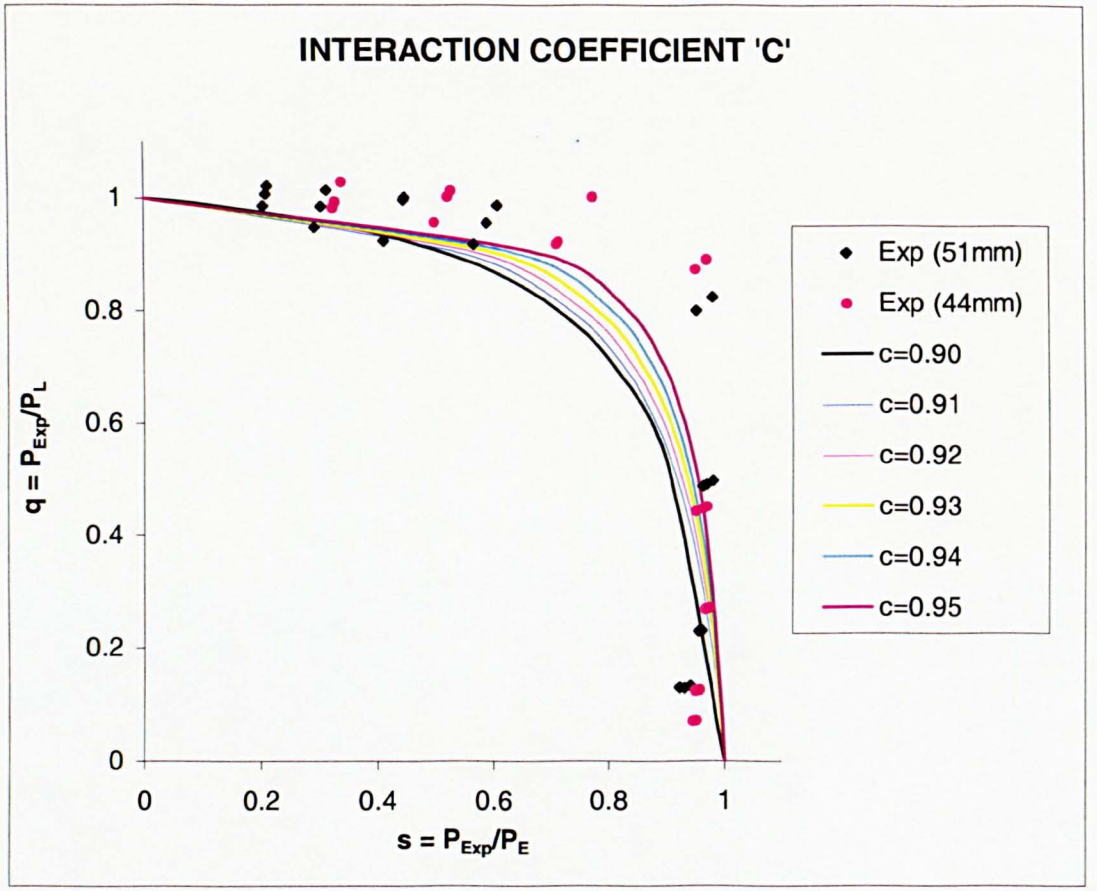

Fig. 4.18 Estimation of interaction coefficient 'c' for the two box-section profiles.

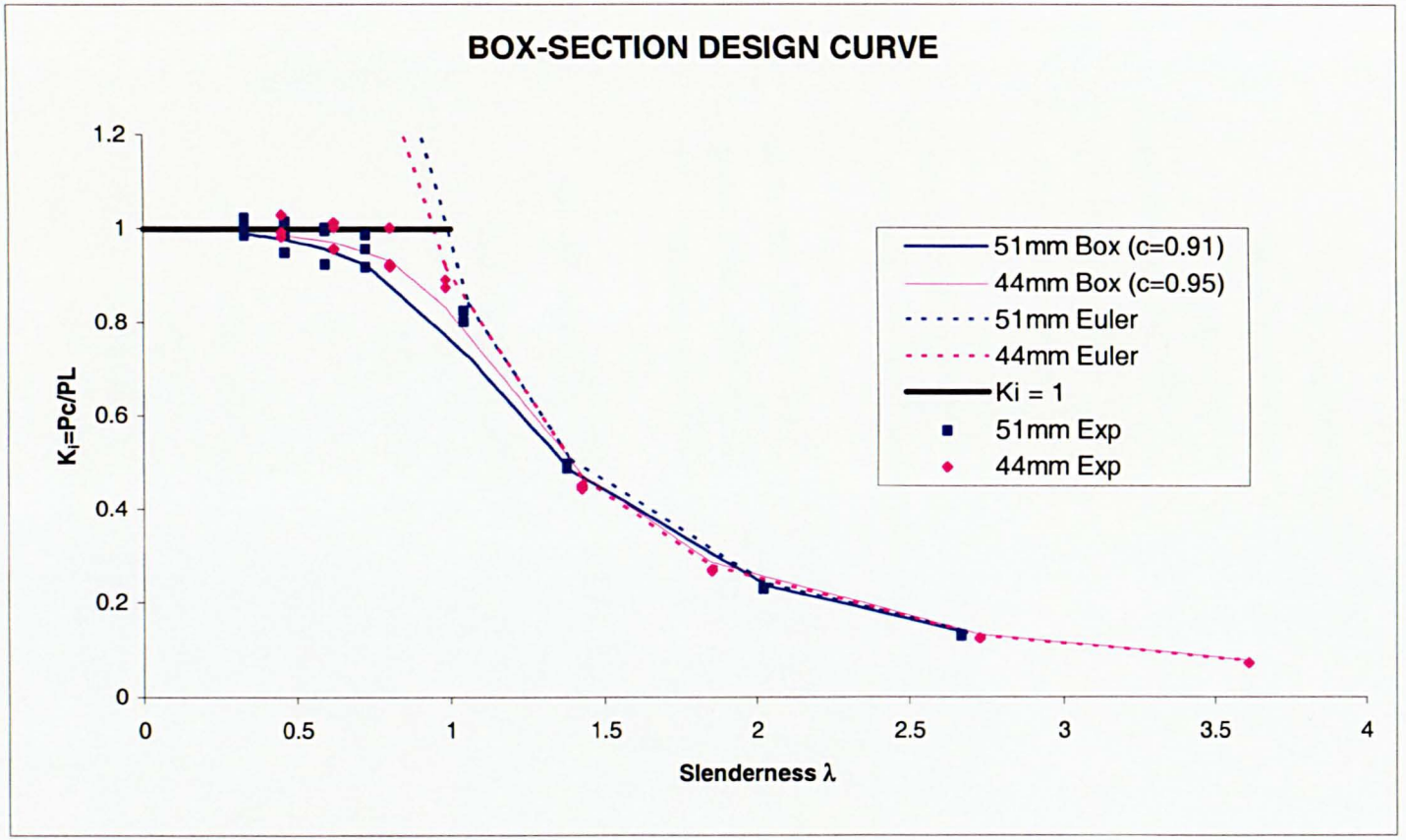

Fig 4.19 Universal design curve for pultruded box-section concentric columns.

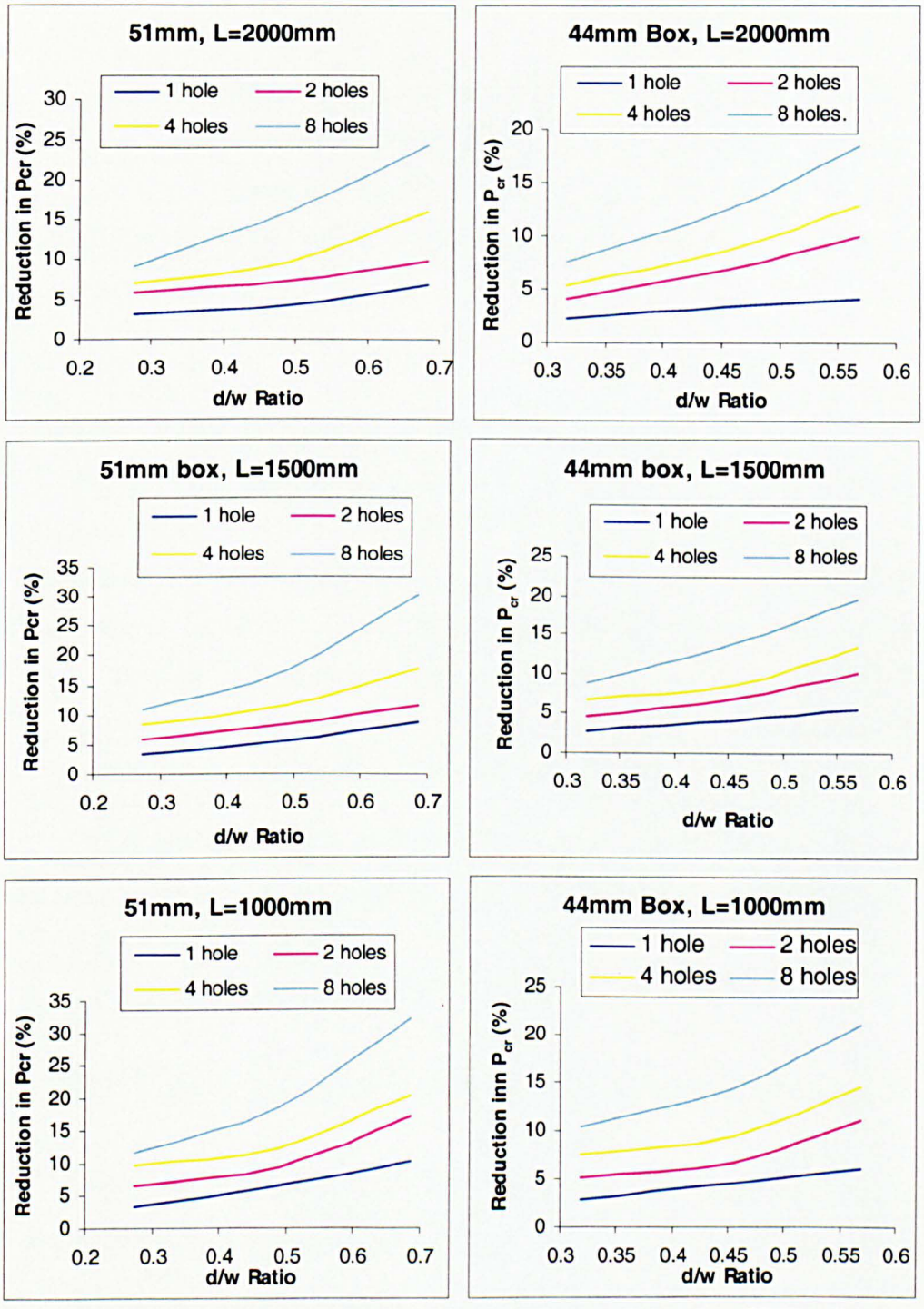

Fig. 4.20 Effect of holes on the buckling stiffness of slender GRP columns.

Table 4.1 Experimental buckling Loads of slender columns

Column No: 1, 51×51×3.2mm, L_{GRP} = 2000mm, L_{eff} = 2055mm, λ = 2.69										
Side	A	-A	B	-B	C	-C	D	-D	Mean	SD
P_{Exp}	15.1	15.1	15.0	15.1	15.5	15.4	15.3	15.3	15.2	0.16
$P_{S.well}$	15.2	15.4	15.5	15.3	15.7	15.7	15.7	15.7	15.5	0.21
Column No: 2, 51×51×3.2mm, L_{GRP} = 2000mm, L_{eff} = 2055mm, λ = 2.69										
Side	A	-A	B	-B	C	-C	D	-D	Mean	SD
P_{Exp}	15.1	15.1	15.3	15.3	15.4	15.4	15.2	15.1	15.2	0.14
$P_{S.well}$	15.1	15.4	15.6	15.6	16.1	15.9	15.4	15.4	15.6	0.30
Column No: 3, 51×51×3.2mm, L_{GRP} = 2000mm, L_{eff} = 2055mm, λ = 2.69										
Side	A	-A	B	-B	C	-C	D	-D	Mean	SD
P_{Exp}	15.2	15.2	15.8	15.6	15.3	15.3	15.8	15.5	15.5	0.24
$P_{S.well}$	15.4	15.5	16.3	16.1	15.5	15.7	16.4	16.1	15.9	0.38
Column No: 4, 44×44×6.0mm, L_{GRP} = 2000mm, L_{eff} = 2055mm, λ = 3.61										
Side	A	-A	B	-B	C	-C	D	-D	Mean	SD
P_{Expt}	15.8	15.8	14.8	14.7	15.7	15.6	14.6	14.7	15.2	0.56
$P_{S.well}$	16.1	16.1	15.2	15.2	15.9	15.8	15.2	15.2	15.7	0.43
Column No: 5, 44×44×6.0mm, L_{GRP} = 2000mm, L_{eff} = 2055mm, λ = 3.61										
Side	A	-A	B	-B	C	-C	D	-D	Mean	SD
P_{Exp}	15.9	15.8	14.8	14.7	15.8	15.7	14.9	14.9	15.3	0.52
$P_{S.well}$	16.0	16.1	15.2	15.3	16.1	16.0	15.2	15.2	15.6	0.44
Column No: 6, 44×44×6.0mm, L_{GRP} = 2000mm, L_{eff} = 2055mm, λ = 3.61										
Side	A	-A	B	-B	C	-C	D	-D	Mean	SD
P_{Exp}	15.1	15.1	15.7	15.7	15.2	15.2	15.6	15.6	15.4	0.28
$P_{S.well}$	15.4	15.4	16.1	16.0	15.4	15.4	16.0	16.0	15.7	0.33

Table 4.1 Experimental buckling Loads of slender columns (continued)

Column No: 1, 51×51×3.2mm, L_{GRP} = 1500mm, L_{eff} = 1555mm, λ = 2.03										
Side	A	-A	B	-B	C	-C	D	-D	Mean	SD
P_{Exp}	27.0	26.8	27.2	27.3	26.9	26.8	27.4	27.4	27.1	0.38
$P_{S.well}$	27.3	27.2	28.1	28.0	27.1	27.2	28.3	28.2	27.7	0.51
Column No: 2, 51×51×3.2mm, L_{GRP} = 1500mm, L_{eff} = 1555mm, λ=2.03										
Side	A	-A	B	-B	C	-C	D	-D	Mean	SD
P_{Exp}	26.9	26.9	27.4	27.3	26.7	26.7	27.4	27.4	27.1	0.32
$P_{S.well}$	27.4	27.1	27.9	28.2	27.0	27.1	28.2	28.3	27.6	0.54
Column No: 3, 51×51×3.2mm, L_{GRP} = 1500mm, L_{eff} = 1555mm, λ=2.03										
Side	A	-A	B	-B	C	-C	D	-D	Mean	SD
P_{Exp}	26.0	26.0	27.5	27.3	25.7	25.9	27.4	27.4	26.6	0.81
$P_{S.well}$	26.7	26.8	28.4	28.3	26.7	26.7	28.1	28.4	27.5	0.86
Column No: 4, 44×44×6.0mm, L_{GRP} = 1500mm, L_{eff} = 1555mm, λ=2.73										
Side	A	-A	B	-B	C	-C	D	-D	Mean	SD
P_{Exp}	25.9	25.8	26.9	26.7	26.0	25.6	26.7	26.9	26.3	0.53
$P_{S.well}$	27.9	28.0	27.3	27.0	27.9	27.8	26.8	27.1	27.5	0.48
Column No: 5, 44×44×6.0mm, L_{GRP} = 1500mm, L_{eff} = 1555mm, λ=2.73										
Side	A	-A	B	-B	C	-C	D	-D	Mean	SD
P_{Exp}	25.4	25.3	26.4	26.3	25.0	25.0	26.0	26.3	25.7	0.61
$P_{S.well}$	26.6	26.7	28.0	27.8	26.7	26.7	27.8	27.6	27.2	0.61
Column No: 6, 44×44×6.0mm, L_{GRP} = 1500mm, L_{eff} = 1555mm, λ=2.73										
Side	A	-A	B	-B	C	-C	D	-D	Mean	SD
P_{Exp}	25.4	25.7	27.0	26.8	25.2	25.2	26.8	27.0	26.14	0.83
$P_{S.well}$	26.7	26.7	27.9	27.9	26.5	26.5	28.2	27.9	27.3	0.74

Table 4.1 Experimental buckling Loads of slender columns (continued)

Column No: 1, 51×51×3.2mm, L_{GRP} = 1000mm, L_{eff} = 1055mm, λ = 1.38										
Side	A	-A	B	-B	C	-C	D	-D	Mean	SD
P_{Exp}	54.0	53.8	54.4	57.0	53.8	54.3	56.7	56.8	55.1	1.45
$P_{S.well}$	58.1	57.5	59.9	60.2	57.1	57.1	60.6	61.0	59.0	1.64
Column No: 2, 51×51×3.2mm, L_{GRP} = 1000mm, L_{eff} = 1055mm, λ = 1.38										
Side	A	-A	B	-B	C	-C	D	-D	Mean	SD
P_{Exp}	51.8	53.8	53.8	56.4	54.7	54.2	56.6	56.6	54.8	1.70
$P_{S.well}$	57.5	57.1	59.5	60.0	57.1	56.8	59.9	59.9	58.6	1.55
Column No: 3, 51×51×3.2mm, L_{GRP} = 1000mm, L_{eff} = 1055mm, λ = 1.38										
Side	A	-A	B	-B	C	-C	D	-D	Mean	SD
P_{Exp}	56.2	56.6	54.9	54.3	56.8	57.3	54.8	55.0	55.7	1.11
$P_{S.well}$	59.9	59.9	60.6	60.6	57.4	58.1	60.7	60.1	59.7	1.22
Column No: 4, 44×44×6.0 mm, L_{GRP} = 1000mm, L_{eff} = 1055mm, λ = 1.85										
Side	A	-A	B	-B	C	-C	D	-D	Mean	SD
P_{Exp}	55.3	55.9	58.3	55.6	55.7	55.3	57.6	58.8	56.6	1.43
$P_{S.well}$	57.8	59.5	58.8	58.5	61.0	59.2	58.8	59.5	59.1	0.93
Column No: 5, 44×44×6.0mm, L_{GRP} = 1000mm, L_{eff} = 1055mm, λ = 1.85										
Side	A	-A	B	-B	C	-C	D	-D	Mean	SD
P_{Exp}	56.1	56.3	59.0	58.5	56.8	56.3	56.3	56.4	56.7	1.14
$P_{S.well}$	59.2	59.9	60.2	59.5	60.6	60.6	58.2	58.5	59.6	0.92
Column No: 6, 44×44×6.0mm, L_{GRP} = 1000mm, L_{eff} = 1055mm, λ = 1.85										
Side	A	-A	B	-B	C	-C	D	-D	Mean	SD
P_{Exp}	55.5	55.1	51.0	51.5	54.5	52.4	52.8	51.1	53.0	1.81
$P_{S.well}$	58.6	58.5	59.2	59.6	58.2	57.5	60.9	60.2	59.1	1.13

Table 4.1 Experimental buckling Loads of slender columns (continued)

Column No: 1, 44×44×6.0 mm, L_{GRP} = 750mm, L_{eff} = 805mm, λ = 1.42										
Side	A	-A	B	-B	C	-C	D	-D	Mean	SD
P_{Exp}	87.9	86.9	85.0	85.1	86.7	87.2	84.2	84.4	85.9	1.41
$P_{S.well}$	96.2	95.0	99.0	97.1	99.0	95.2	104	103	98.6	3.46
Column No:2, 44×44×6.0mm, L_{GRP} = 750mm, L_{eff} = 805mm, λ = 1.42										
Side	A	-A	B	-B	C	-C	D	-D	Mean	SD
P_{Exp}	76.0	80.8	81.5	81.4	82.9	80.2	81.2	80.7	80.6	2.0
$P_{S.well}$	96.2	97.1	93.5	94.3	101	100	98.0	99.0	97.4	2.66
Column No: 3, 44×44×6.0mm, L_{GRP} = 750mm, L_{eff} = 805mm, λ = 1.42										
Side	A	-A	B	-B	C	-C	D	-D	Mean	SD
P_{Exp}	81.5	81.2	89.1	82.2	80.0	81.3	81.4	81.1	82.2	2.82
$P_{S.well}$	98.0	98.0	96.2	96.2	106	102	98.0	99.0	99.2	3.43

Table 4.2 Short Column Failure loads for box-sections

Specimen section (mm)	Specimen Length		Specimen No:			Mean (kN)	SD (kN)
	L_{GRP} (mm)	L_{eff} (mm)	1	2	3		
51×51×3.2	500	555	118	115	110	114	4.2
	400	455	120	111	120	117	5.2
	300	355	114	118	122	118	4.0
	200	255	123	118	121	121	2.1
44×44×6.0	400	455	202	220	203	208	10.2
	300	355	221	223	210	218	6.6
	200	255	226	216	219	220	5.3

Table 4.3 Mode-interaction in intermediate column heights

Specimen section (mm)	Specimen Length		Specimen No:			Mean (kN)	SD (kN)
	L_{GRP} (mm)	L_{eff} (mm)	1	2	3		
51×51×3.2	750	805	96.2	99.0	96.2	97.1	1.7
44×44×6.0	500	555	196	192	196	195	2.2

Table 4.4 Comparison of experimental and theoretical results (long columns)

Column Section and Properties	Length of Specimen		$P_{S.well}$[‡‡] (kN)	$P_{E.sh} = P_{EDC}$ (kN)		$P_{Strongwell}$ $E_{L.c}$ Fibreforce (kN)
	L_{GRP} (mm)	L_{eff} (mm)		$E_{L.c}$ Measured	$E_{L.c}$ Fibreforce	
51×51×3.2 mm $A_{ave} = 628.mm^2$ $I_{ave} = 238000mm^4$	2000	2055	15.7	16.7	9.5	32.5
	1500	1555	27.6	28.8	16.5	46.8
	1000	1055	59.1	61.0	35.9	77.4
	750	805	97.1	101	61.7	110
44×44×6.0 mm $A_{ave} = 882mm^2$ $I_{ave} = 217000mm^4$	2000	2055	15.6	16.6	8.6	34.5
	1500	1555	27.3	28.7	15.1	49.5
	1000	1055	59.3	61.2	32.7	82.0
	750	805	98.4	102	56.2	117
	500	555	195	202	118	189

Table 4.5 Comparison of experimental and theoretical Results (short columns)

Column Section and Properties	Length of Specimen		$P_{L(Exp)}$‡‡ (kN)	Classical Ortho-tropic plate[§§] P_L (kN)	P_{EDC} (kN)		$P_{Strongwell}$ (kN)
	L_{GRP} (mm)	L_{eff} (mm)			$E_{L.c}$ Meas-ured	$E_{L.c}$ Fibre-force	$E_{L.c}$ Fibre-force
51×51×3.2 mm $A_{ave} = 628mm^2$ $I_{ave} =$ $238000mm^4$	500	555	114	80.3 to 252	126 (242)	88.0 (130)	67.8
	400	455	117				
	300	355	118				
	200	255	121				
44×44×6.0 mm $A_{ave} = 882mm^2$ $I_{ave} =$ $217000mm^4$	400	455	208	705 to 2181	1111 (461)	706 (185)	197
	300	355	218				
	200	255	220				

‡‡ Average of several tests

§§ Minimum and maximum buckling loads corresponding to simply supported and fixed long edge supports

Table 4.6 Design parameters for 51×51×3.2mm box-section

L_{eff} (mm)	$\lambda = \frac{L}{\pi}\sqrt{\frac{P_L}{EI}}$	$P_{E.sh}$ (kN)	P_{Exp} (kN)	$q = \frac{P_{Exp}}{P_L}$	$s = \frac{P_{Exp}}{P_E}$	$c = \frac{q+s-1}{qs}$	ki	P_c (kN) $= k_i P_L$
255	0.33	582	123	1.02	0.21	1.08	0.99	119
255	0.33	582	118	0.99	0.20	0.94	0.99	119
255	0.33	582	121	1.01	0.21	1.03	0.99	119
355	0.46	389	114	0.95	0.29	0.87	0.98	117
355	0.46	389	118	0.99	0.30	0.97	0.98	117
355	0.46	389	122	1.01	0.31	1.03	0.98	117
455	0.60	270	120	1.00	0.45	1.00	0.96	115
455	0.60	270	111	0.92	0.41	0.88	0.96	115
455	0.60	270	120	1.00	0.44	1.00	0.96	115
555	0.73	195	118	0.99	0.61	0.99	0.92	111
555	0.73	195	115	0.96	0.59	0.97	0.92	111
555	0.73	195	110	0.92	0.56	0.93	0.92	111
805	1.05	101	96.2	0.80	0.95	0.99	0.73	88.2
805	1.05	101	99.0	0.83	0.98	1.00	0.73	88.2
805	1.05	101	96.2	0.80	0.95	0.99	0.73	88.2
1055	1.38	61	59.0	0.49	0.97	0.96	0.49	59.0
1055	1.38	61	58.6	0.49	0.96	0.96	0.49	59.0
1055	1.38	61	59.7	0.50	0.98	0.98	0.49	59.0
1555	2.03	28.8	27.7	0.23	0.96	0.86	0.24	28.7
1555	2.03	28.8	27.6	0.23	0.96	0.86	0.24	28.7
1555	2.03	28.8	27.5	0.23	0.95	0.84	0.24	28.7
2055	2.69	16.7	15.5	0.13	0.93	0.50	0.14	16.7
2055	2.69	16.7	15.6	0.13	0.92	0.52	0.14	16.7
2055	2.69	16. 7	15.9	0.13	0.94	0.67	0.14	16.7

Table 4.7 design parameters for 44×44×6mm box-section

L_{eff} (mm)	$\lambda = \frac{L}{\pi}\sqrt{\frac{P_L}{EI}}$	$P_{E.sh}$ (kN)	P_{Exp} (kN)	$q = \frac{P_{Exp}}{P_L}$	$s = \frac{P_{Exp}}{P_E}$	$c = \frac{q+s-1}{qs}$	k_i	P_c (kN) $= k_i P_L$
255	0.45	672.28	226	1.03	0.34	1.06	0.99	217
255	0.45	672.28	216	0.98	0.32	0.96	0.99	217
255	0.45	672.28	219	0.99	0.33	0.99	0.99	217
355	0.62	426.60	221	1.00	0.52	1.00	0.97	214
355	0.62	426.60	223	1.01	0.52	1.01	0.97	214
355	0.62	426.60	210	0.96	0.49	0.95	0.97	214
455	0.80	287.22	202	0.92	0.70	0.96	0.93	205
455	0.80	287.22	220	1.00	0.77	1.00	0.93	205
455	0.80	287.22	203	0.92	0.71	0.97	0.93	205
555	0.98	204.08	196	0.89	0.96	1.00	0.83	183
555	0.98	204.08	192	0.87	0.94	0.99	0.83	183
555	0.98	204.08	196	0.89	0.96	1.00	0.83	183
805	1.42	103.36	98.6	0.45	0.95	0.94	0.47	104
805	1.42	103.36	97.4	0.44	0.94	0.92	0.47	104
805	1.42	103.36	99.2	0.45	0.96	0.95	0.47	104
1055	1.85	61.71	59.1	0.27	0.96	0.88	0.29	63.0
1055	1.85	61.71	59.6	0.27	0.97	0.90	0.29	63.0
1055	1.85	61.71	59.1	0.27	0.96	0.88	0.29	63.0
1555	2.73	28.96	27.5	0.12	0.95	0.62	0.13	29.3
1555	2.73	28.96	27.2	0.12	0.94	0.55	0.13	29.3
1555	2.73	28.96	27.3	0.12	0.94	0.57	0.13	29.3
2055	3.61	16.70	15.7	0.07	0.94	0.20	0.08	16.8
2055	3.61	16.70	15.6	0.07	0.94	0.11	0.08	16.8
2055	3.61	16.70	15.7	0.07	0.94	0.17	0.08	16.8

Table 4.8 Percentage loss in buckling resistance due to holes

Column Size & length	Column NO:	d/w	No of holes in one set			
			1 Hole	2 Holes	4 Holes	8 Holes
51×51×3.2mm L = 2000mm	1	0.28	3.1	5.8	7.1	9.1
	2	0.49	4.3	7.3	9.6	16.0
	3	0.69	6.8	9.8	16.1	24.3
51×51×3.2mm L = 1500mm	1	0.28	3.4	5.9	8.2	10.7
	2	0.49	5.5	8.2	11.6	17.5
	3	0.69	8.8	11.3	17.8	30.3
51×51×3.2mm L = 1000mm	1	0.28	3.4	6.6	9.6	11.7
	2	0.49	6.5	9.5	12.3	18.5
	3	0.69	10.2	17.0	20.1	32.2
44×44×6.0mm L = 2000mm	1	0.32	2.1	4.2	5.4	7.5
	2	0.46	3.5	6.8	8.5	12.5
	3	0.57	4.2	10.0	11.7	18.4
44×44×6.0mm L = 1500mm	1	0.32	2.7	4.7	6.8	8.7
	2	0.46	4.12	6.95	8.46	13.8
	3	0.57	5.64	10.2	13.4	19.6
44×44×6.0mm L = 1000mm	1	0.32	2.8	5.3	7.5	10.4
	2	0.46	4.6	6.7	9.5	14.4
	3	0.57	6.2	11.2	14.7	21.1

Plate 4.1 Measurement of initial imperfections.

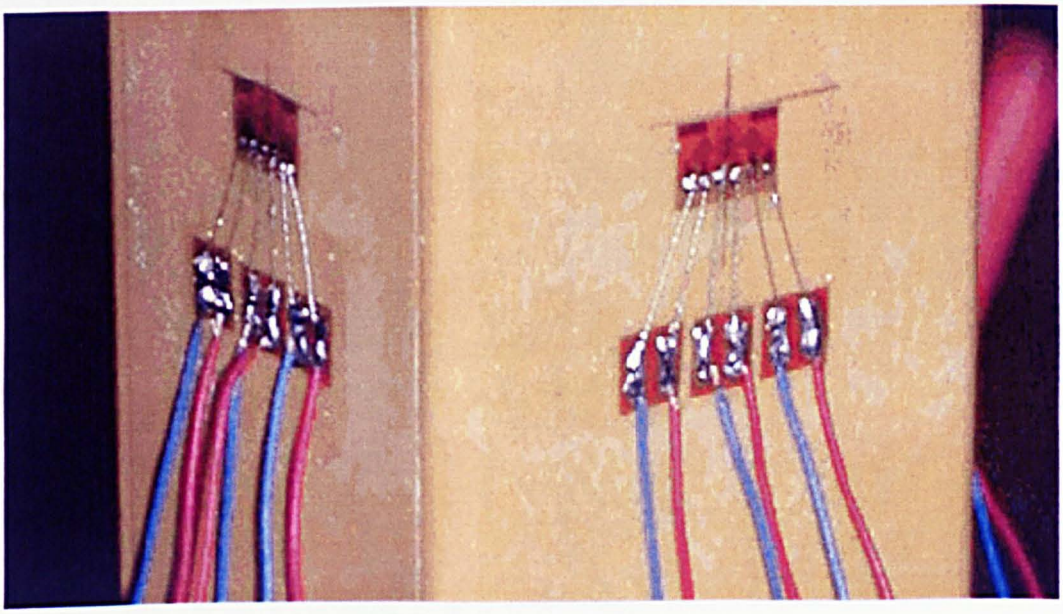

Plate 4.2 Strain rosettes and bondable terminals with wires.

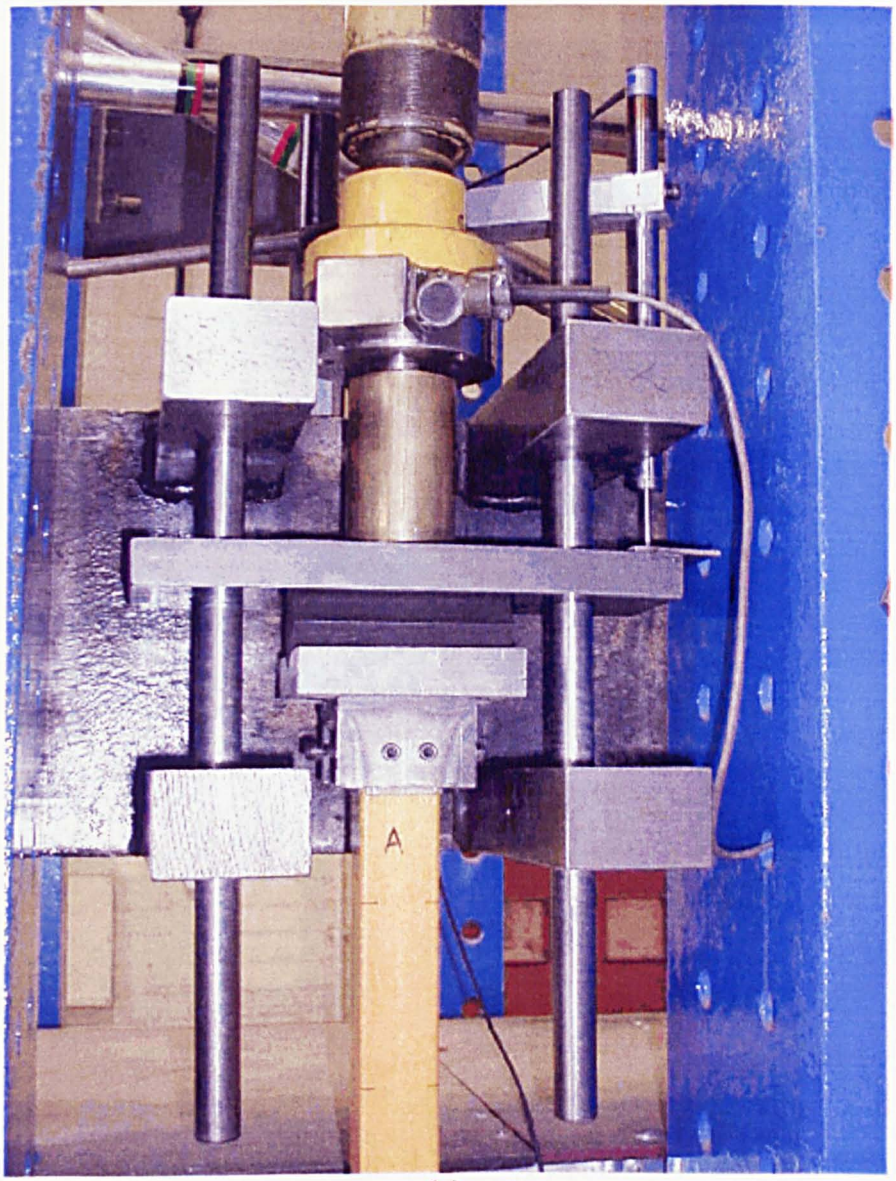

(a)

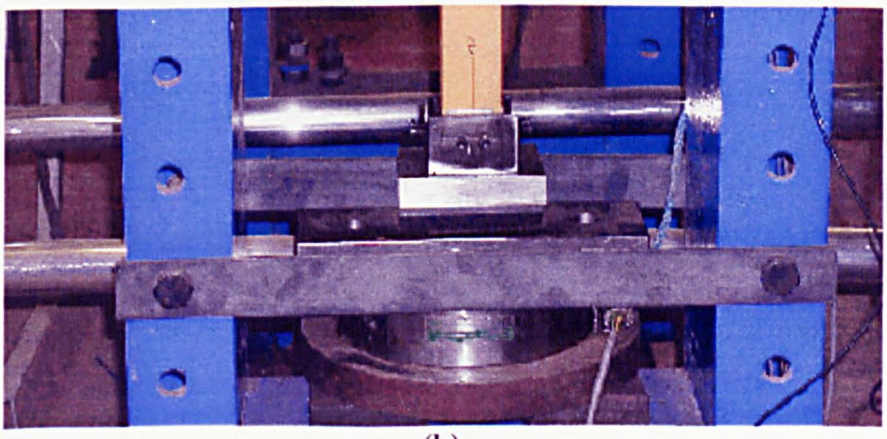

(b)

Plate 4.3 (a) Upper knife-edge, load cell and support assembly and (b) Lower knife-edge, load cell and alignment strip.

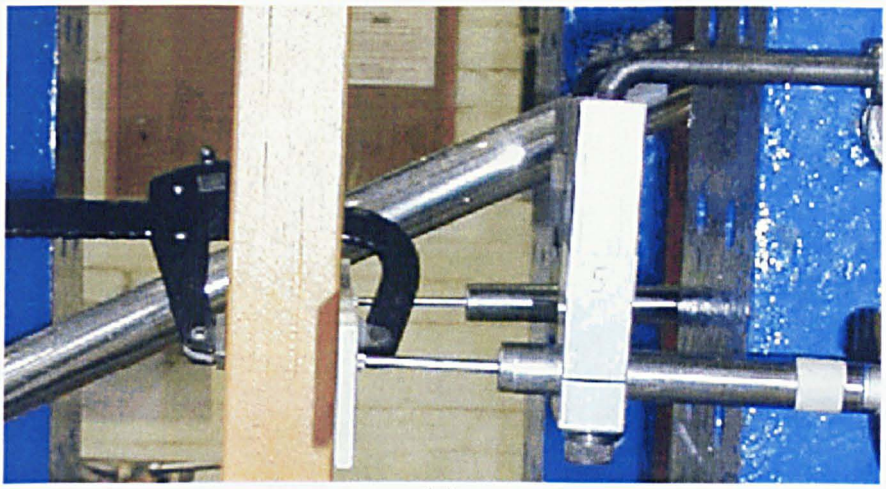

(a)

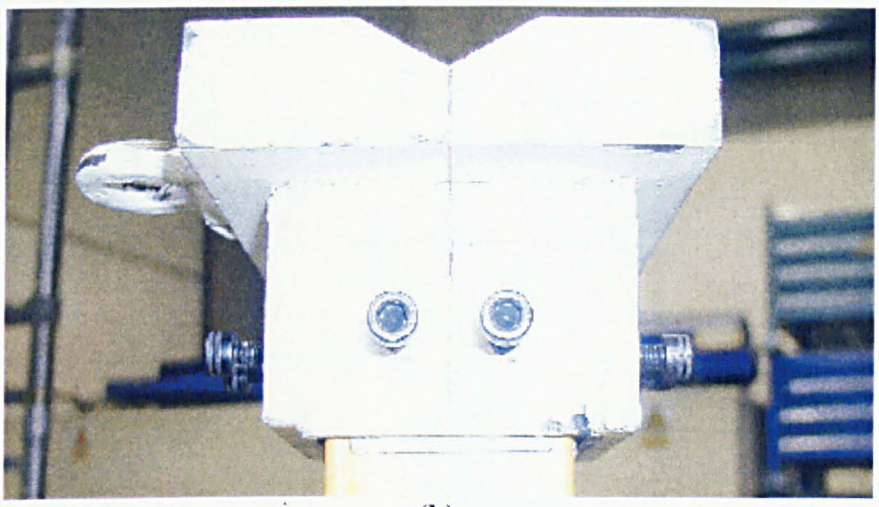

(b)

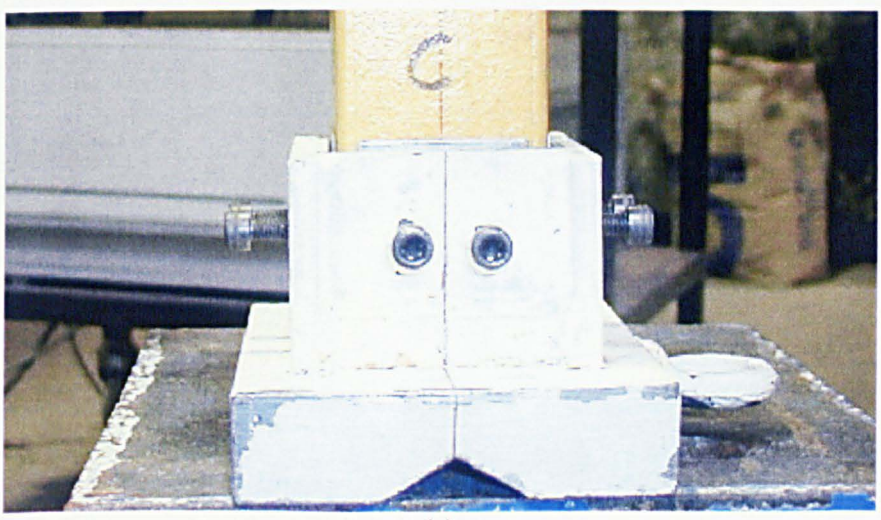

(c)

Plate 4.4 (a) Mid-height rotation check, (b) upper shoe and (c) lower shoe.

Plate 4.5 Test rig and complete set up of axial compression test.

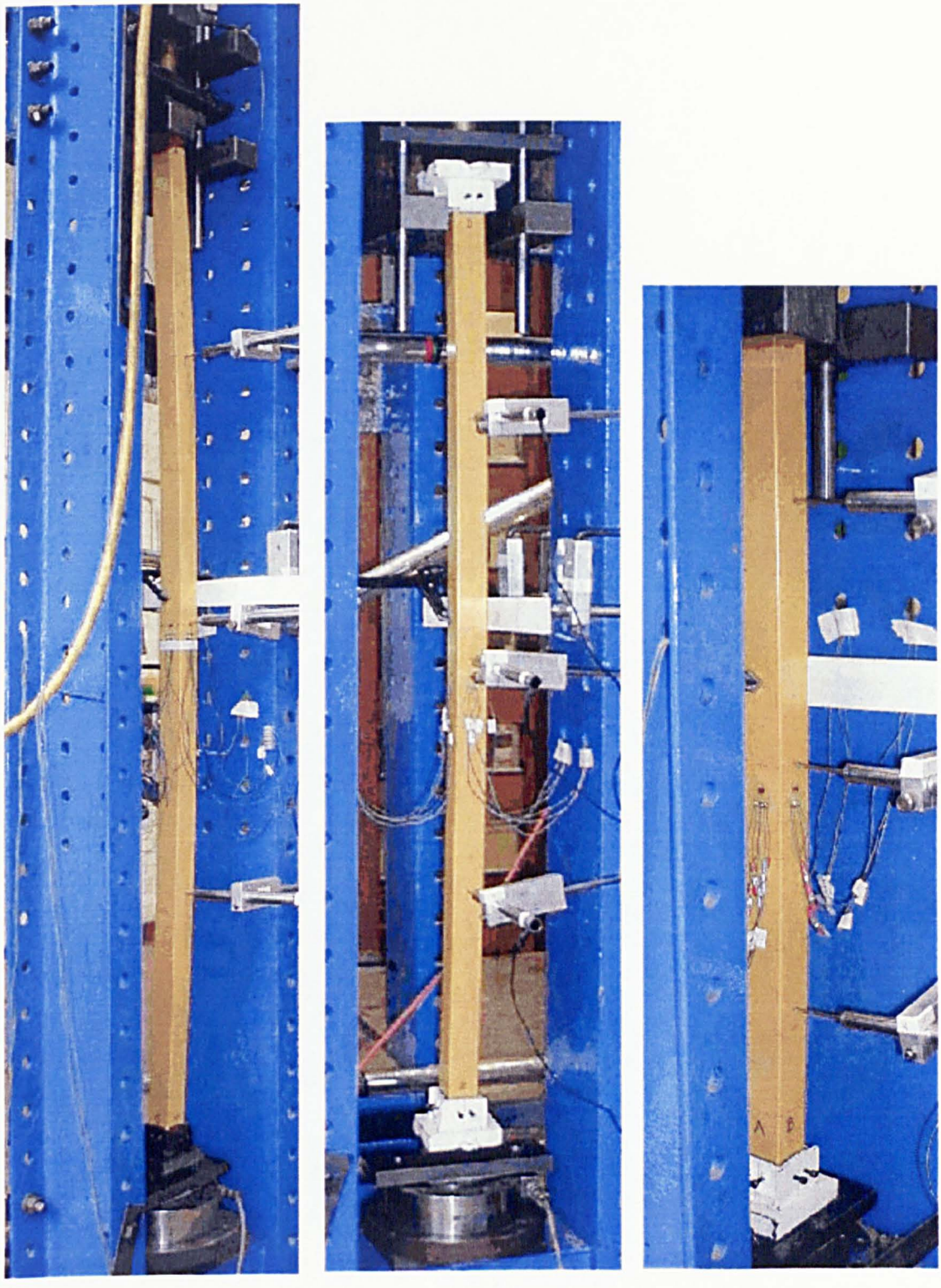

(a) (b) (c)

Plate 4.6 Global buckling in 51mm box-section specimens of height; (a) 2000mm, (b) 1500mm, and (c) 1000mm.

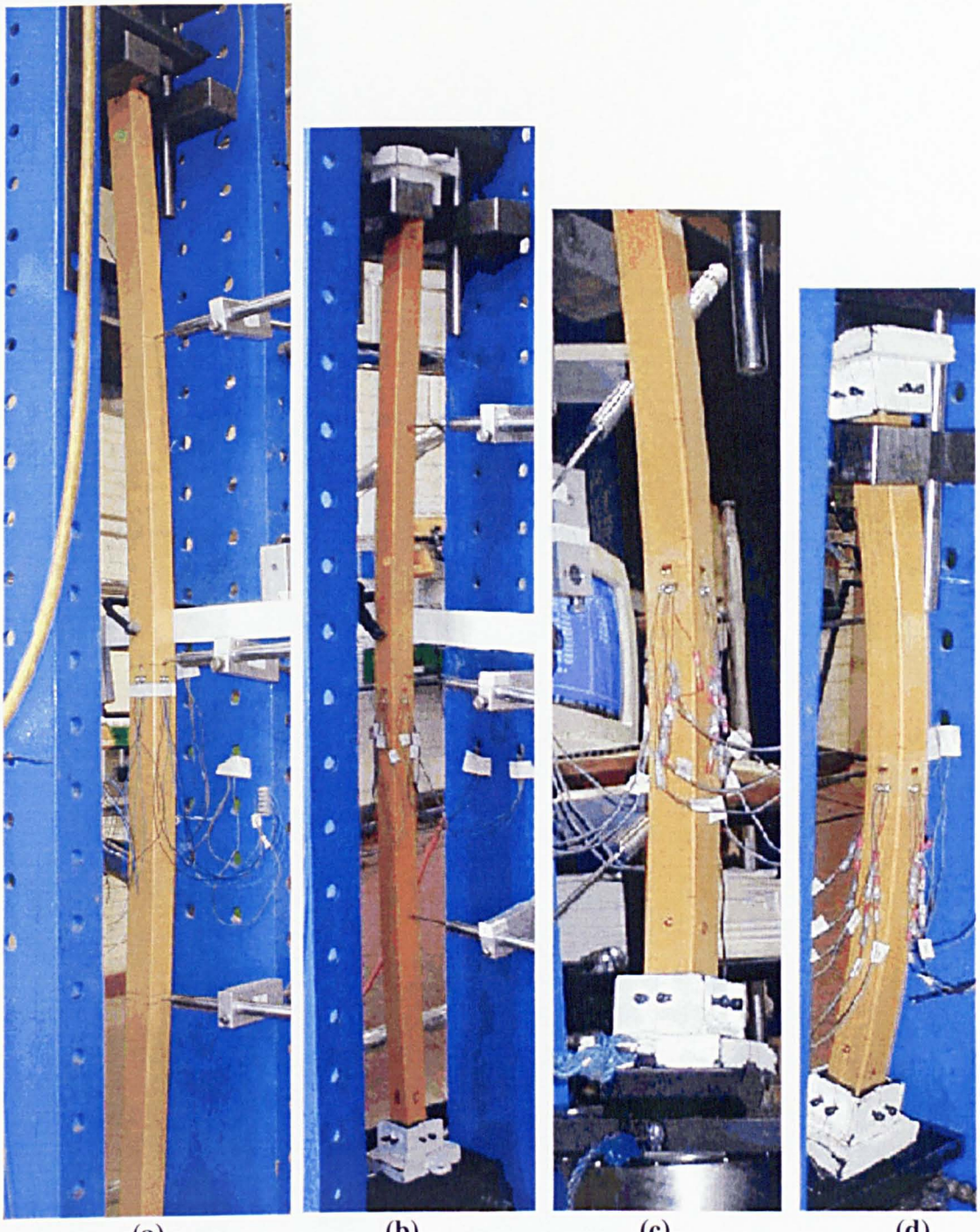

(a) (b) (c) (d)

Plate 4.7 Global buckling in 44mm box-section specimens of height; (a) 2000mm, (b) 1500mm, and (c) 1000mm, and 750mm.

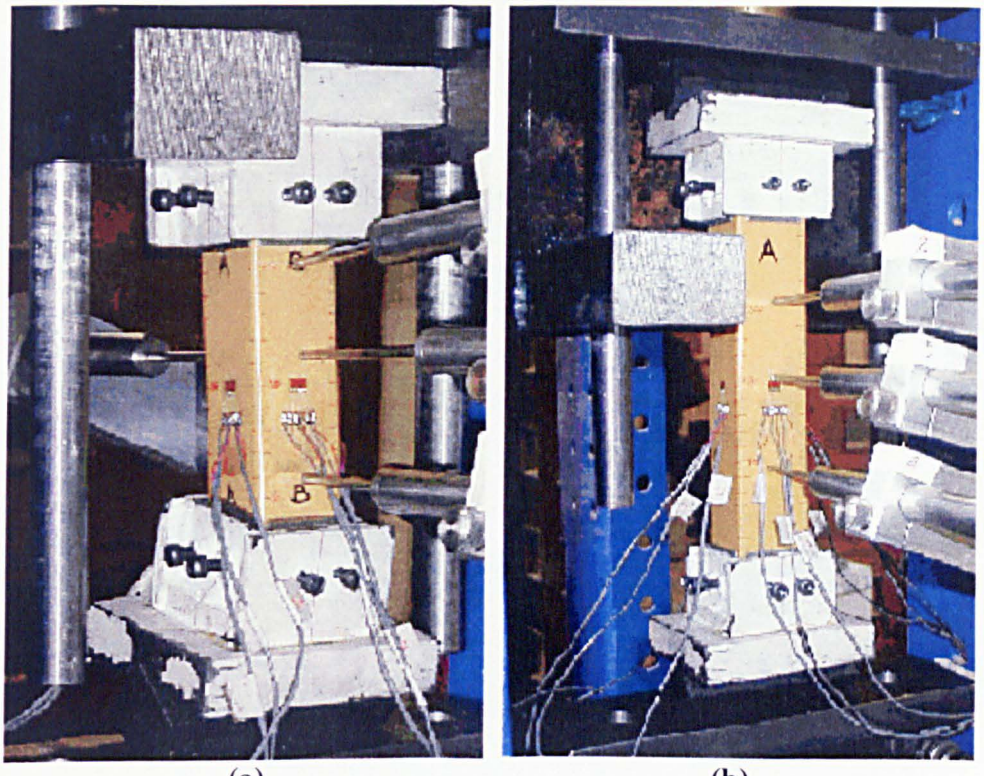

(a) (b)

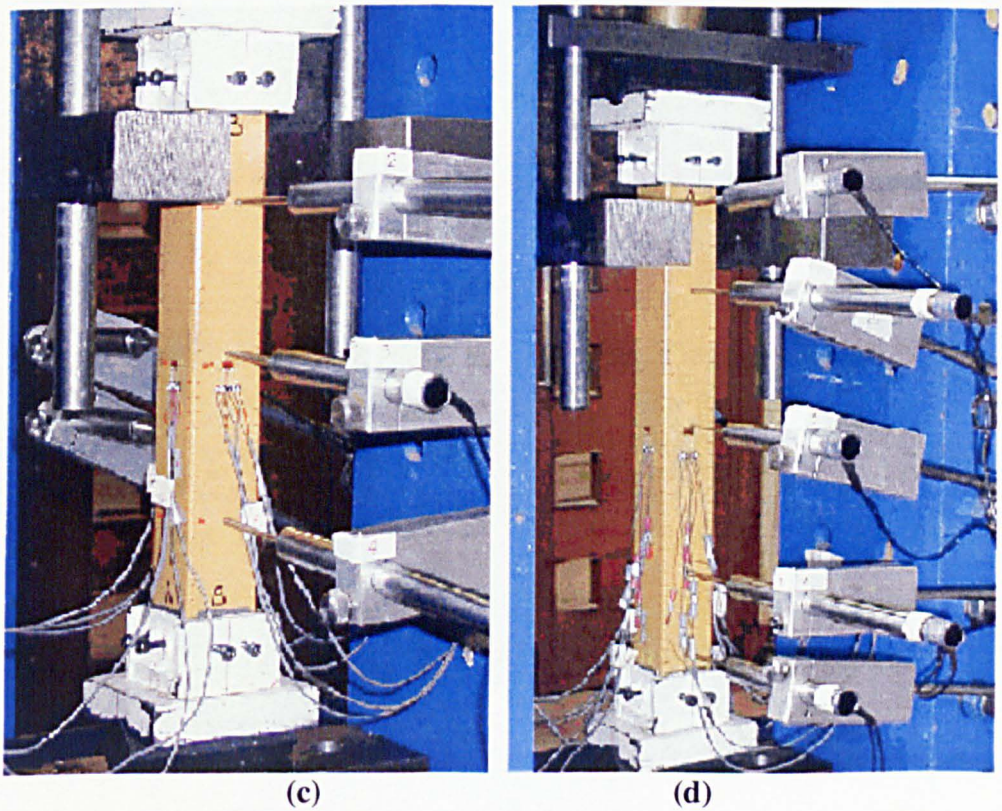

(c) (d)

Plate 4.8 Number and position of LVDTs to measure lateral deflection in short specimens (a) 200mm, (b) 300mm, (c) 400mm and (d) 500mm.

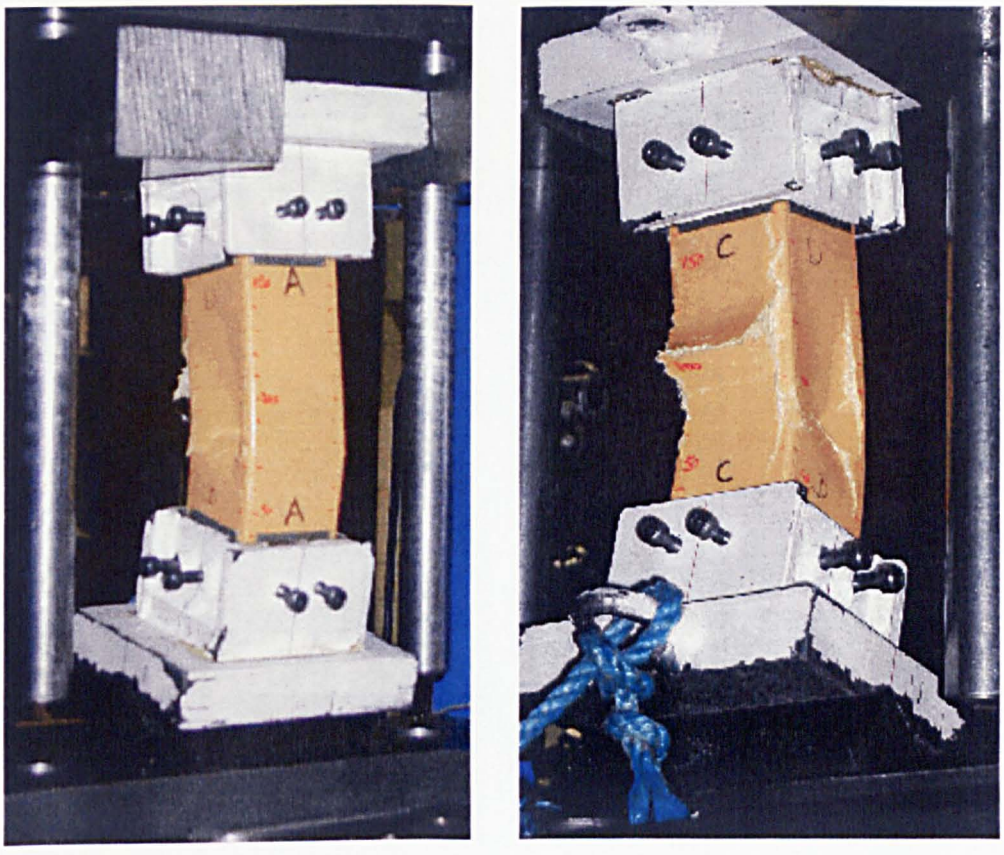

(a) (b)

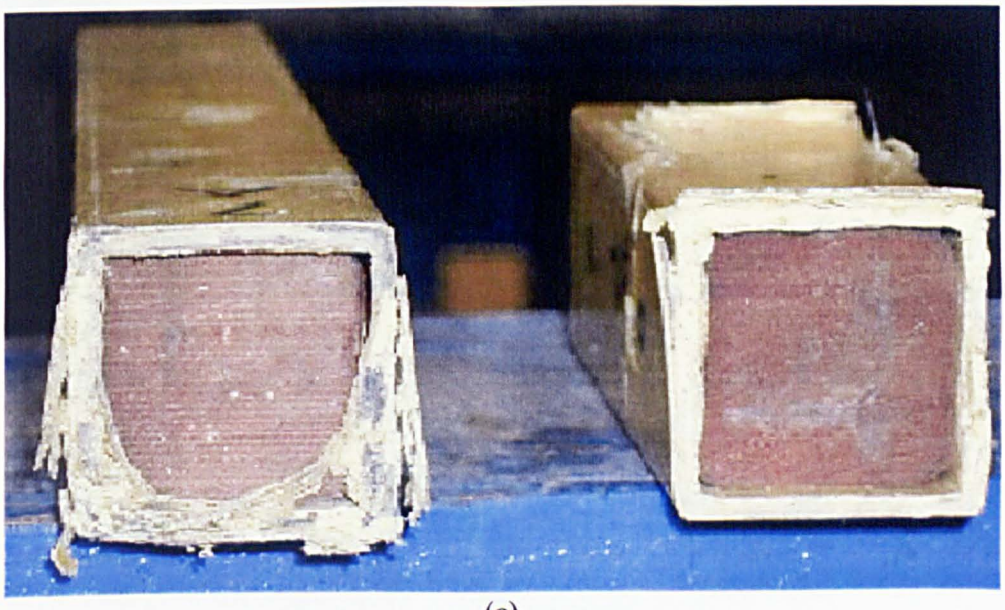

(c)

Plate 4.9 Local buckling of 200mm high, 51mm box-section specimen (a) front web bulging out, orthogonal web moving in; (b) rear (opposite) web bulging out and broken in compression; (c) compression failure at the lower end.

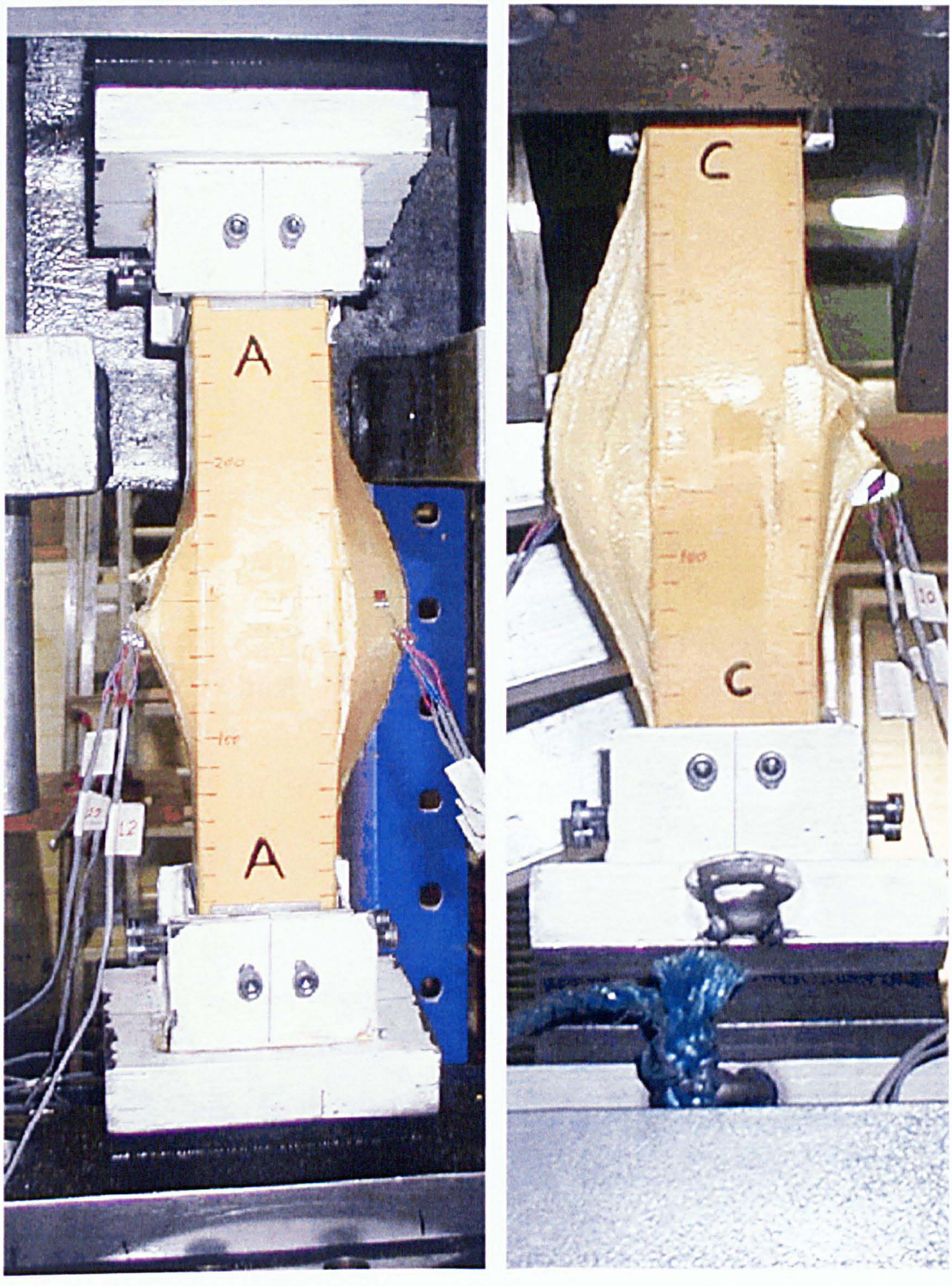

(a) b)

Plate 4.10 Failure mode of 300mm high, 51mm box-section specimen; (a) front view, (b) rear view

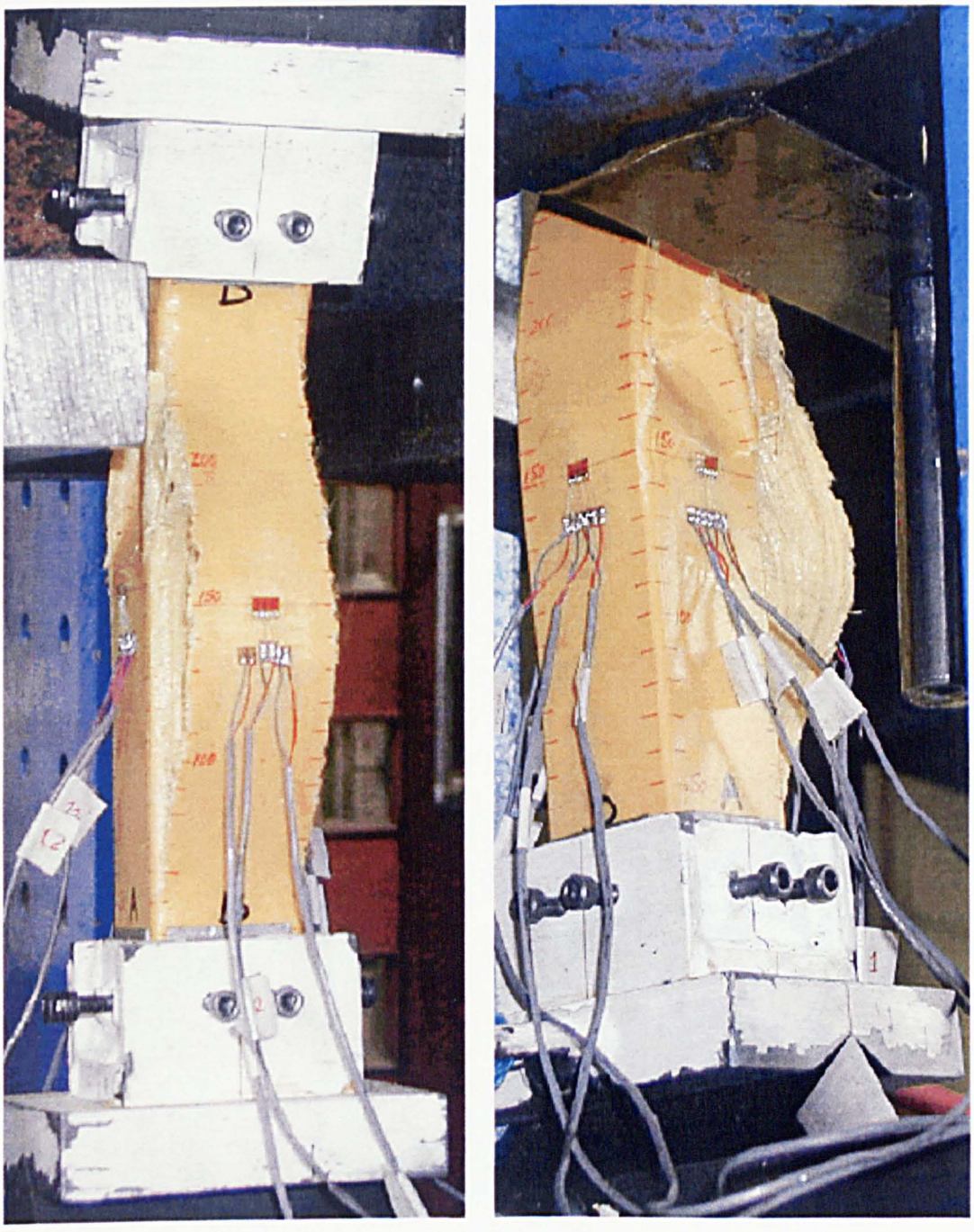

(c) (d)

Plate 4.10 (continued) Failure mode of 300mm high, 51mm box-section specimen; (a) front view, (b) rear view

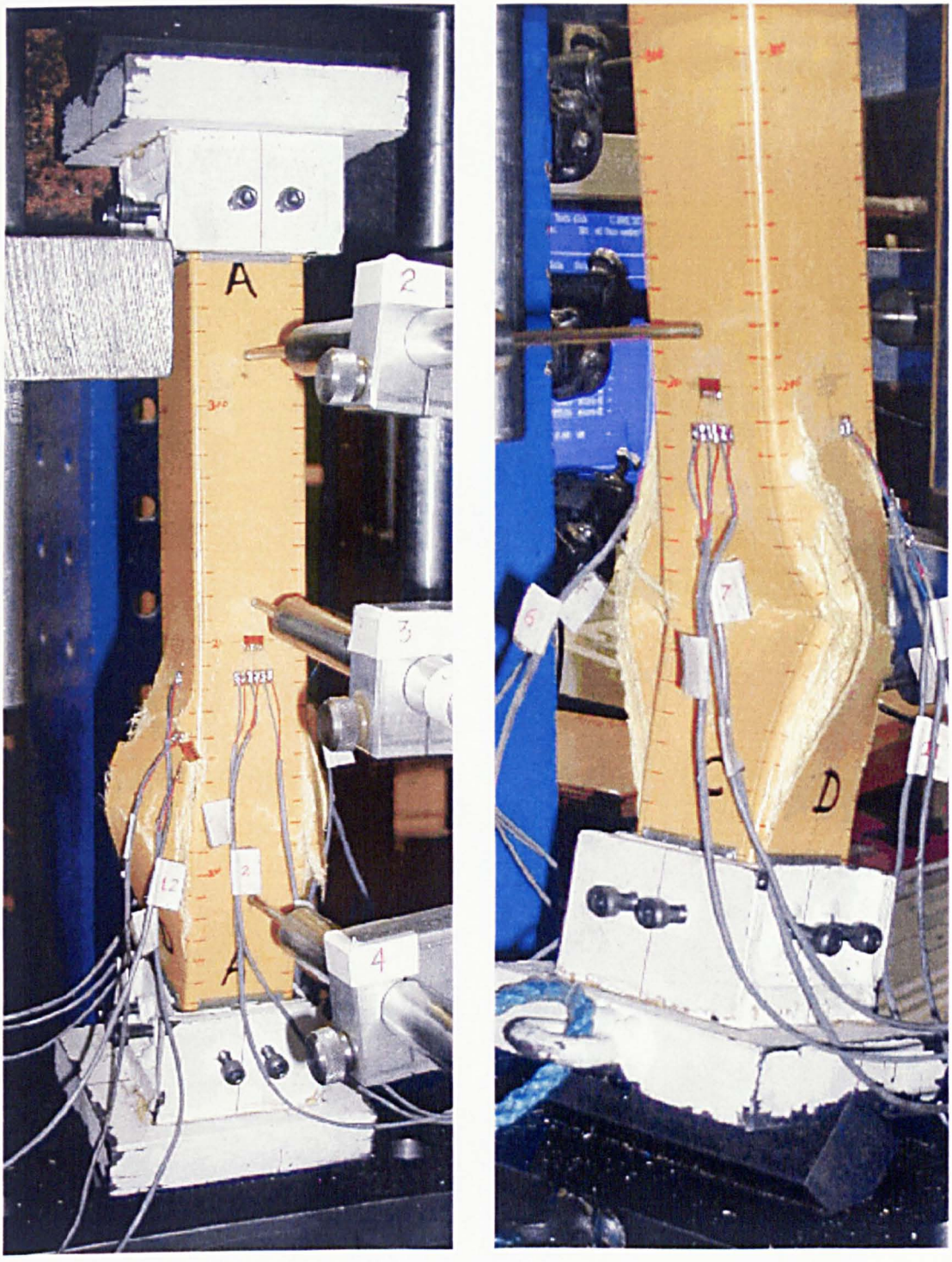

(a) (b)

Plate 4.11 Failure mode of 400mm high, 51mm box-section specimen; (a) front view, (b) rear view

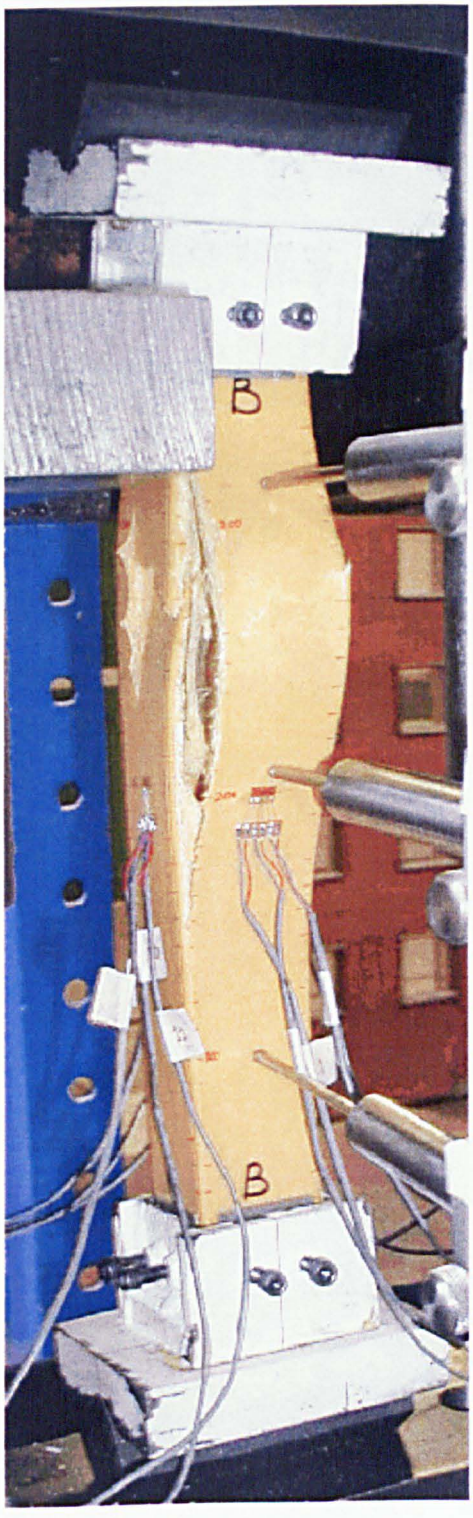

(c)

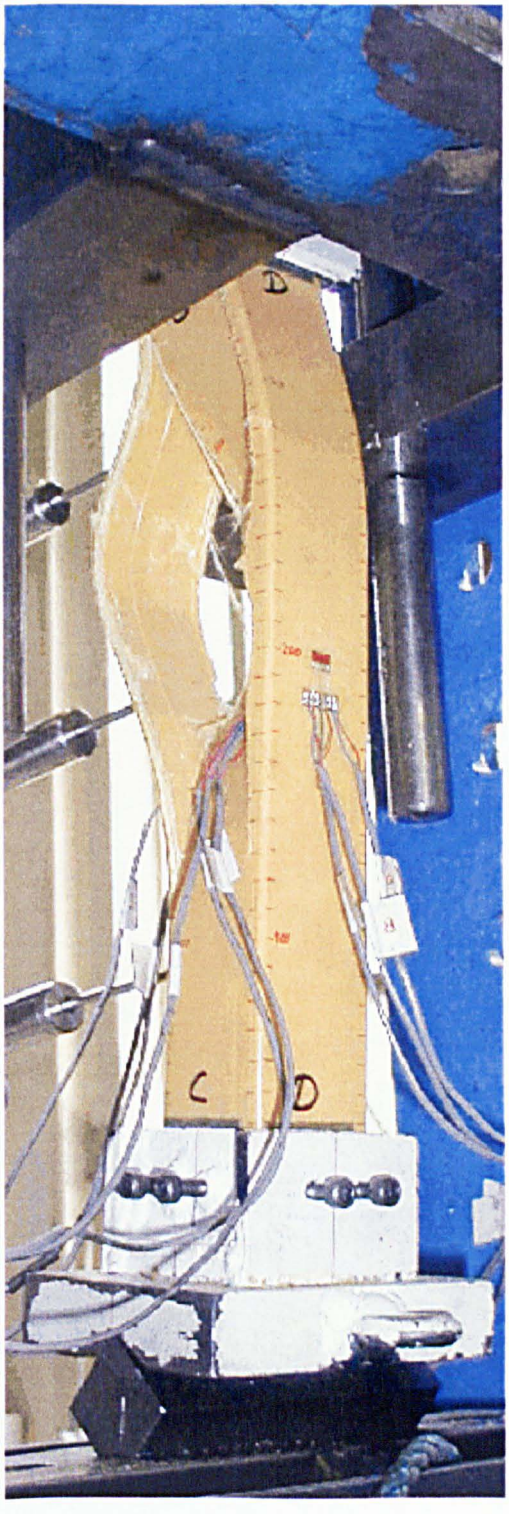

(d)

Plate 4.11 (continued) Failure mode of 400mm high, 51mm box-section specimen; (c) front view, (d) rear view

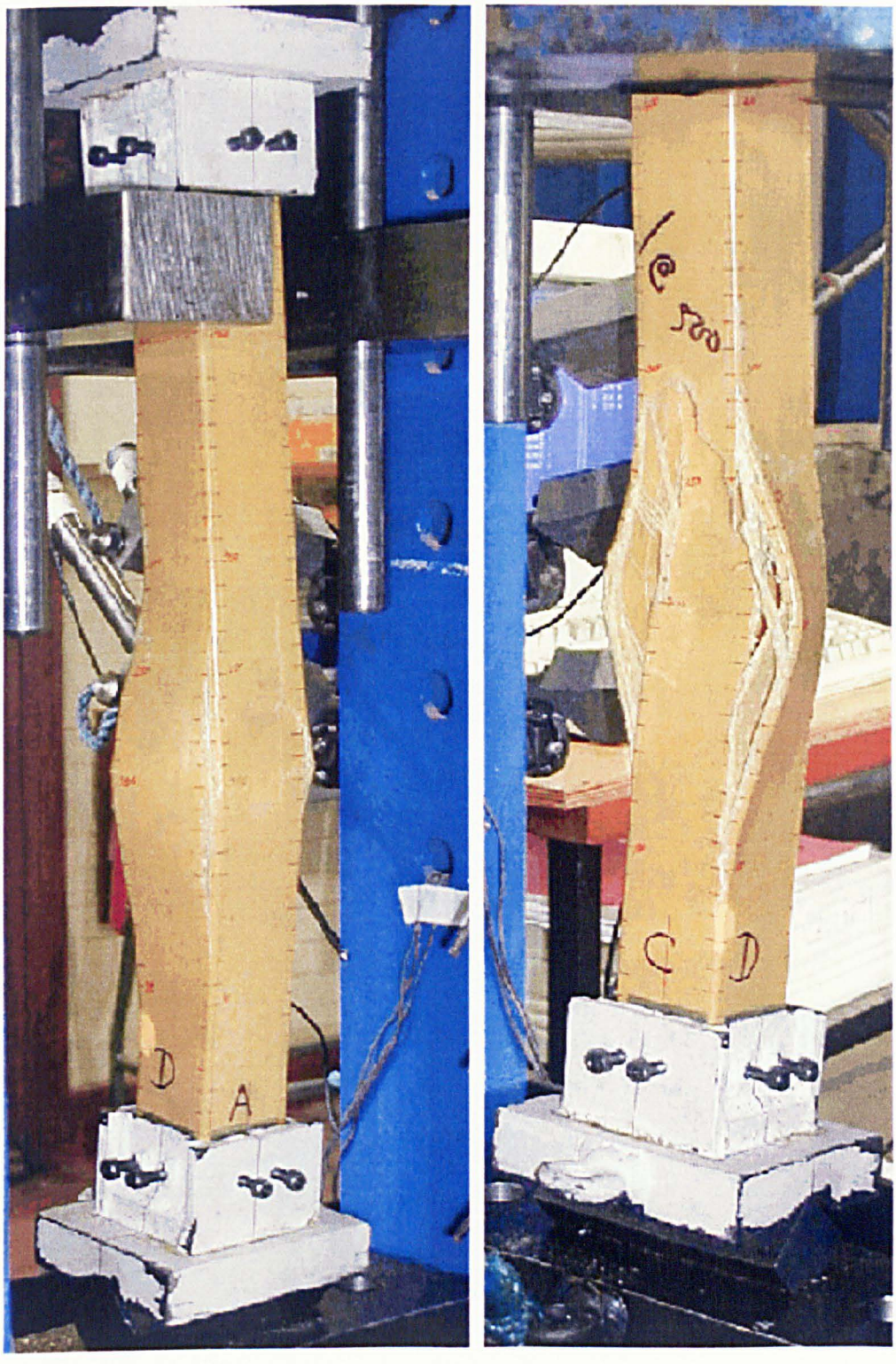

(a) (b)

Plate 4.12 Failure modes of 500mm high 51mm box-section specimen; (a) front and (b) rear view.

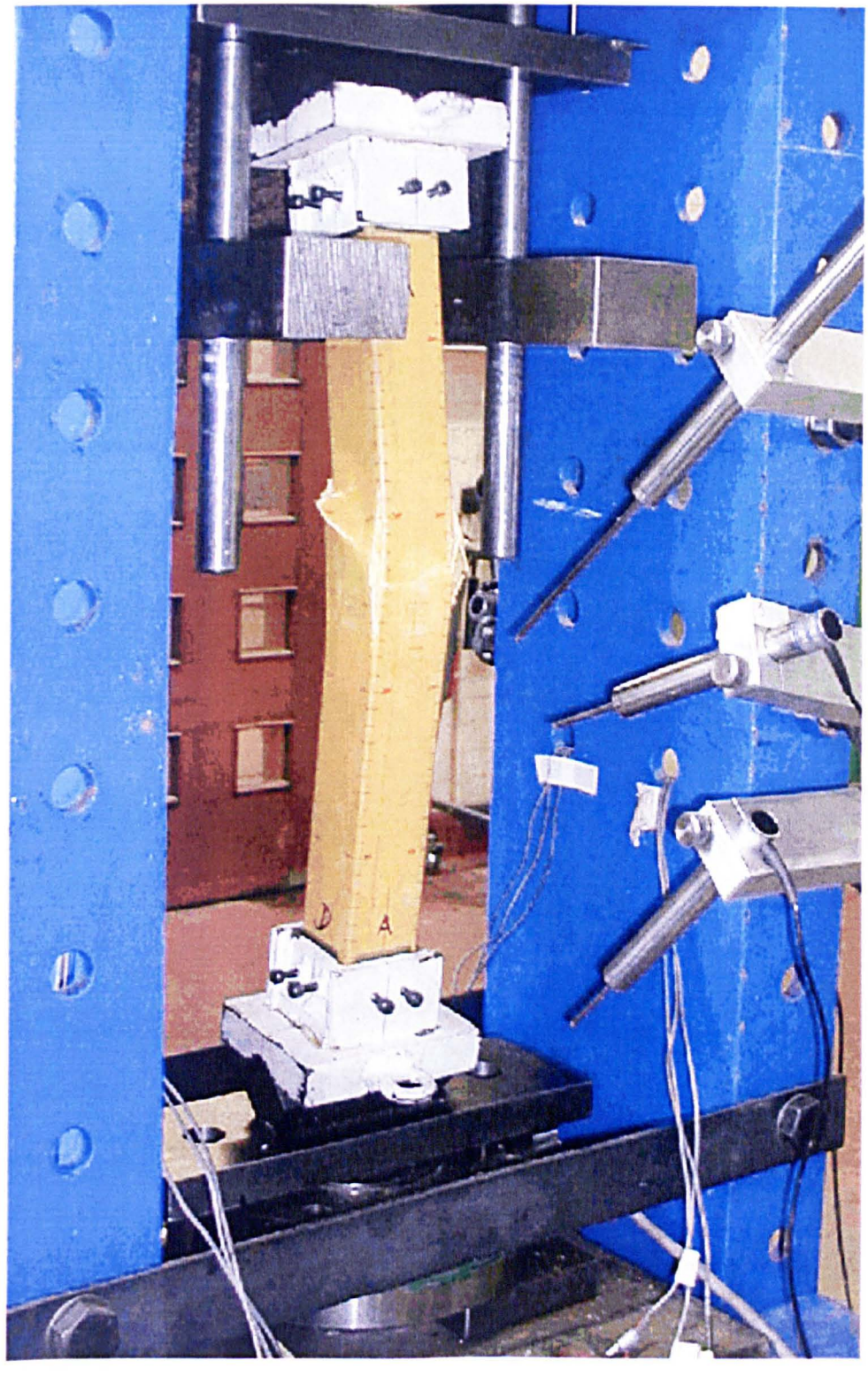

(c)

Plate 4.12 (continued) Failure modes of 500mm high 51mm box-section specimen; (c) front view.

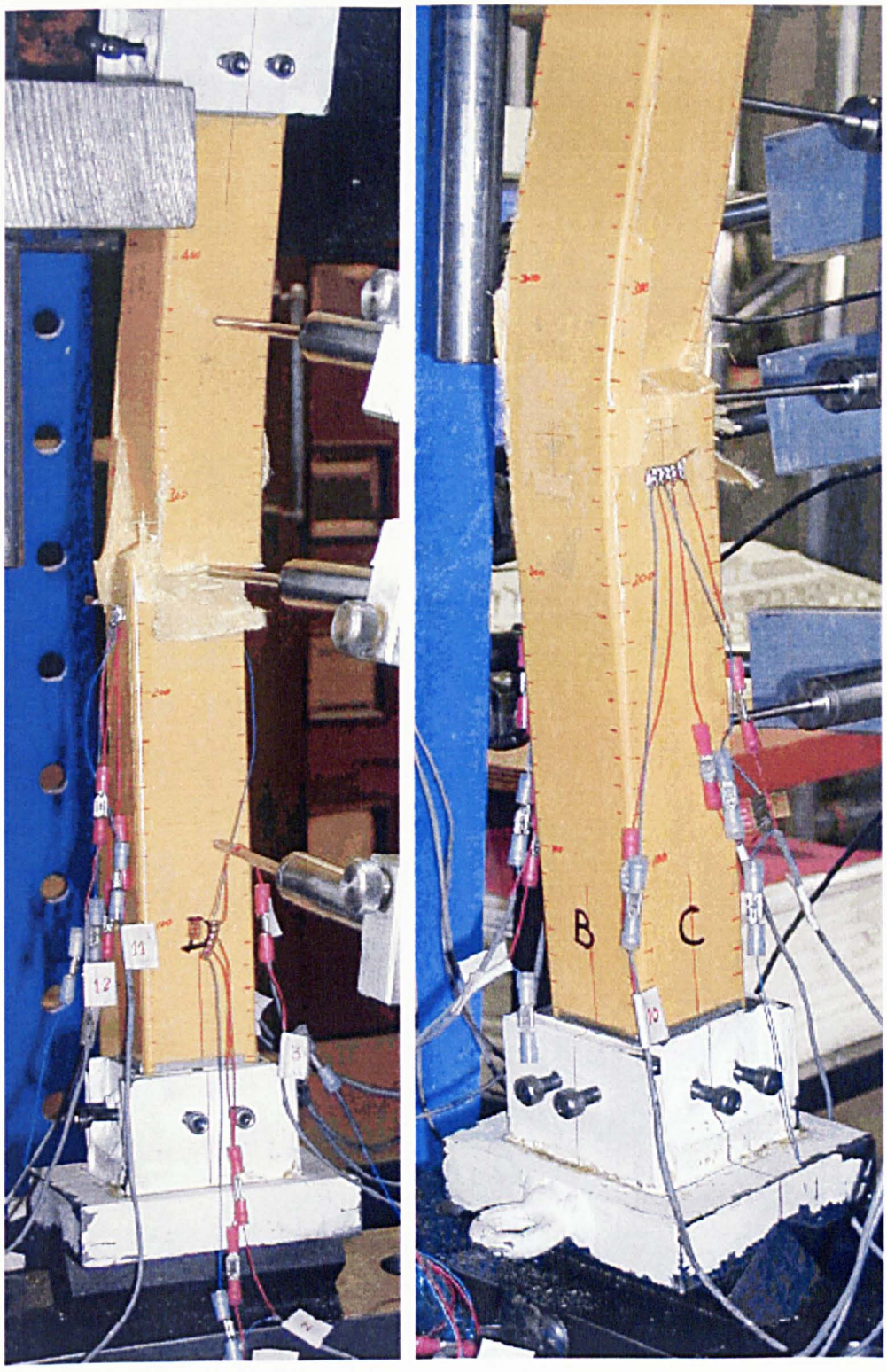

(d) (e)

Plate 4.12 (continued) Failure modes of 500mm high 51mm box-section specimen; (d) front and (e) rear view.

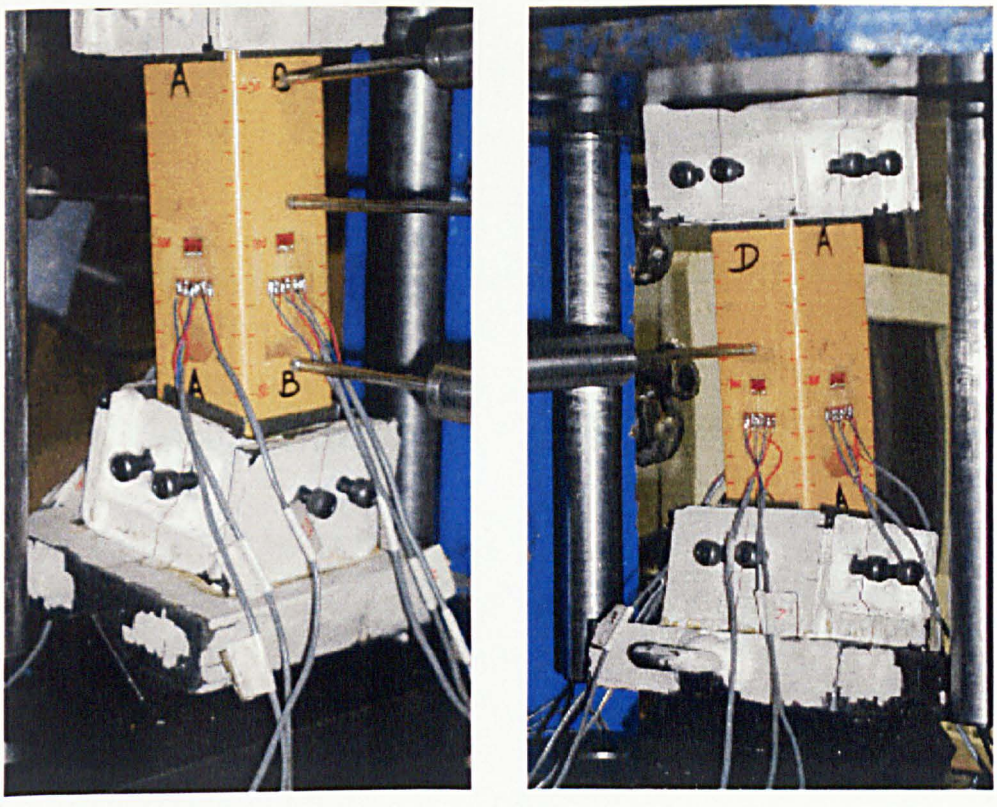

(a) (b)

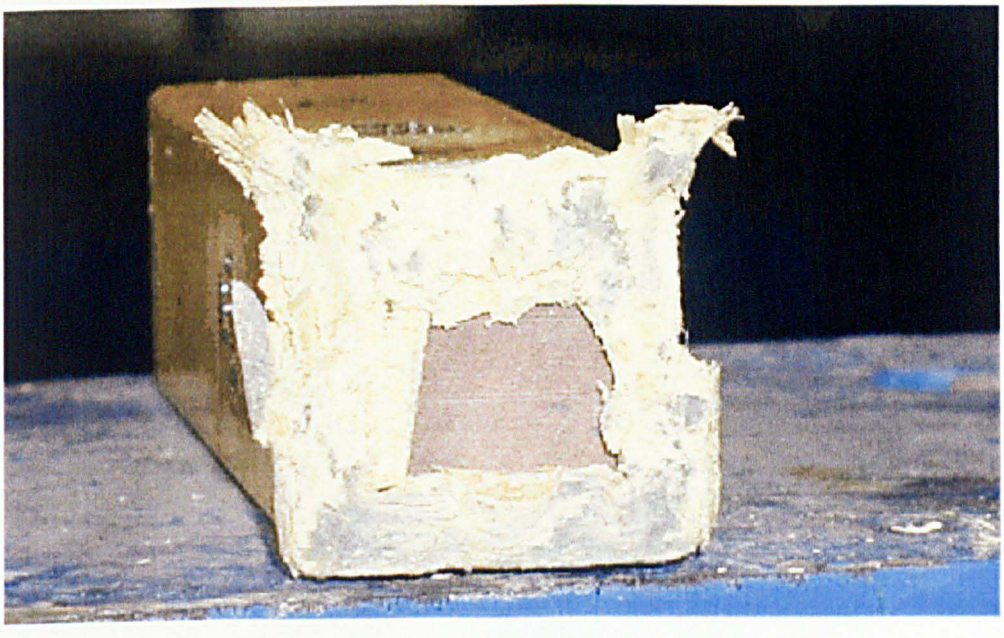

(c)

Plate 4.13 Failure mode of 200mm high 44mm box-section specimen; (a), front view (b), rear view (c) compressive failure at end.

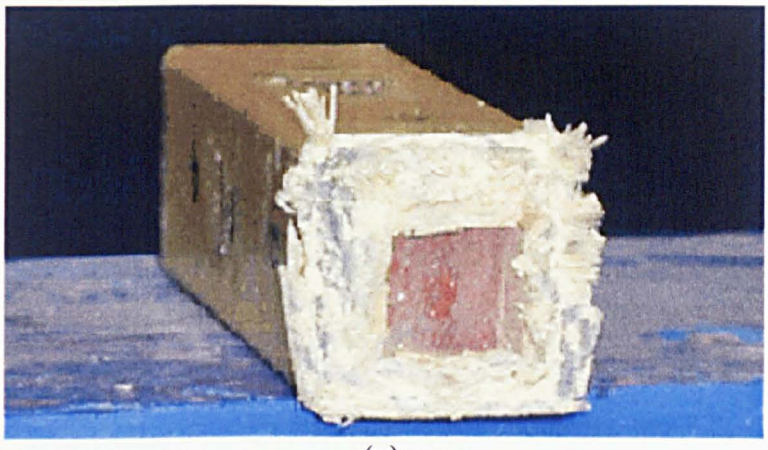

(a)

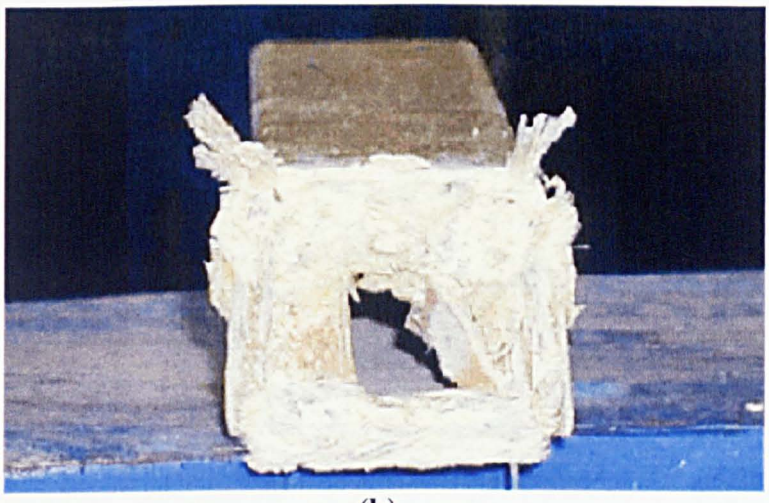

(b)

(c)

Plate 4.14 Material failure mode in (a) 300mm, (b) 400mm and (c) 500mm high, 44mm box-section specimens.

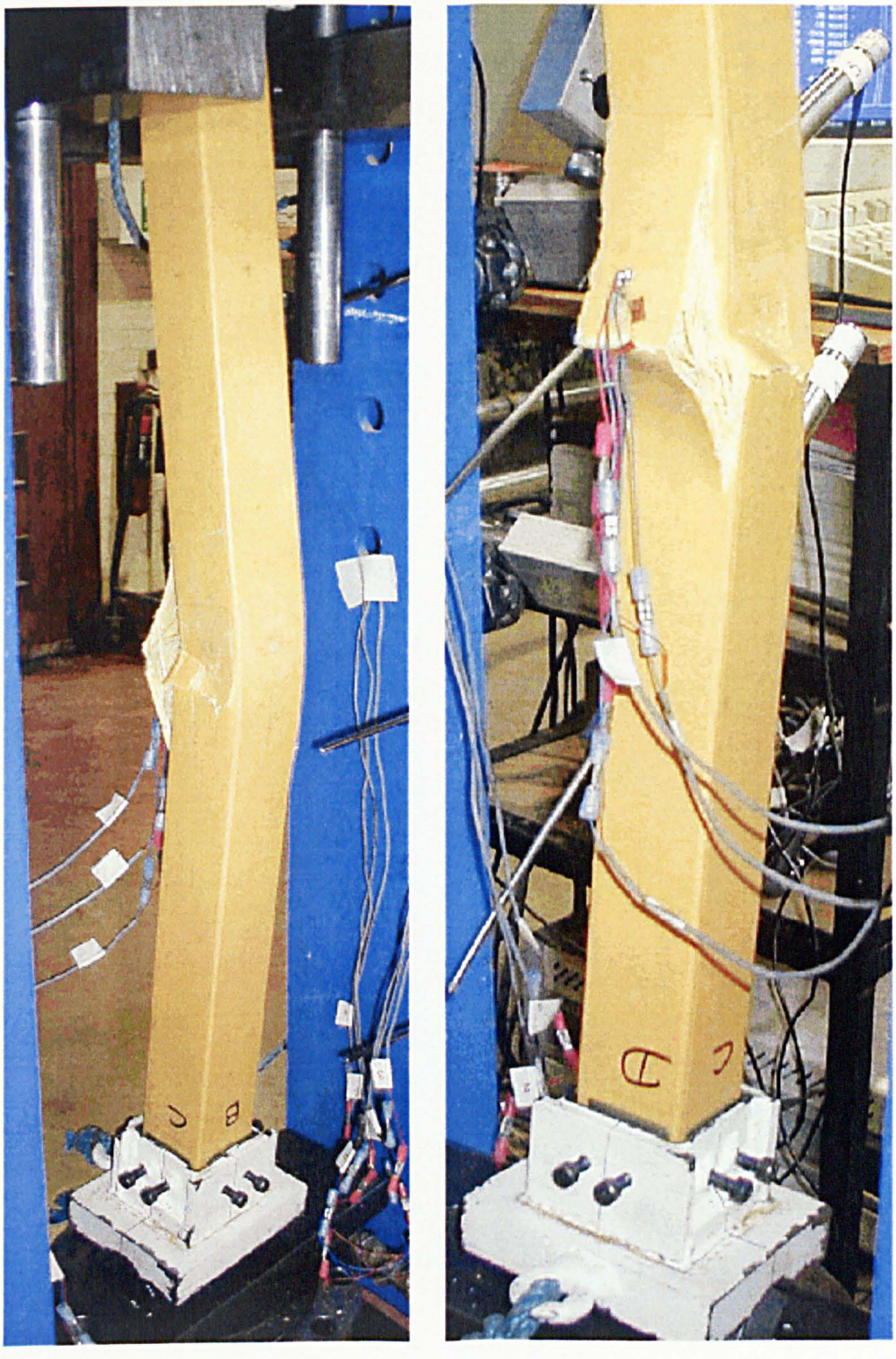

(a) (b)

Plate 4.15 Buckling mode-interaction in 750mm high, 51mm box-section specimen; (a) front and (b) rear view.

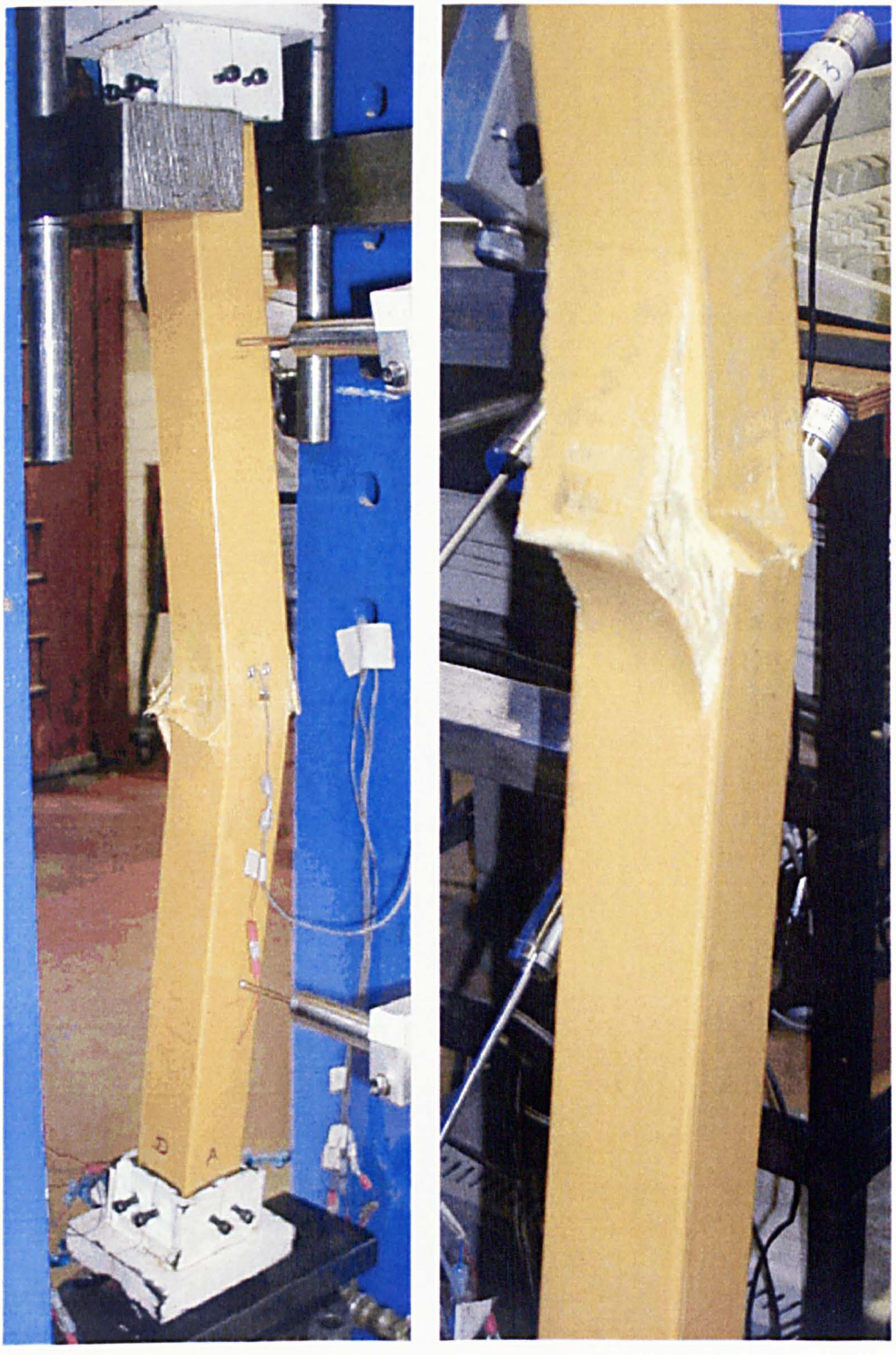

(c) (d)

Plate 4.15 (continued) Buckling mode-interaction in 750mm high, 51mm box-section specimen; (c) front and (d) rear view.

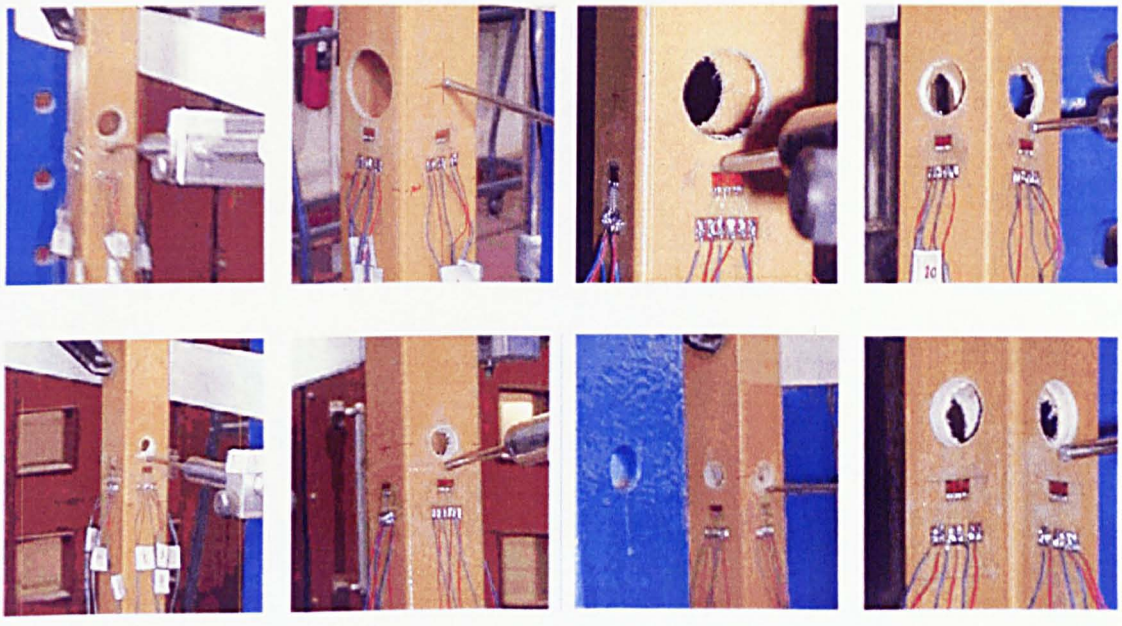

Plate 4.16 Various sizes and combination of holes drilled through the webs of the two box-sections

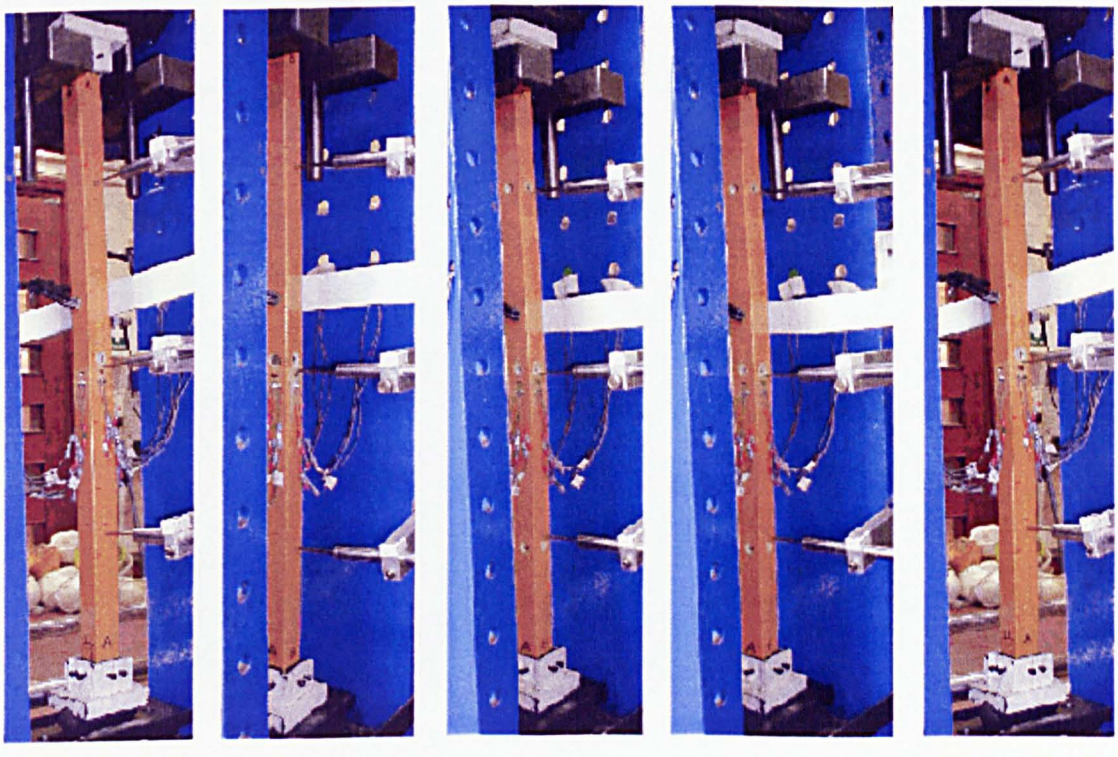

Plate 4.17 Global buckling in 1000mm GRP specimens with holes.

Plate 4.18 Global buckling in 1500mm GRP box-section specimens with holes.

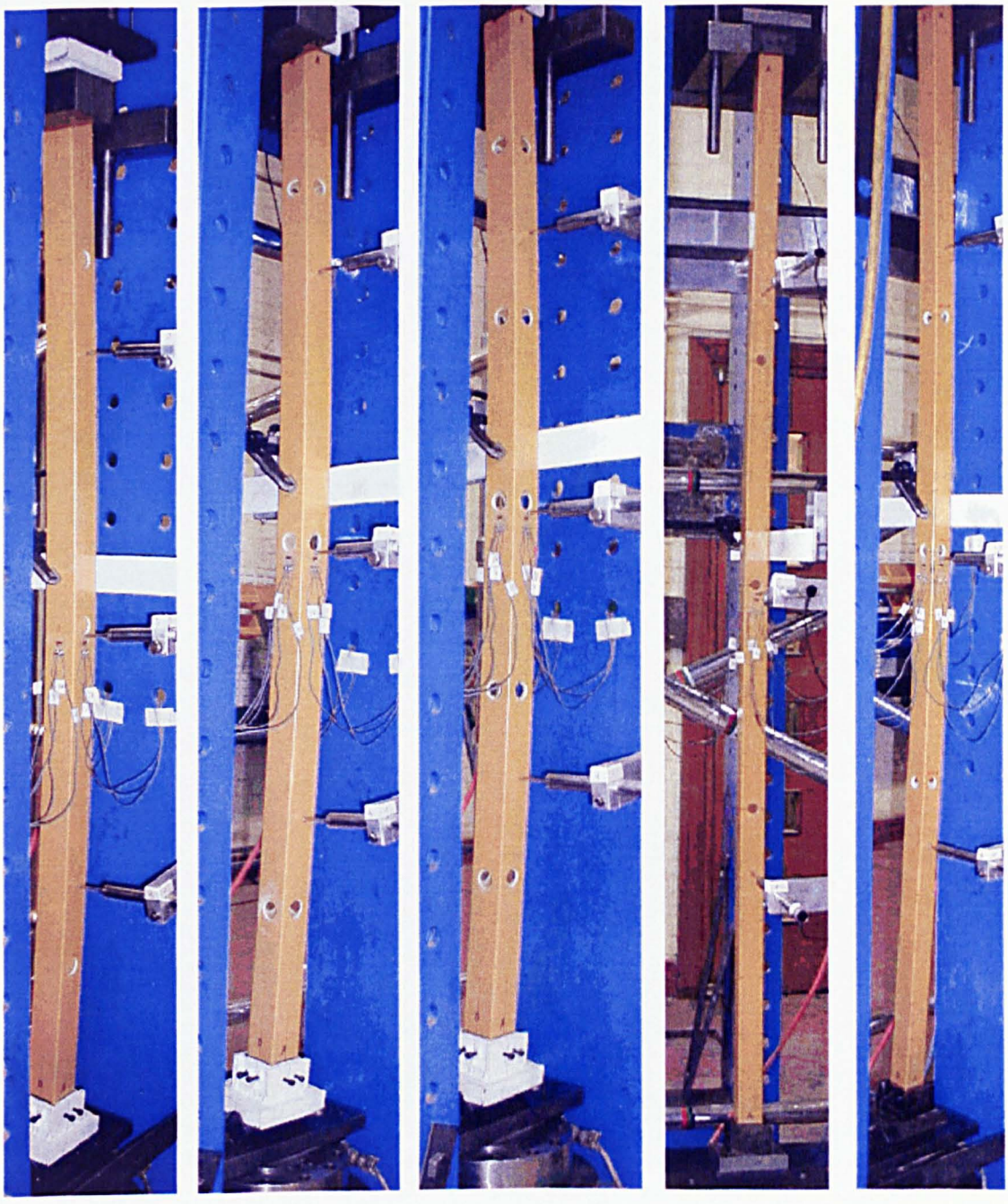

Plate 4.19 Global buckling in 2000mm GRP box-section specimens with holes.

CHAPTER 5

BUCKLING OF GRP BOX COLUMNS—NUMERICAL STUDY

5.1 INTRODUCTION

The ultimate failure loads of axially loaded composite columns of various heights have been measured experimentally and estimated analytically in Chapter 4. In this chapter the failure loads and failure modes of the same box-section columns have been simulated and predicted numerically using finite element modelling. Included in the numerical investigations are the effects of physically measured imperfections e.g. variations in the cross-sectional dimensions. The effects of load eccentricity and initial curvature (bow) have been studied by adding known (measured) amounts of load eccentricities and deflections at the mid-height of the specimen models. The investigations have further been extended to include the effects of holes formed in the webs of the GRP profiles representing changes to the section arising from connections or services details and also to demonstrate the effective zones of the columns. Circular holes of various sizes have been considered for the estimation of the buckling stiffness loss of the composite columns. The outcomes of the numerical studies have been compared with the experimental and closed form analytical results.

Finite element (FE) models representing the true cross-section geometry of the box-sections (shape, parametric dimensions of wall thickness and column heights), have been analysed using a commercial finite element code "LUSAS". A typical base model representing both the box-section profiles, with a GRP height of 1000mm has been constructed (Fig 5.1). The effective height of the column becomes 1055mm after adding 27.5mm thick steel plates to the specimen at the upper and lower ends to simulate the steel shoes used to restrain the specimens and distribute the axial load uniformly as in the experimental configuration. Finite element models of various heights and different boundary conditions have been produced by making respective changes to the base models. The most common boundary conditions found in the literature e.g., simply supported, hinged and fully fixed supports have been applied to the axially loaded columns. Different boundary conditions and the initial assumption of GRP material as isotropic (taking $E=E_L$) have been adopted to establish the

satisfactory benchmarking of the software. Load eccentricity has been introduced (in intervals) by altering the loading positions in the base model. Initial out of straightness (curvature) at mid heights of the columns have been modelled by introducing the imperfections as half sine waves (the most critical imperfections corresponding to the first mode shape). Additional finite element models of the composite columns, with holes in the webs (walls), have been developed to predict the potential loss in the buckling strength of composite columns in the presence of these holes. The sizes of holes have been varied in terms of d/w ratios, where d is the diameter of the hole and w is the web-width. The study has been limited to longer columns (1000 to 2000mm GRP heights) for both box-sections as experimental results are available for comparison. Recommendations regarding the sizes and gaps between the holes are presented.

The main objectives of the numerical investigations are to:

- Develop suitable finite element models representing the true geometry of the box-profiles, simulating the constraints (boundary and loading) of the experimental set up, that exhibit similar behaviour (failure modes and deformations) when analysed using numerical formulations.
- Establish the suitability of different types of analysis. Concepts of elastic stability have been applied through linear analysis. Analytical methods assume axial columns as perfectly straight whereas actual columns are not free from imperfections. In the presence of imperfections, initial loadings path exhibit lateral deformation and the load changes with deflections. Also deformations may be very large in some buckling modes. Non-linear analyses, therefore, are required to trace the predicted behaviour of the member under applied load. Non-linearity may be only geometrical if the dimensional of shape imperfections are present and the failure stresses (and hence failure mode) are within the elastic range of the material. Conversely, if failure modes (experimental) indicate bursting of the material, nonlinearity in the material becomes necessary to consider.
- To establish the effects of specimen height, boundary conditions, degree of orthotropy, in-plane shear modulus, load eccentricity, initial curvature and

hole-size on the buckling strength of the composite columns through parametric studies.

- To establish general rules governing the numerical prediction of ultimate failure loads of GRP pultruded columns. Similar rules are also defined for the composite columns having holes in their webs.
- To establish numerical results (with confidence) containing safe loads for various column heights of the two box-sections (51 and 44mm square). The results have been used for the construction of a design curve for pultruded GRP columns. The universal slenderness ratio 'λ' (2.19) defined for composite columns in Chapter 2 has been used to define a universal design equation for the design of pultruded GRP columns.
- To compare failure loads (and modes) predicted by finite element analyses with those obtained using conventional procedures e.g., elastic stability theory, Strongwell design manual (Strongwell, 1989), ASCE design manual (ASCE, 1984), and design equations in the ECD (Clarke, 1996).

5.2 FINITE ELEMENT MODEL OF COLUMN

The model (geometric details given in Fig. 5.1) comprises a GRP specimen of a specified (variable) height and two steel plates (27.5mm thick) attached to the upper and lower ends simulating the bearing surfaces of the shoes used to restrain the specimen in the experimental study (Chapter 4). As the GRP specimens were restrained laterally in the shoes, the steel plates in the numerical model have been considered as integral parts of the composite specimen.

To represent the geometrical dimensions of the square cross-section of the GRP profiles and the covering steel plates, a 3-dimensional volume model has been developed. Side-walls (webs) of the GRP profile joined to make a square cross-section are represented by volumes (v13 to v20, Fig 5.1) of specified thickness. The terminal steel plates have also been represented by volumes, each comprising 12 volumes (lower v1 to v12 and upper v21 to v32, Fig 5.1). All volumes have identical orientations with respect to the global axes of the model i.e., the orientation of the axes (indicated by black arrows on all the volumes) are parallel to the global *X, Y* and *Z* direction (Fig 5.1).

The volumes have been discretised by dividing into a mesh using three dimensional (volume) solid continuum finite elements (HX20)*. The elements are hexagonal (brick) defined by 20 nodes i.e., 8 at corners and 1 at half-length of each side. Each node has 3 translational degrees of freedom (d.o.f), *u*, *v*, and *w*. The elements are of quadratic order where up to a linear variations of field variables (stress, strain etc), between the nodes, can be represented. The elements belong to the isoprametric family. A regular mesh has been assigned to discretise the rectangular volumes using rectangular finite elements (HX20). H-refinement has been adopted with inference from multi-mesh extrapolation to obtain an adequate mesh (measured as deviations of strain contour plots using averaged and unaveraged nodal values). To maintain the element's aspect ratio within limits (<10 e.g., Cook et al 2002, Lusas theory manual 2001) at least two elements width-wise and four elements per 100mm specimen height have been used. However for shorter lengths (750mm and less) the mesh has been further refined to four divisions in the transverse (width-wise) dimension and eight divisions per 100mm of specimen length in the longitudinal direction. A typical finite element model for the GRP box-section profile of height 1000mm (Fig. 5.2) has been used as the base model for both sections (51 and 44mm square).

Material properties for the steel and GRP composite materials have been defined using data sets and assigned to the volumes representing the corresponding materials. For example, an isotropic material data set, with properties E = 205kN/mm^2 and ν = 0.3, have been defined for steel and assigned to volumes 1 to 12 and 21 to 32 (Fig 5.1a, and c). An orthotropic material data set defines the material properties (established in Chapter 3) for the GRP composite using nine constants as follows;

51×51×3.2mm box-section

E_x = 30.3kN/mm^2, E_y = 9.2 kN/mm^2, E_z = 9.2kN/mm^{2†}, G_{xy} = 2.85kN/mm^2,

G_{yz} = G_{zx} = 3.95kN/mm^2, ν_{xy} = 0.29 and ν_{yz} = ν_{zx} = 0.15 ,

44×44×6.0mm box-section

E_x = 33.2kN/mm^2, E_y = 9.2 kN/mm^2 E_z = 9.2kN/mm^{2†}, G_{xy} = 2.85kN/mm^2

---

* Lusas element library.

† Transverse material properties has been taken equal in X and Z direction (transversely homogeneous).

$G_{yz} = G_{zx} = 3.95\text{kN/mm}^2$, $\nu_{xy} = 0.29$, $\nu_{yz} = \nu_{zx} = 0.15$†

The base model assumes simply supported boundary conditions with respective restraints along the mid-line of the lower and upper steel plates. Each support is defined by specifying the restraints that support applies to the assigned component of the structure. For example, support R1 (Fig 5.2b) three transitional displacements in the x, y and z directions have been restrained ($u = v = w = 0$), but rotation about the x-axis is admissible. This simulates the knife-edge supporting the lower steel shoe in the experimental set up. At support R-2 (Fig 5.2 b), displacements in x and z directions are restrained but not in y direction ($u = w = 0, y \neq 0$) to allow axial shortening under the applied load. Rotation about the x-axis is again admissible. Further, rotations about the y and z axes are restrained in both support-sets (R-1 and R-2) to simulate the knife edge support (KES) used in the experimental test-configuration (Plate 4.3a-b).

The axial compressive load has been applied in the vertically downward direction ($-y$) along the central line of the top steel plate. Typically a unit load distributed along the centre line (51mm long) has been defined. This simplifies the implementation of subsequent analyses by using a load factor approach for both linear and nonlinear analysis. This downward load has been assigned to the lines defining the centre line of the upper plate (see the blue downwards arrows in Fig 5.2 a) to simulate the knife edge loading in experimental configuration. The idealised loads 1.96E-02kN/mm and 2.27E-02kN/mm have been applied along the centre line of 51mm and 44mm box-sections respectively. The FE models of various GRP heights have been obtained by simply changing the length of the base models for each cross-section profile.

Types of analyses

Three types of analyses; linear elastic (eigenvalue), geometrically nonlinear elastic and fully non-linear have been used to predict the buckling loads and failure modes. The linear elastic solution assumes that both the geometry and the material properties remain unchanged up to failure. A geometrically non-linear analysis recognises contributions of changes in the geometry of the structure (column) to the failure mode and load within a constant material framework. A fully nonlinear analysis (geometric and material) recognises both geometric and material nonlinearities in the solution. All three types of the analysis methodology have been considered in this numerical study with recommendations made regarding their selection and application, given

that computational expense escalates dramatically with increased assumed levels of nonlinearity.

5.3 LINEAR ELASTIC (EIGENVALUE) ANALYSIS

Theoretical fundamentals

The instability of the axially compressed columns has been associated with the phenomenon referred as "bifurcation of equilibrium" (Chen and Lui 1987, Farshad 1994, Galambos 1998). In the process, a perfect member when subjected to increasing load initially deforms in one mode and at a load referred to as the critical load, the deformation suddenly changes into a different pattern. For example, an axially loaded column initially shortens due to axial compression. The axial strains are also known as "membrane strains" and the energy stored during the process as "membrane energy". At the critical load, the column suddenly bends. At this bifurcation in the load-displacement behaviour the membrane strain energy is converted into bending strain energy without any change in the externally applied load. In slender columns (and in thin plates) membrane stiffness is much greater than bending stiffness, giving rise to large membrane strain energy for relatively small deformations and displacements. When buckling occurs comparatively large bending deformations are needed to absorb the released strain energy, producing excessive bending deformations.

The critical load at this assumed bifurcation can be determined by an eigenvalue analysis. In the analysis all the possible equilibrium configurations that the system can assume at the bifurcation load are taken into account. These possible displaced configurations of the system are described by specifying a set of generalised displacements. The stiffness matrix relates the generalised forces to the generalised displacements of the system. The stiffness of the system is measured by the determinant of the stiffness matrix. At the critical load the stiffness of the system vanishes. Thus, by setting the determinant of the system's tangent stiffness matrix equal to zero, the system's critical conditions can be identified. The critical conditions are represented by the eigenvalues of the system's stiffness matrix and the displaced configurations are represented by eigenvectors. The lowest eigenvalue corresponding to an axially loaded state (in this case) is the critical load of the system. The

bifurcation or eigenvalue approach is an idealised mathematical approach to determine the critical conditions of a geometrically perfect system.

Initially, to predict the critical buckling load P_{cr} for the base model of 51mm box-section 1000mm high, a linear elastic analysis has been performed by defining the eigenvalue buckling control as the base model is perfectly straight and of slender height (§ 4.7). In this case the assumption of linearity is justified as the overall structural response implies both geometric and material linear responses. A converged solution of 59.3kN to P_{cr} is obtained (Table 5. 2). This value of P_{cr} is close to the experimental load of 59.1kN and analytical load $P_{E\text{-}sh}$ of 61kN (Table 4.4). Furthermore, the deformed shape obtained from the linear elastic analysis (Fig 5.4a) predicted global buckling with a maximum transverse deflection at column mid height and rotation of lower and upper steel plate about the central axis in the x-direction. The deformed shape is identical to the shape observed in the experimental study i.e. half sine wave of the order of the column effective length (Plate 4.6c). This observation serves as an initial indication of the satisfactory performance of the FE model, type of element chosen and the type of analysis performed for this particular case. It also demonstrates that 1000mm GRP high column (L_{eff} = 1055mm) is in the category of slender columns.

Different support conditions at the lower and upper ends (steel plates) of the column model also serve to demonstrate the validity of the numerical predictions. Normally the nature of a support is defined by the displacement or rotational prescriptions. For example in the base model, the simple support assigned to the central line of lower steel plate R-1 (Fig 5.2b) is defined as;

$$u = v = w = 0,\ \theta_x \neq 0,\ \theta_y = \theta_z = 0$$

where u, v, w, are translational displacements and θ_x, θ_y, and θ_z are rotational displacements with respect to X, Y and Z axis. A displacement set equal to zero infers the respective restraint.

The following four support conditions have been analysed for critical buckling loads:

(a) Simple-Simple (SS): Column is simply supported at both ends as described in the base model with lower support as $u = v = w = 0$ and $\theta_x \neq 0$, $\theta_y = \theta_z = 0$. Upper support condition is $u = w = 0$, $v \neq 0$, $\theta_x \neq 0$, $\theta_y = \theta_z = 0$.

(b) Fixed-Simple (F-S): Lower support is fixed i.e., restraint to all translational and rotational degrees-of-freedom as; $u = v = w = 0$, $\theta_x = \theta_y = \theta_z = 0$. Upper support as given in (a) above.

(c) Fixed-Fixed (F-F). Lower support fixed as described in (b) above. Upper support is also fixed but allows vertical shortening as; $u = w = 0$, $v \neq 0$, $\theta_x = \theta_y = \theta_z = 0$.

(d) Fixed-Free (F-Free). Lower support as described in (b) above and no restraints at the upper end of the column.

The outcomes of linear analyses of 1000mm high GRP box-sections (51×51×3.2mm and 44×44×6.0mm) with different boundary conditions are given in Table 5.1. The corresponding buckling modes for the respective box-sections are indicated in Figs 5.4 and 5.5 respectively. Critical buckling loads for F-S boundary conditions (case b) factor the P_{cr}s obtained with simple supports (case a) by 2.04 and 2.02 respectively, as compared with analytical value of 2 (Galambos, 1998). For the F-F boundary conditions (case c) the predicted critical loads, the factors are 4.07 and 4.04 as compared with 4 (analytical, Galambos, 1889). Similarly for F-Free boundary conditions, the predicted critical loads are 0.26 and 0.25 of the S-S case (c.f. 0.25, Galambos, 1998). These results support the implied validity of the numerical model under linear assumptions.

Critical loads for various column heights

Simply supported boundary conditions and application of concentrated load along the centre line of upper steel covering plate remain constant in the FE models of various column heights (of both box-section profiles in the range of 200mm to 2000mm) simulating the experimental set-up (knife edge supports and concentric loading as shown in Fig 5.2). Orthotropic material properties have been used to represent the GRP material in all models. Eigenvalue buckling analyses, with a convergence norm[‡] of 1.0×10^{-6}, predict critical bucking (or failure) loads, under linear assumptions, for 51mm and 44mm box-sections (Tables 5.2 and 5.3 respectively).

---

‡ During analysis, the numerical solution is reffered to a criterion with which to measure its convergence. It is assumed that the eigensolution has converged on iteration k when $\frac{\lambda_i^k - \lambda_i^{k-1}}{\lambda_i^k} \leq$ norm for all eigenvalues λ_i.

51×51×3.2mm box-section

Linear elastic solutions for the column heights of 655mm (GRP height 600mm) and above converged to the required norm (1.0E-06) giving the minimum eigenvalues as the critical buckling loads (Table 5.2). The failure modes (Fig 5.6), of these specimens, obtained as deformed shapes show global (Euler) buckling with maximum lateral deflections at the mid-height. Therefore, columns with effective heights of 655mm and above are grouped as slender columns. The numerical results in Table 5.2 indicate the tendency of the buckling load to depend on column height. Initial comparison of the outcomes of the linear analyses with the experimental and theoretical studies (Table 5.10) indicate the adequacy of eigenvalue solution in predicting critical buckling loads (to within 3%) in the Euler mode (e.g., $L_{eff} \geq$ 655mm for the box sections assumed) and where no material damage (fibre or matrix failure) is observed.

For shorter heights (L_{eff} = 255 to 555mm), however, the linear solutions failed to converge to the required norm. Furthermore, the deformed shapes do not show any type of (global or local) buckling (Fig 5.6). The predicted loads are significantly higher than the experimental and theoretical loads (Table 5.10). Notably, if the required convergence norm is lowered (e.g. 1.0E-01), the predicted buckling loads and deformed shapes are inconsistent. For example, the buckling load for the 555mm column is higher than that of 455 and 355mm columns (Table 5.2) contrary to expectations and the physics of the problem. The deformed shapes of the two columns 255mm and 355mm (Fig. 5.8) show similar buckling-waves in opposite walls, where opposite directions are expected. Failure to comply with the required convergence norm suggests that the equivalent test specimens may have failed by material degradation rather than buckling of the walls or the section as a whole.

44×44×6.0mm box-sections

Linear analysis for column heights L_{eff} = 455mm and above (Table 5.3), converged to the required norm, showing global buckling in the deformed shapes (Fig 5.7). Buckling loads for 455mm and 555mm high columns significantly over predicted compared with experimental loads (Table 5.11), while for heights 655mm and above the predicted loads correlate well (maximum 9%). However, the analyses for the short columns (L_{eff} = 255 and 355mm), failed to converge and gave inconsistent

failure loads e.g., failure loads for 255mm and 355mm columns are 790kN and 471kN respectively, greater than the maximum crushing strength of the section (461kN, Table 4.5). It clearly implies that these profiles fail by material crushing as evidenced by experimental observations.

It is concluded therefore, that linear elastic analysis is valid for the numerical prediction of buckling loads for slender columns that exhibit purely global buckling modes. The lateral deflections at the critical loads appear to be small enough to validate the assumption of linear response. The predicted loads for both the square box-section specimens are close to the Euler (theoretical) loads[§] and are higher than the experimental loads with the latter reduced by imperfections and experimental limitations. Notably, all the converged specimens showed global buckling, confirming the slender column range established experimentally in § 4.3.1. Conversely, if the solution does not converge, numerical predictions are not reliable, as incorrect solutions are obtained. Furthermore, the analysis indicates the range of column heights which are short enough not to show global buckling, suggesting the need for other types of analyses for the safe prediction of failure loads.

5.4 NONLINEAR ELASTIC ANALYSIS

Theoretical fundamentals

Geometric nonlinearities arise from significant changes in the structural configuration during loading e.g., in vertically loaded columns progressive eccentricity of the applied load due to lateral bending. Furthermore, the presence of geometric imperfections introduces lateral deflections at the onset of loading and the problem then becomes a coupled load-deflection problem. Linear elastic (bifurcation) analysis assumes no coupling between membrane (axial) and bending (lateral) deformations and does not take into account either material limits or material nonlinearity (elastic or elasto-plastic). For practical problems (real columns) linear analysis may overestimate the actual collapse load, particularly in those cases where significant imperfections exist and/or the material elastic limit would be exceeded prior to achieving the critical load predicted as an eigenvalue (see §5.3 for example). Therefore a nonlinear analysis is required to account for the changes in loading (or its

[§] For comparison of numerical, theoretical and experimental results see Tables 5.10-11

direction) with geometric variations. However, in a geometrically nonlinear analysis the material properties assigned are elastic (for both steel plates (isotropic) and GRP profiles (orthotropic)) with solutions reflecting only influences of geometric parameters (e.g. imperfections in the current examples).

In the non-linear analysis (a load deflection problem) an iterative numerical procedure successively approximates the equilibrium path (Riks 1979, Godoy et al 1995). The required total load is applied in a number of increments (load steps). Within each increment a linear prediction of the nonlinear response is made, and subsequent iterative corrections are performed to restore equilibrium by the elimination of the residual or 'out of balance' forces. The iterative corrections are referred to a 'convergence' criterion** which indicates to what extent an equilibrate state has been achieved. In each load step, a number of iterations may be required to reach the required level of convergence. The solution procedure is, therefore, commonly referred to as an 'incremental-iterative method. The Newton-Raphson algorithm has been adopted in the present study. In this incremental iterative method, for each load step, the initial prediction of the incremental solution is based on the 'tangent stiffness' from which incremental deformations and their iterative corrections are derived. Each iterative calculation is based upon the current tangent stiffness. This involves the formulation (and factorisation) of the tangent stiffness matrix at the start of each equilibrium iteration. Although the continual manipulation of the stiffness matrix is expensive, the standard Newton-Raphson method generally converges rapidly and is preferred for geometrically non-linear problems (Riks 1979, Crisfield 1981).

The "Total Lagrangian" formulation has been coupled with nonlinear solution procedure. In this formulation the undeformed configuration (in each load step) is taken as a reference configuration i.e. the limits of integration are carried out over the

---

** The convergence criteria, generally incorporated in the nonlinear anlayses are the "root mean square residual norm" and the "displacement norm". In the formar criterion, the norm is the square root of the average of the squares of the residual forces and is dependent upon the units being used. The later (displacement) norm is the sum of the squares of all the iterative displacements as a percentage of the sum of the squares of the total displacement. It is the measure of how much the structure has 'moved' duringan iteration. Being a scaled norm it is not affected by the units.

undeformed configuration. The formulation is numerically stable, convergent under large load increments, valid for small strains and considered more appropriate in the absence of large nodal rotations. In the non-linear control data set of the software, Total Langrangian formulation has been opted, among the other available formulations.

In the solution algorithm the applied load is modified during each increment by a load factor for which the system equilibrium is restored to a required convergence norm, as the displacements increase. At the critical load factor, the plot of load verses displacement becomes horizontal, implying zero stiffness at failure. Buckling or failure of the columns is not indicated as rupture in the numerical model. A zero or negative pivot is interpreted as numeric instability by the gauss elimination algorithm during the forward reduction procedure. At the critical load (or load factor) a zero or negative pivot indicates that the equilibrium is lost.

In the incremental procedure two control methods are available. The incremental path is usually initially controlled under a "constant load level" in which displacement solutions are sought to each segmental load increment. At failure to converge, control is switched to "arc length" in which the incremental load factor is modified to a value consistent with predefined displacement limits. The latter is typically used in stability analyses, especially where the buckled-deformation path is required (e.g. snap-through analyses).

Irrespective of the method being used, incrementation for nonlinear analysis has been specified by automatic incrementation using an incrementation control data set. In this case the starting load factor, amount and number of further increments, and the total load factor, are specified. In uniform incrementation, for each increment the starting load factor will be multiplied by the specified load components and added to the previous level. Termination may be specified in three ways: limiting the maximum load factor, limiting the maximum number of applied increments, limiting the maximum value of named freedom. Where more than one criterion is specified, termination will occur on the first criteria to be satisfied. In addition, the solution will be terminated if, at the beginning of an increment, more than two negative pivots are encountered during the frontal elimination phase.

Geometrically nonlinear results

51×51×3.2mm box-section

The failure loads predicted by the geometrical nonlinear analysis for various simulated columns heights have been given in Table 5.4. The predicted loads for columns heights 655 to 2055 (GRP heights 600 to 2000mm) are in good agreement with the linear (< 2%), theoretical (< 5%) and experimental (< 4%) results (Table 5.10). The axial stress contours (Figs 5.9-5.11) show high compression stresses at the ends under steel plates whilst stress distribution is uniform along the column height.

However the global buckling modes (observed in experimental study) have not been detected in the deformed shapes of non-linear analyses (Figs 5.9-5.11). Instead failure has been manifested by the loss of equilibrium, as indicated by a negative pivot in the reduced stiffness matrix at the critical load. However, whilst the non-linear analysis is capable of predicting the ultimate load carrying capacities in the slender columns, it is unable to predict the buckling modes[††]. In the absence of local buckling and predicted loads near to the global analytical loads these column heights are categorised as slender columns.

In the case of short columns (L_{eff} = 555mm and less), local web buckling has been predicted by the nonlinear analyses. The shortest model analysed comprises 200mm GRP height. The deformed shapes and the axial-stress contours have been shown in Fig 5.12. Three half sine waves are clearly visible in the 2- and 3-dimentional views indicating the alternate amplitudes of the buckled waves. The central half sine wave is fully developed in contrast to the end waves. From the geometry of the mesh, the length of the central half sine wave is deduced to be 62.5mm. It appears that buckling deformation starts at mid-length and propagates towards ends resulting in an odd number of sine waves. Careful inspection of the deformed shapes reveals that the web-interface has also undergone some buckling. The "solution" was achieved at a high convergence norm (1.0×10^{-01}kN) giving a failure load of 274kN. The predicted load is higher than the crushing strength of the cross-section i.e. 236kN (Table 5.10). Experimentally, an average failure load of 121kN (Table 4.2) has been measured with

---

[††] It is shown in § 5.5 that global buckling mode has been predicted by introducing a small initial imperfection in the geometry of the cross-section.

failure accompanied by tearing through the box walls. Furthermore, the experimental failure mode showed only a mid-height buckling wave (Plate 4.9). Apparently, the steel shoes prevented the development of the end waves. Numerically, the contours of axial stresses (Fig 5.12) along the column height range from 0.117 to $-0.496 kN/mm^2$. The first stress plot shows the shear stress distribution just before the failure (+ve pivot showing system still in equilibrium). At this stage the stress concentrations at the peaks of the buckled half sine wave are within the ultimate allowable axial stress of the material ($0.385 kN/mm^2$). The second plot shows increase in the intensity of axial stresses at failure load when solution converges with negative pivot (loss of equilibrium). High axial stresses at the predicted failure compared with the material limits suggest the development of complex non-linear deformations leading to the bursting and tearing failure.

The simulated column height (GRP = 300mm, L_{eff} = 355mm), buckled locally with five half sine waves (Fig 5.13). The three middle waves are fully developed while those towards each end are under developed. This confirms the proposition that buckling starts at mid-height and propagates towards the ends giving an odd number of half sine waves. The three central developed half sine waves again indicate a wave length of 62.5mm. Whilst the numerical predicted load of 211kN (Table 5.4) is lower than the crushing strength of the section (235kN), the axial stresses at the wave crests range from 0.113 to $-0.482 kN/mm^2$ with the latter exceeding the material limit ($0.385 kN/mm^2$) implying material failure (not detected in the deformed shape) at the failure load (second contour plot in Fig 5.13). Therefore, the poor convergence norm at failure suggests that predicted load is unreliable and beyond simple stability (buckling) failure.

For the 400mm column (L_{eff} = 445mm), the nonlinear analysis converges to the required norm and a failure load of 155kN (Table 5.4) is predicted. The deformed shape (Fig 5.14) indicates seven half sine waves out of which middle five has been developed leaving the extreme two under developed. At mid-height a wave length of 62.5mm is interpreted using the mesh geometry. A height of 440mm of GRP is therefore theoretically required to obtain seven fully developed half sine waves (without rotational restraint on the box-face), predicting the minimum local buckling

load[‡‡]. The axial stress distribution (contours of S_y) suggests a range from 0.111 to $-0.473kN/mm^2$ while the compressive stress is $0.385kN/mm^2$, confirming material failure in physical laboratory tests. However the stress concentrations just before failure are lower than the ultimate limit.

Similar behaviour has been predicted for the 500mm GRP column (L_{eff} = 555mm). Seven half sine waves have been predicted (Fig 5.15), five of which are developed. The length of the half sine wave at centre measures 62.5mm suggesting that wave length is constant over the column heights in short range. However, the nonlinear solution converged to a predicted P_L of 150kN (Table 5.4), again higher than the experimental load (Table 5.10). Axial stress contour plots just before and after the failure have been included. The stresses at the failure load on the wave crests are (0.082 to $-0.444kN/mm^2$), indicating material rupture.

44×44×6.0mm box-section

Table 5.5 presents the ultimate failure loads predicted for the B44 profile at various heights from 255 to 2055mm. Deformed shapes for these profiles are shown in Figs 5.16-5.19. All the models display identical failure modes i.e., no local or global buckling is visible. Instead axial shortening with transverse strains are exhibited. This is supported by the axial stress plots along the length showing uniform stress along the whole heights (Figs 5.16-5.19). Ultimate loads for heights 555mm and above (GRP height 500mm and above) are comparable with the experimental, linear and theoretical results for slender columns (Table 5.11). These are heights for which the solutions converged. No local buckling is indicated.

There are two short heights i.e., 255 and 355mm (GRP heights 200, 300m) for which the predicted loads exceeded the crushing strength (477kN) of the material (Table 5.11). The solutions for these column heights did not converge. The stress contours indicate the highest stress intensity at the central (support) line of steel plate (simulating knife edge). Whilst the ultimate allowable compressive stress for 44mm box-section profile is $0.523kN/mm^2$ (Table 3.13), predicted stresses in GRP material

---

‡‡ A similar study has been included in the next section (§ 5.3.4) to determine minimum local buckling load.

adjacent to the steel-plates, range from –0.7 to –0.99kN/mm^2 (Fig. 5.19), confirming that this will be material failure at the ends in the experimental tests.

Weak convergence of the solution for shorter heights of both 51 and 44mm box-section columns, leading to unreliable results, indicates that column behaviour cannot be predicted assuming geometric nonlinearity without the inclusion of material nonlinearity. Furthermore, the absence of the experimental end half sine waves is attributed to the restrictions imposed by steel plates in very short columns. This finding is in line with that of Mottram (2000), who recommended that for the determination (or measurement) of the local buckling load (that must be uniform in a range of short column lengths) of composite columns, the length of column should accommodate at least four half sine-waves.

5.5 ELASTIC DEGRADING (FULLY NONLINEAR) MODEL

5.5.1 Theoretical fundamentals

The evidence emerging from the experimental failure modes (tearing and bursting of the walls and interfaces) of the short columns suggested nonlinear behaviour of the composite material at the failure loads. Large strains modify (reduce) the elastic modulus in the longitudinal and transverse directions and the in-plane shear moduli. Non-linear response of the pultruded GRP materials has been modelled as elastic degrading of the material stiffness under large complex strains (Haj-Ali and Kilic, 2002). Referring, to the orthotropic nature of the GRP material an "Hoffman Criterion" has been adopted for the prediction of the nonlinear behaviour. This is a general failure criterion describing yield (linear limit) of anisotropic materials. Several models, including the well known Von Mises yield criterion are special cases of the Hoffman criterion. The criterion includes the stress hardening in longitudinal and transverse directions of the material. Hardening in the Hoffman criterion has been assumed to be proportional in tension and compression in a particular direction, maintaining the form of the initial yield surface.

The nonlinearity of GRP material (in a particular direction) has been represented by the change in slopes or degree of curvature of the stress strain plots. The "linear limit" σ_L has been identified at the location where initial linearity in the stress-strain curve diverges. Beyond the linear limit a non-linear behaviour has been assumed with a reduced elastic modulus. Linear elastic and nonlinear degrading strains have been

combined to define a reduced modulus (Fig. 5.20) with degrading strains defined as those beyond the elastic limit. For example, assuming that the stress-strain response of a material is beyond linear range is represented by a tri-linear stress-strain curve, the degrading modulus, E_d, (Fig. 5.20) can be represented by a pseudo modulus C_i, where

$$C_i = \frac{E_{di}}{\left(1 - \frac{E_{di}}{E}\right)}, \qquad i = 1,2,3 \tag{5.1a}$$

$$E_{d1} = \frac{\sigma_1 - \sigma_L}{\varepsilon_1 - \varepsilon_L}, \qquad E_{d2} = \frac{\sigma_2 - \sigma_1}{\varepsilon_2 - \varepsilon_1}, \quad E_{d3} = \frac{\sigma_3 - \sigma_2}{\varepsilon_3 - \varepsilon_2} \tag{5.1b}$$

and

$$\varepsilon_L = \frac{\sigma_L}{E}, \quad \varepsilon_1 = \varepsilon_1^e + \varepsilon_1^d, \quad \varepsilon_2 = \varepsilon_2^e + \varepsilon_2^d, \quad \text{with } \varepsilon_1^e = \frac{\sigma_1}{E} \text{ for example} \tag{5.1c}$$

The limit of applicability of C_1, C_2 and C_3 (for example) are defined by effective nonlinear strain limits, L_1, L_2 and L_3 with

$$L_1 = \varepsilon_1 - \varepsilon_1^e = \varepsilon_1 - \frac{\sigma_1}{E}, \; L_2 = \varepsilon_2 - \varepsilon_2^e = \varepsilon_2 - \frac{\sigma_2}{E} \text{ and } L_3 = \varepsilon_3 - \varepsilon_3^e = \varepsilon_3 - \frac{\sigma_3}{E} \tag{5.2}$$

The appropriate values of E, E_{di}, ε_L, and ε_i for the GRP material have been derived from the average of all the quadratic polynomials fitted to the experimentally obtained stress-strain data from coupon tests. For example the average of the quadratic polynomials fitted to the transverse tensile data (5 coupons) is shown in Fig 5.21 (Saribiyik, 2000). To this average quadratic polynomial, linear regression analysis (with $R^2 > 0.99$) has been applied to fit a series of straight line-approximations such that Fig 5.21 resembles Fig. 5.20. From this exercise, the "linear limit" of GRP material in transverse tension is defined as 0.0243kN/mm^2 at a strain of 0.0025, and Young's modulus, E is 9.2kN/mm^2. The values of E_{di}, and ε_i are given in Table 5.6a in addition to the pseudo-modulus C_i and effective plastic strain limit L_i.

Similarly the nonlinear idealisation of the average compression polynomial curves for 3.2mm and 6.0mm thick box-sections are presented in Fig 5.22(a,b). Corresponding values of degrading modulus, pseudo modulus and limits of nonlinear strains (before breaking) have been calculated using (5.1) and (5.2) and presented in Tables 5.6b and 5.6c.

Notably, (as discussed in § 3.5), in the present numerical representation, transverse compression properties of both the box-sections have been assumed to be equal to the tensile properties of the 51mm box-section as measured by Saribiyik (2000). Furthermore, the tensile properties in the longitudinal direction for each box-section have been taken equal to the compression properties measured for each corresponding box-section (Chapter 3). The in-plane shear moduli in the orthotropic directions are assumed to remain constant throughout the analysis[§§].

The same incremental-iterative method (as employed in the geometrically nonlinear analysis) with nonlinear control and Hoffman failure criterion has been used for the full nonlinear analysis. Buckling or failure of the system is not manifested as rupture in the numerical model. Instead, the load factor, plotted against the iteration number, converges to a plateau and appropriate nonlinear strains are identified. Essentially, the solution algorithm maintains numerical stability through arc-length control (i.e. the displacements do not tend to infinity) as zones of the numerical model reaches and attains their stress and nonlinear strains capacities. The converged load factor has been used to calculate the ultimate load (i.e. *load factor* × *applied load*) with the vectors of nonlinear strains used to identify critical component areas. The applied load has been taken as unity and the converged load factor directly gives the ultimate applied load.

Outcomes of materially nonlinear (Hoffman model) analysis

51×51×3.2mm box-sections

Non-linear (Hoffman) results have been presented in Table 5.7. Models with effective heights 655mm and above (GRP heights 600mm and above) failed at loads similar to the obtained from the geometrically nonlinear analysis indicating that the buckling stresses in the columns are lower than the assumed yield stress of the GRP material (Fig 5.22a). Also, the deformed shapes for these columns exhibited similar modes of failure i.e., axial shortening and increases in transverse volumetric strains (Figs 5.9-5.11) with no mid-height lateral deflections, indicative of global buckling. Notably, for straight columns the nonlinear analysis does not indicate a buckled configuration.

[§§] Although the experimental shear stress-strain curves (Figs 3.32-34) are nonlinear, the adopted Hoffman failure criterion does not admit yielding or strain hardening of the in-plane shear stresses.

Representing physical columns (not perfectly straight), small initial curvatures 'Δ_0' (0.5% of the GRP height) have been introduced in the non-linear Hoffman models. As expected, the inclusion of initial curvature at the mid-height reduces the buckling loads and the deformed shapes exhibit global buckling modes in the slender columns (GRP lengths 600mm and above) as shown in Figs 5.23-5.24. These results demonstrate numerically that the imperfection (disturbance) initially induces the onset of global buckling i.e., bifurcation of the primary equilibrium path. In the absence of imperfections, the straight column continues to follow its primary path, even if the critical point is approached. The predicted loads for slender columns with initial curvature (0.5% of the GRP height) correlate with the experimental results e.g., Table 5.10, implying that the GRP columns as tested have initial imperfections of the order 0.5% or less of their heights. Measured imperfections were of the order of 0.2-0.02% of the column height (e.g. see chapter 4, § 4.2.1 and Fig 4.2). The columns heights of 655mm (GRP height 600mm) and above are confirmed as slender columns exhibiting global buckling.

The nonlinear solutions for the short columns 255 and 355mm (GRP heights of 200 and 300mm) terminated with a low convergence norm of 1.0E-01 (Table 5.7). However, whilst the predicted loads are unreliable, the deformed shapes indicated local buckling (Figs 5.25-5.26) of the webs in a sine mode, characteristic of web-buckling in thin walled structures. The shortest modelled length i.e., 255mm (200mm of GRP) exhibited only three half sine waves with indications that these results should not be used for the prediction of the local buckling load as at least four half sine waves are recommended (Mottram 2000). However the 355mm high column buckled locally with 5 half sine waves. Buckled modes in Figs 5.25-5.26 suggest a sine wave of 62.5mm interpreted from the mesh size***.

To investigate the effect of the number of fully developed sine waves of a locally buckled column, on its ultimate load, the height of the column (GRP) has been increased in small intervals of 25mm, from 350 to 475mm and reanalysed. The buckled shapes of these models are shown in Fig. 5.27. Interestingly, nonlinear Hoffman analyses predicted similar ultimate loads (134 to 139kN) for all the models

*** Each 100mm height of GRP is divided into 8 elements, giving element height as 12.5mm. The zoomed half sine wave in Fig 5.25 spans 5 elements, indicating a length of 62.5mm.

having GRP lengths ranging from 350mm to 500mm (L_{eff} = 405 to 555mm). This infers the important result that the numerically predicted buckling load is constant for a range of short column heights exhibiting local buckling. From these numerical results, the straight short column load P_L is around 135kN for the 51mm box section. This compares with an experimentally average value of approximately 120kN (§ 4.5). A second important observation made from Fig 5.27 (and also from Figs 5.12-5.15) is that a constant wave length of 62.5mm is interpolated (using the mesh size) in various column heights among the short column range (local buckling only)[†††]. This numerically predicted length of half-sine wave can be compared with the theoretically calculated length of 64.4mm (§ 4.4.2). Buckling starts from the mid-height and proceeds towards the ends. If the column height is only sufficient to accommodate an integer (odd) number of sine waves, the outer half waves are under developed. Conversely if the column height is increased, either the extremities of the column remain laterally undeformed (L_{GRP}= 375mm) or the number of sine waves is increased by 2 (one at each end) and these new peaks may not be fully developed (e.g. L_{GRP}= 425mm in Fig 5.27). Finally, at the onset of web buckling, strains that are combinations of elastic and nonlinear strains are developed. Elastic strains are uniformly distributed along the height of the column whilst nonlinear strains are only developed at the crests of the buckling wave (and locally along the stress singularity along the line of load application of the load platens). The vectors of elastic and nonlinear strains have been separately plotted on the two adjacent webs (half the cross-section) of the column in Fig 5.28.

The ultimate load predicted for straight columns is generally higher than the experimental loads, given the absence of imperfections in the former and their influence on the latter. Whilst the predicted P_L is over predicted using a straight (perfect) simulation by approximately 10 – 15%, geometric imperfections have been included to provide an improved prediction for P_L for the 51mm box-section and an indication of the nature of the imperfections and their simulation. The variations of cross-sectional dimensions, including the outer widths of the GRP sections, have been measured during the experimental studies. For example, for a 51mm box-section GRP

[†††] Measurements of the half sine wave lengths were not possible because short columns failed by tearing of webs and the cross-sections into long strips.

specimen of height 400mm, the measured outer dimensions along the height have been plotted in Fig 5.29. The imperfections have been evaluated by subtracting the mean dimension from the measured widths. In introducing the imperfections in the fully nonlinear models, four options have been implemented:

Option 1 Wall-thickness has been kept constant, distributing the cross-section with respect to the longitudinal axis of the profile at four heights i.e. 100, 200, 300 and 400mm, with the load remaining concentric.

Option 2 Moving the outer faces only, varying the wall thicknesses and keeping internal dimension constant. The central longitudinal axis passing through all the sections is straight and loading is concentric. However, stresses (and strains) vary along the height depending on the cross-sectional areas.

Option 3 Wall-thickness kept constant, moving the cross-sections as a whole (varying the internal dimensions). The centres of the cross-sections are eccentric, generally, with respect to the line of application of the load.

Option 4 A known load eccentricity, constant wall-thickness and an averaged constant cross-section. Five values of load eccentricities; 0.25, 0.5, 1.0, 1.5, and 2.0mm have been used.

Results for option-4 and combinations of other options with option-4 have been presented in Table 5.8. Results listed for load eccentricity equal to zero correspond to the respective options 1, 2, and 3. Option-1 without load eccentricity caused the minimum reduction in the load as the load is concentric and imperfections divided symmetrically about the side walls. However, the stiffness further reduced with load eccentricity. Combining options 3 and 4 exhibited the most adverse effects on load capacity as explicit load eccentricity was combined with out of straightness along the column height. For example, the predicted failure load for a 400mm GRP specimen with a load eccentricity of 2mm and an out of straightness on average 0.5mm (±0.25mm) reduced from 139kN (perfect column) to 117kN. This latter value is in agreement to the average experimental results of 117kN (Table 5.10). The outcomes combined with the accurate simulations of the behaviour of the long columns establishes the ability of the nonlinear numerical analysis to predict buckling loads for all the practical heights of the composite columns provided, an average estimate of the geometric imperfection is available. Furthermore, imperfections may be reasonably

introduced by assuming constant cross section geometry but that is translated laterally as a function of the height of the column. It is also evident that load eccentricity by itself is not significantly onerous on the failure load of a buckled member, but can be highly degrading when coupled with section geometry imperfections. This is clear when considering the case of a load eccentricity of 2.0mm in the absence of other geometry imperfections (130kN) and section imperfection only (135kN) with the load and section imperfections combined (117kN).

An initial curvature of 0.5% of the column height has been introduced to the models for column heights representing 555 to 2055mm in the fully nonlinear analysis. The predicted loads for imperfect columns (Table 5.10) indicate that the effect of initial curvature reduces with column height. The predicted loads for imperfect columns of heights 805 and 1055mm are much lower than experimental loads indicating small initial imperfections in the physical columns ($e_0 \leq 0.2\%$ measured).

44×44×6.0mm box-sections

Results of the Hoffman nonlinear analysis for thicker box-section (Table 5.9) failed to converge for shorter heights (255 and 355mm) predicting ultimate loads that are lower than the crushing strength of the material but are far greater than the experimental loads. Predicted loads for the taller columns (L_{eff} = 455 to 2055mm) are close to the linear outcomes (Table 5.11) suggesting that columns in this height range are slender. Ultimate failure loads for the slender imperfect (0.5% of GRP height) columns correlate well with the experimental loads (2.7 -3.4%) with global buckling modes (Fig. 5.30). For column heights of 455mm to 805mm (GRP length 400 to 750mm) no local deformations were indicated. Given the nominal dimensions of the column walls (44mm wide by 6mm thick) these results are to be expected.

5.6 EFFECTS OF INITIAL CURVATURE

GRP profiles used as columns have been manufactured by pultrusion and possess dimensional imperfections. Although the imperfections are within the tolerances stated by the design guides, these imperfections reduce the load bearing capacities of the composite columns. Outer dimensions and wall thickness vary from section to section along the length of the profile. Being practically not feasible to separate out-of-straightness and wall thickness variations in assessing P_L in §5.5, these parameters were considered in a semi-adhoc manner. Of practical interest, however, is an initial

curvature (out of straightness). An assumed average imperfection has been assumed in the form of an approximate half sign wave of the order of the full column height and maximum amplitude at the mid height. In the numerical (FE) simulation, the initial curvature has been defined by three points (at mid and end points) lying on a sine curve, with the mid-point controlling the magnitude (Δ). The initial curvature (Δ) has been taken as percentage of the height of the GRP column in the FE model. The effects on the buckling stability for initial curvatures of 0.5, 1, 2 and 3% of GRP height (Fig. 5.32) have been simulated using the fully non-linear finite element model.

The numerical predictions for composite columns having initial curvatures have been plotted in Fig 5.33 for 51mm box and Fig 5.34 for 44mm box-section. The results indicate initially that the loss of buckling stiffness is proportional to the initial curvature and inversely proportional to the column height. Furthermore, the 44mm box-section is significantly less sensitive to this type of imperfection even though the failure loads at higher column heights are comparable with the 51mm box.

5.7 EFFECT OF IN-PLANE SHEAR

GRP box sections have different in-plane shear modulus in the longitudinal and transverse directions. The longitudinal shear modulus G_{xy} is parallel to the fibres whilst transverse moduli G_{yz} and G_{zx} are normal to the fibre direction. Experimentally measured values of shear moduli, for the 51mm box-section in the directions parallel and normal to the fibres, are G_{xy} = 2.85kN/mm^2 and G_{yz} = G_{xz} = 3.95kN/mm^2 respectively (Tables 3.8-3.11).

The effect of longitudinal in-plane shear modulus is investigated by varying G_{xy} from 2kN/mm^2 to 5kN/mm^2 with a uniform interval of 1kN/mm^2 whilst transverse shear moduli are kept constant at G_{yz} = G_{xz} = 3.95kN/mm^2. The results (Fig 5.35a) indicate that the shear effects are not significant in the slender columns (≤ 4%). In short models however, a loss of 6% is predicted if the G_{xy} is reduced from 5 to 2kN/mm^2.

The loss in buckling resistance by varying transverse shear moduli G_{yz} = G_{xz} from 2 to 5kN/mm^2 with a constant G_{xy} of 2.85kN/mm^2 for various column heights are plotted in Fig 5.35b. Again the effects are not significant for the slender column. However, for short columns the effects are considerable (10-12%). Furthermore, the transverse shear effects are higher in magnitude than the longitudinal shear effects.

5.8 NUMERICAL DESIGN CURVE

A universal design curve based on the numerical failure loads, for the two box-section columns has been developed using the procedure described in Chapter 4 (§ 4.5). The experimental loads have been replaced by fully nonlinear FEA results (Tables 5.10-5.11) and slenderness ratios 'λ' recalculated using (2.19) and measured E_L and moment of inertia 'I' of the modelled cross-sections[‡‡‡]. The minimum short column load 'P_L' has been decided from the failure loads for 400mm GRP high columns (L_{eff} = 455mm), for which FEA solutions converged (51mm box-section) exhibiting local buckling with more than four half sine-waves. The interaction coefficient 'c' for each section, to account for imperfections like the material non-homogeneity and out of straightness (§ 2.2.2.3), has been established graphically by plotting the buckling strength ratios 'q' and 's' (2.5), using numerical (non-linear FEA), P_L and Euler loads (Tables 5.10-5.11). The non-dimensional load factors k_i for all column heights have been calculated using (2.24). The failure loads corresponding to initial imperfections of 0.5 and 1.0% have been used for the development of the numerical design curve.

The P_L for 400mm high GRP columns having 0.5% curvature are 130 and 210kN for 51 and 44mm box-sections respectively. From the FEA results for Δ = 0.5%, the interaction coefficients (Fig 5.36(a) have been established as c = 0.95 for both sections. For the 400mm high GRP columns having imperfections Δ = 1.0%, P_L are 120 and 210kN and interactions coefficients as 0.85 and 0.90 (Fig 5.36(b)), for the 51 and 44mm box-sections respectively. The numerical design curves for the real (imperfect) columns having imperfection equivalent to typically assumed initial central curvatures of 0.5 and 1.0% of the GRP heights, are given in Fig 5.37. The experimental curve (Fig 4.19) has also been include for comparison and limiting 'λ' to 2 to enlarge the area of interest.

Fig 5.37 shows that by increasing imperfections, P_L and column slenderness λ reduces while loss of resistance increases due to interaction and the range of column heights subjected to interaction buckling. Design loads represented by the "imperfect

---

‡‡‡ Moments of inertia 'I' of the two box-section have been calculated using the sectional dimensions (51×51x3.2 and 44×44×6.0mm) and differ from those measured for average sections in § 4.4. However, measured properties ($E_{x,c}$ and G_{yz}) have been used for the calculation of 'λ' and Euler loads.

curves" with a 1.0% initial curvature are conservative as the experimental values are above these curves. The design loads are comparable to the experimental outcomes. Notably, the initial imperfection of 1.0% does not necessarily mean an initial mid-height curvature of 1.0% of the GRP height in the physical columns. Rather, this imperfection is equivalent to any combination of out of straightness, cross-sectional variations, wall thickness variations or load eccentricities. Therefore the curves for the two box-sections corresponding to the initial imperfections of 1.0%, presented in Fig. 5.38, have been recommended as the numerically developed design curves for the safe design columns made from GRP box-section profiles under investigation.

These results establish that inclusion of imperfections (of appropriate intensity) is necessary for the development of a safe design curve (Fig. 5.38). Imperfections, typically in the form of initial curvature, can be included in the FE models of the composite columns to simulate the physical columns. Furthermore, fully nonlinear FE analyses are required to obtain a minimum P_L to draw a safe and representative design curve. The accurate estimation of an interaction coefficient by plotting FEA failure loads is vital as it has a substantial effect on the load factor k_i, for the calculation of design loads.

5.9 EFFECTS OF HOLES

Models have been developed with circular holes in one, two and all four side-walls of the box-section (Fig 5.39). Only slender columns i.e., 1000, 1500 and 2000mm high GRP columns (L_{eff} 1055, 1555 and 2055) have been considered to investigate the effects of introducing openings for services or connections for example. The holes have been typically located at the columns mid-height expecting maximum lateral deflections and axial stresses at the buckling loads. The size of the holes are specified in terms of the d/w ratios where 'd' is the diameter of the hole and 'w' is outer width of the cross-sections. The diameters of the holes in most FE models correspond to the hole-sizes actually employed in the experimental study. For example d/w ratios of 0.3, 0.5 and 0.7 correspond to correspond to 15, 25 and 35mm diameter holes in 51mm box-sections. Similarly d/w ratios of 0.32, 0.45 and 0.57 correspond to 14, 20 and 25mm diameter holes made in the 44mm box-sections. The spacing (interval) between the holes is 20d for 1, 2, and 4 holes. The columns with 8 holes represent models having 4 holes, one in each side, but spacing between the holes is reduced to half i.e.,

10d. Therefore columns with 8 holes have double the number of holes as compared with similar height columns with 4 holes. Columns have been analysed using simple supports and concentric loading and assuming no imperfections. Recognising the heights of the columns as slender, linear elastic (eigenvalue buckling) analysis has been performed. FEA solutions converged and all the models exhibited global buckling modes at failure.

The failure loads for the columns of three GRP heights 1000, 1500, and 2055mm have presented in Tables 5.13-14 and are plotted for various hole-sizes in Figs. 5.40-43. Failure loads have been reduced with the introduction of holes. Generally the reduction is directly proportional to the size of holes and inversely proportional to the heights of the columns. The loss of resistance for 51mm box-sections (Fig 5.40), with 1-4 holes for small holes ($d/w \leq 0.3$) is minimal ($\leq 5\%$), but increase to15% for larger holes ($d/w = 0.7$). By reducing the spacing to $10d$ (8 holes), buckling loads decreased by more than 28%.

Similar trends of loss in buckling stiffness with holes have been exhibited by the 44mm box-sections (Figs 5.42-5.43). However the reduction in the failure loads is less when compared to the 51mm box-section. This infers that thicker walls (webs) are less affected by the perforations. For smaller holes ($d/w \leq 0.32$) loss of stiffness is less than 5% and increases to 11% for bigger holes for 1000mm high columns with 1-4 holes. For columns with 8 holes (spacing $=10d$) the loss of stiffness is 17.5%.

Comparing the loss of stiffness due to the spacing between the holes, especially in the thin walled section, it is recommended that interval between the holes should be limited to $20d$.

Experimental loads for columns with similar holes have also been added to the Figs 5.40-5.43, for comparison. Experimental loads are lower than predicted (Figs 5.40, 5.42) with a greater loss of buckling load (Figs 5.42, 5.43). This is because: firstly, FEA loads are for perfect column overestimating the failure loads for physical columns; and secondly, the failure loads used for the calculation loss, for columns with loads for perfect columns are also higher than the experimental loads of columns without holes.

The axial stresses around the holes (Figs. 5.44-5.46) are well within the ultimate compressive stresses, however the stress zones further spread in the case of bigger

holes. The stress distributions are symmetric outer side of the holes indicating uniform compression.

5.10 CONCLUSIONS

1. Linear elastic (Eigenvalue) analysis has successfully been used for the prediction of critical buckling loads of slender columns. In slender columns failure is due to bifurcation of the primary equilibrium path into a secondary (stable or unstable) path. Linear analysis is capable of predicting this bifurcation point and the critical load. At critical loads, slender columns deform into half sine wave (global buckling) of length equal to the effective length of the column. Buckling occurs within elastic limits without any failure or damage of the material (column recovers its shape if the load is removed). 51mm and 44mm box-sections of the type analysed (and tested in chapter 4) are classified as slender for heights 655mm and 555mm, respectively, assuming simple end restraints. The predicted loads have been confirmed by both analytical (Euler including shear effects) and experimentally measured loads. The applicability and reliability of the linear analysis using actual orthotropic properties has been established for slender columns.

2. For short columns, not exhibiting global buckling modes, linear buckling analyses are inappropriate. Reduction in the convergence norm to force "convergence", leads to the prediction of inaccurate and unreliable failure loads. If the solution fails to converge, a failure mode different to buckling may be implied (e.g. material crushing in short columns). In this case a nonlinear analysis should be undertaken. For the 51mm and 44mm box-sections tested, column heights of less than 455mm are included in this category.

3. Geometrically non-linear (Total Lagrangian) analysis has predicted local buckling in the 51mm box-section short columns. The side-walls (webs) show inward and outward deformations (sine-waves) along the length of columns. It is concluded that wave like formation starts at the mid-height and propagates towards ends giving rise to an odd number of half sine waves. The number of half sine waves in local buckling depends upon the height of the GRP specimen. If the column is high enough to accommodate an integer number of

waves, all waves are fully developed. Otherwise, the waves towards the supports are of reduced amplitude. The length of half sine-waves remained approximately constant at 62.5mm for various heights of short columns compared with an analytical value of 64.4mm. However, an experimental value is not available.

4. The reliability of the numerical results obtained from a geometrically nonlinear analysis depends on the numerical convergence of the solution. Simulation models of 200 and 300mm GRP columns failed to converge and predicted incorrect and unreasonable buckling loads. For column heights of 400mm and above, the analyses converged providing good estimates of failure loads. The stress contours plotted on the deformed shape provided an indication of the failure mode. At the wave crests, predicted stresses exceeded the physical material limits, implying that in physical tests bursting and tearing across the section would have occurred. The most developed half sine wave at the mid-height of the column initiated failure by bursting of the specimen in the experimental observations.

5. Short columns failure loads, considering material nonlinearity, are lower than the geometrically nonlinear analyses. Plots of the stress contours just before the failure reveal that stresses (and strains) are within the limit of the defined nonlinearity. The strains (and hence the stresses) are high due to reduced elastic moduli beyond the elastic limit. It is after reaching the failure loads, strains (and hence stresses) increase rapidly and exceed the ultimate limits, implying bursting and tearing of the section. Nonlinear strains are only seen at the crests of local buckling waves and at column end under the steel plate subjected to high stresses. Conversely plots of the elastic strains show a uniform distribution along the length of the column. It is further concluded that nonlinear analyses in the short column range are needed to establish the local buckling mode, number of half sine waves, length of the half sine wave, and most importantly to predict P_L for the construction of design curve. The half sine wave length predicted for the 51mm box-section (62.5mm) is comparable with the theoretically calculated value (64.4mm in § 4.4.2). Half sine wave length for 44mm box-section is not available as no local buckling was predicted for this section. P_L for the 51 and 44mm box-sections are

predicted as 135 and 210kN respectively in comparison to the 120 and 220kN established experimentally. The difference between the values can be attributed to the imperfections involved both in geometry and testing configurations.

Critical buckling loads for the slender columns (of both sections) predicted from fully non-linear analyses are comparable to the linear elastic predictions. In slender columns the strains (and hence the stresses) were below the ultimate limits of the material and sections did not rupture. Furthermore, the failure loads for elastic and nonlinear analyses are similar because the material is not highly nonlinear. Infact, a pseudo type nonlinearity with minimal stress hardening has been assumed in the material properties. No nonlinear strains have been observed in the case of slender columns. Rather, elastic strains are uniformly distributed along the heights of slender columns.

However, the fully-nonlinear (elastic degrading) predictions for the straight columns are higher than the experimental results. Introduction of the load eccentricity and initial curvature at mid-height as the sources of imperfection decreased the failure loads. The effect of initial curvature is more pronounced than load eccentricity. The failure loads considering eccentricity and curvature combined, are lower than the experimental loads. This demonstrates that accurate predictions using nonlinear analysis (particularly) for short columns, are possible provided that imperfections can be accurately estimated.

Deformed geometries obtained by nonlinear analyses (both elastic and nonlinear) for the slender perfect columns (of both box-sections) fail to indicate global buckling. However, the buckling mode shapes are recovered by introducing imperfections in the form of initial curvature. This establishes that global buckling is initially induced by the presence of geometric imperfections.

6. Buckling resistance is sensitive to initial curvature (as a source of imperfection) and inversely proportional to the column height and the thickness of the section walls (webs). For the box-sections analysed, an initial curvature of 0.5% of GRP length can reduce critical buckling loads by 15% in short to 10% in long columns for 51mm box-section, and 12% in short and 7%

in long columns for the 44mm box-section. When combined, eccentricity and initial curvature induce substantial reductions in the load carrying capacities of the composite columns.

7. The effects of in-plane shear stiffness are negligible in the slender columns of both box-sections. However, the effect of transverse shear modulus is significant particularly in short columns. For example, the buckling stiffness of 455mm high column can be reduced by 15% if the transverse shear modulus is decreased by 50%.

8. A numerical "FEA design curve" has been plotted using predicted P_L and ultimate failure loads for various heights of the both box-section perfect and imperfect columns. The ultimate failure loads for columns assumed as perfect overestimate the ultimate failure loads and not represent the real columns. Perfect columns do not exhibit interaction of modes, observed in the physical testing for a range of column heights between short and slender columns. FEA design curve corresponding to the imperfect columns can predict safe buckling loads. The predicted FEA loads using fully non-linear analyses have successfully been used for the development of the design curve yielding design loads for all the practical heights of both the 51 and 44mm box-section columns. Imperfections in the FEA models can typically be included in the form of initial curvature representing accumulation of all kinds of physical imperfections. Interaction coefficient 'c' representing the interaction between the isolated buckling modes and reducing the column stiffness, mainly depends upon length of the column, minimum column load P_L and the cross-section. Choosing a suitable single interaction constant can aggregate design curves for various box-section profiles. Recommended design curves to the tested box-sections are given in Fig.5.38.

9. Circular holes can be formed (drilled) in the sidewalls (webs) of the GRP box-section profiles without loosing considerable loss of stiffness (loss $\leq$ 5%), if the size of the holes is kept small ($d/w \leq 0.3$). However, for bigger holes the loss in the stiffness can reduce considerably (up to 25%). An interval (spacing) between the consecutive holes, equal to 20 times the diameter of the hole, has been recommended limiting the maximum loss of buckling stiffness lower than 15%.

5.11 RECOMMENDATIONS RELATED TO THE USE OF FEA AND THE INTERPRETATION OF NUMERICAL SOLUTIONS.

The finite element method has been successively used for the prediction of ultimate failure loads of composite columns of various heights. The predicted loads, when compared with experimentally measured and analytical calculated failure loads, have shown a reasonable correlation. The predicted loads have also been used for the development of FEA design curves for the GRP two box-sections. For the efficient performance of the FEA procedures and to obtain accurate results, the following recommendations are made.

Appropriate finite element models, representing the true geometrical configuration of the structure (concentric columns in this study) are developed. Boundary conditions i.e., external supports applied to the FE modes should simulate the restraints applied by the actual physical supports to the structures. The expected behaviour of the physical structure under the applied load can provide the guidance in providing extra restraints and the location and type of load in the FE model. The type, order, shape and degrees of freedom for finite elements used for discretisation of the structure should be decided considering the nature of deformations exhibited by the physical structure. The type of analyses may also depend upon the required results. For example, linear analysis is needed if the deformations are small and do not alter the boundary or loading conditions during the analysis. Or eigenvalue buckling analysis is performed when linear stability formulations are applicable. Similarly a full nonlinear analysis is performed when both geometry and material undergo changes as the load increases. Preliminary analysis with coarse mesh may be performed to establish the proper working of the analyses and resulting behaviour of the structures. Once the finite elements modelling the structure, boundary and loading conditions and type of analysis is established, mesh may be refined to increase the accuracy of the predictions.

After preparing the numerical models of vertically oriented, simply supported, and concentrically loaded straight GRP columns, FEA analyses are performed for the predictions of failure loads. For this, the following rules are recommended:

A linear elastic (eigenvalue analysis) should be performed initially to infer the nature of the failure mode of a column. If the deformed shape indicates Euler (global)

buckling, the column height is grouped as slender and the eigenvalue load taken as the critical buckling load. If the solution fails to converge or converges without indicating any failure mode, a nonlinear may be performed to find out the type of buckling.

If a geometrically nonlinear analysis indicates local web-buckling and the number of developed half sine waves is more than four and the peak stresses and peak stresses are lower than the material strength, then the predicted loads should be taken as the ultimate failure loads for the corresponding heights. However, the quality of the prediction of these loads may further be improved by performing a fully nonlinear analysis, especially if the material exhibits any nonlinearity at higher stresses. A fully non-linear analysis is essential if the peak stresses exceed the material capacity. Fully nonlinear analyses may also improve the prediction of failure loads for slender columns, but the difference decreases with the height of the column. To simulate the real columns, initial imperfections can be introduced in the form of wall thickness variation, load eccentricity, out of straightness or a combination of these imperfections. These rules are also applicable for the prediction of failure loads of the columns with circular holes in the webs.

FEA design curve developed using the FEA predicted loads for perfect columns, overestimates the design loads. To simulate the buckling of real columns, imperfection in the form of initial curvature has been included. The intensity of the initial imperfections may be decided by the ultimate loads when compared with the experimental results. The FEA design curve for the imperfect columns successfully indicates local, interaction and global buckling characteristic of the actual column behaviour for different heights. This establish that Design curve for the two box-section profiles may be developed using fully nonlinear numerical analyses of imperfect columns. The procedure can be used to develop design curves for other GRP box-sections, if the accurate mechanical properties and initial imperfections can be estimated.

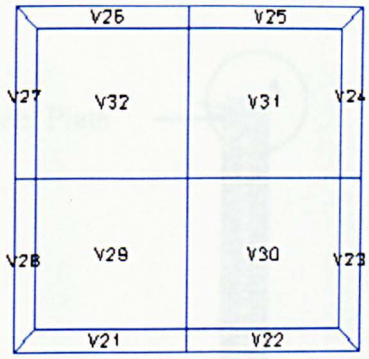

(c)

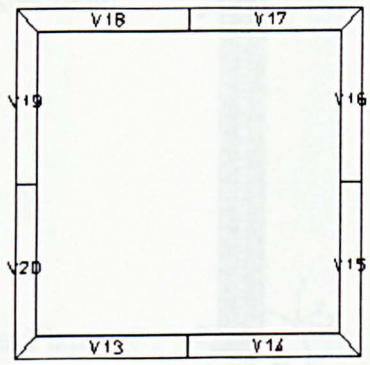

(b)

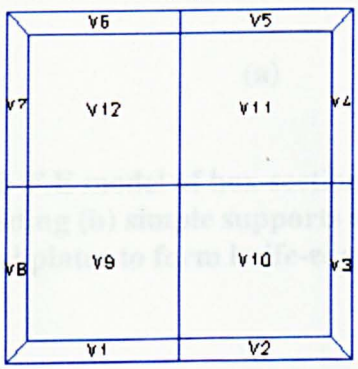

(a)

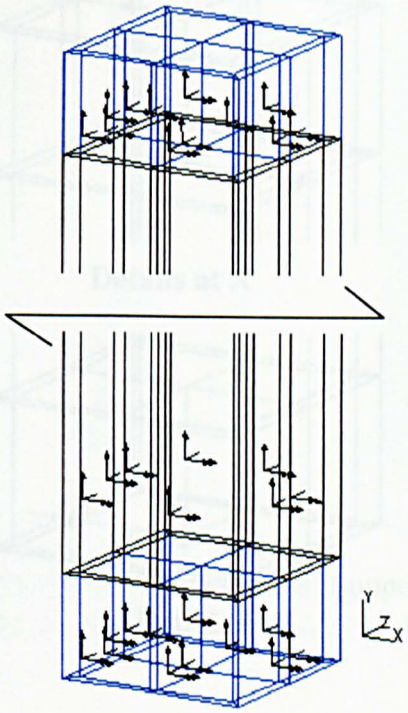

(d)

Fig 5.1 A typical 3-dimensional finite element model of composite column fixed with steel plates at both ends; (a) lower steel plate presented by 12 volumes, (b) GRP thin wall section presented by 8 volumes, (c) upper steel plate presented by 12 volumes and (d) three dimensional configuration of the model.

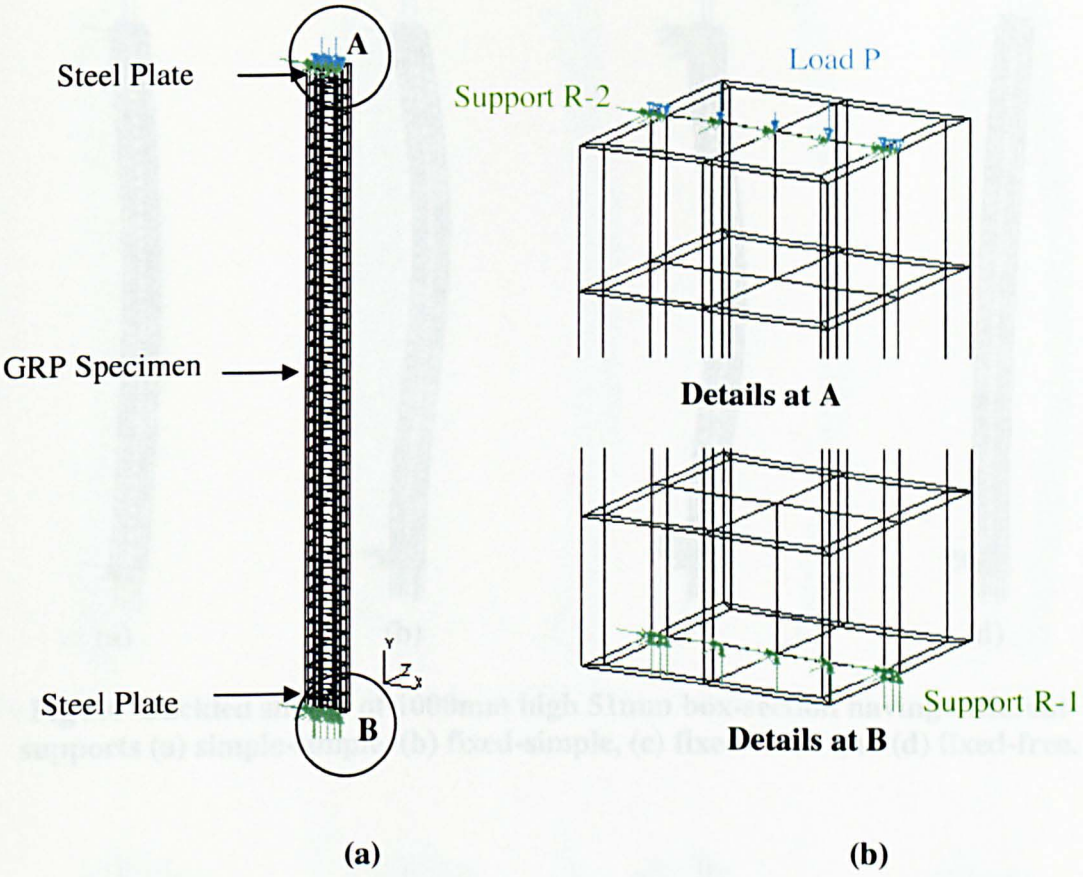

Fig. 5.2 F.E model of box-section column, (a) showing regular mesh , supports and loading (b) simple supports assigned to the central line of lower and upper steel plates to form knife-edge supports and axial compressive loading.

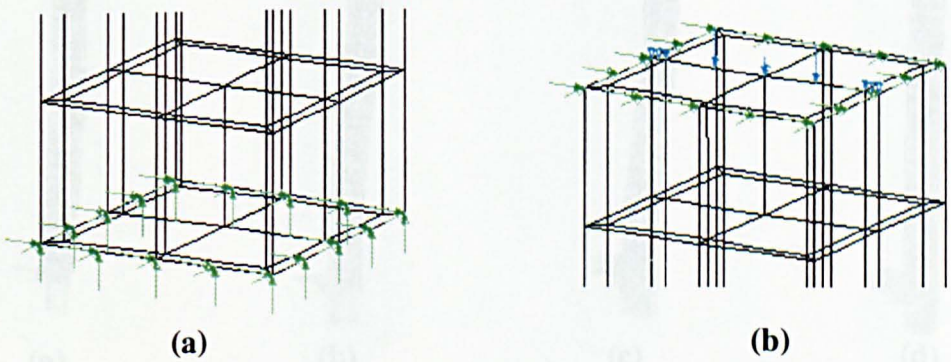

Fig 5.3 Fixed supports (green) assigned to (a) lower and (b) upper, steel plates.

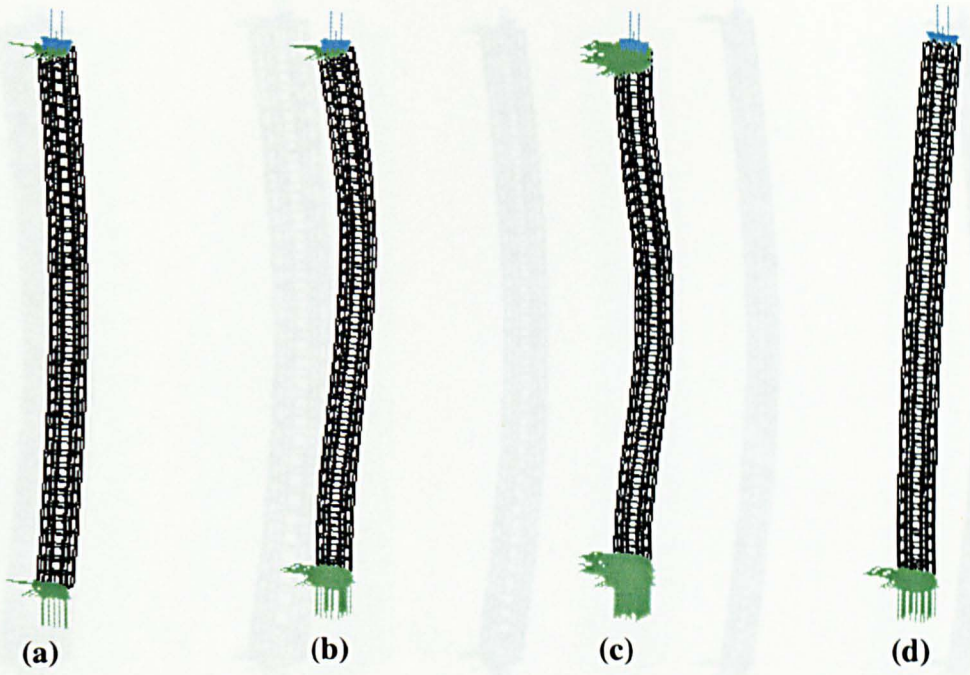

Fig 5.4 Buckled shapes of 1000mm high 51mm box-section having different supports (a) simple-simple, (b) fixed-simple, (c) fixed-fixed and (d) fixed-free.

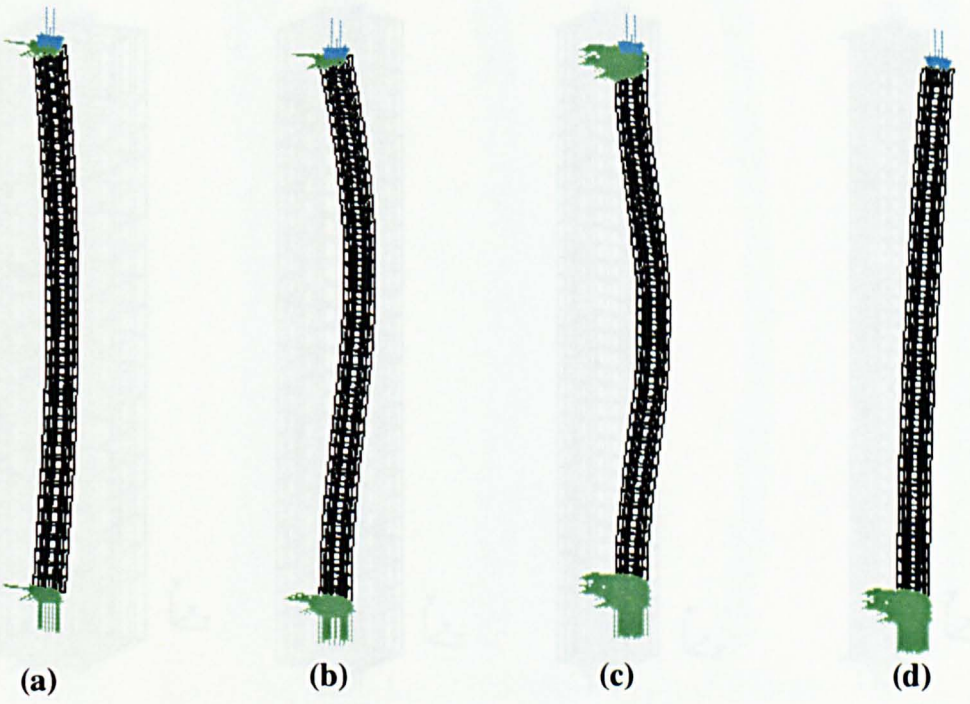

Fig 5.5 Buckled shapes of 1000mm high 44mm box-section having different supports (a) simple-simple, (b) fixed-simple, (c) fixed-fixed and (d) fixed-free.

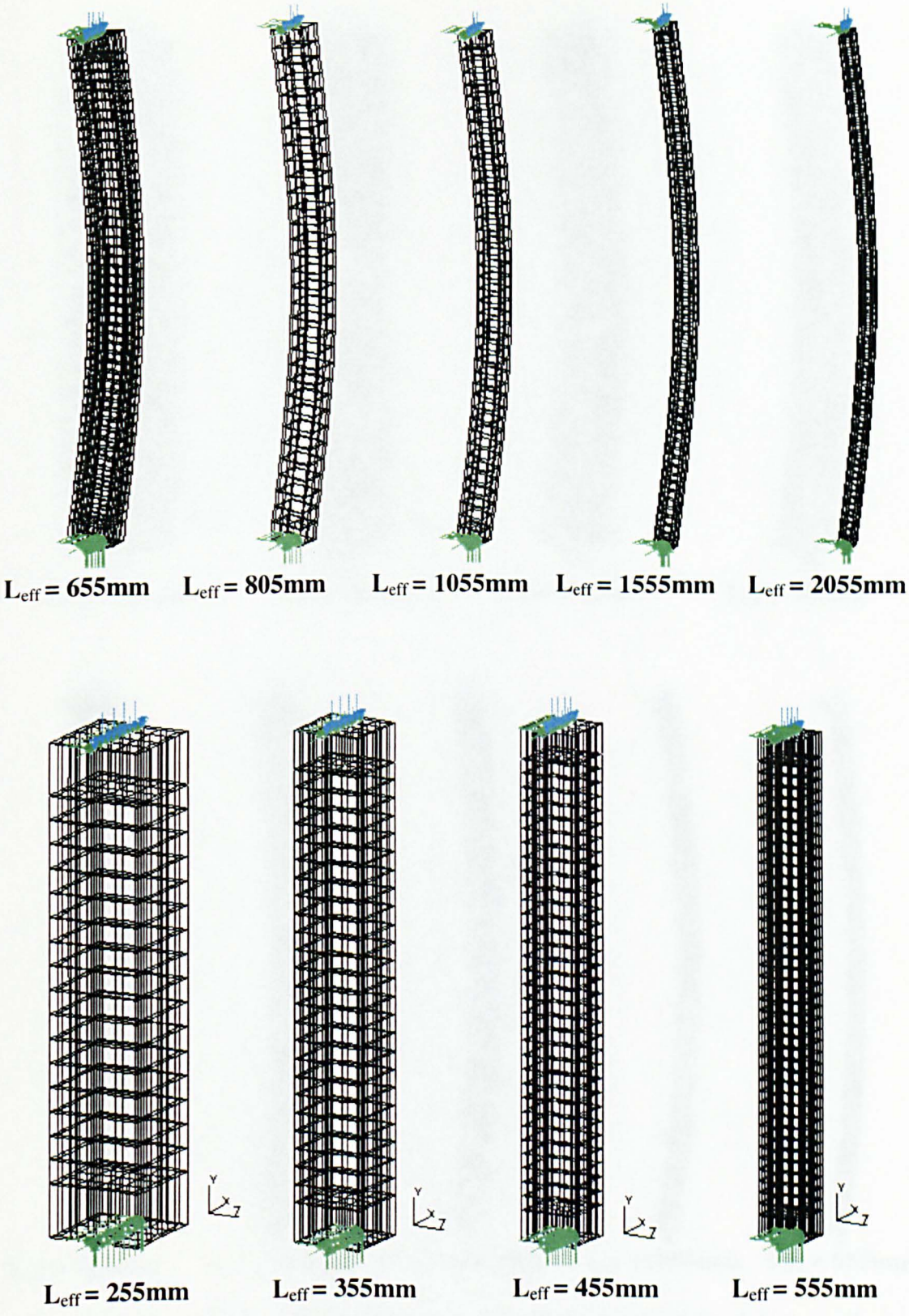

Fig 5.6 Linear elastic (Eigenvalue) buckling of the 51×51×3.2mm box-sections.

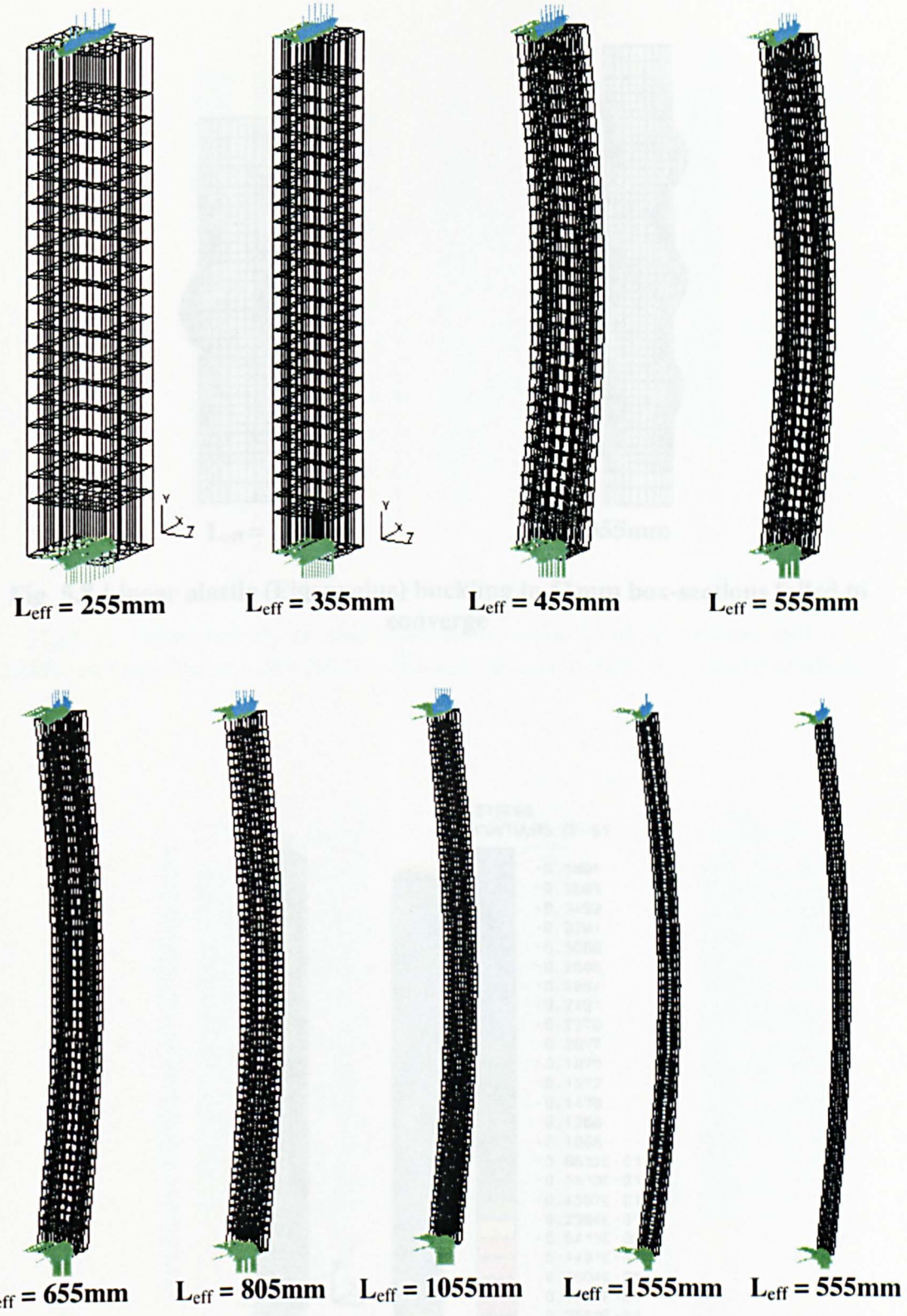

Fig 5.7 Linear elastic (Eigenvalue) buckling of the 44×44×6.0mm box-sections

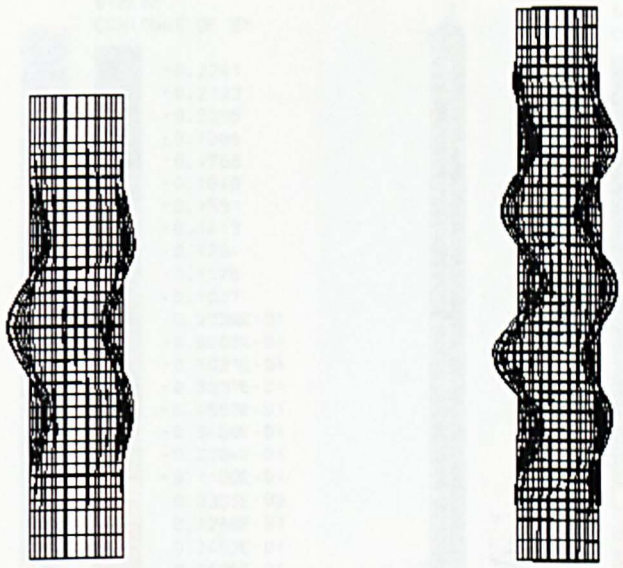

L_{eff} = 255mm L_{eff} =355mm

Fig 5.8 Linear alastic (Eigenvalue) buckling in 51mm box-sections failed to converge

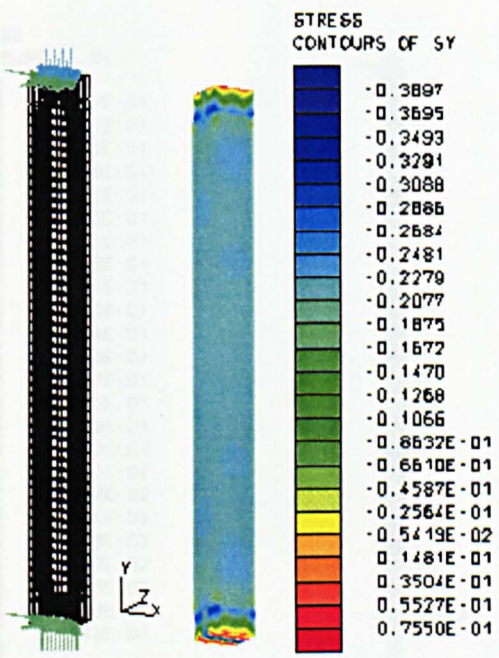

Fig 5.9 Deformed shape and axial stress contours of 655mm high 51mm box-section (geometrically non linear analysis).

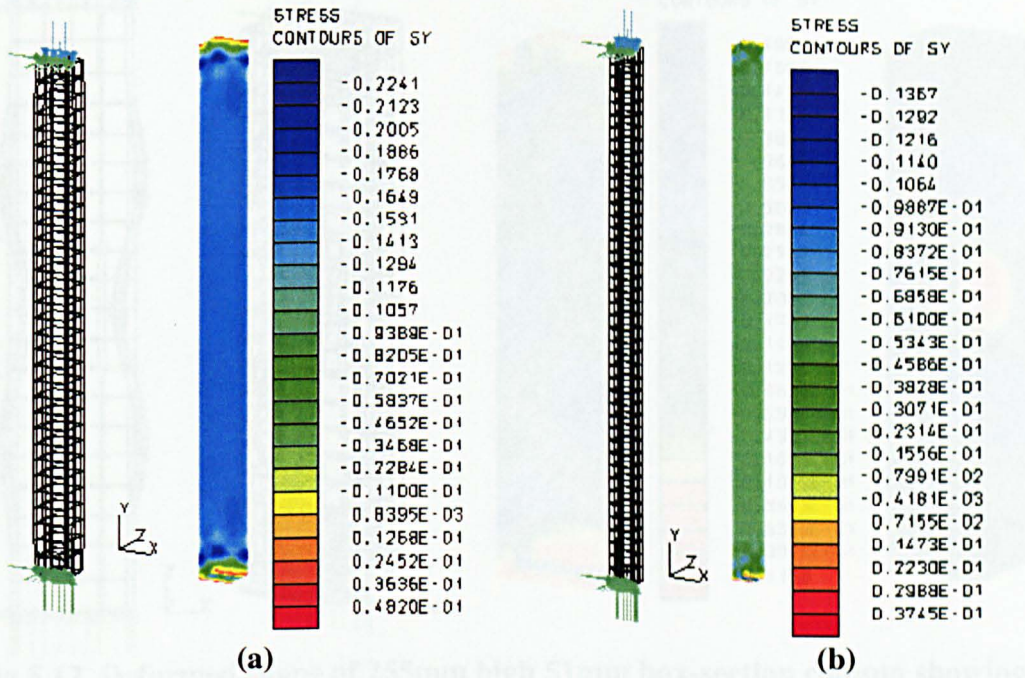

(a) (b)

Fig 5.10 Deformed shape and axial stress contours of (a) 805mm and (b) 1055mm high 51mm box-section columns (geometrically non linear analysis).

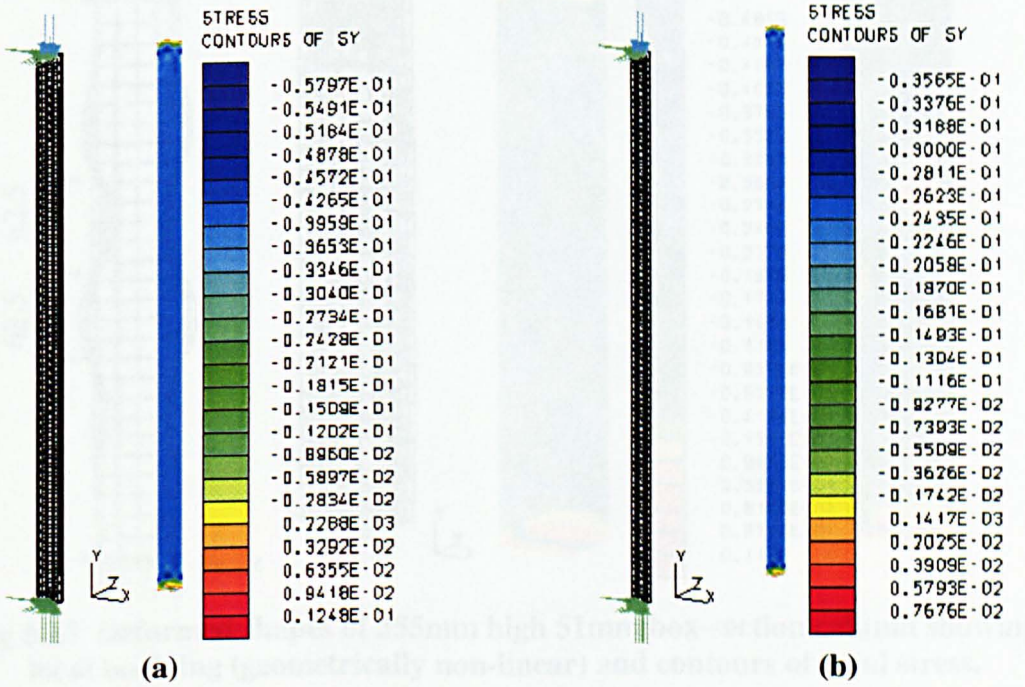

(a) (b)

Fig 5.11 Deformed shape and axial stress contours of (a) 1555mm and (b) 2055mm high 51mm box-section columns (geometrically non linear analysis).

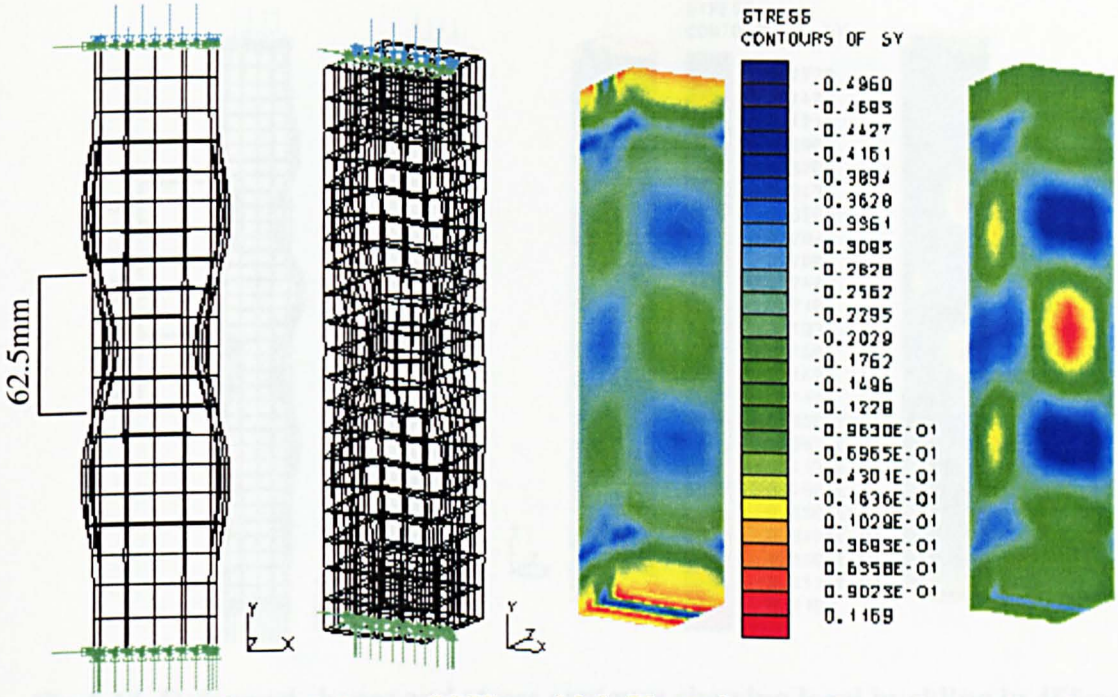

Fig 5.12 Deformed shape of 255mm high 51mm box-section column showing local buckling (geometrically non-linear) and contours of axial stress.

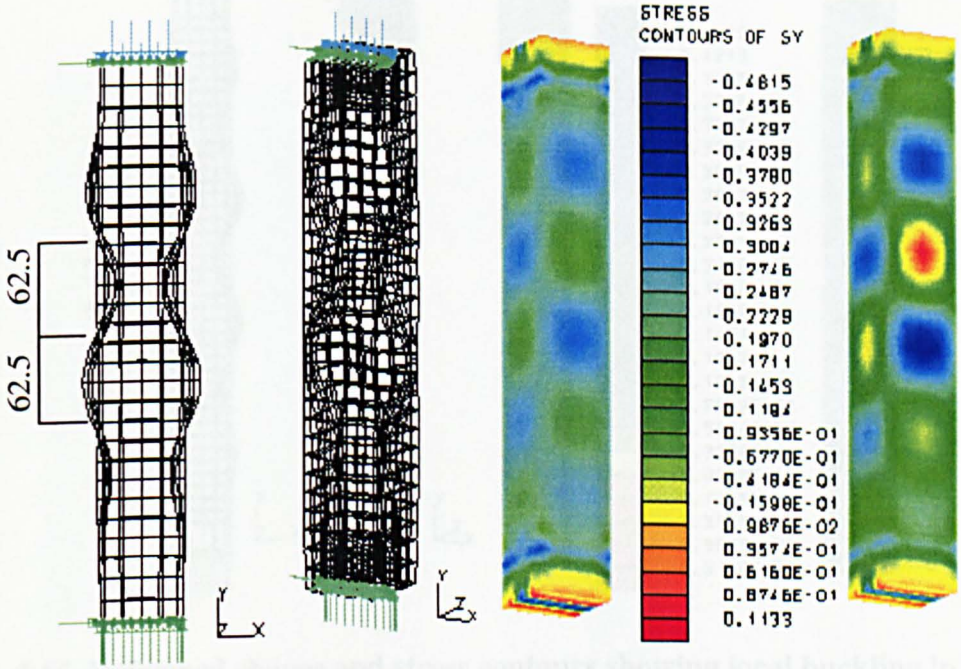

Fig 5.13 Deformed shapes of 355mm high 51mm box-section column showing local buckling (geometrically non-linear) and contours of axial stress.

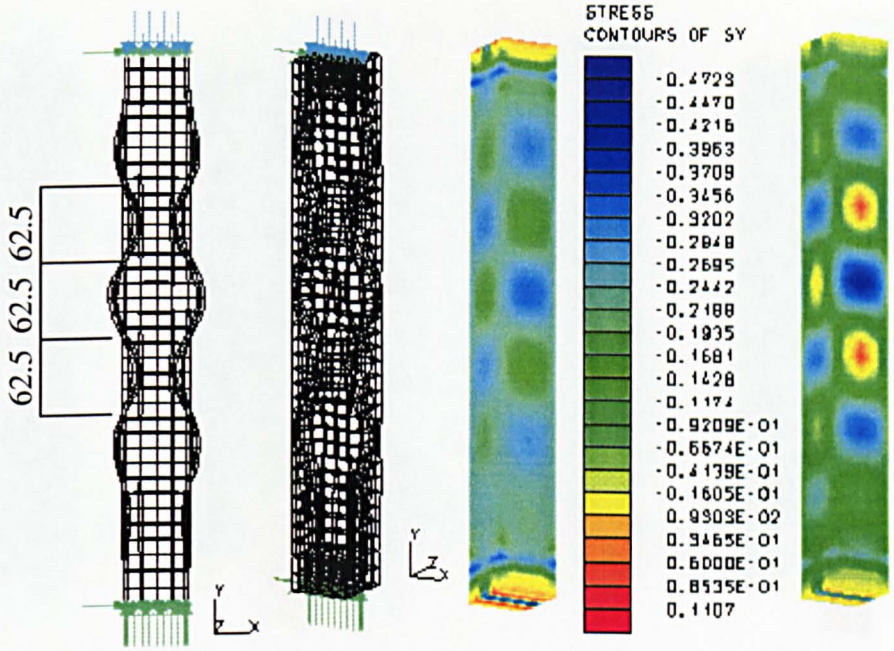

Fig 5.14 Deformed shapes and stress contours showing local buckling in 455mm high 51mm box-section (geometrically non-linear). 5 half sine waves are visible.

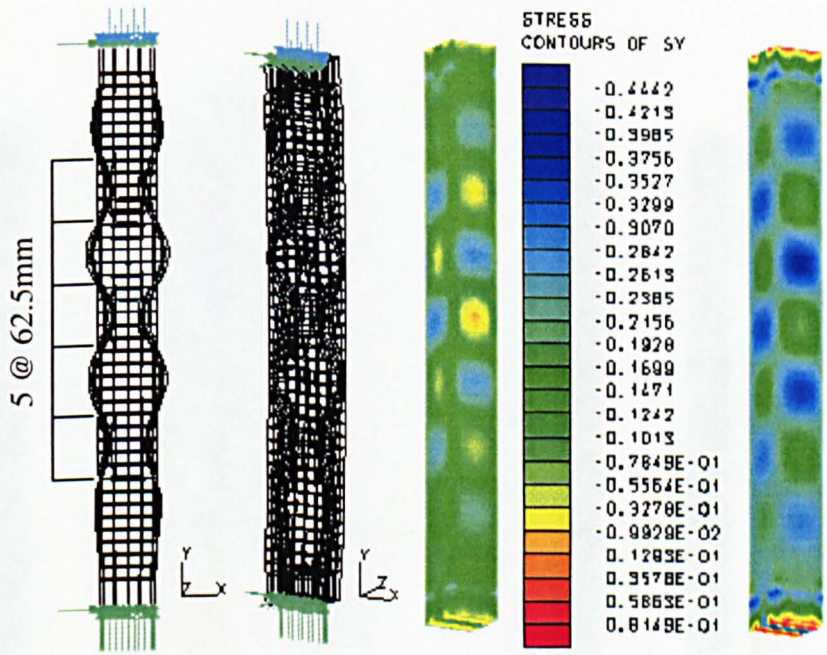

Fig. 5.15 Deformed shapes and stress contours showing local buckling in 555mm high 51mm box-section (geometrically non-linear). 7 half sine waves are visible.

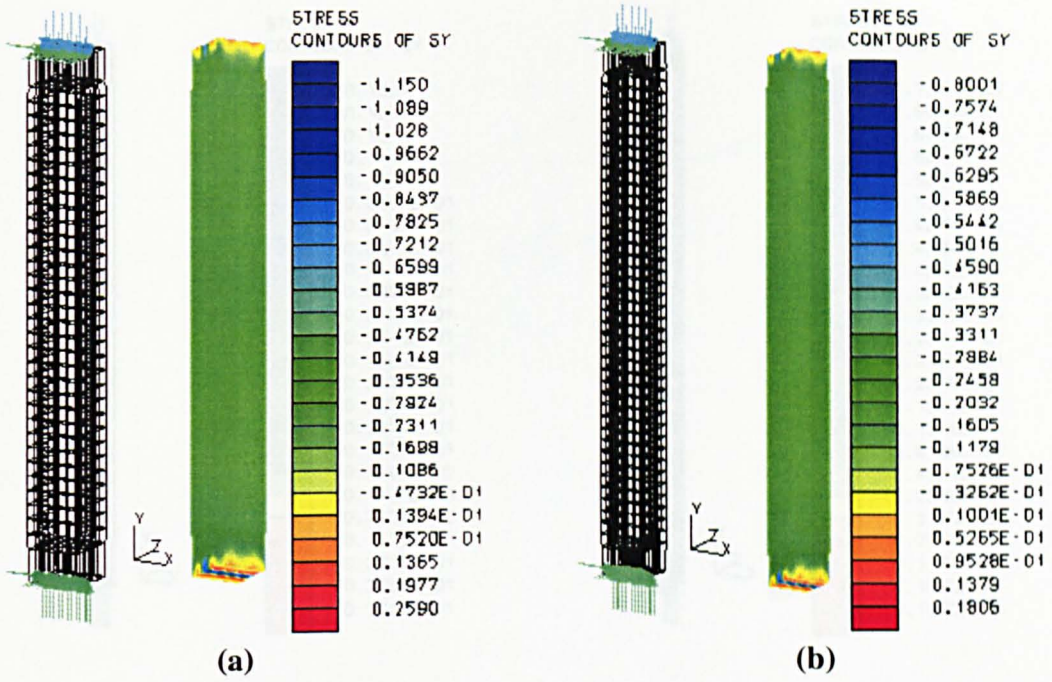

(a) (b)

Fig 5.16 Deformed shapes and stress contours of (a) 455mm and (b) 555mm high 44mm box-section columns, obtained by nonlinear analysis.

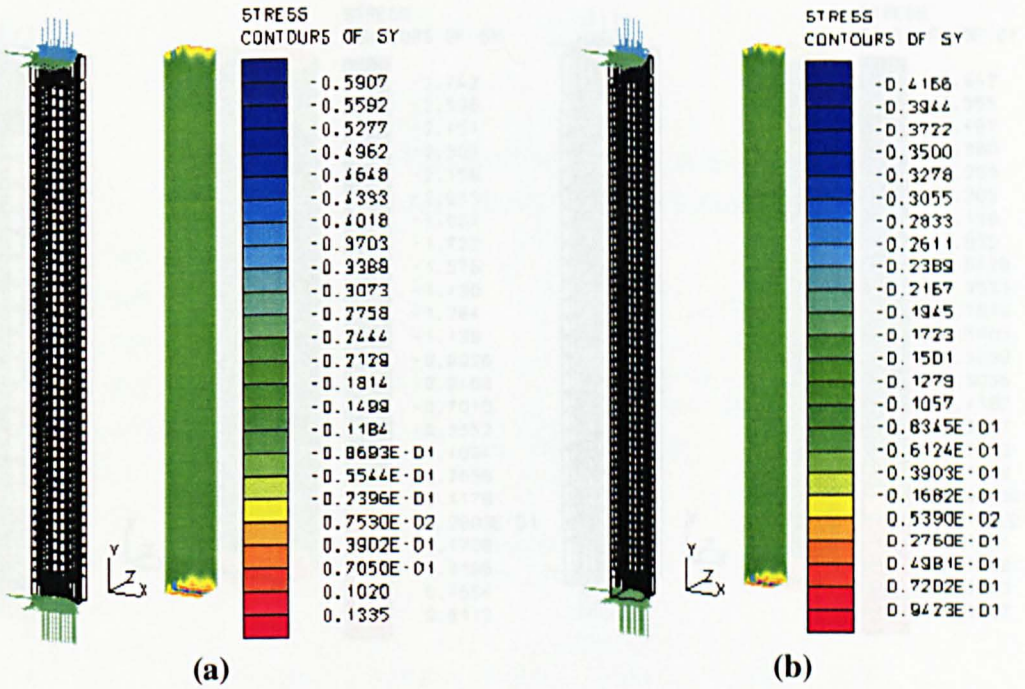

(a) (b)

Fig 5.17 Deformed shapes and stress contours of (a) 655mm and (b) 805mm high 44mm box-section columns, obtained by nonlinear analysis.

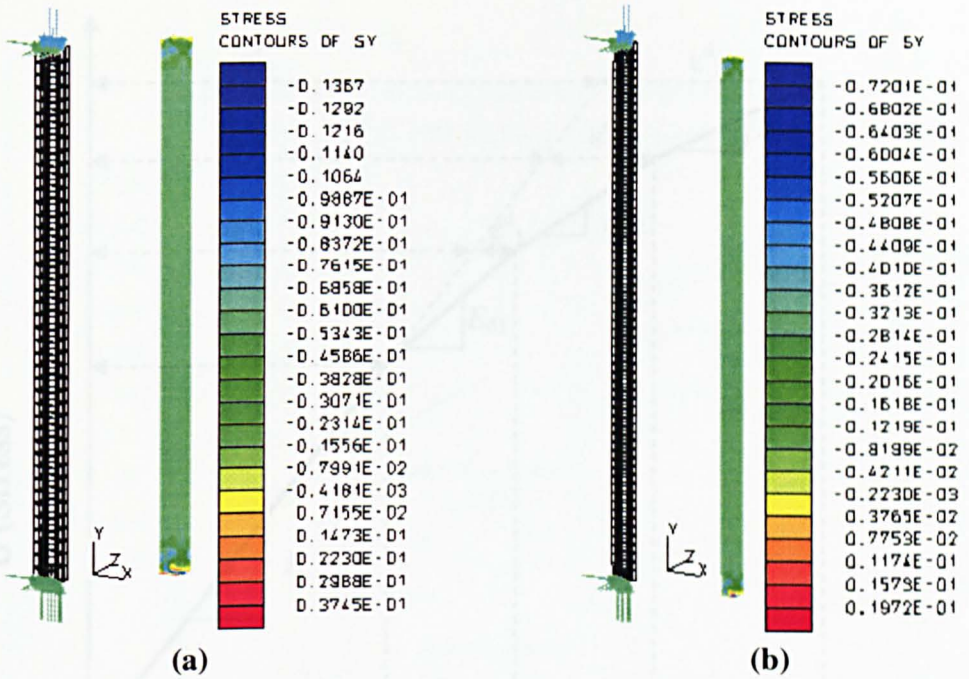

Fig 5.18 Deformed shapes and stress contours of (a) 1055mm and (b) 1555mm high 44mm box-section specimens, obtained by nonlinear analysis.

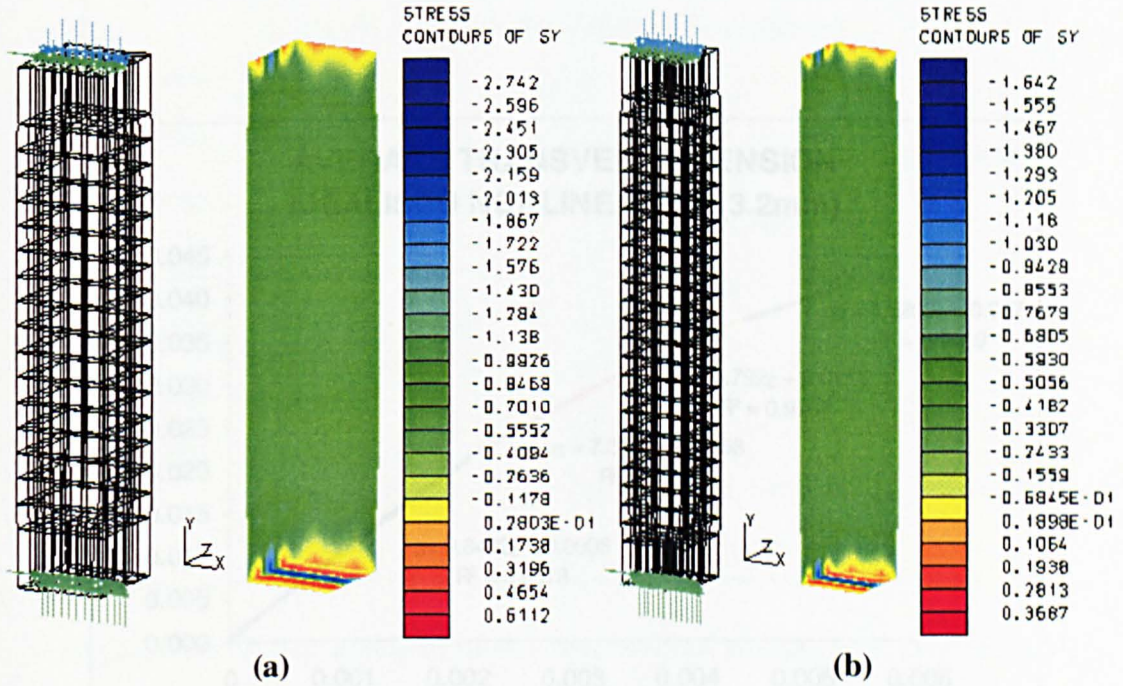

Fig 5.19 Deformed shapes and stress contours of (a) 255mm and (b) 355mm high 44mm box-section specimens, obtained by nonlinear analysis.

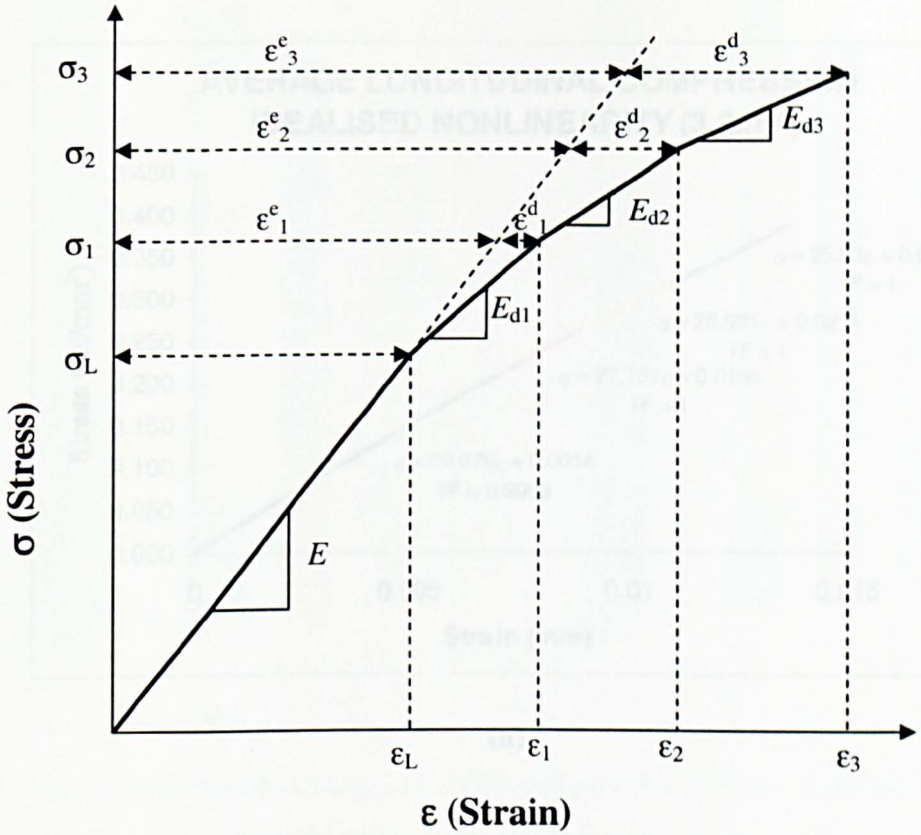

Fig 5.20 Nonlinear idealization of the material response.

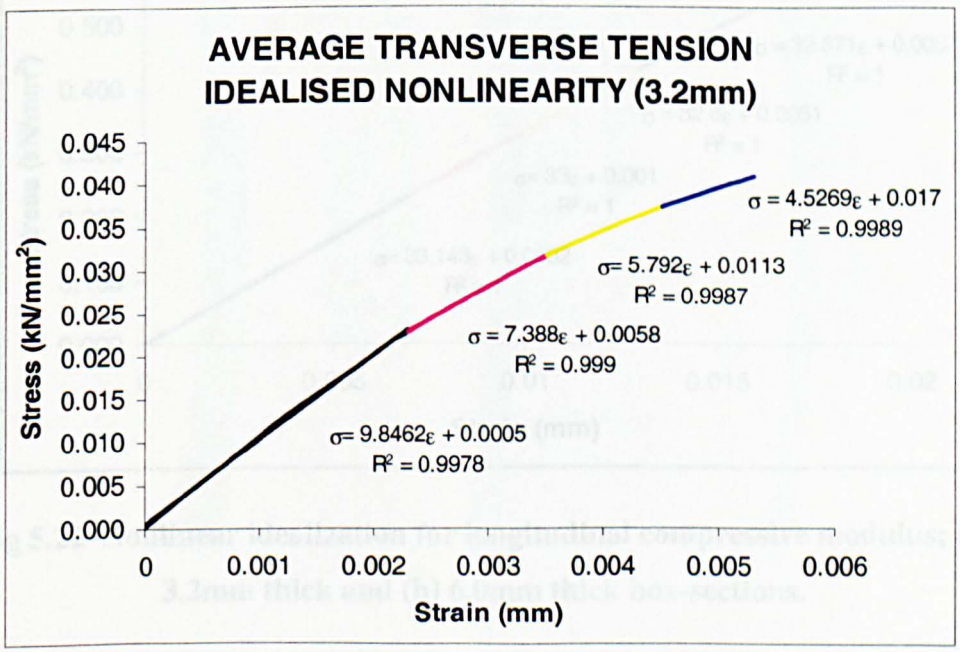

Fig 5.21 Nonlinear idealization for transverse tensile elastic modulus

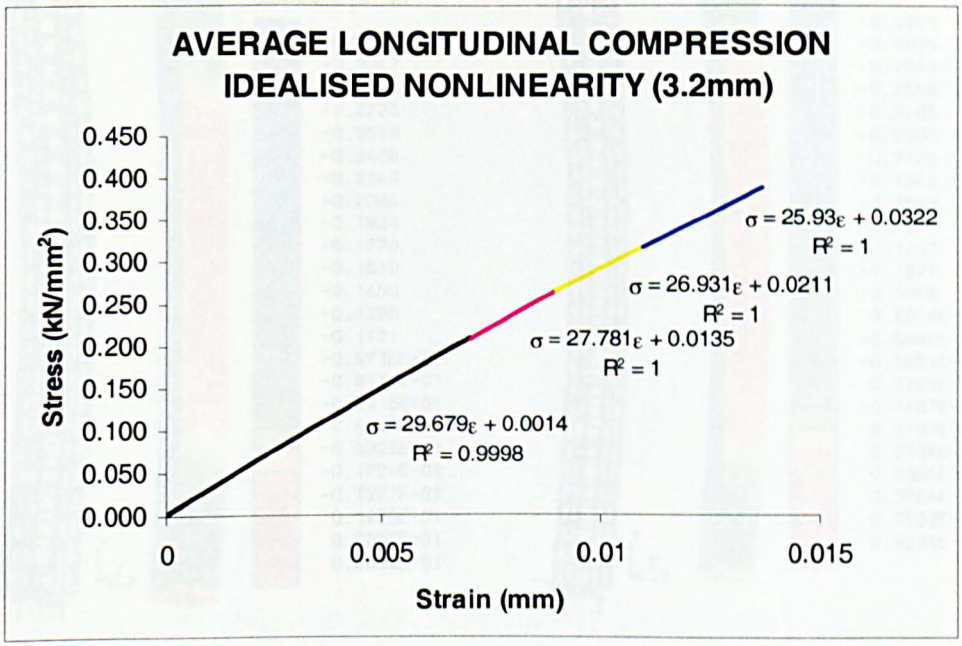

(a)

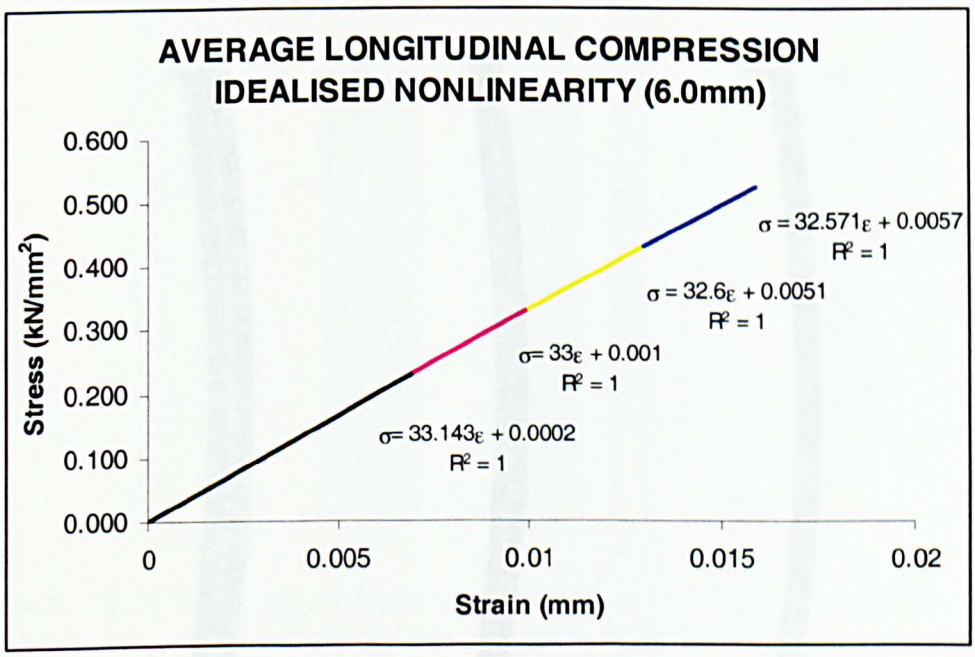

Fig 5.22 Nonlinear idealization for longitudinal compressive modulus; (a) 3.2mm thick and (b) 6.0mm thick box-sections.

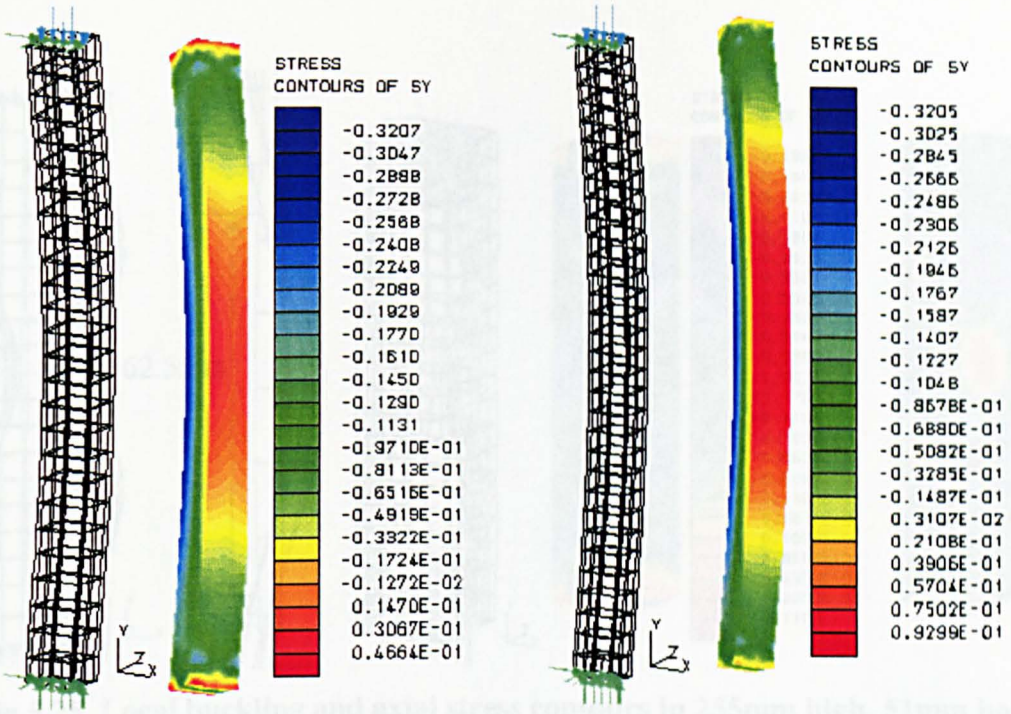

(a) (b)

Fig. 5.23 Global buckling in (a) 655mm and (b) 805mm high nonlinear (Hoffman) models of 51mm box-section

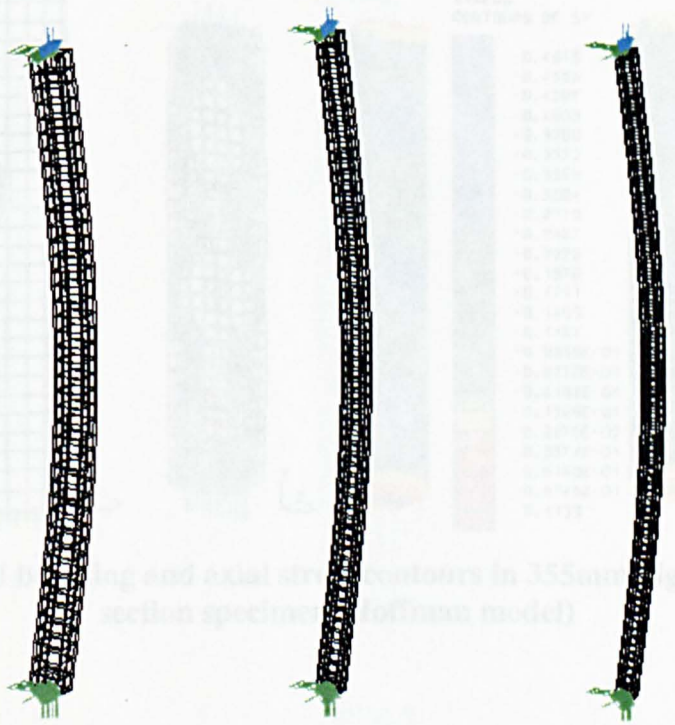

(a) (b) (c)

Fig. 5.24 Global buckling in (a) 1055mm (b) 1555mm and (c) 2055mm high nonlinear (Hoffman) models of 51mm box-section

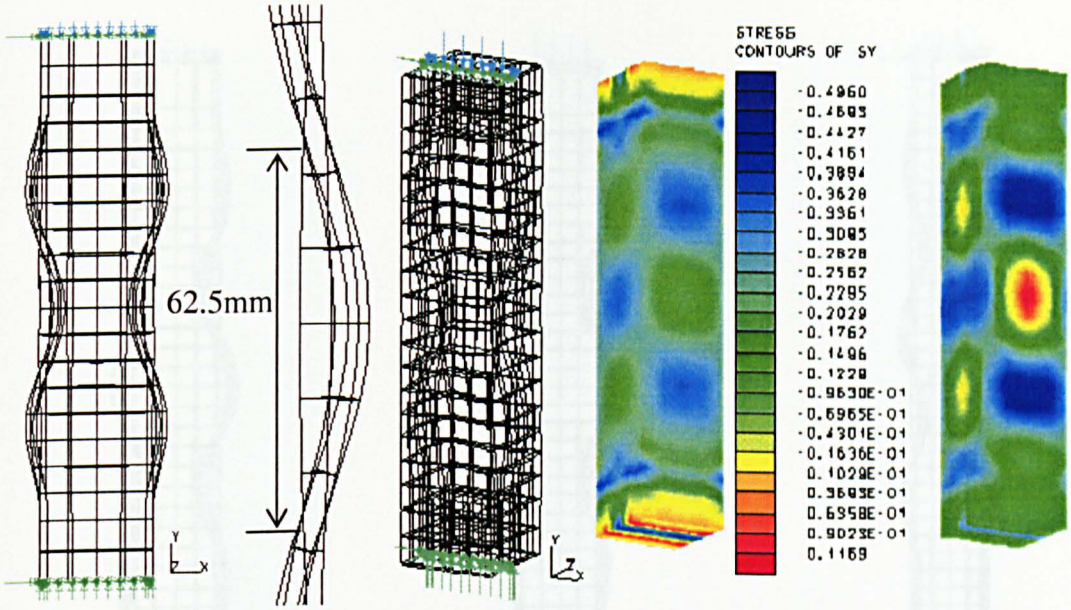

Fig 5.25 Local buckling and axial stress contours in 255mm high, 51mm box-section specimen (Hoffman model)

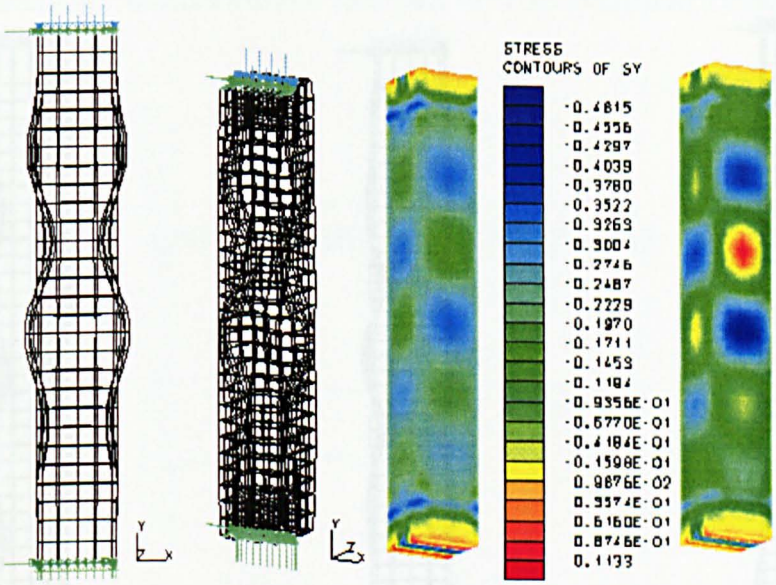

Fig 5.26 Local buckling and axial stress contours in 355mm high, 51mm box-section specimen (Hoffman model)

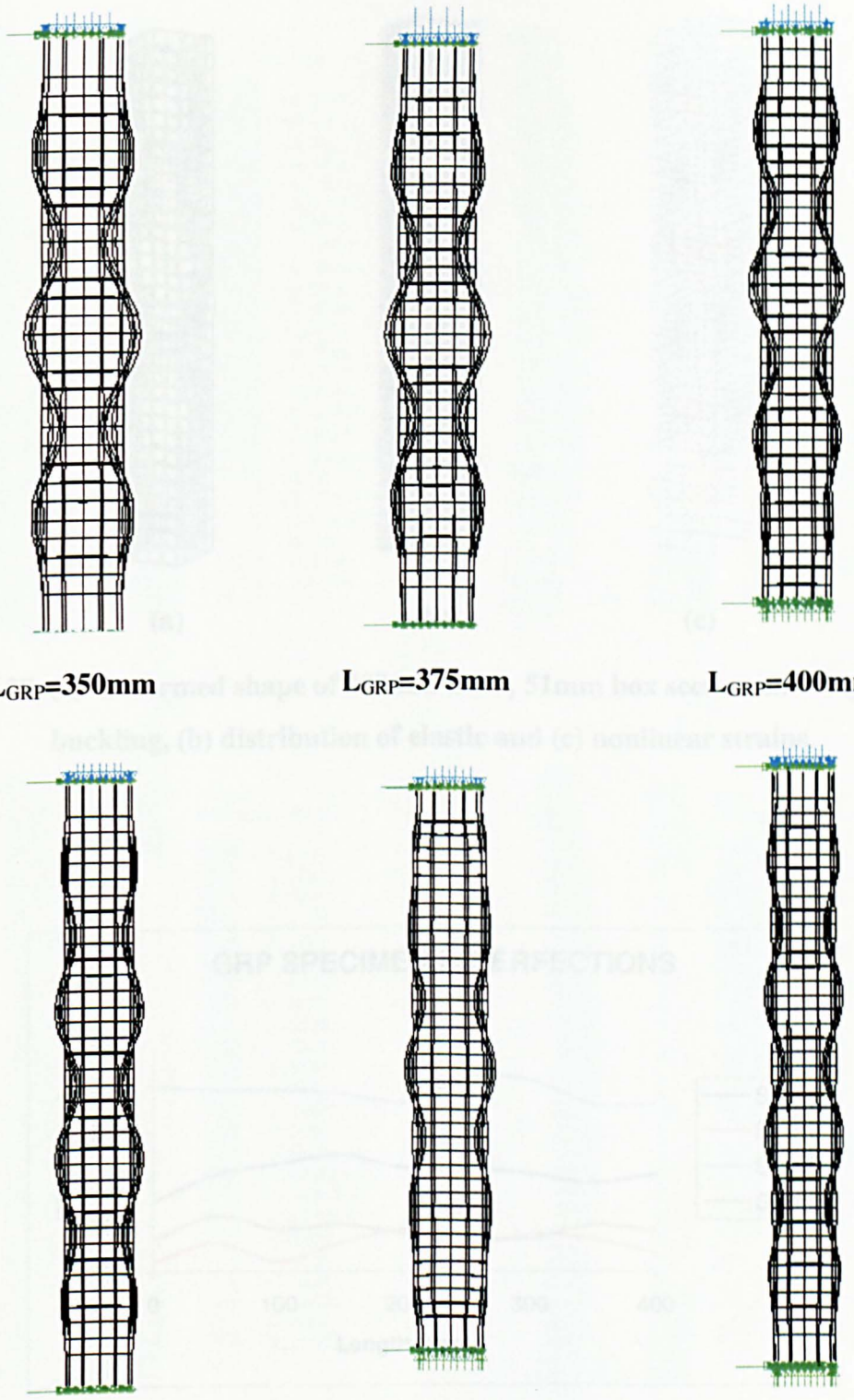

Fig 5.27 Local buckling modes of 51mm box-sections showing number and lengths of half sine waves (Hoffman model).

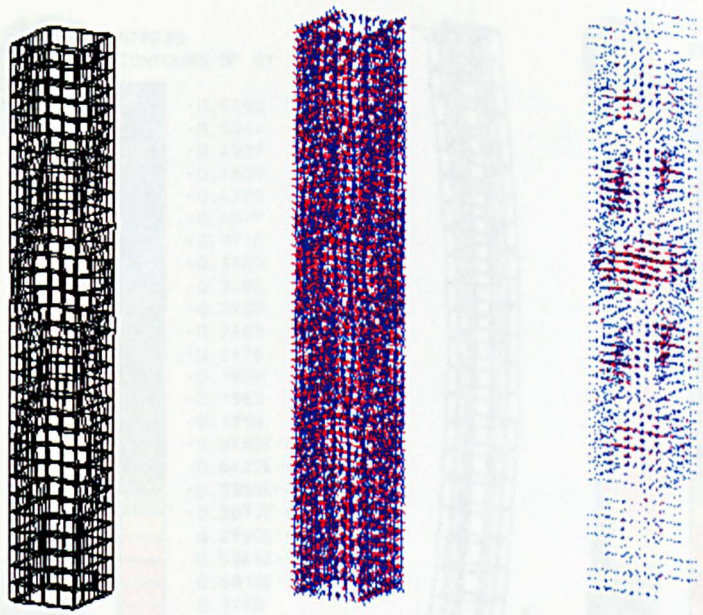

Fig 5.28, (a) Deformed shape of 400mm GRP, 51mm box section showing local buckling, (b) distribution of elastic and (c) nonlinear strains.

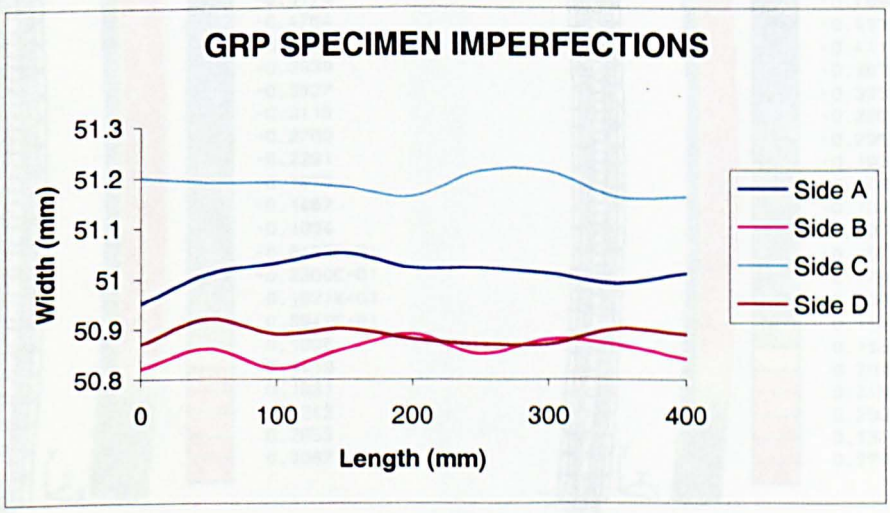

Fig 5.29 Measured dimensions for 400mm high 51mm GRP specimen.

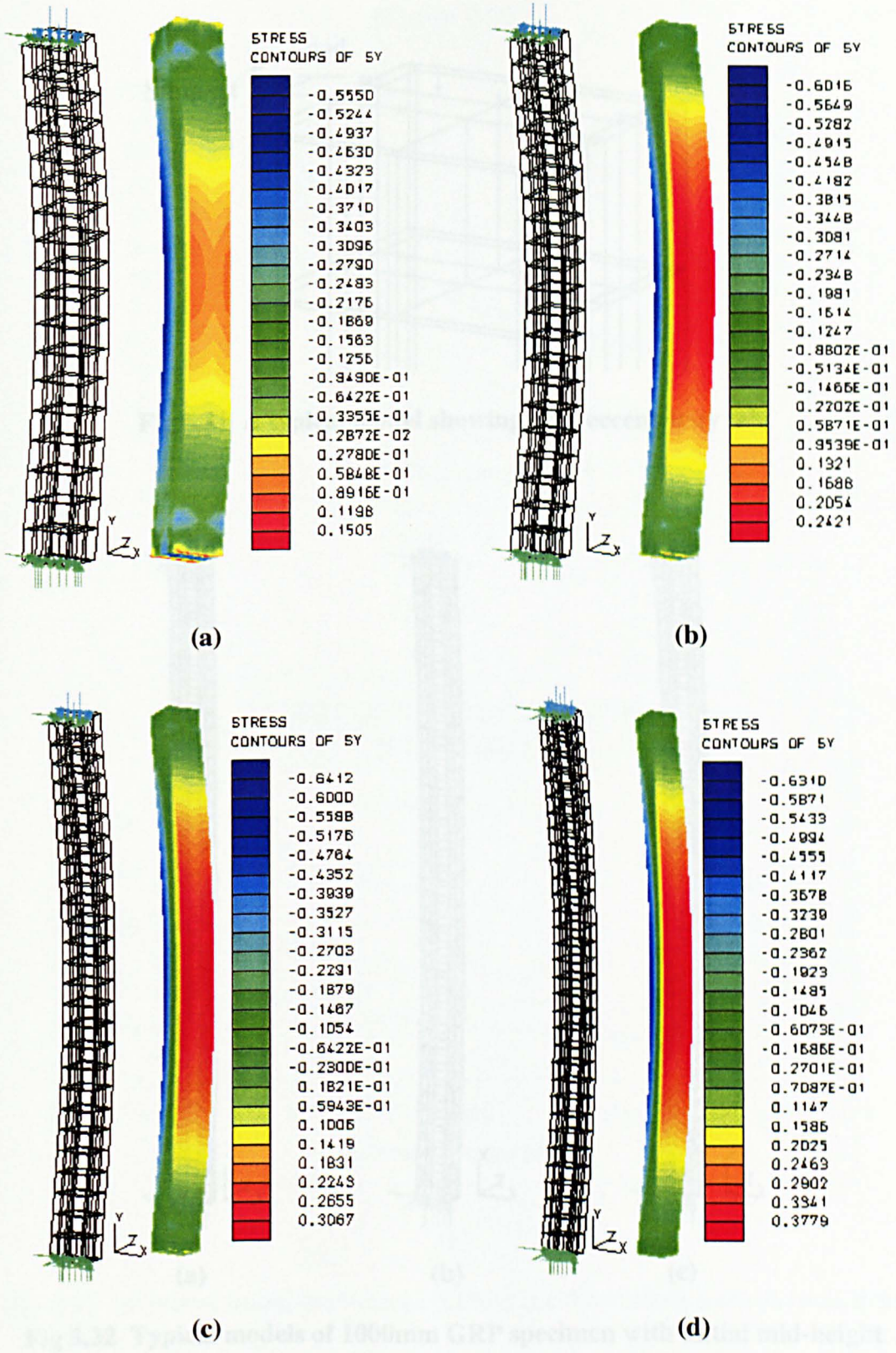

Fig 5.30 Deformed shapes of 44mm box-section columns (Hoffman model): (a) 455mm, (b) 555mm, (c) 655mm and (d) 805mm

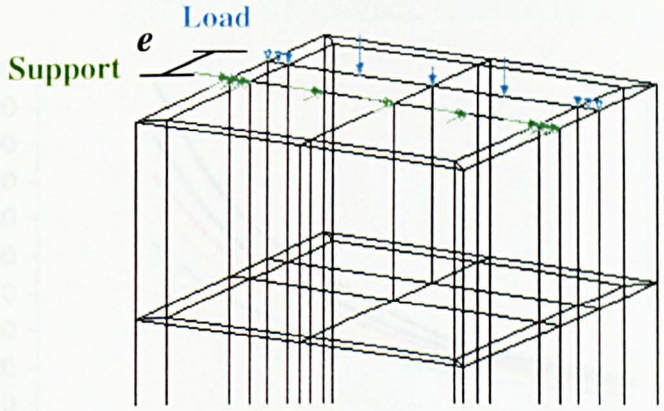

Fig 5.31 A typical model showing load eccentricity '*e*'.

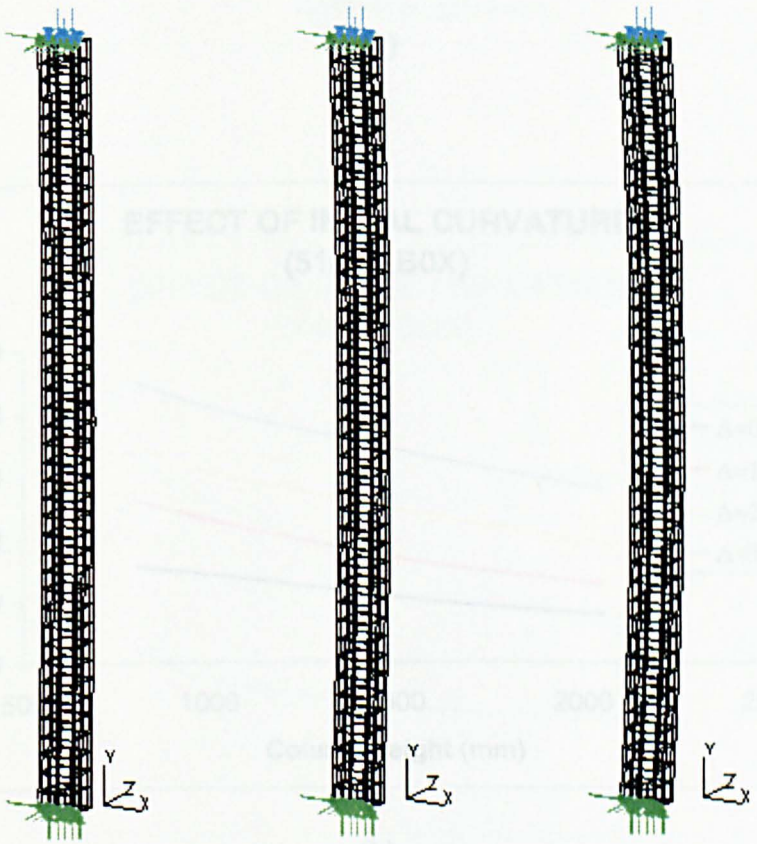

(a) (b) (c)

Fig 5.32 Typical models of 1000mm GRP specimen with initial mid-height curvature of (a) 1%, (b) 2% and (c) 3%.

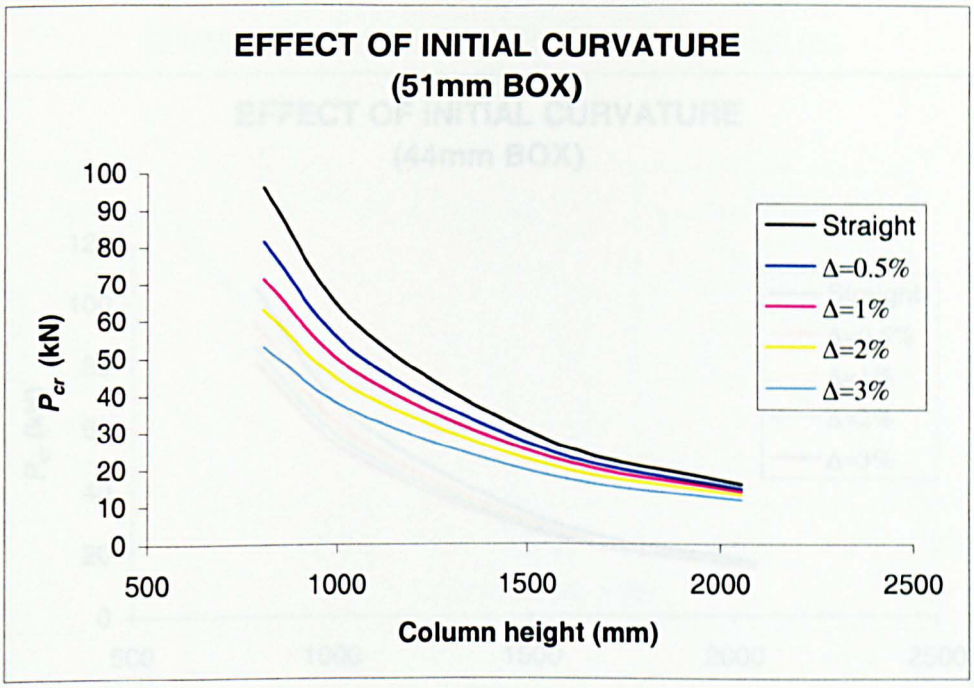

(a)

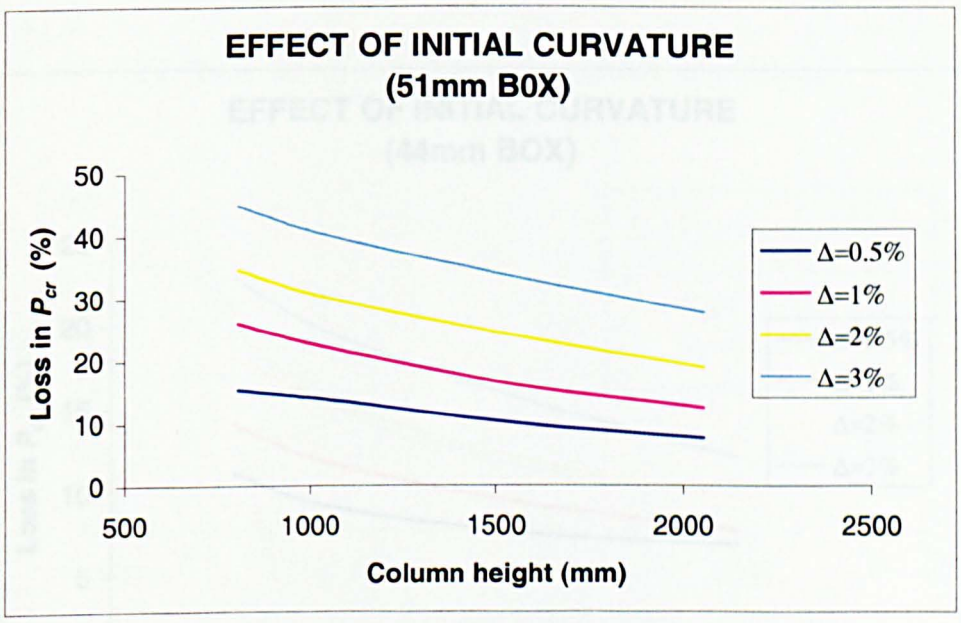

(b)

Fig 5.33 Effects of initial curvature on the critical buckling loads (51mm box).

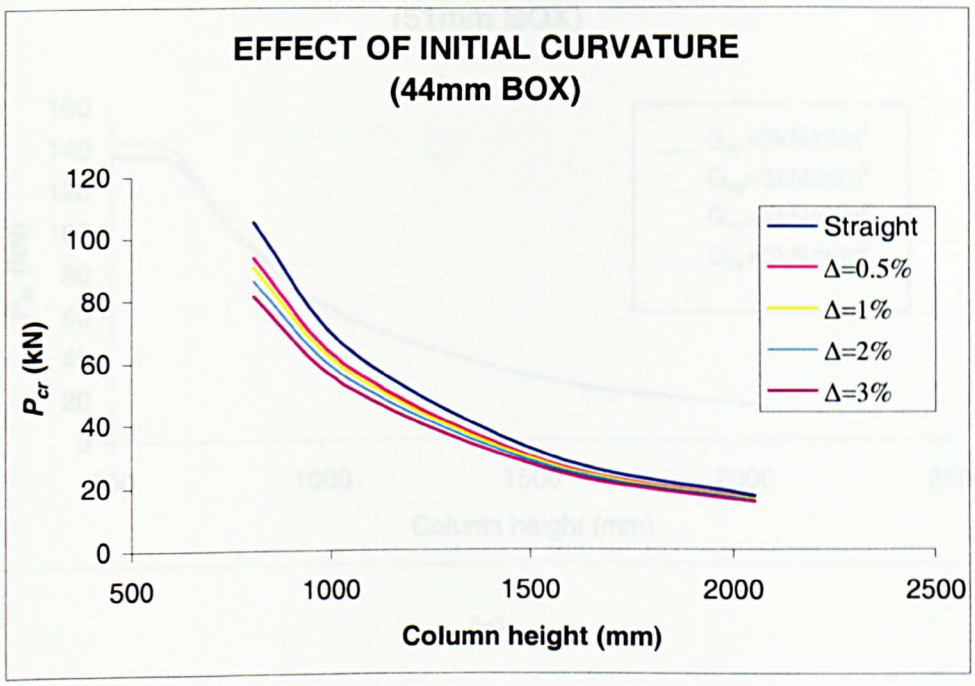

(a)

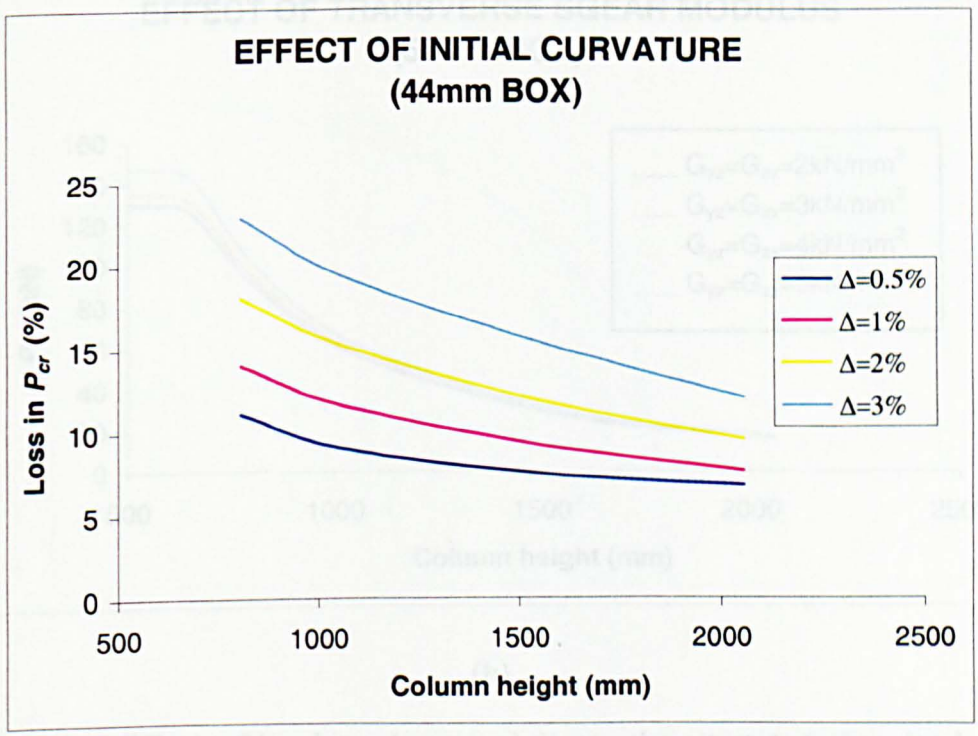

(b)

Fig 5.34 Effects of initial curvature on the critical buckling loads (44mm box).

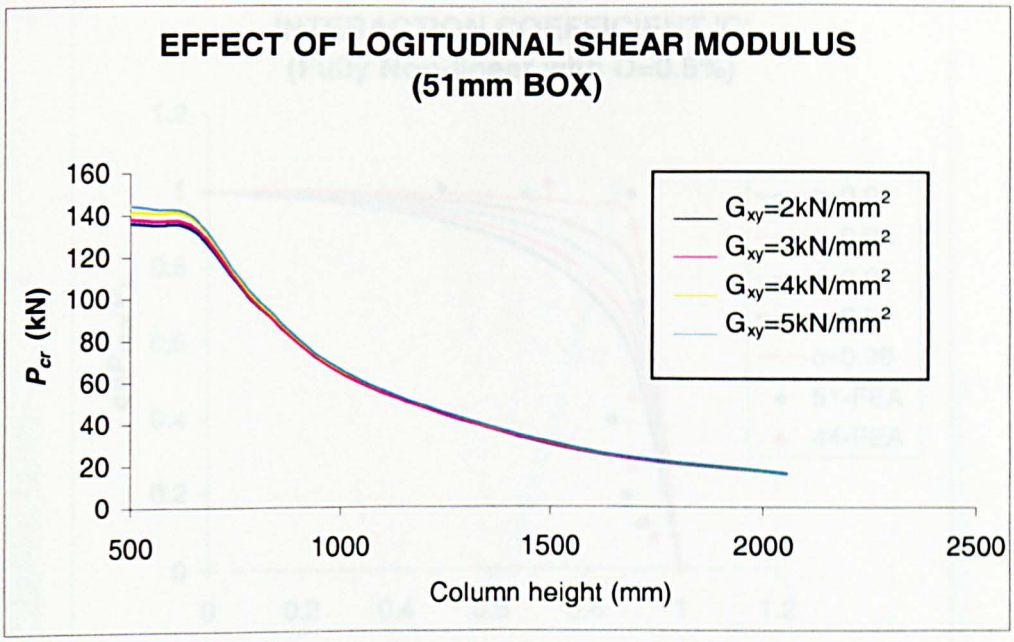

(a)

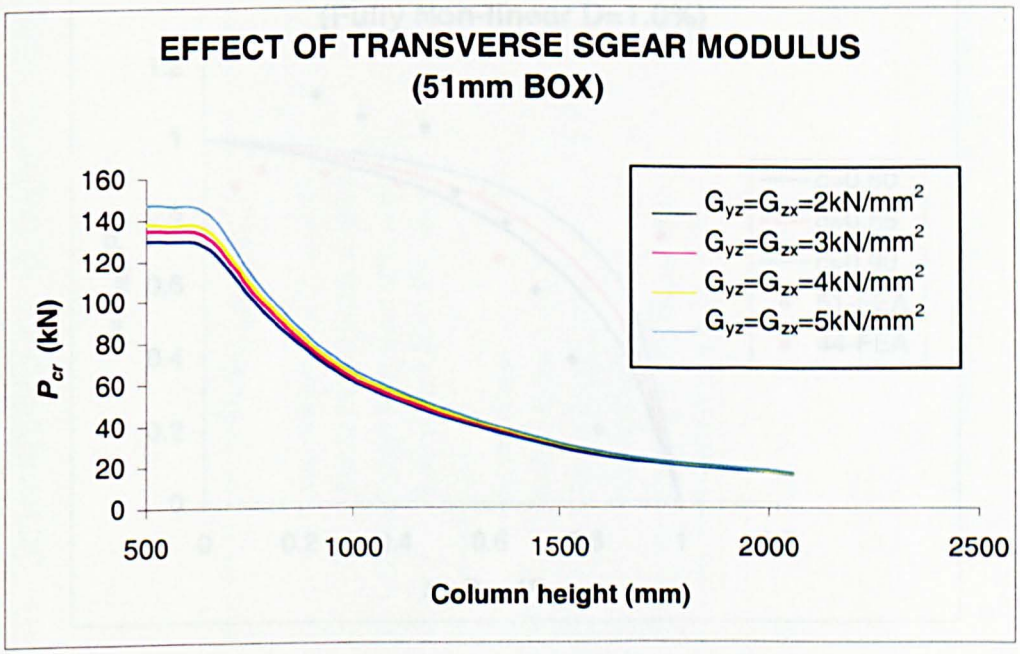

(b)

Fig 5.35 Effects of in-plane shear modulus on the ultimate failure loads.

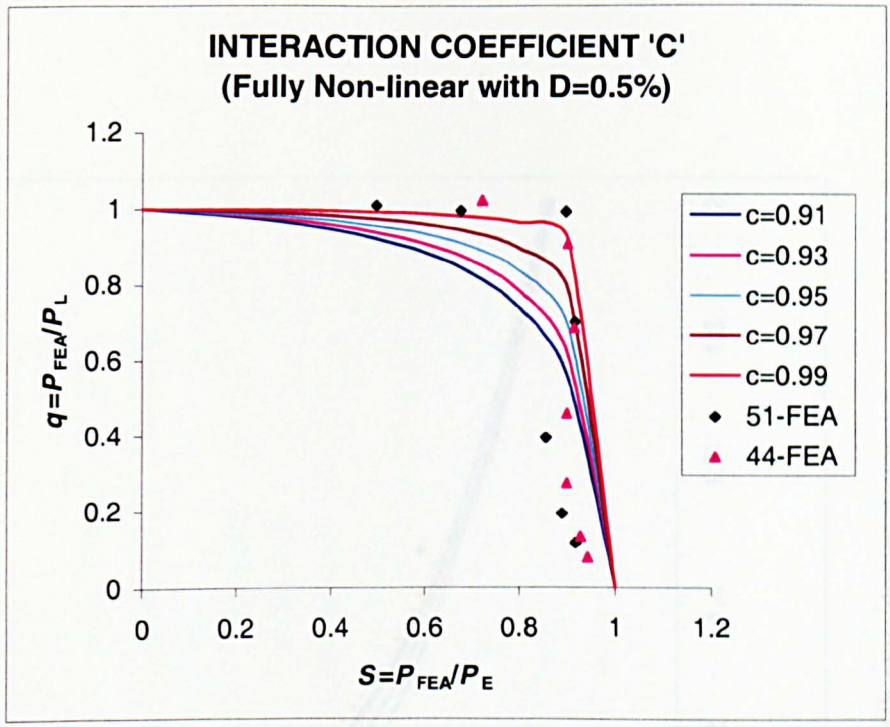

(a)

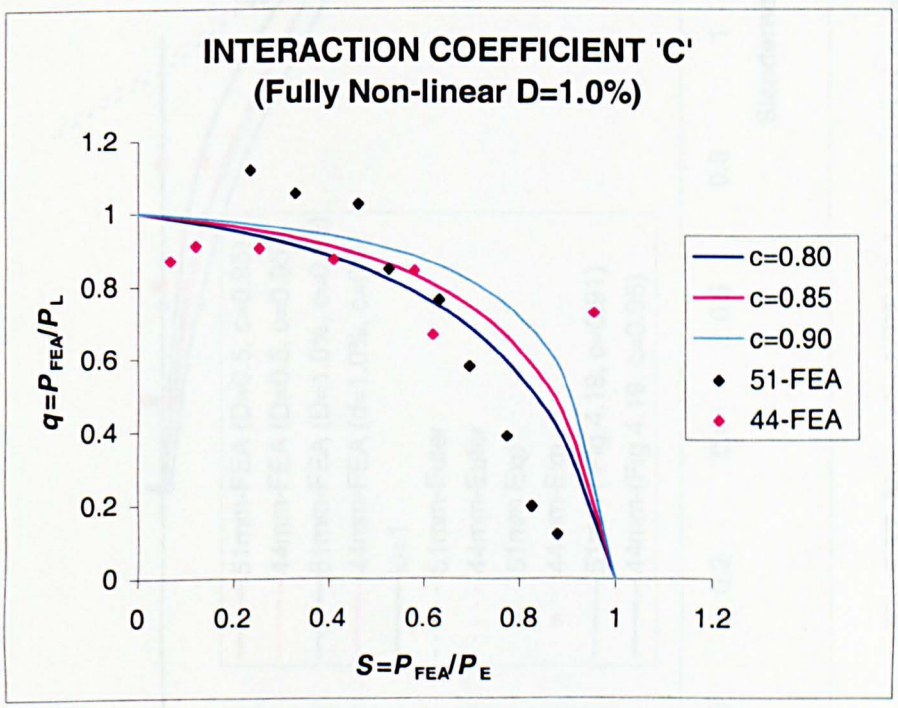

(b)

Fig. 5.36 Estimation of interaction coefficient using FEA predictions.

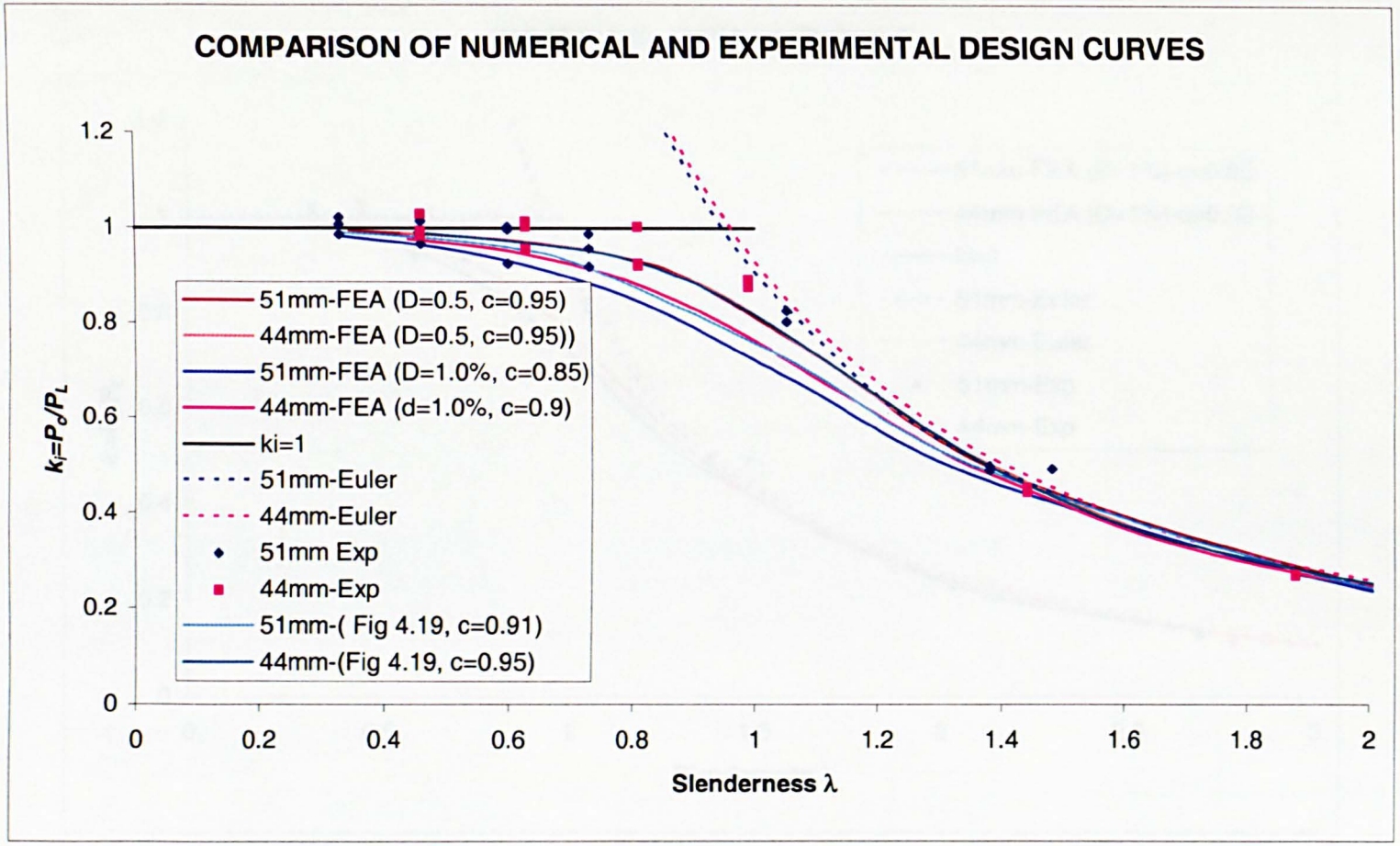

Fig 5.37 Numerical (FEA) design curves compared with experimental curves.

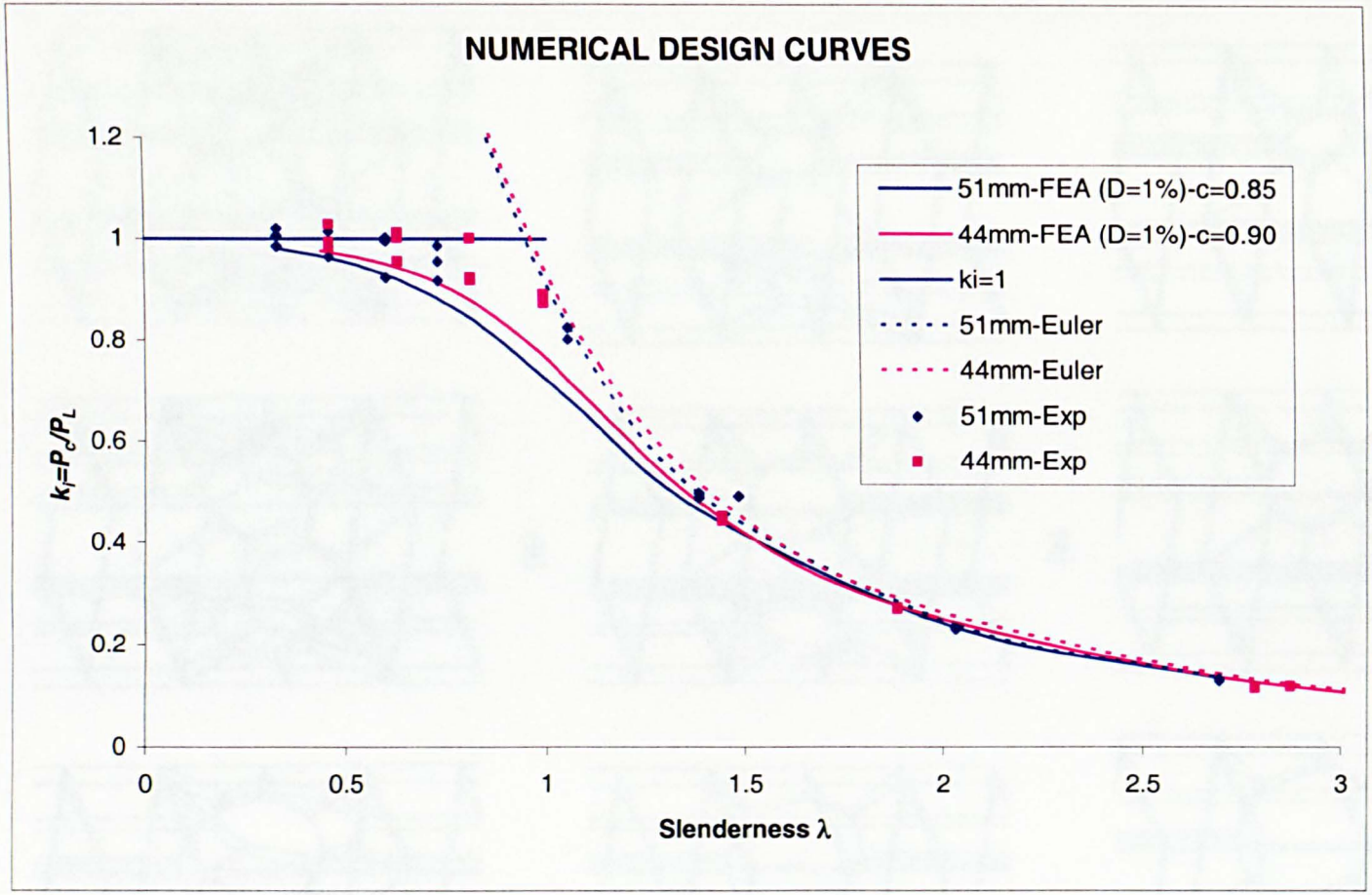

Fig 5.38 Numerical (FEA) design curve for the box-section profiles.

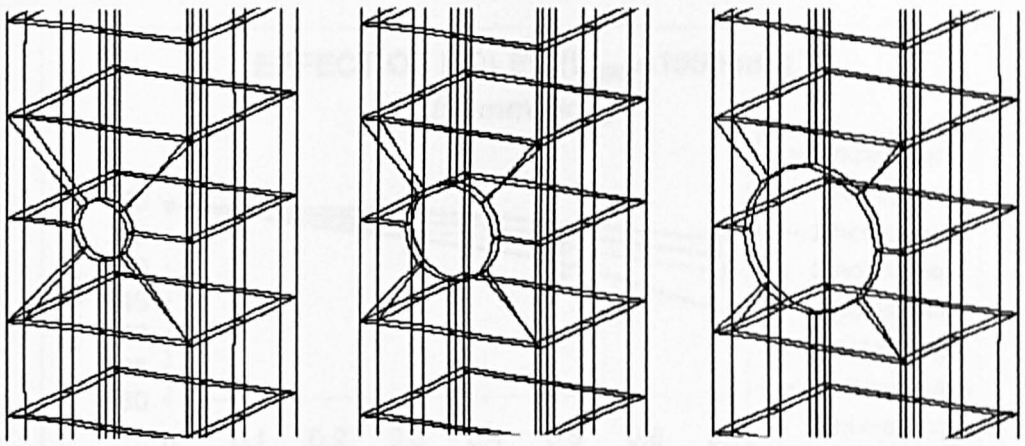

(a)

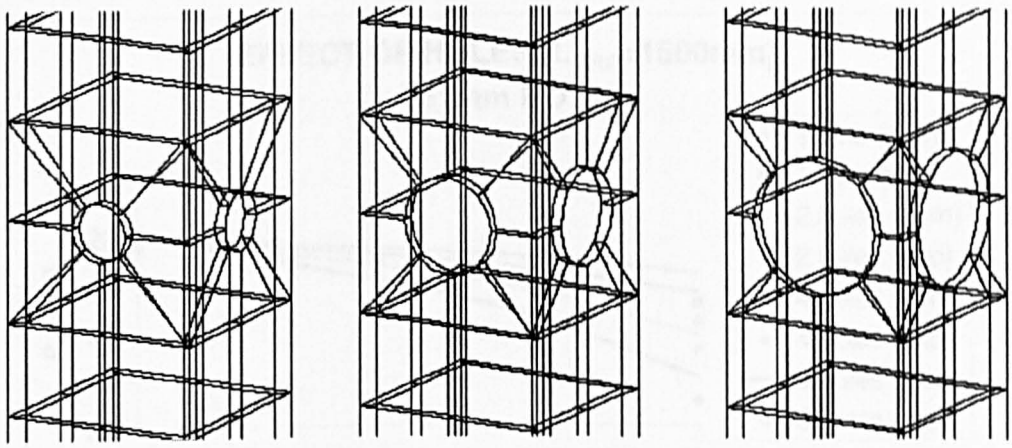

(b)

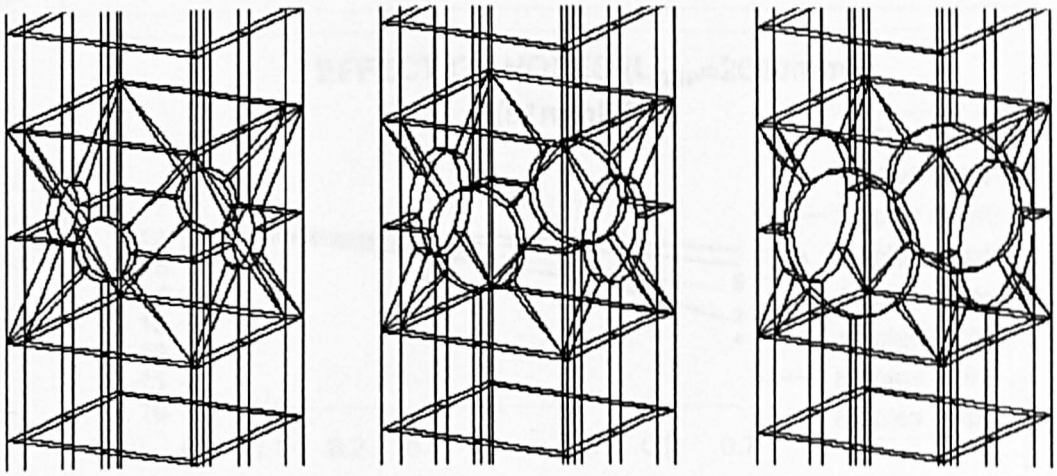

(c)

Fig. 5.39 Typical FE models of columns with holes (d/w = 0.3, 0.5 and 0.7); (a) hole in one side, (b) holes in two sides and (c) holes in four sides.

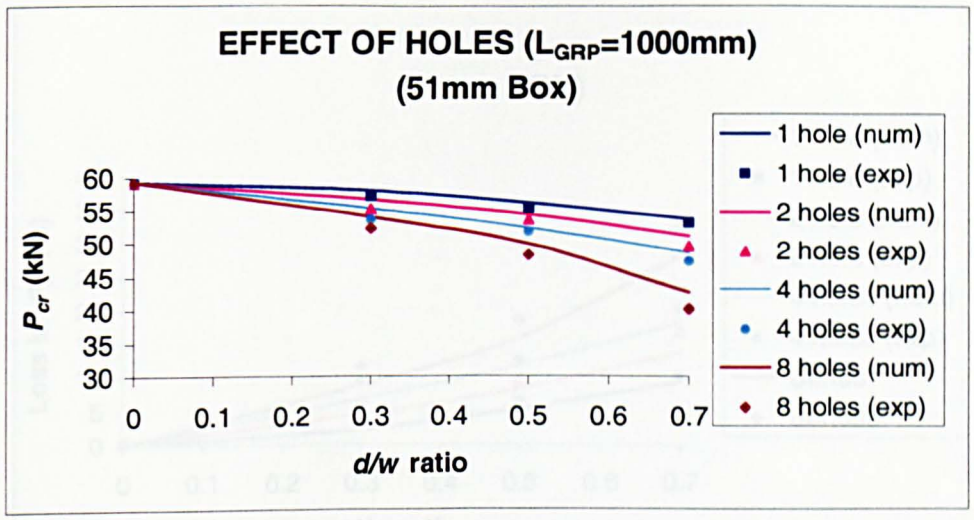

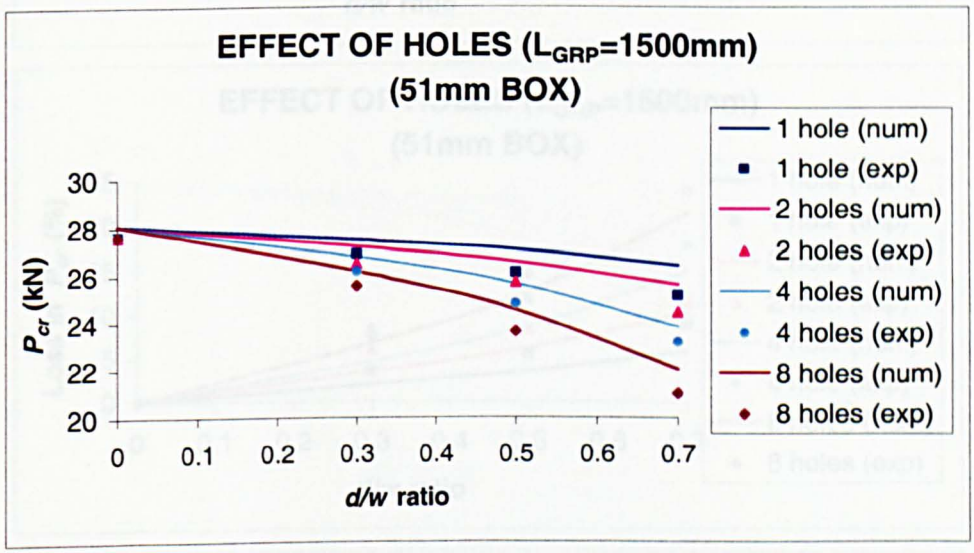

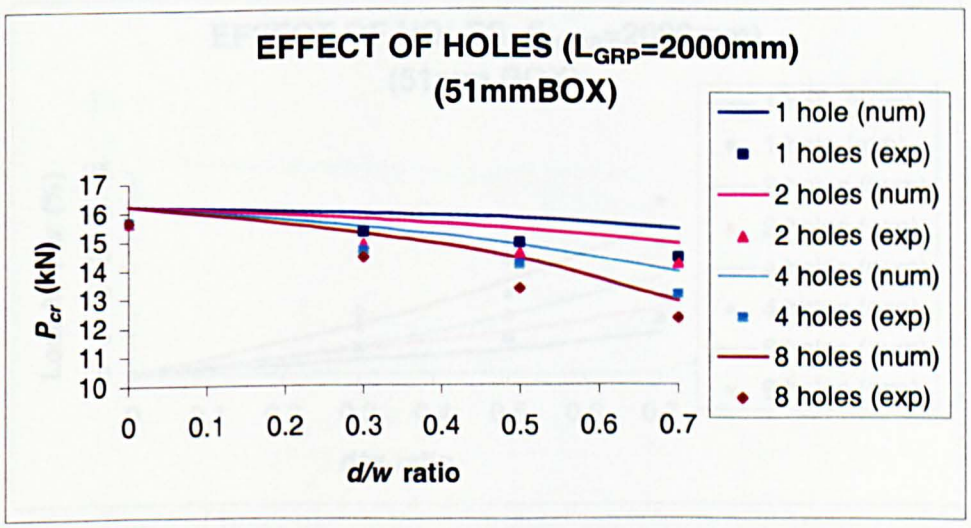

Fig 5.40 Effects of holes on the buckling loads in 51mm box-section columns.

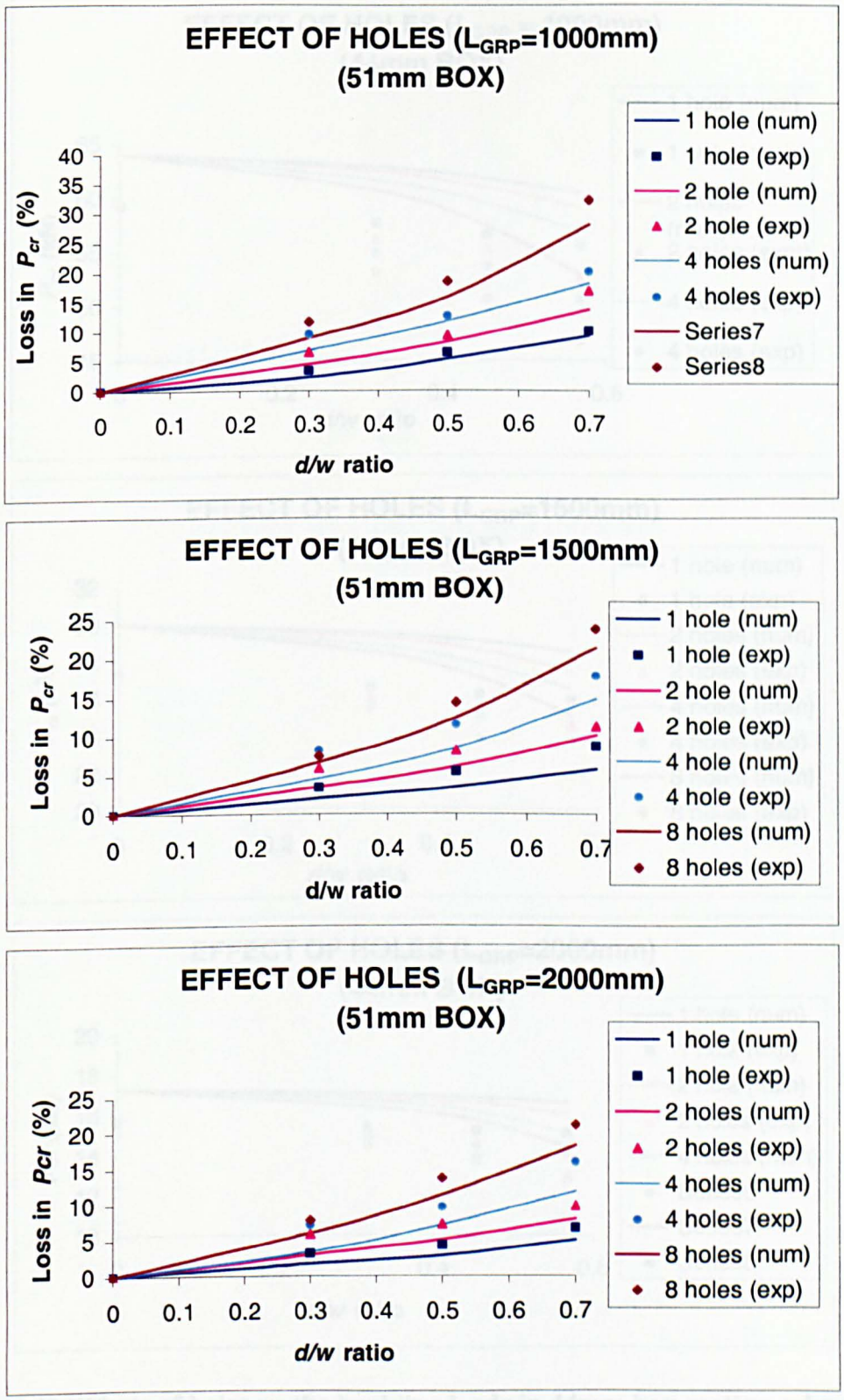

Fig 5.41 Loss of buckling stiffness due to holes in 51mm box-section columns.

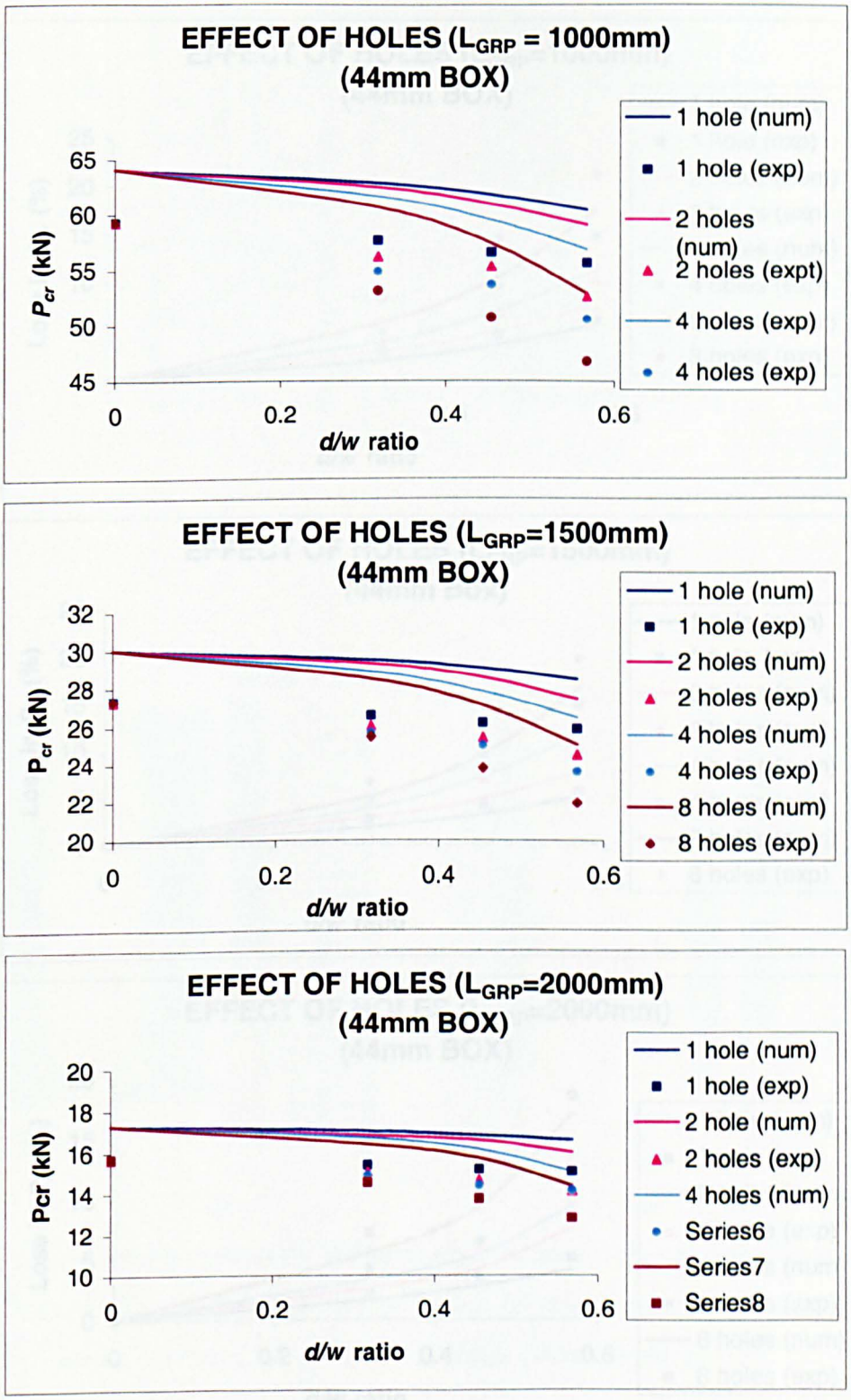

Fig 5.42 Effects of holes on the buckling loads in 44mm box-section columns.

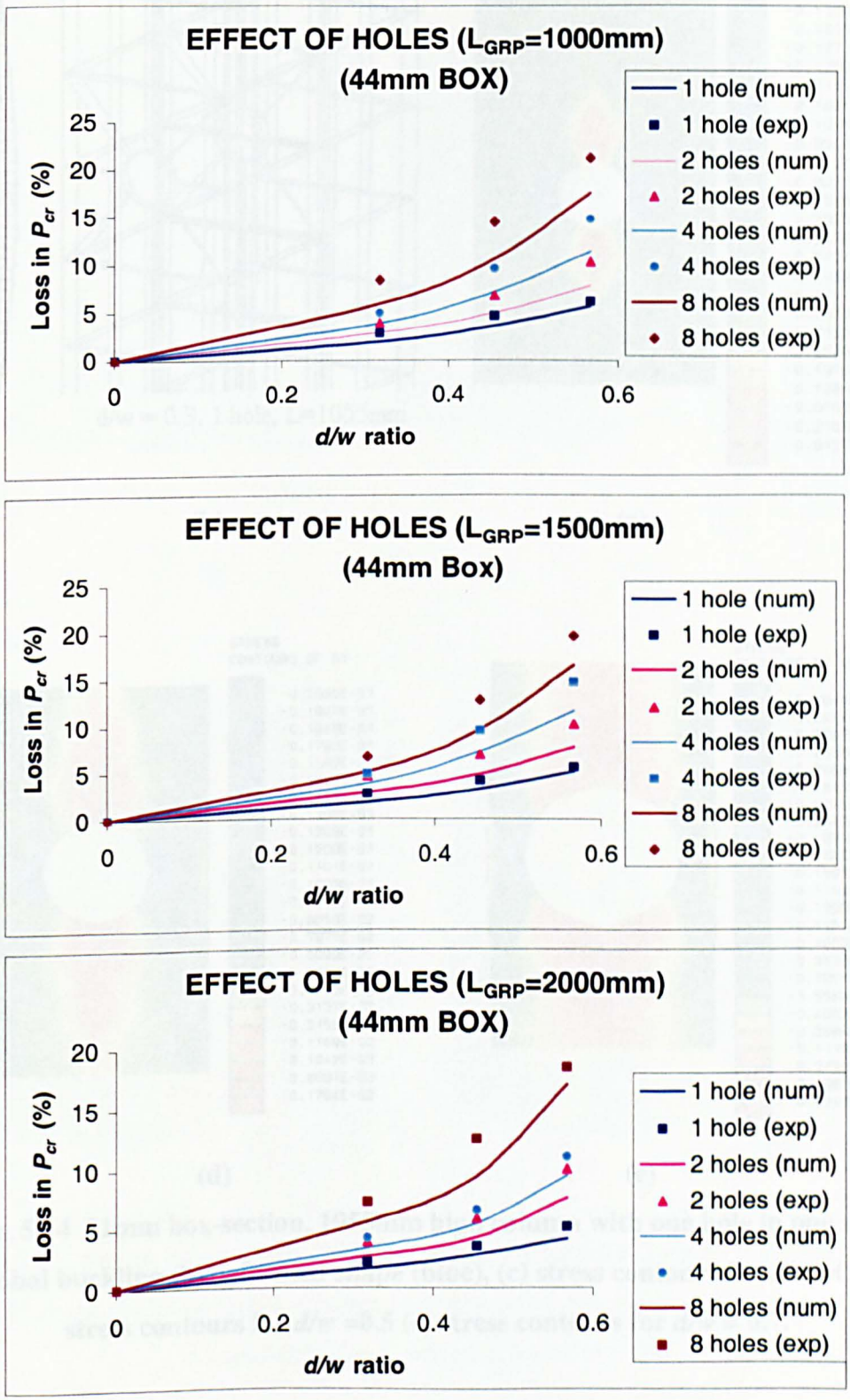

Fig 5.43 Loss of buckling stiffness due to holes in 44mm box-section columns.

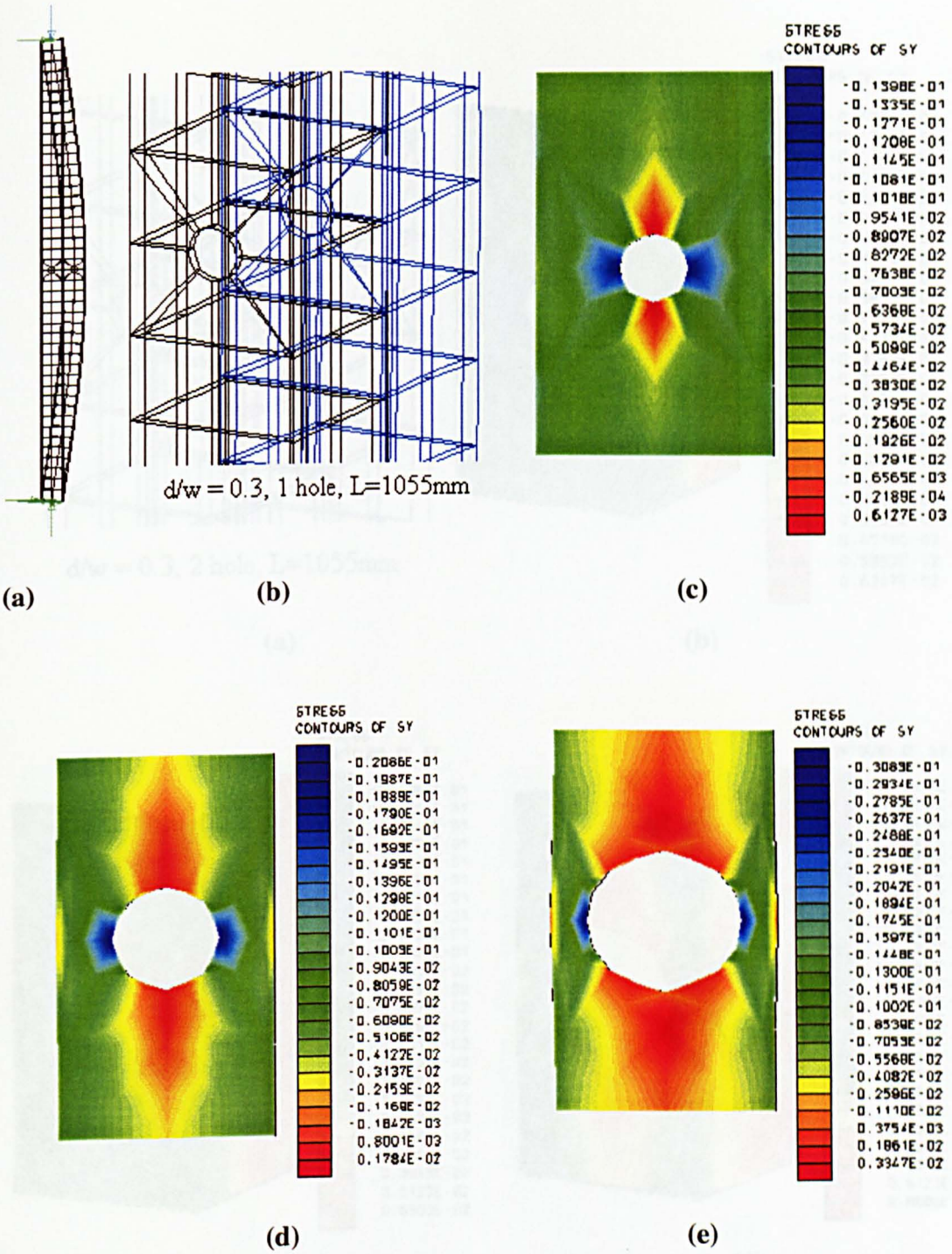

Fig 5.44 51mm box-section, 1055mm high column with one hole in one side (a) global buckling (b) deformed shape (blue), (c) stress contours for *d/w* =0.3, (d) stress contours for *d/w* =0.5 (c) stress contours for *d/w* = 0.7.

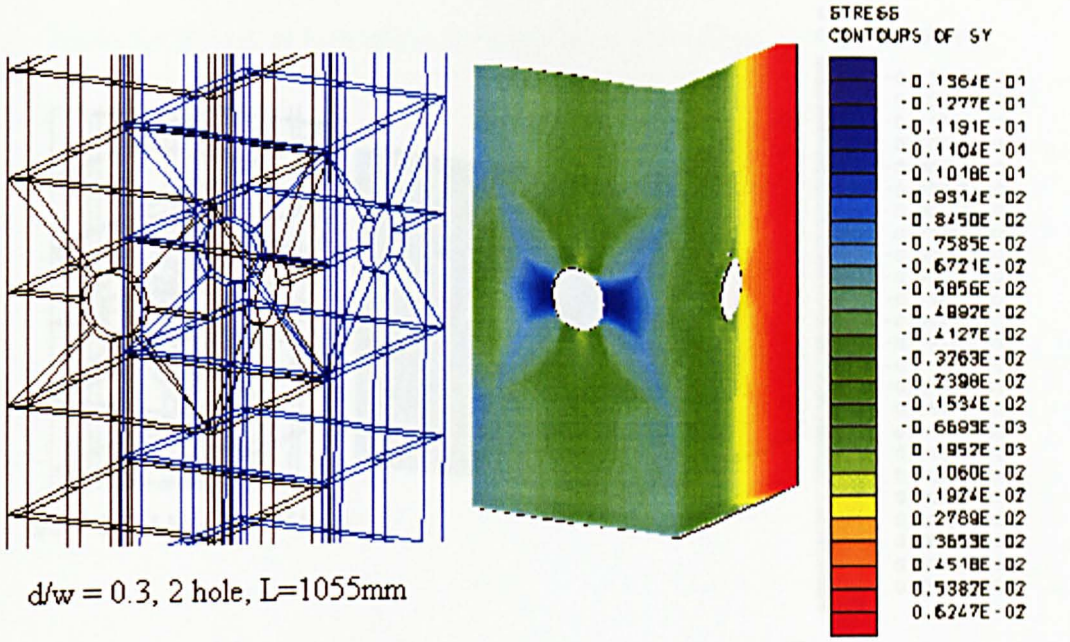

(a) (b)

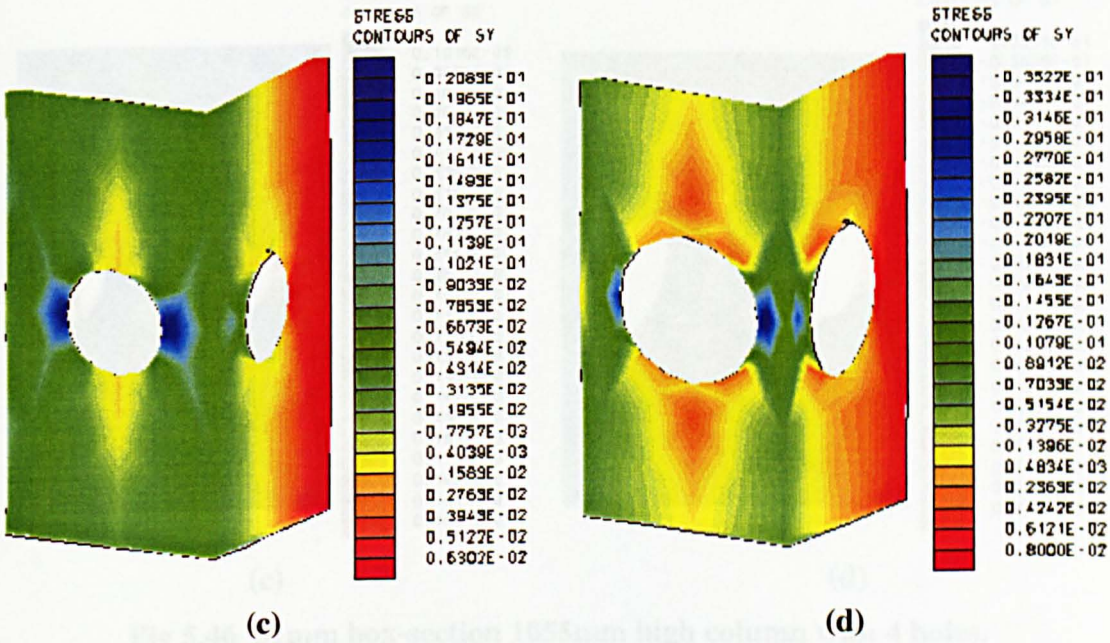

(c) (d)

Fig 5.45 51mm box-section 1055mm high column with 2 holes (a) deformed shape (blue), (b) axial stress contours for *d/w* = 0.3, (c) stress contours for *d/w* = 0.5 and (d) stress contours for *d/w* = 0.7.

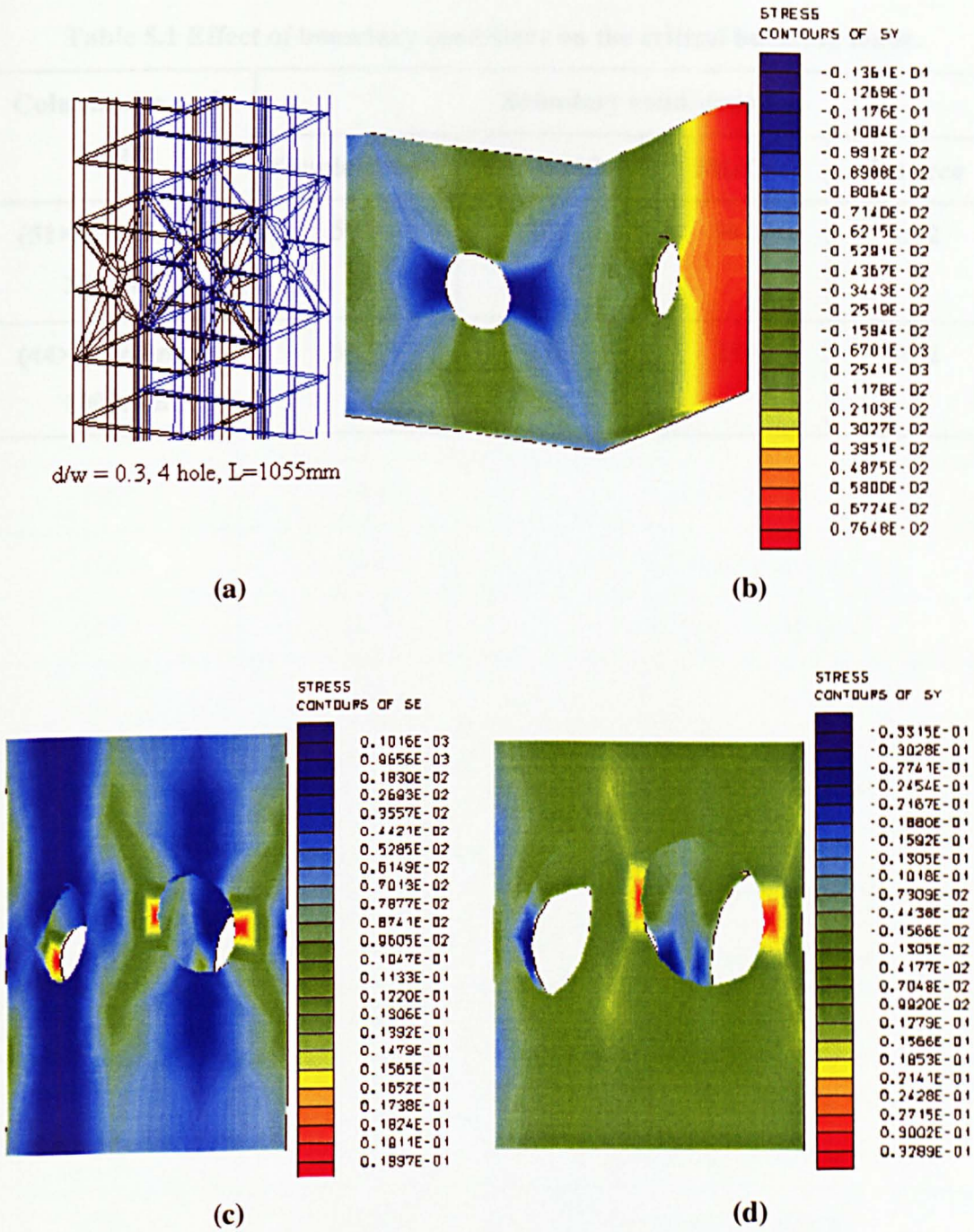

Fig 5.46 51mm box-section 1055mm high column with 4 holes.

(a) deformed shape (blue), (b) axial stress contours for *d/w* = 0.3 (c) stress contours for of *d/w* = 0.5 and (d) stress contours for *d/w* = 0.7.

Table 5.1 Effect of boundary conditions on the critical buckling loads.

Column size and length	Boundary conditions			
	Simple-simple	Fix-simple	Fix-fix	Fix-free
(51×51×3.2mm) 1000mm	59.3	121	241	15.2
(44×44×6.0mm) 1000mm	64.1	130	259	16.2

Table 5.2 Linear elastic (eigenvalue) analysis results of 51×51x3.2mm section.

Length (mm)	Eigenvalue Load	Failure Mode
255	*189*[§§§]	Solution not converged (no buckling)
355	*171*	Solution not converged (no buckling)
455	*166*	Solution not converged (no buckling)
555	*192*	Solution not converged (no buckling)
655	143	Global buckling
805	98.4	Global buckling
1055	59.3	Global buckling
1555	28.1	Global buckling
2055	16.2	Global buckling

Table 5.3 Linear elastic (eigenvalue) analysis results of 44×44×6.0 section.

Length (mm)	Eigenvalue Load	Failure Mode
255	*790*[§§§]	Solution not converged
355	*471*	Solution not converged
455	308	Global buckling
555	216	Global buckling
655	159	Global buckling
805	108	Global buckling
1055	64.1	Global buckling
1555	30.0	Global buckling
2055	17.3	Global buckling

[§§§] The values in italics are non-converged solutions.

Table 5.4 Geometrically non-linear analysis results of 51×51×3.2mm section.

Length (mm)	Failure Load	Failure Mode
255	*274*[****]	Local buckling with 3 half sine waves
355	*211*	Local buckling with 5 half sine waves
455	155	Local buckling with 5 half sine waves
555	150	Local buckling with 7 half sine waves
655	143	Axial shortening, no buckling
805	97.0	Axial shortening, no buckling
1055	58.6	Axial shortening, no buckling
1555	27.9	Axial shortening, no buckling
2055	16.2	Axial shortening, no buckling

Table 5.5 Geometrically non-linear analysis results of 44×44×6.0mm section.

Length (mm)	Failure Load	Failure Mode
255	*774*[****]	Axial shortening, no buckling
355	*465*	Axial shortening, no buckling
455	305	Axial shortening, no buckling
555	216	Axial shortening, no buckling
655	158	Axial shortening, no buckling
805	107	Axial shortening, no buckling
1055	62.5	Axial shortening, no buckling
1555	29.5	Axial shortening, no buckling
2055	17.2	Axial shortening, no buckling

[****] The values in italics are non-converged results.

Table 5.6a Elastic degraded gradients for transverse tension test (51mm and 44mm box-sections).

Degraded modulus E_d (kN/mm^2)	Total strain 'ε'	Stress/Strain gradient, C (pseudo modulus) (kN/mm^2)	Effective nonlinear strain limit, L
7.2	0.0035	27.8	0.00026
5.8	0.0045	14.4	0.00066
4.5	0.0053	8.4	0.00109

Table 5.6b Elastic degrated gradients for longitudinal compression test (51mm box-section).

Degraded modulus E_d (kN/mm^2)	Total strain 'ε'	Stress/Strain gradient, C (pseudo modulus) (kN/mm^2)	Effective nonlinear strain limit, L
27.5	0.009	370	0.000148
27.0	0.011	296	0.00033
25.9	0.0138	203	0.00068

Table 5.6c Elastic degraded gradients for longitudinal compression test (44mm box-section).

Degraded modulus E_d (kN/mm^2)	Total strain 'ε'	Stress/Strain gradient, C (pseudo modulus) (kN/mm^2)	Effective nonlinear strain limit, L
33.0	0.01	7648	0.000013
32.7	0.013	2289	0.0001
32.6	0.0159	2151	0.001

Table 5.7 Fully Nonlinear (Hoffman analysis results of 51×51×3.2mm section.

Length (mm)	Failure load (Straight column) (kN)	Failure Modes / comments
255	*188*[††††]	Local buckling with 3 half sine waves.
355	*157*	Local buckling with 5 half sine waves.
455	139	Local buckling with 5 half sine waves.
555	137	Local buckling with 7 half sine waves.
655	134	Global buckling with initial imperfections.
805	96.2	Global buckling with initial imperfections.
1055	58.5	Global buckling with initial imperfections.
1555	27.9	Global buckling with initial imperfections.
2055	16.2	Global buckling with initial imperfections.

Table 5.8 Initial imperfections effecting the P_{cr} of 400mm high 51mm section.

Load eccentricity (mm)	P_{cr} for options (kN)			
	4	1+4	2+4	3+4
0	139	138	135	135
0.25	134	134	132	134
0.5	138	137	131	130
1.0	136	135	126	125
1.5	134	133	124	122
2.0	130	129	124	117

[††††] The values in italics are non-converged solutions.

Table 5.9 Nonlinear (Hoffman) analysis results of 44×44×6.0 section.

L_{eff} (mm)	Failure load (Straight column) (kN)	Failure modes / comments
255	*453*‡‡‡‡	Axial shortening, no buckling
355	*446*	Axial shortening, no buckling
455	305	Axial shortening, no buckling in straight columns. Global buckling with initial imperfections.
555	214	Axial shortening, no buckling in straight columns. Global buckling with initial imperfections.
655	158	Axial shortening, no buckling in straight columns. Global buckling with initial imperfections.
805	105	Axial shortening, no buckling in straight columns. Global buckling with initial imperfections.
1055	62.1	Axial shortening, no buckling in straight columns. Global buckling with initial imperfections.
1555	29.2	Axial shortening, no buckling in straight columns. Global buckling with initial imperfections.
2055	17.1	Axial shortening, no buckling in straight columns. Global buckling with initial imperfections.

‡‡‡‡ The values in italics are non-converged solutions.

Table 5.10 Failure loads (comparison) for 51×51×3.2 mm box-section columns.

Effective Length (mm)	Numerical (kN)					Theoretical (kN)			Experi-mental §§§§ (kN)
	Linear (perfect)	Nonlinear (geometric) (perfect)	Nonlinear (geometric+material)			Euler & EDC (including shear effects)	Strongwell (crushing strength)		
			Perfect	Imperfect			$E_{L,c}$ Measured	$E_{L,c}$ FibreForce	
				Δ_0=0.5%	Δ_0=1.0%				
255	*189******	*274*	*188*	*185*	*134*	570	120	66.1	121
355	*171*	*211*	*157*	*151*	*123*	381	(236)	(127)	118
455	*166*	155	139	131	123	264			117
555	*192*	150	137	129	101	191			108
655	143	143	134	129	91.2	144	257	146	-
805	98.4	97.0	96.2	91	69.23	99.2	196	112	97.1
1055	59.3	58.6	58.5	51.1	46.2	59.8	138	78.6	59.1
1555	28.1	27.9	27.9	25.1	23.4	28.3	83.4	47.5	27.6
2055	16.2	16.2	16.2	15.0	14.1	16.4	58.0	33.1	15.7

§§§§ Average of three tested columns

***** The values in italics are non-converged solutions.

Table 5.11 Failure loads (comparison) for 44×44×6.0 mm box-section columns.

Effective Length (mm)	Numerical (kN)					Theoretical (kN)			Experi-mental[†††††] (kN)
	Linear (perfect)	Nonlinear (geometric) (perfect)	Nonlinear (geometric+material)			Euler & EDC (including shear effects)	Strongwell (crushing strength)		
			Perfect	Imperfect			$E_{L,c}$ Measured	$E_{L,c}$ FibreForce	
				Δ=0.5%	Δ=1.0%				
255	*790*[‡‡‡‡‡]	*774*	*453*	*350*	*220*	696	381	204	220
355	*471*	*465*	*446*	*350*	*220*	442	(477)	(189)	218
455	308	305	305	215	210	298	464	248	209
555	216	216	214	190	137	211	358	192	195
655	159	158	158	144	128	157	289	155	-
805	108	107	105	96.3	90.6	107	221	118	98.4
1055	64.1	62.5	62.1	57.4	56.1	64	155	83.3	59.3
1555	30.0	29.5	29.2	27.9	26.5	30.0	93.9	50.3	27.3
2055	17.3	17.2	17.1	16.3	14.6	17.3	65.4	35	15.7

[†††††] Average of three tested columns.

[‡‡‡‡‡] The values in italics are non-converged solutions.

Table 5.12 Effects of holes on the buckling loads of 51mm box-section profiles.

d/w	L_{GRP} (mm)	P_{cr} (kN)				
		No Holes	1 Hole	2 Holes	4 Holes	8 Holes
0.3	1000	59.3	57.9	56.5	55.2	54
	1500	28.1	27.5	27.2	26.8	26.2
	2000	16.2	16.0	15.7	15.4	15.3
0.5	1000	59.3	56.1	54.3	52.2	49.8
	1500	28.1	27.1	26.6	25.7	24.6
	2000	16.2	15.8	15.4	14.9	14.4
0.7	1000	59.3	53.7	51.1	48.5	42.6
	1500	28.1	26.4	25.6	23.9	22.1
	2000	16.2	15.4	14.9	13.9	12.9

Table 5.13 Effects of holes on the buckling loads of 44mm box-section profiles.

d/w	L_{GRP} (mm)	P_{cr} (kN)				
		No Holes	1 Hole	2 Holes	4 Holes	8 Holes
0.32	1000	64.1	62.8	62.6	61.6	60.6
	1500	30.0	29.5	29.3	28.9	28.5
	2000	17.3	17.0	16.8	16.7	16.3
0.46	1000	64.1	61.8	61.0	59.5	57.4
	1500	30.0	29.1	28.6	27.8	27.1
	2000	17.3	16.8	16.6	16.1	15.7
0.57	1000	64.1	60.5	59.1	56.8	52.9
	1500	30.0	28.5	27.5	26.5	25.1
	2000	17.3	16.6	16.0	15.0	14.4

CHAPTER 6

CONCLUSIONS AND FUTURE SUGGESTIONS

6.1 GENERAL OVERVIEW

Buckling is the most common failure mode associated with compression members having thin walled cross-sections. This has been further emphasised for the GRP structural profiles comprising thin composite walls and lower stiffness constants. The design guidance presently available mainly consists of classical solutions for steel profiles (plates and columns) or empirical equations derived from limited experimental studies on individual profiles conducted by manufacturers. The need to establish effective methods of analysis for the prediction of safe buckling loads for these profiles has been recognised. Potential advantages of using finite element analyses for the prediction of ultimate failure/buckling loads, of GPR box-section columns, for the development of appropriate design curves have been investigated in this study. The numerical predictions have been validated by comparison with experimental evidence.

Two GRP box-section profiles having cross-sections 51×51×3.2 and 44×44×6.0mm have been investigated to determine the buckling and the ultimate failure loads for various column heights. The investigations comprise experimental and numerical studies. In the experimental phase, three specimen of each height of the two box-sections have been tested to measure the failure loads. The failure modes and material behaviour at failure have been observed. In the numerical phase, finite element models of simply supported and axially compressed composite columns have been analysed for the ultimate loads and the respective failure modes. Both linear and nonlinear analyses have been considered to investigate the failure behaviour, witnessed in the experimental observations. Numerical analyses have been used for parametric studies to establish the effects on the ultimate loads of various factors e.g., different boundary conditions, material orthotropy, load eccentricities, initial curvature and making holes through the walls of the profiles.

For use in the numerical analysis, the material properties of the GRP profiles have been determined. The micromechanics approach, in conjugation with the classical

lamination theory, has been used to calculate the theoretical properties of the GRP material (E_x, E_y, ν_{xy} and G_{xy}) from the properties of the constituent materials and their configuration. In-plane shear properties have been measured experimentally, testing the material coupons obtained from the two profiles. A simple AFPB fixture for the testing of shear coupons have been proposed, validated using FE analysis, fabricated and subsequently used for the measurement of shear properties. To meet dimensional constraints, shorter coupon and AFPB fixture have been proposed, validated and used for the determination of shear properties.

The investigations undertaken in this study can be divided into following thematic sections:

- Determination of the material properties using analytical and experimental methods.
- Experimental testing of simply supported and axially loaded GRP specimens (columns) of various heights, for the measurement of the buckling/ultimate loads.
- Numerical prediction of the ultimate loads and failure modes using finite element analyses.
- Development of a universal design equation for the prediction of safe buckling loads for the two box-section profiles.

6.2 CONCLUSION

6.2.1 MATERIAL PROPERTIES

Material properties of the two GRP box-sections profiles, in the longitudinal and transverse directions, have been established using analytical and experimental methods. Analytically, four orthotropic material constants (E_x, E_y, G_{xy}, and ν_{xy}) have been estimated using micromechanics and classical lamination theory (CLT). Experimentally, coupons (specimens) extracted from the sides of GRP box-sections have been tested in the laboratory to measure these properties. Estimated (analytical) properties has been used in the (FE) analyses of standard and short shear coupons (Chapter 3) whilst measured (experimental) outcomes are used in the numerical

representations of GRP columns for the prediction of buckling loads and modes (Chapter 5).

In-plane shear properties have been measured using V-notched beam method (ASTM-D5379M-93). Shear coupons of standard length (76mm) have been extracted, from the walls of the box-sections, in the longitudinal direction. A short shear coupon (40mm) has been proposed for extraction from the webs in the width-wise (transverse) direction (one of the box-sections is only 44mm wide). The potential performance of the short shear coupon has been investigated numerically using finite element (FE) method. Representative FE models of standard ASTM and short shear coupons have been developed. Numerical representation of the standard ASTM coupon has been validated by the FE analyses enforcing a selection criterion, set as the lowest divergent strain field across the centre of the coupon. Numerically validated ASTM shear coupon provides a bench mark against which the performance of the short coupon has been measured. An insight into the performance of the short coupon has been gained by investigating the effects of geometric parameters including width, thickness, notch-depth and interval between the loading points. Addition of the aluminium tabs in the FE models of short transverse coupons, to avoid local failure under the loading bars and to achieve a true shear failure at the centre has also been validated for adequate performance. FE models of the proposed AFPB (asymmetric four point bending) test fixtures for the ASTM and short coupons have been developed and analysed prior to fabrication. FE presentations of the shear coupons (ASTM and short) without and with AFPB test fixtures have been used to establish and validate the performance of these fixtures under the applied loads.

In-plane shear properties have been measured experimentally using ASTM and short shear coupons extracted from both box-profiles. Short coupons with the main reinforcement perpendicular to the notch tips gave consistent and similar results to the ASTM outcomes, validating the performance of short shear coupon for the measurement of in-plane shear properties. Aluminium tabs have been bonded to the short shear coupons with main reinforcement parallel to the notch tips.

The following principal conclusions have been drawn:

- Material properties of the composite GRP materials can be effectively predicted theoretically, from the properties of the constituent materials and the

constitutive information (manufacturer supplied), using principals of micromechanics and classical lamination theory (CLT). Material properties of the two GRP box-sections, to be used in the numerical analyses, have been theoretically predicted.

- Experimentally, material coupons (specimens) extracted from the composite walls of the profiles can be physically tested to confirm these properties and to validate the theoretical procedure.
- Finite element analyses have been successfully used to investigate the performance and behaviour of material coupons when subjected to shear loading. FE models of both ASTM standard and short shear coupons without and with test fixtures have been analysed to check their performance under the applied loads. The performance of the coupons has been judged by the quality of shear strain and stress distributions across the central section (between the notches).
- Surface models using plane stress elements can represent thick prismatic coupon and fixture components. This is validated through the comparison of the FEA results of 2D and 3D coupon models
- It has been established numerically that the schematic loading of the ASTM and short coupons produce no bending moment at the centre. The loads applied by the upper loading bars and the reactions in the lower loading bars produce equal and opposite couples cancelling each other at the centre.
- Numerically predicted shear force resultant (and hence the shear stress) across the central test section of the ASTM coupon, loaded in the AFPB fixture, is identical to the theoretical calculations using the schematic shear force diagram given in the ASTM standard, validating the adequacy of the fixture. However, in the case of short shear coupon, the numerical shear force resultant is 7.5% less than the theoretical value obtained using shear force diagram. This decrease in the applied shear force has been attributed to the slight bending of the top loading beam in the short AFPB fixture, changing the force distribution across the contact area between loading bars and coupon, from uniform to triangular. Resultants, however, remained equal and opposite and no bending effects at central section are induced. This implies that the

resultant shear force applied at the central test section of a different (non-standard) coupon, loaded by an AFPB fixture, can be predicted using finite element analyses. This maintains the validity and capability of the short coupon and fixture to be used for measuring the in-plane shear properties in directions where material for the standard ASTM coupon is not available due to dimensional constraints.

- Most importantly, the AFPB shear fixture reduced the high compressive stresses under the load application points. For example, in the case of the ASTM coupon subjected to standard loading, the strain intensity under the inner loading point is 1.8 times the uniform shear strain at centre and can cause premature failure of the coupon under the point loads. This strain intensity reduces to half the value of the uniform central shear stress, when ASTM coupon is loaded using AFPB shear fixture, ensuring coupon failure at central test section at the ultimate shear stress. This demonstrates the adequate performance of the shear coupon and test fixture.

- Finite element analyses have been successively used for the parametric study of the behaviour of the coupons. FE analyses of short coupon (when assumed as isotropic) loaded in fixture established that 90° notches produced the lowest deviation of the numerical shear strain distribution across the central test section from the uniform theoretical. Furthermore, a notch depth of 20 to 25% of the coupon depth produces the numerical shear stress nearest to the theoretical value.

- Material orthotropy, causing strain concentrations at notch roots, have been recognised as the most adverse parameter effecting the magnitude and quality of the shear strain distribution at the central section of the coupon. The effect is more pronounced in transverse coupons. According to the present numerical outcomes, an orthotropy of 1:3 causes 13% and 44% higher strain concentrations at notch roots than at centre, in the longitudinal and transverse coupons respectively. Whereas an orthotropy of 1:6 produces 60 and 100% higher strain concentrations at notch roots in the longitudinal and transverse coupons.

- Separation between the loading points has been predicted not to effect the shear strain distribution.
- The short shear coupon, 40×10mm rectangular with 90° v-notches at mid-length of the long sides, notch depth of 2.5mm (25% of overall depth) has been recommended in the light of numerical and experimental results presented.

6.2.2 EXPERIMENTAL INVESTIGATIONS

Columns of various heights ranging from 200 to 2000mm, extracted from the two GRP box-section profiles have been tested for ultimate load capacities and failure modes. Three specimens for each column height have been tested. All the specimens are simply supported and concentrically loaded in a vertically aligned testing rig. Specimen ends have been squared and the cross-sectional dimensions measured to establish the imperfections, with the sections held in place by steel shoes and aligned vertically using survey techniques.

Experimental data has been recorded at regular intervals (every 2 seconds) during a specified test time (10 minutes) by a data-logger, giving applied load, axial shortening, 3 lateral deflections (mid and quarter heights), axial strains (on four sides at mid height) and the ultimate failure loads. Columns exhibiting global buckling e.g., 1000mm and above for 51mm box-section and 750mm and above for 44mm box-section profiles are categorised as slender columns. Global buckling occurred without material failure and the lateral deflections were restricted to 1.0% of the column height. The Southwell method has been used to establish the critical buckling loads for the slender columns without imperfections. The slender columns have been retested after rotating about the longitudinal axis of symmetry and lengthwise by 180°. Short columns of 51mm box-section, however, exhibited negligible transverse deflections, before an abrupt and irreversible failure, eliminating any possibility of retesting the specimens or the use of Southwell method. The short 44mm box-section columns failed by material degradation at the both ends under the high compressive stresses at the ultimate loads. The maximum short column loads 'P_L' for the two box-sections have been established from the experimental ultimate loads.

The experimental outcomes have been initially compared with the theoretically predicted results using classical approaches and the design guidance from Eurocomp

design code and the manufacture's design manuals. A unified design curve for the two box-sections has been produced using experimental and analytical results.

Circular holes have been drilled through the walls of the box-section columns and retested to establish the effects of perforations on the critical buckling loads of slender columns. Three sizes of holes with *d/w* ratios of 0.3, 0.5 and 0.7 for 51mm and 0.32, 0.46 and 0.57 for the 44mm box-sections have been considered.

The main conclusions of the experimental study are:

- Using the cross-sectional measurements (outer widths and wall thickness) at the two column ends, mean cross-sections have been established. The variations in the measurements are within ±0.25mm from the mean dimensions, i.e., with in the standard tolerance (ASTM 3917-94). Mean cross-section has been used for the calculation of cross-sectional area and moment of area in the subsequent calculations of stresses, strains and analytical critical buckling loads.

- Ultimate failure/buckling loads of composite columns depend upon their heights, material properties and the cross-section dimensions. These factors have been combined into one characteristic parameter 'λ', the slenderness ratio. As the latter two factors are constant for a particular box-section profile, the ultimate loads and failure modes depend upon column heights.

- The 51mm box-section columns of GRP height 1000mm and above buckled globally and categorised as slender columns. The 44mm box-section columns of GRP height 750 and above exhibited global buckling and grouped as slender columns. Slender columns buckled in a half sine wave with maximum deflections at mid sections. The measured lateral deflection at mid and quarter heights confirmed the deflected shape as half sine wave of the order of the effective column length.

- Slender columns buckled without material failure and regained their straight configuration on unloading establishing that global buckling occurred in the elastic range of material. Specimens retained there stiffness after failure whilst the lateral deflections increased continuously without further increase in applied load. However, the columns unloaded after lateral deflection reached 1% of the GRP length, to avoid material damage. The stress-strain plots

confirm the linear elastic buckling of the slender columns. The Southwell method adequately predicted the Euler buckling load for slender columns.

- Short 51mm box-section columns failed by tearing of the joints and breaking of webs. Deformed geometries indicated that local buckling was initiated initially at mid height followed by excessive deformations leading to a catastrophic tearing failure of the specimen. The phenomenon has been reported previously in the literature and is dependent on the ratio of web thickness to its width. The failure loads for the short specimens range from 110 to 123kN with a difference of -8.2 to +2.1% from the implied P_L whilst these loads are nearly half of the crushing strength (242kN) of this section. However, experimental loads are comparable to the analytical predictions (126kN) calculated using EDC design equation (taking safety factor 1 for comparison). Closed form expressions using linear elastic theory predict a range of critical buckling loads from 80.3 to 252kN for simply supported and fixed long edges. Experimental loads fall with in this range, establishing intermediate torsional stiffness of interface between elastic and fully rigid for the pultruded profiles. It further demonstrates that EDC equation accounts for the interface stiffness. Experimental failure loads for short column further demonstrate that P_L is independent of the column heights in the short range.

- Short 44mm box-section columns did not exhibited local buckling or tearing of the webs, but failed by material crushing at the ends. Stress-strain plots confirmed that material behaved linearly prior to the failure followed by nonlinearity at failure. The failure loads for these specimens range from 202 to 226kN with a difference of -8.1 to 2.9% from the implied P_L of 220kN. However, the ultimate failure loads are nearly half (44 to 49%) of the crushing strength of the material (461kN).

- Mode interaction has been observed in the box columns of intermediate heights of both the sections. The 750mm high 51mm box-section columns initially exhibited global buckling with lateral deflections at mid-height, but later failed by tearing of material under local compression on the concave side, demonstrating interaction of global and local modes exhibited by the slender and short columns of 51mm box-sections. Similarly 500mm high 44mm box-section columns initially developed global buckling, but later failed by

material degradation at the ends, establishing interaction of the two modes exhibited by slender and short 44mm box-section columns.

- The loss in the buckling resistance is minimal (≤ 10.0%) for smaller circular holes ($d/w \leq 0.3$), provided the interval between holes is not less than 20 times the diameter of the holes. For bigger holes ($d/w = 0.7$) and an inter hole spacing of 10 times the diameter, a loss of 30% have been measured.

6.2.3 NUMERICAL INVESTIGATIONS

Ultimate loads and failure modes for the columns of two box-section profiles have been predicted numerically using the finite element method (FEA). The method comprises the formation of models simulating the columns physically tested in the experimental study, and analysing them under the action of applied loads and boundary conditions. Both linear and nonlinear analyses have been included to establish the effects of geometrical and material nonlinearities on the failure modes. Physical imperfections affecting the ultimate loads e.g., variations in the outer and cross-sectional dimensions, out-of-straightness and eccentric loading have been considered. Assumed initial mid-height curvatures (percentage of GRP heights) have been included into the models of imperfect columns to account for these imperfections. The fully nonlinear numerical results for imperfect columns (minimum load capabilities) have been used to derive a design curve with an appropriate value of interaction coefficient accounting for the loss of stiffness in the composite columns due to mode interaction and physical imperfections. Separate models of the columns having circular holes of different sizes in the walls have been prepared and analysed for ultimate failure loads. The main outcomes of the numerical investigations are:

- 3-Dimensional volume elements with three translational degrees of freedom have been successfully used to model the orthotropic composite walls of the square cross-sections and the isotropic steel plates at the column ends. All the models are simply supported (knife edges) and axially loaded (along the middle line of the plate).
- Linear elastic (eigenvalue buckling) analyses adequately predicted the buckling loads of slender columns. The failure modes, in the form of a half sine wave of the order of effective column heights, exhibited by the linear analyses confirmed the global buckling in slender columns. The range of the

column heights for which the linear analysis exhibited global buckling, has been categorised as the slender columns. Column heights of 655mm and above in the case of 51mm square box-section and 555mm and above in the case of 44mm box-sections have been grouped as slender columns, and short otherwise.

Buckling loads and the global modes predicted using linear elastic analyses, confirm that global buckling of composite columns occurs due to bifurcation at the critical loads, and can be solved by linear elastic theory (eigenvalues). The predicted loads are close to the Euler buckling and experimental loads, establishing that not only the physical imperfections in the composite columns are small, but also the deformations (axial and lateral deflections) are small at critical loads, and the columns behave linearly. Furthermore, stress contours drawn along the length of the columns, confirm that the stresses at critical loads are within the elastic limits of the material.

However, in the case of shorter columns, the linear elastic solutions failed to converge without indicating buckling modes. Only axial shortening and volumetric strains are exhibited. This suggests that buckling modes other than global buckling or material failure occurs beyond the elastic limit of the analysis.

- Geometrically nonlinear analyses predicted the local buckling modes in short 51mm box-section columns. The number of half sine waves depends upon the GRP column height. The FE solution for the shortest column having a GRP height of 200mm failed to converge, exhibiting three half sine waves. The failure load predicted by the non-converged solution, more than twice the experimental load, is incorrect. It is concluded therefore that FE solutions which fail to converge are not reliable. It also supports the observation made by Mottram (2000) that for measuring the short column load the minimum height of the column should be long enough to accommodate at least four half sine waves. The stress contours plotted along the column heights show that although the stress concentrations at the peaks of the initiated buckled waves, is less than the elastic limit, stresses immediately after the onset of local buckling increase abruptly and exceed the elastic limits (causing rupture of

material). The need for a fully nonlinear analysis including the material nonlinearity is implied by these results.

No local buckling has been predicted in the short 44mm box-sections models whilst the geometrically non-linear solutions failed to converge, giving unreliable failure loads. Stress contours indicate a uniform stress distribution along the entire height indicating only axial and no lateral stresses. The absence of the local buckling has been attributed to low b/t and the strong interface restricting the local deformations.

For slender columns, the geometrically nonlinear analyses failed to exhibit the expected failure modes i.e., global buckling in perfect columns. It infers that nonlinear solutions for the slender columns converge (maintaining equilibrium) beyond the bifurcation point, if no disturbance or imperfections enhance the lateral deformation. Inclusion of initial curvatures in the nonlinear analyses, confirmed global buckling mode in slender columns.

- Fully nonlinear (geometrically and materially) analyses have been used to provide buckling solutions to perfect and imperfect composite columns. For perfect columns, the results (failure loads and modes) are similar to the geometrically nonlinear findings i.e., global buckling not indicated in the slender columns whilst local buckling exhibited in the short 51mm columns. For shorter column heights (200 and 300mm GRP) the solutions failed to converge giving incorrect and unreliable loads. The converged solutions for the short and slender columns are higher than the experimental results.

  Imperfections in the form of assumed initial curvatures has been introduced to simulate the numerical models with the real (tested in Chapter 4) columns. The converged solutions of imperfect columns exhibited representative buckling modes and the predicted loads which are closer to the experimental results. Imperfect nonlinear solutions have confirmed slender heights of 655mm and above for 51mm and 555mm and above for 44mm box-sections.

- Fully nonlinear solutions for short 51mm box-section imperfect columns, 400-500mm GRP heights (converged solutions), established that the maximum short column load remains constant for a range of short column heights exhibiting four or more half sine waves in the buckled shape. This maximum

short column load is taken to be the P_L. It is shown that the P_L is sensitive to geometric imperfections. Furthermore, the length of half sine wave remained constant at 62.5mm irrespective of the column height between 400 and 500mm. These important conclusions are in line with the previous findings of studies on pultruded columns reported in the literature (Mottram 2000, Barbero and Turk 2000). No local buckling has been predicted in the 44mm box-section short columns inferring material (crushing) failure. Experimental observations confirmed material failure of the short 44mm box-section columns.

- A general rule for applying FE analyses for the prediction of ultimate (design) loads has been outlined. Initially, a linear elastic analysis should be performed indicating the buckling mode and behaviour (deformed shape) of the model. If the solution converges and a definite buckling mode is exhibited, the failure load is taken as the buckling load for the column. If the linear solution fails to converge exhibiting local web buckling with underdeveloped or fewer than four sine waves, a nonlinear solution procedure is recommended as follows. An imperfection of reasonable amplitude i.e., 0.5 to 1% should be included to specify an imperfect column and a geometrically nonlinear analysis should be performed. If the predicted stresses are less than the ultimate strength of the material, then the load can be the failure load. Conversely, if the predicted stresses are higher than ultimate strength of the material, a full nonlinear (Hoffman failure criterion) analysis should be performed.

- The results from the fully nonlinear FE analyses clearly demonstrate that failure loads depends upon the column height (L_{eff}), longitudinal stiffness $E_{L,c}$, load eccentricity and initial curvature. Of these, the first two parameters are included in establishing column slenderness ratio 'λ', and the imperfections are accounted for by the interaction coefficient 'c'. Whilst, the numerical solutions predicted only two isolated buckling modes, global and local, exhibited by the slender and short columns, the predicted loads for the intermediate column heights (λ=0.5-1.5) are lower than theoretical loads for isolated modes. This loss of buckling resistance has been attributed to the mode interaction (not indicated by the deformed shapes) and is represented by interactions coefficient 'c'. The interaction coefficient is established by

plotting numerical data, for certain imperfection amplitude, normalised by the P_E and P_L, into interaction plots and best fitted with the empirical interaction curves. The value of 'c' also accounts for the effects of slenderness because all the data for various slenderness values is represented by a single value of 'c' corresponding to a given imperfection amplitude.

- A numerical design curve has been developed using failure loads predicted from fully nonlinear analyses of the imperfect columns. A single curve represents short and slender columns depending on the slenderness ratio. The values of c for 0.5% imperfection are $c = 0.95$ for both the box-sections. For the imperfection amplitude of 1.0% of column height, 'c' values have been estimated as 0.85 and 0.9 for 51mm and 44mm box-sections respectively. The proposed design curve has been verified by including experimental results located above the curve.

- Perforations (holes) reduce the buckling resistance of the slender columns, but the loss is minimal ($\leq 5\%$) provided the size of the holes is small ($d/w \leq 0.3$) and interval between the holes not less than twenty times the diameter of the holes. Buckling stiffness is further reduced by increasing the holes size and reducing the interval between the holes. It is recommended to limit the holes size to $d/w = 0.6$.

6.3 SUGGESTIOS FOR FUTURE WORK

The following recommendations for the future work, based on the experimental and numerical result, are suggested:

- Standard pultruded box-sections with larger dimensions should be investigated for the ultimate loads and column behaviour using the fully non-linear imperfect numerical models proposed in this study.

- Numerical simulation can predict the critical height of the box-section columns exhibiting maximum loss of stiffness due to mode interaction. Additional specimens in the range of $\lambda = 0.5$ to 1.5 should be tested experimentally to achieve a fully representative value of interaction coefficient 'c'.

- Influences of various parameters on c should be investigated.

- Consider new definitions for slenderness ratio λ, which correspond to observed mode of failure.
- Buckling or failure capacities of the pultruded sections verses the ultimate material strengths should be investigated.
- Present study considered mainly simply supported boundary conditions in the experimental and numerical investigations. Other types of supports (e.g., fixed-fixed) should be included to simulate the columns behaviour in non-idealised structural scenarios.

REFERENCES

ABAQUS (1998), Hibbitt, Karlsson and Sorensen, Inc., User's Manual.

Abdallah, M. G. and Gsacoigne, H. F. (1989), "The influence of Test Fixture Design on the Iosipescu Shear Test for Fibre Composite materials", ASTM STP 1003, C. C. Chamis (Ed), American Society for Testing and Materials, Philadelphia, PA. Pp. 231

Adams, D. F. and Walrath, D.E. (1987), "Further Development of the Iosipescu Shear Test Method", *Experimental Mechanics*, Vol. 27, No. 2, Pp. 113-199.

Akasaka, T. (1974), "Practical Methods of Evaluating the Isotropic Elastic constants of Glass Mat Reinforced Plastic", *Composite Material Structures*, (Japan), 3, 21, in Mechanics of Composite materials, R. M. Jones (Ed), Hemisphere Publishing Corporation, New York.

Arcan, M., Hashin, Z. and Voloshin, A. (1978), "A method to Produce Uniform Plane-Stress States with Applications to Fibre-Reinforced Materials." *Experimental Mechanics*, Vol. 8, No. 4, Pp. 141-146.

Arcan, M. (1984), "The Iosipescu Shear Test as Applied to Composite Materials—Discussion," *Experimental Mechanics*, Vol. 24, No. 1, Pp. 66-67.

Ballinger, C. A. (1990), "Structural FRP Composites," *Civil Engineering*, ASCE, Vol. 6, No. 7, Pp. 63-65.

Ballinger, C. A. (1991), "Development of Composites for Civil Engineering", *Proceedings of Speciality Conference on Advanced Composite Materials in Civil Engineering*, Las Vegas.

Banks, W. M., and Rhodes, J., (1983), "The Instability of Composite Sections", *2nd Int. Conference on Composite Structures*, Paisley, UK, Elsevier, 442-452.

Bank, L. C. (1987), "Shear Coefficients for Thin-Walled Composite Beams", *Composite Structures*, Vol. 8, No.1, Pp. 47-61.

Bank, L. C. (1989), "Properties of Pultruded Fibre Reinforced Plastic Structural Members", *Transportation Research Record 1223, Transportation Research Board, Washington D.C.*, Pp. 117-124.

Bank, L. C. (1989a), "Flexural and Shear Moduli of Full-Section Fibre-Reinforced Plastic (FPR) Pultruded Beams", *Journal of Testing and Evaluation*, Vol. 17, No. 1, Pp. 40-45.

Bank, L. C. (1990), "Shear properties of Pultruded Glass FRP Materials", *Journal of Materials in Civil Engineering*, ASCE, Vol. 2, No. 2, Pp. 118-122.

Bank, L. C., Nadipelli, M., and Gentry, T. R. (1993), "Local Buckling and failure of Pultruded Fiber-Reinforced Beams", *American Society of Mechanical Engineers*, Material Division (Publication) MD, Vol. 46, Pp. 499-519.

Bank, L. C., Nadipelli, M., Gentry, T.R. and Yin, J. (1994), "Local Buckling of Pultruded FRP Beams: Theory and Experiment", *ASCE Proceedings of Structural Congress*, Apr 24-28, Atlanta, Georgia, USA, N. C. Baker and B. J. Loodno (Eds), ASCE, New York, Pp. 417-422.

Bank, L. C., Nadipelli, M. and Gentry, T. R. (1994a), "Local Buckling and Failure of Pultruded Fiber-Rrinforced Plastic Beams", *Journal of Engineering Materials and Technology, Transactions of The ASME*, Vol. 116, No. 2, Pp. 233-237.

Bank, L. C., Yin, J. and Nadipelli, M. (1995), "Local Buckling of Pultruded Beams – Nonlinearity Anisotropy and Inhomogeneity", *Construction and Buildnding Materials*, Vol. 9, No. 6, Pp. 325-331.

Bank, L. C., Gentry, T. R. and Nadipelli, M. (1996), "Local Buckling of Pultruded FRP Beams—Analysis and Design", *Journal of Reinforced Plastics And Composites*, Vol. 15, Pp. 283-294.

Bank, L. C. and Yin, J. (1996), "Buckling of Orthotropic Plates with Free and Rotationally Restrained Unloaded Edges", *Thin-Walled Structures*, Vol. 24, Pp. 83-96.

Bank, L. C. and Yin, J. (1999), "Failure of Web-Flange Junction in Postbuckled Pultruded I-Beams", *Journal of Composites for Construction*, Vol. 3, No. 4, Pp. 177-184.

Barbero, E. J. and Fu, S. H. (1990), "Local Buckling as Failure Initiation in Pultruded Composite Beams", *Impact and Buckling of Structures*, D. Hui (Ed), ASME AD-Vol. 20, AMD-Vol. 114, pp. 41-45.

Barbero, E. J. and Raftoyiannis, I. (1990), "Buckling Analysis of Pultruded Composite Column", *Impact and Buckling of Structures*, D. Hui (Ed), ASME AD-Vol. 20, AMD-Vol. 114, pp. 47-52.

Barbero, E. J. (1991), "Pultruded Structural Shapes—From the Constituent to the Structural Behaviour", *SAMPE Journal*, Vol. 27, No. 10, Pp. 25-30.

Barbero, E. and GangaRao, H. V. S. (1991), "Structural Applications of Composites in Infrastructure", Part 1. *SAMPE Journal*, Vol. 27, No. 6, Pp. 9-16.

Barbero, E. J. and Sonti, S. S. (1991), "Micro Mechanical Models for Pultruded Composite Beams", *32nd SDM Conference*, April 8-10, Baltimore, MD.

Barbero, E. J. and Tomblin, J. (1992), "Buckling Testing of Composite Columns", *AIAA Journal*, Vol. 30, No. 11, Pp. 2798-2800.

Barbero, E. J. and Raftoyiannis, I. G. (1993), "Euler Buckling of Pultruded Composite Columns", *Composite Structures*, Vol. 24, No. 2, Pp. 139-147.

Barbero, E. J., Raftoyiannis, I. G. and Godoy, L. A., (1993), "Mode Interaction in FRP columns," *Mechanics of Composite Materials: Non-Linear Effects*, M. H. Hyer (Ed), AMD, Vol. 159, NewYork, American Society of Mechanical Engineers, Pp. 9-18.

Barbero, E. J., Lopez-Anido, R. and Davalos, J. F. (1993), "On the Mechanics of Thin-Walled Laminated Composite Beams", *Journal of Composite Materials*, Vol. 27, Pp. 806-829.

Barbero, E. J. and Tomblin, J. (1994), "A Phenomenological Design Equation for FRP Columns with Interaction Between Local and Global Buckling", *Thin-Walled Structures*, Vol. 18, Pp. 117-131.

Barbero, E. J., Raftoyiannis, I. G. and Godoy, L. A. (1995), "Finite Element for Post-Buckling Analysis. II—Application to Composite Plate Assemblies", *Composites and Structures*, Vol. 56, No. 6, Pp. 1019-1028.

Barbero, E. J., Godoy, L. A., and Raftoyiannis, I. (1996), "Finite Elements for Three-Mode Interaction in Buckling Analysis", *International Journal of Numerical Methods in Engineering*, Vol. 39, Pp, 469-488.

Barbero, E. J. and Tomblin, J. (1996), "A Damage Mechanics Model for Compression Strength of Composites", *International journal of Solids and Structures*, Vol. 33, No. 29, 1996, Pp. 4379-4393.

Barbero, E. J. and Evans, D. (1997), "Guidelines for Design of FRP Columns", *Structures Congress Proceedings*, ASCE, Portland USA, Vol. 2, Pp. 1484-1488.

Barbero, E. J. and Trovillion, J. (1998), "Prediction and Measurement of the Post-Critical Behaviour of Fibre-Reinforced Composite Column", *Composite Science and Technology*, Vol. 58, No. 8, pp. 1335-1341.

Barbero, E. J. (1998), "Prediction of Compression Strength of Unidirectional Polymer Matrix Composites", *Journal of Composite Materials*, Vol. 32, No. 5, 483-502.

Barbero, E. J. (1999), *Introduction to Composite Material Design*, Taylor and Francis, Philadelphia, PA.

Barbero, E. J. and DeVivo, L. (1999), "Beam-Column Design Equations for Wide-Flange Pultruded Structural Shapes", *Journal of Composites for Construction*, Vol. 4, No. 4, Pp. 185-191.

Barbero, E. J. (2000), "Prediction of Buckling-Mode interaction in Composite Columns", *Mechanics of Composite Materials and Structures*, Vol. 7, Pp 269-284.

Barbero, E. J. and Turk, M. (2000), "Experimental Investigation of Beam-Column Behaviour of Pultruded Structural Shapes", *Journal of Reinforced Plastics and Composites*, Vol. 19, No. 3, Pp. 249-265.

Barbero, E. J., Dede, E. and Jones, S. (2000), "Experimental Validation of Buckling Mode Interaction in Intermediate Length Composite Columns", *International Journal of Solids and Structures*, Vol. 37, Pp. 3919-3934.

Barker, A. J., and Balasundarm, V. (1987), "Compression Testing of Carbon Fibre-Reinforced Plastics Exposed to Humid Environments", *Composites*, Vol.18, No. 3, Pp. 217-226.

Bento, R. and Sridharan, S. (1985), "Interactive Buckling Analysis with Finite Strips", *International Journal of Numerical Methods in Engineering*, Vol. 21, Pp. 145-161.

Bento, R. and Sridharan, S. (1985), "Mode Interaction in Thin-Walled Structural Members", *Journal of Structural Mechanics*, ASCE, Vol. 12, Pp. 517-542.

Bodamer, D. (1998), "A Composite Sketch", *Civil Engineering*, January 1988, Pp. 56-59.

Bogner, B. R. (1990), "Isopolyester Pultrusion Resin Study", *Proceedings of SPI Composite Institution*, 45th Annual conference, New York.

Brooks, R. J. and Turvey, G. J. (1995), "Lateral Buckling of Pultruded GRP I-Section Cantilevers", *Composite Structures*, Vol. 32, Pp. 203-215.

Brown, N. D., Mottram, J. T. and Anderson, D. (1998), "The Behaviour of Columns for the Design of Pultruded Frames: Tests on Isolated Columns", *Proceedings of 2nd International Conference on Composites in Infrastructure*, University of Arizona, Vol. 2, Pp. 248-260.

Brunelle, E. J. and Oyibo, G. A. (1983), "Generic Buckling Curves for Specially Orthotropic Plates", *AIAA Journal*, Vol. 21, No. 8, Pp. 1150-1156.

Chen, W. F. and Lui, E. M. (1987), *Structural Stability: Theory and Implementation*. Elsevier, New York.

Chilver, A. H. (1956), "End-Fitting Effects in Strut Tests", *Journal of Royal Aeronautical Society*, Vol. 60, Pp. 175-277.

Chin, C-K., Al-Bermani, F. G. A., and Kitipornchai, S. (1993), "Finite Element Method for Buckling Analysis of Plate Structures", *Journal of Structural Engineering*, ASCE, Vol. 119, No. 4, Pp. 1048-1068.

Clarke, J. L. (Ed) (1996), "*Structural Design of Polymer Composite – EUROCOMP Design code and handbook*", S. & F. N. Spon, London.

Cook, R. D., Malkus, D. S., Plesha, M. E. and Witt, R. J. (2002), *Concepts and Applications of Finite Element Analysis*, Fourth Edition, John Wiley & Sons. Inc, New York.

Crisfield, M. A. (1981), "A Fast Incremental/Iterative Solution Procedure that Handles Snap-Throug", *Computers and Structures*, Vol. 13, Pp. 55-62.

CSA (1994), *Limit States Design of Steel Structures*, CAN/CSA-S16.1-94, Canadian Standards Association, Rexdale Ontarion, Canada.

Datoo, M. H. (1991), *Mechanics of Fibrous Composites*, Elsevier Applied Science, London, New York.

Davalos, J. F., Qiao, P. and Barbero, E. J., (1996), "Multiobjective Material Architecture Optimization of Pultruded FRP I-Beams", *Composite Structures*, Vol. 35, Pp. 271-281.

Davalos, J. F., and Qiao, P. (1997), "Analytical and Experimental Study of Lateral and Distortional Buckling of FRP Wide-Flange Beams", *Journal of Composite for Construction*, Vol. 1, No. 4, Pp. 150-159

Davalos, J. F. and Qiao, P. (1998), "Engineering Design Analysis Equations for Local Buckling of FRP Structural Shapes", *2nd Int. Conference On composites in Infrastructure*, Vol. 2, 248-260, Tucson, AZ.

Dickson, T. and Munro, N. (1995), "Selection of an In-Plane Shear Test Method Based on the Shear Sensitivity of Laminate Tensile Modulus", *Composites*, Vol. 26, No. 1, Pp. 17-24.

ECS (1992), *Eurocode 3: Design of Steel Structures*, European Committee for Standardisation, Brussels, Belgium.

Engesser, F. (1889), "Die Kinckfestigkeit Gerader Stabe", *Zeitschrift Fur Architekter und Ingenieur Vereins zu Hannover*, Weisbaden, Germany, Vol.35 455 (in German).

Euler, L. (1744), "*De curvis elastics*," Lausanne and Geneva, pp. 267-268. (Leonhard Euler's Elastic Curves, translated and annotated by W. A. Oldfather, C. A. Ellis, and D.M. Brown, reprinted from Isis, Vol. 20, No. 58, 1933, The St. Catherine Press, Bruges, Belgium).

Euler, L., (1759), "Sur La Force de Colonnes," *Memoires de L'Accademie* de Berlin.

EXTREN Fibre-Glass Structural Shapes Design Manual, (1989), Strongwell, Bristol, Virginia.

Faella, C., Mozzolani, F. M. Piluso, V. and Rizzano, G. (2000), "Local Buckling of Aluminium Members: Testing and Classification", *Journal of Structural Engineering*, Vol. 3, Pp. 353-360.

Farshad, M. (1994), *Stability of Structures*, Elsevier, Amsterdam, London, New York.

Fibreforce, (2000), *FIBREFORCE Replacing Metals Where it Matters*, Fibreforce Composites Limited, Runcorn, Cheshire, UK, (http://www.fibreforce.u-net.com).

Foster, D. C., Richards, D. and Bonger, B. R. (2000), "Design and Installation of Fiber-Reinforced Polymer Composite Bridge", *Journal of Composite for Construction*, ASCE, Vol. 4, No. 1, Pp. 33-37.

Fukumoto, Y. and Kubo, M. (1982), "Buckling in Steel U-Shaped Beams", *Journal of Structural Division*, ASCE, Vol. 108 (ST5), Pp. 1174-1190

Galambos, V. G. (1998), *Guide to Stability Design Criteria for Metal Structures*, Fifth Edition, John Wiley & Sons, New York.

Godoy, L. A., Barbero, E. J. and Raftoyiannis, I. G. (1993), "Finite Elements for Post-Buckling Analysis I—The *W*-Formulation", *Composite and Structures*, Vol. 56, No. 6, Pp. 1009-1017.

Godoy, L. A., Barbero, E. J. and Raftoyiannis, I. G. (1995), "Interactive Buckling Analysis of Fiber-Reinforced Thin-Walled Columns", *Journal of Composite Materials*, Vol. 29, No. 5, Pp. 591-613.

Godoy, L. A. and Croll, J. G. A. (1995), "Energy Contribution in the Buckling of Fiber-Reinforced Thin-Walled Columns", *Stability of Structures*, Vol. 1, S. Rajasekaran and S. Sridharan (Eds), Allied Science Publishers, Bombay, Pp. 209-218.

Godoy, L. A. and Almanzar, L. I. (1996), "Improving Design in Composite Thin-Walled Columns", *Proceedings of the Engineering Mechanics*, ASCE, Vol. 2, Pp. 1155-1158.

Green, A. (1987), "Glass-Fiber-Reinforced Composites in Building Construction", Transportation Research Record 1118, National Research Council, Washington, D.C, Pp. 73-76.

Green, A., Bisarnsin, T. and Love, E.A. (1994), "Pultruded Reinforced Plastics for Civil Engineering Structural Applications", *Journal of Reinforced Plastics and Composites*, Vol. 13, Pp. 942-951.

Goltermann, P. and Mollmann, H. (1989), "Interactive Buckling in Thin-Walled Beams II- Applications", *International Journal of Solids and Structures*, Vol. 25, Pp. 729-749

Haaijer, Geerhard. (1959), "Plate Buckling in the Strain-Hardening Range", *Paper No.2968, Transactions of American Society of Civil Engineers*, Vol. 124, Pp. 117-148.

Haeberle, J. and Matthews, F. L. (1990), "Studies on Compressive Failure in Unidirectional CFRP Using an Improved Test Method", *Proceedings of ECCM-4, European association for Composite Materials*, Elsevier, London, England, Pp. 517-523.

Haj-Ali, R. and Kilic, H. (2002), "Nonlinear Behaviour of Pultruded FRP composite", *Composites*, Part B, Vol. 33, No. 3, Pp. 173-179.

Hashem, Z. A. (1993), "Structural Behaviour of Plastic Composite Columns", *PhD dissertation, University of Texas at Arlington, Texas.*

Herakovich, C. T. and Bergner Jr, H. W. (1980), "Finite Element Stress Analysis of a Notched Coupon Specimen for In-Plane Shear Behaviour of Composites", *Composites*, Pp. 149-154.

Hewson, P. J. (1978), "Buckling of Pultruded Glass Fibre-Reinforced Channel Sections", *Composites*, Vol. 9, No. 17, Pp. 56-60.

Holston, A. Jr. (1970), "Buckling of Orthotropic Plates with One-Free Edge", *AIAA Journal*, Vol. 8, No. 7, Pp. 1352-1354.

Iosipesscu, N. (1967), "New Accurate Procedure for Single Shear Testing of Metals", *Journal of Materials*, Vol. 2, No. 3, Pp. 537-566.

Johnson, A. F. (1985), "Simplified Buckling Analysis for R.P Beams and Columns", *1st European Conference on Composite Materials*. Pp. 541-549.

Johnston, B. G. (1983), "Column Buckling Theory: Historic Highlights", ACSE Journal of Structural Engineering, Vol. 109, No. 9, Pp. 2086-2096.

Jones, R. M. (1975), *Mechanics of Composite Materials*, Hamisphere Publishing, New York.

Kato, B., (1982), "Cold formed Welded Steel Tubular Members", *Axially Compressed Structures*, R. Narayanan, ed., Applied Science Publishers, London, 149-180.

Kennedy, J. B. and Neville, A. M. (1976), *Basic Statistical Methods for Engineers and Scientists*, Harper & Row, New York, London.

Key, P. W., Hasan, S. W. and Hancock, G. J. (1988), "Column Behaviour of Cold-Formed Hollow Sections", *Journal of Structural Engineering*, ASCE, Vol. 114, No. 2, Pp. 390-407

Lee, D. J. and Hewson, P. J. (1979), "The Use of Fibre-Reinforced Plastic in Thin-Walled Structures", *In Stability Problems in Engineering Structures and Components*, T.H. Richards and P. Stanley (Ed), Applied Science Publishers, London, 23-55.

Lee, S. and Munro, M. (1986), "Evaluation of In-Plane Shear Test Methods for Advanced Composite Materials by the Decision Analysis Technique", *Composites*, Vol. 3, No. 1, Pp 13-22.

Lee, S. Munro, M. and Scott, R. F. (1990), "Evaluation of Three In-Plane Shear Test Methods for Advanced Composite Materials", *Composites*, Vol. 21, N0. 6, Pp 495-502.

Leissa, A. W. (1983), "Buckling of Composite Plates", *Composite Structures*, Vol. 1, Pp. 51-66.

Liskey, K. A. (1985), "Pultruded Fibreglass-Reinforced Plastics (FRP): a Structural Solution for Corrosive Environment", *Chemical Engineering*, Vol. 92, Part. 23, 221-224.

Liskey, K. A. (1991), "Structural Applications of Pultruded Composite Products", *Proceedings of Speciality Conference on advanced Composite Material in Civil Engineering*, ASCE, New York, Pp. 182-193.

Liu, K. and Piggot, M. R. (1995), "Shear Strength of Polymers and Fibre Composites: 1. Thermoplastics and Thermoset Polymers", *Composites*, Vol. 26, Pp. 829-840.

Liu, K. and Piggot, M. R. (1995), "Shear Strength of Polymers and Fibre Composites: 2. Carbon/Epoxy Pultrusions", *Composites*, Vol. 26, Pp. 841-848.

Lopez-Anido, R., Davalos, J. F. and Barbero, E.J. (1995), "Experimental Evaluation of Stiffness of Laminated composite Beam Element under Flexure", *Journal of Reinforced Plastics and Composites*, Vol. 14, No. 4, Pp. 349-361.

Luciano, R. and Barbero, E. J. (1994), "Formulas for the Stiffness of Composites with Periodic Microstructure", *International Journal of Solids and Structures*, Vol. 31, No. 21, Pp. 2933-2944.

Lusas Theory Manual (2001), *LUSAS Finite Element System*, FEA Ltd, Surrey UK, (www. feauk.co.uk).

Martin, J. D. and Sumerak, J. E. (1987), *Pultrusion in Composites*, Dostal, C.A. et al (Eds), Engineering Materials Handbook, Vol. 1, ASM International, Pp. 533-543.

Measurement Group (1990), *Strain Gage Rosettes-Selection, Application data Reduction,* Measurement Group UK Ltd, Technical Note (TN-515), Basingstoke, Hants, Uk.

Miller, D. M. (1987), *Glass Fibers in Composites*,. Dostal, C.A. et al (Eds), Engineering Materials Handbook, Vol. 1, ASM International, Pp. 45-48.

Morton, J., Ho, H., Tsai, M. Y. and Farley, G. L. (1992), "An Evaluation of the Iosipescu Specimen for Composite Material Shear Property Measurement", *Journal of Composite Materials*, Vol. 26, No. 5, Pp. 708.

Mottram, J. T. (1991), "Structural Properties of a Pultruded E-Glass Fiber-Reinforced Polymeric I-Beam", *Composite Structures, 6th International Conference on Composite Structures*, Elsevier Applied Science, London, Pp. 1-28.

Mottram, J. T. (1991a), "Evaluation of Design Analysis for Pultruded Fibre-Reinforced Polymeric Box Beams", *Structural Engineer*, Vol. 69, No. 11/4, Pp. 211-220.

Mottram, J. T. (1992), "Lateral-Torsional Buckling of a Pultruded I-Beam", *Composites*, Vol. 23, No. 2, Pp. 81-92.

Mottram, J. T. (1994), "Compression Strength of Pultruded Flat Sheet Material", *Journal of Materials in Civil Engineering*, Vol. 6, No. 2, Pp. 185-200.

Mottram, J. T. (1996), "Closure by J. T. Mottram", *Journal of Material in Civil Engineering*,

Mottram, J.T. (1999), Personal communication with the Author.

Mottram, J. T. (2000), "Review of Beam Column Design Equation for Wide-Flange Pultruded Sturctural Shapes". Research Report CE65. University of Warwick, Coventry, UK.

Mottram, J. T., Brown, N. D. and Anderson, D. (2003), "Physical Testing For Concentrically Loaded Columns of Pultruded Wide-Flange Profile." *Proceedings of the Institution of Civil Engineers, Structures & Buildings*, Vol. 156, No. 2, Pp. 205-219.

Nagaraj, V. and GangaRao, H. V. S. (1997), "Static Behaviour of Pultruded GFRP Beams" *Journal of Composites for Construction*, ASCE, Vol. 1, Pp. 120-129.

Naughton, B. P., Panhuizen, F. and Venmeulen, A. C. (1985), "The Elastic Properties of Chopped Strand Mat and Woven Roving in GRP Laminae", Journal of Reinforced Plastics and Composites, Vol. 4

Palmer, D. W., Bank, L. C. and Gentry, T. R. (1998), "Progressive Tearing Failure of Pultruded Composite Box Beams: Experiment and Simulation", *Composite Science and Technology*, Vol. 58, 1353-1359.

Pecce, M., Lazzaro, F. and Cosenza, E. (1998), "Local Buckling of FRP Profiles: Experimental Results and Numerical Analysis", *European Conference on Composite Materials* ECCM-8, 331-338, Napoli, Italy.

Qiao, P. (1997), "Analysis and Design Optimization of Fibre-Reinforced Plastics (FRP) Structural Beams", *Ph.D Dissertation*, West Virginia University, Morgantown , West Virginia.

Qiao, P., Davalos, J. F. and Barbero, E. J. (1998), "Design Optimization of Fibre Reinforced Plastic Composite Shapes", *Journal of Composite Material*, Vol. 32, No. 2, Pp. 177-196.

Qiao, P., Davalos, J. F. and Wang, J. (2001), "Local Buckling of Composite FRP Shapes by Discrete Plate Analysis", *Journal of Structural Engineering*, ASCE, Vol. 127, No. 3, Pp. 245-255.

Raftoyiannis, I. G. (1991), "Buckling of Pultruded Composite Columns", *MSC Thesis*, West Virginia University, Morgantown, M.V.

Raftoyiannis, I. G. (1994), "Buckling Mode Interaction in FRP Columns", *Ph.D Dissertation,* West Virginia University, Morgantown, M.V

Raftoyiannis, I., Godoy, L. A. and Barbero, E. J. (1995), "Buckling Mode Interaction in Composite Plate Assemblies", *Applied Mechanics Reviews*, Vol. 48, (11. Part 2), 52-60.

Rasmussen, K. J. R. and Rondal, J. (1997), "Strength Curves For Metal Columns", *Journal of Structural Engineering*, ASCE, Vol. 123, No. 6, Pp. 721-728.

Riks, E. (1979), "An Incremental Approach to the Solution of Snapping and Buckling Problems", International journal of Solids and Structures, Vol. 15, No. 7-B, Pp. 529-551.

Robbins, J. (1992), "Links to a Tee" in Bridges, *New Civil Engineer*, 13 August 1992, Pp. 20-23.

Salim, H. A., Davalos, J. F., Barbero, E. J., Lopez-Anido, A. and Qiao, P. (1995), "Design of FRP Shapes for Civil Structures", *Proceedings of Engineering Mechanics,* Vol. 1, Pp. 405-408.

Saribiyik, M. (2000), "Analysis of a Bonded Connector for Pultruded GRP Structural Elements", *Ph.D thesis*, University of Newcastle upon Tyne, UK.

Scott, D., Yoon, S. J. and Zureick, A. (1992), "Full Scale Test on Concentrically Loaded Fibre Reinforced Pultruded Columns", *Proc of Material Engineering Congress*, ASCE, New York., Pp. 572-576.

Scott, D. W. and Zureick, A. H. (1998), "Compression Creep of A Pultruded E-Glass/ Vinylester Composite", *Composites Science and Technology*, Vol. 58, Pp. 1361-1369.

Singer, J., Arbocz, J. and Weller, T. (1998), *Buckling Experiments: Experimental Methods in Buckling of Thin-Walled Structures*. John Wiley & Sons, New York.

Slepetz, J. M., Zagaeski, T. F. and Novello, R. F. (1978), "In-Plane Shear Test for Composite materials", Report No. AMMRC TR 78-30, *Army Material and Mechanics Research Center,* Watertown, MA.

Sonti, S. S. and Barbero, E. J. (1995). "Determination of Shear Properties for FR Pultruded Composites", *Journal of Reinforced Plastics and Composites*, Vol. 14, Pp. 390-401.

Speier, E. E. (1980). "On Experimental Versus Theoretical Incipient Buckling of Narrow Graphite/Epoxy Plates in Compression," American Institute of Aviation and Aeronautics, May, Pp. 187-193.

Spigel, B. S., Parbhakaran, R. and Sawyer, J.W. (1987). "An investigation of the Iosipescu and Asymmetrical Four-Point Bend Test", Experimental Mechanics, vol. 27, No. 1, Pp. 57-63.

Sridharan, S., and Ali, A., (1986), "An Improved Interactive Buckling Analysis of Thin-Walled Columns Having Doubly Symmetric Cross-Sections," *International Solids and Structures*, Vol. 22, No. 4, Pp. 429-443.

Southwell, R. V. (1932). "On the Analysis of Experimental Observations in Problems of Elastic Stability," *Proceedings of the Royal Society of London*, Series A, Vol. 135, Pp. 601-616.

Starr, T. F. (1983). "Structural Application for Pultruded Profiles" *Composite Structures*, Vol. 2, Pp. 192-213.

Strongwell Design Manual. (1998). Strongwell, Bristol, Va.

Structural Plastic Design manual, (1984). American Society of Civil Engineers, Manual and Reports on Engineering Practice, No. 63, ASCE, New York.

Timoshenko, S. P., and Gere, J. M. (1961). *Theory of Elastic Stability*. New York: McGraw-Hill Book Company

Tomblin, J. S. (1991), "A Universal Design Equation for Pultruded Composite Columns" *MSC. Thesis*, Mechanical and Aerospace Engineering, West Virginia University, Morgantown, WV.

Tomblin, J. S., (1994). "Compressive Strength Models for Pultruded Glass Fibre Reinforced Composites", *Ph.D. Dissertation*, West Virginia University, Morgantown, WV.

Tomblin, J. S. and Barbero, E. J. (1994). "Local Buckling Experiments on FRP Columns" *Thin-Walled Structures*, Vol. 18, No. 2, 97-116.

Toneff, J. D., Stiemer, S. F. and Osterrieder, P. (1987). "Local and Overall Buckling in Thin-Walled Beams and Columns" *Journal of Structural Engineering*, ASCE, Vol. 113, No. 4, Pp. 769-786.

Tsai, W. T. (1986). "Note on Southwell,s Method for Buckling of Struts," *Journal of Applied Mechanics,* ASME, Vol. 53, Pp. 953-954.

Tsai, S. W. (1989). *Composite Design*, 4th Edition, Think Composites.

Turvey, G. J., (1992). "Tension/Compression Strength of Unnotched/notched Pultruded GRP Plate", *ECCM 1st Testing and Standardisation Conference, European Association for Composite Material*, Elsevier, London, England, Pp. 167-176.

Turvey, G. J. (2000). "Bolted Connections in PFRP Structures", *Structural Engineering Materials*, Vol. 2, Pp. 146-156.

Usami, T. and Fukumoto, Y. (1982). "Local and Overall Buckling of Welded Box Columns." Journal of the Structural Division, *Proc of the American Society of Civil Engineers*, ASCE, Vol. 8, No. ST3, Pp. 525-542.

Vakiener, A. R., Zureick, A. and Will, K. M. (1991). "Prediction of Local Flange Buckling in Pultruded Shapes by Finite Element Analysis," *Proc of ASCE Speciality Conference on Advanced Composite Material in Civil Engineering*, S. L. Iyer (Ed), Las Vegas, Pp. 302-317.

Walrath, D. E. and Adams, D. F. (1983), "The Iosipescu Shear Test as Applied to Composite Materials", *Experimental Mechanics*, Vol. 23, No.1, Pp. 105-110.

Wang, Y. and Zureick, A. H. (1994), "Compression Creep of a Pultruded E-glass/ Vinylester Composite", *Composite Science and Technology*, Vol. 58, Pp 1361-1369.

Wang, Y. and Zureick, A. H. (1994), "Characterisation of the Longitudinal Tensile Behaviour of Pultruded I-Shape Structural Members Using Coupon Specimens", *Composite Structures*, Vol. 29, Pp. 463-472.

Webber, J. P. H., Holt, P. J. and Lee, D. A. (1985), "Instability of Carbon Fibre Reinforced Flanges of I-Section Beams and Columns", *Composite Structures*, Vol. 4, Pp. 245-265.

Werner, R. I. (1984), "Pultrusion Process Engineering-Where are We Headed", *Proceedings of the 39th Annual Conference, Reinforced Plastic/Composite Institute*, The Society of the Plastic Industry, Pp. 1-8.

Wilson, D. W. and Carlson, L. A. (1997), "Mechanical Property Measurements", in *Composite Engineering Handbook*, Mallic, P. K, (Ed) Marcel Dekker, New York.

Yoon, S. J., Scott, D. and Zureick, A. (1992). "An experimental Investigation of the behaviour of concentrically loaded pultruded columns." *Proc of 1st International Conference on Advanced Composite Materials in Bridges and structures.*, K. W. Neale and P. Labossiere (Eds), Montreal, Canada, Pp. 309-317.

Yoon, S. J. (1993). *Local Buckling of Pultruded I-shape Columns*, Ph.D dissertation, Georgia Institute of Technology, Atlanta.

Yuan, L. R., Hashem, Z., Green, A. and Bisarnsin, T. (1991). "Fiber-Reinforced Plastic Composite Columns" *Advanced Composite Materials in Civil Engineering Structures*, S. L. Iyer, (Ed), ASCE, New York, 205-211.

Zahn, J. J. (1992). "Re-Examination of Ylinen and Other Column Equations," *ASCE, Journal of Structural Engineering*, Vol. 118, No. 10, Pp. 2716-2728.

Zureick, A., Yoon, S. and Scott, D. (1992). "Experimental investigation on concentrically loaded pultruded columns." *Proceedings of the 2nd International Symposium on Textile Composites in building Construction*, P. Hamlin and G. Verchery (Eds), Paris, France, Part 2, Pp. 207-215.

Zureick, A. and Scott, D. (1997). "Short-Term Behaviour and Design of Fiber-Reinforced Polymeric Slender Members under Axial Compression." *Journal of Composites for Construction*, Vol. 1, No. 4, Pp. 140-149.

Zureick, A., Shih, B. (1998). "Local Buckling of Fiber-Reinforced Polymeric Structural Members under Linearly-Varying Edge Loading—Part 1. Theoretical Formulation" *Composite Structures*, Vol. 41, Pp. 79-86.